

Hydraulic modelling of liquid-solid fluidisation in drinking water treatment processes

Kramer, O.J.I.

DOI

[10.4233/uuid:b49b0f3f-3f23-4179-a17e-2a0c754c53a5](https://doi.org/10.4233/uuid:b49b0f3f-3f23-4179-a17e-2a0c754c53a5)

Publication date

2021

Document Version

Final published version

Citation (APA)

Kramer, O. J. I. (2021). *Hydraulic modelling of liquid-solid fluidisation in drinking water treatment processes*. [Dissertation (TU Delft), Delft University of Technology]. <https://doi.org/10.4233/uuid:b49b0f3f-3f23-4179-a17e-2a0c754c53a5>

Important note

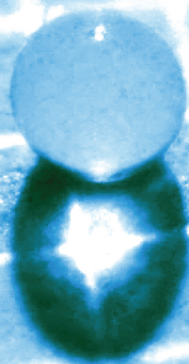
To cite this publication, please use the final published version (if applicable). Please check the document version above.

Copyright


Other than for strictly personal use, it is not permitted to download, forward or distribute the text or part of it, without the consent of the author(s) and/or copyright holder(s), unless the work is under an open content license such as Creative Commons.

Takedown policy

Please contact us and provide details if you believe this document breaches copyrights. We will remove access to the work immediately and investigate your claim.



*“If you don’t look closely,
you will not see it.”*


$$\epsilon = 1.5 \frac{Fr_p^{0.4}}{Re_p^{0.1}}$$

$$Re_p = \frac{\rho_f v_s d_p}{\eta}$$

$$Fr_p = \frac{v_s}{\sqrt{\left(\frac{\rho_p}{\rho_f} - 1\right) g d_p}}$$

Hydraulic modelling of liquid-solid fluidisation in drinking water treatment processes

Onno Kramer

Preface

In drinking water treatment plants, multiphase flows are a frequent phenomenon. Examples of such flows are pellet-softening and filter backwashing where liquid-solid fluidisation is applied. A better grasp of these fluidisation processes is needed to be able to determine optimal hydraulic states. In this research, models were developed, and experiments performed to gain such hydraulic knowledge. As a result, treatment processes can be made more flexible. In a rapidly changing environment, drinking water production must be flexible to ensure robustness and to tackle challenges related to sustainability and long-term changes. In the hydraulic models, the voidage in the fluidised bed and the particle size of the suspended granules are crucial variables. Voidage prediction is challenging as the fluidised bed is a dynamic environment showing highly heterogeneous behaviour that is hard to describe with an effective model. And particle size causes a conundrum due to the irregular shapes of the applied granules. Through the combination of hydraulic dimensionless Reynolds and Froude numbers, an accurate voidage prediction model has now been developed. With a straightforward pseudo-3D image analysis for non-spherical particles measuring particle mass and density, the dimensioned shapes of, for instance, ellipsoids can be determined. Particle shape factors included in models are not constant as is commonly believed, but dynamic. Applying advanced computational fluid dynamics simulations confirmed significant heterogeneous particle-fluid patterns in fluidised beds. Comprehensive sedimentation experiments showed that the average drag coefficient and terminal setting velocity of individual grains can be estimated reasonably well, but with a significant degree of data spread around the mean values. For engineering purposes, this is relevant information which should be taken into consideration. A new soft-sensor was designed to determine the voidage gradient and particle size profile in a fluidised bed. The expansion degree of highly erratic, polydisperse and porous granular activated carbon grains can be predicted with a model, but in full-scale processes the grains are subject to change, and therefore it is most likely that the prediction accuracy will deteriorate rapidly. For reliable drinking water quality, smart models provide solutions to complex challenges, but they are only effective when they are calibrated and validated in advanced pilot plants and are applied in full-scale processes with diligence and commitment on the part of multidisciplinary teams.

Hydraulic modelling of liquid-solid fluidisation in drinking water treatment processes

Proefschrift

ter verkrijging van de graad van doctor aan de Technische Universiteit Delft,
op gezag van de Rector Magnificus, Prof.dr.ir. T.H.J.J. van der Hagen,
voorzitter van het College voor Promoties,
in het openbaar te verdedigen op
10 September 2021 om 10:00 uur

door

Onno Johannes Ignatius KRAMER
Ingenieur in de chemische technologie, Universiteit Twente, Nederland
geboren te Amsterdam, Nederland

Dit proefschrift is goedgekeurd door de promotoren.

Samenstelling promotiecommissie:

Rector magnificus, voorzitter

Prof. dr. ir. J.P. van der Hoek, Technische Universiteit Delft, promotor

Prof. dr. ir. J.T. Padding, Technische Universiteit Delft, promotor

Onafhankelijke leden:

Dr. ir. K.A. Buist, Technische Universiteit Eindhoven

Prof. dr. ir. N.G. Deen, Technische Universiteit Eindhoven

Prof. dr. ir. J.R. van Ommen, Technische Universiteit Delft

Prof. dr. ir. L.C. Rietveld, Technische Universiteit Delft

Overige leden:

Prof. dr. E.S. Boek, Queen Mary University of London, United Kingdom

Reserve lid:

Prof. dr. ir. W.S.J. Uijttewaal, Technische Universiteit Delft

ISBN/EAN: 978-94-6366-436-3

Published by Gildeprint Drukkerijen, Enschede

Copyright © 2021 by O.J.I. Kramer

All rights reserved. No part of the material protected by the copyright may be reproduced or utilised in any form or by any means, electronic or mechanical, including photocopying, recording or by any information storage and retrieval system, without written permission from the copyright owner.

Cover design: K. Dieters

Printed in the Netherlands

An electronic open access version of this document is available in the Delft University Repository at repository.tudelft.nl.

Summary

The starting point of this research ([Chapter 1](#)) was the need to determine the hydraulic states in liquid-solid fluidisation systems, often applied in full-scale drinking water treatment plants. In determining the hydraulic state, the voidage as well as the size of particles in fluidised state play a vital role. In accurate voidage prediction, highly non-spherical particles and unsteady behaviour in the fluidised bed have proven to be complex factors, and recent sustainability-driven changes in the use and re-use of granular materials have shown enormous variety in terms of particle size and shape. Important goals of the current research were the development of hydraulic models that are suitable for drinking water treatment plants and the calibration and validation of these models, based on reliable experimental data obtained in advanced experimental set-ups.

The hydraulic states of flow through a pipe, flow around a fixed object in setting state and flow through a bed of particles, elucidated in [Chapter 2](#) follow similar principles: laminar flow at low fluid velocities, where the drag coefficient is inversely proportional to the Reynolds number, to turbulent flow at high fluid velocities, where the drag coefficient becomes constant. Fluidisation, a phenomenon in which a fluid flows through a bed of solid particles and the bed is converted from a static, solid-like state to a dynamic, fluid-like state, played a vital role in this research. Reasons for applying fluidisation are the enhancement of the mixing properties of fluid and particles as well as the creation of a large surface area per unit volume. Especially for the latter reason, the operational window in many water treatment operations, such as pellet-softening, lie in the vicinity of minimum fluidisation. Particles in the pellet-softening process vary from almost spherical to highly irregularly shaped. Non-sphericity and a high degree of polydispersity makes accurate modelling of voidage particularly complex. Accordingly, in many existing models, spheres are used for the sake of convenience. However, efforts to describe the dimension of a three-dimensional non-spherical particle by one single number, for instance with an equivalent particle diameter, resulted in a conundrum about the appropriate choice of a suitable particle measure in models.

New experimental set-ups were designed at Waternet to obtain reliable expansion data for a myriad of particle types ([Chapter 3](#)). These expansion columns consisted of circuits in which water was pumped in an upward direction through a cylindrical

tube to allow particles to enter a fluidised state. Besides flow, the temperature could also be controlled. The set-up was equipped with differential pressure measurement. In addition, a new experimental set-up was designed for the longitudinal determination of the hydraulic state in a fluidised bed with an immersed object by means of a hydrostatic weighing technique. This soft-sensor was designed to determine the voidage gradient from which the particle size profile could be estimated. Furthermore, an advanced set-up was used at TU Delft to obtain precision terminal settling data through particle path trajectories 3D in a quiescent fluid; this was done with high-speed cameras.

Comprehensive sedimentation experiments, discussed in [Chapter 4](#), showed that the average drag coefficient and terminal setting velocity of individual grains can be estimated reasonably well with a collection of prediction models available in the literature, such as the model proposed by Brown and Lawler. Unfortunately, these models provide little information about the significant degree of data spread around the mean values. A thorough analysis showed that the extent of data spread can be elucidated and that this spread is caused by variations in particle density, path trajectory instabilities and in particular by variations in particle size, shape and orientation. For engineering purposes, this is relevant information which should be taken into consideration.

The terminal settling velocity is an important input parameter in the Richardson–Zaki model, which is still widely used for the voidage prediction in fluidised beds. Nevertheless, the minimum fluidisation velocity is not included in this model, while the voidage is kept relatively low in multiphase drinking water treatment processes to maintain optimal process and control conditions. As a consequence, the Richardson–Zaki model tends to overestimate the minimum fluidisation velocity and results in less accurate predictions with respect to voidage values. The Richardson–Zaki model was subsequently enhanced with proven hydraulics-based models, such as the model proposed by Carman. This significantly improved voidage prediction accuracy as discussed in [Chapter 5](#).

[Chapter 6](#) addressed the fact that many voidage prediction models are based on a traditional drag relation as a function of the modified particle Reynolds number. Based on accurate experimental data, an apparent and persistent spread as well as deviations in drag were observed, supporting the hypothesis that the effective full-

scale drag in a fluidised bed cannot be assumed to be a function of the Reynolds number only. By adding the densimetric particle Froude number as a third dimension to the traditional 2D plot (drag against Reynolds number), the spread in effective full-scale drag could be visualised and explained by means of a 3D plot. As a result, a new drag relation was developed showing that the degree of overall expansion is not only dependent on the ratio of laminar-turbulent flow, but also on the amount of homogenous versus heterogeneous flow.

With respect to modest superficial fluid velocities, the current literature shows that liquid-solid fluidisation systems are generally considered to be homogeneous. However, during fluidisation experiments with calcite grains, open spaces of water were observed between the fluidised particles, even at relatively low fluid velocities. In addition to this, as discussed in [Chapter 7](#), significant heterogeneous particle-fluid patterns were detected at higher fluid velocities. To obtain information about voids in bulk regions, complementary Computational Fluid Dynamics - Discrete Element Method simulations were performed and found to agree reasonably well with the experimental results for validation. The simulations showed that throughout the range of considered water velocities, heterogeneous behaviour exists and cannot be neglected.

Numerous voidage prediction models are available in the scientific literature ([Chapter 8](#)). Many of these models are based on semi-empirical porous-media-based drag relations such as Ergun or semi-empirical terminal-settling based models such as Richardson–Zaki and fitted for monodisperse, almost perfectly round particles. They are also often implicit. In water treatment processes, granules are *de facto* non-spherical, which means that the voidage prediction in the above-mentioned models is most likely less accurate and hence unsuitable. In order to provide an effective applicable solution, a new explicit data-driven voidage prediction model is proposed based on the dimensionless Reynolds and Froude numbers using non-linear symbolic regression methods. The model was calibrated on accurate data obtained from elaborate pilot plant experiments and can be used for a wide range of particle sizes, fluid velocities and temperatures. The model can therefore be used directly in water treatment processes such as drinking water pellet-softening.

[Chapter 9](#) focuses on fluid flow through a bed of solid particles, an important process that frequently occurs in full-scale water treatment operations. For estimating the

resistance across the bed, the Carman–Kozeny model remains popular. Up-flow filtration experiments showed that the drag coefficient across the bed decreased considerably in the laminar and transition regions. This was most likely caused by particle re-orientation, realignment and positional rearrangement. Based on measurements, it was shown that the shape factor, commonly used to match the predicted drag coefficient with experimentally obtained drag coefficients, is not a constant particle property but is also dependent on the fluid properties viscosity and velocity. A thorough hydraulic analysis showed that up-flow filtration in rapid sand filters, under backwash conditions, caused the particle bed to collapse almost imperceptibly. As a result, it was possible to unravel the successful method using optimisation of the extended terminal sub-fluidisation wash filter backwashing procedure, reducing turbidity peaks with a positive effect on water quality. Furthermore, to investigate the morphological properties and preferred particle orientation, a new straightforward pseudo-3D image analysis was developed for particles with an irregular shape. When the measured mass and density of a particle sample is combined with 2D flatbed scanning, the dimensioned shapes of for instance ellipsoids can be determined. Particle analysis using the 2D scanning technique with pseudo-3D image processing is superior to commonly used 1D sieve analyses.

Granular activated carbon filtration ([Chapter 10](#)) is an important treatment step in full-scale drinking water treatment plants. Periodically, filters have to be rinsed through a backwashing procedure. The prediction of the effective voidage of granular activated carbon grains is exceptionally complex because the grains are highly irregular, non-spherical and polydisperse, and they have internal porous structures. In the literature, hardly any general expansion prediction models are available for these types of carbon grains. Extensive experimental measurements confirmed the high level of complexity with regard to accurate voidage prediction for these types of grains. However, a combination of fluidisation and laboratory experiments, such as wetting degree, density and evaporation measurements, could solve expansion enigmas.

Process control and optimisation of fluidised beds in full-scale pellet-softening reactors is complicated due to a large variation in granule types. A stratified bed consists of highly irregularly shaped crushed calcite grains in the top region of the bed while the larger, more spherical calcite pellets migrate to the lower region of the

bed. To distinguish the gradient for local voidage and particle accretion in a pellet-softening fluidised bed, a movable immersed object with a hydrostatic weighing technique was developed and used as a soft-sensor to determine the hydraulic state gradient (Chapter 11). This hydrometer could be used to measure the buoyant force and, accordingly, to determine the bed voidage. Using a data-driven model, the particle size profile over the height of the whole fluid bed could be predicted. The hydrometer offers possibilities to derive the hydraulic performance of full-scale pellet reactors.

Chapter 12 describes the importance of the research for drinking water production. Drinking water production is of vital importance for public health. Reliable and impeccable drinking water quality can be achieved by means of advanced treatment plants that consist of concatenated unit operations. In many of these unit operations, multiphase flows occur with a variety of irregularly shaped particles. Due to an ongoing change in conditions, requirements and external drivers, such as the need for more sustainable granules, process set-points have to be adjusted on a regular basis. Furthermore, in order to cope not only with short-term but also long-term changes and to ensure robustness, a more flexible design of full-scale installations is needed. Using effective models, the hydraulic states in these treatment processes can be predicted accurately, which enhances the daily operations. Intelligent models can contribute to better water quality, uninterrupted supply, cost efficiency, sustainability and client comfort.

In Chapter 13 the overall conclusions of the research are presented. New insights into hydraulic phenomena were gained and used to develop new effective voidage prediction models. The occurrence of heterogeneous behaviour in liquid-solid fluidised beds was proven both experimentally and numerically. The predictive accuracy of effective voidage models was improved by inclusion of the densimetric particle Froude number. New insights were obtained from precision up-flow filtration experiments. It was found that non-spherical particles tend to reorientate and change their position in the bed, considerably affecting the net available surface for flow-through. With these new insights, it was possible to discover the cause of the success behind the extended terminal sub-fluidisation wash method. For pragmatic applications, using spheres and, more in particular, average sieve diameters in data-driven models might work, but in case of natural granules with an irregular shape, this can only be done if experimental data can be obtained. However, for future-proof

flexible water treatment plants, a next step is needed in the development of hydraulic models that includes the erratic shapes of drinking water-related granules. The transition from garnet sand to re-used calcite in the pellet-softening process illustrated the significant effects of altering particle properties on the bed expansion behaviour and the subsequent need for these advanced models.

Finally, [Chapter 14](#) discusses areas for further exploration. For ongoing research, the operation and performance of the pellet-softening process can be improved when the new hydraulic insights are combined with chemical insights in an advanced process model. For future studies, computational fluid dynamics modelling holds great promise as a useful tool to reveal new insights into water treatment processes, such as the influence of non-spherical particles in multiphase flows. Probably the best academic and applied research results can be obtained when fundamental and experimental efforts are combined and discussed, in particular via education. After all, this is not only what young professionals need, but also what is needed for a sustainable society with access to safe drinking water for all.

Samenvatting

Het uitgangspunt van dit onderzoek ([Hoofdstuk 1](#)) was de noodzaak om de hydraulische condities te kunnen bepalen in vloeistof-vast fluïdisatiesystemen, die vaak worden toegepast in grootschalige drinkwaterzuiveringsinstallaties. Bij het bepalen van de hydraulische condities spelen zowel de porositeit (volumefractie lege ruimte) als de grootte van zwevende korrels in gefluïdiseerde toestand een cruciale rol. Complicerende factoren bij het nauwkeurig voorspellen van de porositeit zijn de niet-ronde deeltjes en onstabiel gedrag in het gefluïdiseerde bed. De transitie van lineaire naar circulaire procesvoering bij de drinkwaterbehandeling heeft geleid tot wijzigingen in het gebruik en hergebruik van granulaire materialen. Het gevolg daarvan is dat de deeltjesgrootte, de verdeling en de vorm van de korrels aanzienlijk kunnen variëren. Een belangrijke doelstelling van dit onderzoek was het ontwikkelen van hydraulische voorspellingsmodellen die kunnen worden gebruikt bij drinkwaterzuiveringsinstallaties. Doordat geavanceerde meetopstellingen zijn ontworpen en nauwkeurige experimenten zijn uitgevoerd, konden de modellen worden gekalibreerd en gevalideerd met de verkregen betrouwbare meetgegevens.

De hydraulische condities van een stroming door een buis, een stroming rond een vast object in sedimentatiestoestand en stroming door een gefluïdiseerd bed van deeltjes worden toegelicht in [Hoofdstuk 2](#). Deze condities volgen vergelijkbare principes: laminaire stroming bij lage vloeistofsnelheden, waarbij de weerstandscoefficiënt omgekeerd evenredig is met het Reynoldskengetal, en turbulente stroming bij hoge vloeistofsnelheden, waarbij de weerstandscoefficiënt constant wordt. Fluïdisatie is een fenomeen waarbij een vloeistof stroomt door een bed van vaste deeltjes en deze deeltjes vanuit een statische, vaste toestand worden gebracht in een dynamische, vloeistofachtige toestand. Vloeistof-vast fluïdisatie speelt een cruciale rol in dit onderzoek. Fluïdisatie wordt toegepast om de menigeenschappen van vloeistof en korrels te verbeteren en om een grote oppervlakte per volume-eenheid te creëren. Vooral vanwege dat tweede gevolg ligt het operationele werkgebied bij veel waterbehandelingsoperaties, zoals bij pelletontharding, in de buurt van het minimale fluïdisatiepunt. De kalkkorrels in de pelletontharding variëren van bijna bolvormig tot zeer onregelmatig gevormde gebroken calcieteeltjes. De hoge mate van niet-rondheid en een hoge mate van polydispersiteit maken nauwkeurige modellering van de porositeit bijzonder complex. Dienovereenkomstig worden in veel bestaande modellen gemakshalve

perfecte ronde bollen gebruikt. Het beschrijven van de afmeting van een driedimensionaal niet-rond *natuurlijk* deeltje met één enkel getal, zoals met een equivalente deeltjesdiameter, leverde echter een raadsel op over de toe te passen korreldiameter in de modellen.

Voor dit onderzoek zijn nieuwe meetopstellingen ontworpen om betrouwbare hydraulische meetgegevens te verkrijgen voor een groot aantal watergerelateerde korreltypen (Hoofdstuk 3). Deze zogenaamde expansiekolommen bestonden uit een systeem waarin water in opwaartse richting door een cilindrische buis werd gepompt om deeltjes in een gefluïdiseerde toestand te laten brengen. Behalve de vloeistofsnelheid kon met de meetopstelling ook de temperatuur worden ingesteld en kon de verschildrukmeting worden gemeten. Eveneens werd een nieuwe proefopstelling ontworpen voor de longitudinale bepaling van de hydraulische toestand in een gefluïdiseerd bed met behulp van een hydrostatische weegtechniek en een ondergedompeld object in een gefluïdiseerd bed. Deze sensor werd speciaal ontworpen om de hydraulische drukgradiënt te meten. Hiermee kon de bijbehorende porositeit worden bepaald en kon het deeltjesgrootte profiel worden geschat. Verder is op de TU Delft een geavanceerde opstelling gebruikt om de terminale bezinkingsgegevens van individuele korrels in een stilstaande vloeistof te verkrijgen met behulp van hogesnelheidscamera's die de valbeweging van deze deeltjes konden volgen.

Met uitgebreide sedimentatie-experimenten (Hoofdstuk 4) is aangetoond dat de gemiddelde weerstandscoefficiënt en de uiteindelijke terminale bezinkingsnelheid van individuele korrels redelijk goed kunnen worden voorspeld met een verzameling aan voorspellingsmodellen die beschikbaar zijn in de literatuur, zoals het bekende model van Brown en Lawler. Helaas bieden deze modellen weinig informatie over grote verschillen tussen de meetgegevens rondom de gemiddelde waarden. Een grondige analyse toonde aan dat de mate van spreiding kan worden verklaard en wordt veroorzaakt door variaties in deeltjesdichtheid, door de instabiliteit van het valtraject en in het bijzonder door variaties in deeltjesgrootte, vorm en oriëntatie van de deeltjes. Voor praktische industriële toepassingen is dit relevante informatie waarmee rekening moet worden gehouden.

De terminale bezinkingsnelheid is een belangrijk uitgangspunt bij het Richardson–Zaki model. Dit model wordt nog steeds veelvuldig gebruikt voor de voorspelling van

de porositeit in gefluidiseerde bedden. Het punt van minimale fluïdisatie is echter geen onderdeel van dit model. Bij drinkwaterbehandelingsprocessen wordt de porositeit relatief laag gehouden voor optimale procesconditie. Het gevolg hiervan is dat het Richardson–Zaki model de minimale fluïdisatiesnelheid overschat, wat resulteert in minder nauwkeurige voorspellingen van de porositeit. Het Richardson–Zaki-model kon worden verbeterd dankzij de invoering van de hydraulische context. Door gebruik te maken van de modellen van Brown–Lawler en Carman–Kozeny wordt de voorspelling van de porositeit aanzienlijk verbeterd, zoals besproken in [Hoofdstuk 5](#).

[Hoofdstuk 6](#) behandelt het gegeven dat veel porositeitsvoorspellingsmodellen zijn gebaseerd op de traditionele weerstandscoefficiënt als functie van het Reynoldsgetal. Op basis van nauwkeurige experimentele expansiegegevens werden significante verschillen waargenomen in de weerstandscoefficiënt. Dit ondersteunde de hypothese dat de weerstandscoefficiënt bij de toepassing voor grootschalige gefluidiseerde bed reactoren niet enkel geldt als functie van het Reynolds kengetal. Door het Froude kengetal als derde dimensie toe te voegen aan de traditionele 2D-weergave (weerstandscoefficiënt tegen het Reynoldsgetal), kon de spreiding worden gevisualiseerd en vervolgens worden verklaard door middel van een 3D-weergave. Als resultaat werd een nieuw voorspellingsmodel ontwikkeld voor de weerstandscoefficiënt dat aantoont dat de porositeit niet alleen afhankelijk is van de verhouding tussen laminaire-turbulente stroming, maar ook van de hoeveelheid homogene versus heterogene stroming.

Met betrekking tot lage superficiële vloeistofsnelheden laat de huidige literatuur zien dat vloeistof-vaste stof fluïdisatiesystemen over het algemeen worden beschouwd als homogeen. Bij fluïdisatie-experimenten met kalkpellets werden in het bed echter open holtes waargenomen in het bed tussen de gefluidiseerde deeltjes in. Ondanks het gegeven dat dit fenomeen ook werd waargenomen bij relatief lage vloeistofsnelheden werden bij hogere vloeistofsnelheden significante heterogene deeltjes-vloeistofpatronen gedetecteerd ([Hoofdstuk 7](#)). Om informatie te verkrijgen over de porositeit werden geavanceerde rekenkundige vloeistof dynamica (CFD) simulaties uitgevoerd. Deze bleken tamelijk goed overeen te komen met de experimentele meetresultaten. De simulaties toonden ook aan dat over het hele bereik van vloeistofsnelheden heterogeen gedrag voorkomt en dat dit niet zonder meer kan worden verwaarloosd.

In de wetenschappelijke literatuur zijn tal van voorspellingsmodellen voor de porositeit beschikbaar (Hoofdstuk 8). Veel van deze modellen zijn gebaseerd op semi-empirische poreuze media-gebaseerde weerstandsrelaties, zoals Ergun, of semi-empirische terminale bezinkingsmodellen, zoals Richardson–Zaki. Deze modellen zijn afgeleid voor monodisperse perfect ronde deeltjes. Daarnaast zijn vele hiervan impliciet voor de porositeit, hetgeen het gebruik ervan bemoeilijkt. Bij drinkwaterproductieprocessen zijn korrels in de regel niet rond, wat inhoudt dat de voorspelling van de porositeit in de bovengenoemde modellen hoogstwaarschijnlijk minder nauwkeurig is, en daarmee veelal ongeschikt. Om een effectieve toepasbare oplossing te bieden, werd een nieuw expliciet data-gestuurd porositeitvoorspellingsmodel voorgesteld. Hierbij is uitgegaan van de dimensieloze Reynolds- en Froude kengetallen met behulp van niet-lineaire symbolische regressiemethoden. Het model is vervolgens gekalibreerd en gevalideerd op basis van nauwkeurige meetgegevens. Deze expansiegegevens zijn verkregen na een uitgebreide reeks van experimenten en konden ze worden gebruikt voor een breed scala aan deeltjesgroottes, vloeistofsnelheden en temperaturen. Het resultaat was dat het model daarom goed kan worden gebruikt bij de drinkwaterproductie, zoals bij de ontharding van drinkwater.

Hoofdstuk 9 is gericht op vloeistofstroming door een bed van vaste korrels zoals de snelle zandfiltratie. Dit proces is een belangrijk proces dat vaak voorkomt bij grootschalige waterzuiveringsinstallaties. Voor het schatten van de weerstand over het korrelbed is het Carman–Kozeny model nog steeds populair. Opwaartse filtratie-experimenten toonden aan dat de weerstandscoefficiënt over het bed aanzienlijk afnam in het laminaire gebied en in het overgangsgedebied. Dit werd hoogstwaarschijnlijk veroorzaakt door heroriëntatie en herrangschikking van de zandkorrels. Nog vaak wordt een vormfactor gebruikt om de voorspelde weerstandscoefficiënt te laten overeenkomen met de experimenteel verkregen weerstandscoefficiënt. Met experimentele metingen werd echter aangetoond dat de vormfactor geen constante deeltjeseigenschap is, maar dat deze ook afhankelijk is van de vloeistofeigenschappen zoals de viscositeit en de snelheid. Een grondige hydraulische analyse toonde aan dat de opwaartse filtratie in snelfilters, onder terugspoelcondities, ervoor zorgde dat het deeltjesbed haast onmerkbaar ineensloot. Daardoor was het mogelijk om de succesvolle (Extended terminal subfluidisation wash) ofwel de ETSW-methode te ontrafelen. Deze methode is succesvol en geschikt om het terugspoelen van de snelfilters te optimaliseren.

Hierdoor worden troebelheidspieken sterk verminderd met een positief effect op de waterkwaliteit. Om de morfologische eigenschappen en de voorkeur van de deeltjesoriëntatie te onderzoeken, werd bovendien een nieuwe rechtstreekse pseudo-3D-beeldanalyse methode ontwikkeld voor deeltjes met een onregelmatige vorm. Als de afgewogen massa en dichtheid van een deeltjesmonster wordt gecombineerd met een 2D scanner, kunnen de gedimensioneerde vormen van bijvoorbeeld ellipsoïden worden bepaald. De deeltjesanalyse met behulp van de 2D-scanteknik met pseudo-3D-beeldverwerking is superieur ten opzichte van veelgebruikte klassieke 1D-zeefanalyses.

In grootschalige drinkwaterzuiveringsinstallaties is granulaire actieve koolfiltratie een cruciale behandelingsstap voor het verwijderen van onder meer organische (micro)verontreinigingen uit het water ([hoofdstuk 10](#)). Periodiek moeten de filters worden gereinigd door middel van een terugspoelprocedure waarbij de kooldeeltjes worden geëxpandeerd. De voorspelling van de effectieve expansie van de kooldeeltjes is uitzonderlijk complex, doordat de korrels doorgaans een grillige vorm hebben, uitermate polydispers zijn en bovendien een interne poreuze structuur hebben. Voor dit soort kooldeeltjes zijn in de literatuur nauwelijks algemene voorspellingsmodellen voor expansie beschikbaar. Uitgebreide experimentele metingen bevestigden de hoge mate van complexiteit voor een nauwkeurige voorspelling van de porositeit. Een combinatie van fluïdisatie en laboratoriumexperimenten, zoals metingen van bevochtigingsgraad, dichtheid en verdamping, biedt mogelijkheden om de complexiteit te ontrafelen.

Procesbesturing en optimalisatie van gefluïdiseerde bedden in pelletonthardingsreactoren is complex vanwege een grote variatie aan korrelmaterialen. Een gestratificeerd korrelbed bestaat uit een combinatie van zeer onregelmatig gevormde gebroken calciëtkorrels boven in het bed, terwijl de grotere, meer ronde calciëtpellets zich in het onderste deel van het bed bevinden. Om de gradiënt voor lokale porositeit en deeltjesgrootteverdeling in het gefluïdiseerd bed van een korrelreactor te onderscheiden, werd een beweegbaar ondergedompeld object met een hydrostatische weegtechniek ontwikkeld. Deze sensor werd vervolgens gebruikt om de hydraulische toestandsgradiënt te bepalen ([Hoofdstuk 11](#)). Deze hydrometer meet de opwaartse kracht in het bed en dienovereenkomstig de porositeit van het bed. Met behulp van een data-gestuurd model kon het deeltjesgrootteprofiel over de hoogte van het gehele gefluïdiseerd bed worden

voorspeld en werd het mogelijk om de hydraulische prestatie van een pelletreactor af te leiden.

Hoofdstuk 12 beschrijft het belang van het onderzoek voor de drinkwaterproductie. Drinkwaterproductie is van levensbelang voor de volksgezondheid. Een betrouwbare en onberispelijke drinkwaterkwaliteit kan worden bereikt met behulp van geavanceerde zuiveringsinstallaties die bestaan uit aaneengeschakelde zuiveringsprocessen. Bij veel van deze processen komt meefasestroming voor met een verscheidenheid aan niet-ronde *natuurlijke* deeltjes. Door voortdurende veranderingen in omstandigheden, eisen en externe drijfveren, zoals de behoefte aan het gebruik van duurzamere granulaten, moeten processtuurwaarden regelmatig worden bijgesteld. Bovendien is een flexibeler ontwerp van installaties op ware grootte zeer wenselijk om niet alleen het hoofd te kunnen bieden aan veranderingen op de korte termijn, maar vooral ook op de lange termijn en om robuustheid te kunnen blijven garanderen. Met behulp van effectieve voorspellingsmodellen kunnen de hydraulische toestanden in deze waterzuiveringsprocessen nauwkeurig worden voorspeld, wat de dagelijkse werkzaamheden ten goede komt. Intelligente voorspellingsmodellen kunnen bijdragen aan een betere waterkwaliteit, een ononderbroken levering, kostenefficiëntie, duurzaamheid en klantcomfort.

In **Hoofdstuk 13** worden de algemene conclusies van het onderzoek besproken. Nieuwe inzichten in hydraulische verschijnselen zijn verkregen en gebruikt om nieuwe effectieve voorspellende modellen van de porositeit te ontwikkelen. Het optreden van heterogeen gedrag in vloeibaar-vast gefluidiseerde bedden is zowel experimenteel als numeriek aangetoond. De nauwkeurigheid van de porositeitmodellen is verbeterd door gebruik te maken van zowel het Reynolds als het Froude kengetal. Nieuwe inzichten werden verkregen uit nauwkeurige opwaartse filtratie-experimenten. Het bleek dat niet-ronde deeltjes de neiging hebben om zich te heroriënteren en hun positie in het bed te veranderen, wat het netto beschikbare oppervlak voor doorstroming aanzienlijk beïnvloedt. Met deze nieuwe inzichten was het mogelijk om de oorzaak van het succes achter de ETSW methode voor filterterugspoeling te achterhalen.

Voor pragmatische toepassingen zou het gebruik van ronde bollen en meer in het bijzonder van de gemiddelde zeefdiameters in data-gestuurde modellen kunnen werken. Maar in het geval van *natuurlijke* niet-ronde korrels is dit alleen mogelijk als

zeer gedegen en zeer nauwkeurige experimentele gegevens kunnen worden verkregen. Voor toekomstbestendige flexibele waterzuiveringsinstallaties is echter een volgende stap nodig in de ontwikkeling van hydraulische modellen waarin de grillige vormen van drinkwatergerelateerde korrels worden meegenomen. De overgang van granaatzand bij de ontharding naar hergebruikt gebroken calciet in de pelletontharding, illustreerde de significante gevolgen en de invloed van de verandering van deeltjeseigenschappen op het expansiegedrag van het zwevende korrelbed en de hieruit volgende wens naar meer geavanceerde modellen.

Ten slotte bespreekt [Hoofdstuk 14](#) de mogelijkheden voor verdere verkenning. Voor lopend onderzoek kunnen de werking en prestaties van het pelletonthardingsproces worden verbeterd wanneer de nieuwe hydraulische inzichten worden gecombineerd met de opgedane chemische inzichten om zodoende te komen tot een nieuw geavanceerd procesmodel.

Voor toekomstige studies is numerieke vloeistofdynamica-modellering (CFD) een grote belofte als een nuttig hulpmiddel om nieuwe inzichten te verkrijgen in waterbehandelingsprocessen, zoals de invloed van niet-ronde deeltjes in meerfasestromen.

Waarschijnlijk kunnen de beste academische en toegepaste onderzoeksresultaten worden behaald wanneer fundamentele en experimentele inspanningen met elkaar worden gecombineerd, in het bijzonder als dat gebeurt bij onderwijssituaties. Dit is immers niet alleen wat jonge talenten nodig hebben, maar ook wat nodig is voor een duurzame samenleving met toegang tot veilig drinkwater voor iedereen.

Table of contents

Table of contents



Contents

Summary	iv
Samenvatting	x
Table of contents	xviii
Nomenclature	xxx
1 General introduction	1
1.1 Drinking water challenges	1
1.2 Multiphase flows and drinking water granules	2
1.3 Processing granules	4
1.4 Classical models to estimate expansion behaviour	4
1.5 Particle size conundrum	5
1.6 Fluidisation quality	6

1.7	Consequences for full-scale operation pellet-softening	8
1.8	Computational Fluid Dynamics modelling	9
1.9	Experimental data	9
1.10	Data-driven modelling	10
1.11	Full-scale water treatment considerations	11
1.12	Knowledge gaps and research questions	12
1.12.1	The classical Richardson–Zaki model.....	12
1.12.2	Terminal settling	12
1.12.3	Particle orientation in the vicinity of incipient fluidisation	13
1.12.4	Drag relations in fluidised beds	13
1.12.5	CFD	14
1.12.6	Data-driven modelling	14
1.12.7	Expansion characteristics of carbon granules	15
1.12.8	A soft sensor for the fluidised bed state indication.....	15
1.12.9	Relationship Application-Research-Education	15
1.13	Approach.....	16
1.14	Aim	17
1.15	Outlook.....	17
2	Basics of fluidisation and pellet-softening.....	21
2.1	Introduction to fluidisation	21
2.1.1	Applied fluidisation processes.....	21
2.1.2	Fluidisation states.....	22
2.2	Fluidisation in practice: pellet-softening	25
2.3	Flow phenomena.....	28
2.3.1	The Reynolds number	28
2.3.2	Flow through tubes.....	29
2.3.3	Flow around objects	29
2.3.4	Hindered settling and fluidisation	32
2.4	Particle size conundrum.....	34
3	Materials and methods	37
3.1	Experimental set-up	37
3.1.1	Expansion columns	37

3.1.2	Terminal settling set-up	44
3.1.3	Set-up for immersed objects in fluidised beds	46
3.2	Physical properties of water	48
3.3	Physical properties of particles	48
3.3.1	Particle selection	49
3.3.2	Representative particle samples	50
3.3.3	Particle size and shape analysis	50
3.3.4	Average particle diameter	52
3.3.5	Particle density	53
3.4	Fluidisation expansion experiments	55
3.4.1	Standard operating procedure	55
3.4.2	Bed voidage and expansion	57
4	Can terminal settling velocity and drag of natural particles in water ever be predicted accurately?	61
4.1	Abstract	61
4.2	Introduction	62
4.2.1	Deviations in the prediction of settling in water treatment processes	62
1.1.1	Terminal settling and drag coefficient: models from the literature	63
4.2.2	Terminal settling velocity calculation	64
4.2.3	Aim	65
4.3	Materials and methods	67
4.3.1	Experimental approach	67
4.3.2	Particle selection	67
4.3.3	Experimental set-up	69
4.3.4	Reference data	69
4.4	Results and discussion	70
4.4.1	Standard drag curve with average values	70
4.4.2	Drag coefficient and terminal settling velocity prediction versus spread in measured data	72
4.4.3	Uncertainty analysis	74
4.4.4	Path trajectories	82

4.4.5	Data from the literature.....	83
4.4.6	Propagated effect of parameter uncertainties on terminal settling	86
4.4.7	Consequences of uncertainty in settling velocity for water treatment processes.....	88
4.5	Conclusions.....	89
4.6	Supplementary material	91
5	Improvement of the Richardson–Zaki liquid-solid fluidisation model on the basis of hydraulics	97
5.1	Abstract	97
5.2	Introduction	98
5.3	Richardson–Zaki model analyses	100
5.3.1	Model principle	100
5.3.2	Model boundaries.....	101
5.3.3	The Richardson–Zaki index n	103
5.3.4	The Richardson–Zaki curve	105
5.3.5	Richardson–Zaki on the basis of hydraulics	107
5.4	Richardson–Zaki models and theory related to the fluidised bed pellet-softening process.....	108
5.4.1	Richardson–Zaki water treatment constraints.....	108
5.4.2	Hydraulics-based Richardson–Zaki index.....	109
5.4.3	Simplified analytical expressions	111
5.5	Materials and Methods.....	115
5.5.1	Particle selection	115
5.5.2	Particle and fluid characterisation and expansion experiments	115
5.5.3	Terminal settling velocity experiments	116
5.5.4	Fluidisation expansion experiments	117
5.6	Results and discussion	118
5.6.1	Obtained particle properties	118
5.6.2	Expansion experiments.....	119
5.6.3	Minimum fluidisation velocity prediction.....	122
5.6.4	Voidage prediction.....	124

5.6.5	Richardson–Zaki index.....	125
5.7	Conclusions.....	128
5.8	Supplementary material	129
6	Improvement of voidage prediction in liquid-solid fluidised beds by inclusion of the Froude number in effective drag relations	133
6.1	Abstract.....	133
6.2	Introduction	134
6.3	Theory	137
6.3.1	Hydraulic models in porous media	137
6.3.2	Hydraulic models based on the Reynolds and Froude numbers	141
6.4	Materials and Methods.....	146
6.4.1	Particle selection and fluidisation experiments	146
6.4.2	Particle and fluid characterisation and expansion experiments	147
6.5	Results and discussion	147
6.5.1	Expansion experiments.....	147
6.5.2	Fluidisation characterisation observations	149
6.5.3	Persistent drag deviation.....	150
6.5.4	Estimation of the Kozeny coefficient	152
6.5.5	Drag relations based on the Reynolds number.....	153
6.5.6	Hydraulic models based on the Reynolds and Froude numbers	157
6.5.7	Voidage prediction.....	160
6.6	Conclusions.....	162
6.7	Research data.....	164
6.8	Supplementary material	164
7	Numerical study on unsteady liquid-solid behaviour in drinking water softening reactors	169
7.1	Abstract.....	169
7.2	Introduction	170
7.2.1	Liquid-solid fluidisation applied in drinking water softening processes	170

7.2.2	Fluidisation quality.....	172
7.2.3	Full-scale experience and reactor performance.....	174
7.2.4	Aims.....	175
7.3	Materials and Methods.....	175
7.3.1	Simulations.....	175
7.3.2	Experimental set-up	176
7.3.3	Camera experiments	177
7.4	Results and discussion	177
7.4.1	Expansion experiments.....	177
7.4.2	Fluidisation characterisation observations	178
7.4.3	Simulation results and discussion	179
7.5	Conclusions.....	189
7.6	Recommendations	190
7.6.1	Supplementary material	191
8	Accurate voidage prediction in fluidisation systems for full-scale drinking water pellet-softening reactors using data-driven models	195
8.1	Abstract.....	195
8.2	Introduction	196
8.2.1	Drinking water softening.....	196
8.2.2	Sustainability goals.....	198
8.2.3	Reactor technology conditions and research objective.....	200
8.3	Prediction models and performance indicators.....	202
8.3.1	Voidage prediction models.....	202
8.3.2	Reactor performance indicators	205
8.4	Materials and Methods.....	206
8.4.1	Empirical data-driven voidage prediction models	206
8.4.2	Experimental set-up	210
8.4.3	Particle selection	211
8.4.4	Particle and fluid characterisation and expansion experiments	211
8.5	Results	212

8.5.1	Particle selection, properties, experimental set-up and fluidisation experiments.....	212
8.5.2	Obtained physical properties of particles	212
8.5.3	Voidage prediction.....	214
8.5.4	Reactor performance indicators	220
8.6	Discussion	225
8.6.1	Voidage prediction models	225
8.6.2	Reactor performance indicators	230
8.7	Conclusions.....	231
8.8	Research data	233
8.9	Supplementary material	234
9	New hydraulic insights into rapid sand filter bed backwashing using the Carman–Kozeny model	239
9.1	Abstract	239
9.2	Introduction	240
9.3	Hydraulic drag	241
9.3.1	Hydraulic models for fluid flow in particle beds	241
9.3.2	Particle correction shape factors	243
9.4	Research aims	245
9.5	Materials and methods.....	245
9.5.1	Particle selection and physical properties	245
9.5.2	Hydraulic experimental set-up.....	246
9.5.3	Dynamic shape factor determination.....	247
9.6	Results and discussion	248
9.6.1	Particle properties	248
9.6.2	Hydraulic experiments and expansion curves	251
9.6.3	Measured and predicted drag coefficients	253
9.6.4	Hydraulic explanation for up-flow filtration and ETSW	257
9.6.5	Preliminary considerations of hydraulics-based ETSW	259
9.6.6	Full-scale consequences of utilising the ETSW procedure ..	260
9.7	Conclusions.....	261
9.8	Recommendations	262
9.8.1	Supplementary material	263

10	Fluidisation characteristics of granular activated carbon in drinking water treatment applications	267
10.1	Abstract	267
10.2	Introduction	268
10.3	Materials and Methods.....	272
10.3.1	Particle selection - a wide variety in properties and sources 272	
10.3.2	Porous media - dry and wet conditions.....	274
10.3.3	Laboratory measurements - particle characterisation.....	277
10.3.4	Fluidisation measurements - expansion characteristics	281
10.3.5	Modelling aspects - voidage and incipient fluidisation	281
10.4	Results and discussion	283
10.4.1	Porous media - dry and wet conditions.....	283
10.4.2	Laboratory measurements - particle characterisation.....	285
10.4.3	Fluidisation measurements - expansion characteristics	289
10.4.4	Modelling aspects – voidage, morphology and incipient fluidisation	291
10.5	Conclusions.....	297
10.6	Recommendations	298
10.7	Supplementary material.....	299
11	A novel sensor measuring local voidage profile inside a fluidised bed reactor	305
11.1	Abstract.....	305
11.2	Introduction	306
11.2.1	Liquid-solid fluidisation applied in drinking water softening processes.....	306
11.2.2	Hydraulic state determination of pellet-softening fluidised beds 308	
11.3	Materials and methods.....	309
11.3.1	Particle selection	310
11.3.2	Fluidisation experiments.....	310
11.3.3	Data transformation model.....	311
11.4	Theoretical hydraulic state determination	312

11.4.1	Suspension density	312
11.4.2	Force balance.....	313
11.4.3	Suspension density	313
11.4.4	Total particle mass and differential pressure	314
11.4.5	Submerged object corrections	315
11.4.6	Discretisation modelling	317
11.4.7	Particle size estimation.....	319
11.4.8	Model-based hydraulic state determination and reactor performance indicators.....	320
11.5	Results and discussion	321
11.5.1	Preliminary full-scale experiment	321
11.5.2	Particle selection	322
11.5.3	Proof of concept of the hydrostatic weighing technique.....	323
11.6	Conclusions.....	333
11.7	Recommendations	334
11.8	Supplementary material	337
12	Synthesis of research findings.....	341
12.1	From a robust to a flexible process design	341
12.2	Hydraulic modelling of liquid-solid fluidisation processes	342
12.3	Particle size conundrum.....	343
12.4	Model consideration	343
12.4.1	Classical models	344
12.4.2	Data-driven models	344
12.4.3	Numerical models.....	345
12.4.4	Model selection	345
13	Conclusions.....	351
13.1	Lessons learned through modelling and experiments	351
13.2	Terminal settling and data spread.....	351
13.3	Laminar-turbulent and homogeneous-heterogeneous flows	351
13.4	Computational fluid dynamics	352
13.5	Data-driven models	353
13.6	From fixed to dynamic particle shape factors	353
13.7	Expansion of granular activated carbon grains.....	354

13.8	A soft-sensor to determine the hydraulic state.....	355
13.9	From robust to more flexible water treatment	356
13.10	The expansion column benefits	356
14	Recommendations	359
14.1	Objectives for optimisation	359
14.1.1	Relating hydraulic and chemical reactor performance indicators 359	
14.1.2	Optimal reactor performance and fluidisation quality	360
14.2	Related ongoing research	360
14.2.1	Alternatives to particles diameter in fluidisation models	361
14.2.2	Distortion layers in the pellet-softening reactors	361
14.2.3	Computational fluid dynamics modelling.....	363
14.2.4	General theory of liquid-solid and gas-solid fluidisation.....	364
14.3	Avenues for future research.....	365
	Annexes.....	369
	Annex 1: Photos	370
	Annex 2: Wall effects.....	375
	Annex 3: Obtained particle properties.....	376
	Annex 4: Morphological properties.....	378
	Annex 5: Statistical analysis.....	379
	Annex 6: Overview uncertainty analysis equations.....	380
	Annex 7: Where research, education and professional practice meet.....	383
	References	389
	List of publications	415
	Acknowledgements.....	427
	Curriculum Vitae	430

Nomenclature

Nomenclature

Symbols

a, b, c	Radius of major axes of spheroids	[m]
A, B, C, D	Coefficients	[-]
A_1	Surface area of one spherical particle	[m ²]
A_c	Specific space velocity	[s ⁻¹]
A_i	Projected particle area using static image analysis	[m ²]
Ar	Archimedes number	[-]
A_p	Particle projected area	[m ²]
A_s	Area of spherical particle	[m ²]
$A_{s,r}$	Specific surface area (reactor volume)	[m ² /m ³]
$A_{s,w}$	Specific surface area (water phase)	[m ² /m ³]
A_{\perp}	Cross sectional area of the object perpendicular to the flow	[m ²]
b/l_3	Aspect (width-to-length) ratio (volume based)	[-]
c_i	Coefficients	[-]
c_p	Specific heat	[J/(kg·K)]
C_D	Fluid dynamic drag coefficient	[-]
$\overline{C_D}$	Average drag coefficient	[-]
C_D'	Error / uncertainty introduced in drag coefficient	[-]
C_w	Drag coefficient	[-]
d	Sieve mesh width or measured diameter	[m]
d_i	Effective size where $i\%$ of particles is smaller than the particular size	[m]
$d_{i,max}$	Maximum diameter (minor axis of ellipse)	[m]
$d_{i,min}$	Minimum diameter (minor axis of ellipse)	[m]
Δd_p	Distance between the centres of two spherical particles	[m]
D	Inner column or cylinder vessel diameter	[m]
D_{co}	Diameter cylindrical object	[m]
D_{hm}	Inner column diameter hydrometer	[m]
D_H	Hydraulic diameter	[m]
d_g	Average seeding material diameter	[m]
d_i	Effective size of a sample i	[m]
d_p	Effective or average or particle equivalent diameter	[m]

$\langle d_p \rangle$	Mean particle diameter	[m]
$d_{s,i}$	Sieve mesh diameter	[m]
<i>error</i>	1.96 times standard spread	
e	Absolute roughness of interior pipe material	[m]
e_p	Particle coefficient of restitution, ratio of final to initial relative velocity	[-]
E	Bed expansion	[%]
$E_{H,50}$	Ellipsoid height (cumulative 50% point)	[m]
$E_{L,50}$	Ellipsoid length (cumulative 50% point)	[m]
$E_{W,50}$	Ellipsoid width (cumulative 50% point)	[m]
f	Friction factor in the Moody's chart	[-]
f_c	Correction factor	[-]
f_L	Dimensionless drag coefficient (laminar representation)	[-]
$f_{L,CK}$	Dimensionless drag coefficient (for Carman–Kozeny)	[-]
f_T	Dimensionless drag coefficient (turbulent representation)	[-]
$f_{T,CK}$	Dimensionless drag coefficient (for Carman–Kozeny)	[-]
F_b	Buoyancy force	[N]
F_{col}	Force caused by particle collisions	[N]
F_d	Drag or frictional force of a spherical particle during terminal settling	[N]
F_g	Force by the gravitational field	[N]
F_s	Upward strain force	[N]
F_p	Net force exerting on spherical particle for terminal settling conditions	[N]
Fr	Froude number	[-]
Fr_p	Densimetric or particle Froude number	[-]
g	Gravitational acceleration	[m/s ²]
Ga	Galileo number	[-]
H	Column height	[m]
h	Convective heat transfer coefficient of the flow	[J/(m ² ·s·K)]
h_{bed}	Bed height (numerical)	[m]
i, j, k	Parameters	[-]
k	Wall effects correction multiplier	[-]
k_{koz}	Kozeny pore shape factor	[-]
k_{La}	The volumetric mass-transfer coefficient	[1/s]
k_{tc}	Thermal conductivity	[J/(m·s·K)]
K	Kozeny coefficient	[-]
l, m, n	Coefficients	[-]

l	Characteristic length	[m]
L	Fluid bed height	[m]
ΔL	Relative total fluid bed height	[m]
L_0	Fixed bed height	[m]
m	Total particle mass	[kg]
m_c	Carbon particle (theoretical)	[kg]
m_g	Object mass (in air)	[kg]
m_i	Single particle mass	[kg]
m_{meas}	Submerged SSD particle mass weighed under water	[kg]
m_{od}	Carbon particle mass (oven dry)	[kg]
m_{op}	Open pore mass (entirely wetted carbon particle)	[kg]
m_{ssd}	Total mass of (internally wetted carbon particle)	[kg]
m_{strain}	Object mass apparent (mass while submerged in fluidised bed)	[kg]
m_{sub}	Submerged object mass (in water)	[kg]
n	Richardson–Zaki coefficient, expansion index	[-]
n_L	Richardson–Zaki coefficient at laminar terminal Reynolds conditions	[-]
n_T	Richardson–Zaki coefficient at turbulent terminal Reynolds conditions	[-]
N	Total number of experiments	[#]
N_p	Total number of particles	[#]
N_r	Number of reactors	[#]
Nu	Nusselt number, the ratio of convective to conductive heat transfer	[-]
OPV	Open pore volume	[L/kg]
$\Delta P/L$	Pressure drop head loss	[kPa/m]
ΔP_{max}	Total maximum differential pressure over the bed	[kPa]
Pr	Nusselt number, ratio momentum diffusivity to thermal diffusivity	[-]
Q_w	Water flow rate	[m ³ /h]
r	Radial coordinate	[m]
r_{cp}	Closed pore ratio (dry)	[vol%]
r_{wd}	Ratio wet / dry carbon particle mass	[wt%]
Re	Reynolds number, ratio of inertial forces to viscous forces within a fluid	[-]
Re_{co}	Reynolds number for submerged cylindrical objects	[-]
Re_p	Reynolds particle number	[-]
Re_t	Reynolds particle for terminal velocity conditions	[-]
Re_ϵ	Modified Reynolds particle number corrected for the voidage	[-]
$Re_{\epsilon,mf}$	Modified Reynolds particle number at minimum fluidisation	[-]

Re_1	Blake Reynolds particle number	[-]
RF	Modified Reynolds–Froude number	[-]
S	Strain / stress	[V]
$SPHT$	Sphericity calculated from the perimeter P and project area	[-]
St	Stokes number	[-]
$Symm$	Symmetry	[-]
t	Time	[s]
Δt	Time step	[s]
t_f	Fluid response	[s]
t_p	Particle response	[s]
T	Temperature	[°C] [K]
UC	Non-uniformity coefficient d_{60}/d_{10}	[-]
v_E	Apparent free-falling particle settling velocity in an infinite dilution	[m/s]
v_i	Interstitial fluid velocity or phase-averaged bulk fluid velocity	[m/s]
V_{object}	Immersed object volume	[m ³]
v_p	Particle phase velocity	[m/s]
v_s	Linear superficial velocity or empty tube fluidisation velocity	[m/s]
v_t	terminal settling velocity	[m/s]
\bar{v}_t	Average terminal settling velocity	[m/s]
v_t'	Error / uncertainty introduced in velocity	[m/s]
$v_{t,BL}$	Terminal settling velocity according Brown–Lawler	[m/s]
V	Volume	[m ³]
V_a	Absolute carbon and components volume without closed pores	[m ³]
V_c	Pure or (theoretical) solid carbon volume without closed pores	[m ³]
V_{cp}	Closed pore volume (dry)	[m ³]
V_{ext}	Volume occupied by or air or water (outside) between particles	[m ³]
V_{opw}	Open pore volume (wetted part)	[m ³]
V_{op}	Open pore volume (entirely wetted)	[m ³]
V_p	Volume of an individual particle or porous (solid and internal pores)	[m ³]
V_p	Volume of porous particles (solid and internal pores)	[m ³]
V_s	Skeletal carbon volume with closed pores	[m ³]
V_{tot}	Total particle volume	[m ³]
V_{tp}	Volume of total carbon pores (open and closed internal pores)	[m ³]
W	Weight of object in air	[N]
W_{sub}	Weight of submerged object in water	[N]

z	Axial coordinate	[m]
x	Average particle diameter between top and bottom sieves	[m]
Δx	Cell size	[m]
y_{calc}	Predicted calculated value	
y_{exp}	Experimentally determined value	
Y_p	Particle Young's modulus of elasticity in tension	[MPa]

Greek symbols

α, β	Coefficients	[-]
α	Linear heat expansion coefficient	[m/(m.K)]
β	Di Felice power coefficient	[-]
δ	Uncertainty	
ε	Voidage of the system	[-]
$\hat{\varepsilon}$	Voidage, integration variable	[-]
$\langle \varepsilon \rangle$	Mean voidage	[-]
ε_0	Fixed bed voidage	[-]
ε_1	Voidage at situation 1 (with no distorted bed)	[-]
ε_2	Voidage at situation 2 (constriction caused by the object in the bed)	[-]
ε_i	Internal porosity is formed by the voids inside the particle	[-]
ε_{ext}	External porosity activated carbon equal to voidage	[-]
ε_{max}	Maximum achievable voidage before particle entrainment	[-]
ε_{mf}	Voidage at minimum fluidisation	[-]
η	Dynamic fluid viscosity	[Pa·s]
η_{mix}	Dynamic viscosity of mixture	[Pa·s]
κ, λ	Coefficients	[-]
λ	Ratio between particle grain diameter and inner column diameter	[-]
μ	Statistical mean	
μ_p	Particle coefficient of friction, amount of friction between two surfaces	[-]
$\bar{\rho}$	Specific gravity number, particle to fluid density ratio	[-]
ρ_a	Absolute density of solid carbon without closed pores	[kg/m ³]
ρ_{air}	Density of ordinary air	[kg/m ³]
ρ_{bulk}	Bulk or bed density is the mass of adsorbent in a specific volume	[kg/m ³]
ρ_f	Fluid density	[kg/m ³]

ρ_p	Particle density	[kg/m ³]
ρ_c	Density of calcium carbonate	[kg/m ³]
ρ_{co}	Density cylindrical object	[kg/m ³]
ρ_f	Fluid density	[kg/m ³]
ρ_g	Seeding material density	[kg/m ³]
ρ_{mix}	Suspension density (particles and fluid)	[kg/m ³]
ρ_p	Particle density or dry envelope carbon particle density	[kg/m ³]
ρ_s	Solid skeletal density of carbon with closed pores	[kg/m ³]
ρ_{sub}	Submerged particle mass	[kg/m ³]
ρ_w	Density of ordinary water	[kg/m ³]
ρ_{wet}	Same as ρ_p when internal pores are 100% filled with water	[kg/m ³]
ν_p	Particle Poisson ratio of the relative contraction strain	[m/m]
ν_T	Kinematic fluid viscosity	[m ² /s]
ξ	Number of particles in layer (thickness) around submerged object	[#]
σ	Standard deviation	
σ_ε	Voidage standard deviation	[-]
σ_p	Particle diameter standard deviation	[m]
ϕ_m	Time-averaged vertical solid mass flux	[kg/(m ² /s)]
ϕ_s	Shape of diameter correction factor	[-]
Φ	Sphericity	[-]
Φ_\perp	Crosswise sphericity	[-]
Φ_\parallel	Lengthwise sphericity	[-]
Ψ	Particle shape descriptor	[-]
Ξ	Circularity	[-]
Ω	Mathematical group in adjusted voidage model	[m ³ /m ³]

Subscripts, superscripts and abbreviations

0	Fixed bed state
ACC	Amorphous calcium carbonate
AOC	Assimilable organic carbon
ARE	Average relative error
BACF	Biological activated carbon filtration
BL	Brown and Lawler model

c	Calcium carbonate (CaCO ₃)
calc	Calculated value
CCCP	Calcium carbonate crystallisation potential
CDF	Cumulative distribution function
CFD	Computation fluid dynamics
CH	Three-dimensional chaotic (regime path trajectory)
CK	Carman–Kozeny model
CP	Calcite pellet
CRP	Constant rate period
crit	Critical
CS	Camsizer
CISTR	Completely ideally stirred tank reactor
DNA	Dimensionless numbers application
DNS	Direct numerical simulation
DEM	Discrete element method
DOC	Dissolved organic carbon
DPI	Dots per inch
DTM	Data transformation model
EBCT	Empty bed contact time
EC	Electrical conductivity
EG	Ergun model
Eq.	Equation number
ETSW	Extended terminal sub-fluidisation wash
EXC	Expansion column
exp	Experimental value
f	Fluid properties
FG	Fair and Geyer
FRP	Falling rate period
FTU	Formazin turbidity units
g	Garnet
GAC	Granular activated carbon
GSF	Gas-solid fluidisation
GB	Glass bead
HF	Steady oblique: high-frequency oscillating (regime path trajectory)
HU-ILC	Hogeschool Utrecht, Institute for life sciences & chemistry
HSV	Colour model (hue, saturation, value) in graphic design

i	Index number
IJ	ImageJ
IEX	Anionic exchange polymer resins
KPI	Key performance indicator
KZ	Kozeny model
LDN	Drinking water treatment plant Leiduin of Waternet
LF	Steady oblique: low-frequency oscillating (regime path trajectory)
LRMSE	Logarithmic root mean squared error
LVN	Pre-treatment plant Loenderveen of Waternet
LW	Lewis
LSF	Liquid-solid fluidisation
MAE	Mean average error
max	Maximum
mf	Minimal fluidisation conditions
Mic	Microscope
NaOH	Sodium hydroxide
NRMSE	Normalised root mean square error
OD	Oven dry
OMP	Organic micro pollutants
OPV	Open pore volume
p	Particle properties
PBL	Problem based learning
PCC	Porous calcium carbonate coating
PDF	Probability density function
pH	Pondus hydrogenium <i>i.e.</i> acidity or alkalinity of water
PLC	Programmable logic controller
PFR	Plug flow reactor
P&ID	Piping and instrumentation diagram
PO	Chaotic: high-frequency planar chaotic oblique oscillating (regime path trajectory)
PSD	Particle size distribution
QMUL	Queen Mary University of London
QR	Chaotic: low-frequency rotating quasi periodic oblique oscillating (regime path trajectory)
R ²	Pearson's correlation coefficient
ref	Reference value

Rep1Frp	Single Reynolds–Froude model
Rep2Frp	Double Reynolds–Froude model
RF	Reynolds–Froude number
RIO 2	Reynolds–Froude based model
RSF	Rapid sand filtration
RZ	Richardson–Zaki model
SDC	Standard drag curve
SI	Saturation index
SI	International system of units
SO	Steady oblique (regime path trajectory)
SON	Stokes–Oseen–Newton inspired model
SRM	Symbolic regression modelling
SSA	Specific crystallisation surface area
SSD	Saturated surface dry
SSV	Specific space velocity
Sv	Sieve
t	Terminal settling conditions
TDS	Total dissolved solids
TSA	Total surface area
TU Delft	Delft university of technology
TU/e	Eindhoven university of technology
UC	Uniformity coefficient (sieve analysis)
VP	Chaotic: vertical periodic oscillating planar (regime path trajectory)
VPP	Voidage prediction polynomials
wt	Weight
w/w	Weight by weight, the proportion of a particular substance within a mixture, as measured by weight or mass
Waternet	Water cycle organisation for Amsterdam and surrounding areas
WHO	World Health Organisation
WPK	Drinking water treatment plant Weesperkarspel of Waternet
WS	Wet surface condition

Dimensionless numbers

Table 1 Dimensionless numbers

Number	Equation	Equation number
Reynolds tube	$Re = \frac{\rho_f v_s D}{\eta}$	(1)
Reynolds cylinder	$Re_{co} = \frac{\rho_f v_s D_{co}}{\eta}$	(2)
Reynolds terminal	$Re_t = \frac{\rho_f v_t d_p}{\eta}$	(3)
Reynolds particle	$Re_p = \frac{\rho_f v_s d_p}{\eta}$	(4)
Incipient Reynolds particle	$Re_{p,mf} = \frac{\rho_f v_{mf} d_p}{\eta}$	(5)
Reynolds modified particle	$Re_\varepsilon = \frac{\rho_f v_s d_p}{\eta} \frac{1}{1-\varepsilon}$	(6)
Incipient Reynolds modified particle	$Re_{\varepsilon,mf} = \frac{\rho_f v_{mf} d_p}{\eta} \frac{1}{1-\varepsilon}$	(7)
Blake Reynolds	$Re_1 = \frac{1}{6} \frac{\rho_f v_s d_p}{\eta} \frac{1}{1-\varepsilon}$	(8)
Archimedes	$Ar = \frac{g d_p^3 \rho_f \rho_p - \rho_f }{\eta^2}$	(9)
Galileo	$Ga = \sqrt{\frac{g d_p^3 \rho_f \rho_p - \rho_f }{\eta^2}}$	(10)
Specific gravity	$\bar{\rho} = \frac{\rho_p}{\rho_f}$	(11)
Froude	$Fr = \frac{v_s^2}{g d_p}$	(12)
Stokes	$St = \frac{\rho_p d_p v_s}{9\eta}$	(13)
Densimetric particle Froude	$Fr_p = \frac{v_s}{\sqrt{\left(\frac{\rho_p}{\rho_f} - 1\right) g d_p}}$	(14)
Modified Reynolds–Froude	$RF = RF(Re_\varepsilon, Fr_p)$	(15)
Drag coefficient (turbulent)	$f_T = \frac{\Delta P}{\Delta L} \frac{d_p}{\rho_f v_s^2} \frac{\varepsilon^3}{1-\varepsilon}$	(16)
Drag coefficient (turbulent)	$f_T = \left(\frac{\rho_p}{\rho_f} - 1\right) \frac{g d_p}{v_s^2} \varepsilon^3$	(17)
Drag coefficient (laminar)	$f_L = \frac{\Delta P}{\Delta L} \frac{d_p^2}{\eta v_s} \frac{\varepsilon^3}{(1-\varepsilon)^2}$	(18)
Drag coefficient (laminar)	$f_L = \frac{g d_p^2 (\rho_p - \rho_f)}{v_s \eta} \frac{\varepsilon^3}{1-\varepsilon}$	(19)
Nusselt	$Nu = \frac{h}{k_{tc}}$	(20)
Prandtl	$Pr = \frac{c_p \eta}{k_{tc}}$	(21)

Glossary

Sources: (Allen, 1990; Crittenden *et al.*, 2012; Grace, 2020)

Activated carbon: Adsorption granules with a high porous structure and adsorption capacity to remove organic matter and dissolved gases from water

Agglomeration: The process of bringing smaller particles together to form a larger mass by which precipitation particles grow larger by collision or contact with other particles

Aggregative fluidisation: Fluidisation characterised by the formation of bubbles usually occurring where the fluidising medium is a gas but also with liquids

Air scour: Optional feature during backwash in which air is introduced into filter underdrains along with backwash water; the vigorous scouring action helps clean deep-bed filters

Alkalinity: Buffering capacity of water to neutralise itself. It prevents the water pH levels from becoming too acid or basic. Alkalinity stabilises water at pH levels around seven. The total alkalinity of water is the sum carbonate, bicarbonate and hydroxide alkalinity

Attrition: Break-up of particles due to collisions or other interactions and stresses

Apparent density: See bulk density

Archimedes: Greek physicist (B.C. 287–212) the first-known who worked on hydrostatics outlining the concept of buoyancy of floating bodies'

Archimedes number: The ratio of gravitational forces to viscous force

Aspect ratio: The ratio of width to height ratio of an elongated particle

Backwash: Process for removing accumulated solids from a filter bed by reversing the water flow

Basset force: Unsteady forces due to acceleration of a submerged body with respect to the fluid

Bed expansion: Height of operating fluidised bed divided by static bed height or bed height at minimum fluidisation

Brazil nut effect: Or granular convection is a phenomenon in which granular material containing a mixture of particles of different size and shape subjected to vibration or shaking moves upwards and end up on the surface

Bulk density: The mass under specified conditions of a unit volume of GAC including its pore volume and interparticle voids

Buoyancy: The force exerted on an object that is immersed in a fluid *i.e.* the magnitude of the buoyant force is equal to the weight of the fluid displaced by the body

Bubbles: Voids containing few, if any, particles, rising relative to the particles above them and behaving in a somewhat analogous manner to bubbles in liquids

Bubbling fluidisation: See aggregative fluidisation

Calcium carbonate crystallisation potential: The amount of supersaturated calcium in the reactor effluent that could still precipitate from solution in the form of calcite before reaching thermodynamic equilibrium which determines the efficiency of the entire pellet-softening process

Carry over: Entrained suspended particles which leave the fluidised bed column entirely caused by contamination of dosed chemicals, pellet erosion, undissolved flushed calcium carbonate particles and/or homogeneous nucleation *i.e.* spontaneous precipitation not on seeding material

Circularity: Perimeter of sphere of the same projected area divides by the actual projected perimeter of the particle

Cluster: Group of particles travelling together due to hydrodynamic factors

Constriction: A submerged object in the fluidised bed causes a restricted flow

Creeping flow regime: laminar flow regime

Data transformation model: The gradient in the fluidised measured by the submerged object, starting with voltage, is converted into suspension density, voidage, particle size and reactor key performance indicators

Darcy–Weisbach friction factor: Dimensionless parameter characterising the friction loss in a fluid flow, named after the French civil engineer Henri Philibert Gaspard Darcy (1805–1858)

De-fluidisation: Under certain conditions, such as increasing temperature, decreasing flow rate or when particles grow, a well-fluidised bed loses fluidised bed expansion, whether partial or total

Dense phase: Region where the concentration of particles is sufficiently high that there are significant particle-particle interactions and contacts

Dilatancy: The observed volume change in compacted dense granular materials as it is subjected to shear deformations

Dilute phase: Region where particle concentration is low enough that interparticle contacts are relatively rare

Distributor: Horizontal plate with perforations, nozzles, or other openings or other means of introducing a fluidising fluid to support the weight of particles and cause

them to move while also supporting the dead weight of the particles when the flow of fluid is interrupted

Disperse phase: The region of decreasing solids concentration occupying the freeboard

Drag: The drag force that counteracts the force of gravity which results in the bed being fully suspended

Effective size: The particle size which corresponds to 10 percent finer on the cumulative particle size distribution curve

Elutriation: Progressive selective removal of finer particulates by entrainment

Energy dissipation: The result of an irreversible process that takes place where energy transforms from an initial form to a final form. In fluidised beds this is caused by the interaction between particles and the surrounding fluid

Empty bed contact time: Measure of the time during which a water to be treated is in contact with the treatment medium in a bed, assuming that all fluid passes through the bed at the same velocity

Entrainment: Particles, especially fine ones, are carried upwards by the exhaust or product gas and leave the column through the exit. To minimize their losses, entrained particles must normally be continuously captured and returned to the bottom of the vessel

Expanded bed: A bed of particles through which a fluid flows upward at a rate sufficient to elevate and separate the particles without changing their relative positions

Expansion column: Experimental set-up for liquid-solid fluidisation and filtration, as well as sedimentation experiments

Ferret diameter: Distance between two parallel tangents on opposite sides of the image of a randomly oriented particle

Fines: Relatively small particles, smaller than the smallest nominal specification particle size typically those smaller than 37 or 44 μm

Fixed bed: Or packed bed is a vessel that is filled with a granular material through which a fluid flows without causing substantial movement of the bed

Filtration: A process of separating particulate matter from a fluid by passing it through a permeable material

Filtrate: A fluid that has passed through a filter medium

Flotsam: Component that floats to the top of the bed

Fluid: Either gas or liquid, usually the former in the context of fluidisation

Fluid bed: An alternative term for fluidised bed

Fluidisation: is a process whereby a granular material is converted from a static solid-like state to a dynamic fluid-like state. This occurs when a fluid (gas or liquid) passes through a bed of granular material

Fluidised bed: A bed of solid particles in which the fluid flows upward at a rate sufficient to suspend the particles completely and randomly in the fluid phase as in liquid-like properties of the solids

Freeboard: Region extending from dense fluidised bed upper surface to top of vessel

Froude number: Dimensionless number proportional to the ratio of the inertial force over the gravitational force, named after an English naval architect and hydrodynamicist William Froude (1810–1879)

Geldart classification: A system of classifying particles into four groups (A, B, C and D) according to their fluidisation behaviour, named after an English Professor of Powder Technology Derek Geldart (1931–2012)

Granular: Particles having approximately an equidimensional irregular shape

Granular activated carbon: heating process of carbon grains to encourage active sites to absorb micro pollutants

Grid: Alternate name for gas distributor supporting the fluidised bed and assuring uniform entry of gas at its base

Hagen–Poiseuille: A physical law that gives the pressure drop in an incompressible and Newtonian fluid in laminar flow flowing through a long narrow cylindrical tube

Hardness: Hardness in water is determined by the concentration of multivalent cations in the water such as: calcium (Ca^{2+}) and magnesium (Mg^{2+}). Hard water is high in dissolved minerals such as: bicarbonates (HCO_3^-)

Head loss: A measure of the reduction in the total head (sum of elevation head, velocity head and pressure head) of the fluid as it moves through a fluid system

Heterogeneous fluidisation: See aggregative fluidisation

Homogeneous fluidisation: See particulate fluidisation

Hydraulic classification: The rearrangement of particles as the water flows up through a bed wherein the larger particles settle, and the smaller particles rise to the top of the bed

Hydraulic conductivity: A physical property which measures the ability of the material to transmit fluid through pore spaces and fractures in porous media. It depends on the intrinsic permeability of the material, the degree of saturation, and on the properties of the fluid

Hydrometer: An instrument to measure the relative density of fluids based on the concept of buoyancy

Incipient fluidisation: See minimum fluidisation

Inertia: The resistance of any physical object to any change in its velocity

Inertial flow regime: Turbulent flow regime

Influent: The stream of water that enters a treatment unit operation

Interface: The boundary layer between two substances such as between a solid particle and water

Interstitial velocity: The velocity obtained by flow through a particle bed between the particles

Irregular: Lacking any symmetry

Jetsam: Component that ultimately sinks

Laminar flow: A flow which is characterised by fluid particles following smooth paths in layers with little or no mixing and in which rapid fluctuations are absent

Liquid-solid flows: Flows where solid particles are carried by a liquid

Lubrication force: Hydrodynamic force due to the fluid inertia arising from the pressure gradient in the interstitial fluid being squeezed from the space between two particle surfaces

Macropore: GAC pores with widths exceeding 50 nanometres

Mesopore: GAC pores of widths between 2 and 50 nanometres

Micropore: GAC pores with widths not exceeding 2 nanometres

Minimum fluidisation: The state forming the boundary between a fixed bed and a fluidised bed. The point at which the drag force on a particle is equal to its net weight

Minimum fluidisation velocity: The superficial fluid velocity at and beyond which the bed is said to be fluidised

Monodisperse distribution: The particles all having effectively the same size, at least 90% lies within 5% of the median size

Packed bed: A stationary bed of particles up through which a fluid passes at low fluid velocities

Particle: Discrete piece of material

Particle load: The mass of particulates per unit volume of fluid

Particulate: Free suspended solids

Particulate fluidisation: Fluidisation characterised by continuous and uniform bed expansion in general

Particle size distribution: The percentage, commonly by mass and occasionally by number or particle count, in each size fraction into which a sample of granules has been classified such as the percentage retained on each *sieve* in a given size range

Parvoids: Inhomogeneities in the form of bubbles, travelling waves or particle clusters in fluidised beds

Pellet-softening: Reduction of calcium in water through seeded crystallisation in fluidised bed reactors producing calcite pellets

PHREEQC: pH, redox, equilibrium, calculation, program written in C++, to perform a wide variety of aqueous geochemical calculations

Polydisperse distribution: A collective of particles having significantly different sizes, more than 10% deviates at least 5% from the median size

Pore: An opening in granular medium that allows fluid to pass through

Porosity: Ratio of volume of voids included intergranular voids to the total volume

Porous medium: Pores between the particulate phase

Precipitate: An insoluble often irreversible reaction product in an aqueous chemical reaction

Pressure drop: A decrease in water pressure during its flow due to internal friction between molecules of water, and external friction due to irregularities or roughness in surfaces past that the water flows

Probability density function: A statistical expression that defines a probability distribution for a discrete random variable as opposed to a continuous random variable *i.e.* the likelihood of an outcome

Reynolds number: Dimensionless number proportional to the ratio of the inertial force over the viscous force, named after a British physicist and mathematician Osborne Reynolds (1842–1912)

Ripening: Process of granular material conditioning at the beginning of a filter run during where clean media captures particles

Riser: Tall column in which particles are carried, on average, upwards by an ascending fluid

Sand filtration: A frequently used and robust process to remove suspended solids from water. The filtration medium consists of multiple layers of sand with a variety in size and density

Sedimentation: Settling of solid particles in a liquid system driven by gravity

Segregation: Tendency for particles of different physical characteristics (*e.g.* different size, density, and/or shape) to preferentially become more concentrated in different spatial regions

Shape factor: Dimensionless quantities used as a correction factor in image analysis and engineering that numerically describe the shape of a particle, independent of its size

Sieve analysis: A gradation procedure to assess the particle size distribution of a granular material by allowing the material to pass through a series of sieves of progressively smaller mesh size

Slugging fluidisation: During the formation of bubbles in a fluidised bed, they can grow in size until they start to coalesce when the ratio of the bubble to tube diameter is larger than 0.8. The bubble occupies the majority of the bed cross-section and moves in upward direction through the bed

Softening: Water softening is the removal of calcium and optional certain other metal cations dissolved in hard water such as magnesium to reduce the water hardness

Solidity: The area of a particle divided by its convex hull area; the imaginary convex hull around it

Solids: Generic term referring to solid particles

Specific gravity: The ratio of the particle to the fluid density

Surface saturated dry: The condition of a particle in which the surface of the particle is dry *i.e.* surface adsorption is no longer taking place, but the internal voids are saturated with water

Stokes number: Dimensionless number proportional to the ratio of the characteristic particle response time to a characteristic fluid response time, named after an Anglo-Irish physicist George Gabriel Stokes (1819 –1903)

Specific space velocity: The rate in which the water passes the surface area or how often the water is renewed at the water layer above the particle surface *i.e.* the contact area per second per square meter of transfer surface area

Specific surface area: The particle surface area per unit of volume available for crystallisation

Spherical: Surface area of a sphere of the same volume as the particle divides by the actual exterior surface area of the particle

Sphericity: The ratio of the surface area of an equal volume sphere to the surface area of the grain

Straining: Filtration mechanism in which particles are captured at the surface of a filter because they are too large to fit through the pore spaces in the filter

Superficial velocity: The volumetric flow rate of fluidising fluid divided by the cross-sectional area of the bed

Surface roughness: Asperities on the surface of particles increase the frictional resistance to particles that slide past each other due to fluid across the particles

Suspension: Dispersion of solid particles in a liquid, in which they are not soluble

Terminal settling velocity: Or free-fall velocity or the maximum allowable velocity

Turbulent fluidisation: At very high superficial gas velocities, discrete bubbles or slugs are no longer present and the bed is characterised by significant pressure fluctuations

Tortuosity: commonly used to describe curved or twisted paths of fluid flow in porous media

Trickle flow: Liquid-solid-gas systems such as filter backwashing assisted by auxiliary scouring with air

Uniformity coefficient: Measure of the uniformity and variation of granular media; the ratio of the 60th percentile (d_{60}) to the 10th percentile (d_{10}) media sizes as determined by a sieve analysis

Viscosity: The syrupiness and the tendency of a fluid to resist flowing due to internal forces. When the temperature rises, the viscosity decreases

Voidage: Fraction of bed volume or local volume occupied by fluid

Voidage function: A function to express effects of the particle concentration on the drag force on a sphere in a multiparticle to the drag force on a single particle


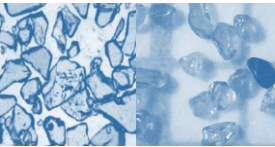

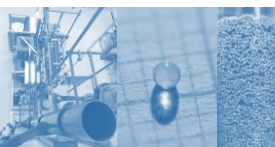
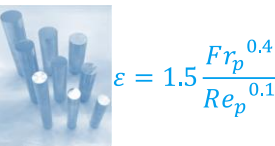


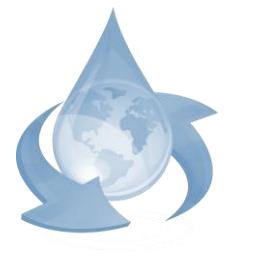
Volume diameter: Diameter of a sphere having the same volume as the particle

Waddell sphericity: Ratio of surface area of a sphere with the same volume as a particle to its actual surface area

Wall effects: Retardation of the settling velocity due to water displacement or wall contact interactions

Water: A chemical substance composed of the chemical elements hydrogen and oxygen H₂O which can occur in gaseous, liquid, and solid states. In this research the liquid phase is important. It is one of the most plentiful and essential of all compounds. Water is tasteless, transparent, odourless and has the ability to dissolve many other substances. The versatility of water is essential for all known forms of life.

Road map

<h2>Problems</h2>	<ul style="list-style-type: none"> - Global water stress - Access to reliable drinking water - Call for more sustainable processes - Increasing complexity of treatment processes 	
<h2>Gaps</h2>	<ul style="list-style-type: none"> - Multiphase flows with irregularly shaped particles - Erratic expansion behaviour of fluidised beds - Consequences for full-scale pellet-softening - Particle-fluid behaviour and modelling challenges 	
<h2>Aims</h2>	<ul style="list-style-type: none"> - Developing hydraulic prediction models - Key performance indicators for pellet-softening - Increase water quality and process reliability - Reduce raw materials, re-use waste materials 	
<h2>Approach</h2>	<ul style="list-style-type: none"> - Exploration classical popular hydraulic models - Conducting accurate pilot-plant experiments - Investigating expansion behaviour of spheres - Synthesising smart voidage prediction models 	
<h2>Results</h2>	<ul style="list-style-type: none"> - Straight forward voidage prediction models - Validated CFD model describing inhomogeneities - Filtration backwash working (ETSW) revealed - Developed online sensor for system analysis 	 $\varepsilon = 1.5 \frac{Fr_p^{0.4}}{Re_p^{0.1}}$
<h2>Solutions</h2>	<ul style="list-style-type: none"> - Terminal settling data spread is now proven - Sand filtration backwash optimisation is possible - Granular activated carbon grains can be modelled - Determining hydraulic state in FBR is promising 	
<h2>Spin-offs</h2>	<ul style="list-style-type: none"> - Pellet-softening chemistry better understood - Valuable expansion data-sets for CFD modelling - Link between research-application-education - Completely new water-hydraulics curriculum 	
<h2>Future</h2>	<ul style="list-style-type: none"> - Water quality improvement and cost reduction - Integral and intelligent water treatment approach - Flexible circular treatment processes achievable - Safe and reliable drinking water for everyone 	

Chapter 1

General introduction

1 General introduction

1.1 Drinking water challenges

Water is the source of life. Our planet holds approximately 1,386 billion km³ of water, but only a small portion of it, 0.007%, is suitable for drinking water purposes. According to the World Health Organization, over 1 billion people globally lack access to safe drinking water supplies, and by 2025 half of the world's population will be living in water-stressed areas (World Health Organization and UNICEF, 2017). To deal with water stress caused by water pollution, increasing population numbers as well as climate change, and to answer the call for a more sustainable society, increasingly complex treatment strategies are required (Filho and Sümer, 2015; van Engelenburg *et al.*, 2021).

Almost all households in the Netherlands have unhindered access to clean tap water and reliable, high quality drinking water thanks to robust treatment plants (de Moel *et al.*, 2006). The Dutch purification philosophy is based on a multibarrier system (van der Kooij *et al.*, 1995; Smeets *et al.*, 2009) that protects against pathogens and (micro)pollutants: harmful constituents are removed from the water using a sequence of sophisticated unit operations (Bolisetty *et al.*, 2019). For decades, process control and optimisation of unit operations were primarily based on operator knowledge and field experience. More recently, water quality improvements have been made and optimal supply has been ensured through the implementation of advanced prediction models and intelligent control schemes (van der Helm, 2007). To cope with the increasingly complex quest for sustainability, the public water utility of Amsterdam, Waternet, focuses on a carbon neutral policy for the entire water cycle. This includes surface water management, wastewater treatment and, last but not least, the supply of drinking water (van der Hoek *et al.*, 2017). Energy recovery and the re-use of waste as raw materials in treatment plants are part of the solution for developing an effective circular economy (Filho and Sümer, 2015). To facilitate the necessary industry wide implementation of current developing research and technology, the transition from linear to circular processes raises the need for considerable adjustments in terms of operations, optimisation, maintenance and control (Edzwald, 2011). This also applies to drinking water treatment processes in which granules are used in multiphase flow systems.

1.2 Multiphase flows and drinking water granules

Multiphase flows are frequently encountered in water treatment plants (Crowe and Group, 2006). Multiphase flow is a type of interactive flow that is composed of more than one distinct phase. These mixtures contain a combination of a liquid and a gas, liquids and solids or a combination of liquids, solids and gas. Examples are ozone gas dosage in water for the oxidation of organic micropollutants, backwashing procedures to remove small particles from filters and seeded crystallisation in fluidised bed reactors to soften drinking water. In this research, the focus lies on liquid-solid systems in drinking water treatment. Four types of multiphase flows are presented in Table 2 below.

Table 2 *Examples of multiphase flows in drinking water treatment processes*

Process	Filtration ¹⁾	ETSW ²⁾	Pellet softening	Flushing
Flows ³⁾	s	l-s	l-s	l-s or l-s-g
Goal	Retain suspended solids	Increase filter packing	Large surface area	Entrainment of remnant fine particles
Problems	Mud balls	Filter ripening	Carry over	Trapped sediment
State	Fixed	Incipient	Fluidised	Terminal
Velocity ⁴⁾	$v_s < v_{mf}$	$v_s \approx v_{mf}$	$v_s > v_{mf}$	$v_s \rightarrow v_t$

1) Rapid sand filtration or activated carbon filtration

2) Extended Terminal Sub-Fluidisation Wash in filters (Chapter 9)

3) l = liquid, s = solid, g = gas

4) s = superficial, mf = minimum fluidisation, t = terminal settling

In many drinking water treatment processes, a wide number of granule varieties is used. Examples are activated carbon grains in adsorption filters (Figure 1A), sand grains (Figure 1B, Figure 1C) and calcite particles in water softeners (Figure 1D). Additional photographs of granules can be found in Annex 1: Photos. When these granules are processed, for example by crushing (Figure 1E), or when they are being replaced with more sustainable alternatives, such as eco-based activated carbon sources (Figure 1A), substantial changes during the treatment processes have been observed and must be taken into account. Often, changes are seen in terms of particle density, size and shape; this affects aspects such as the expansion degree of filter beds during backwash procedures or the expansion degree of calcite grains in a softening fluidised bed reactor. To deal with these changes, a thorough understanding of this phenomena is required in order to increase the resiliency of process control (van Schagen, 2009) and maintain optimal process conditions.



Figure 1A Granular carbon
 $d_p=1.0$ mm



Figure 1B Rapid filter sand
 $d_p=1.1$ mm

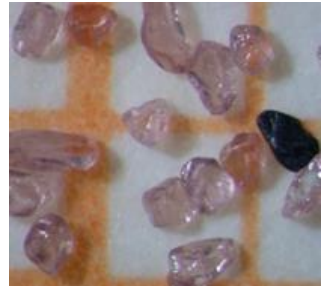


Figure 1C Garnet sand
 $d_p=0.25$ mm



Figure 1D Calcite pellet
 $d_p=1.05$ mm



Figure 1E Crushed calcite
 $d_p=0.50$ mm

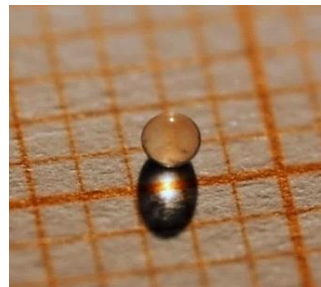


Figure 1F Glass pearl
 $d_p=1.0$ mm

Adapting to substantial changes requires new knowledge derived from many disciplines such as hydraulics, fluid dynamics, mathematics, physics, chemical engineering, particle technology, aquatic chemistry, numerical modelling, system and control and finally process optimisation.

In the literature, models to predict the expansion are traditionally based on perfect spheres (Figure 1F), even though in full-scale operations particles are irregularly shaped. In addition, these granules are naturally polydisperse and sometimes even porous. This makes an accurate prediction of particle expansion behaviour an ongoing challenge. (Michaelide *et al.*, 2017). Water treatment and supply is subject to a host of requirements with respect to water quality, water quantity, sustainability, cost effectiveness, safety, public opinion and innovation drivers (Crittenden *et al.*, 2012). These requirements create an urgent need for the development of accurate prediction models to estimate the expansion degree of particles in liquid-solid expanded beds, as it relates all the mentioned topics.

1.3 Processing granules

Particle size, shape, and density can vary substantially due to granule handling and processing. Two examples can be given to explain adverse consequences. Carbon grains in granular activated carbon filtration are typically manufactured from a raw coal material. When the coal feedstock is substituted by a sustainable material (Naushad and Lichtfouse, 2020) such as wood or coconut shells, the particle density is likely to decrease (Kwiatkowski, 2012). Grains with lower density tend to show a larger degree of expansion during backwashing. This can result in an unwanted flush out of precious grains if the expansion cannot be predicted with accuracy.

In drinking water softening reactors, water hardness is reduced through crystallisation of calcium carbonate on seed particles in a fluidised state (Graveland *et al.*, 1983). These particles grow into semi-spherical calcite pellets and are periodically removed from the reactors. For sustainability purposes, these grains are crushed and partially re-used (Schetters *et al.*, 2015). The ground calcite grains have an erratic shape compared to the almost spherical calcite pellets and consequently show different expansion behaviour in the fluidised bed. The ensuing challenge is to control the expanded bed height and to estimate overall softening performance (Rietveld *et al.*, 2010).

1.4 Classical models to estimate expansion behaviour

In full-scale operational water treatment plants, the expansion degree is determined by means of voidage prediction models. Voidage stands for the fluid phase fraction, *i.e.* the fraction of the bed volume that is occupied by the voids. Popular and frequently applied models are the Richardson–Zaki model, based on the settling of particles, and the Carman–Kozeny model, which is based on flow through assumed channels in porous media.

The underlying principle of the Richardson–Zaki model (Richardson and Zaki, 1954) is the terminal settling velocity of an individual grain, from which the bed voidage can be predicted using an empirical index. The model is reasonably accurate for diffusive gas systems with high voidages and large particle velocities. In water treatment processes however, the voidage is often kept in the proximity of minimum fluidisation conditions, to obtain a high surface area (Seville and Yu, 2016), which leads to a

larger degree of prediction uncertainty. Additional research is required to further the reliability of this popular model.

The Carman–Kozeny model (Kozeny, 1927; Carman, 1937) was derived for flow through capillary tubes in a packed system of particles. The Carman model parameters were predominantly calibrated for gas-solid systems. A small dataset of a mere six data points (Green and Ampt, 1911) was based on a water-solid system. An improved substantiation of this model and its parameters is therefore both relevant and worthwhile.

1.5 Particle size conundrum

In the two models mentioned above, spherical particles are generally taken as a starting point. Since spherical particles are exceptional in full-scale industrial treatment processes, engineers and researchers often apply particle shape factors correcting for the irregularity of granules (Dallavalle, 1948). The well-known Ergun model, for instance, a model based on the Carman model, includes a shape factor for that reason (Ergun, 1952). A typical value of a sand grain's shape factor is around 0.85. Shape factors are subsequently used to correct the calculated pressure drop in fixed bed states. When these models are also used to predict the bed voidage in the fluidised state, the shape factor corrections, from a pragmatic perspective, are omitted and set to 1 (Crittenden *et al.*, 2012). This remarkable correction is confusing, given that the particle size itself remains unchanged. There is enough reason to take note of this when studying these porous media-based models for the effect of irregularly shaped particles in fixed and fluidised beds.

When a fluid flows in upward direction through a particle bed in fixed state, the fluid exerts a certain drag on the particles (Clift *et al.*, 1978). The transition from a fixed bed to a fluidised bed occurs when the pressure drop across a packed bed reaches a constant maximum value, corresponding to the buoyant weight of the particles, at which point the fluid flow equals the minimum fluidisation velocity. For higher flow velocities, the particles start to elevate, and irregularly shaped particles also show changing orientation, realignment, and rearrangement in their packing position. This happens in such a manner that the bed offers the maximum flow passage, *i.e.* voidage to the fluid (Hassett, 1961). Initially, both the flow-through interface availability in the bed, as well as the drag decrease and accordingly increase for larger fluid flows. These phenomena also affect the volume-based voidage

prediction, something that has not been elucidated in the literature and needs to be clarified. In the field of engineering, shape factors are applied to compensate for this aspect in the fixed and incipient fluidisation but omitted for the fluidised state.

In practice, samples of granules are still commonly sieved to obtain information about the particle sizes and distribution for process monitoring purposes. With this method, the morphological properties of the particles are lost. The straightforward acquired particle information, *i.e.* average particle size, is entered accordingly in the voidage or pressure drop prediction model. In practice, this classical *i.e.* conventional method works well for spherical particles, but it is rather inaccurate for irregularly shaped particles. Rod-like particles, in particular, can realign and pass to lower sieves, which gives a distorted view of the actual particle sizes. Irregularly shaped particles experience anisotropic drag in fluidised state, due to the surrounding fluid and interactions with adjacent particles (Mahajan *et al.*, 2018). The altered drag and collision characteristics have a direct influence on the existence of local voids and fluidisation dynamics (Grace, 2020).

It remains unknown to what extent the phenomena mentioned above, negatively or positively determine the chemical crystallisation efficiency in softening fluidised bed reactors in operational settings. In full-scale reactors, a myriad of particles varying in size and shape are stratified in the expanded bed state. Larger spherical calcite pellets migrate due to their larger gravitational pull, while the smaller irregularly shaped ground calcite grains tend to fluidise in the higher regions of the bed (van Dijk and Wilms, 1991). This wide variety of particles in this process also entails a wide range of fluidisation quality classifications. To be able to optimise these complete process units, a thorough fluidisation quality analysis is needed.

1.6 Fluidisation quality

A fluidisation quality classification was described by Geldart (1973) who defined four types of fluidisation behaviour in ambient air. Geldart's classification is expressed in terms of the average particle diameter and the density difference between the particles and the fluid. According to this classification, most of the granules applied in drinking water treatment belong to groups B and D shown in Table 3.

Table 3 Geldart type of fluidisation

Group	Type ¹⁾	Classification	Examples applied drinking water granules
A	Aeratable	Smooth fluidisation	IEX, GAC
B	Sandlike	Bubbly flow	CP, GB, garnet, crystal sand, calcite, GAC
C	Cohesive	Flushing	-
D	Spoutables	Channeling	CP, GB, Nylon, GB, metal balls, RSF

¹⁾ IEX = Anionic exchange polymer resins, GAC = Granular activated carbon, CP = Calcite pellets, RSF = Rapid sand filter grains and GB = Glass beads

However, this classification is based on fluidised particles mainly on the basis of bubbling behaviour. Goossens (1998) proposed a relatively simple industrial tool to classify and predict the fluidisation behaviour of any given fluid-particle system under consideration based on the dimensionless Archimedes number, taking into consideration the determination of the representative particle diameter and of the related shape factor. A greatly simplified classification for liquid-solid fluidisation beds was proposed by Wilhelm and Kwauk (1948), who were the first to propose an empirical criterion for the transition between particulate or idealised fluidisation with complete homogeneity and aggregative or heterogeneous fluidisation (Liu *et al.*, 1996).

There is no general agreement in the literature on the existence of completely homogeneous fluidisation in water particulate systems (Gibilaro, 2001), nor is a refined model given for a precise determination from homogeneous to heterogeneous fluidised state. It is, however, generally assumed that liquid-solid fluidised beds expand homogeneously (Albright, 2009; Michaelide *et al.*, 2017), implying that the particles are uniformly distributed spatially (Yang, 2003). This deceiving assumption owes its popularity to the fact that the large majority of experimental observations has been made visually (Di Felice, 1995). Numerical simulations, that take the presence of particle interactions into consideration, show a rather different picture of the system's behaviour (Di Renzo and Di Maio, 2007). No liquid-solid fluidised bed behaves in a strictly homogeneous manner (Grace, 2020). Inhomogeneities appear, in the form of bubbles, travelling waves or particle clusters (parvoids) depending on the system's physical parameters (Hassett, 1961). What follows this observation, is the question to which extent the fluidisation quality determines the voidage. Many porous media-based models such as Kozeny, Ergun and Carman are based on a drag-Reynolds number relationship, where viscous and inertial forces are considered. Inhomogeneities in the fluidised beds caused by clustering of particles, local voids of water and velocity fluctuations are not taken into account.

1.7 Consequences for full-scale operation pellet-softening

With respect to drinking water pellet-softening, it remains unclear to which degree heterogeneous behaviour, as mentioned above, affects the efficiency of chemical crystallisation, either negatively or positively. The main advantage of seeded crystallisation is that CaCO_3 precipitates onto the surface of grains instead of creating spontaneous unwanted precipitation in the liquid (Burhenne *et al.*, 2017). Larger open water spaces might increase spontaneous precipitation, while a heterogeneous flow regime could have a positive effect on the supply and distribution of chemical reactants in the water phase, due to vigorous agitation of the particles in contact with the fluid.

The scientific literature does not provide governing key performance indicators to determine the overall performance of seeded crystallisation reactors, but process improvement is only possible if multiple key performance indicators can be defined. The focus in this research mainly lies on hydraulic key performance indicators. In addition, some other indicators are also considered, like parameters related to chemical conversion, process control, biological processes and economic factors, among other things.

With a view to pellet-softening, the specific surface area is a decisive indicator that is based on the particle size and voidage. This indicator provides information about the available area for crystallisation purposes per unit reactor volume or in the existing water phase. The pellet size, and consequently, the specific surface area, has a significant influence on performance with respect to the water quality. To keep the super-saturation in the pellet-softening reactor at acceptable levels, the surface area must be known to determine the crystallisation rate over the height of the reactor (van Schagen *et al.*, 2008a). Here, the voidage, particle size and temperature are important (Rietveld, 2005). The disadvantage of the specific surface area, as a key performance indicator, is that no optimum condition, that fits in the operational window, can be found as a function of fluid velocity, water temperature or particle size. Other possible indicators, such as specific space velocity representing the rate in which the water passes the transfer surface area, should be investigated.

1.8 Computational Fluid Dynamics modelling

Popular models like Carman–Kozeny and Richardson–Zaki have a theoretical foundation for their scaling in certain limits, but they are also largely based on empirical fits and assumptions. These models can be used to estimate an average voidage on a macro-scale, but they do not provide any information about voidage on a micro-scale.

Computational fluid dynamics (CFD) is a powerful and popular tool, based on local conservational laws, for the prediction of the fluid dynamics in various types of multiphase systems. CFD enables a proper design of these systems. It is a sophisticated way to analyse the fluid flow behaviour. The availability of affordable high-performance computing hardware and the introduction of user-friendly interfaces have led to the development of CFD packages available for both commercial and research purposes.

In the literature, CFD is focused on gas-solid fluidisation and to a lesser extent on liquid-solid fluidisation. The classical CFD Discrete Element Method (CFD-DEM) approach does not include closures for the lift, virtual mass and basset history forces (Nijssen *et al.*, 2020) which are needed for a complete description of a liquid-solid system. With the help of a reliable model, local information about voidage distribution and wall effects, an analysis can be made of specific surface area. Reliable CFD modelling requires solid training to accurately describe a real reactor. While CFD modelling is promising, the numerical results should always be validated using accurate experimental data.

1.9 Experimental data

In the literature, some expanded bed data can be found (Wilhelm and Kwauk, 1948; Loeffler, 1953), but this data applies to natural grains, e.g. sand, or to glass beads and metal balls that lack morphologic properties. No expanded bed data is available for monodisperse highly spherical grains, nor is there any data available for calcite pellets. In order to calibrate derived models, highly spherical monodisperse grains are essential as a reference; calcite pellets are needed to validate these models for use in a full-scale environment.

1.10 Data-driven modelling

The modelling of full-scale fluidised bed reactors is a challenging affair because of their complex flow behaviour and numerous particle interactions (Cornelissen *et al.*, 2007). Using advanced CFD modelling such as Direct Numerical Simulation, the entire range of spatial and temporal scales can be resolved in the computational mesh, which therefore necessarily contains only a few particles ($N \sim 100$ to 1000). Using a Discrete Element Method model, in which the mesh is actually larger than the particles and therefore flow around the particles is no longer resolved, allows more particles to be simulated ($N \sim 10,000$ to 1,000,000). Regarding full-scale industrial fluidised bed reactors, such as water pellet-softening ($N \sim 10,000,000,000$), CFD simulations could potentially be achievable. However, this can only be done by approximating the particle interactions and particle-fluid drag to an even greater extent. Examples can be observed in Filtered Two-Fluid Models (Cloete *et al.*, 2018). However, from a computational perspective such CFD models are very expensive, making them less suitable for process optimisation and plant-wide control. To cope with constantly changing operational conditions in full-scale installations, there is a demand for less complex models that will increase optimisation and enhance robustness of process controlling. To be more concise; there is an exceeding demand for prediction models that address pressure drop and overall voidage in fluidised beds. In addition to that, these models would need to take the local and global multiphase flow phenomena, occurring in full-scale installations, effectively into account.

Another approach to acquire the average bed voidage is the use of data-driven models, based on accurate experimental data, which can also be used for straightforward application. The voidage can be predicted with an empirical data model that include n^{th} -order polynomials. The corresponding polynomial coefficients are based on the fluid and particle properties, *i.e.* flow, temperature, diameter and density. Drag relations in fluidised beds are based on hydraulic dimensionless numbers, in which the Reynolds number is mostly used. Similarly, data-driven models can be based on dimensionless numbers. In order to incorporate more hydraulic information of the system, other dimensionless numbers can also be considered, such as the Archimedes or Froude number.

To conclude, there are instances where a trade-off must be observed between the advantage of simple mathematical expressions, convenient programmable in industrial process automation environments, and the disadvantage of losing

scientific depth and nuances. Data-driven models could provide a solution in case a myriad of particles occurs with different sizes, shapes and densities that would quickly lead to very complex modelling. If accurate experimental data can be obtained, model parameters can easily be fitted. The disadvantage of this method is that it will no longer work in the event of drastic process change, such as the use of different grain materials.

1.11 Full-scale water treatment considerations

Granular material is often applied in full-scale water treatment plants. In softening fluidised bed reactors, a complex modelling situation arises due to a variation of particle properties in different sections over the height of the reactor. Other factors that increase this complexity include, but are not limited to, aquatic and chemical reactor phenomena, water and chemical dosage through nozzles and the degree of mixing within the particle bed, biological activities, process fluctuations with the risk of unwanted flushing material and/or fixed bed state conditions and, in general, process scale-ups.

In filter backwash procedures such as rapid sand filters applied in drinking water treatment plants, process performance, *i.e.* in terms of effluent water quality, is highly dependent on the hydraulic condition of the process. In this unit operation, a third phase is involved. Besides water, air is decisive too. In carbon filtration, another complexity should be mentioned. Granular activated carbon (GAC) grains have pores for adsorption purposes, and besides being porous, they are also highly irregularly shaped and polydisperse. This makes an accurate voidage prediction even more difficult.

The complex aspects mentioned above are relevant, but the gas phase remain unaddressed in this research. In order to assess overall process performances, accurate hydraulic models must first be developed based on a thorough understanding of the principles behind the liquid-solid multiphase flows.

1.12 Knowledge gaps and research questions

It is noteworthy that several knowledge gaps exist on some relevant subjects. These subjects are discussed in the following paragraphs and include the classical Richardson–Zaki model, terminal settling, particle orientation, drag relations, CFD, data-driven modelling, expansion characteristics, soft sensors and finally the relationship between application, research and education.

1.12.1 The classical Richardson–Zaki model

- The popular Richardson–Zaki model is based on the assumption of homogeneous expansion through a logarithmic relationship between the voidage and superficial fluid velocity, and the assumption that the maximum voidage coincides with the terminal settling velocity of individual grains. However, the voidage in water treatment processes lies in the vicinity of incipient fluidisation.

? Knowledge gap: It is not clear whether this model is suitable for voidage prediction covering the full fluidised state range, starting from terminal settling to minimum fluidisation.

► Research questions: Is the Richardson–Zaki model accurate for predicting the minimum fluidisation velocity accurately and how to derive an index formula with a more hydraulic meaning?

1.12.2 Terminal settling

- The Richardson–Zaki model uses the maximum superficial velocity, *i.e.* the terminal settling velocity, for the dilute state. In the literature, many prediction equations are given. The starting approach is the standard drag curve where the dimensionless drag coefficient is plotted against the particle terminal Reynolds number for a very wide range:

? Knowledge gap: Based on the standard drag curve, where the dimensionless drag coefficient is plotted against the particle terminal Reynolds number for a very wide

range, it not evident that the terminal settling velocity of natural particles in water can be predicted accurately.

▶ Research questions: Which model is suitable for an accurate prediction of drinking water-related granules and what is the extent of spread around an average estimated value? A follow-up question asks whether there are any insights to be gained in terms of robust process designs and adequate process optimisation for fluidisation and sedimentation of natural granules considering the influence of natural variations of the settling velocity when using predictive models.

1.12.3 Particle orientation in the vicinity of incipient fluidisation

- When the superficial fluid velocity is increased from a fixed to a fluidised state in a bed of granules, the estimated Kozeny coefficient, according to the Carman–Kozeny model, is assumed to remain constant.

? Knowledge gap: The literature does not provide an explanation why this Kozeny coefficient, assumed to be constant, is not constant for irregularly shaped particles.

▶ Research questions: Can the classical way of representing the drag, using logarithmic scales, be modified to reveal hidden information about particle rearrangements, and can academic insights be obtained regarding the altering available surface for flow-through in other water treatment processes?

1.12.4 Drag relations in fluidised beds

- The overall fluidised bed voidage is a crucial process parameter which can be estimated by means of drag relations. Traditionally, in drag relations, the emphasis of the dimensionless standard drag coefficient, defined as a function of the Reynolds number, is focused on the turbulent flow regime and less on the laminar and transition flow regimes

? Knowledge gap: A traditional drag plotted against the particle Reynolds number results to apparent and persistent data dispersion which cannot be explained.

▶ Research questions: Is it possible to incorporate fluidisation quality, taking into account laminar-turbulent as well as homogeneous-heterogeneous fluidisation

characteristics? In addition, can the drag relation and voidage prediction accuracy for liquid-solid fluidisation be improved by including the Froude number in addition to the Reynolds number?

1.12.5 CFD

- Computational fluid dynamics modelling holds great promise for fluidised bed modelling and aims to discover the main mechanisms of interest for accurately predicting characteristics of fluidised beds for optimisation and improvement reasons. Unsteady liquid-solid behaviour in fluidised beds can only be observed through transparent walls of experimental set-ups.

? Knowledge gap: It is impossible to analyse particle-fluid behaviour inside a fluidised bed.

► Research questions: In this respect, can the numerical model developed by Nijssen *et al.* (2020) be validated using expanded bed data experimentally obtained in this research, and accordingly, is it possible to confirm the existence of local voids and voidage distribution?

1.12.6 Data-driven modelling

- Many empirical and semi-empirical models are available for predicting the voidage in fluidised beds. A data-driven model can also be used to achieve comparable or better results.

? Knowledge gap: It is unclear if traditional and frequent applied models have a higher accuracy compared to data-driven models based on experimental data.

► Research questions: Are experimentally determined expansion characteristics suitable for modelling purposes? Furthermore, can the voidage be estimated accurately using straightforward polynomials, or are other data-driven and symbolic regression models suitable for generating an accurate prediction model? Accordingly, can these voidage prediction models be used to determine reactor key performance indicators to be used in full-scale pellet-softening reactors?

1.12.7 Expansion characteristics of carbon granules

- Granular activated carbon filtration is a very important unit operation applied in full-scale drinking water treatment plant. Periodically, filters have to be cleaned through a backwashing procedure.

? Knowledge gap: The literature does not provide general expansion prediction models for GAC grains which are polydisperse, irregularly shaped and porous.

► Research questions: With respect to determining particle properties, which method can be used to measure the morphological and particle properties of GAC grains precisely? Accordingly, how can expanded bed datasets be acquired as a function of fluid velocity and viscosity?

1.12.8 A soft sensor for the fluidised bed state indication

- Process control and optimisation of fluidised beds in full-scale pellet-softening reactors is complex due to a large variation in granule types. Therefore, the processes are often individually controlled, maintained and improved on the basis of *rules-of-thumb*, field experience of operators and sensitive pressure drop sensors.

? Knowledge gap: No straightforward sensor exist to obtain longitudinal hydraulic states in pellet-softening reactors.

► Research questions: Is a cylindrical object submerged in the fluidised bed suitable for measuring the weight that is considered representable for the buoyant force and whether this can be used as a soft-sensor to determine the bed voidage. As a result, can the particle size profile over the height of the whole fluid bed be predicted using fluid properties and voidage?

1.12.9 Relationship Application-Research-Education

- Today's world is facing a number of major issues that require effective and sustainable long-term answers, such as the need to address global water stress, the growing lack of precious resources and the call for a circular economy. With an increasingly complex society and in view of the complexity this entails in terms of

intertwining and overlapping problems, engineers of the future may well be the right people to provide sustainable solutions.

? Knowledge gap: In terms of agendas and programmes, the alignment between educational institutions and the professional field is challenging. Actors in the process industry strive to find solutions in order to make highly complex transitions from linear to more circular-oriented processes, but talented graduate engineers are not automatically well prepared for addressing these questions where advanced technical skills are required. The chemical engineering curriculum may be improved by enhancing students' understanding and performance through merging research, education and operations via problem-based learning. To this end, concrete and effective technical training equipment is needed to prepare engineering students for their future tasks. As yet, there is no effective low-cost multiphase flow fluidised bed set-up that represents a full-scale drinking water treatment process for sustainability studies in an environment where academia, practice and education can meet.

► Research question: Is the liquid-solid fluidisation expansion column suitable for gaining accurate experimental data that in turn are suitable for academic research purposes, for training engineers and for helping them develop next-century skills?

1.13 Approach

The preliminary approach of the current research study was to examine the most popular and frequently applied prediction models available in the literature. Accordingly, precise experiments were executed to obtain highly accurate expanded bed data for drinking water-related granules supplemented with advanced laboratory experiments. The numerical results, obtained with the popular and frequently applied models, were compared with the experimental data to examine their prediction accuracy.

Based on the experimental data, the opportunity arose to study the changes in drag caused by particle rearrangements in fixed bed states. Furthermore, based on newly gained insight, fluidisation models were developed to improve the prediction accuracy of voidage in liquid-solid fluidised beds. Accordingly, expansion data was used to calibrate the model parameters as well to validate the accuracy of the models. Symbolic regression techniques and non-linear regression were used to support the modelling. Computational fluid dynamics modelling was compared with experimental results, using a high-speed camera. Additionally, particle-fluid

behaviour inside a fluidised bed was investigated. Based on highly accurate prediction models, development of a soft-sensor was started to obtain a voidage and particle size distribution across the reactor height which enabled the development of key performance indicators.

1.14 Aim

The aim of this research is to develop hydraulic models that are suitable for drinking water treatment plants, in particular for softening in fluidised bed reactors. Accordingly, the focus is on calibrating these prediction models using reliable experimental data obtained in accurate experimental set-ups. Furthermore, it is intended to use these models to develop more advanced key performance indicators to acquire hydraulics process states.

1.15 Outlook

Each chapter in this dissertation is based on a published article or one that has been submitted for publication. Since each chapter covers different subjects, the relationship between the chapters is elaborated below.

Chapter 1 starts with the general context and sets the general framework for this research.

Chapter 2 provides insight into the background basic theory that forms the fundament for this research. In addition, the similarity between drag through a (hollow or porous) object and around objects is explained. As fluidisation is a prominent topic in this research, the chapter also elaborates on the basics of fluidisation theory.

Chapter 3 lists the materials and methods used in the study and describes experimental set-ups and devices. The chapter also presents columns for fluidisation experiments, for terminal settling experiments and for emerging objects. The analyses of particle and fluid properties are

explained, as is the methodology for conducting fluidisation expansion experiments aimed at gaining accurate expanded bed data.

- Chapter 4** discusses why terminal settling does not stand on its own. In successive chapters, it will be made clear how the terminal settling velocity must be known in order to estimate the voidage. In this chapter, the occurrence of natural spread around an approximated value is discussed, crucial information for engineers and researchers. The various causes of spread are elucidated in detail.
- Chapter 5** is dedicated to the most common voidage prediction model by far: the Richardson–Zaki model. Voidage prediction is important in this research and therefore this model should be examined in great detail for its applicability in water treatment processes.
- Chapter 6** discusses the need to adapt the Carman–Kozeny model. This model is based on a drag relation with a dependency of the dimensionless Reynolds number, and this chapter will elucidate how observed heterogeneous phenomena in fluidised beds can be captured in this model by including the Froude number.
- Chapter 7** considers computational fluid dynamics modelling as the most promising tool for discovering multiphase flow secrets. Based on a new CFD model, experimental results are validated and local voids and unsteady parvoids are shown.
- Chapter 8** focuses on industrial full-scale reactors, which are still dependent on straightforward effective voidage prediction models. Based on accurate expanded bed data, empirical and semi-empirical models are compared with the most frequently applied prediction models.
- Chapter 9** deals with the Carman–Kozeny model, a highly popular model in both porous media and civil engineering. The foundation of this model is the drag exerted on particles by the surrounding fluid. This chapter demonstrates the effect on visibility by modifying the way in which drag

is presented. It will be made clear that irregularly shaped particles show orientation from the fixed to fluidised bed.

Chapter 10 concentrates on granular activated carbon filtration, a very important water treatment process. Filters must be cleaned through backwashing the filter beds. Expanded bed prediction is complex due to the non-spherical and polydisperse properties of the carbon grains. The modelling results will be evaluated with the experimental data.

Chapter 11 is based on the prediction models that have been developed; it will be shown how a soft sensor based on the principles formulated by Archimedes is suitable for predicting the hydraulic state in a fluidised bed.

Chapter 12 is the final chapter in this dissertation. It synthesises Chapters 1 to 11 and combines their conclusions and recommendations. Consequences of these are discussed with a view to the possibilities and opportunities for future operational process optimisation as well as the control and design of drinking water treatment plants.

Chapter 13 in this chapter overall conclusions are drawn from Chapters 1 to 12. The consequences of the conclusions are discussed for liquid-solid fluidisation processes applied in drinking water treatment plants.

Chapter 14 finally, an overview of related ongoing research is given.

Chapter 2

Basics

“The beginning of knowledge is the discovery of something we do not understand.”

(Frank Herbert, 1920 – 1986)

2 Basics of fluidisation and pellet-softening

This chapter elucidates the basics of fluidisation and pellet-softening. Accordingly, hydraulic states and flow resistances relevant for pellet-softening fluidised bed reactors are explained. These hydraulic states consist of flow through a pipe, flow around a fixed object, and flow through a bed of particles, assuming the bed is a collection of pipes. These hydraulic states follow similar principles: laminar flow at low fluid velocities, where the drag is inversely proportional to the Reynolds number, to turbulent flow at high fluid velocities, where the drag becomes constant.

2.1 Introduction to fluidisation

2.1.1 Applied fluidisation processes

Liquid-solid fluidisation is an operation by which a liquid flows continuously through a bed of solid particles which is converted from a static, solid-like state to a dynamic, fluid-like state. In the fluidisation state, the interaction between the fluid phase and solid particles (drag force) balances the gravity acting on the particles, causing the particles to float and move freely in the reactor. This leads to a large available surface area per unit volume and enhances the mixing properties. Liquid-solid fluidisation is frequently encountered in industrial practice in a variety of water treatment processes (Di Felice, 1995; Epstein, 2003; Yang, 2003; Grace *et al.*, 2020) such as:

- Backwashing of filter media (*e.g.* rapid sand filtration)
- Crystallisation (*e.g.* calcite, struvite (magnesium ammonium phosphate))
- Adsorption (*e.g.* granular activated carbon filtration)
- Particle classification and separation (*e.g.* flushing fines from seeding materials)
- Flocculation (*e.g.* in pre-treatment water processes: removal of suspended solids)
- Ion exchange (*e.g.* water softening)

Liquid-solid fluidisation has many other applications, for instance in heat exchangers, thermal energy, leaching and washing, electrolysis, incineration, fertiliser production, petrochemical processes, granulation, catalytic cracking, pharmaceutical

applications, combustion, gasification, pyrolysis, food processing, biochemical processing and transport.

In fluidised bed processes, the particle-fluid interactions and chemical reactions involve a large number of variables and challenges, making modelling the process (e.g. for optimisation) extremely complex. Challenges in industrial full-scale fluidisation reactors, for instance, are caused by irregularly shaped particles, wide particle size distributions and fluid distribution in reactors, all of which affect the hydrodynamics. There is no universal model for an accurate description of the process. For this reason, fluidised bed modelling and simulation to predict and analyse different process states is an active field of research. In the literature, many models are proposed and discussed which describe the behaviour of the particle-fluid interactions and behaviour in multiphase flows (Davidson *et al.*, 1985; Kunii and Levenspiel, 1991; Gibilaro, 2001; Yang, 2003; Rhodes, 2008; Michaelide, 2017).

2.1.2 Fluidisation states

The following states are encountered when a fluid flows with increasing rate through a particle bed (Figure 2):

1. Filtration and flow through a packed bed
2. Minimum fluidisation at maximum pressure drop
3. Fluidisation and flow through a bed of floating grains
4. Flushing and terminal settling

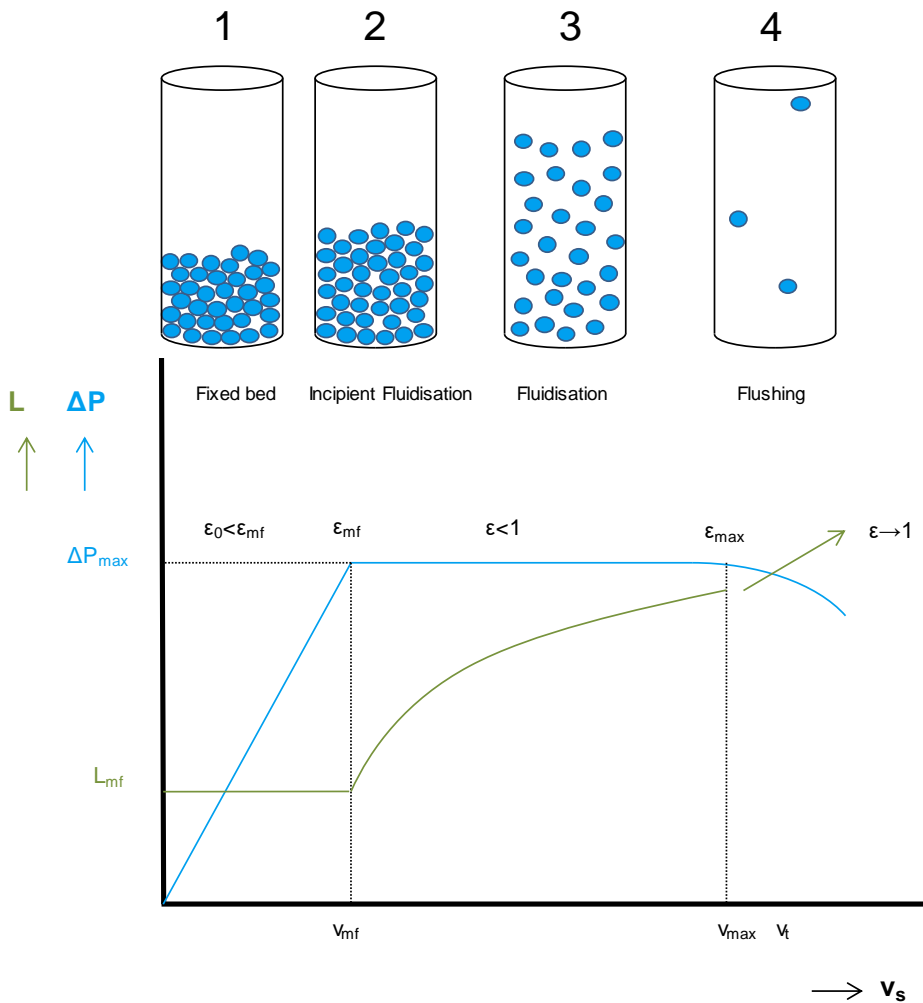


Figure 2 Different fluidisation states in a particle bed for increasing fluid velocity conditions, voidage and pressure drop.

1/4 Filtration and flow through a packed bed

The first representation in Figure 2 describes the particle bed in a fixed state. When a fluid flows in an upward direction through a packed bed, the pressure drop ($\Delta P/L$) in the bed will increase with the fluid velocity as the hydraulic resistance increases (area 1 in Figure 2). In this state, the upward flow provides insufficient force to

counteract the gravitational force, causing the particles to remain stationary in the particle bed.

2/4 Minimum fluidisation at maximum pressure drop

In the second regime, the upward flow has sufficient force to support the grains. The pressure drop will rise to a maximum value. The bed is then on the cusp of fluidisation (point 2 in Figure 2). The bed is both fixed and fluid. The superficial velocity at which this occurs is called the minimum fluidisation velocity v_{mf} . The maximum pressure drop over a fixed bed is equal to the buoyant weight (apparent weight) of the particle bed (Di Felice, 1995; Crowe and Group, 2006; Michaelide *et al.*, 2017).

$$\frac{\Delta P_{max}}{L_{mf}} = (\rho_p - \rho_f)g(1 - \varepsilon_{mf}) \quad (\varepsilon > \varepsilon_{mf}) \quad (22)$$

Where ρ_p is the particle density, ρ_f is the fluid density, g the gravitational acceleration, L the bed height and ε the voidage or fraction of the total volume of the bed which is free space available for the fluid flow. When the fluid velocity is gradually increased beyond the incipient minimum fluidisation, the pressure drop shows a small increase before it drops again to become constant. The amount of pressure drop increase depends on the previous history of the bed. A determining factor here is whether the bed is a well-settled i.e. more dense bed or a well-expanded and loose settled bed (Gupta and Sathiyamoorthy, 1999). This pressure increase does not occur when the fluidisation velocity is decreased, a process called de-fluidisation.

3/4 Fluidisation and flow through a bed of floating grains

In the fluidised state, the particles are fully supported by the fluid. With increasing fluid velocity, the pressure drop across the bed will remain constant as there is no more gravitational resistance for the increasing drag force to overcome. Instead, the effect of increasing fluid velocity is an expansion of the bed of particles (region 3 in Figure 2). The bed expansion E , defined as the relative increase in bed height, can be used to calculate the voidage ε from a known initial fixed bed voidage ε_0 .

$$E = \frac{L}{L_0} - 1 = \frac{\varepsilon - \varepsilon_0}{1 - \varepsilon} \quad (23)$$

$$\varepsilon = 1 - \frac{L_0}{L}(1 - \varepsilon_0) \quad (24)$$

4/4 Flushing and terminal settling

As the liquid velocity is increased further, a point is reached at which the particles are entrained by the liquid flow (region 4 in Figure 2). This occurs when the liquid flow velocity is larger than the sedimentation velocity of a single particle, also known as the terminal settling velocity.

2.2 Fluidisation in practice: pellet-softening

Liquid-solid fluidisation is frequently encountered in a variety of water treatment processes. A specific application is pellet-softening. Central softening is widely used in large-scale drinking water production plants in the Netherlands, not only for its benefits to public health and client comfort but also for economic and environmental reasons (Beefink *et al.*, 2021). Almost 500 million cubic meters of water are softened annually by means of seeded crystallisation in fluidised bed reactors. In the pellet-softening reactor (Figure 3), calcium carbonate (CaCO_3) is removed by utilising the principles of fluidisation and seeded crystallisation (van Dijk and Wilms, 1991). Hard water is treated in an up-flow fluidised cylindrical bed reactor with a superficial velocity of 60-120 m/h. A strong chemical base, often caustic soda, is dosed and mixed well in the reactor to increase the pH level of the water and to obtain supersaturated conditions (Graveland *et al.*, 1983). By doing so, the calcium carbonate equilibrium is altered, causing calcium carbonate to precipitate. Seeding materials, such as garnet sand or crushed calcite, are introduced and fluidised by the upward stream, providing a large surface area for a controlled and efficient crystallisation process.

Calcium carbonate crystallises on the surface of the seeding material, thereby forming pellets. The crystallisation on the seeds mainly occurs in the lower region of the reactor (van der Veen and Graveland, 1988). Due to the crystallisation, the calcite pellets grow and migrate to the bottom of the reactor. When a defined grain

size threshold is exceeded, a certain portion of the pellets is extracted from the bottom of the reactor (1-2 mm). Garnet sand (0.25 mm) or crushed calcite pellets (0.5 mm) are used to replenish the removed particles at 1-meter height of the reactor. The softening unit is an installation consisting of several cylindrical reactors in parallel. Each of the reactors has a diameter of 2.6-3.0 m and a height of 5.5-6.0 m. The influent has a calcium content of 1.8-2.4 mmol/L. The target hardness of the softened effluent is 1.4 mmol/L after the addition of caustic soda (25% w/w NaOH), but lime or soda are also choices of used chemicals. Different types of reactors can be applied for softening, such as cylindrical reactors with flat bottom called the *Amsterdam reactor* (van der Veen and Graveland, 1988) and reactors with varying diameters over height with conical bottom part and tangential inlet (Groenendijk *et al.*, 2008). The bottom of a typical *Amsterdam Reactor* has a distinct plate containing 35 nozzles per m² which separate water and NaOH at the bottom (Figure 4). The dosing point and incoming water jet create turbulence at the bottom of the reactor for rapid mixing. NaOH flows upward through small channels in the nozzles. In the upper part of the reactor, axial mixing takes place. A stratification process occurs when larger calcite pellets migrate to the bottom of the reactor and the smallest particles move to the top of the fluidised bed. The softening process is elucidated in greater detail in Chapter 8. Photographs of full-scale reactors can be found in the Supplementary material (Section 2) of (Kramer *et al.*, 2020b).

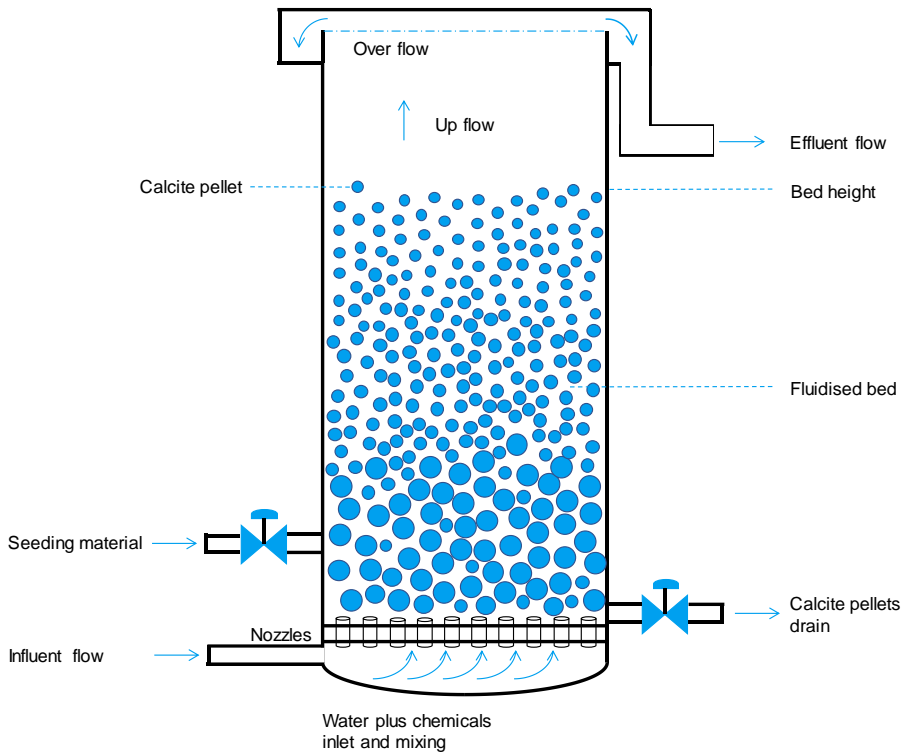


Figure 3 Schematic overview of a pellet-softening reactor with hard water influent, soft water effluent, chemical dosing, seeding material dosing and a fluidised bed of calcite pellets and seeding material

- Three flow phenomena can be defined in the pellet-softening fluidised bed reactor:
- Empty tube flow
 - Terminal or maximum settling velocity (entrainment or flushing) of individual grains
 - Flow through an agglomeration of particles and water (fluidisation)

The different flow phenomena and flow regimes are presented in Table 4, and discussed in the following section.

Table 4 Flow phenomena and flow regimes in a pellet-softening fluidised bed reactor

Flow phenomenon	Media	Flow regimes
Tube flow	Water	Turbulent
Terminal settling	Water, granule	Laminar + transitional
Fluidisation	Water, granules	Laminar + transitional

2.3 Flow phenomena

2.3.1 The Reynolds number

In the flow of liquids and gases, a distinction is made between laminar flow (smooth non-crossing flow paths) and turbulent flow (oscillations, vortices and eddies with crossing flow paths). For flow through a tube, the transition from laminar to turbulent is very sudden with increasing fluid velocity (Munson *et al.*, 2020). For flow through a particle bed, however, the transition is very diffuse (Bird *et al.*, 2007).

The Reynolds number is a dimensionless quantity, commonly used to distinguish between turbulent and laminar flow patterns and to predict how a fluid will behave under different circumstances. The Reynolds number is defined as the ratio of inertial forces to viscous forces according to Equation (1).

$$Re = \frac{\rho_f v_s D}{\eta} \quad (1)$$

Where η is the kinematic viscosity and v_s the superficial fluid velocity. To define the Reynolds number, it is important to decide on the relevant length scale. For flow through a cylinder, in Equation (1), the tube diameter D is used. When considering flow around objects, the hydraulic diameter D_H is taken, using the cross-sectional area and the wetted perimeter. Other situations require the use of other Reynolds numbers that include different hydraulic diameters, velocities and the bed voidage or open void fraction (Table 5).

Table 5 Hydraulic diameter used in definition of Reynolds number

Flow pattern	Velocity	Hydraulic diameter	
Tube flow	Linear flow rate	Tube diameter	$D_H = D$
Terminal settling	Terminal settling velocity	Particle diameter	$D_H = d_p$
Fluidisation	Superficial velocity	Voidage	$D_H = \varepsilon / (1 - \varepsilon) \cdot d_p / 6$

2.3.2 Flow through tubes

In the field of engineering, Moody's diagram (Moody, 1944) is a well-known graph relating the dimensionless friction factor f , Reynolds number and dimensionless surface roughness e/D for a fully developed flow in a round tube. This diagram, given in Figure 4, can be used to predict the pressure drop given the flow rate, or *vice versa* (Munson *et al.*, 2020). The laminar flow regime ($f = 64/Re$) declines fast for increasing Reynolds numbers; the emphasis lies on turbulent flow regimes where the friction factor becomes independent of Reynolds number but dependent on e/D , and is usually shown on a logarithmic scale.

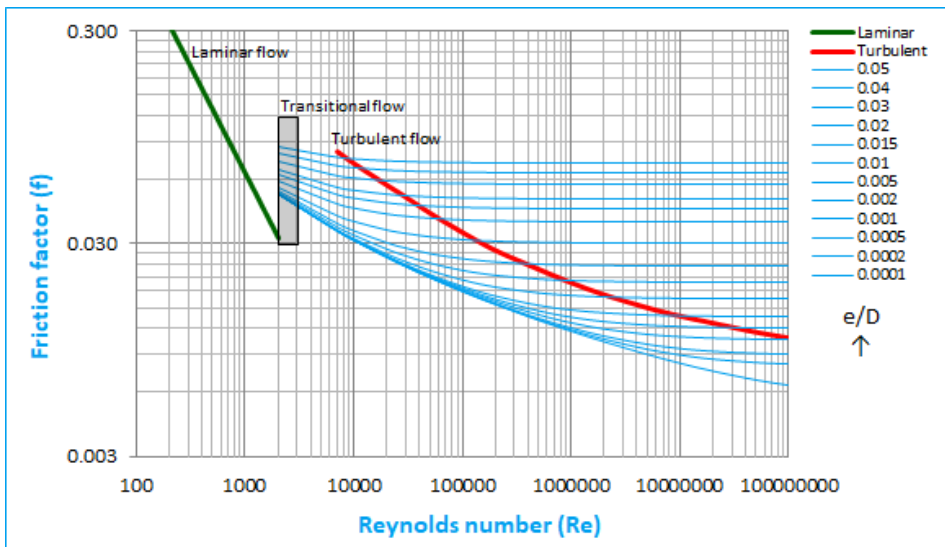


Figure 4 Moody's diagram for flow through pipes (Moody, 1944). The green line represents laminar flow and the red line represents complete turbulence.

2.3.3 Flow around objects

External fluid flows past objects involve a variety of fluid mechanical phenomena and has a wide variety of engineering applications (Munson *et al.*, 2020). The character of the flow field depends on the shape of the object. Even the simplest shaped objects, such as a sphere, produce fairly complex flows (Batchelor, 2012). For a given shaped object, the flow pattern and related forces are highly dependent on

various factors such as object size, shape, orientation, velocity and fluid properties (White, 2016).

The forces on an individual particle in upward fluid flow are the same as the ones determining the terminal settling velocity (Grace *et al.*, 2020), namely fluid-particle interactions (*e.g.* drag, added mass, Basset, lift, magnus) and forces imposed by external fields (*e.g.* gravitational, magnetic). For this *basics* Section, only drag, buoyancy and gravitational forces are considered. The particle will settle when downward forces predominate, be flushed out when upward forces predominate, or remain suspended or fluidised when the forces are balanced. The downward force is the gravity, while the upward force is the sum of the buoyant weight of the particle and the drag caused by the (local) fluid flow. The sum of gravitational, buoyant and drag forces acting on a particle is represented by Equation (25) (Clift *et al.*, 1978).

$$\sum F = F_g - F_b - F_d \quad (25)$$

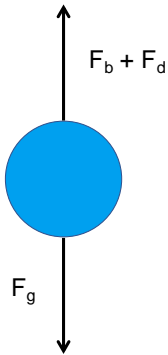


Figure 5 Forces acting on settling particle

With a projected surface area A_p in the direction of the gravitational field, Equation (25) can be rewritten as follows (Newton, 1726):

$$\sum F = \rho_p V_p g - \rho_f V_p g - C_{D\frac{1}{2}} A_p \rho_f v_t^2 \quad (26)$$

If a particle starts at rest, it will accelerate due to an imbalance in forces (Crittenden *et al.*, 2012) as the particle velocity increases, and the drag force increases until the vertical forces are balanced (*i.e.* $\sum F = 0$). At that point, the particle reaches a

constant velocity known as its terminal settling velocity v_t , with a corresponding terminal Reynolds numbers, as shown in Equation (3).

$$Re_t = \frac{\rho_f v_t d_p}{\eta} \quad (3)$$

Figure 6 shows the standard drag curve for terminal settling of a spherical particle. In the viscous dominated (Stokes) regime, an exact calculation shows that the drag coefficient is given by $C_D = 24/Re_t$ (Clift *et al.*, 1978). In the inertia dominated (Newtonian) regime (Newton, 1726), the drag coefficient of a sphere can be approximated by a constant: $C_D = 0.43$. This constant value implies that the efficiency of energy transfer from the fluid is independent of the settling velocity. This occurs at high terminal Reynolds numbers in the turbulent flow regime, and is caused by boundary layer separation, forming wakes and vortices behind a spherical object. In Figure 6 this is represented by a horizontal line. At extremely high Reynolds numbers, super-critical flow separation occurs (White, 2016), causing the drag to decrease further. This phenomenon lies outside the scope of our current research. For both the Stokes and Newtonian regimes it is easy to find an explicit analytical expression for the terminal settling velocity of a sphere. However, in the intermediate region between Stokes drag and Newtonian drag, a transitional regime exists in which both viscous and inertial forces matter. The transitional regime applies to many water treatment processes. Many empirical and semi-empirical equations are given in the literature to estimate the drag coefficient. A very common and still popular equation was given by Schiller and Naumann (1933). Many researchers have proposed improvements covering the entire Reynolds range (Morrison, 2013). In this regime however, calculating the terminal settling velocity is not as straightforward, and numerical methods are required. Moreover, in water treatment processes, granules usually have an irregular shape, which leads to an inaccurate prediction of the terminal settling velocity. A more comprehensive account of drag and terminal settling characteristics is presented in Chapter 4.

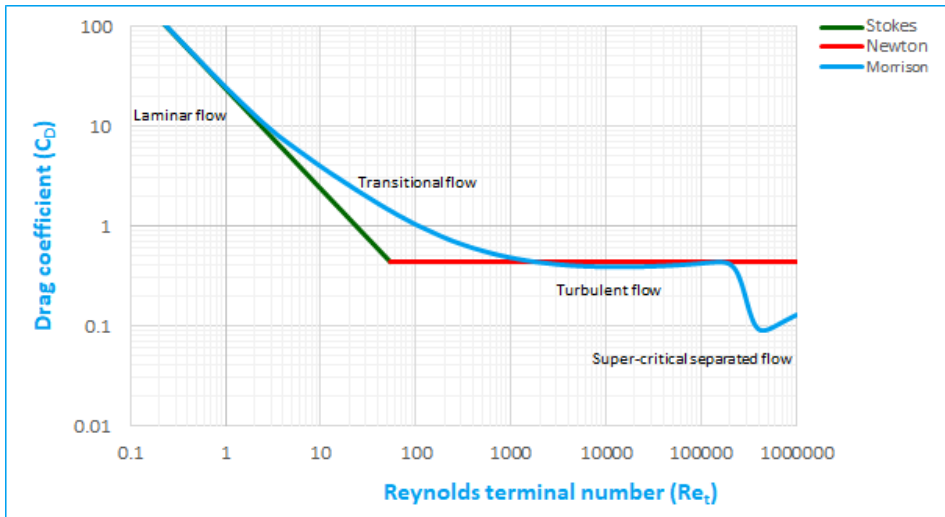


Figure 6 Standard drag curve for terminal settling of a sphere (Stokes, 1850; Newton, 1726; Morrison, 2013).

2.3.4 Hindered settling and fluidisation

Stokes, transitional settling and Newtonian settling all define terminal settling as the unhindered descent of an individual particle in an infinitely large space. In practical applications in water treatment processes, however, this approach falls short (Camp, 1946). Usually, particles have interaction with other particles or with the container wall that considerably affect the settling behaviour. Settling that takes these interactions into account is known as hindered settling (Crittenden *et al.*, 2012), and is usually relevant when particle volume concentration is larger than approximately 1 percent (Edzwald, 2011). In a fluidised bed reactor, sedimentation and fluidisation are hydrodynamically similar. In fluidisation, the particles are sustained in suspension by the upward fluid flow and experience no net movement, whereas in the sedimenting suspension, the particles move downwards (Coulson and Richardson, 1957); (Batchelor, 1988). Additional details are given in Chapter 5. The terminal Reynolds number (according to Equation (3)) is related to the maximum velocity of an individual grain relative to the fluid. For hindered settling, we instead make use of the particle Reynolds number (Equation (4)), in which the terminal settling velocity is replaced by the superficial fluid velocity (Yang, 2003).

$$Re_p = \frac{\rho_f v_s d_p}{\eta} \quad (4)$$

For very dense particle suspensions the fluid needs to find its way through a labyrinth of voids between particles, which may be viewed as a series of tortuous tube-like channels. This analogy between flow through a tube and flow through voids in a bed of particles was first proposed by Kozeny (1927). On the basis of this analogy, a modified particle Reynolds number (Equation (6)) was defined, this time using the hydraulic mean diameter of a *channel* and the interstitial fluid velocity, which makes the equation applicable to the flow conditions through particle beds (Carman, 1937; Chhabra and Basavaraj, 2002; Crittenden *et al.*, 2012).

$$Re_\varepsilon = \frac{\rho_f v_s d_p}{\eta} \frac{1}{1 - \varepsilon} \quad (6)$$

Analogous to tube flow and terminal settling, a dimensionless drag coefficient can be defined for packed and fluidised beds by relating the pressure drop to the superficial flow velocity. This so-called friction factor f_T is often plotted against the modified Reynolds number Re_ε , as illustrated in Figure 7.

Under laminar flow conditions, the friction factor is described as $f_T = 180/Re_\varepsilon$, proposed by Kozeny (1927) based on work by earlier researchers (Darcy, 1856; Blake, 1922). For fully turbulent flow regime conditions, the friction factor becomes a constant $f_T = 1.75$, as proposed by Burke and Plummer (1928). Neither completely laminar nor completely turbulent flow conditions occur in water treatment processes (Crittenden *et al.*, 2012). Therefore, drag relations given by Ergun (1952) and Carman (1937) for the transitional flow regime were based on Forchheimer (1930).

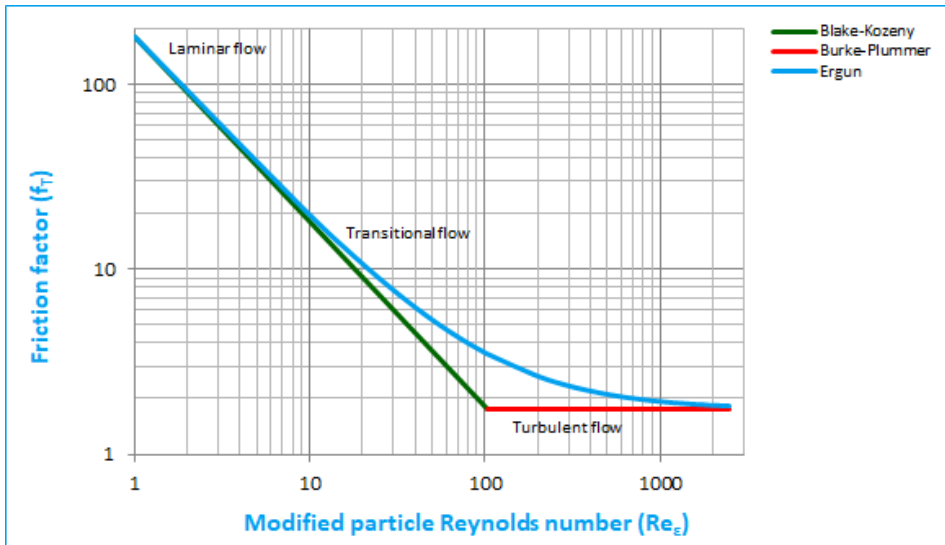


Figure 7 Friction factors for packed and fluidised beds (Blake, 1922; Kozeny, 1927; Burke and Plummer, 1928). The superposition of laminar and turbulent flow over the entire Reynolds number range was proposed by Ergun (1952).

The most commonly used equation for expressing the relationship between permeability, voidage, particle size and tortuosity is the Carman–Kozeny equation. This equation is applied in various fields, such as groundwater flow, water treatment, water processes and a variety of chemical engineering applications (Holdich, 2002; Yang, 2003; Oka and Anthony, 2003; Peker *et al.*, 2008; Xu and Yu, 2008). The Carman–Kozeny equation is important not only for the determination of permeability in porous media, but also for the estimation of the voidage in a fluidised bed. In groundwater flow, the flow regimes are generally considered to be laminar. In fluidised beds, however, not only laminar, but also transitional and, to a certain degree, turbulent flow regimes occur. More information about the Carman–Kozeny model is given in Chapter 9 and 6.

2.4 Particle size conundrum

Natural or processed granules are frequently used in water treatment processes. These granules are often not only irregularly shaped, but also polydisperse and sometimes even porous. This must be borne in mind especially for modelling purposes, where particle size is a vital parameter. Surprisingly, a sphere is the only

shape that can be described by one unique number. Unfortunately, for all other particles, more numbers are needed to describe the shape precisely. Even for a cube, this number could also refer to an edge or diagonal. So, a sphere is unique. This is why, for the sake of convenience, the equivalent sphere is still the most popular representative measure in the case of non-spherical particles in models. The particle size conundrum arises when a three-dimensional object needs to be described by one single number: by a single or equivalent particle diameter. In the literature several solutions can be found for natural non-spherical particles like sand grains. Examples are sphere of same volume, sphere of same surface area, sphere of same weight, sphere passing same sieve aperture, sphere of same minimum length, sphere of same maximum length or sphere having same sedimentation rate (Figure 8).

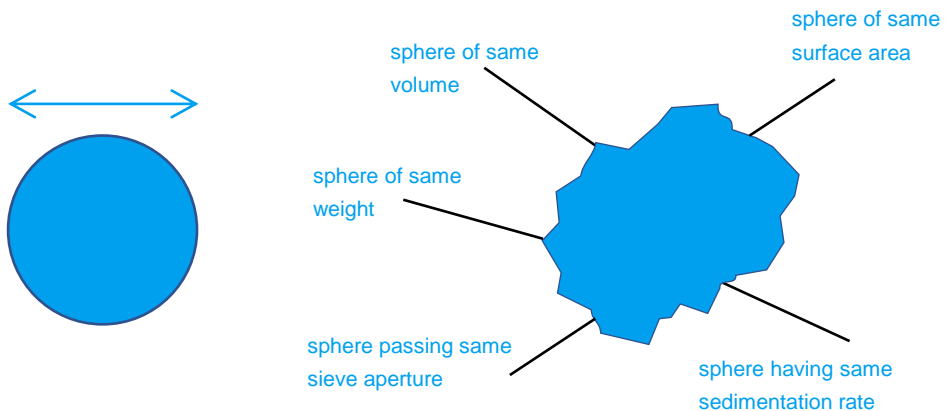


Figure 8 *The size of a sphere can be determined easily. The size of a non-spherical particle can also be determined but depends on the measuring technique.*

None of these examples are either ‘right’ or ‘wrong’. Their particular application determines which one is preferable. Different particle properties are measured. This can be done through image analysis (Allen, 1990), for which several methods and techniques are available to measure particles properties, with size and shape being the most important. An example is ImageJ (Ferreira and Rasband, 2012), a Java-based image processing programme developed at the National Institutes of Health and the Laboratory for Optical and Computational Instrumentation and suitable for the analysis of water-related grains.

Chapter 3

Materials and methods

“Mistakes are the portals of discovery.”

(James Joyce, 1882 – 1941)

3 Materials and methods

This chapter provides an overview of the materials and methods common to most chapters described in this thesis. Experimental columns are described in Section 3.1, physical properties of water are included in Section 3.2, physical properties of particles are included in Section 3.3 and standard operational procedures are described in Section 3.4.

3.1 Experimental set-up

To accommodate this research, three types of experimental columns were designed:

- Columns for fluidisation experiments (Section 3.1.1)
- Columns for terminal settling experiments (Section 3.1.2)
- Columns for submerged objects (Section 3.1.3)

3.1.1 Expansion columns

Experimental columns ($D = 57$ mm) were designed at Waternet for liquid-solid fluidisation and terminal settling experiments. They were installed at three locations: in Waternet's Weesperkarspel drinking water pilot plant in Amsterdam (Figure 9), at Queen Mary University of London (Figure 10) and at the University of Applied Sciences Utrecht, the Netherlands (Figure 11 and Figure 12). A schematic overview can be found in Figure 14. The set-up consists of a 4-meter-high transparent PVC pipe with an inner diameter of 57 mm.

Locally produced drinking water was used for the experiments. An overflow at the top of the column was used to recirculate the water through a buffer vessel and a reservoir. The reservoir was connected to a boiler, a cooler, and a programmable thermostat to regulate the water temperature.



Figure 9 *Waternet expansion column in Amsterdam*



Figure 10 *QMUL mobile expansion column in London*

The bottom section of the column was equipped with a membrane with a mesh of $120\ \mu\text{m}$; this membrane functioned as the base of the bed. The purpose of the membrane distributor was to allow water to flow through the bed as a plug flow reactor with a uniform velocity profile across the bed cross section, thereby preventing inhomogeneities.



Figure 11 *Experimental pilot set-up in Utrecht HU-ILC*

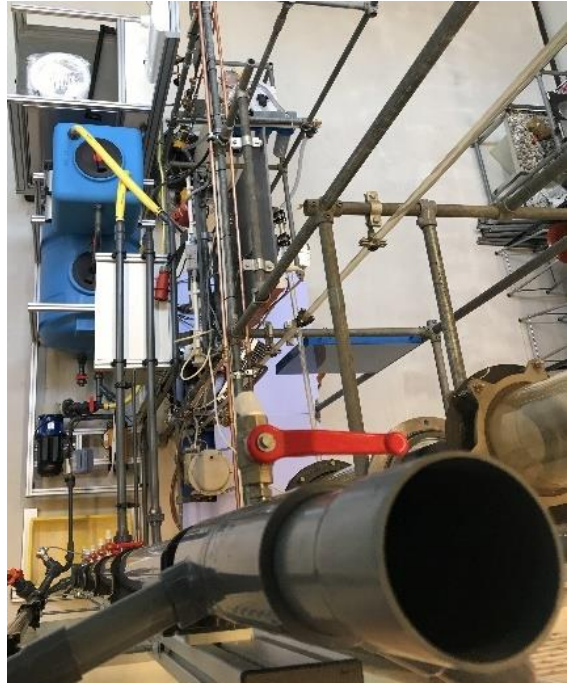
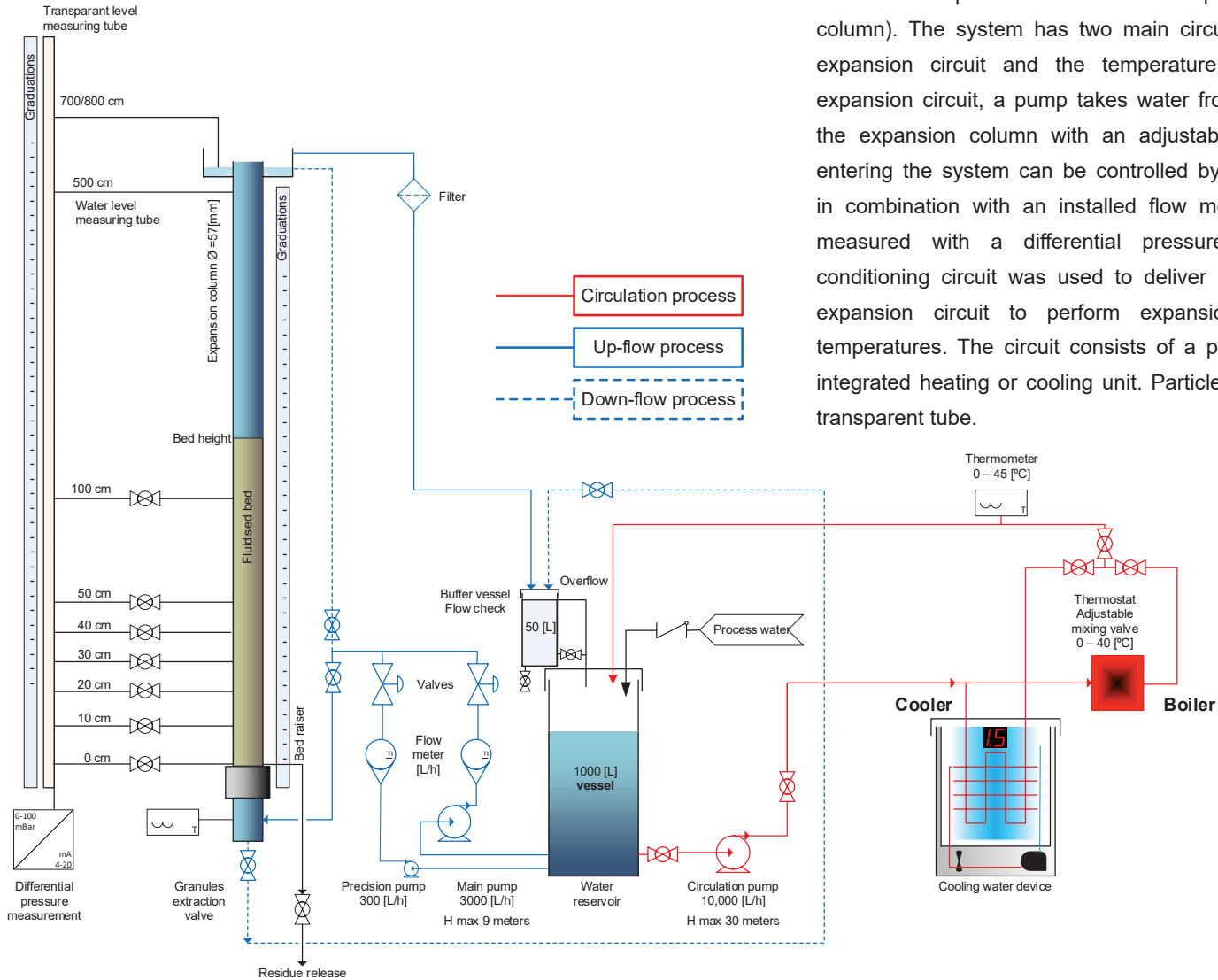


Figure 12 *Column top view $D = 57 \text{ mm}$, $L = 4 \text{ m}$*



Schematic representation of the experimental set-up (expansion column). The system has two main circuits in which water flows: the expansion circuit and the temperature conditioning circuit. In the expansion circuit, a pump takes water from a reservoir and feeds it to the expansion column with an adjustable water flow. The flow rate entering the system can be controlled by opening and closing a valve in combination with an installed flow meter. The pressure drop was measured with a differential pressure sensor. The temperature conditioning circuit was used to deliver a desired temperature to the expansion circuit to perform expansion experiments at different temperatures. The circuit consists of a pump that feeds water into an integrated heating or cooling unit. Particles are fluidised in a cylindrical transparent tube.

Figure 13 Schematic representation of the expansion column experimental set-up

The set-up has two main circuits in which water flows, the expansion circuit, and the temperature conditioning circuit. The set-up has two main circuits in which water flows: the expansion circuit and the temperature conditioning circuit. In the expansion circuit, a pump takes water from a 1000 L reservoir and feeds it to the expansion column with an adjustable water flow. The flow rate entering the system can be controlled through opening and closing a valve in combination with an installed flow meter (Bürkert Electro-Magnetic Inductive Flow measurements, type 8051, Figure 16). The pressure drop was measured with a differential pressure sensor (Endress+Hauser Ltd, Differential Pressure Measurement, Deltabar S, type: XD30-AADA, Figure 15). A second column was assembled with additional taps to measure differential pressures over the height of the column. From the bottom to 0.5 m, every 0.1 m and up to 4 m, ever 0.5 m, taps could be used to measure the pressure drop.

The temperature conditioning circuit is used to deliver a desired temperature to the expansion circuit to perform expansion experiments at different temperatures. This circuit consists of a pump that feeds water into an integrated heating or cooling unit. The cooling unit can condition the water to a temperature as low as 3 °C and the heating unit up to a temperature of 40 °C.



Figure 15 Flow meter



Figure 16 Differential pressure sensor

The effluent of the conditioning unit feeds the flow-checking unit, which is directly connected to the buffer reservoir. The supporting instruments of the experimental set-up are a flow-checking unit, a differential pressure measurement unit, a flow measuring unit, a measuring tape, a stopwatch and a thermometer.

To measure the particle bed height, a metallic measuring tape (Vogel Precision Measuring Tools DIN EN ISO 9001:2015) was secured on the outer wall of the expansion column.

The hydrostatic differential pressure measurement unit consists of two hydrostatic hoses (Figure 17), one measuring the pressure on the bottom of the bed and one on the upper part of the bed. The difference of heights outputs the pressure difference in centimetres of water column (Dacomba Torres, 2018).



Figure 17 Hydrostatic measurement board with longitudinal taps

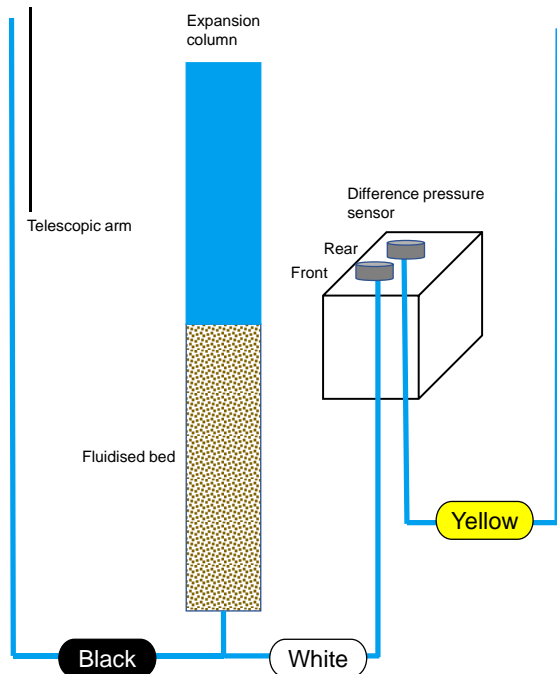


Figure 18 Differential pressure measurement scheme

3.1.2 Terminal settling set-up

Terminal settling experiments were conducted in the experimental columns ($D = 57$ mm) as given in Section 3.1.1. During terminal settling experiments, the water pump was turned off. Additional cylindrical columns ($D = 125$ mm) were used (Figure 19) to reduce wall-effects influences. (Figure 9, Figure 10, Figure 11 and Figure 12).



Figure 19 Terminal settling column $D = 125$ mm

The settling behaviour of single particles was determined for various materials and for different grain sizes. The temperature was carefully controlled by flowing water through the column of the exact temperature before each experiment and by regularly repeating this process throughout the experiment. Individual particles were dropped at the top of the column. Steady state velocities were reached within one second and before a distance of $L = 0.1$ m. The condition to be met for steady state velocity is that the particle travels a distance of at least $O(100 \cdot d_p)$ or greater before the stop clock is switched on. After the steady state velocity had been reached, the time required to travel a defined vertical distance ($L = 0.50\text{--}3.75$ m) was measured visually by the laboratory researcher and the assistant. More aspects are discussed in Chapter 11.

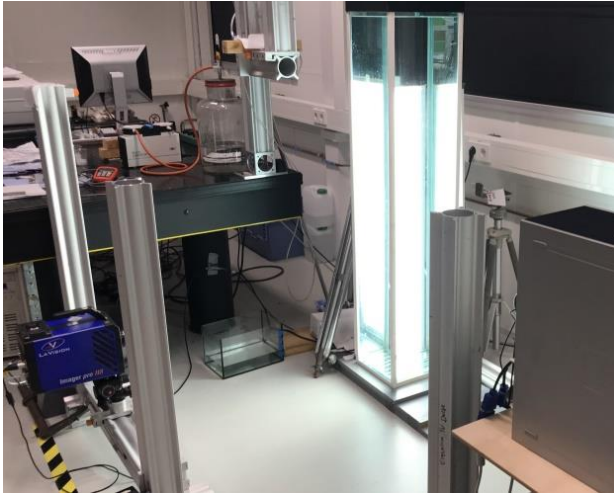


Figure 20 Experimental pilot set-up at TU Delft, $D = 300$ mm, to determine particle path trajectories 3D in a quiescent fluid.

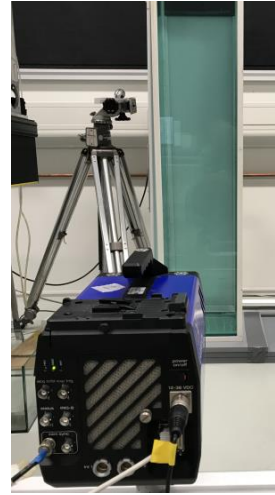


Figure 21 High-speed camera

In addition, an advanced experimental pilot set-up at TU Delft was used to determine particle 3D path trajectories in a quiescent fluid. The design of the experiment involved tracking the 3D position of a sphere falling in a tank containing still water, using 3D particle tracking velocimetry, to accurately capture the path instabilities. Installed components included a temperature conditioned tank, controlled high-speed cameras (LaVision Imager pro HS camera + sCMOS), data acquisition, particle release mechanism, LEDs and a water bath for pre-wetting purposes. The sphere is able to travel several hundred sphere diameters (Jenny *et al.*, 2004) before it reaches the field of view of the cameras. It is possible to track the sphere for sufficiently large distances $70 d_p$ for the largest sphere in the current study and $375 d_p$ for the smallest one). The advanced experimental set-up is thoroughly explained and discussed in (Raaghav, 2019).

3.1.3 Set-up for immersed objects in fluidised beds

The hydrometer column

An experimental set-up was designed at Waternet and at the University of Applied Sciences Utrecht, the Netherlands (Figure 23). A transparent 2 m cylindrical PVC column (Figure 24) with an inner diameter of 123 mm was used for the fluidisation experiments. The bottom section of the column was equipped with a membrane with a mesh of 120 μm ; this membrane functioned as the base of the bed. The purpose of the membrane distributor was to allow water to flow through the bed with a uniform velocity profile across the bed cross section, thereby preventing inhomogeneities. Locally produced drinking water was used for the experiments. An overflow at the top of the column was used to recirculate the water through a buffer vessel and a reservoir. The column was mounted in an aluminium frame to accommodate the measuring apparatus and ensure a levelled column. A centrifugal pump with valves created an adjustable upward flow that was measured by a calibrated flow meter. The flow rate entering the system could be controlled through opening and closing a valve in combination with an installed flow meter (Bürkert Electro-Magnetic Inductive Flow measurements, Type 8051). Water temperature could be regulated with a boiler, a cooler and a thermostat by recirculating water through a buffer vessel connected to a water reservoir. To measure the particle bed height, a metallic measuring tape was secured on the outer wall of the expansion column. A schematic overview can be found in (Figure 14). Additional technical information about materials is given in (Kramer *et al.*, 2021e) and the Supplementary material (Section 3).



Figure 23
Experimental set-up

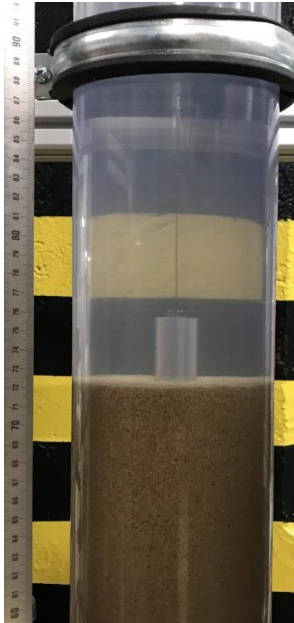


Figure 24
Submerged object



Figure 22
Pulley system, from left to right: distance encoder, load cell, support pulley, stepper motor



Figure 25
Data transfer unit

Hydrometer pulley system

A pulley system driven by a stepper motor was mounted above the expansion column to move a cylindrical object vertically through the fluidised bed (Figure 24). A distance encoder was used to measure the number of rotations (Figure 22), which was then converted to the longitudinal position of the object. A load cell measured the amount of strain in voltage, which was converted to the weight of the object. The stepper motor, distance encoder and load cell were connected to a I/O hardware module (Q.monixx) (Instruments GmbH, 2021a). The module (Figure 10) transmitted the data stream of and from a Gantner GI.Bench data acquisition software environment running on a computer. Within the GI.Bench configuration (Instruments GmbH, 2021b), hardware controls and data log settings were defined as well as the calibration values for conversion of strain [V] to mass [kg] and number of revolutions [#] to distance travelled [m]. The pulley system (Figure 22) is composed of four components to move the object up and down the column and log its weight and distance. From left to right, the object is attached to a thin, braided fishing line. The

line is strung over the first pulley and encoded with a step counter which transmits the number of steps from a set zero point to an attached data processor. This relates to the area of the column in which the object resides. The line passes under the second pulley equipped with a load cell that measures the amount of strain in voltage. This strain is directly correlated to the submerged weight of the object which is calculated by calibrated values within the GI.bench software. The line is threaded over the third pulley for support and connected to the stepper motor used to move the object up and down the column. Additional technical details are provided in (Kramer *et al.*, 2021e) and the Supplementary material (Section 3).

3.2 Physical properties of water

The density of ordinary water as a function of temperature was retrieved from Rumble (2017), Perry and Green (2007) and Albright (2009). The dynamic viscosity is given by the Vogel–Fulcher–Tammann equation (Vogel, 1921; Civan, 2007). In Equation (27), the influence of the combined content of all inorganic and organic substances (Total Dissolved Solids, TDS = 400 mg/L) is small (0.03% for the density and 0.07% for the dynamics viscosity (Sharqawy *et al.*, 2010)), and has not been taken into account, as appropriate for applied drinking water.

$$\eta = 0.001 e^{\left(\frac{578.919}{(T+273)-137.546} - 3.7188\right)} \quad (273 < T [K] < 373) \quad (27)$$

3.3 Physical properties of particles

The following particle properties are considered:

- Particle selection (Section 3.3.1)
- Representative particle samples (Section 3.3.2)
- Particle size and shape analysis (Section 3.3.3)
- Average particle diameter (Section 3.3.4)
- Particle density (Section 3.3.5)

Note that particle shape factors will be described in Chapter 9.

3.3.1 Particle selection

In this research, the focus was on the investigation into hydraulic behaviour of granules applied in full-scale drinking water treatment unit operations. These granules are in general irregularly shaped, polydisperse and sometimes even porous. In addition, highly spherical and monodispersed particles and data tabature from publications were examined as a reference. The following granules were selected from full-scale installation, purchased or obtained from literature sources (Table 6):

Table 6 *Particles used in this research*

Granule type	Process	Particle diameter [mm]
Calcite		
Calcite pellets	Pellet-softening	0.35-2.80
Garnet pellets	Pellet-softening	0.25-3.35
Sand pellets	Pellet-softening	0.60-2.00
Crushed calcite	Pellet-softening	0.40-0.60
Distortion layer ¹⁾	Pellet-softening	0.30-0.36
Natural particles		
Crystal sand	Pellet-softening	0.40-0.60
Garnet sand	Pellet-softening	0.13-0.30
Rapid filter sand	Rapid sand filtration	0.80-2.00
Olivine	Research	0.50-0.90
Mined Italian calcite	Pellet-softening	0.43-1.00
Synthetic particles		
Granular activated carbon	Carbon filtration	0.44-3.15
IEX anionic exchange resins	Research	0.90-1.18
Spherical particles		
Glass beads	Research	0.70-3.50
Steel shots	Research	3.00
Nylon resin balls	Research	2.00-3.00
Zirconium balls	Research	0.10-3.00
Other particles		
Literature data ²⁾	Research	0.10-6.35

¹⁾ Fluffy garnet pellets resulting from deteriorated softening

²⁾ Raw data is included in articles' Supplementary material

3.3.2 Representative particle samples

A Retsch (RT 6.5) sample splitter was always used to obtain representative granule samples for the reproducibility of the research analyses.



Figure 26 Retsch sieve shaker



Figure 27 Sample splitter

3.3.3 Particle size and shape analysis

Particles like calcite pellets were fractionated using a Retsch AS 200-control sieve device and calibrated US mesh sieves regulated by standards such as ISO 3310-1, ISO 565, EN 933-2 and ASTM E11 (NEN-EN 933-2, n.d.), represented in Figure 26. Morphological particle properties, such as the sphericity, were determined with a Retsch Camsizer XT (Retsch-Technology, 2007) (Figure 29). Accordingly, ImageJ software (Figure 30) was used for image analysis purposes (Ferreira and Rasband, 2012). Additional photos of granules were taken with a Nikon SMZ800 laboratory Stereo Microscope (480x) (Figure 28).



Figure 28 Stereo microscope



Figure 29 Retsch Camsizer XT

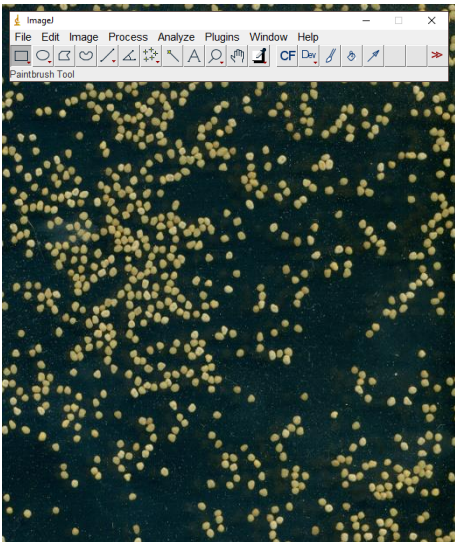


Figure 30a ImageJ version 1.53j

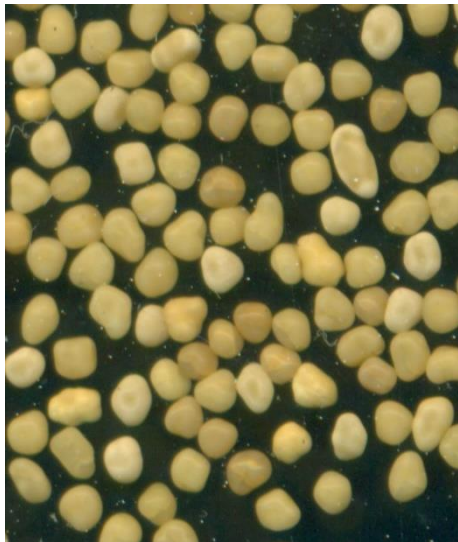


Figure 30b Calcite pellets scan

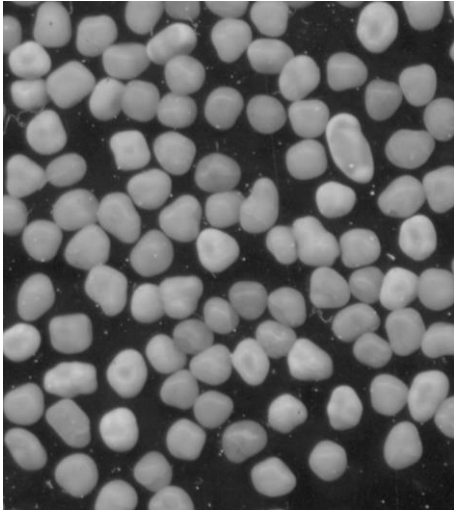


Figure 30c Image processing

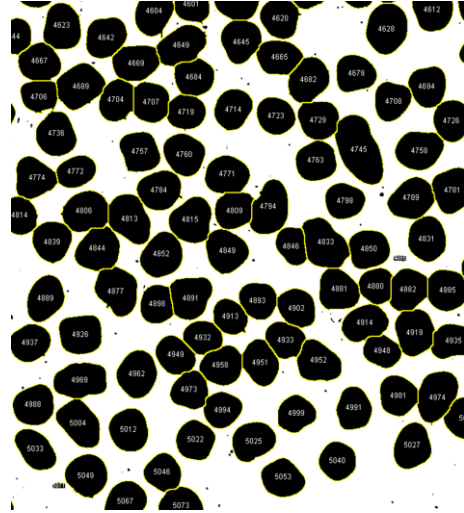


Figure 30d Particle numbering

More information about particle image analysis can be found in Chapter 9.

3.3.4 Average particle diameter

The effective or average hydraulic equivalent particle diameter d_p of examined natural particles, such as calcite pellets, was based on the applied sieve method in which particles were divided over the successively smaller sieve openings and calculated according to the appropriate geometric mean for two sieves. In this research, the ratios $d_{s,2}/d_{s,1}$ between two successive sieve openings were 1.12 and 1.20. The hydraulic equivalent particle diameter (Dallavalle, 1948; Davis, 2010; Crittenden *et al.*, 2012) was calculated using Equation (28):

$$d_p = \sqrt{d_{s,1}d_{s,2}} \quad (28)$$

Additionally, the particle size of examined particles was determined through static image analysis. Based on a scan of a sample using specialised software such as ImageJ (Ferreira and Rasband, 2012) that analyses pixels, it is possible to compute the size and different morph parameters of each particle in the picture.

$$d_p = 2 \sqrt{\frac{\sum_i^N A_i}{N\pi}} \quad (29)$$

3.3.5 Particle density

The particle density was determined through several methods, based on particle counting, static image analysis, differential pressure and/or pycnometer.

Particle counting

A straightforward way to calculate the particle density ρ_p is particle counting N with Equation (30):

$$\rho_p = \frac{\sum_i^N m_i}{N \frac{\pi}{6} d_p^3} \quad (30)$$

Static image analyses

Using ImageJ software, the particle density can also be calculated when this is combined with a mass measurement, also discussed in Section 9.5.

Laboratory pycnometer

A traditional laboratory tool to determine the particle density is the pycnometer (Figure 31). The particle density of grain material was measured with a 50 mL pycnometer (Geldart, 1990). To increase measurement accuracy, the laboratory experiment is repeated at least 10 times.

Differential pressure

In the steady state of homogeneous fluidisation of particulate solids (Gibilaro, 2001; Yang, 2003), the constant frictional pressure drop equals the weight of the bed material in suspension, reduced by the buoyancy forces, per unit of bed surface according to Equation (31):

$$\frac{\Delta P}{\Delta L} = (\rho_p - \rho_f)g(1 - \varepsilon) \quad (31)$$

The differential pressure ΔP or pressure drop in a homogenous fluidisation state is independent of the prevalent superficial fluid velocity (Gibilaro, 2001). Using Equation (22), the particle density ρ_p can be determined according:

$$\rho_p = \rho_f + \frac{\frac{\Delta P}{\Delta L}}{g(1 - \varepsilon)} \quad (32)$$

In addition, when the total mass m of the granules in the fluidised bed is known as well as the differential pressure sensor value ΔP the particle density can also be determined using Equation (33) and is therefore independent on the bed height.

$$\Delta P = \frac{mg}{\frac{\pi}{4}D^2} \left(1 - \frac{\rho_f}{\rho_p}\right) \quad (33)$$

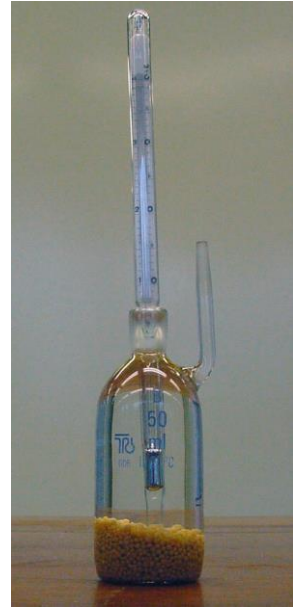


Figure 31 Calibrated laboratory pycnometer to determine the particle density

Rewriting gives:

$$\rho_p = \frac{\rho_f}{1 - \frac{\pi D^2}{4} \frac{\Delta P}{m g}} \quad (34)$$

Different particle densities

Due to crystallisation of CaCO₃ at the particle surface of calcite pellets, the particle size increases over time. Since the density of the seeding material, for instance garnet grains, is different from the density of calcium carbonate, the average density changes during the softening process. Equation (35) was used to estimate average particle density for garnet pellets based on the assumption that round particles contain an equally distributed layer of pure chalk with a density of 2,711 kg/m³, as postulated by Anthony *et al.* (2003).

$$d_p^3 \rho_p = d_g^3 \rho_g + (d_p^3 - d_g^3) \rho_c \quad (35)$$

3.4 Fluidisation expansion experiments

This section details the study's fluidisation expansion experiments and includes the following:

- Standard operating procedure (Section 3.4.1)
- Bed voidage and expansion (Section 3.4.2)

3.4.1 Standard operating procedure

Procedure expansion experiments

Fluidisation behaviour was examined for a set of different grains varying in size, shape and composition. The test column was filled with approximately 0.3 - 3.0 kg of uniform particles. To prepare the experiments, the particles were initially gently fluidised until the suspension was stratified on size, shape and particle density. The flow was then stopped, and after the particle bed had settled into a fixed state, the

fixed bed height was measured. Then, the flow velocity was slowly increased. For each flow velocity, bed height and differential pressure were recorded individually. The differential pressure was measured with a device as well as hydrostatically. The differential pressure was corrected for both the hydrodynamic influence $\frac{1}{2}\rho v^2$, which had a minor effect (< 0.5%), as well as for missing mass ($L/(L-0.025)$), since the lowest pressure sensor tap was assembled at 2.5 cm above the bottom of the column.



Figure 32 *Lowest section of the expansion column with the lowest tab and the grid at the bottom*

The water flow was gradually increased until the particles were in an incipient state and started to fluidise. The minimum fluidisation bed height was not only measured visually but also determined based on the intersection of linearly increasing differential pressure in the fixed bed state and the maximum differential pressure in the homogeneous fluidisation condition. During the experiments, the water temperature was kept constant

(standard deviation approximately 1 °C) and was measured at the overflow of the column and directly in the column. Expansion experiments were conducted for garnet grains and calcite pellets for at least four different water temperatures between 3 and 36 °C. For each individual experiment, the temperature was recorded at least four times. For crushed calcite, the temperature was recorded for every single measurement. Since the experimental set-up had been improved technically, pressure differences were absent in some of the experiments.

Procedure filtration experiments

During the extended terminal sub-fluidisation wash experiments, both a filtration cycle and backwash procedure with ETSW were simulated using the expansion/filtration experimental set-up (Figure 9 and Figure 11). During the experiments, approximately three kilograms of rapid sand filtration granules with a sieve diameter ranging between 0.85 to 1.25 mm were loaded in the expansion column, using an upward flow to prevent inhomogeneous channels. To simulate a

filtration cycle and an effectively packed RSF bed, the experimental set-up was operated in filtration mode for one hour while the filtration speed alternated between 0 and 50 m/h. Following the filtration procedure, a backwash was simulated by switching the experimental set-up to expansion mode and expanding the filtration bed by 10%, or approximately 30 m/h, for 10 minutes. Afterwards, the fluid velocity was gradually reduced to 5 m/h and kept constant for 30 minutes. During this period, at five minutes intervals, the differential pressure, fluid velocity, temperature and bed height were determined individually.

The flow-checking unit is a water reservoir of 50 litres, it has an integrated transparent tube where the water level can be measured with a ruler. With the known water level, the volume can be measured, making it possible to calculate volume in a given time with the help of a stopwatch.

3.4.2 Bed voidage and expansion

Based on the known total mass m of all the granules, the fixed and fluid bed voidage as well as the expansion degree of the bed can be calculated (Michaelide *et al.*, 2017) using Equations (36) and (23):

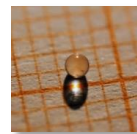
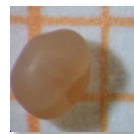
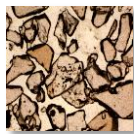
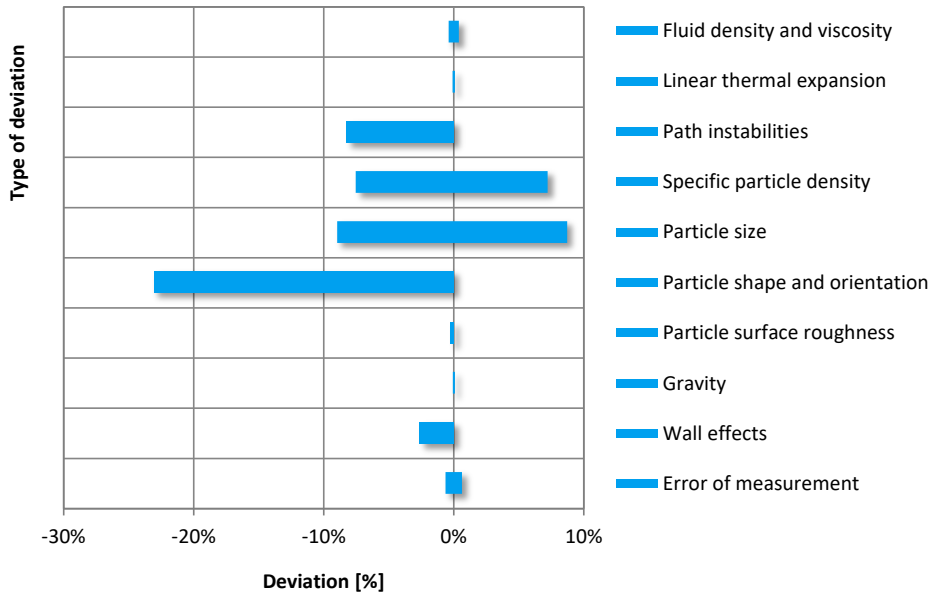
$$\varepsilon = 1 - \frac{m}{\frac{\pi}{4}D^2L\rho_p} \quad (36)$$

$$E = \frac{L}{L_{mf}} - 1 = \frac{\varepsilon - \varepsilon_{mf}}{1 - \varepsilon} \quad (37)$$

The particle mass is an extremely important value. Since it is also vital to reduce the risk of making experimental and logging mistakes, the volume of the grains in a jar can be measured and compared with the calculated value using Equation (38) and an estimated fixed bed porosity for spherical particles $\varepsilon \approx 0.4$. The incipient porosity can be estimated according the following rule-of-thumb: $\varepsilon_{mf} \approx 1.05 \varepsilon_0$.

$$V = \frac{m}{\rho_p(1 - \varepsilon_0)} \quad (38)$$

Terminal settling velocity of particles in water



- ▶ The Brown–Lawler equation is suitable to predict drag for perfectly round spheres
- ▶ Experiments with natural non-spherical particles show considerable deviation in drag
- ▶ A numerical parameter variation analyses explains the influence on deviation
- ▶ Measured deviation is primarily caused by particle properties

Keywords Drinking Water; Terminal Settling Velocity; Calcium Carbonate Grains; Drag Coefficient; Natural Particles; Data Spread

Chapter 4

Terminal Settling

*“A conundrum about the definition regarding the effective particle size:
“What is the diameter of a banana? And how should one use that in a model?”*

This article has been published as:

Can terminal settling velocity and drag of natural particles in water ever be predicted accurately?

O.J.I. Kramer, P.J. de Moel, S.K.R. Raaghav, E.T. Baars, W.H. van Vugt, W.P., Breugem, J.T. Padding, J.P. van der Hoek

Drinking Water Engineering and Science. **14** (2021) pp. 1–19.

The article can be found online at: <https://doi.org/10.5194/dwes-14-53-2021>

4 Can terminal settling velocity and drag of natural particles in water ever be predicted accurately?

4.1 Abstract

Natural particles are frequently applied in drinking water treatment processes in fixed bed reactors, in fluidised bed reactors, and in sedimentation processes to clarify water and to concentrate solids. When particles settle, it has been found that in terms of hydraulics, natural particles behave differently when compared to perfectly round spheres. To estimate the terminal settling velocity of single solid particles in a liquid system, a comprehensive collection of equations is available. For perfectly round spheres, the settling velocity can be calculated quite accurately. However, for naturally polydisperse non-spherical particles, experimentally measured settling velocities of individual particles show considerable spread from the calculated average values.

This work aimed to analyse and explain the different causes of this spread. To this end, terminal settling experiments were conducted in a quiescent fluid with particles varying in density, size and shape. For the settling experiments, opaque and transparent spherical polydisperse and monodisperse glass beads were selected. In this study, we also examined drinking water related particles, like calcite pellets and crushed calcite seeding material grains, both applied in drinking water softening. Polydisperse calcite pellets were sieved and separated to acquire more uniformly dispersed samples. In addition, a wide variety of grains with different densities, sizes and shapes were investigated for their terminal settling velocity and behaviour. The derived drag coefficient was compared with well-known models such as Brown–Lawler.

A sensitivity analysis showed that the spread is caused to a lesser extent by variations in fluid properties, measurement errors and wall effects. Natural variations in specific particle density, path trajectory instabilities and distinctive multi-particle settling behaviour caused a slightly larger degree of spread. In contrast, greater spread is caused by variations in particle size, shape and orientation.

In terms of robust process designs and adequate process optimisation for fluidisation and sedimentation of natural granules, it is therefore crucial to take into consideration the influence of natural variations of the settling velocity when using predictive models for round spheres.

4.2 Introduction

4.2.1 Deviations in the prediction of settling in water treatment processes

The settling behaviour of *natural* grains in drinking water treatment processes is of great importance (Camp, 1946; Cheremisinoff, 2002; Edzwald, 2011; Howe *et al.*, 2012; Crittenden *et al.*, 2012). Examples include pellet-softening in fluidised bed reactors (Graveland *et al.*, 1983), sedimentation, flotation and flocculation, filtration processes (Amburgey, 2005; Tomkins *et al.*, 2005), backwashing of filter media, and washing columns in which fine material and impurities are separated from seeding material (Cleasby *et al.*, 1977; Soyer and Akgiray, 2009). In processes such as pellet-softening (Rietveld, 2005; van Schagen, 2009), it is important always to keep the particles in fluidised state, *i.e.* to prevent fixed bed state (which sets the minimum superficial velocity) or flushing state (which sets the maximum superficial velocity). In contrast, in sand filter backwash processes, exceeding the maximum settling velocity, *i.e.* flushing of impurities and fine materials, is the objective. In these processes, the particle size mostly varies between 0.3 - 2 mm, and the particle density varies between 1.2 - 4 kg/L.

The societal call for a circular economy (Filho and Sümer, 2015; Marques *et al.*, 2015) has put pressure on water utilities to change their policies (Ray and Jain, 2011), also in terms of making treatment processes more sustainable. The re-use of waste materials is an example of this transition from a linear to a circular approach. Pellet-softening, for instance, is an example of a sustainable process (Beefink *et al.*, 2021) where full-grown calcium carbonate pellets are crushed and re-used as raw material in the process itself (Schetters *et al.*, 2015). The disadvantage, however, is that the processed calcite grains become completely irregularly shaped and show a considerably different hydraulic settling behaviour compared to the generally spherical full-grown calcite pellets. In case of pellet-softening processes using fluidisation, the spread in settling velocity can cause the unwanted flushing of smaller grains out of the reactor and the settling of larger grains to the lower region of the reactor, which leads to a fixed bed state. In other processes, like granular activated carbon (GAC) filtration, where bio-based raw materials are getting more attention compared to fossil fuel-based materials, the settling behaviour is important during filter bed backwashing. The physical properties of bio-based grains are often

different compared to conventional grain types, which affects the settling behaviour in backwashing processes as well.

The accurate calculation of the terminal settling velocity of a single particle in water is based on the fluid dynamic drag coefficient, which is empirically known for spherical particles (Clift *et al.*, 1978). However, accurate prediction models for settling behaviour of polydisperse highly non-spherical and porous grains applied in filter backwash systems are limited (Dabrowski *et al.*, 2008; Huncce *et al.*, 2018). Note that the term 'highly spherical' stands for sphere-shaped particles with a sphericity ($\Phi \approx 1$), the term 'medium spherical' stands for grains with sphericities ($0.85 < \Phi < 0.99$) and the term 'lightly non-spherical' stands for irregularly shaped grains with sphericities ($\Phi < 0.95$). The sphericity of a particle is the ratio of the surface area of a sphere with the same volume as the given particle to the surface area of the particle.

It is important, especially in the field of engineering design and operations for optimal control and optimisation purposes, not only to accurately predict the drag coefficient and terminal settling velocity, but also to take into consideration the degree of variation. Aspects such as natural variations in fluid and particle properties, the degree of polydispersity and other factors that influence the terminal settling velocity will be investigated in this work. In this work, we will investigate the amount and the causes of this spread, something which is hugely underexposed in the popular and often cited prediction models presented in the literature *e.g.* (Cheng, 1997; Khan and Richardson, 1987; Brown and Lawler, 2003; Zhiyao *et al.*, 2008; Barati and Neyshabouri, 2018).

1.1.1 Terminal settling and drag coefficient: models from the literature

The literature provides a comprehensive collection of models for the accurate prediction of the terminal settling velocity and drag coefficient for perfectly round spheres. More recently, advanced drag equations for non-spherical particles have been proposed, based on geometrical particle properties. With the help of advanced particle image analysis, it is increasingly possible to determine morphological properties such as sphericity and circularity to predict drag coefficients more accurately. Nearly all prediction models, based on thorough literature surveys, can be found in the publications listed in Table 7.

Table 7 Publications with overviews of drag coefficient models

Spherical particles	Irregularly shaped particles
Clift (1978)	Haider–Levenspiel (1989)
Concha–Almendra (1979)	Ganser (1993)
Brown–Lawler (2003) ¹⁾	Loth (2008)
Almedeij (2008)	Hölzer–Sommerfeld (2008)
Cheng (2009)	Yang (2015)
Barati (2014)	Ouchene (2016)
Song (2017)	Bagheri–Bonadonna (2016)
Auguste–Magnaudet (2018)	Dioguardi (2018)
Goossens (2019)	Breakey (2018)

¹⁾ Popular drag coefficient prediction models from the literature and a more detailed explanation of the Brown–Lawler model are included in the Supplementary material (Section 5).

A very common form of the standard drag coefficient prediction (Equation (28)) is an arrangement of groups: laminar ($24/Re_t$), according to Stokes, transitional (ARe_t^B) and turbulent (C), according to (Clift *et al.*, 1978; Haider and Levenspiel, 1989):

$$C_D = \frac{24}{Re_t} (1 + ARe_t^B) + \frac{C}{1 + \frac{D}{Re_t}} \quad (39)$$

with Re_t referring to the (terminal) Reynolds number described in Equation (3). Well-known examples for spherical particles are the conventional equation proposed by (Schiller and Naumann, 1933), the equation proposed by (Fair *et al.*, 1971), often applied in water treatment, and the equation proposed by (Brown and Lawler, 2003), covering a wide range of terminal Reynolds numbers. Prediction models for non-spherical particles are also based on the appearance of Equation (28). Examples can be found (Bagheri and Bonadonna, 2016) and (Dioguardi *et al.*, 2018).

4.2.2 Terminal settling velocity calculation

The most common way to calculate the terminal settling velocity v_t is to predict the dimensionless drag coefficient C_D of a single solid sphere in a Newtonian fluid as a function of the Reynolds numbers Re_t . The dimensionless particle Reynolds number under terminal settling conditions is the ratio of the inertial force on the particle to the

viscous force with a characteristic length and velocity scale, typically the volume-equivalent particle diameter d_p and terminal velocity v_t :

$$Re_t = \frac{\rho_f d_p v_t}{\eta} \quad (3)$$

To actually predict the steady terminal velocity of a given particle with a projected surface area A_p in the direction of the gravitational field from these correlations, one needs to consider a force balance in which the drag force balances the difference between buoyancy and weight (Yang, 2003; Gibilaro *et al.*, 1985; Clift *et al.*, 1978).

$$(\rho_p - \rho_f)gV = C_D A_p \frac{1}{2} \rho_f v_t^2 \quad (40)$$

For spheres this leads to an analytic *dimensionless* drag coefficient as proposed by (Bird *et al.*, 2007):

$$C_D = \frac{4}{3} \frac{g d_p |\rho_p - \rho_f|}{v_t^2 \rho_f} \quad (41)$$

This means that the terminal settling velocity can be calculated by combining Equations (28), (3) and (41), assuming that the fluid and particle properties are known. The disadvantage of this set of equations is that the terminal settling velocity must be solved numerically.

The literature also provides empirical equations to predict the terminal settling velocity for specific grains (Concha and Almendra, 1979; Cheng, 1997); (Brown and Lawler, 2003; Zhiyao *et al.*, 2008; Terfous *et al.*, 2013; Goossens, 2019).

4.2.3 Aim

The aim of this work was to illustrate the existence of considerable spread in the prediction of terminal settling, a process which is mostly determined through the prediction of the drag coefficient. This spread becomes relevant as soon as treatment processes must be designed, controlled and optimised. Professionals active in fields where the settling of grains is relevant should be aware of this

phenomenon. Merely predicting the drag coefficient and terminal settling velocity based on an estimated average particle diameter, using models derived for perfectly round spheres, is insufficient and likely to be highly inaccurate.

Academic research is predominantly focused on improving the standard drag curve (SDC) for a wide range of Reynolds numbers, from completely laminar to fully turbulent, and researchers regularly present accuracy improvements on a relatively small scale (Almedeij, 2008; Barati *et al.*, 2014; Yang *et al.*, 2015; Whiten and Özer, 2015; Song *et al.*, 2017) etc. The engineering approach, on the other hand, is focused on higher accuracies mainly for a much smaller operational range. With respect to pellet-softening reactors as applied in drinking water treatment processes, the relevant regime is typically $10 < Re_t < 200$. The present study aimed to improve our understanding of the principles governing the terminal settling velocity of *natural* irregularly shaped particles; the numerical prediction of their terminal settling velocity is much more complex than would be the case for perfectly round particles. To address this, a significant number of terminal settling experiments were carried out and compared with the conventional drag force coefficient equations proposed in the literature (Table 7). Additionally, shape descriptors such as sphericity were measured.

Improved knowledge in this field enables the accurate modelling and optimisation for system and control purposes in automated drinking water treatment processes. This is of value not only for the softening process itself, but also for other processes like the sand-washing processes of seeding material in which dust and undesired materials, such as bacteria, are flushed and released from the process. This is particularly important as unreliable prediction models increase the risk of contamination of the treatment processes, which may adversely affect drinking water quality.

4.3 Materials and methods

4.3.1 Experimental approach

A sequence of different experiments was executed (Table 8). The experimental work started with *old-school* settling experiments with natural, highly irregularly shaped particles and ended with terminal settling experiments using an advanced calibrated set-up with high-speed cameras. *Old-school* settling entails measuring the vertical fall velocity of grains, visually, in a quiescent fluid using a timer.

The goal of these experiments was to identify the influence of particle size and shape and fluid properties on the terminal settling velocity and settling behaviour.

4.3.2 Particle selection

For the terminal settling experiments, opaque and transparent spherical polydisperse and monodisperse glass beads were selected. We also examined drinking water related particles such as calcite pellets and crushed calcite seeding material grains, both of which are applied in drinking water softening. Polydisperse calcite pellets were sieved and separated to acquire more uniformly dispersed samples. In addition, a wide variety of grains with different densities, sizes and shapes were investigated for their terminal settling velocity and behaviour. The morphological particle properties were obtained with the help of laboratory instruments (Retsch Camsizer XT) and image analysis software (ImageJ).

Table 8 Different types of terminal settling experiments

Nr.	Grain type	Study research topic	Shape	Uniformity	Observation
1	Natural and processed	Degree of spread and orientation	Highly non-spherical	Highly polydisperse	Visual
2	Water softening ¹⁾	Effects of particle growth	Lightly non-spherical	Polydisperse	Visual
3	Glass beads	Effect of polydispersity	Spherical	Polydisperse	Visual
4	Glass beads	Agreement prediction models	Highly spherical	Monodisperse	Visual
5	Glass beads	Wall effects	Highly spherical	Monodisperse	Visual
6	Glass beads	Individual grain variations	Highly spherical	Monodisperse	Cam ²⁾
7	Glass beads	Influence column diameter	Highly spherical	Monodisperse	Visual
8	Glass beads	Fall length variations	Highly spherical	Monodisperse	Visual
9	Synthetic	Particle size variations	Spherical	Polydisperse	Visual
10	Metal balls	Surface roughness	Highly spherical	Monodisperse	Visual
11	Metal balls	Path trajectories	Highly spherical	Monodisperse	Visual
12	Calcite pellets and others ⁵⁾	Advanced settling	Lightly non-spherical	Polydisperse	3D cam ^{3) 4)}

¹⁾ Calcite pellets, crushed calcite and garnet sand

²⁾ Default traditional camera

³⁾ 3D trajectory of particle paths using particle tracking velocimetry in a quiescent fluid

⁴⁾ Path trajectory videos are shared by (Kramer et al., 2020f)

⁵⁾ Metal balls, glass beads and synthetic material

Note: Photographs of granules are presented in Annex 1: Photos.

4.3.3 Experimental set-up

The experimental set-up is presented in Section 3.1.2, physical properties of water in Section 3.2 and photographs of granules in Annex 1: Photos. Standard operating procedure of terminal settling experiments is elucidated in Section 3.1.2.

Experimental columns ($D = 57$ mm and $D = 125$ mm) were designed for terminal settling experiments, installed at two locations: in Waternet's Weesperkarspel drinking water pilot plant located in Amsterdam, the Netherlands and at the University of Applied Sciences Utrecht, the Netherlands (Figure 12 and Figure 19). Moreover, an advanced experimental pilot set-up at Delft University of Technology was used to determine particle 3D trajectories using particle tracking velocimetry in a quiescent fluid (Figure 20 and Figure 21).

4.3.4 Reference data

In addition to the experiments, a large dataset obtained from the literature was examined; this will be discussed in Section 4.4.5.

The Supplementary material section includes technical information about experimental set-up devices and flow chart diagram and procedures (Section 1), photographic pictures of grains used in water treatment processes (Section 2) and steady state conditions (Section 11).

4.4 Results and discussion

4.4.1 Standard drag curve with average values

In total 3,629 new individual terminal settling experiments were executed (Table 8), which marked the starting point of the spread analysis. Raw data is included in the Supplementary material (Section 17). The results, in accordance with the standard drag curve approach (Lapple and Shepherd, 1940), are plotted in Figure 33, where experimental results for repeated experiments on sets of the same type and size of particles have been averaged (symbols). Additionally, the figure includes popular prediction models (lines). The prediction model equations are included in the Supplementary material (Section 5). A preliminary evaluation (Figure 33) indicates that the prediction accuracy is reasonably good for most of the grains. Exceptional outliers are wetted-GAC Norit ROW 0.8 Supra grains (rods), due to particle rotation and their delayed settling behaviour, and the 10 mm glass beads, due to wall effects ($d_p : D = 10 : 57$). Note: wall effects are discussed in Annex 2: Wall effects.

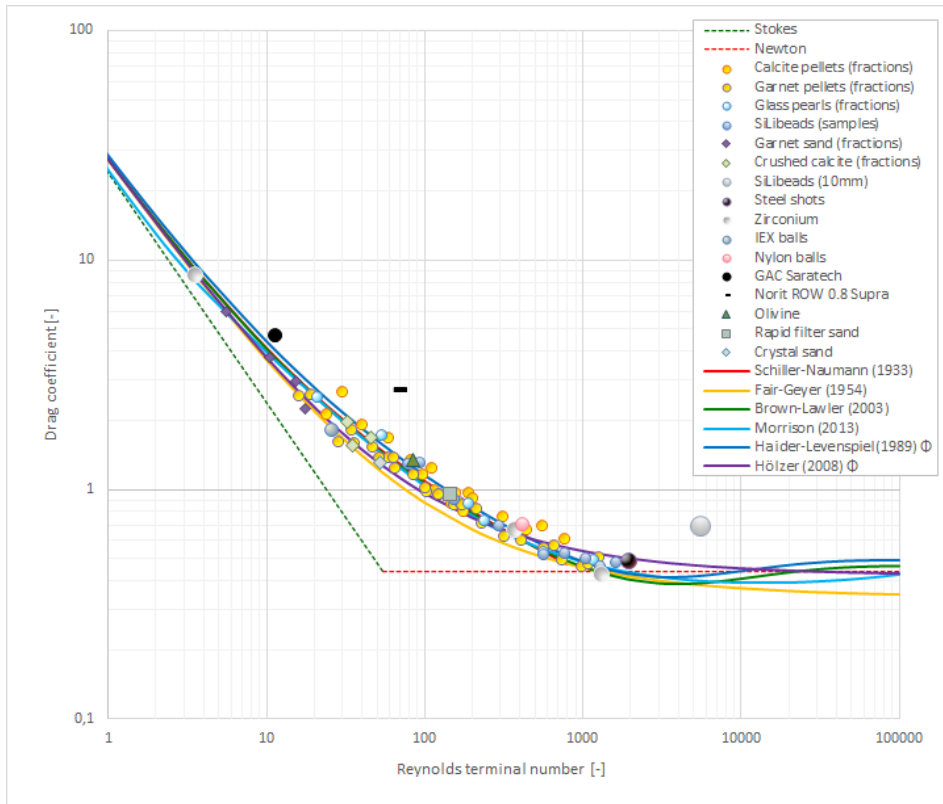


Figure 33 Standard drag curve (SDC) for 3,629 grains, using averaged values over multiple experiments, for 16 types of materials compared with popular prediction models for spherical and non-spherical particles. Φ indicates that the measured sphericity is included in the model. Extended SDC with all examined models is given in the Supplementary material (Sections 5 and 7).

Experimental and model results were compared using two statistical error definitions and correlation coefficients; findings are presented in Table 9. To cope with the irregularity of *natural* particles, the measured sphericity Φ was used for models developed for non-spherical particles. With respect to the terminal velocity, the calculated normalised root mean Brown–Lawler square error for the best-known models derived for spherical particles, such as and Schiller–Naumann, is in the range of 9-11%.

4.4.2 Drag coefficient and terminal settling velocity prediction versus spread in measured data

Many drag coefficient prediction models found in the literature (Table 7) are based on fits through datasets provided in the literature. Most of the data is based on previous experimental work. In most cases it remains unexplained, and thus unverifiable, whether the literature data represent raw data from single experiments or were processed, for example filtered (by removing outliers), averaged (using statistics) or corrected (for instance by correcting for wall effects). In the current work we will be explicit about all data processing steps.

To see the amount of variation on an individual particle level, *i.e.* when no average is calculated, the ratio of the measured to calculated settling velocity (according to Brown–Lawler) was plotted against the calculated settling velocity in Figure 34. To identify statistical outliers, a 3.5σ bandwidth was added to Figure 34. Of the experimental data, 0.9% can be identified as outliers. The largest spread is shown for non-spherical particles such as granular activated carbon, olivine, anionic exchange resin (IEX) and garnet grains. In case of garnet sand, outliers can be attributed to the distinctive experimental method of multi-particle settling, *i.e.* hindered settling (Loeffler, 1953; Baldock *et al.*, 2004; Tomkins *et al.*, 2005). As the smallest garnet grains were difficult to detect, multiple grains were settled instead of one single grain. The trends in Figure 34 are prominent, which indicates that individual variability cannot simply be ignored.

Table 9 Drag coefficient and terminal settling velocity prediction accuracy for individual terminal settling experiments ($N = 3,629$).
 Note: Average relative error (ARE), Normalised root mean square error (NRMSE) and correlation coefficient (R^2).
 The symbol Φ indicates that the measured sphericity is included in the model.

Model	ARE (C_D)	ARE (v_t)	NRMSE (C_D)	NRMSE (v_t)	R^2 (C_D)	R^2 (v_t)
Schiller–Naumann (1933) ¹⁾	13.0%	7.0%	18.4%	11.3%	0.91	0.93
Fair–Geyer (1954)	16.7%	10.1%	20.2%	13.1%	0.89	0.96
Clift–Gauvin (1971)	12.4%	6.2%	17.4%	9.0%	0.91	0.96
Clift (1978)	12.4%	6.3%	17.9%	9.1%	0.91	0.96
Turton–Levenspiel (1986)	12.7%	6.4%	17.9%	9.1%	0.91	0.96
Flemmer–Banks (1986)	13.0%	6.8%	18.4%	9.8%	0.91	0.97
Khan–Richardson (1987)	12.0%	6.2%	17.1%	9.1%	0.91	0.96
Difelice–Dalavalle (1997) ¹⁾	22.0%	9.1%	27.3%	10.8%	0.91	0.98
Haider–Levenspiel (1989)	12.6%	6.4%	18.0%	9.1%	0.91	0.97
Brown–Lawler (2003)	12.1%	6.2%	17.1%	9.0%	0.91	0.96
van Schagen (2008) ¹⁾	30.2%	11.8%	36.7%	13.7%	0.90	0.97
Cheng (2009)	12.6%	6.3%	18.0%	9.0%	0.91	0.96
Terfous (2013)	12.1%	6.3%	17.2%	9.2%	0.91	0.96
Morrison (2013)	11.8%	6.2%	16.8%	9.1%	0.91	0.96
Barati (2018)	12.4%	6.3%	18.1%	9.2%	0.91	0.96
Goossens (2019)	28.5%	19.8%	31.6%	23.3%	0.86	0.96
Haider–Levenspiel (1989) Φ	14.0%	6.5%	20.0%	8.8%	0.91	0.97
Ganser (1993) Φ	17.6%	8.6%	24.5%	11.1%	0.89	0.96
Chien (1994) Φ	17.3%	9.9%	22.0%	13.1%	0.87	0.96
Hölzer (2008) Φ	29.1%	11.5%	35.6%	13.2%	0.89	0.96
Bagheri (2016) Φ	39.3%	15.3%	74.6%	19.3%	0.60	0.82
Dioguardi (2017) Φ	16.4%	7.4%	23.4%	9.9%	0.91	0.96

¹⁾ Results were rejected when boundary conditions (known limits of applicability) were violated

Note: Statistical methods are given in Annex 5: Statistical analysis.

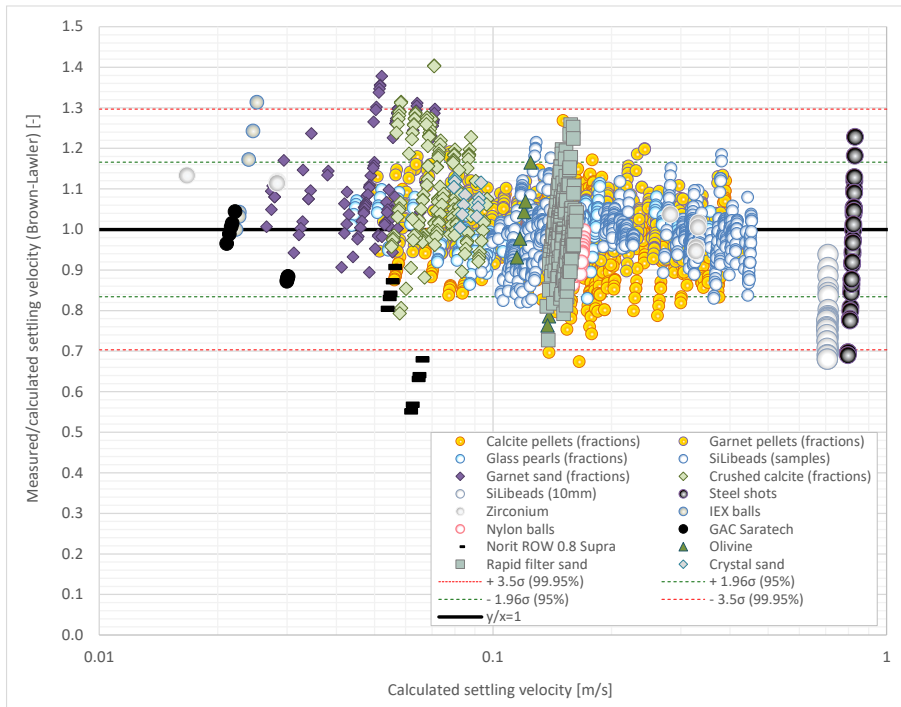


Figure 34 Ratio of measured and calculated terminal settling velocities (Brown–Lawler) against calculated settling velocity. Statistical probability estimation 95% ($\mu \pm 1.96\sigma$) plot and the ($\mu \pm 3.5\sigma$) to show the outliers (0.9%) 32 of 3,629 experimental values. A similar graph for the drag coefficient is given in the Supplementary material (Section 9).

4.4.3 Uncertainty analysis

To better estimate the consequences of spread and accordingly to be able to compensate this in full-scale operational processes, it is important to know which parameters cause the spread in drag and observed settling velocity. We started with an uncertainty analysis to estimate the degree of deviation in variables caused by the following uncertainties in measured parameters (Table 10), to be able to add error bars to the standard drag curves. The estimates of uncertainty in C_D and Re_t as well as in ρ_p and v_t were calculated according to the propagation of errors method (Ku, 1966).

Table 10 Decisive variable and parameter investigation

Variables	Parameters
C_D is determined by:	$g, d_p, \rho_p, \rho_f, v_t$
Re_t is determined by:	d_p, ρ_f, v_t, η
Direct measurements:	Particle properties: d_p, ρ_p, Φ Fluid properties: ρ_f, T Experimental: g, D, L, t

Figure 35 shows typical results for the uncertainty in C_D versus Re_t for 16 selected particle types, expressed with error bars. Results for all other particle types as well as detailed derivations of the contribution to the errors can be found in Annex 6: Overview uncertainty analysis equations and in the Supplementary material (Sections 6 and 7).

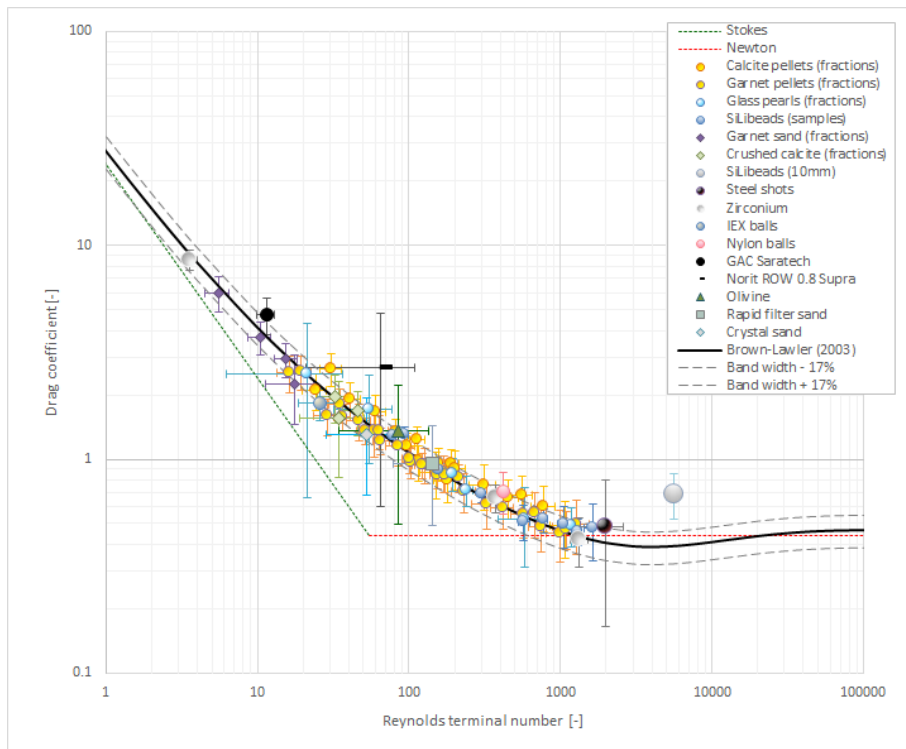


Figure 35 Standard drag curve with error bars based on uncertainty analyses for 16 types of materials compared with the Brown–Lawler prediction model. A bandwidth of 35% is added, based on a summarised propagated effect of errors on the uncertainty of the experimental measurements. Error bars for specific particle types and specific research aims (Table 8) can be found in the Supplementary material (Section 6 and 7).

Natural and processed highly non-spherical polydisperse particles

Natural irregularly shaped particles often used in water treatment processes, such as olivine, calcite, GAC grains and several sand types, cause the largest degree of spread in the standard drag curve. C_D values for GAC grains are higher compared to the calculated value according to (Brown and Lawler, 2003). However, spherical GAC grains show a slightly lower spread, with an error $\delta C_D \approx 1$. The error for the rod-shaped GAC grains is considerable larger due to the combination of a large particle size distribution (PSD), non-spherical shape, particle orientation and particle porosity. During the experiments, it was visually observed that the GAC rods tended to settle horizontally. Additionally, they showed wobbling and zigzag behaviour.

The settling behaviour in terms of drag for olivine, crystal sand, garnet sand and rapid filter sand is less erratic. It is notable that particularly for rapid filter sand grains the error in Re_t is large compared to the error in C_D (Haider and Levenspiel, 1989). This is mainly due to a large PSD, *i.e.* grains were originally mined and not sieved in advance. The non-spherical particle properties are less decisive. The observed spread for other natural grains is similar. However, for grains smaller than 0.5 mm, detecting the settling velocity became more complex and challenging.

For crushed calcite pellets, the error in C_D mainly results from the grains' irregular shape caused by their processing, *i.e.* grinding (Schetters *et al.*, 2015). As the grains were sieved, the PSD is less wide.

The SDC curve for natural and processed highly non-spherical polydisperse particles is given in the Supplementary material (Section 7.1).

Medium non-spherical polydisperse particles used in water softening

Calcite pellets were extracted from the water softening reactor, dried and fractionated using calibrated sieves. Detailed morphological properties such as sphericity and circularity were also measured; these are included in the Supplementary material (Section 2). The extra information was used in the prediction models. The prediction accuracy for C_D was calculated for models derived for spherical particles and for models derived for non-spherical particles. Table 11 presents the accuracy, where the symbol Φ stands for including the particles' morphological properties. No prediction model can predict the drag coefficient with an error level below 10%. The 'best' results are obtained by the classical Haider–Levenspiel model and, with a slightly lower score, the Brown–Lawler model.

Table 11 Drag coefficient prediction accuracy for calcite pellets ($0.36 < d_p < 2.8$ mm) based on individual terminal settling experiments ($N = 1,163$). The symbol Φ indicates that the measured sphericity is included in the model.

Model	ARE (C_D)	NRMSE (C_D)	R^2 (C_D)
Fair–Geyer (1954)	15.4%	17.2%	0.91
Brown–Lawler (2003)	12.1%	13.5%	0.90
Morrison (2013)	12.7%	14.5%	0.91
Goossens (2019)	37.1%	38.1%	0.88
Haider–Levenspiel (1989) Φ	10.0%	11.2%	0.91
Ganser (1993) Φ	13.1%	15.7%	0.91
Chien (1994) Φ	19.6%	21.0%	0.91
Hölzer–Sommerfeld (2008) Φ	21.0%	24.5%	0.87
Bagheri (2016) Φ	15.2%	19.8%	0.85
Dioguardi (2018) Φ	25.7%	28.6%	0.92

Figure 36 presents the average C_D values for calcite pellets where, from a visual perspective, the dots show a reasonable fit with the majority of the models. The error bars clearly show that the variation in the measured data constrains the prediction accuracy. Detailed morphological data of calcite pellets and crushed calcite and the standard drag curve for natural and processed highly non-spherical polydisperse particles are given in the Supplementary material (Section 2 and 7.2).

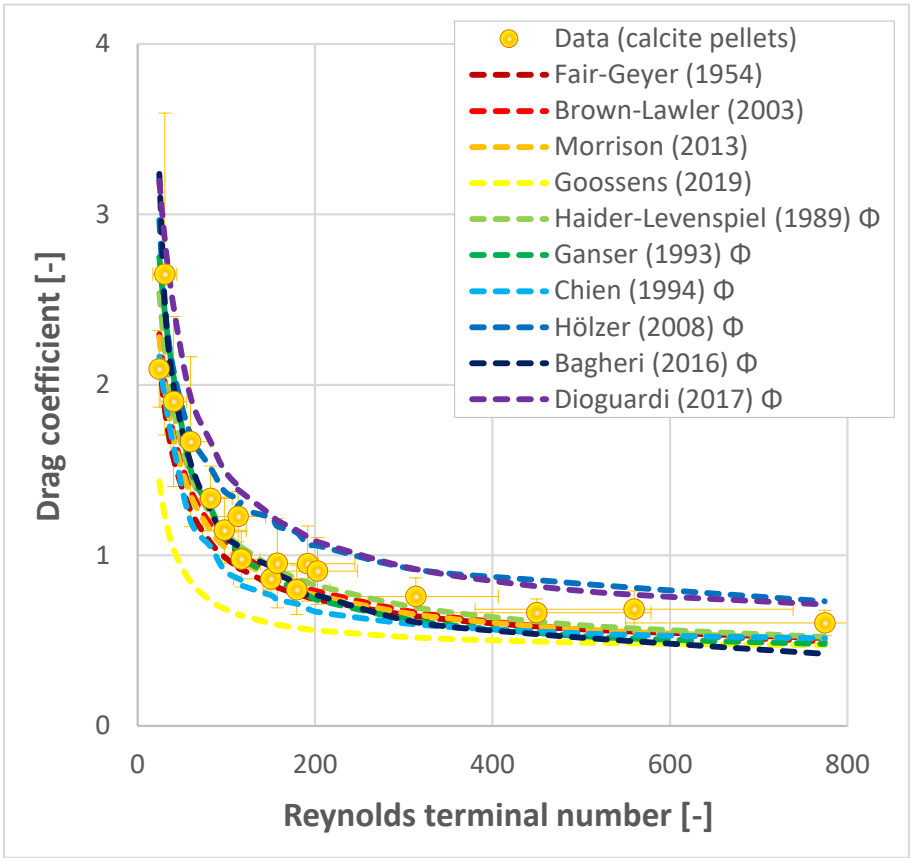


Figure 36 Drag coefficient prediction (average values on lin-lin scale) accuracy for calcite pellets ($0.36 < d_p < 2.8 \text{ mm}$) including (measured) error bars, based on individual terminal settling experiments ($N = 1,163$). Φ indicates that the measured sphericity is included in the model.

Highly spherical polydisperse and monodisperse glass beads

In the literature, glass beads are popular and frequently used for model calibration and validation purposes. In this work, 288 individual spherical glass pearls were settled. The C_D values show reasonable agreement with the Brown–Lawler curve. Data spread is caused by polydispersity ($UC > 1$), albeit less pronounced than for calcite pellets. A whole sequence of highly spherical ($\Phi \rightarrow 1$) monodisperse ($UC \rightarrow 1$) glass beads ($N = 911$) was studied in terms of their settling behaviour. For these particles, diagonal trends in the SDC plots were noticeable, despite the fact that the average C_D coincides fairly well with the Brown–Lawler curve. These trends are related to the way the estimated drag coefficient depends on the measured settling

velocity (Equation (41)) and have been observed by (Veldhuis *et al.*, 2009) and (Raaghav, 2019). The slope in the standard drag curve equals approximately -2, corresponding to $C_D'/\overline{C_D} \sim -2 v_t'/\overline{v_t}$. A mathematical basis for this trend is explained in the Supplementary material section with the help of a simple scaling analysis (Section 10) and the SDC curve (Section 7.3).

Repetitive experiment with highly spherical monodisperse single glass beads

To eliminate the human factor, one sequence was executed where one and the same single glass bead ($d_p = 3$ mm) was used 30 times. The start and end times were filmed, and hence the error in δt and δL was negligible. We observed that the spread in C_D decreased when human error was excluded. Nevertheless, similar to spherical monodisperse glass beads, the previously observed trend (slope -2) was observed. The SDC curves for highly spherical polydisperse and monodisperse single glass beads are given in the Supplementary material (Section 7.4).

Highly spherical monodisperse glass beads and wall effects

Additional to the highly spherical monodisperse glass beads, larger glass beads ($d_p = 10$ mm) were tested in a small cylindrical column ($D = 57$ mm). In this particular case, wall effects evidently played a role in the retardation of the terminal settling velocity. In addition, it became apparent during the experiments that the glass beads tended to move to the wall, followed by a prominent zigzag movement due to side drifting motions caused by a high Galileo number (Zhou and Dušek, 2015). The Galileo number is expressed in Equation (10):

$$Ga = \sqrt{\frac{g d_p^3 \rho_f |\rho_p - \rho_f|}{\eta^2}} \quad (42)$$

Note: The majority of literature which addresses path instabilities use the Galileo number based on the regime map (Jenny *et al.*, 2004; Veldhuis and Biesheuvel, 2007; Zhou and Dušek, 2015), and not the Archimedes number (Karamanev, 1996).

In the standard drag curve, C_D is higher compared to the Brown–Lawler curve, but this can be attributed to wall effects and non-vertical settling trajectories. Wall effect

correction equations given by (Di Felice and Gibilaro, 2004; Gibilaro *et al.*, 1985) and (Chhabra *et al.*, 2003), often empirically based, could not compensate for these non-ideal phenomena and circumstances. The SDC curve and a video fragment illustrating the wall effects for a highly spherical monodisperse glass bead are given in the Supplementary material (Section 7.5).

Highly spherical monodisperse glass beads in different columns and with different fall lengths

To explore the influence of the column diameter, the same experiments were executed in two columns with different sizes ($D = 57$ mm and $D = 125$ mm) for three different glass bead sizes (1.5, 2.5 and 3.5 mm). The successive experiments aimed to determine whether the fall length plays a role. An important aspect here is that the settling velocity was measured merely in a steady state situation. Based on the results and figures given in the Supplementary material (Sections 7.6 and 7.7), no distinction can be made.

Highly spherical polydisperse synthetic particles

Spherical polydisperse particles with a low particle to fluid density ratio ($\bar{\rho} = 1.4$) have similar settling behaviour. Nylon balls and IEX resin balls are spherical and have a relatively high uniformity coefficient. IEX balls are more polydisperse compared to nylon balls and show more spread in C_D . The SDC curve for highly spherical polydisperse synthetic particles is given in the Supplementary material (Section 7.8).

Highly spherical monodisperse metal balls

The outside layer of the examined zirconium balls is ZrO_2 , so the surface is not smooth. To investigate if this affects the drag, we tested highly spherical, monodisperse zirconium balls with three different sizes (0.1, 1.0 and 2.0 mm). The individual measured drag coincides well with the Brown–Lawler curve. Generally speaking, surface roughness can cause the boundary layer to become turbulent and the wake region behind the sphere to become considerably narrower than if it were laminar, which results in a considerable drop in pressure drag with a slight increase in friction drag (Munson *et al.*, 2020; Loth, 2008; Bagheri and Bonadonna, 2016). Nevertheless, the influence of particle surface roughness on the drag coefficient for

Reynolds ($Re_t < 40,000$) can be neglected. The range for Reynolds in this work for all experimental data is $1.2 < Re_t < 7,500$; surface roughness effects were not found and therefore further neglected.

Additionally, the settling behaviour of highly spherical and monodisperse metal balls ($d_p = 3$ mm) with a high particle to fluid density ratio ($\bar{\rho} = 8$) was studied in a cylindrical column ($D = 125$ mm). Based on the average measured C_D , the experimental drag was 7% smaller than the Newton constant drag ($C_D = 0.44$), but 20% above the Brown–Lawler predicted value in this particular range of Reynolds number. The measured drag had a small calculated spread ($C_D = 0.41 \pm 0.01$). The experiments, however, prove the existence of a substantial discrepancy at the individual level. We observed four different settling behaviours and path trajectories (Table 12). An average drag coefficient $C_D = 0.48 \pm 0.17$ was determined for $N = 35$ individual measurements. Nonetheless, a lower $C_D = 0.34 \pm 0.04$ was determined for metal balls with a vertical path trajectory, and $C_D = 0.44 \pm 0.04$ for particles which tended to move to the wall but did not touch it. For particles that came into contact with the wall of the tube, a significantly higher $C_D = 0.68 \pm 0.14$ was found. In this particular case, the wall effect, causing retardation of the settling velocity due to water displacement, is another factor to be considered. Here, the wall effect implies wall contact interactions. Similar to what was found for 10 mm glass beads, we observed a vertical bouncing effect on the wall caused by a chaotic zigzag fall trajectory (Zhou and Dušek, 2015). The SDC curves for highly spherical monodisperse metal balls are given in the Supplementary material (Section 7.9).

Table 12 Path trajectories of 3.0 mm steel shots

Wall interaction	Description trajectory
None	No wall effects, a straight vertical fall path
Minor	Tends to move to the wall but does not touch it
Moderate	Moves towards the wall and touches it
Considerable	Touches the wall from the beginning

4.4.4 Path trajectories

The path trajectories of fractionated calcite pellets (1.0 mm - 2.8 mm) were recorded using an advanced experimental set-up. Figure 37 and Figure 38 present the path trajectories of single calcite pellets, demonstrating the non-linear fall trajectory of grains.

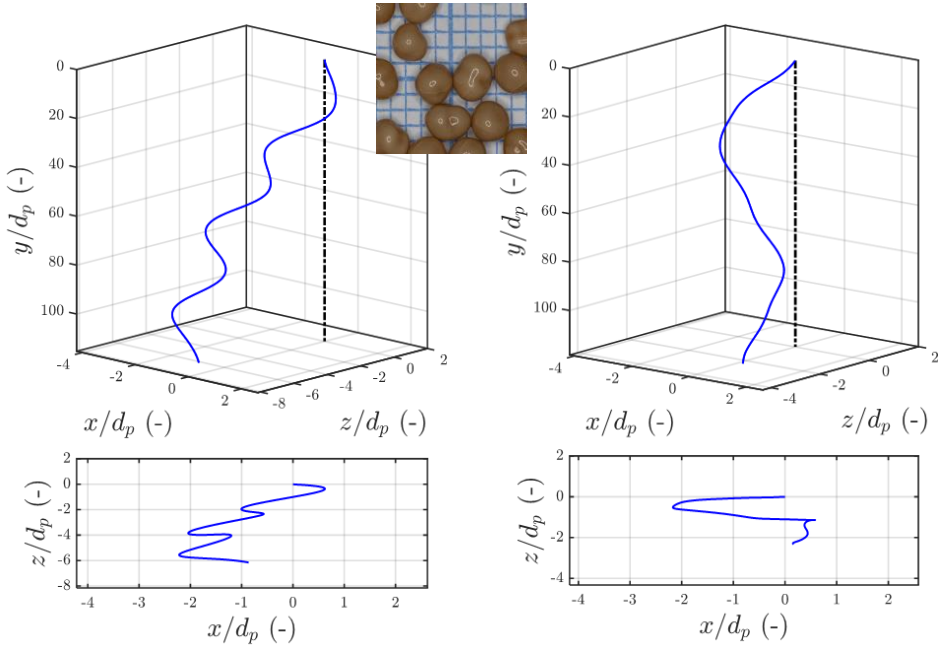


Figure 37 Calcite pellets: $2.36 < d_p < 2.8$ mm, $T = 20$ °C, $C_D = 0.55$, $\bar{\rho} = 2.7$, $Re_t = 809$, $Ga = 522$, $v_t = 0.32$, $v_{t,BL} = 0.34$, angle = 2.8° , $-\%v_t = 7\%$, path: CH

Figure 38 Calcite pellets: $2.36 < d_p < 2.8$, $T = 20$ °C, $C_D = 0.57$, $\bar{\rho} = 2.7$, $Re_t = 800$, $Ga = 522$, $v_t = 0.32$, $v_{t,BL} = 0.34$, angle = 2.1° , $-\%v_t = 8\%$, path: CH

Chaotic paths of freely falling and ascending spheres, path instabilities and transitions in Newtonian fluid have been discussed by many (Jenny *et al.*, 2004; Veldhuis and Biesheuvel, 2007; Horowitz and Williamson, 2010; Zhou and Dušek, 2015; Auguste and Magnaudet, 2018; Riazi and Türker, 2019) and experimentally proven by (Raaghav, 2019). To investigate the path trajectories expected for our particles, we investigated the state diagram (Zhou and Dušek, 2015) of Galileo number Ga versus density ratio ρ_p/ρ_f in Figure 39, magnified in Figure 40. The state diagram contains different areas with typical settling behaviours. Several areas

overlap, which means that different trajectories might occur. The regime map proposed by Zhou and Dušek is derived for perfect spheres. Path trajectories for calcite pellets will not follow the regime map completely, due to their less regular shape, as the regimes are sensitive to the anisotropic nature of the particles.

The measured sphericities of calcite pellets, given in the Supplementary material (Section 2), however, have values larger than $\Phi > 0.9$, so we expect a qualitatively similar path trajectory behaviour.

As shown in Figure 40, about 3/4 of all examined grains belong to the steady oblique regime and 1/4 to the three-dimensional chaotic regime. Calcite pellets show a similar pattern: 4/5 steady oblique and 1/5 chaotic. Glass beads: 1/2 steady oblique and 1/2 chaotic. Synthetic material and metal balls belong almost completely to the chaotic regime.

Individual path trajectory behaviour of the examined calcite pellets and of other particles are given in the Supplementary material (Section 8). Path trajectory videos are shared by (Kramer *et al.*, 2020f).

4.4.5 Data from the literature

In the literature, raw and processed settling data is available for research purposes. The dataset generated by (Brown and Lawler, 2003) is a composition of previous research experiments on spherical particles ($N = 480$). Other researchers (Wu *et al.*, 2006; Almedeij, 2008; Cheng, 2009; Dioguardi and Mele, 2015; Song *et al.*, 2017; Dioguardi *et al.*, 2018; Breakey *et al.*, 2018) shared data for both spherical and non-spherical particles. Based on literature data, C_D versus Re_t for $N = 3,655$ data points is plotted in Figure 41. Figure 42 shows a smaller area, focusing on covering the relevant regime for water treatment, where the data spread reconfirms the apparent spread and deviations also found in our work. A data spread of, for instance, $\pm 50\%$ in C_D means a factor 0.8 - 1.4 in v_t . The consequences for a sand wash installation, for example, is an error in v_t of $\pm 20\%$, which could raise the question whether this is sufficiently accurate and suitable for process control. Drag coefficient prediction accuracy, similar to the data in Table 9 and data from the literature, is given in the Supplementary material (Sections 5.7 and 17).

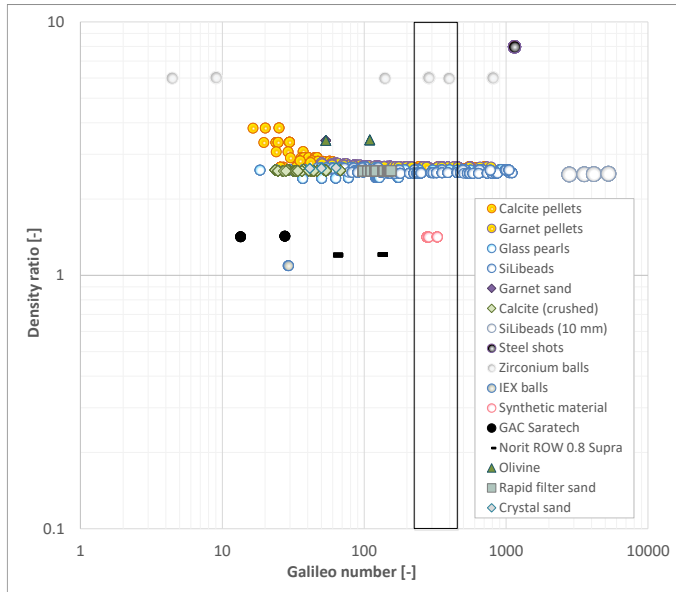


Figure 39 State diagram. Galileo number Ga versus specific gravity number $\bar{\rho}$ with examined particles.

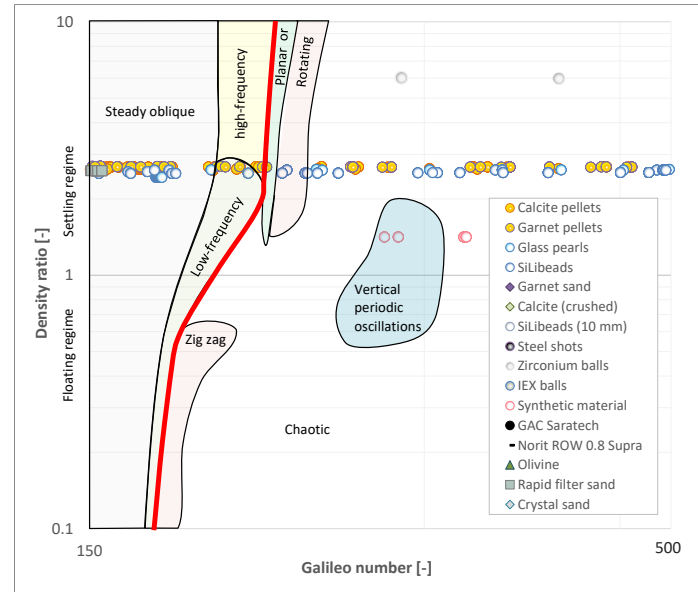


Figure 40 Path trajectory regime plot according (Zhou and Dušek, 2015; Raaghav, 2019) (zoomed area in Figure 39). The chaotic regime applies to the right of the red line.

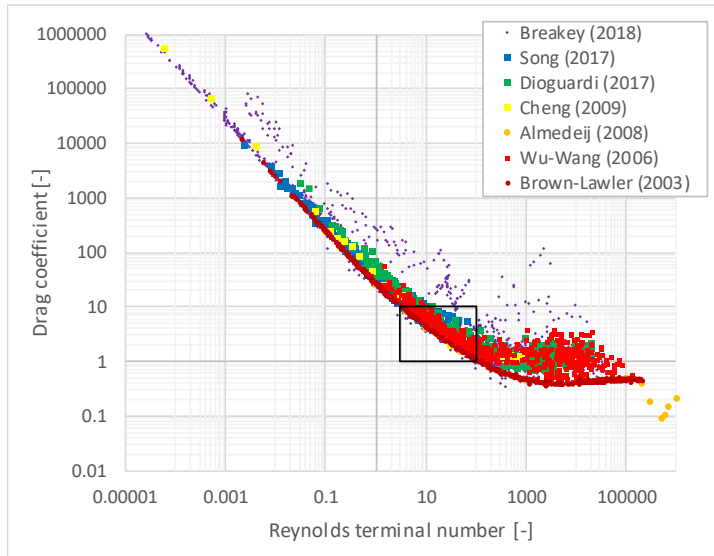


Figure 41 SDC (log-log) data from literature sources with 4,135 data point in total.

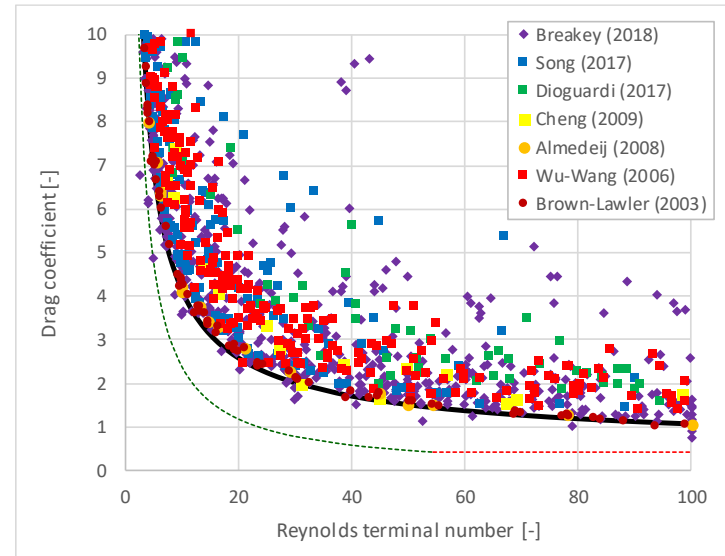


Figure 42 SDC (lin-lin) data from literature sources, zoomed in on an area that is important for drinking water treatment. Solid lines represent the Brown-Lawler drag model and dashed lines the Stokes and Newton drag models, respectively.

4.4.6 Propagated effect of parameter uncertainties on terminal settling

Figure 43 shows the influence of the uncertainty in various parameters on uncertainty in the settling velocity v_t . The summarised propagated effect of errors on the uncertainty of the experimental measurements are 35% for the terminal settling velocity and 56% for the terminal Reynolds number. The graphically summarised propagated effect of errors for C_D and Re_t are presented in the Supplementary material (Section 6). The figure shows that some causes, like variation in gravity, surface roughness and linear expansion due to temperature changes, can be neglected.

Uncertainties in the fluid density and viscosity as well as in the estimated (human) error of measurements have a relatively minor effect on the error in v_t . For instance, the error in v_t resulting from the human error in measurements is estimated at 1.3%, based on human response time inaccuracies. Depending on the tube and particle dimensions, also wall effects, leading to retardation of the settling velocity, can be ignored, certainly in full-scale systems. Based on the wall effect equation proposed by (Arsenijević *et al.*, 2010), which has gained wide acceptance in the literature, the error on v_t is estimated to be 2.6% for all measurements made in this study. Further details and an explanation with respect to wall effects and error analysis can be found in the Supplementary material (Section 13).

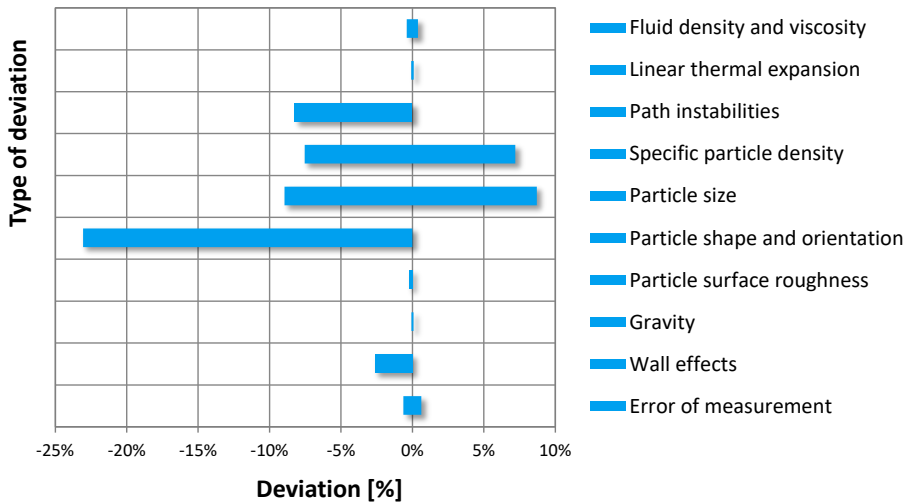


Figure 43 Summarised propagated error on the terminal settling velocity resulting from different causes.

Figure 43 shows that the vast majority of the spread is caused by variations in specific particle density, particle size and shape, particle orientation and path instabilities. The error caused by natural variations in particle density *combined* with the relative error of experimentally measured particle density in the laboratory was approximately 7%. The error in v_t was calculated at 14.8%.

Regarding particle size, in this work pellets were sieved to produce more monodisperse particle samples. On the assumption that spheres are round and pass the sieves, the variation in size (Δd_p) is 19.0%, but this depends on the type of sieve used. The variation in diameter had a considerable effect (17.7%) on spread for v_t . A special case is included in the Supplementary material (Section 12), based on the assumption that irregularly shaped particles behave like spheroids. It is illustrated how particles pass through a sieve and rotate and settle, and this is compared with a particle on another projected surface.

The literature shows that the effect of particle orientation on the drag coefficient depends on particle shape, (Abraham, 1970; Bird *et al.*, 2007; Loth, 2008; Bagheri and Bonadonna, 2016). As the particle shape becomes less spherical, the effect of particle orientation becomes more significant due to the increase of the ratio between maximum and minimum projected areas. In the Stokes regime, the particles do not have a preferred orientation and for a statistically representative run of experiments they can adopt any random orientation.

An easy preliminary approach for non-spherical shapes can be adopted through the sphericity Φ , which is frequently used in drinking water treatment processes to correct for irregular particles (Yang, 2003). In the case of sand grains, the drag coefficient increases from 1.2 to 1.7 when the sphericity decreases from $\Phi = 1.0$ to $\Phi = 0.7$, which corresponds to a 20% increase of C_D (US-IACWR, 1957). When the sphericity is decreased stepwise by 10%, the terminal settling velocity decreases linearly by 10% while, in contrast, the drag coefficient increases almost twice as much. For sand, (Đuriš *et al.*, 2013) selected a reasonable sphericity $\Phi = 0.76$. According to (Yang, 2003), the sphericity varies between $\Phi = 0.66$ for sharp sand and 0.86 for round sand, which agrees well with Geldart's observation for measured settling velocity (Geldart, 1990). A sphericity of 0.66 results in a 23.0% decrease of v_t and a 28.6% increase of C_D .

(Albright, 2009) showed that for cylindrical particles towards the laminar regime ($Re_t < 50$) the drag coefficient is lower compared to round spheres. However, this coefficient is higher for more turbulent regimes where $Re_t > 50$. (Dharmarajah, 1982) reported that under creeping conditions all orientations are stable ($Re_t/\Phi < 0.1$) and that in the transitional regime ($0.1 < Re_t/\Phi < 200$) particles are stable since they tend to orient themselves with the largest cross-section in the three mutually perpendicular planes of symmetry in a position normal to the direction of motion. Under more turbulent conditions ($200 < Re_t/\Phi < 500$), the orientation of settling is less predictable: examples include wobbling and rotation. For the inertial regime ($Re_t/\Phi > 500$), the particles' rotation about their axis is frequently coupled with spiral translations. (Haider and Levenspiel, 1989) demonstrated in the drag–Reynolds terminal diagram that for irregular particles with increasing non-sphericity, the drag coefficients also increase considerably: this can rise by as much as 500%. This demonstrates that for higher Reynolds numbers irregularity becomes increasingly important.

4.4.7 Consequences of uncertainty in settling velocity for water treatment processes

The discussion on how to measure the terminal settling velocity of a single particle, or multiple particles, is extremely relevant. What is the most representative for a full-scale system? Not a single particle. Hence, it is important to discuss how single

particle measurements can be extrapolated to information relevant for the full-scale system. Often the settling velocity is expressed as a fraction of the terminal settling velocity. For instance, in their famous article (Richardson and Zaki, 1954) the settling velocity of multiple particles for a voidage extrapolated to 1 equals the apparent free-falling settling velocity of a single particle at infinite dilution, i.e. the terminal settling velocity v_t . Many water treatment processes like pellet-softening and filter backwashing operate at a voidage in the vicinity of the incipient state (Kramer *et al.*, 2019). Therefore, a large uncertainty in v_t has a considerable effect on the voidage prediction, for instance leading to a fixed bed state where a fluidised bed was expected. In this work, we have explicitly shown the causes of uncertainty in v_t . There is no model for the prediction accuracy for terminal settling velocity and drag coefficient, that covers the wide range of differences in particle properties with a low prediction inaccuracy (< 1%). The prediction accuracy for models derived for non-spherical particles (Haider and Levenspiel, 1989; Ganser, 1993; Hölzer and Sommerfeld, 2008; Ouchene *et al.*, 2016), using the sphericity as a shape descriptor, is not significantly improved for drinking water related granules.

4.5 Conclusions

Based on measured average terminal settling velocities, drag prediction models like Brown–Lawler were found to agree reasonably well with experimental observations. However, individual terminal settling velocities showed a considerable amount of spread around the average value. In general, particle size and shape variations as well as chaotic path trajectories during settling are the most decisive reasons why the spread in individual terminal settling velocities occurs. In this work we observed two kinds of wall effects. Besides their decreased settling velocity, the aspect that is the most frequently discussed in the literature, particles also show variations in path trajectories where they touch the vessel wall, thus leading to a reduced velocity. While the majority of the predictive correlations lie within a bandwidth of 6% between each other, the summarised propagated effect of errors on the uncertainty of the experimental measurements is 34% for v_t , 35% for C_D and 56% for Re_t . The data obtained from literature sources also show a considerable degree of spread in C_D . The terminal settling velocities determined with an advanced experimental set-up were compared with *old-school* velocities measured by eye and stopwatch. The average relative error between the two methods was only $4\% \pm 3\%$, so this cannot

explain the observed large spread in individual measurements. Simple models such as $C_D = \frac{24}{Re_t} + 0.44$ (Goossens, 2019) have a relatively low prediction accuracy, based on the data acquired. Nevertheless, one should take into consideration the existing data spread around the average C_D when other models are used with apparently higher prediction accuracies. In other words: more complex expressions do not automatically entail higher accuracy.

Our results have important implications when drinking water treatment processes are optimised or designed, for instance with a new type of grain with specific morphological, density or other particle properties. It is important to take notice of the spread in settling velocities. The considerable degree of spread in terminal settling velocities could result in less optimal process states and lower efficiency in the use of raw materials and should therefore be taken into account in the design, operation and optimisation of water treatment processes.

Finally, the prediction accuracy for terminal settling velocity and drag coefficient should be improved, in particular for non-spherical particles.

In conclusion, to answer our main question whether terminal settling velocity and drag of natural particles in water can ever be predicted accurately, we have to say 'yes, it is possible', at least for spherical particles and using a model such as Brown–Lawler. The answer is 'possibly yes' for non-spherical particles, albeit only when more morphological properties are included besides (equivalent) particle diameter, circularity and sphericity. During the past decades, novel work has been published on the topic of terminal settling. Nevertheless, some puzzles remain unsolved. The prediction accuracy can be improved by means of new advanced research, to be carried out in academia as well as in industry.

4.6 Supplementary material

Supplemental data for this article can be accessed at:
<https://doi.org/10.5194/dwes-14-53-2021-supplement>

Contents		page
1	Materials and methods	5
1.1	Experimental set-up for terminal settling experiments	5
1.2	Flow chart diagram	6
1.3	Concise drinking water treatment processes	8
1.4	Physical properties of water	8
1.5	Procedure	8
1.5.1	Preparations	8
1.5.2	Old-school terminal settling velocity experiments	8
1.5.3	Repeating experiment of one and the same particle	9
1.5.4	Multiple particle experiment	9
2	Particle selection and characterisation	10
2.1	Photos of particles	10
2.2	Particle selection	15
2.3	Average particle diameter	18
2.4	Particle density	20
2.4.1	Particle counting	20
2.4.2	Static image analyses	20
2.4.3	Differential pressure	20
2.4.4	Laboratory pycnometer	20
2.4.5	Grains with different densities	20
2.4.6	Density measurement results	21
2.5	Particle characterisation and morphological properties	21
3	Calculation of the local gravitational field of earth	22
4	Wall effects	23
5	Drag coefficient prediction models from the literature	24
5.1	Spherical particles	24
5.2	Non-spherical particles	25
5.3	More complex prediction models using morphological properties	26
5.4	Brown–Lawler model	27
5.5	Range analysis	28
5.6	Standard drag curve with average values and prediction models	29
5.7	Model prediction accuracy for data from the literature	29
5.8	Comparison old-school and advanced terminal settling velocities	31
6	Uncertainty analysis	32
6.1	Basic equations	32
6.2	Overview uncertainty analysis equations and contribution to error	33
6.3	Simplifications	34
6.3.1	Archimedes and Galileo numbers	34
6.3.2	Linear thermal expansion	34
6.3.3	Kinematic viscosity	35

6.4	Drag Reynolds relationships	35
6.5	Uncertainty expressions	36
6.6	Reynolds uncertainty	36
6.6.1	First term	36
6.6.2	Second term	37
6.6.3	Third term	39
6.7	Drag uncertainty	41
6.7.1	First term	41
6.7.2	Second term	42
6.7.3	Third term	44
6.7.4	Fourth term	45
6.7.5	Fifth term	47
6.8	Particle density uncertainty	49
6.8.1	First term	49
6.8.2	Second term	49
6.9	Terminal settling velocity uncertainty	50
6.9.1	First term	50
6.9.2	Second term	50
6.9.3	Relative velocity:	51
6.9.4	Human response time inaccuracy correction	52
6.10	Uncertainty analysis parameters and coefficients	52
7	Uncertainty in drag coefficient	53
7.1	Natural and processed highly non-spherical polydisperse particles	53
7.2	Medium non-spherical polydisperse particles applied in softening	53
7.3	Spherical polydisperse and monodisperse glass beads	54
7.4	Repetitive experiment with round monodisperse single glass beads	55
7.5	Highly spherical monodisperse glass beads and wall effects	56
7.6	Highly spherical monodisperse glass beads in different columns	56
7.7	Highly spherical monodisperse glass beads different fall lengths	57
7.8	Highly spherical polydisperse synthetic particles	57
7.9	Highly spherical monodisperse metal balls	58
8	Recorded path instabilities	59
8.1	Path trajectories	59
8.2	Path trajectory tables	69
8.3	Path trajectory videos	71
9	Measured and calculated drag coefficient	72
10	Drag-Reynolds experimental data spread trends	73
10.1	Observed drag-Reynolds data trends	73
10.2	Error made by the laboratory researcher	73
10.3	Correlation error in CD with error in Ret	75
10.4	Direct dependency of the deviation to variation in particle diameter	76
11	Steady state velocity	77
12	Oblate spheroids	78
13	Statistical analysis	80
13.1	Statistical equations	80
13.2	Propagated effect of parameter uncertainties on drag and Reynolds	81
14	Acknowledgments	83

15	Nomenclature	84
	15.1 Symbols	84
	15.2 Greek symbols	85
	15.3 Subscripts, superscripts and abbreviations	85
16	Bibliography	87
17	Source data	91
	17.1 Experimental data (this work)	91
	17.2 SDC data (this work)	121
	17.3 SDC data (literature)	151-184

Improved Richardson–Zaki Based on hydraulics

$$\epsilon^n = \frac{v_s}{v_t}$$

Index

Superficial velocity

Voidage

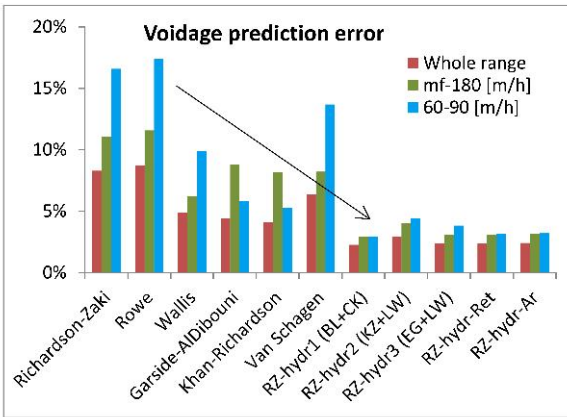
Terminal velocity

$$\frac{\Delta P}{\Delta L} = 180 \frac{v_{mf} \eta (1 - \epsilon_{mf})^2}{d_p^2 \epsilon_{mf}^3} + 2.87 \frac{\rho_l^{0.9} v_{mf}^{1.9} \eta^{0.1} (1 - \epsilon_{mf})^{1.1}}{d_p^{1.1} \epsilon_{mf}^3}$$

Carman–Kozeny (at minimum fluidisation)

$$C_D = \frac{24}{Re_t} (1 + 0.15 Re_t^{0.681}) + \frac{0.407}{1 + \frac{8710}{Re_t}}$$

Brown–Lawler (at terminal settling)



Drinking water pellet softening liquid-solid fluidisation

- ▶ The Richardson–Zaki model can be improved using a hydraulic basis
- ▶ Minimum fluidisation prediction using Richardson–Zaki is inaccurate
- ▶ The index coefficient in the Richardson–Zaki equation is redundant
- ▶ Voidage can be predicted accurately in liquid-solid fluidisation processes

Keywords Liquid-Solid Fluidisation; Drinking Water; Richardson–Zaki; Minimal Fluidisation; Terminal Settling Velocity; Hydraulic Models

Chapter 5

Richardson–Zaki

“The arrival time of a space probe travelling to Saturn can be predicted more accurately than the behaviour of a fluidised bed chemical reactor.”

(Derek Geldart, 1986)

This article has been published as:

Improvement of the Richardson–Zaki liquid-solid fluidisation model on the basis of hydraulics

O.J.I. Kramer, P.J. de Moel, E.T. Baars, W.H. van Vugt, J.T. Padding,
J.P. van der Hoek

Powder Technology. **343** (2019) pp. 465–478

The article can be found online at:

<https://doi.org/10.1016/j.powtec.2018.11.018>

5 Improvement of the Richardson–Zaki liquid-solid fluidisation model on the basis of hydraulics

5.1 Abstract

One of the most popular and frequently used models for describing homogeneous liquid-solid fluidised suspensions is the model developed by Richardson and Zaki in 1954. The superficial fluid velocity and terminal settling velocity together with an index makes it possible to determine the fluid voidage in a straightforward way. The reference point for the Richardson–Zaki model is the terminal settling velocity at maximum voidage conditions. To be able to predict voidage in the proximity of minimum fluidisation conditions, either the minimum fluidisation velocity must be known or the Richardson–Zaki index must be very accurate. To maintain optimal process and control conditions in multiphase drinking water treatment processes, the voidage is kept relatively low. Unfortunately, the Richardson–Zaki index models tend to overestimate the minimum fluidisation velocity and therefore also result in less accurate predictions with respect to voidage values. We extended the Richardson–Zaki model with proven hydraulics-based models. The minimum fluidisation velocity is acquired using the model proposed by Kozeny (1927), Ergun (1952) and Carman (1937). The terminal settling velocity is obtained through the model developed by Brown and Lawler (2003), which is an improved version of the well-known model developed by Schiller and Naumann (1933). The proposed models are compared with data from expansion experiments with calcium carbonate grains, crushed calcite and garnet grains applied in drinking water softening using the fluidised bed process. With respect to voidage, prediction accuracy is improved, with the average relative error decreasing from 15% to 3% when the classic Richardson–Zaki model is extended with these hydraulics-based models. With respect to minimum fluidisation velocity, the average relative error decreases from 100% to 12%. In addition, simplified analytical equations are given for a straightforward estimation of the index n .

5.2 Introduction

The accurate calculation of voidage in water is of major importance in drinking water treatment processes because it determines the process conditions and treatment results. Examples include pellet-softening in fluidised bed reactors (Graveland *et al.*, 1983), sedimentation, flotation and flocculation, filtration processes (Amburgey, 2005), backwashing of filter media and washing columns in which fine material and impurities are separated from seeding material. In these processes, particle size mostly varies between 0.3-2.0 mm, and particle density between 2.5-4.0 kg/L. This study focuses on calcium carbonate particles applied in pellet-softening reactors. The softening process involves the dosing of caustic soda, soda ash or lime in a cylindrical up-flow fluidised-bed reactor, which leads to an alteration of the calcium carbonate equilibrium in which the solubility product is exceeded. The reactor is filled with seeding material such as garnet grains (Figure 1B) or crystal sand grains and pellets. The large specific surface area in the reactor causes the CaCO_3 to crystallise on the particles, called pellets (Figure 1C), as a result of which these grow in size and become increasingly round. If there is no difference in specific density, larger particles will migrate to the lower region of the reactor bed, and a stratified bed will evolve. To retain fluidisation conditions, it is important that the largest pellets, usually those that are larger than 1-2 mm, are extracted from the reactor. These pellets can be used as a by-product in other processes, for instance in industrial and agricultural processes, or they can be re-used as seeding material.

Pellet-softening in a fluidised bed reactor was developed and introduced in the Netherlands in the late 1980s, and by the end of 2018 almost all Dutch drinking water was softened with the help of this technique (Hofman *et al.*, 2007). For more than 30 years, crystal sand and garnet grains have been used as seeding material (van Dijk and Wilms, 1991). Process optimisation (van Schagen *et al.*, 2008b) and control (van Schagen *et al.*, 2008a) has been focused primarily on garnet pellets.

To meet sustainability goals and to promote the development of a circular economy, water companies have modified their pellet-softening processes, in which garnet grains, mined in Australia, have been replaced by calcite seeding particles that are based on crushed, dried, sieved and re-used calcium carbonate pellets (Schetters *et al.*, 2015). A second matter to be considered is that the garnet core inside the pellets hinders their potential application in market segments such as the glass, paper, food and feed industries, and it hinders their direct re-use in the pellet reactor itself when it comes to ensuring a more sustainable and circular process. The pellet

market value and the sustainability of the softening process (Beefink *et al.*, 2021) can be increased through the substitution of the sand grain by a calcite grain of 0.5 mm (100% calcium carbonate). If the calcite pellets are crushed, dried and sieved, they can be re-used as a seeding material (Palmen *et al.*, 2014). Due to the crushing of the relatively round pellets, the calcite seeds have an irregular shape (Figure 1D) and behave differently with respect to settling characteristics in the up-flow fluidisation reactor. In the case of pellet-softening processes using fluidisation, this different sedimentation behaviour can cause unwanted flushing of smaller particles out of the reactor and settling of larger grains to the lower region of the reactor, which leads to a fixed bed state. Photographs of particles used in this study can be found in Annex 1: Photos and in the Supplementary material (Chapter 1).

To maintain or provide optimal process conditions in pellet-softening reactors, it is important to accurately determine the fluidised bed voidage. Voidage is a crucial variable to determine the specific surface area, the minimum fluidisation and flushing conditions as well as the water and particle residence time. At the bottom of the reactor, the voidage is kept relatively low to obtain the highest crystallisation contact area; nevertheless, fixed bed situations must be avoided. The degree of voidage is dependent on the physical properties of the grains and the water viscosity. *De facto*, voidage, or fluid bed height, is kept constant through controlling the water flow in the reactor depending on water temperature and through particle bed management. In pellet-softening reactors, voidage is approximately $\varepsilon \approx 0.5$ at the bottom of the reactor and $\varepsilon \approx 0.8$ at the top.

In the literature, several attempts have been made to predict voidage. Asif (1998) studied binary solids, and Akgiray and Soyer (2006) presented widely used Richardson–Zaki correlations for spherical particles. Slaa *et al.* (2012) showed that the Richardson–Zaki expression underestimates the settling velocities for small particles at high concentrations due to the effect of particle size on the apparent viscosity of the settling silt-water mixture. Đuriš *et al.* (2016) investigated the prediction of bed expansion and minimum fluidisation velocity of sand mixtures in water.

The objective of this paper is to improve the popular Richardson–Zaki model through model enhancement based on hydraulics, which will lead to an improved accuracy of voidage predictions, particularly for pellet-softening. Through the minimum fluidisation velocity and terminal settling velocity, the Richardson–Zaki index can be calculated accurately. In this way, the index acquires a hydraulic meaning. The numerical prediction of voidage in fluidisation reactors using natural particles with an

irregular shape is much more complex than would be the case for perfectly spherical particles. In this work, an improved model is proposed and compared with existing Richardson–Zaki based models, while modelling results are compared with results from a significant number of expansion experiments which were carried out at pilot plant scale. Improved knowledge in this field enables accurate modelling and optimisation for system and control purposes in automated drinking water treatment processes. This is particularly important because unreliable prediction models increase the risk of ineffective treatment processes and higher consumption of chemicals, something which may adversely affect drinking water quality, sustainability goals and costs.

This paper is organised as follows. In Section 5.3, we give a general overview of the current Richardson–Zaki based models and theory. In Section 5.4, we discuss the Richardson–Zaki theory applied to the fluidised-bed pellet-softening process and we propose new Richardson–Zaki index equations based on hydraulics. In Section 5.5, we present our experiments and in Section 5.6 we show and discuss the results. We end with our conclusions in Section 5.7.

5.3 Richardson–Zaki model analyses

5.3.1 Model principle

A fundamental approach for the description of homogeneously fluidised beds is the well-known and most popular expansion law of Richardson and Zaki, introduced in 1954, which describes the steady state velocity-voidage relationship for sedimenting liquid-solid homogeneous suspensions, but which is also used in gas-solid systems. The model is addressed in a number of standard works: (Wilhelm and Kwauk, 1948; Al-Dibouni 1977; Dharmarajah, 1982; Yates, 1983; Rowe 1987; Li and Kwauk, 1994; Gupta and Sathiyamoorthy, 1999; Darby and Chhabra, 2001; Gibilaro, 2001; Holdich, 2002; Yang, 2003; Oka and Anthony, 2003; Crowe and Group, 2006; Rhodes, 2008; Peker *et al.*, 2008; Yates and Lettieri, 2016; Seville and Yu, 2016). When an ensemble of solid particles is settling in a quiescent liquid, additional hindering effects influence its settling velocity. The drag (Gupta and Sathiyamoorthy, 1999) is increased as a result of the proximity of particles within the ensemble and

the up-flow of liquid as it is displaced by the descending particles. According to Richardson and Zaki, the hindering effects are strongly dependent on the voidage ε . Theoretically, Coulson and Richardson (1957), updated in Harker *et al.* (2002), demonstrated that the validity of the Richardson–Zaki equation is limited by the maximum solids concentration that permits solids particle settling in a particulate cloud. This maximum concentration corresponds with the concentration in an incipient fluidised bed or at minimum fluidisation conditions where $\varepsilon = \varepsilon_{mf} \approx 0.4$. In the model, the superficial velocity v_s is linked with particle and fluidised bed characteristics such as the terminal settling velocity v_t of an isolated particle in an unbounded fluid.

$$\varepsilon^n = \frac{v_s}{v_t} \quad (\varepsilon_{mf} < \varepsilon < 1) \quad (43)$$

Equation (43) gives a simple relationship between voidage and sedimentation or fluidisation velocity for systems composed of uniform monodispersed spheres dispersed in a liquid. Other expressions which have been proposed in the literature are generally more complex or more limited in their application.

5.3.2 Model boundaries

Theoretically (Busciglio, 2011), the Richardson–Zaki model intersects two boundary points:

$$\begin{cases} \frac{v_s}{v_t} = 0 & \text{for } \varepsilon = 0 \\ \frac{v_s}{v_t} = 1 & \text{for } \varepsilon = 1 \end{cases} \quad (44)$$

It is known that the index n in the Richardson–Zaki model depends on the flow regime. This influence is visualised in Figure 44 where the ratio of the superficial and terminal settling velocity is plotted against the voidage. For viscous flow using the classic Stokes particle drag equation, the Richardson–Zaki index tends to $n \rightarrow 4.8$; in the inertial regime, the Richardson–Zaki index tends to $n \rightarrow 2.4$ (Rhodes, 2008).

Usually, the voidage is considered to be the dependent variable and the superficial velocity the independent variable (Gibilaro, 2001). Therefore, Figure 44 displays the superficial velocity on the X-axis and the voidage on the Y-axis. The degree of curvature is determined by the index n , as can be seen in Figure 44. Deviations in particle size and shape affect the Richardson–Zaki index, which leads to more inaccurate voidage predictions.

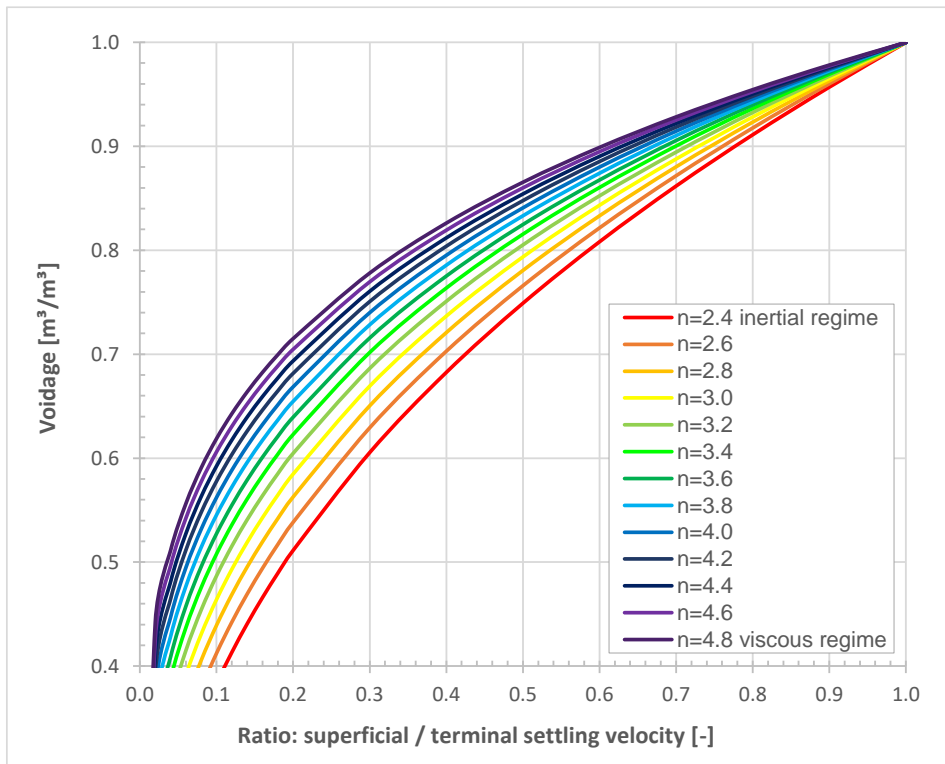


Figure 44 Richardson–Zaki gradients for various Richardson–Zaki indices. The curves are bounded to incipient fluidisation $\varepsilon \approx 0.4$. The relative error in minimum fluidisation (X-axis) is larger compared to the relative error in voidage (Y-axis).

In fact, the Richardson–Zaki model does not consider the incipient fluidisation condition. In the vicinity of minimum fluidisation v_{mf} , small deviations in n cause large deviations in the prediction of the minimum fluidisation point when merely the classic Richardson–Zaki model is used (following the curves from v_t to v_{mf} in Figure 44). Indeed, large deviations in n were already observed in Figures 5 and 6 included in the article by Khan and Richardson (1989). The most obvious and known points

are the inherent terminal settling velocity and the minimum fluidisation velocity. Using these two points, besides the origin (0,0), the index is in fact determined, as we will show in this paper.

5.3.3 The Richardson–Zaki index n

Popular index equations

In the literature, a collection of equations is given to estimate the Richardson–Zaki index n of which the most popular are presented in Table 13. These equations are based on the single particle Reynolds number Re_t under terminal settling conditions or the Archimedes number Ar .

$$Re_t = \frac{\rho_f v_t d_p}{\eta} \quad (3)$$

$$Ar = \frac{g d_p^3 \rho_f (\rho_p - \rho_f)}{\eta^2} \quad (9)$$

Table 13 Richardson–Zaki index equations from the literature

Reference	Reference	Equation	Eq. nr.
Classical Richardson–Zaki equation	(Richardson and Zaki, 1954), (Richardson and Zaki, 1979)	$n = \begin{cases} Re_t < 0.2, & n = 4.65 \\ 0.2 \leq Re_t < 1, & n = 4.4 Re_t^{-0.03} \\ 1 \leq Re_t < 500, & n = 4.4 Re_t^{-0.1} \\ Re_t \geq 500, & n = 2.4 \end{cases}$	(45)
General expression	(Siwec, 2007)	$n = c_1 Re_t^{c_2}$	(46)
Garside and Al-Dibouni equation	(Garside and Al-Dibouni, 1977), (Rowe, 1987)	$\frac{n_L - n}{n - n_T} = \alpha Re_t^\beta$	(47)
Khan and Richardson	(Khan and Richardson, 1987)	$\frac{n_L - n}{n - n_T} = \alpha Ar^\beta$	(48)

Equation index boundaries

As early as 1949, Lewis *et al.* (1949) found that if the particle is settling under conditions where Stokes' law is valid, n has a value of about 4.65. According to Khan and Richardson (1987), Gibilaro (2001), Yang (2003) and others, the Richardson–Zaki index is bounded between the viscous ($n = 4.8$) and the inertial regime ($n = 2.4$). According to (Maude and Whitmore, 1958) and (Richardson and da S. Jerónimo, 1979), the value of n lies between 2.4 and 4.6, or between 2.3 and 4.6, respectively, for a wide range of terminal Reynolds numbers.

Alternative index equations

A different empirical equation was proposed by Garside and Al-Dibouni (1977). Rowe (1987) gave a convenient empirical equation to estimate the Richardson–Zaki index covering the whole Reynolds range: n_L and n_T are the asymptotic values of n at low and high values of Re_t , respectively, while the position and rate of increase of n in the intermediate region are determined by the coefficients α and β . According to Khan and Richardson, Equation (47) given by Rowe is an empirical expression which satisfactorily represents the experimental data for n when the effect of the vessel walls is negligible.

Equation (47) cannot be applied for a given liquid-solid system without prior knowledge of Re_t . Therefore, Khan and Richardson (1989) proposed the same form of equation while using the Archimedes number (Equation (9)) instead of the Reynolds terminal number, albeit with different values of the coefficients α and β .

The Richardson–Zaki model originally included wall effect corrections in Equation (45). In some works, the wall effect corrections are ignored (van Schagen *et al.*, 2008b; Seville and Yu, 2016; Clift *et al.*, 1978; Di Felice, 1995; Pal and Ghoshal, 2013). More info about wall-effects is given in Annex 2: Wall effects.

Siwec (2007) presented different values of the coefficients c_1 and c_2 for several types of grain materials. Di Felice and Gibilaro (2004) and Khan and Richardson (1987) presented an overview of existing empirical equations to calculate the Richardson–Zaki index. A collection of improved equations to calculate the index equation was given by Dharmarajah (1982) and Akgiray and Soyer (2006). Extension and adjustments of the Richardson–Zaki equation to suspensions of multisided irregular particles were examined by Bargieł and Tory (2013), for small fines by Schiaffino and Kytömaa (1993), and the expansion behaviour within fixed packings by Glasserman *et al.* (1994). The relation between the Richardson–Zaki

equation and the apparent drag force has been studied by Yang and Renken (2003), Valverde and Castellanos (2008) and Di Felice (1995), and in addition new equations have been proposed for the intermediate regime. The latest proposal was made by Pal and Ghoshal (2013), albeit with a different approach, to predict the settling velocity of a sedimenting particle which is dispersed in a sediment-fluid mixture during a turbulent flow. Although theoretically the value of n is restricted between $2.4 < n < 4.8$, high values are reported by Capes (1974), Chong *et al.* (1979) and Johnson *et al.* (2016), often due to the irregularity of investigated grains.

Based on experimental data, some works like (Khan and Richardson, 1989) on the Richardson–Zaki index n show significant deviation. In other works (Đuriš *et al.*, 2016), particle size distributions (Siwiec, 2007; Akgiray and Soyer, 2006; Capes, 1974) affect the linearity of the $\log v_s$ versus $\log \varepsilon$ curves, where particularly at higher flow regimes this leads to deviations in n . Exclusively considering perfectly round monodispersed spheres will show no deviation in n . However, using natural grains, a certain degree of deviation will *de facto* be observed. By applying irregularly shaped particles, a shape factor (Yang, 2003) could be introduced as a correction for the particle diameter used in the Richardson–Zaki model. Shape factors are often applied in fixed bed processes. In fluidised processes, however, shape factors as a constant correction factor are less accurate due to the re-orientation of irregularly shaped particles that takes place at different voidage values. Since the Richardson–Zaki model can solely be used for the fluidised state, pragmatic shape factors are therefore less useful. To be able to cope with irregularity accurately, the Richardson–Zaki model must be extended thoroughly by introducing complex models, even if this might adversely affect the ‘elegance’ of the simple expression 43. We based our model on spheres, as is commonly done and reported in the literature. Including the irregularity of particles is recommended for future research; at this moment, our measurements lack a detailed quantification of these irregularities.

5.3.4 The Richardson–Zaki curve

The index n can be determined through the linear relationship between the logarithm of the superficial velocity and the logarithm of the voidage (Yang, 2003; Coulson and Richardson, 1957). When the plot of $\log v_s$ versus $\log \varepsilon$ for concentrated suspensions is linearly extrapolated to $\log \varepsilon = 1$, the intercept is equal to $\log v_E$, where according

to Coulson and Richardson v_E is the apparent free falling settling velocity of a particle in an unbounded solution and corresponds closely to the free falling or terminal settling velocity v_t of a single particle. Here, wall effects corrections are introduced. Chong *et al.* (1979) found the term v_E obtained by linearly extrapolating below $\varepsilon = 0.9-1$ on a log-log plot of v_s versus ε to be measurably lower than the corresponding terminal settling velocity v_t . Dharmarajah (1982) stated that Richardson and Zaki failed to observe beyond a voidage of approximately $\varepsilon = 0.9$ where the log v_s versus log ε plots deviate significantly from linearity. Dharmarajah mentioned that the curvature is more pronounced with increasing particle Reynolds numbers and that the characteristics of a liquid fluidised system change drastically when the expanded bed voidage approaches unity. Gibilaro (2001) reports that it has been widely verified that a plot of v_s against ε on logarithmical co-ordinates approximates closely to a straight line of bed expansion, regardless of flow regime. However, small deviations from this behaviour have been reported for high void fractions $\varepsilon > 0.95$ (Altenburg, 2019).

Di Felice (1995) described two types of expansion characteristics in which the first region concerns lower voidages and in which a straight line with extrapolation to voidage equal to 1 is below the predicted value of the single particle terminal velocity. In the second region, the slope increases with increasing void fraction, approaching the correct value for v_t . Later, Di Felice and Rotondi (2013) reported that values of v_E can also exceed the value of v_t . Analysis of the data sets reported by Girimonte and Vivacqua (2011) and Girimonte and Vivacqua (2013) indicates that calculated values of v_E are regularly smaller than experimental ones, with an average error of about 25% and a level of inaccuracy that increases as the size of the fluidised particles decreases. Their plotted experimental data clearly deviate increasingly at voidage values higher than 0.8.

The intercept velocity or the extrapolated value of the fluid superficial velocity to $\varepsilon = 1$ agreed quite well with the mean terminal settling velocity of a cloud of particles experimentally determined by Đuriš *et al.* (2013). The experimental data reported by Đuriš *et al.* (2016) at a higher velocity of approximately 10%, however, indicate a deviation of v_E through linear extrapolation of v_s and the terminal settling velocity resulting from the influence of the particle roughness on the behaviour of the bed in high voidage regions during the fluidisation of sand mixtures.

5.3.5 Richardson–Zaki on the basis of hydraulics

In Yang (2003), Harker *et al.* (2002) and Khan and Richardson (1987) a more hydraulics-based approach can be found in which Equation (43) is rearranged for an explicit equation for the index n at incipient conditions:

$$n = \frac{\log\left(\frac{v_{mf}}{v_t}\right)}{\log \varepsilon_{mf}} \quad (49)$$

Under extreme conditions, in other words when the minimum fluidisation velocity as well as the terminal settling velocity are known, the index n could be determined. Using the particle Reynolds numbers for terminal settling (Equation (3)) and the particle Reynolds numbers for minimum fluidisation (Equation (7)), the index can be written as follows (Gibilaro, 2001):

$$n = \frac{\log\left(\frac{Re_{\varepsilon, mf}}{Re_t}(1 - \varepsilon_{mf})\right)}{\log \varepsilon_{mf}} \quad (50)$$

With:

$$Re_{\varepsilon} = \frac{\rho_f v_s d_p}{\eta} \frac{1}{1 - \varepsilon} \quad (6)$$

Where ε becomes ε_{mf} and v_s becomes v_{mf} under minimum fluidisation state:

$$Re_{\varepsilon, mf} = \frac{\rho_f v_{mf} d_p}{\eta} \frac{1}{1 - \varepsilon_{mf}} \quad (7)$$

5.4 Richardson–Zaki models and theory related to the fluidised bed pellet-softening process

5.4.1 Richardson–Zaki water treatment constraints

In pellet-softening reactors, the calcium carbonate pellets range from 1-2 mm in size, while for the seeding materials particle size varies between 0.2 mm in case of garnet grains (Figure 1B) and 0.5 mm when crushed calcite grains are used (Figure 1D). In full-scale reactors, the superficial velocity is controlled between 60 and 90-120 m/h. In Figure 45, the operational field is marked green in which the influence of particle size is plotted using the Richardson–Zaki equation.

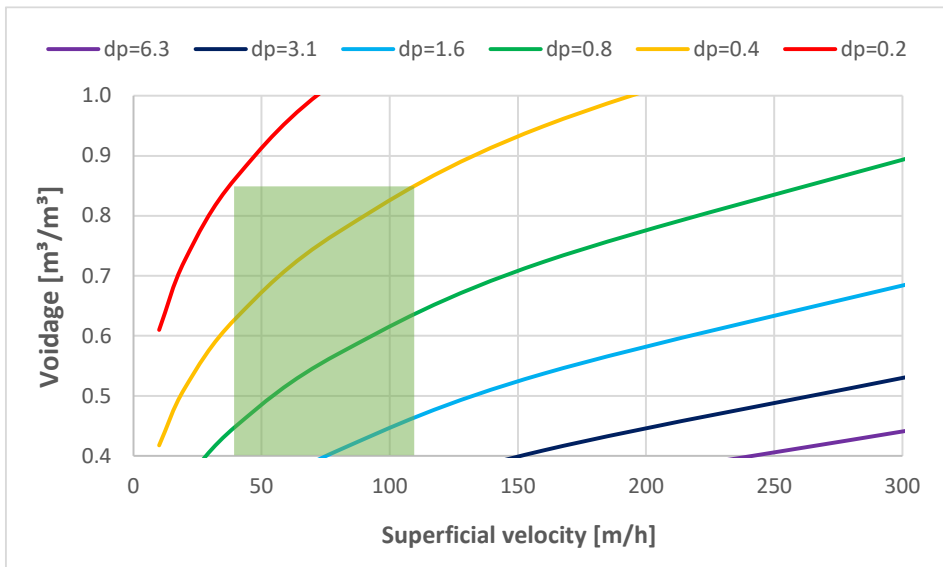


Figure 45 The effect of particle size (values in mm at the top) and superficial velocity (X-axis) on voidage predicted by Richardson–Zaki. The green area marks the operation range of drinking water pellet-softening fluidisation processes regarding seeded calcium carbonate crystallisation.

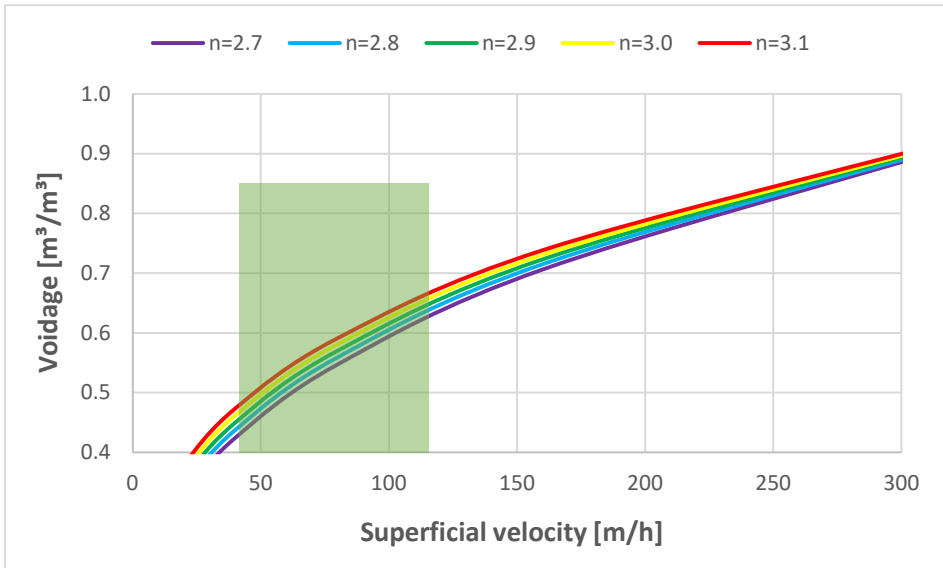


Figure 46 The influence of the Richardson–Zaki index for a particular grain, e.g. $d_p = 0.8$ mm. The green area marks the operation range of drinking water pellet-softening fluidisation processes. The effect of e.g. 10% deviation in v_t or v_E on voidage in drinking water softening process is relatively small, 12%, but larger for minimum fluidisation velocity, 47%.

Figure 46 shows the effect of the magnitude of n on voidage in relation to the superficial velocity for a given particle size. The terminal settling velocity increases when particles grow in size: this can be determined with the Richardson–Zaki equation with an assumed voidage $\varepsilon \rightarrow 1$. In case the terminal settling velocity is known, the index n can be calculated for several models. For a given minimum fluidisation voidage, the subsequently estimated minimum fluidisation velocity leads to significant deviations.

5.4.2 Hydraulics-based Richardson–Zaki index

In the literature (Oka and Anthony, 2003; Tomkins *et al.*, 2005; Baldock *et al.*, 2004), several equations have been proposed for equations for n . These works, however, have not used the latest hydraulic models. To develop an accurate Richardson–Zaki index expression, Equation (49) is used as a starting point. Besides the minimum

fluidisation voidage ε_{mf} , also the terminal settling velocity and the minimum fluidisation velocity are required.

In the literature (Yang *et al.*, 2015; Barati *et al.*, 2014; Cheng, 2009; Gibilaro *et al.*, 1985; Edzwald, 2011), a comprehensive collection of widely used models is available to estimate the drag and terminal settling velocity of particles. A well-known and accepted model is the Brown–Lawler (2003) equation, (Equation (51)), which is an improved model of the well-known equation proposed by Schiller and Naumann (1933). This is discussed in Kramer *et al.* (2021b).

$$C_D = \frac{24}{Re_t} (1 + 0.15Re_t^{0.681}) + \frac{0.407}{1 + \frac{8710}{Re_t}} \quad (Re_t < 200,000) \quad (51)$$

Since terminal settling velocity is an important variable in the Richardson–Zaki Equation (1), the effect of particle properties may considerably affect the numerical outcome of the index n and the estimated minimum fluidisation velocity.

The Richardson–Zaki model does not provide any information about the voidage at minimum fluidisation. This is also the case for hydraulics-based models such as Kozeny, Carman and Ergun. Nevertheless, using the steady state force balance for suspensions at incipient fluidisation state, makes it possible to introduce the voidage at minimum fluidisation.

A frequently used equation to calculate the pressure drop of a fluid flowing through a packed bed of solids for laminar flow is the Kozeny equation (Kozeny, 1927):

$$\frac{\Delta P}{\Delta L} = 180 \frac{v_s \eta (1 - \varepsilon)^2}{d_p^2 \varepsilon^3} \quad (52)$$

The corresponding Kozeny dimensionless friction factor f_T states:

$$f_T = \frac{180}{Re_\varepsilon} \quad (Re_\varepsilon < 2) \quad (53)$$

where Re_ε is defined in Equation (6). Carman (1937) as well as Forchheimer (1901) and Happel and Epstein (1954) proposed an extension, resulting in a second term for the transitional flow regime and valid for a higher particle Reynolds number

(Equation (6)). Information regarding Kozeny, Carman and Ergun equations is given in the Supplementary material (Section 4).

$$f_T = \frac{180}{Re_\varepsilon} + \frac{2.9}{Re_\varepsilon^{0.1}} \quad (Re_\varepsilon < 600) \quad (54)$$

For higher flow regimes, Ergun (1952) is frequently used to calculate the dimensionless friction factor f_T according to Equation (55):

$$f_T = \frac{150}{Re_\varepsilon} + 1.75 \quad (55)$$

Accordingly, the Richardson–Zaki index n can be determined by combining the rearranged Equation (49) with the Carman–Kozeny Equation (54) and the Brown–Lawler Equation (51). For both equations, numerical solver methods are required to solve the voidage for applied boundary conditions: ($Re_t < 200,000$) and ($Re_\varepsilon < 600$). Today, using this model should not present any obstacles. This model is abbreviated to *RZ-hydr1 (CK+BL)*.

5.4.3 Simplified analytical expressions

Although numerical solvers can be used for the voidage, it is desirable to have available analytical expressions that do not need an iterative numerical approach. Accordingly, several analytic models are given. It is possible to derive an explicit model using a simplified drag equation based on Lewis *et al.* (1962), Clark (2009) and Kunii and Levenspiel (1969):

$$C_D = \frac{10}{\sqrt{Re_t}} \quad (0.4 < Re_t < 500) \quad (56)$$

A more general form (Oka and Anthony, 2003) of Equation (56) is:

$$C_D = \alpha Re_t^\beta \quad (57)$$

in which the Lewis coefficients are $\alpha = 10$ and $\beta = -0.5$. For other frequently used equations, e.g. Oka and Anthony (2003), the coefficients are $\alpha = 18.5$ and $\beta = -0.6$. The value $\beta = -0.5$ results in a linear relationship between drag and the terminal settling velocity (Kramer *et al.*, 2015), which confirms that calcite pellets are in the middle of the transitional flow regime.

Kozeny–Lewis hydraulic analytic model

Using the particle Reynolds terminal Equation (3) and the Kozeny drag Equation (52), the Richardson–Zaki index equation becomes the following:

$$n = \frac{\log\left(\frac{\frac{3}{4}\alpha Re_t^{\beta+1} \varepsilon_{mf}^3}{180(1-\varepsilon_{mf})}\right)}{\log \varepsilon_{mf}} \quad (5 < Re_t < 500) \quad (58)$$

Equation (58) is bounded between thresholds for the particle Reynolds numbers (Equation (7)) at minimum fluidisation conditions and for the terminal Reynolds number at intermediate range.

In the literature, expressions are also given for the Archimedes number (Equation (9)), as a result of which Equation (58) becomes the following:

$$n = \frac{\log\left(\frac{Ar^{\frac{\beta+1}{\beta+2}} \varepsilon_{mf}^3}{180(1-\varepsilon_{mf})} \left(\frac{3}{4}\alpha\right)^{\frac{1}{\beta+2}}\right)}{\log \varepsilon_{mf}} \quad (10 < Ar < 80,000) \quad (59)$$

This model is abbreviated to: *RZ-hydr2 (KZ+LW)*. The derivations of equation Kozeny–Lewis n equations (58), (59), van Dijk variants (62), (63), Ergun–Lewis equations (65) and floating parameters (67), (66), (69) and (68) can be found in the Supplementary material (Section 5).

Kozeny–Lewis hydraulic extended analytic model

Gibilaro (2001) presented the Kozeny Equation (52) with a friction factor according to:

$$\frac{\Delta P}{\Delta L} = f_T \frac{\rho_f v_{mf}^2}{d_p} \frac{1 - \varepsilon_{mf}}{\varepsilon_{mf}^3} \quad (60)$$

Van Dijk and Wilms (1991) adjusted the Kozeny equation through the adjustment of the friction factor and used different coefficients $\kappa = 130$ and $\lambda = -0.8$. A more general form of f_T is:

$$f_T = \kappa Re_\varepsilon^\lambda \quad (61)$$

Now, the Richardson–Zaki index equation becomes as follows:

$$n = \frac{\log \left(Re_t^{\frac{\beta-\lambda}{\lambda+2}} \left(\frac{\varepsilon_{mf}^3 (1 - \varepsilon_{mf})^\lambda}{\kappa} \right)^{\frac{1}{\lambda+2}} \left(\frac{3}{4} \alpha \right)^{\frac{1}{\lambda+2}} \right)}{\log \varepsilon_{mf}} \quad (62)$$

$$n = \frac{\log \left(Ar^{\frac{\beta-\lambda}{(\beta+2)(\lambda+2)}} \left(\frac{\varepsilon_{mf}^3 (1 - \varepsilon_{mf})^\lambda}{\kappa} \right)^{\frac{1}{\lambda+2}} \left(\frac{3}{4} \alpha \right)^{\frac{1}{\beta+2}} \right)}{\log \varepsilon_{mf}} \quad (63)$$

Equation (58) is retrieved for the Kozeny coefficients $\kappa = 180$ and $\lambda = -1$.

Ergun–Lewis hydraulic analytic model

The next model is abbreviated to *RZ-hydr3 (EG+LW)* and is based on the Ergun–Archimedes Equation (64) and the Lewis Equation (56).

$$Ar = \left(A Re_{\varepsilon, mf} + B Re_{\varepsilon, mf}^2 \right) \frac{(1 - \varepsilon_{mf})^2}{\varepsilon_{mf}^3} \quad (64)$$

where $A = 150$, $B = 1.75 = 7/3$.

The following analytic Richardson–Zaki index equation can be derived:

$$n = \frac{\log \left(\frac{\sqrt{\left(\frac{1}{2} \frac{A}{B} (1 - \varepsilon_{mf}) \right)^2 + \frac{\varepsilon_{mf}^3}{B} Ar - \frac{1}{2} \frac{A}{B} (1 - \varepsilon_{mf})}}{\left(\frac{4}{3} \frac{Ar}{\alpha} \right)^{\frac{1}{\beta+2}}} \right)}{\log \varepsilon_{mf}} \quad (10 < Ar < 300,000) \quad (65)$$

When the second term of Equation (55) or (64) is ignored, Equation (58) is retrieved; however, this is done with the Ergun coefficient 150 instead of the Kozeny value 180.

Floating parameters

It is also possible to find an implicit analytical solution for Equation (58) with the same numerical output of the Brown–Lawler and Carman–Kozeny models. This can be achieved by using the principle of simple drag Equations (57) and (61) with so-called floating coefficients α , β as a function of the particle Reynolds terminal number and κ , λ as a function of the particle Reynolds minimal fluidisation number. The result is as follows:

$$\beta = \frac{\frac{c_1(c_2(c_3 - 1)Re_t^{c_3} - 1)}{Re_t^2} + \frac{c_4c_5}{(Re_t + c_5)^2}}{\frac{c_1}{Re_t}(1 + c_2Re_t^{c_3}) + \frac{c_4}{1 + \frac{c_5}{Re_t}}} Re_t \quad (66)$$

$$\alpha = \frac{\frac{c_1}{Re_t}(1 + c_2Re_t^{c_3}) + \frac{c_4}{1 + \frac{c_5}{Re_t}}}{Re_t^\beta} \quad (67)$$

$$\lambda = \frac{-\frac{c_1}{Re_\varepsilon^2} - c_2c_3Re_\varepsilon^{-c_3-1}}{\frac{c_1}{Re_\varepsilon} + \frac{c_2}{Re_\varepsilon^{c_3}}} Re_\varepsilon \quad (68)$$

$$\kappa = \frac{\frac{c_1}{Re_\varepsilon} + \frac{c_2}{Re_\varepsilon^{c_3}}}{Re_\varepsilon^\lambda} \quad (69)$$

Finally, the coefficients in Equations (47) and (48) can be numerically fitted with the Brown–Lawler + Carman–Kozeny index functions (Equations (51) and (54)). These models are abbreviated to *RZ-hydr-Ret* and *RZ-hydr-Ar*.

5.5 Materials and Methods

5.5.1 Particle selection

In this study, we examined predominantly natural particles which are frequently applied in drinking water treatment processes, in particular in the softening process. Investigations started with garnet grains, the most frequently utilised seeding material in the Netherlands, calcite pellets, which is seeding material with a substantial layer of crystallised CaCO_3 coming from the softening process and also re-used crushed calcite, processed in the Netherlands. Garnet grains and calcite pellets were dried at room temperature; crushed calcite grains were dried in an oven at 150-200 °C for hygiene purposes.

Particles were initially sieved and separated in order to acquire more uniformly dispersed samples with a defined sieve diameter in which the hydraulic equivalent particle diameter could be calculated using Equation (28). Available sieve sizes are usually regulated by standards such as ISO 3310-1 (NEN–norm (NEN-EN 933-2, n.d.)) and ASTM E11:01 (US). The distance between succeeding sieve openings varies between 2, $\sqrt{2}$ and 1.20 and 1.12. In this research, the ratios between two succeeding sieve openings were 1.12 and 1.20.

5.5.2 Particle and fluid characterisation and expansion experiments

The method to calculate the physical properties of water is given in the Materials and Methods Section 3.2. The methods to determine the physical properties of particles is given in Section 3.3. Accordingly, bed voidage and differential pressure equations are given in Section 3.4. Photographs of granules are shown in Annex 1: Photos.

able 14 Particle materials

Grain material	Mesh bottom sieve [µm]	Mesh top sieve [µm]	Average grain size [mm]	Frequency [#]
Garnet grains (mesh 80)	212	250	0.23	5
Garnet grains (mesh 30/60)	250	300	0.27	8
Crushed calcite	400	500	0.45	4
"	400	600	0.49	4
"	500	600	0.55	4
"	500	630	0.56	8
Calcite pellets	425	500	0.46	4
"	500	600	0.55	4
"	600	710	0.65	4
"	710	800	0.75	4
"	800	900	0.85	4
"	900	1120	1.00	11
"	1120	1400	1.25	4
"	1400	1700	1.54	4
"	1700	2000	1.84	4

5.5.3 Terminal settling velocity experiments

In the current study, the settling behaviour of single particles was determined through adjusting the water temperature for various materials and for different grain sizes. The temperature was carefully controlled by flowing water through the column of the exact temperature before each experiment and by regularly repeating this process throughout the experiment. Individual particles were dropped at the top of the column. After steady state velocity had been reached, the required time to elapse a defined distance ($L = 2$ m) was measured visually. All fractions in able 14 were tested for temperatures between 3 and 36 °C. A powerful flashlight at the top of the column supported the visual determination of the free falling particles (Kramer et al., 2021b).

5.5.4 Fluidisation expansion experiments

In total, 76 fluidisation expansion experiments were carried out. Regarding calcite pellets and garnet grains, the superficial velocity was increased to approximately 180 m/h and for crushed calcite to approximately 260 m/h.

The data derived from the expansion experiments were used to calculate pressure difference, bed voidage and average particle size. The calculated pressure difference was compared with the measured sensor and hydrostatic values. The calculated voidage was compared with the voidage derived directly from the experimental data. The average particle diameter was derived from the applied sieve fractions. For every experiment, an expansion curve was plotted with bed voidage, pressure difference and transitions from fixed to fluidised state.

Bed voidage, expansion and differential pressure

Because the initial amount of grains is known, the fixed and fluid bed voidage and expansion can be calculated using Equations (36) and (23), given in the Materials and Methods Section 3.4. The experimental differential pressure data can be validated using Equation (22).

Statistical methods

To compare the experimental data with the prediction models, the average relative error (Brown and Lawler, 2003; Haider and Levenspiel, 1989) is determined as:

$$ARE = \frac{1}{n} \sum_{i=1}^n \left(\frac{|y_{calc,i} - y_{exp,i}|}{y_{exp,i}} \right) \quad (70)$$

Note: Statistical methods are given in Annex 5: Statistical analysis.

In Section 5.6, we will compare the various equations presented in Section 5.4 with data obtained from our experimental set-up in Section 5.5. We will evaluate the performance and accuracy of the various equations, and we will formulate our advice on the best approach for practical applications.

5.6 Results and discussion

The experimental set-up is discussed in Section 3.1. The physical properties of water is given in Section 3.2. Photographs of granules are shown in Annex 1: Photos. Standard operating procedure of fluidisation experiments is elucidated in Section 3.4.

5.6.1 Obtained particle properties

The experimentally measured particle density of examined grains is given in Table 4. An average relative error of 2% was found in the particle density, caused by both the laboratory experiments and natural variations of the particle properties. The average particle density was derived (Equation (33)) from the fluidised bed set-up based on the pressure drop measurement. The average relative error here was 3%. The measured fixed bed voidage for calcite pellets (Table 4) agrees with an expected value of 0.4 for round spheres. Garnet grains, which were mined and had a more irregular shape, show a higher fixed bed voidage. The fixed bed voidage of crushed calcite seeding material, with a much more irregular shape due to crushing, is significantly higher, which also agrees with findings reported by Wen and Yu (1966), Yang (2003) and Đuriš (2016).

Table 15 Grain materials

Grain material	N	Grain size	Particle density measured	Particle density ³⁾	Fixed bed voidage ⁴⁾	Incipient voidage
	[#]	[mm]	[kg/m ³]	[kg/m ³]	[m ³ /m ³]	[m ³ /m ³]
Garnet grains ¹⁾	13	0.21-0.30	4,175 ± 25	4,040 ± 125	0.44 ± 0.02	0.46 ± 0.03
Crushed calcite ¹⁾	20	0.40-0.63	2,575 ± 5	2,570 ± 50	0.49 ± 0.01	0.51 ± 0.01
Calcite pellets ²⁾	43	0.43-2.00	2,625 ± 35	2,703 ± 50	0.38 ± 0.01	0.40 ± 0.01

1) S = Seeding material

2) P = CaCO₃ grains

3) Validated with Equation (33)

4) Equation (36)

5.6.2 Expansion experiments

The acquired experimental data set consisted of a matrix with varied temperature, grain size and flow, as was required for a comparison of the theoretical fluidisation models. In total, 76 fluidisation experiments were carried out for calcite pellets, garnet and crushed calcite grains. Figure 47 shows, as an example, a typical expansion curve in which the voidage and pressure difference was measured for increasing superficial velocity. All experimental data of expansion experiments can be found in the Supplementary material (Section 8).

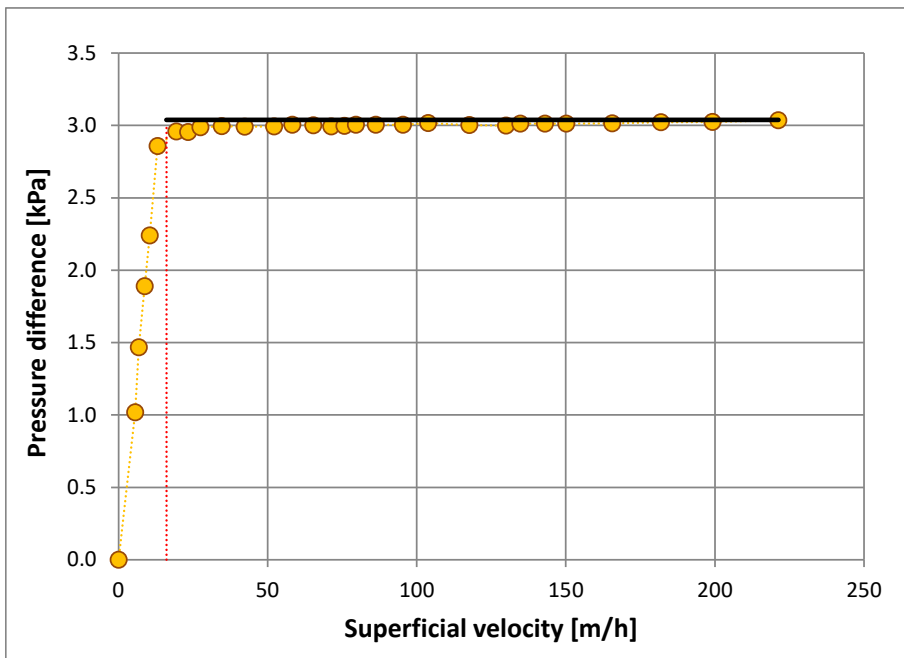


Figure 47a A typical expansion experiment concerning crushed calcite grains $0.5 < d_p < 0.6$ mm at $T = 25^\circ\text{C}$.

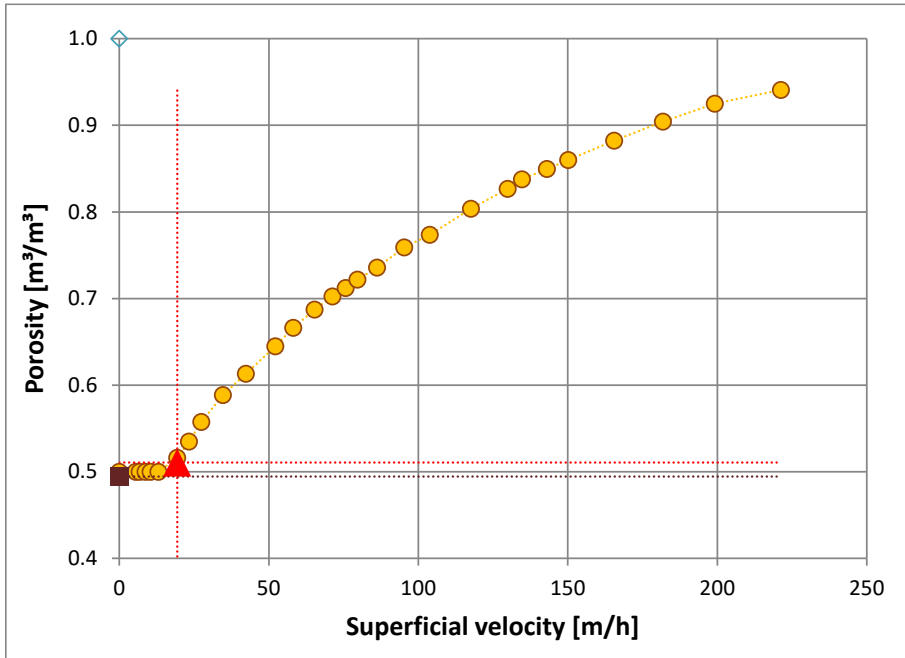


Figure 47b A typical expansion experiment concerning crushed calcite grains $0.5 < d_p < 0.6$ mm, $T = 25^\circ\text{C}$ with measured differential pressure (Equation (22)) and voidage (Equation (36)). The vertical red line indicates the minimum fluidisation velocity. I-s fluidisation experiment nr.: 63.

In their original article, Richardson and Zaki plotted superficial velocity in the opposite way on logarithmic scales. Both in Figure 47 and Figure 48, the incipient fluidisation points are clearly visible. The Richardson–Zaki line intercepts at $\varepsilon = 1$ the apparent free-falling settling velocity v_E of a particle at infinite dilution. Note that in this example, v_E is 4% lower than the estimated terminal settling velocity calculated with Equation (51).

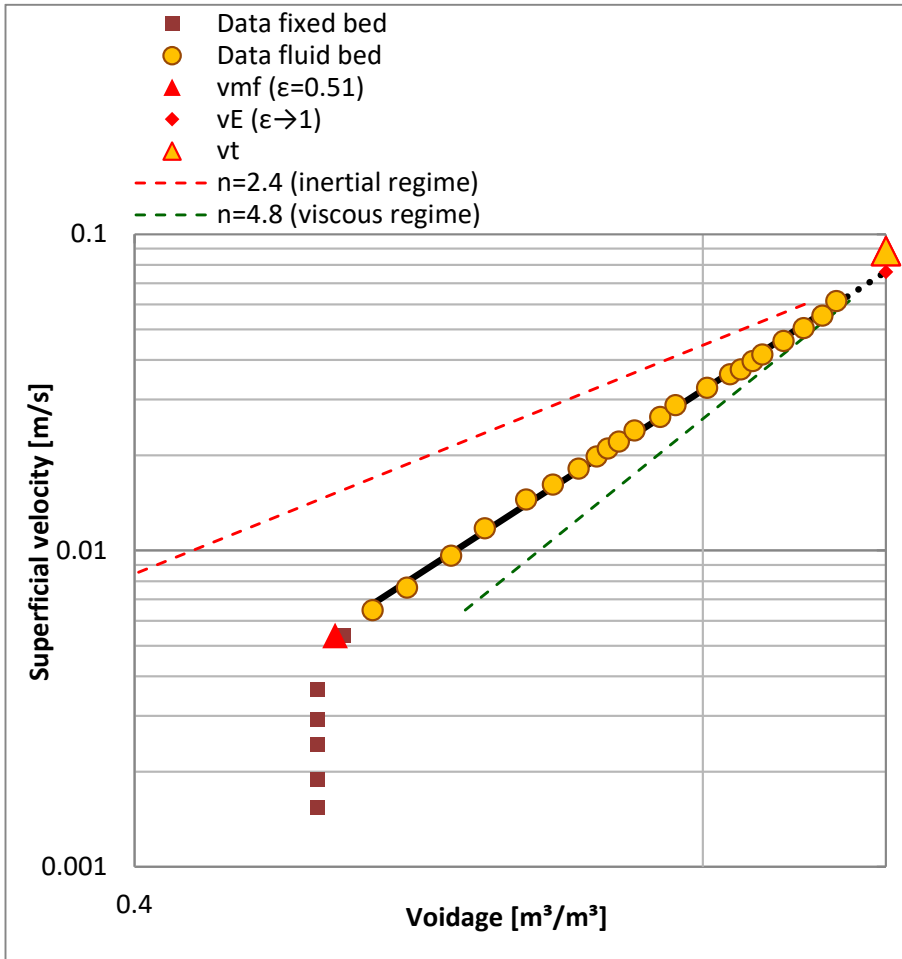


Figure 48 Richardson–Zaki representation. *I-s fluidisation experiment nr.: 63.*

For the 76 fluidisation experiments, the extrapolated fluid velocity v_E was determined: this is displayed in Figure 49, showing that in particular for higher velocities, the deviations increase. For the calcite pellets, the deviations may be caused by inaccurate extrapolation to $\epsilon \rightarrow 1$ since the maximum obtained voidage was 0.6 for large pellets ($d_z > 1.4$ mm) during the expansion experiments. The value of v_E for crushed calcite is lower than v_t , which is due to the highly irregularly shaped particles - something that becomes more apparent for higher fluid velocities, which in turn leads to more unsteady drag behaviour.

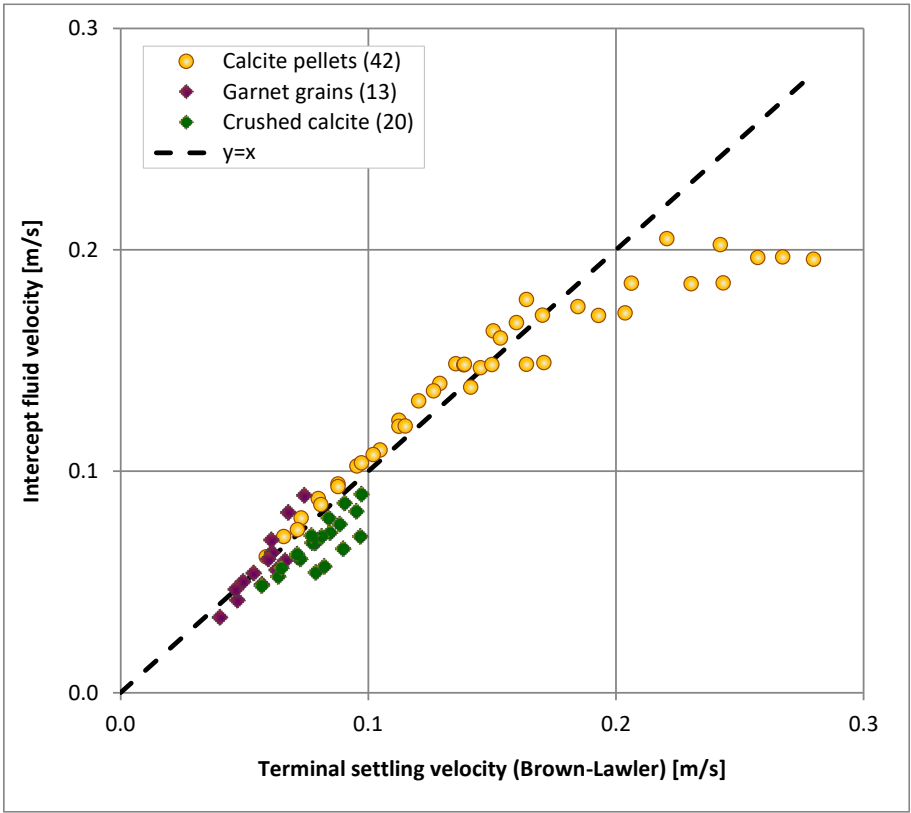


Figure 49 Richardson–Zaki intercept velocity v_E against the terminal settling velocity v_t calculated with the Brown–Lawler Equation (51).

5.6.3 Minimum fluidisation velocity prediction

The voidage at minimum fluidisation is a crucial parameter and in fact more important than the terminal settling point, since the process state in pellet-softening reactors and apparent voidage are closer to the state of minimum fluidisation. With Equations (36) and (23), both the fixed and incipient bed voidage were calculated for 76 experiments.

Three groups of models were compared with respect to their ability to predict the minimum fluidisation velocity accurately. Table 16 shows the results for Richardson–Zaki-based models, followed by frequently used hydraulic models as reported in the literature and thirdly by Richardson–Zaki hydraulics-based models. The prediction

accuracy of the first group is generally low, compared to the second group. This result can also be observed in Figure 50. A global explanation is that Richardson–Zaki starts with the terminal settling point and has to predict v_{mf} using a slope n over a large voidage ‘distance’ ($\Delta\varepsilon \approx 0.6$) with the possibility of overestimation. Because the models of the second group are based on the principle of fixed state, it seems evident that their prediction is much more accurate. Based on the experiments, the Carman–Kozeny model was found to have the lowest error: it can therefore be considered the best model to predict the minimum fluidisation point. The models in the third group are based on both Richardson–Zaki and the classical hydraulic models and provide a lower error compared the first group. The hydraulics-based Richardson–Zaki numerical model *RZ-hydr1 (BL+CK)* is slightly less accurate than the Carman–Kozeny model.

Table 16 Minimum fluidisation velocity prediction

Model and Reference	Equations	Average relative error [%]
Group 1: Richardson–Zaki models from literature		
(Richardson and Zaki, 1954)	43, 3, 45	100.4%
(Rowe, 1987)	1, 4, 47	106.3%
(Wallis, 1969)	43, 3, 47	63.6%
(Garside and Al-Dibouni, 1977)	43, 3, 47	52.9%
(Khan and Richardson, 1987)	43, 9, 48	51.9%
(van Schagen, 2009)	43, 3, 45	87.6%
Group 2: Hydraulic models		
(Kozeny, 1927)	22, 52	26.2%
(Carman, 1937)	22, 54	12.4%
(Ergun, 1952)	22, 55	29.6%
Group 3: Richardson–Zaki hydraulics-based models		
RZ-hydr1 (BL+CK)	43, 54, 51	13.1%
RZ-hydr2 (KZ+LW)	43, 58	15.7%
RZ-hydr3 (EG+LW)	43, 65	20.6%
RZ-hydr-Ret	43, 3, 71	16.4%
RZ-hydr-Ar	43, 9, 72	16.8%

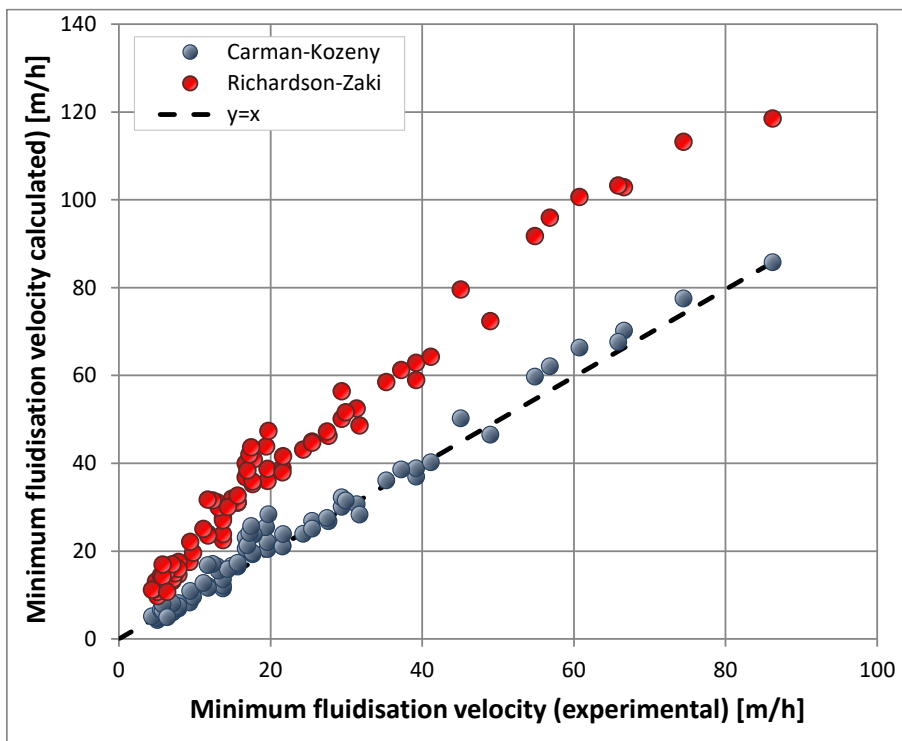


Figure 50 The experimentally determined minimum fluidisation velocity versus the calculated minimum fluidisation velocity using Richardson–Zaki (Equation (43)) and Carman–Kozeny (Equation (54)). Richardson–Zaki overestimates the minimum fluidisation velocity.

5.6.4 Voidage prediction

Voidage prediction accuracy was determined for three different ranges. This was first done for a wide operation range regarding pellet-softening: 60 -90 m/h, for superficial velocities up to 180 m/h and for a wide examined fluid flow range applied in the expansion experiments. The average relative errors (Equation (70)) were calculated for 76 experiments: these are listed in Figure 51. The original Richardson–Zaki model has an error of 8% for a wide range of fluid velocity. This error increases to 17% for grains applied in the drinking water pellet-softening process. The Richardson–Zaki model built on a hydraulic basis, as derived in this work, provides

much lower errors of approximately 3%. A particular point of interest concerns taking into account the validity of the working area.

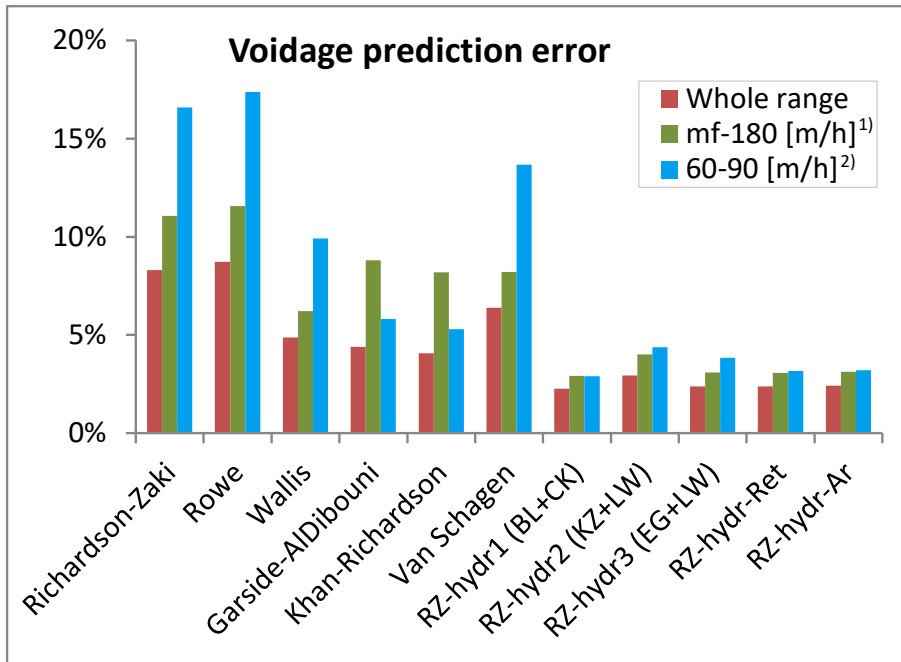


Figure 51 Relative errors of predicted voidage according to different models from the literature and from this work. 1) Starting with the lowest minimum fluidisation velocity. 2) Waternet operational area in softening reactors.

5.6.5 Richardson–Zaki index

The models proposed by Richardson–Zaki, Rowe, Wallis, Garside–Al Dibouni and Khan–Richardson use the index n to predict voidage (Equation (43)). In Figure 52, the determined indices n for 76 experiments are plotted (dots) as well as the curves for given models. All examined grains applied in the softening process have a higher value compared to the expected Richardson–Zaki values (red curve) and coincide quite well with the Richardson–Zaki hydraulics-based models. This has been confirmed and reported in earlier publications by Siwiec (2007) and is due to the irregularity of the grains which will re-orientate during fluidisation, causing the

exerting drag to increase and behave like virtually smaller grains with a corresponding higher n value.

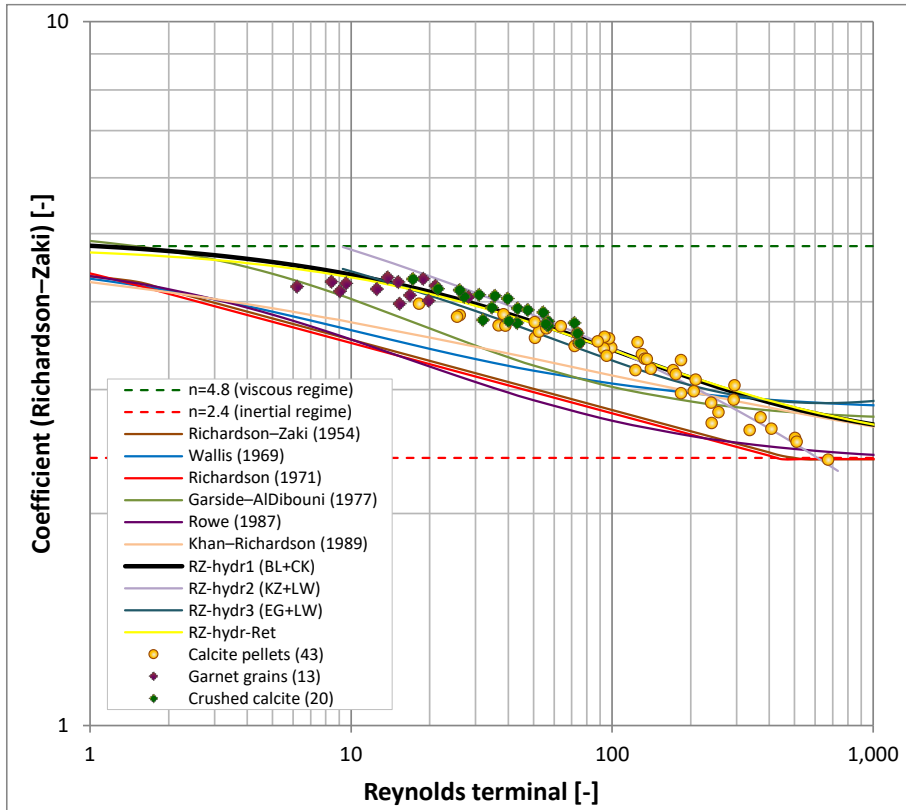


Figure 52 The experimentally determined Richardson–Zaki index for investigated grains

Figure 53 shows the influence on n of having different particles with different hydraulic physical properties, such as incipient voidage ε_{mf} and particle density ρ_p . Despite the fact that at Reynolds terminal ($Re_t \approx 100$) all three curves coincide, the index value increases up to 2% for garnet grains and 7% for calcite grain, both at lower and higher Reynolds terminal values.

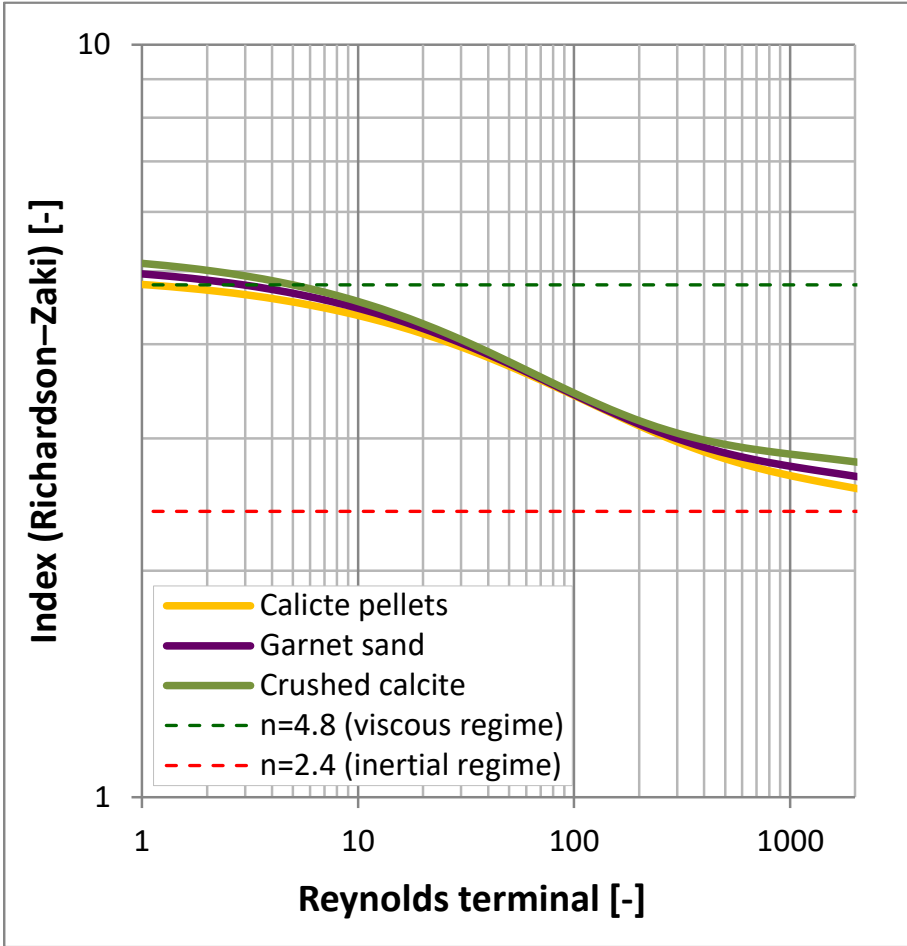


Figure 53 The influence of specific density and voidage at minimum fluidisation of garnet grains, crushed calcite grains and calcite pellets. See Table 4 for physical properties of particles.

In summary, we find that the hydraulics-based Richardson–Zaki model *RZ-hydr1* (*BL+CK*) enables us to predict the voidage with a low error, but unfortunately numerical iteration remains necessary. From a pragmatic point of view, it is desirable to be able to predict the voidage with an explicit analytical equation such as Equations (47) and (48). Furthermore, the elegance of Richardson–Zaki is the simplicity of the particular model itself. To allow for fast evaluations, we numerically fitted the coefficients, based on Brown–Lawler + Carman–Kozeny (Equations (51) and (54)): they are presented in Table 17.

Table 17 Coefficients in Equations (47) and (48)

Model and Reference	n_L	n_T	$\alpha(Re_t)$	$\beta(Re_t)$	$\alpha(Ar)$	$\beta(Ar)$
Theoretical, (Harker <i>et al.</i> , 2002)	4.8	2.4				
(Richardson and Zaki, 1954)	4.65	2.4				
(Wallis, 1969)	4.7	2.79	0.253	0.687		
(Garside and Al-Dibouni, 1977)	5.09	2.73	0.104	0.877		
(Garside and Al-Dibouni, 1977) (simplified)	5.1	2.7	0.1	0.9		
(Dharmarajah, 1982) (forced through ε_{mf})	5.09	2.73	0.194	0.877		
(Rowe, 1987)	4.7	2.35	0.175	0.75		
(Khan and Richardson, 1987)	2.084	4.94	3.24	-0.37		
(Khan and Richardson, 1987)	4.8	2.4			0.043	0.57
This study, RZ-hydr-Ret	4.8	2.4	0.043	0.75		
This study, RZ-hydr-Ar	4.8	2.4			0.015	0.5

This leads to simplified equations:

$$\frac{4.8 - n}{n - 2.4} = 0.043 Re_t^{0.75} \quad (71)$$

$$\frac{4.8 - n}{n - 2.4} = 0.015 Ar^{0.5} \quad (72)$$

5.7 Conclusions

The well-known Richardson–Zaki model is frequently cited and successfully applied in varied industries. The reason is its simple mathematic appearance. Its starting point is the falling velocity of a suspension relative to a fixed horizontal plane that equals the upward velocity of the liquid, based on the empty tube, required to maintain a suspension at the same concentration. Thanks to this simple method, the expansion of a liquid-solid fluidised bed can be predicted. However, the prediction of voidage in drinking water treatment processes in the proximity of minimum fluidisation on the basis of the traditional index equations overestimates the measured values of minimum fluidisation. Using an extra hydraulic point with an actual physical meaning makes the voidage prediction a much more accurate one. Based on the Brown–Lawler equation combined with the Carman–Kozeny equation, voidage can be predicted with an error of approximately 3% for particles applied in pellet-softening processes for drinking water production purposes. When the index n is used to estimate voidage, the influence of n for lower superficial velocities is

much higher compared to conditions in the proximity of terminal settling conditions or higher voidage values.

The determined index n values in this research show a higher value compared to those expected on the basis of the classic Richardson–Zaki model, something which is due to the irregularity of the considered drinking water grains. The Richardson–Zaki model that is constructed on a hydraulic basis is an improvement on the classical Richardson–Zaki model: the average relative error for voidage decreases from 15% to 3% in the operational working area of liquid-solid pellet-softening within a voidage range of $0.5 < \varepsilon < 0.8$. With respect to minimum fluidisation velocity, the average relative error decreases from 100% to 12%. Finally, with simplified analytical equations it is possible to make a straightforward estimation of the index n .

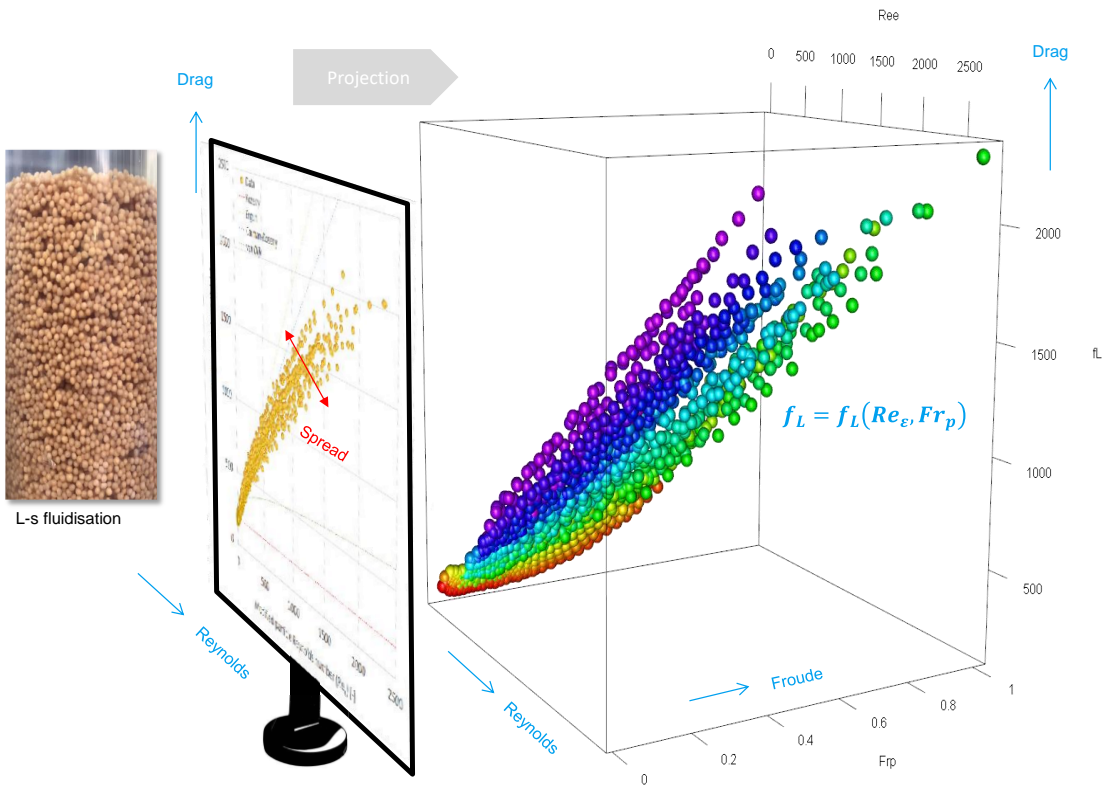
5.8 Supplementary material

Supplemental data for this article can be accessed at:

<https://doi.org/10.1016/j.powtec.2018.11.018>

<https://ars.els-cdn.com/content/image/1-s2.0-S0032591018309227-mmc1.docx>

Contents	page
1. Photos of examined particles	1
2. Richardson–Zaki model	2
1.1 Richardson–Zaki index equations	2
1.2 Richardson–Zaki plot	3
1.3 Richardson–Zaki wall effects	3
1.4 Richardson–Zaki model influence	4
3. Estimating the terminal settling velocity	4
4. Hydraulic equations for the minimum fluidisation velocity	5
4.1 RZ-hydr1 (BL+CK)	7
4.2 RZ-hydr2 (KZ+LW)	7
4.3 RZ-hydr2 (KZ+LW) extended	9
4.4 RZ-hydr3 (EG+LW)	10
4.5 RZ-hydr-Ret	12
4.6 RZ-hydr-Ar	12
5. Floating parameters	13
5.1 Brown–Lawler floating parameters	13
5.2 Carman–Kozeny floating parameters	16
6. Bibliography	19
7. Acknowledgments	21
8. Experimental data	22-47



- ▶ I-s fluidisation experiments show open spaces of fluid in the fluidised particle bed
- ▶ Drag cannot be described completely with the Reynolds number only
- ▶ Drag should be expressed through a linear representation for more accurate analysis
- ▶ Voidage prediction accuracy is improved from 5% to 1% by including Froude

Keywords Liquid-Solid Fluidisation; Drinking Water; Carman–Kozeny Equation; Drag Relations; Accurate Voidage Prediction; Hydraulic Models

Chapter 6

Homogeneous-Heterogeneous

“Behind the familiar 2D plot (Drag vs Reynolds number), a 3D representation lies hidden: an additional axis (Froude number) yields information about the degree of heterogeneity of a fluidised bed.”

This article has been published as:

Improvement of voidage prediction in liquid-solid fluidised beds by inclusion of the Froude number in effective drag relations

O.J.I. Kramer, J.T. Padding, W.H. van Vugt, P.J. de Moel, E.T. Baars, E.S. Boek, J.P. van der Hoek

International Journal of Multiphase Flow. **127**, 103261 (2020) pp. 1–13

The article can be found online at:

<https://doi.org/10.1016/j.ijmultiphaseflow.2020.103261>

6 Improvement of voidage prediction in liquid-solid fluidised beds by inclusion of the Froude number in effective drag relations

6.1 Abstract

A novel effective drag relation for liquid-solid fluidisation is proposed, suitable for application in full-scale installations. This is achieved by presenting new insights related to the influence of the temporal-spatial heterogeneity on the effective hydrodynamic drag for large fluidised systems. While heterogeneous flow behaviour can be predicted increasingly accurately in CFD simulations that explicitly model the heterogeneous solids distribution, for the operation of many large-scale applications it is infeasible to perform such computationally intensive simulations. Therefore, there is a clear need for full-scale drag relations that effectively take into account the heterogeneous behaviour and irregular spatial particle distributions. Our new drag relation is based on a large set of experiments, which shows that the degree of overall expansion is not only dependent on the ratio of laminar-turbulent flow, but also on the amount of homogenous versus heterogeneous flow, which is not included in current full-scale drag relations. To include the effect of heterogeneity, the standard drag relation, based on the Reynolds number, is extended with a specific type of Froude number. Because fully turbulent flow regimes are rare in applications of liquid-solid fluidisation, our focus is not on the turbulent flow regime but instead on laminar and transitional flow regimes. In these regimes, three types of models are investigated. The first type is based on a theoretical similarity with terminal settling, the second is based on the semi-empirical Carman–Kozeny model and the third is based on empirical equations using symbolic regression techniques. For all three types of models, coefficients are calibrated on experimental data with monodisperse and almost spherical glass beads. The models are validated with a series of calcium carbonate grains applied in drinking water treatment processes as well as data obtained from the literature. Using these models, we show that the voidage prediction average relative error decreases from approximately 5% (according to the best literature equations which use Reynolds number only) to 1-2% (using both Reynolds and Froude numbers). This implies that our new models are more suitable for operational control in full-scale fluidised bed applications, such as pellet-softening in drinking water treatment processes.

6.2 Introduction

Liquid-solid fluidisation (LSF) is frequently used in drinking water treatment processes, for instance in seeded crystallisation softening processes (Crittenden *et al.*, 2012). For optimal process conditions, *i.e.* fast calcium carbonate crystallisation (van Schagen, 2009), a large surface area in the fluidised bed is required. Therefore, in the field of water treatment, and specifically in pellet-softening LSF reactors, accurate voidage prediction models are crucial (Kramer *et al.*, 2020b). In a fluidised bed, the voidage, particle size and physical properties of the fluid and particles are inter-related. In the literature, numerous multiphase models are given to predict the overall voidage in fluidised bed reactors, mainly aimed at gas-solid systems (Di Felice, 1995; Gibilaro, 2001; Yang, 2003; Crowe and Group, 2006; Rhodes, 2008; Seville and Yu, 2016; Yates and Lettieri, 2016; Johnson, 2016). Specifically, for liquid-solid systems, the overall voidage can be predicted using classical models, such as the Richardson–Zaki approach based on terminal settling velocity, or an improved version also using the incipient fluidisation (Kramer *et al.*, 2019). The other frequently applied method is based on the idea of a flow through an assumed collection of channels in a bed of particles (Kozeny, 1927; Carman, 1937). The well-known Carman–Kozeny equation is an important drag relation for the determination of permeability in porous media, such as filters, as well as for the estimation of the voidage in a fluidised bed in water treatment processes. The simplicity of this model is a consequence of an evident direct relationship between the particle Reynolds number and the drag exerted by the fluid on the particles (Bird *et al.*, 2007) where viscous and inertial forces are balanced. This drag model, however, does not consider homogeneous or heterogeneous flow patterns.

Homogeneous fluidisation for uniform particles was observed by Wilhelm and Kwauk (1948) and Richardson and Zaki (1954). Fluidisation quality was characterised by Geldart (1973) who made a distinction between non-bubbling (particulate, homogeneous) and bubbling (aggregative heterogeneous) fluidisation. However, this was for gas-liquid fluidisation. According to Couderc (Davidson *et al.*, 1985), two modes of fluidisation occur in liquid-solid fluidised systems, *i.e.* particulate and aggregative fluidisation (Davidson *et al.*, 1985). Based on experimental studies (Didwania and Homsy, 1981; Ham *et al.*, 1990; Li and Kwauk, 1994), at least five flow regimes can be identified: stable uniform fluidisation, particulate regime, wavy flow, wavy flow with traverse structure, fine scale turbulent flow and bubbling regime as the liquid velocity is increased. Di Felice (1995) reported inhomogeneities in LSF

systems where the degree of heterogeneous behaviour depended on particular system characteristics such as morphological particle properties, particle size distribution and fluid-to-solid density ratio. Small particles with a density closer to that of the fluidising medium are more easily fluidised compared to large and heavy particles, since the gravitational pull is larger for the latter particles. The interparticle forces on small particles are relatively more important than the same forces acting on large particles, causing small particles to exhibit a certain velocity range of homogeneous expansion (Beetstra, 2005). For larger particles, throughout the bed, large inhomogeneities may occur: these include clustering of particles and voids of water as well as velocity fluctuations due to bubbling and spouting effects.

The importance of the fluid-particle interaction problem is considerable (Wu and Yang, 2019). The modelling of full-scale fluidised bed reactors is challenging because of their complex flow behaviour and numerous particle interactions (Cornelissen *et al.*, 2007). Using Direct Numerical Simulation (DNS), the whole range of spatial and temporal scales can be resolved in the computational mesh, which therefore necessarily contains only a few particles ($N \sim 100$ to 1000). The advantage of DNS is that no explicit drag relations need to be imposed. Rather, the drag is resolved for each particle, taking into account the effects of particle-particle collisions and other forces acting on the particles (Al-Arkawazi *et al.*, 2017). The computational costs, however, are very high. These costs can be lowered by using a coupled Computational Fluid Dynamics - Discrete Element Method (CFD-DEM) model (Ghatage *et al.*, 2014), in which the mesh is actually larger than the particles and therefore flow around the particles is no longer resolved. Although this allows for more particles to be simulated ($N \sim 10,000$ to 1,000,000), a drawback is that the interactions between the fluid phase and solid phase must be modelled explicitly by a drag relation, for instance the Ergun model (Liu *et al.*, 2015). In CFD-DEM, it is important to not choose the mesh size too large either, to be able to assume a more-or-less homogeneous particle distribution at the scale of a single CFD cell. Regarding full-scale industrial fluidised bed reactors, like water pellet-softening ($N \sim 10,000,000,000$), CFD simulations could perhaps be achievable, but only by approximating the particle interactions and particle-fluid drag even more, such as in Filtered Two-Fluid Models (Cloete *et al.*, 2018). Such CFD models are computationally very expensive, making them less suitable for process optimisation and plant-wide control. To cope with constantly changing operational conditions in full-scale installations, more straightforward models are needed for optimal and robust process control. In particular, there is a need for drag relations that can predict

the pressure drop and overall voidage in fluidised beds, effectively taking into account the local and global multiphase flow phenomena occurring in full-scale installations.

The aim of the current work is to determine an improved full-scale drag relation considering the abovementioned homogeneous and heterogeneous flow regimes. The majority of drag relations given in the literature is based on the Reynolds number only and assumes static and homogeneous particle arrangements. Because these drag relations ignore temporal-spatial fluctuations, they are not suitable to accurately cope with the transition from homogeneous to heterogeneous flow regimes. Here, we hypothesise that the popular Carman–Kozeny model can be improved through the introduction of the Froude number, in addition to the Reynolds number, to incorporate the heterogeneous aspects. In fluid mechanics (Wilkes, 2019), the dimensionless Froude number is used to indicate the influence of gravity on fluid motion (Di Felice, 1995). Wilhelm and Kwauk (1948) observed that the Froude number was a reliable parameter for discriminating between two extreme situations, with the fluidisation behaviour ranging from extremely smooth to violently bubbling. We will validate our new drag models by comparing their predictions with a large set of experimental results from our laboratories as well as experimental data from the available literature.

6.3 Theory

Section 6.3.1 below elucidates the fundamental principles of drag relations, in particular Carman–Kozeny. The extension of the drag relation with the Froude number to cope with the heterogeneous flow aspects is introduced in Section 6.3.2.

6.3.1 Hydraulic models in porous media

Laminar flow regime: Blake–Kozeny equation

At low Reynolds numbers, the relation between the fluid flow velocity through a dense porous medium and the pressure drop over this system is described in general by Darcy's law. Accordingly, the head loss, or hydraulic gradient, has the following form for laminar flow in a packed bed of particles:

$$\frac{\Delta P}{\Delta L} = K \frac{v_s \eta (1 - \varepsilon)^2}{d_p^2 \varepsilon^3} \quad (73)$$

The hydraulic gradient (Ergun, 1952) is often given in terms of a drag coefficient (f_T)

$$\frac{\Delta P}{\Delta L} = f_T \frac{\rho_f v_s^2}{d_p} \frac{1 - \varepsilon}{\varepsilon^3} \quad (74)$$

The dimensionless drag coefficient in Equation (74) is often given as a function of the modified particle Reynolds number Re_ε :

$$f_T = f_T(Re_\varepsilon), \quad (75)$$

where the modified particle Reynolds number Re_ε is defined as:

$$Re_\varepsilon = \frac{\rho_f v_s d_p}{\eta} \frac{1}{1 - \varepsilon} \quad (6)$$

Laminar flow regime: Kozeny equation

The corresponding Kozeny drag coefficient f_T is given as (Kozeny, 1927):

$$f_T = \frac{180}{Re_\varepsilon} \quad (Re_\varepsilon < 2) \quad (53)$$

Turbulent flow regime: Burke–Plummer equation

For the complete turbulent flow regime given by Burke and Plummer (1928), the corresponding Burke-Plummer drag coefficient f_T (Bird *et al.*, 2007) states:

$$f_T = 1.75 \quad (Re_\varepsilon > 2,000) \quad (76)$$

Transitional flow regime: Ergun and Carman–Kozeny

Ergun (1952) combined the Kozeny and Burke–Plummer equations and added these together, producing a mathematically blended model (Equation (55)) to predict laminar, transitional and turbulent flow, which satisfies the linear and nonlinear terms in the Reynolds number. The Ergun drag coefficient is based on experimental data between $2 < Re_\varepsilon < 4,000$ and is often used in CFD modelling (Beetstra, 2005; Kolev, 2012; Erdim *et al.*, 2015; Tavassoli *et al.*, 2015):

$$f_T = \frac{150}{Re_\varepsilon} + 1.75 \quad (55)$$

However, we will show below that there is a considerable discrepancy between the Ergun model and our experimental data for $Re_\varepsilon > 500$.

For the transitional flow regime, the Carman–Kozeny drag coefficient (Carman, 1937) is given by:

$$f_T = \frac{180}{Re_\varepsilon} + \frac{2.9}{Re_\varepsilon^{0.1}} \quad (Re_\varepsilon < 600) \quad (54)$$

The Carman–Kozeny equation is, *de facto*, the most commonly used equation and applied in various fields such as ground water flow, water treatment processes and a variety of chemical engineering applications (Xu and Yu, 2008). According to

Sobieski and Zhang (2014), both Ergun (55) and Carman–Kozeny (54) equations are sensitive to voidages and more pronounced at lower voidage. Since in water treatment the operational field lies in the vicinity of incipient fluidisation and, in addition, turbulent flow regimes are exceptional, there is a preference for using the Carman–Kozeny drag relation. Additionally, van Dijk and Wilms (1991) proposed an empirical simplified drag relation based on the Kozeny Equation (53) valid for the transition region.

$$f_T = \frac{130}{Re_\epsilon^{0.8}} \quad (5 < Re_\epsilon < 100) \quad (77)$$

Kozeny coefficient

Initially, Kozeny (1927) proposed a fixed pore shape factor $k_{koz} = 5$ in Equations (73) and (78) to fit the model results to experimental data.

$$K = 36 k_{koz} \quad (78)$$

Ergun (1952) proposed a slightly lower value ($K = 150$ instead of 180) for the Kozeny coefficient in Equation (55), which is confirmed in standard works (Di Felice, 1995; Bird *et al.*, 2007; Crowe and Group, 2006). However, it has been demonstrated through experiments and CFD modelling (Gupta and Sathiyamoorthy, 1999; Crittenden *et al.*, 2012; Ebrahimi Khabbazi *et al.*, 2013; Ozgumus *et al.*, 2014) that the k -value is dependent on the permeability for different porous media of varying voidage values (Teng and Zhao, 2000).

Traditional drag versus Reynolds number

In general, drag relations, where the drag is given as a function of the Reynolds number, are commonly plotted on *log-log* scales to comprise a wide range of Reynolds numbers. The most common drag relation is pipe flow friction given in Moody's diagram (Moody, 1944), (Section 2.3.2). Here, the laminar flow regime declines fast for increasing Reynolds numbers, as the emphasis lies on turbulent flow regimes, represented by horizontal lines.

For porous media, drag relations and plots in the literature show a similar pattern. The laminar drag declines with increasing Reynolds numbers following Kozeny

(Equation (53)), after which the drag deflects in the transitional flow regime towards the constant drag predicted by Burke–Plummer (Equation (76)), which is valid in the turbulent flow regime (Forchheimer, 1930). As turbulent flow regimes are rare in applications of LSF, the emphasis should not lie on the turbulent flow regime. To place greater emphasis on the drag in the laminar and transitional regions, it is better to focus on deviations from the laminar regime by multiplying f_T (drag coefficient in the turbulent ($\sim v_s^2$) representation) with the modified particle Reynolds number Re_ε (Equation (6)) to arrive at f_L (drag coefficient in the laminar ($\sim v_s$) representation) (Erdim *et al.*, 2015):

$$f_L = f_T Re_\varepsilon \quad (79)$$

In the literature, deviations between measurements and drag models are commonly present, but often artificially hidden due to the use of *log-log* scales over many orders of magnitude. In this work, by reporting f_L (Equation (79)) values on a linear scale, we will make these deviations between measured and modelled drag more clearly visible in the transitional regime.

Drag relations for fixed and fluidised beds

Equation (74) can be rewritten to obtain an explicit expression for f_T based on measurements of the hydraulic gradient:

$$f_T = \frac{\Delta P}{\Delta L} \frac{d_p}{\rho_f v_s^2} \frac{\varepsilon^3}{1 - \varepsilon} \quad (16)$$

Another equation for the drag coefficient, denoted by f_L , was given by Erdim *et al.* (2015):

$$f_L = \frac{\Delta P}{\Delta L} \frac{d_p^2}{\eta v_s} \frac{\varepsilon^3}{(1 - \varepsilon)^2} \quad (18)$$

In a steady state of homogeneous fluidisation of particulate solids, the frictional pressure drop equals the weight of the bed material, reduced by the buoyancy forces, per unit of bed surface. This is expressed by Equation (22) (Yang, 2003):

$$\frac{\Delta P}{\Delta L} = (\rho_p - \rho_f)g(1 - \varepsilon) \quad (31)$$

Based on Equation (22), the force balance between the frictional drag and the weight of the particles in the bed yields an alternative expression for the dimensionless drag coefficient f_T or f_L :

$$f_T = \frac{(\rho_p - \rho_f)gd_p}{\rho_f v_s^2} \varepsilon^3 \quad (17)$$

$$f_L = \frac{gd_p^2 (\rho_p - \rho_f)}{v_s \eta} \frac{\varepsilon^3}{1 - \varepsilon} \quad (19)$$

Equations (16) and (18) can be used to determine the dimensionless drag coefficient based on experimental data for both fixed and fluidised bed states, where the differential pressure and voidage must be known. Equations (17) and (19) are dependent on the voidage, albeit independent of the differential pressure, and they are valid only for the fluidised bed state. For accurate drag determination, Equation (19) might be preferable since there is no dependency on sensitive differential pressure measurements. The determination of bed voidage in LSF is relatively accurate due to the straightforward measurement of total mass of particles, bed height and particle density.

6.3.2 Hydraulic models based on the Reynolds and Froude numbers

Froude numbers

Wilhelm and Kwauk (1948) proposed a dimensionless number, known as the Froude number, which is a reliable parameter for discriminating between the two extreme situations, particulate and bubbling behaviour, to explain the quality of fluidisation:

$$Fr = \frac{v_s^2}{gd_p} \quad (12)$$

The Froude number can be viewed as the ratio of inertial to gravity forces. A transition occurs from particulate or smooth homogeneous fluidisation to heterogeneous or aggregative (bubbling) fluidisation at $Fr \approx 1$ with a theoretical maximum value $Fr = 1.5$. According to Gupta and Sathiyamoorthy (1999), this transition occurs at $Fr \approx 0.13$. In general, the transition from a homogeneous to a heterogeneous state is gradual. Many standard works define the Froude number as Equation (12) (Di Felice, 1995; Gupta and Sathiyamoorthy, 1999; Bird *et al.*, 2007; Yates and Lettieri, 2016; Rapp, 2017; Wilkes, 2019). Other standard works (Yang, 2003; Rhodes, 2008) use the square root of the expression given in Equation (12):

$$Fr = \frac{v_s}{\sqrt{gd_p}} \quad (80)$$

In case the particle and fluid densities are taken into account (Grace, 1986; Crowe and Group, 2006), the densimetric or particle Froude number is given by (Wirth, 1991):

$$Fr_p = \frac{v_s}{\sqrt{\left(\frac{\rho_p}{\rho_f} - 1\right)gd_p}} \quad (14)$$

The densimetric Froude number, Equation (14), also contains information about the ratio of the densities of the particle and the fluid. Because the gravitational force on a particle in a fluid is always counteracted by a buoyancy force (a neutrally buoyant particle does not sediment or fluidise), it appears to be the more relevant Froude number.

Proposed model extensions

There are several reasons why we propose an extension of the existing classical drag models with the particle Froude number:

- While the Reynolds number deals with the relationship between viscous and inertial forces, the particle Froude number deals with the relationship between gravity and inertial forces. Notably for larger particles and/or particles with a relatively large solid-to-fluid density, the gravitational forces are dominant. In other words: the Reynolds

number quantifies the laminar-to-turbulent properties, whilst the Froude number quantifies the homogeneous-to-heterogeneous properties of the system.

- When aggregative fluidisation occurs, voids of fluid provide pathways with less resistance to the fluid, resulting in a lower drag compared to the drag assumed for homogeneous fluidisation. This means that, when we look at the form of Equations (55) or (54), the effective Reynolds number should in fact be slightly higher. This might be accomplished through adding an explicit dependency on the Froude number.
- Visual observations of assumed homogeneous fluidisation experiments showed significant voids and trains of particles, which means that the drag cannot be mathematically described merely by the Reynolds number based on viscous and inertial forces. Through inclusion of the Froude number, information regarding such transient fluidisation events is appended. Videos with LSF experiments are shared in the Supplementary material (Section 6) (Kramer *et al.*, 2020d).
- In DNS modelling (Beetstra *et al.*, 2007), drag relations are often proposed for static arrays of particles, whereas in many practical applications, such as pellet-softening, the particles are moving in space, leading to heterogeneities as mentioned above.

Model synthesis incorporating the Reynolds and Froude numbers

To take into account both laminar and turbulent characteristics as well as homogeneous and heterogeneous phenomena, we propose three types of models for liquid-solid fluidised beds, based on the Reynolds number (Equation (6)) along with the Froude number (Equation (14)):

$$f_T = f_T(Re_\varepsilon, Fr_p) \quad (81)$$

The first of our three models is based on a theoretical similarity with terminal settling, the second is based on the semi-empirical Carman–Kozeny model and the third is based on empirical equations using symbolic regression techniques.

Our first model is based on theoretical expressions for the drag on a sphere falling through a quiescent fluid at small but finite Reynolds numbers. According to the principles introduced by Oseen (1927) and Proudman and Pearson (1957), the

singular solution of the basic Stokes Equation (Batchelor, 2012) grows like $-\log(\text{Re})$ instead of decaying like $1/\text{Re}$ towards the transitional region. For increasing Reynolds numbers, the inertial forces become more important and the drag coefficient approaches Newton's law *i.e.* a constant drag coefficient. The newly proposed dimensionless drag coefficient is a combination of the Reynolds number Re_ε and the Froude number Fr_p according to Equation (82):

SON model (Stokes–Oseen–Newton inspired model)

$$f_T = \frac{c_1}{Re_\varepsilon} + \frac{c_2}{Fr_p} - c_3 \ln(Re_\varepsilon) + c_4 \quad (82)$$

Our second model is based on the original Carman–Kozeny Equation (54). To incorporate our observed heterogeneous phenomena in liquid-solid fluidised beds, we propose to replace the Reynolds number in the Carman–Kozeny equation by a new dimensionless number RF :

$$RF = RF(Re_\varepsilon, Fr_p) \quad (15)$$

With the application of our newly proposed dimensionless number RF , the form of Equation (54) is therefore adjusted to:

$$f_T = \frac{c_1}{RF} + \frac{c_2}{RF^{c_3}} \quad (83)$$

Previously, the numerical coefficients c_1 , c_2 and c_3 in Equation (83) were obtained by fitting them to experimental results (Gupta and Sathiyamoorthy, 1999). In this work, however, the coefficients have been fitted through non-linear curve fitting. Note that for small Froude numbers (homogeneous fluidisation), RF should approach the modified Reynolds number Re_ε . Still, this leaves many possibilities with regard to the exact relation in Equation (15). We have explored the following models:

RIO 1 model (Reynolds–Improved–Outlook model)

The first model is inspired by the shape of the equation proposed by Schiller and Naumann (1933):

$$RF = Re_{\varepsilon} \frac{(1 + c_4 Fr_p^{c_5})}{(1 + c_6 Fr_p^{c_5})} \quad (84)$$

RIO 2 model

It is possible to adjust RF in such a way that only one extra fitting parameter remains; c_3 belongs to Carman–Kozeny Equation (83).

$$RF = \left(Re_{\varepsilon} + c_4 Fr_p^{\frac{1}{c_3}} \right) \quad (85)$$

The third model was obtained using symbolic regression techniques as applied in genetic programming. Genetic programming is a random-based technique (Koza, 1992) for automatically learning computer programmes based on artificial evolution. It has been successfully used in many applications (Edwards, 2006; Barati *et al.*, 2014). The advantage of genetic programming is that there is no need to define the structure of a model *a priori*: the technique randomly generates a population of several mathematical operators. Symbolic regression is the process of determining the symbolic function, which describes a data set, thus effectively developing an empirical model (Awange and Paláncz, 2016). These types of models have two main features: complexity and accuracy. Generally, given a certain data set, the process starts with the determination of very simple but inaccurate models. With time, more accurate but also more complex models are obtained. To prevent adverse modelling of measurement errors, data noise or deviation, a model should be taken as a compromise between complexity and accuracy. Despite symbolic regression leading to numerous solutions, *i.e.* multiple equations, occasionally relatively simple equations are found. Following this approach using the software package Eureqa (Nutonian, 2019), Equation (86) is an example of such a simple equation and has been used for modelling purposes.

EUR model (Eureqa symbolic regression model)

$$f_T = \frac{c_1}{Re_{\varepsilon}} + \frac{c_2}{\sqrt{Fr_p}} \quad (Re_{\varepsilon} < 15,000) \quad (86)$$

When in steady-state homogeneous fluidisation the frictional pressure drop Equation (22) is combined with the classical drag relations or with the proposed new drag relations (Equations (82), (83) and (85)) in combination with Equation (84) as well as Equation (86), the voidage in fluidised beds can be calculated. In the new expressions, besides the Reynolds number (Equation 6), also the Froude number is required (Equation 14). It should be noted that all proposed models have different parameters c_i .

6.4 Materials and Methods

The experimental set-up is presented in Section 3.1. The physical properties of water is given in Section 3.2. Photographs of granules is given in Annex 1: Photos. Standard operating procedure of fluidisation experiments is elucidated in Section 3.4.

6.4.1 Particle selection and fluidisation experiments

In this study, we initially examined calcite pellets (100% CaCO_3) applied in drinking water softening. Polydisperse calcite pellets were sieved and separated in order to acquire more uniformly dispersed samples. To investigate hydrodynamic behaviour, also highly monodisperse and almost spherical glass beads were used: two transparent and four opaque solid-coloured SiLibeads glass beads type P.

For validation purposes, LSF data were retrieved from standard references in the literature for a wide range of different particles in fluid water systems (Wilhelm and Kwauk, 1948; Lewis *et al.*, 1949; Richardson and Zaki, 1954; Loeffler, 1953).

Detailed information regarding data tabulation can be found in the Supplementary material (Sections 3-5, 18).

6.4.2 Particle and fluid characterisation and expansion experiments

The method to calculate the physical properties of water is given in Materials and Methods Section 3.2. The methods to determine the physical properties of particles is given in Section 3.3. Accordingly, bed voidage and differential pressure equations are given in Section 3.4.

6.5 Results and discussion

Expansion experiments and fluidisation characterisation observations are given in Section 6.5.1 and Section 6.5.2. The determined drag with persisting deviation is discussed in Section 6.5.3. The experimental data leading to the estimation of the Kozeny coefficient are presented in Section 6.5.4. Accordingly, the drag relations based on the Reynolds number and hydraulic models based on the Reynolds and Froude numbers are discussed in Section 6.5.5 and Section 6.5.6, respectively. Finally, the voidage prediction results are given in Section 6.5.7.

6.5.1 Expansion experiments

The acquired experimental data set consisted of a matrix with varying temperatures, grain sizes and flow rates, as was required for a comparison of the theoretical fluidisation models. In total, 97 fluidisation experiments were carried out for calcite pellets (61) and glass beads (36) which were compared to fluidisation characteristics obtained from the literature (42). Figure 47 shows, as an example, a typical expansion curve in which the voidage and pressure difference along the whole bed was measured for increasing superficial velocities at different temperatures. For increasing temperature, total differential pressures in the fixed bed and bed voidage in the fluid state decrease due to the decrease in viscosity *i.e.* less interaction force on each particle brought about by the fluid.

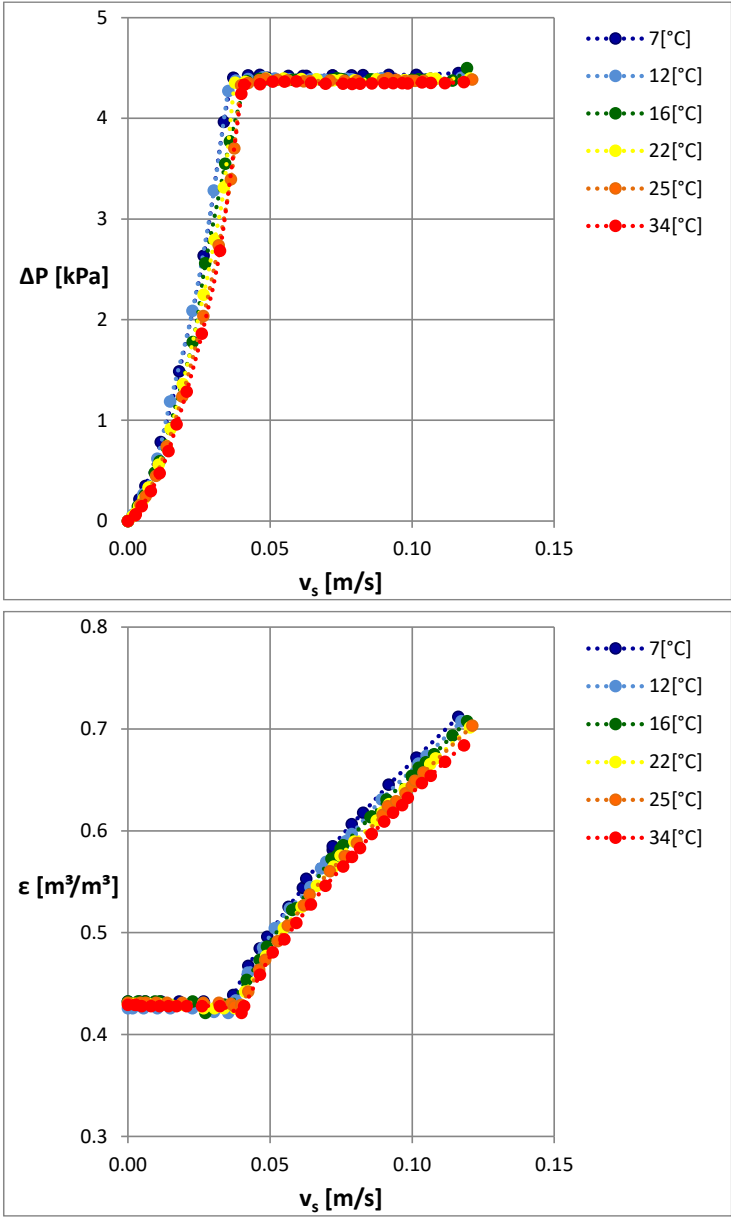


Figure 54 A typical expansion experiment with SiLibeads glass beads ($d_p = 2.5$ mm), ($6 < T$ °C < 27), with measured differential pressure along the whole bed and voidage against the superficial fluid velocity.

6.5.2 Fluidisation characterisation observations

During fluidisation experiments with calcite grains, we observed open spaces of water between the fluidised particles, even at relatively low fluid velocities (Figure 4). Moreover, significant heterogeneous particle-fluid patterns were detected at higher fluid velocities, even though in the literature LSF systems are generally considered to be homogeneous at lower superficial fluid velocities (Di Felice, 1995). Supporting videos showing LSF experiments are shared in the Supplementary material (Section 6) (Kramer *et al.*, 2020d) to visualise the voids and bubbly flow aspects for both calcite pellets and glass beads.

To eliminate the influence of particle shape and polydispersity, the experiments were repeated with highly spherical monodisperse glass beads and we saw that the heterogeneous flow phenomena emerged yet again. The voids of water were found to provide pathways of lower resistance to the fluid, resulting in a lower drag compared to the assumed drag for homogeneous fluidisation.



Figure 55
Fluidised calcite pellets in water at normal fluidisation: voids are clearly visible (1.4-1.7 mm 20 °C, 22 mm/s)



Figure 56
Fluidised glass beads in water at relatively low fluidisation (1.5 mm 12 °C, 25 mm/s)



Figure 57
Fluidised glass beads in water just above incipient fluidisation (2.5 mm 22 °C, 39 mm/s)

6.5.3 Persistent drag deviation

The experimentally determined drag coefficients f_T and f_L for calcite pellets, glass beads and data obtained from the literature are plotted in Figure 58 and Figure 59. Classical models (Kozeny, Ergun, Carman–Kozeny and van Dijk) have been added; they are not constrained by boundary conditions to emphasise the effects of laminar and turbulent behaviour. Wall effect corrections have not been implemented because they are insignificant under our experimental conditions. A further and more detailed explanation can be found in Annex 2: Wall effects and in the Supplementary material (Section 9).

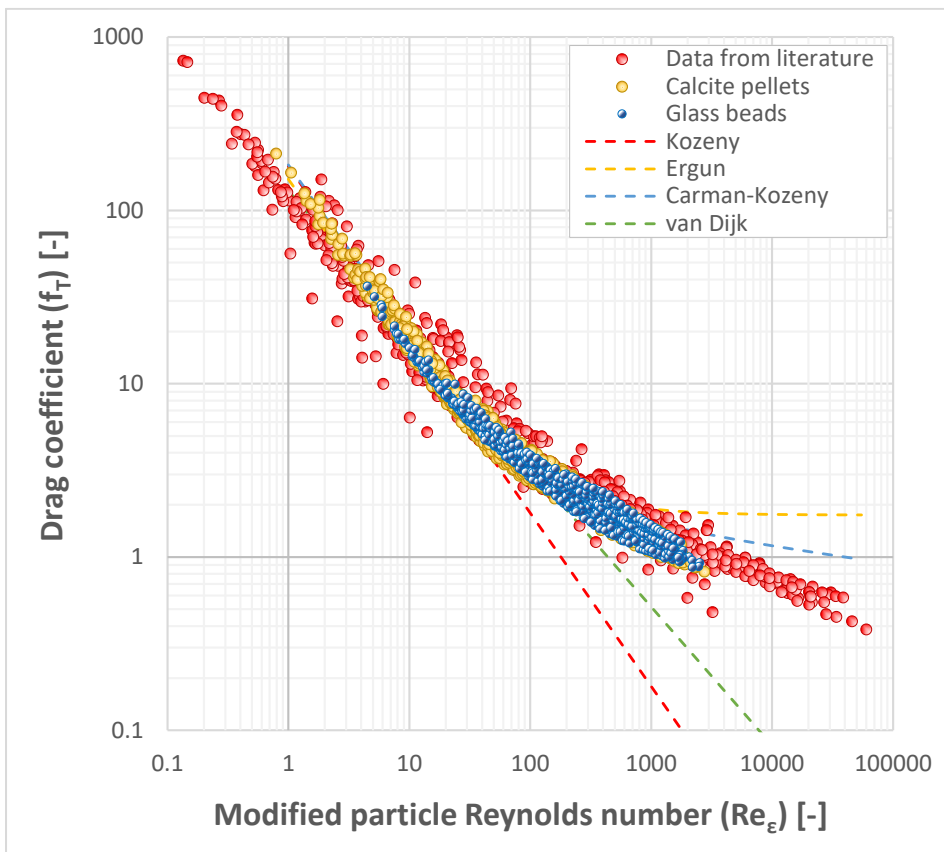


Figure 58 Drag curve f_T (turbulent representation) for calcite pellets, glass beads and data from the literature.

When the drag f_T based on the Reynolds number had been determined for calcite pellets, a certain degree of spread in the data was found (Figure 58). To eliminate the influence of particle shape and polydispersity, the experiments were repeated using highly spherical and monodisperse glass beads. Yet again, a similar degree of spread in the data was found. To accentuate the spread of drag measurements in the transitional region and to eliminate the *log-log* effect, the standard drag f_T was converted into f_L using Equation (79). Accordingly, the quadratic fluid velocity term in Equation 17 is converted into a linear inversely proportional relationship between f_L and velocity (Equation 19), which reduces the magnitude of drag. The presence of the spread is evident in Figure 59.

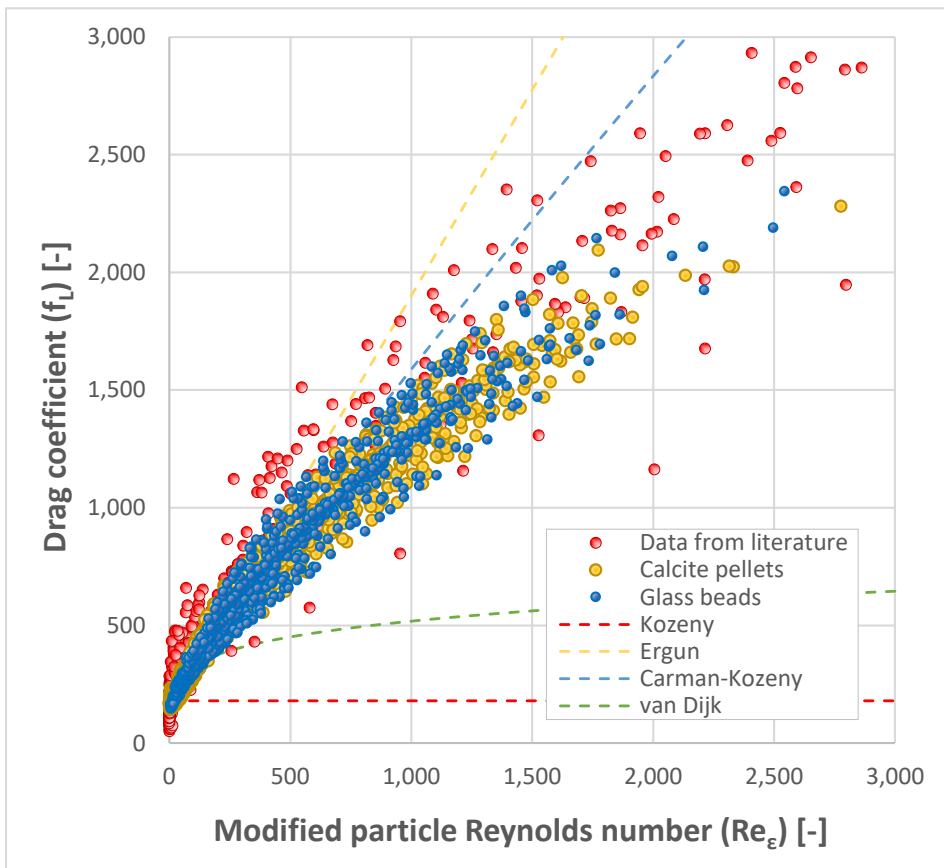


Figure 59 Drag curve f_L (laminar representation) for experimental data and classical models.

Data obtained from the literature was added, which shows a substantially larger spread compared to the experimentally determined drag in this work. Data from the literature, however, has a wider variance due to the use of different types of grain material.

6.5.4 Estimation of the Kozeny coefficient

The experimentally obtained fluidisation characteristics for glass beads in fixed bed states was used to calculate the Kozeny-coefficient K . The drag relation Equation (18) given by Erdim *et al.* (2015), which is based on the differential pressure, can be used. In Figure 60, f_L is plotted against Re_e where the original coefficients were used (Carman, 1937). In the vicinity of the fixed bed (voidage close to 0.4), the deviation is substantial, which can be attributed to the fixed packing irregularity. The plot shows that the original value $K = 180$ is slightly too high. Using non-linear curve fitting, the optimal Kozeny-coefficient K gives a value close to 150, which agrees with Ergun (1952), Yang (2003) and many others, despite the fact that the Kozeny-coefficient K does not have a fixed value for different conditions. Regarding spherical calcite pellets, the deviation is even higher compared to glass beads due to the influence of irregularly shaped grains. To continue the modelling, a fixed value of $K = 150$ is assumed henceforward. Graphs and data regarding calcite pellets are given in the Supplementary material (section 10).

Table 18 Carman–Kozeny coefficients for fixed bed state

Carman–Kozeny model	Grain type	c_1	c_2	c_3	R^2
Original Equation (54)	Glass beads	180	2.87	0.10	0.721
Fitted model		151	3.38	0.12	0.866

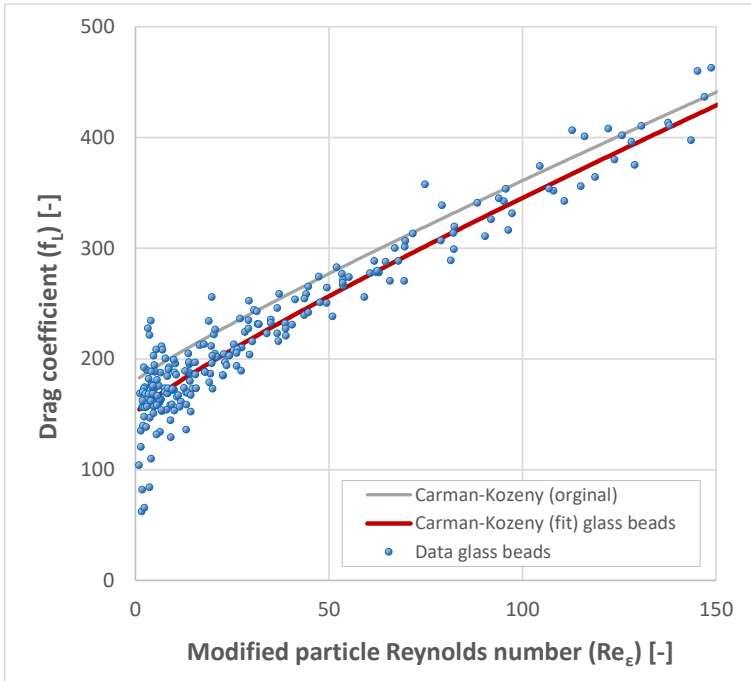


Figure 60 Original Carman–Kozeny Equation (54) glass beads f_L versus Re_ϵ in the fixed bed state.

6.5.5 Drag relations based on the Reynolds number

First, the results for classical models will be discussed. The experimentally obtained fluidisation characteristics data were used to calculate the drag (f_T and f_L) as a function of the modified particle Reynolds number Re_ϵ , which is presented in Table 19; graphs are given in the Supplementary material (Section 11). In general, when f_T is used, *i.e.* in the laminar flow regime, drag at lower Reynolds values is emphasised. In the transitional regime when f_L is used, *i.e.* in the intermediate flow regime, drag at intermediate Reynolds values are more determinative. The scope of this work focuses on water systems, so f_L will primarily be used. Additional graphs for comparison purposes with classical models can be found in the Supplementary material (Section 11).

Table 19 Drag relation models based on the modified particle Reynolds number

Grain type	Model	Eq. nr.	Note	c_1	c_2	c_3	R^2	c_1	c_2	c_3	R^2
				f_T				f_L			
Calcite pellets	Kozeny	53	Original	180	-	-	0.974	180	-	-	0
	Burke–Plummer	76	Original	-	1.75	-	0	-	1.75	-	0.740
	Ergun	55	Original	150	1.75	-	0.980	150	1.75	-	0.328
	"	"	Fit	169	1.46	-	0.989	210	1.12	-	0.944
	Carman–Kozeny	54	Original	180	2.87	0.100	0.977	180	2.87	0.100	0.790
	"	"	Fit	150 ¹⁾	4.84	0.206	0.987	150 ¹⁾	5.70	0.232	0.980
	Van Dijk	77	Original	130	-	0.800	0.966	130	-	0.800	0.147
	"	"	Fit	134	-	0.833	0.971	27.7	-	0.446	0.976
Glass beads	Kozeny	53	Original	180	-	-	0.845	180	-	-	0
	Burke–Plummer	76	Original	-	1.75	-	0	-	1.75	-	0.466
	Ergun	55	Original	150	1.75	-	0.980	150	1.75	-	0.294
	"	"	Fit	150	1.44	-	0.985	206	1.13	-	0.930
	Carman–Kozeny	54	Original	180	2.87	0.100	0.981	180	2.87	0.100	0.776
	"	"	Fit	150 ¹⁾	2.21	0.0789	0.987	150 ¹⁾	5.49	0.226	0.967
	Van Dijk	77	Original	130	-	0.800	0.842	130	-	0.800	0
	"	"	Fit	45.3	-	0.550	0.917	23.0	-	0.417	0.967
Literature data	Kozeny	53	Original	180	-	-	0.516	180	-	-	0
	Burke–Plummer	76	Original	-	1.75	-	0	-	1.75	-	0
	Ergun	55	Original	150	1.75	-	0.813	150	1.75	-	0
	"	"	Fit	113	2.02	-	0.964	291	0.646	-	0.893
	Carman–Kozeny	54	Original	180	2.87	0.100	0.500	180	2.87	0.100	0.138
	"	"	Fit	150 ¹⁾	-29.0	1.300	0.970	150 ¹⁾	8.11	0.262	0.981
	Van Dijk	77	Original	130	-	0.800	0.966	130	-	0.800	
	"	"	Fit	124	-	0.884	0.972	14.1	-	0.320	0.981

¹⁾ Fixed value $c_1 = 150$

For all data regarding the fluidised state, the Kozeny model violates the laminar boundary conditions and can therefore not be used to predict the drag or bed voidage. In general, the majority of LSF flow regimes occur in the transition region, in particular when the fluid is water. Exclusively laminar and turbulent flow regimes barely occur. Therefore, the Burke–Plummer model is not suitable for prediction purposes either. Conversely, the Ergun model is relatively accurate at low Reynolds numbers, but for higher Reynolds numbers, drag is increasingly overestimated. Fitting the Ergun parameters increases the prediction accuracy.

When Carman–Kozeny is examined for both calcite pellets and glass beads, drag is slightly overestimated. The most obvious explanation is that the Kozeny constant K is not constant and more likely approaches 150 rather than 180. In addition, Carman (1937) mainly used experimental data based on gas-solid systems to calibrate the Carman–Kozeny model parameters (Figure 61). A minority of Carman’s dataset (Green and Ampt, 1911) consisted of a few water-solid experiments at laminar conditions. Another disadvantage of this semi-empirical model lies in the assumptions that the particles are perfectly round, and that the particle distribution remains homogeneous. Since these assumptions are not fulfilled in practice, the model parameters must be adjusted, often empirically, to increase the voidage prediction accuracy. In other words, the Carman–Kozeny model parameters often used in the literature are not automatically suitable for LSF. This supports our attempts to use a fitting method to find the most reliable model parameters based on our experiments. In Table 19, the fitted Carman–Kozeny equation has the highest R^2 .

The van Dijk model (van Dijk and Wilms, 1991) is valid in the transitional region but provides very diverse correlation coefficients (f_T and f_L). However, fitted van Dijk parameters provide reasonable R^2 values but cannot cope with the apparent deviation. In summary, drag prediction based merely on the Reynolds number in classical models is only accurate to some extent when the parameters are fitted based on experimental data. The spread of data in terms of drag, however, is not resolved. This can also be seen in the drag plots presented in literature (Hoyland, 2017) where the data spread is less visible due to the use of logarithmic scales. If the experimental data set is examined for glass beads using f_L , the lowest K -value of 150 is confirmed. We observe that the lowest determined drag for glass beads and calcite pellets corresponds to $f_T = 0.86$, which is lower than the minimum of 1.75 proposed in the literature (Burke and Plummer, 1928; Ergun, 1952). The lowest determined drag regarding data obtained from the literature is even lower: $f_T = 0.38$.

These lower drag values are most likely caused by non-homogeneous fluidisation characteristics. This explains why a porous media model is less accurate and not suitable for use. Based on the numerical results in Table 19, classical drag relations with only a Reynolds relationship are less accurate and therefore less suitable for water treatment processes.

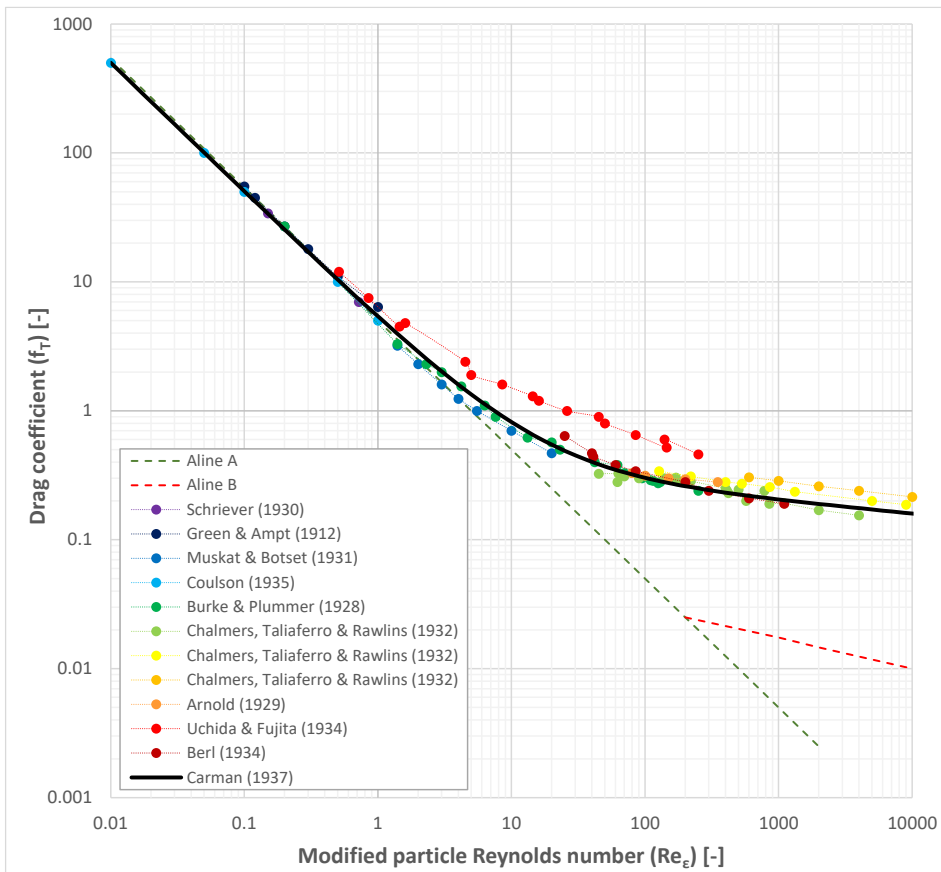


Figure 61 Original data extracted from Carman (1937): correlation for beds of spherical particles (Figure 1).

6.5.6 Hydraulic models based on the Reynolds and Froude numbers

The persistent spread and deviations (in f_T and f_L), in addition to our visible observations, reinforce our hypothesis that drag cannot be estimated accurately as a function of the Reynolds number only. The main reason for this is that crucial information about the fluidisation quality is missing. To take into account laminar-turbulent as well as homogeneous-heterogeneous fluidisation characteristics, an improvement of the drag relation for LSF is proposed based on the Reynolds and Froude numbers. The effect of the extra dimension, expressed by the additional Froude number, can be seen in the 3D plot in Figure 62 for calcite pellets. 3D plots for glass beads and data from the literature are given in the Supplementary material (Sections 8 and 13).

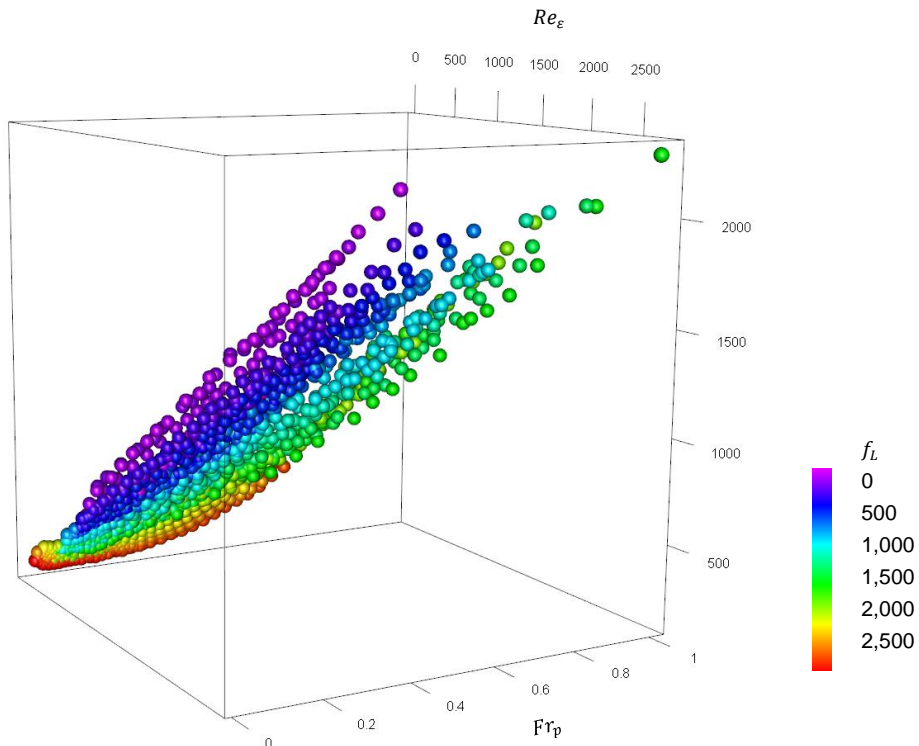


Figure 62 Rotated 3D plot (f_L versus Re_ϵ , Fr_p) based on experimental data (calcite pellets) in the fluidised state.

For all three proposed types of models (cf. Section 6.3.2), $K = 150$ was used. In general, the correlation coefficients for glass beads, calcite pellets and data from the literature are at least 0.95 or higher (Table 2). In case the original Carman parameters are used as input parameters, in all cases, the R^2 is substantially lower. For many models, the highest obtained correlation coefficient was $R^2 = 0.993$, which indicates the quality of the experimental data set and model.

Both RIO 1 and 2 models are based on the Carman–Kozeny equation. The RIO 1 model has three extra parameters and has the highest R^2 value, while the RIO 2 model only has one extra parameter with a slightly lower R^2 value. Although the EUR model is relatively simple and has only one extra parameter and a boundary condition, it still has a reasonable R^2 .

Regarding the RIO 2 model, the transition to turbulence is expected to occur when the two terms in Equation 85 have approximately the same value, *i.e.* when the Reynolds number exceeds $Re_\varepsilon > 1,500\text{-}2,000$ (for the obtained value of the parameter c_4), in accordance with (Ergun, 1952).

Table 20 Drag relation models based on Reynolds-Froude numbers

Grain type	Model	Eq. nr.	c_1	c_2	c_3	c_4	c_5	c_6	R^2
Calcite pellets	SON model	82	150 ¹⁾	0.161	0.205	2.30	-	-	0.989
	RIO 1 model	84	150	11.4	0.260	6.91	1.26	0.0424	0.991
	RIO 2 model	85	150	6.70	0.240	2,166	-	-	0.990
	EUR model	86	150	0.930	-	-	-	-	0.984
Glass beads	SON model	82	150	0.227	0.122	1.61	-	-	0.991
	RIO 1 model	84	150	12.2	0.244	18.9	1.43	0.00903	0.992 ²⁾
	RIO 2 model	85	150	6.33	0.226	3,883	-	-	0.988
	EUR model	86	150	0.891	-	-	-	-	0.987
Literature data	SON model	82	150	0.224	0.139	1.76	-	-	0.990
	RIO 1 model	83+84	150	6.62	0.191	6.87	1.80	0.320	0.992
	RIO 2 model	83+85	150	10.4	0.280	3,750	-	-	0.987
	EUR model	86	150	0.674	-	-	-	-	0.958

¹⁾ Fixed Kozeny coefficient $K = 150$

²⁾ Figure 63 and Figure 64

Fit parameters for other examined granules besides glass beads and calcite pellets are provided in (Kramer et al., 2020c).

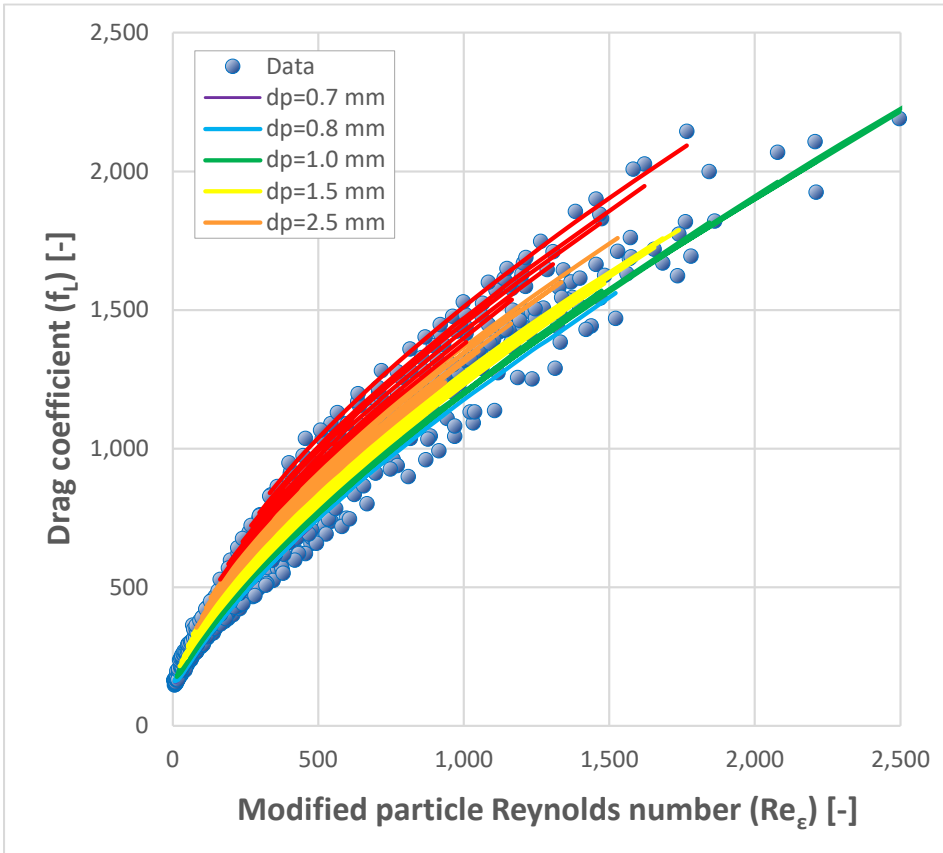


Figure 63 Drag coefficient f_L versus Re_e for glass beads and RIO 1 model (highest R^2).

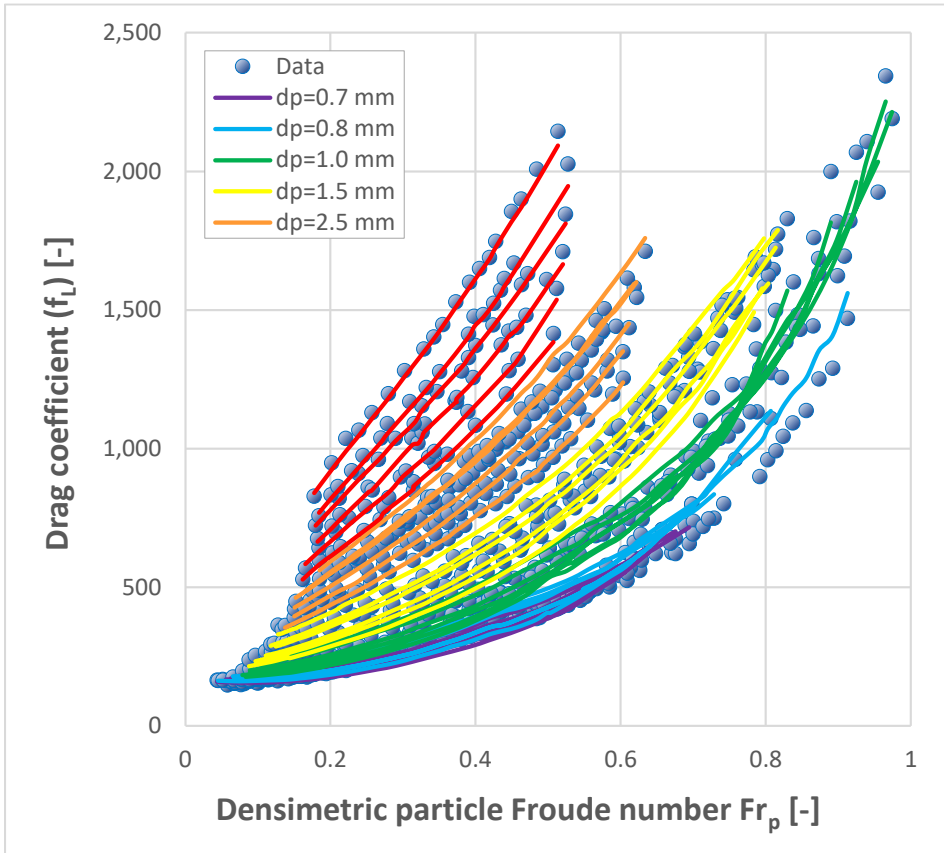


Figure 64 Drag coefficient f_L versus Fr_p for glass beads and RIO 1 model (highest R^2).

In Figure 63, the drag coefficient f_L is plotted against the Reynolds number through a linear plot. In this figure, the effect of the projection of the 3D plot shown in Figure 62 on a single 2D plane, leading to the apparent spread of the drag versus modified Reynolds number, is clearly visible. The influence of the Froude number becomes apparent in Figure 12.

6.5.7 Voidage prediction

The investigated drag models were used to predict the voidage for the fluidised state using the differential pressure Equation (17). The models were compared with experimental data: glass beads and calcite pellets as well as data obtained from the

literature. Results are presented in fit parameters are used in the models. The prediction accuracy for glass beads and calcite pellets is roughly the same. For all models, the prediction accuracy for data from the literature is lower.

Although the laminar flow regime-based Kozeny model seems to predict the voidage quite well, the model is barely valid when the given boundary conditions are respected. This is also the case with the turbulent flow regime-based Burke–Plummer model. The Ergun model is valid for all flow regimes but has a lower accuracy, *i.e.* a higher average relative error, compared to the original Carman–Kozeny equation. The latter model, however, is not valid for the whole regime. The van Dijk model, often applied in water treatment processes, is a little more accurate compared to Ergun. It is, however, only valid for low transition flow regimes.

During the experiments, the fluid flow was increased until voidage values were attained of $\varepsilon \approx 0.95$. This means that the developed models are valid up to $\varepsilon \approx 0.95$. The prediction inaccuracy is 0.8-1.5% for glass beads, 1.2-1.6% for calcite pellets and 3.4-4.4% for data from the literature. The voidage prediction accuracy for glass beads, calcite pellets and data obtained from the literature as given in fit parameters are used in the models is based on fitting parameters based on perfectly monodisperse glass beads. For other specific grain types, besides these glass beads, it is nevertheless possible to increase the prediction accuracy in case specific fit parameters are used in the models.

Table 21 Voidage prediction accuracy

Model	Model	Eq. nr.	Validity ¹⁾	Average Relative Error [%] ²⁾		
				[%] Glass beads	Calcite pellets	Literature data
Classical models	Kozeny	53	4	2.4	2.3	9.0
	Burke–Plummer	76	15	9.4	9.6	13.1
	Ergun	55	100	4.7	4.2	8.1
	Carman–Kozeny	54	58	3.2	2.4	6.3
	van Dijk	77	29	4.4	3.1	6.3
Drag model	SON	82	100	1.3	1.2	3.4
	RIO 1	83+84	100	0.8	1.6	4.0
	RIO 2	83+85	100	1.5	1.4	4.0
	EUR	86	100	1.2	1.4	4.4

¹⁾ Percentage of the data that meets the boundary conditions of the used models

²⁾ Bolzano's numerical intermediate value theorem (Apostol, 1967)

The most accurate model is the Carman–Kozeny-based RIO 1 model, with an overall average relative error below 1. For homogeneous fluidisation, where the Froude number has a minor effect, the models scale to the Reynolds number. For heterogeneous fluidisation, the Froude number has more influence and increasingly reduces the drag.

The choice for one of the four presented models depends on criteria such as correlation coefficient, voidage prediction accuracy, familiarity, required boundary conditions, number of fit parameters, simplicity, applicability and/or user preferences. Despite the fact that the Carman–Kozeny-based RIO 2 model has a slightly lower voidage accuracy for glass beads and slightly higher for calcite pellets, it has two fit parameters less than the RIO 1 model and it meets all selection criteria. This means that this model is slightly more preferable. In future work, thorough CFD modelling is recommended to determine whether the Froude number is a suitable dimensionless number to exactly describe or evaluate the concept of ‘heterogeneous flow phenomena’.

6.6 Conclusions

Liquid-solid fluidisation processes are frequently used in industry, such as drinking water treatment processes. For pellet-softening, the operational field lies in the vicinity of incipient fluidisation to provide a large crystallisation surface area and consequently to obtain optimal process conditions. This operational field falls within the initial transitional flow regime rather than turbulent flow regimes. To obtain optimal process conditions, the overall fluidised bed voidage is a crucial process parameter which can be estimated by means of drag relations. Traditionally, in drag relations, the emphasis of the dimensionless standard drag coefficient, defined as a function of the Reynolds number, is focused on the turbulent flow regime ($\sim v_s^2$) and less so on the laminar ($\sim v_s$) and transition flow regimes.

We propose four adjustments to improve the drag analysis to mathematically describe the fluidisation stability and to increase the overall voidage prediction accuracy. The first and second adjustments are to multiply the standard drag coefficient with the Reynolds number and to use a double linear representation instead of a traditional double logarithmic representation; this improves the distinctive capability of the drag analysis considerably. The third adjustment concerns coping with heterogeneity phenomena in liquid-solid fluidised beds. The

traditional drag relation based on the particle Reynolds number is extended with the particle Froude number. By adding a third dimension to the traditional 2D linear plots, where drag is plotted against Reynolds, the apparent and persistent spread in effective full-scale drag can be explained and visualised by means of a 3D plot. The fourth adjustment increases the accuracy of the dimensionless drag coefficient and therefore also the voidage prediction by using experimental data based on total mass of particles, bed height and particle density measurements rather than using sensitive differential pressure measurements.

Four new prediction models have been synthesised (SON, RIO 1, RIO 2 and EUR) which enable us to predict the voidage in the fluidised state more accurately. The prediction average relative error decreased from approximately 5% using the best literature Equation (exclusively based on Reynolds number) to 1-2% with the new Equation (based on Reynolds and Froude numbers). The RIO 2 model based on Carman–Kozeny has a voidage prediction inaccuracy of only 1% and can be used for calcite pellets as well as for spherical grains used in full-scale drinking water treatment processes such as pellet-softening.

6.7 Research data

Fit parameters for various additional granules regarding liquid-solid fluidisation models such as highly spherical particles and a variety of granules applied in drinking water treatment processes are shared at 4TU.Centre for Research Data: <https://doi.org/10.4121/13537121.v1>

6.8 Supplementary material

Supplemental data for this article can be accessed at:

<https://doi.org/10.1016/j.ijmultiphaseflow.2020.103261>

<https://ars.els-cdn.com/content/image/1-s2.0-S0301932219309723-mmc1.docx>

Contents		page
1	Proposed RIO 2 model based on Reynolds and Froude numbers	1
2	Hydraulic models in porous media	2
3	Photographs of examined particles	3
4	Particle and fluid characterisation	4
	4.1 Average particle diameter	4
	4.2 Particle density	4
	4.3 Physical properties of water	5
	4.4 Particle properties obtained	5
5	Fluidisation expansion experiments	7
	5.1 Standard operating procedure	7
	5.2 Bed voidage and expansion	7
	5.3 Statistical analysis	7
6	Supporting videos of liquid-solid fluidisation experiments	8
	6.1 Calcite pellets	8
	6.2 Glass beads	8
7	Visual observations	9
8	Graphical 3D plots	10
9	Wall effects	11
10	Estimation of the Kozeny coefficient	12
11	Persisting drag deviation based on the Reynolds number	13
	11.1 Calcite pellets	14
	11.2 Glass beads	15
	11.3 Literature data	16
	11.4 Validation with differential pressure data	18
12	Hydraulic models based on the Reynolds and Froude numbers	19
	12.1 Calcite pellets	20
	12.2 Glass beads	21
	12.3 Literature data	21

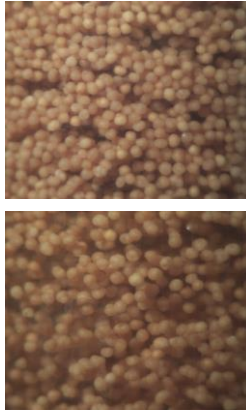
13	Script in R (3D plot: fL, Reε, Frp)	23
14	Future research and recommendations	24
15	Nomenclature	25
16	Bibliography	27
17	Acknowledgments	30
18	Experimental data	31
18.1	Glass beads	31
18.2	Calcite pellets	44
18.3	Data from literature	68
18.3.1	Richardson and Zaki	68
18.3.2	Wilhelm and Kwauk	69
18.3.3	Lewis	73
18.3.4	Loeffler	74-81

Fluidised bed reactor

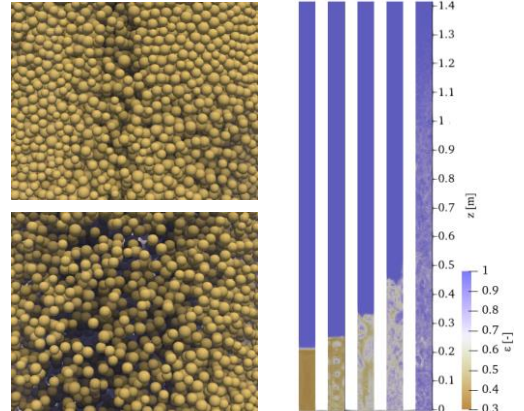
investigations reveal unexpected heterogeneity with implications for drinking water softening



Experimental



Numerical



- ▶ Liquid-solid fluidisation experiments show open spaces at low velocities
- ▶ Heterogeneous particle-fluid patterns are detected at higher fluid velocities
- ▶ CFD-DEM simulations show good agreement with experimental observations
- ▶ Numerical simulations confirm the formation of local voids and instabilities
- ▶ Voidage distributions and solid flux profiles obtained from our computer simulations

Keywords Fluidisation; Unsteady Behaviour; Drinking Water Treatment; Multiphase Computational Fluid Dynamics; Reactor Performance; Void Fraction Distribution

Chapter 7

Computational Fluid Dynamics

“Reliable experimental data using advanced pilot plants is crucial to accurately calibrate and validate numerical models.”

This article has been published as:

Experimental and numerical insights into heterogeneous liquid-solid behaviour in drinking water softening reactors ^{*)}

T.M.J. ^{*)}Nijssen, O.J.I. ^{*)}Kramer, P.J. de Moel, J. Rahman, J.P. Kroon, P. Berhanu, E.S. Boek, K.A. Buist, J.P. van der Hoek, J.T. Padding, J.A.M. Kuipers

Chemical Engineering Science: X, **11**, 100100 (2021) pp. 1–11

The article can be found online at:

<https://doi.org/10.1016/j.cesx.2021.100100>

^{*)} shared authorship on joint work with equal contribution

^{**)} this article has also been selected to feature on the front cover of this prestigious journal

7 Numerical study on unsteady liquid-solid behaviour in drinking water softening reactors

7.1 Abstract

Liquid-solid fluidisation is frequently encountered in drinking water treatment processes, for instance in seeded crystallisation softening processes. For modest superficial fluid velocities, liquid-solid fluidisation systems are generally considered to be homogeneous, as reported in literature. However, during fluidisation experiments with calcite grains, open spaces of water can be observed between the fluidised particles, even at relatively low fluid velocities. Moreover, significant heterogeneous particle-fluid patterns are detected at higher fluid velocities. Such heterogeneous behaviour can beneficially or adversely affect the chemical crystallisation efficiency. To obtain information about voids in bulk regions, complementary Computational Fluid Dynamics - Discrete Element Method (CFD-DEM) simulations were performed and compared with the experimental results for validation. Simulations were performed using different water inlet velocities and fractionised calcite granules obtained from full-scale reactors. Here, the results are analysed using the bed height, voidage and pressure drop of the system. Furthermore, images of the experiments and simulations are visually compared for the formation of voids. The simulations showed distinct differences in void fraction in the cross-section of the column. It is shown that throughout the range of considered water velocities, heterogeneous behaviour exists and cannot be neglected. The heterogeneity and onset of fluidisation behaviour obtained from the simulations and experimental observations were compared and found to agree reasonably well.

7.2 Introduction

7.2.1 Liquid-solid fluidisation applied in drinking water softening processes

Water softening is an important process in water treatment (Crittenden *et al.*, 2012). The removal of calcium carbonate has multiple benefits, for example to counteract limescale (Beeftink *et al.*, 2021; Kramer *et al.*, 2020b). The softening process is frequently performed using liquid-solid fluidised (LSF) bed reactors (Figure 65) (Graveland *et al.*, 1983). In the Netherlands, more than 400 million m³ water is softened annually in drinking water treatment plants employing fluidised bed pellet reactors (Hofman *et al.*, 2007). By adding caustic soda, supersaturated conditions are created. Calcium carbonate crystallisation takes place on the surface of calcite grains, which then grow. Pellets are extracted from the reactor when a defined grain size threshold is exceeded. Larger particles will migrate to the lower region of the reactor bed and, depending on the flow conditions, a stratified bed with a certain particle size profile will evolve. In these softening reactors, sand is generally used as seeding material and calcite pellets are produced as a by-product (van Dijk and Wilms, 1991). To improve sustainability, pure calcite can be used as seeding material, while full-grown calcite pellets, extracted from the reactor, can be dried, grained and sieved and re-used as seeding material (Schetters *et al.*, 2015).



Figure 65 Full-scale pellet-softening reactors located at Waternet (Amsterdam, the Netherlands). The unit consists of 12 Amsterdam reactors with reactor diameter $D = 3.0$ m (van der Veen and Graveland, 1988).

For optimal process conditions, *i.e.* fast calcium carbonate crystallisation (van Schagen, 2009), a large specific surface area (SSA), and therefore small particles, in the fluidised bed is required (Kramer *et al.*, 2020b). Because of the importance of the grain size and subsequent stratification effects, the fluidisation behaviour of these LSF bed reactors must be studied closely. Due to the need to ensure a continuous production of reliable drinking water, experiments in this field are restricted to pilot-scale set-ups. Complementary to these experiments, numerical simulations are used as a reliable tool to gain insight into these processes. Such simulations offer a more detailed view of the fluidisation behaviour inside the reactor without the need for elaborate experimental methods.

7.2.2 Fluidisation quality

Homogeneous fluidisation can be defined as a fluidised state in which solid particles are uniformly dispersed throughout the fluid without observable bubbles (Yang, 2003). The average distance between particles remains relatively constant, such that there is a consistent distribution of neighbour particles around each given particle (Gibilaro, 2001). Mainly, no bubbles or voids are present in homogeneous fluidisation (Grace *et al.*, 2020).

Heterogeneous fluidisation, in contrast, includes any state other than homogeneous. It can be chaotic or non-uniform, it can have bubbles or particles moving in bulk in different directions, and it can have particles moving randomly without maintaining a fixed distance to other particles. Both homogeneous and heterogeneous fluidisation are affected by increasing flow rate and varying particle properties. Fluidisation quality has been studied in great detail for gas-solid fluidisation (GSF) where bubbles play an important role. In LSF, bubbles or voids are pockets of fluid created during fluidisation. Some particles will get closer together to allow for large gaps with little or no particles. The presence of these gaps is one of the main indications of heterogeneous fluidisation (Geldart, 1973).

Homogeneous fluidisation for uniform particles was observed by (Wilhelm and Kwauk, 1948) who proposed a simplified classification and empirical criterion for the transition between a state of particulate or idealised fluidisation with complete homogeneity and a state of aggregative or heterogeneous fluidisation (Liu *et al.*, 1996). (Goossens, 1998) proposed a relatively simple industrial tool to classify and predict the fluidisation behaviour of any given fluid-particle system, based upon the dimensionless Archimedes number (Equation (9)) where gravitational and inertial forces are considered, and taking into consideration a representative particle diameter and related shape factor.

It is widely accepted that fluidisation flow for GSF is heterogeneous or aggregative, while LSF is mainly homogeneous or particulate, implying that the particles are assumed to be uniformly distributed (Ruckenstein, 1964; Davidson *et al.*, 1985; Jamialahmadi and Miiller-Steinhagen, 1992; Yang, 2003; Crowe and Group, 2006; Albright, 2009; Wang *et al.*, 2016; Michaelide *et al.*, 2017). This assumption has formed the basis of many publications. For example, (Richardson and Zaki, 1954) stated that measuring sedimentation would be similar to fluidisation due to the fact that in fluidisation the particles do not undergo any net movement and velocity is only due to the continuous upward movement of fluid, suggesting that the fluidisation

reaches an equilibrium. (Oke *et al.*, 2015) assumed the Richardson–Zaki equation to be correct, implying that homogeneous flow dominates for their numerical calculations. This highlights the large influence that these older publications continue to have. According to (Di Felice, 1995), the main or prevalent regime is homogeneous in LSF, whereas GSF is described to have many regimes and transition states. (Zheng *et al.*, 1999) stated that the flow in a liquid-solid circulating fluidised bed has higher uniformity than is the case for a gas-solid bed and that only some non-uniformity can be seen, implying that the flow is mainly homogeneous. (Liu *et al.*, 2013) described LSF as pseudo-homogeneous for higher viscosity liquids. (Tsuchiya *et al.*, 1997) stated that LSF sometimes demonstrates heterogeneous behaviour, albeit mainly homogeneous. According to (Batchelor, 1988), the conditions for instability of LSF are more complicated compared to GSF. Batchelor described experiments trying to find relationships between flow rate and other variables and found that a non-uniform fluidised bed contains two dependent variables; the local mean particle velocity and the local particle concentration. Batchelor also showed that instability occurs when the particle Froude number (ratio of inertial to gravity forces) exceeds a critical value (Wilhelm and Kwauk, 1948). A transition occurs from smooth homogeneous fluidisation to heterogeneous or aggregative (bubbling) fluidisation at a Froude number ≈ 1 . (Fazle Hussain, 1986) found that the instabilities of local turbulent flows cause the formation of vortices and coherent structures. Based on a stability map proposed by (Gibilaro *et al.*, 1986) and updated later (Gibilaro, 2001), the transition for LSF in ambient water from particulate to aggregate fluidisation depends on both the density and the size of the suspended particles; for a lower particle density, a larger size is necessary for a transition to occur.

While the majority of researchers have used optical methods to investigate LSF, a small number of computational studies is available too. For example, (Ghatage *et al.*, 2014) conducted an extensive literature review on the stability analysis of LSF and studied the transition from homogeneous to heterogeneous regimes with Computational Fluid Dynamics - Discrete Element Method (CFD-DEM) simulations and experiments. This study highlighted that the transition conditions for LSF could be obtained experimentally by observing the behaviour of the (classification) velocity of a single foreign particle at different superficial liquid velocities.

7.2.3 Full-scale experience and reactor performance

The fluidisation quality of softening processes at Waternet, the water utility of Amsterdam and surroundings, was observed visually during full-scale operational conditions and considered to be moderately heterogeneous. It is currently unknown to which extent such heterogeneous behaviour affects the chemical crystallisation efficiency, either negatively or positively, as there are many effects to consider. In addition, carryover at the reactor effluent was detected, a process which adversely affects the calcium carbonate crystallisation potential (CCCP), a quality performance index for the water softening process (Rietveld, 2005).

The cylindrical pellet-softening reactor (*Amsterdam reactor*) (van der Veen and Graveland, 1988) is based on well-mixed water, caustic soda and particular material in the lowest region of the reactor (continuously ideally stirred-tank reactor principle) and a continuous flowing system of cylindrical geometry (plug flow reactor principle) in upward direction. The rate of crystallisation is strongly dependent on the rate of mass transfer of the reactants to the crystallisation surface. As a consequence, the degree of heterogeneity is also important since bubbles cause by-pass and liquid backflow, typically detrimental to the conversion.

The main advantage of seeded crystallisation employed in this reactor is that CaCO_3 precipitates onto the surface of grains instead of creating spontaneous unwanted precipitation in the liquid (Burhenne *et al.*, 2017). The SSA of the seeding material is an important parameter for the softening process, as it influences the calcium carbonate kinetics significantly (van Dijk and Wilms, 1991; van Schagen, 2009). The chemical performance of the seeded crystallisation is based on the growth rate of the seeding calcite particles (Hu *et al.*, 2017) and the growth rate of the seeding material particle depends on the mass transfer of the reactants to the surface of the pellet and the reaction of crystallisation (Tai *et al.*, 2006).

The imposed SSA which is exposed for crystallisation varies through time and space. Larger open water spaces might increase the probability of spontaneous precipitation, while a heterogeneous flow regime could have a positive effect on the dispersion of chemical reactants in the water phase due to vigorous agitation of the particles in contact with the fluid. It is unclear how the crystallisation proceeds in the presence of unsteady local voids during fluidisation. These combined factors mean that it is difficult to predict the influence of heterogeneous fluidisation on the reactor performance *a priori*. For this reason, a scaled pilot experimental set-up was designed to investigate the hydraulic behaviour of the pellet-softening process, and

a CFD-DEM model was developed to study the degree of unsteady liquid-solid behaviour in LSF systems.

7.2.4 Aims

The aim of the current work is to demonstrate the importance of heterogeneous behaviour in LSF beds with calcite pellets in water. To this end, the instability of the local voidage and the overall transport of particles are used as indicators. Numerical modelling is applied using a suitable CFD-DEM model, and results are compared with reliable expansion data obtained from experiments. Additionally, quasi 2D images of inhomogeneities in the expanded beds are presented, taken from experiments as well as simulations. Lastly, the CFD-DEM model is used to explore the three-dimensional flow phenomena inside the LSF bed.

7.3 Materials and Methods

7.3.1 Simulations

The simulations in this work were conducted using the model described in detail by (Nijssen *et al.*, 2020). This model couples Computational Fluid Dynamics (CFD) and the Discrete Element Method (DEM), allowing for the simultaneous description of the water phase and the suspended particles. This work employs the unresolved CFD-DEM methodology, which resolves the fluid flow at a length scale larger than the particles. This allows for the simulation of a large number of particles ($\approx 10^6$) but requires interaction models to evaluate the force exerted by the fluid on the particles and *vice versa*. The model proposed by Nijssen *et al.* is especially suited for simulation of LSF beds as it includes closures for the drag and lift as well as virtual mass and Basset forces. The addition of the Basset force is a significant improvement of the classical drag-only CFD-DEM approach, which is better suited for gas-solid systems (Nijssen *et al.*, 2020). For a complete description of the model, the reader is referred to the original work.

The parameters and settings used in the simulations are summarised in Table 13. The fluid properties are taken at 20 °C, the same temperature at which the experiments were conducted. The coefficients of friction and restitution were estimated based on the experiments using glass spheres as performed by Joseph and Hunt (Joseph and Hunt, 2004) and the Stokes number (Equation 13). Using the liquid velocity as the typical collision velocity, the Stokes number was found to lie in the range of 10 - 60. Typical values were chosen for the Young's modulus and Poisson ratio, as they have a negligible influence on the results (Blais and Bertrand, 2017).

Table 22 *Parameters and settings used in simulations. Fluid properties are taken at 20 °C; coefficients of friction and restitution are based on the work of (Joseph and Hunt, 2004).*

Variable	Symbol	Value	Unit
Column diameter	D	0.057	[m]
Column length	H	2.0	[m]
CFD cell size	Δx	4.65	[mm]
CFD time step	Δt_{CFD}	10^{-3}	[s]
DEM time step	Δt_{DEM}	10^{-5}	[s]
Fluid density	ρ_f	998.20	[kg/m ³]
Fluid dynamic viscosity	η	$1.005 \cdot 10^{-3}$	[Pa·s]
Gravitational acceleration	g	9.81	[m/s ²]
Particle diameter (mean)	$\langle d_p \rangle$	1.55	[mm]
Particle diameter (standard deviation)	σ_p	0.16	[mm]
Particle density	ρ_p	2575	[kg/m ³]
Total particle mass	m_p	0.87	[kg]
Particle Young's modulus	Y_p	5.0	[MPa]
Particle Poisson ratio	ν_p	0.45	[-]
Particle coefficient of restitution	e_p	0.3	[-]
Particle coefficient of friction	μ_p	0.05	[-]

7.3.2 Experimental set-up

Expansion experiments for several materials were carried out at three locations: in Waternet's Weesperkarspel drinking water pilot plant located in Amsterdam, the Netherlands (Figure 9), at the University of Applied Sciences Utrecht, the Netherlands; and at Queen Mary University of London, United Kingdom (Figure 10)

and at the University of Applied Sciences Utrecht, the Netherlands (Figure 11 and Figure 12). A schematic overview can be found in Figure 14. For this research, we examined calcite pellets (100% CaCO₃) applied in drinking water softening. Polydisperse calcite pellets were dried, sieved and fractionated in order to acquire more uniformly dispersed samples. Photographic material are included in Annex 1: Photos and in the Supplementary material (Sections 1 and 2). Standard operating procedure is explained in Section 3.4.

7.3.3 Camera experiments

In this study, we used a Chronos 1.4 high-speed camera to make video recordings of the collective motion of calcite pellets ($1.4 < d_p < 1.7$ mm) in the expansion column at different flow rates. This camera is capable of capturing images at a rate of 1.4 gigapixel per second (Kramer et al., 2020e). We varied the superficial fluid velocity between 15 and 87 mm/s (corresponding to bed voidages between 0.42 and 0.78) and used recording rates increasing from 10 to 1200 fps, as shown in Table 23. In addition, video recordings were made with a Canon LEGRIA HF G25 (1920 x 1080 pixels at 25 fps) for various flow rates. Besides the ($1.4 < d_p < 1.7$ mm) pellets, ($0.8 < d_p < 0.9$ mm) pellets were also recorded (Kramer et al., 2020h).

7.4 Results and discussion

7.4.1 Expansion experiments

Fluidisation characteristics were measured for calcite pellets ($1.4 < d_p < 1.7$ mm, $\rho_p = 2,575$ kg/m³) at 20 °C for five different superficial fluid velocities. Some experiments were executed in *duplo* or *triplo*, as shown in Table 23. Additionally, videos were made for two types of calcite pellets: Geldart's type D ($1.4 < d_p < 1.7$ mm) and Geldart's type B ($0.8 < d_p < 0.9$ mm) (Geldart, 1973). For validation purposes, additional expansion characteristics were acquired for varying temperatures and flow rates. The experimental data is included in full in the Supplementary material (Section 7).

Table 23: Experimental and numerical results for 1.4-1.7 mm calcite pellets in water at 20 °C

Nr.	Superficial fluid velocity	v_s/v_t ¹⁾	Bed voidage		Pressure drop		Frame rate
			numerical	experimental	numerical	experimental	
[#]	[mm/s]	[-]	[m ³ /m ³]	[m ³ /m ³]	[kPa]	[kPa]	[fps]
1,2,3	15	0.015	0.38	0.42	2.06	2.08	10
4,5	30	0.030	0.48	0.54	2.07	2.08	10
6,7,8	61	0.061	0.59	0.68	2.10	2.08	400
9	87	0.087	0.70	0.78	2.15	2.08	600
10	142	0.142	0.89	0.91	2.16	2.08	1200

¹⁾ Ratio superficial to terminal settling velocity

7.4.2 Fluidisation characterisation observations

During the fluidisation experiments with calcite grains, open spaces and voids of water were observed between the fluidised particles (Figure 66), even at relatively low fluid velocities in the vicinity of minimum fluidisation. These voids were found to increase in size when the fluid flow increased (Kramer et al., 2020a).



Figure 66 Sequence of 1.4-1.7 mm calcite pellets in a 57 mm column. Dark zones are caused by local pockets of water, $v_s = 25$ mm/s, $\langle \epsilon \rangle = 0.50$ m³/m³, average interstitial fluid velocity 50 mm/s. White lines represent the progression of waves of voids moving up at 50 mm/s. The time interval between images is 0.17 s, corresponding to 8.5 mm or 5.5 particle diameters. The wave progression can be seen more clearly on the provided video material (Kramer et al., 2020e; Kramer et al., 2020h).

Voids are formed when the pathway between clusters of particles is of lesser resistance than the assumed homogeneous fluidisation state, resulting in a lower energy dissipation. A liquid-solid fluidised bed may appear homogeneous when observed on a larger scale, but locally the fluid flow distribution through the bed may not be completely uniform. These inhomogeneities appear in the form of bubbles, travelling waves or particle clusters (parvoids) depending on the systems physical parameters (Hassett, 1961).

Moreover, significant heterogeneous particle-fluid patterns were detected at higher fluid velocities. The observed voids behaved like bubbly waves (Verloop and Heertjes, 1970) and moved up the bed with a certain wave velocity and frequency. Around these voids, clusters of particles were formed, which had a tendency to linger as a group and show decreased hindered settling. After individual particles broke loose from the particle train and start settling vertically, the remaining particles followed successively. For relatively high fluid velocities, recirculation patterns were observed where particles tended to show both upward and downward flow. At these high fluid velocities, the voids were more equidistantly distributed in the bed. In the vicinity of the column walls, the bed voidage was slightly higher compared to the bulk of the fluidised bed, which consequently implies a slightly different hydrodynamic flow pattern, as confirmed by (Loeffler, 1953). According to the transition model for LSF by (Gibilaro *et al.*, 1986), the considered 1.4-1.7 mm calcite pellets should belong to the fully particulate (homogeneous) region, not to the aggregate region nor to the particulate and aggregate regions. In contrast to the transition model, a homogeneous state for these examined particles was not observed in experiments.

7.4.3 Simulation results and discussion

The mean bed voidage for calcite pellets fraction 1.4-1.7 mm, was predicted on the basis of the CFD-DEM simulations carried out by (Nijssen *et al.*, 2020) and compared with the experimentally determined voidages (Kramer *et al.*, 2020d). In addition, the voidages were estimated with the popular model developed by (Richardson and Zaki, 1954) and an empirical model proposed by (Kramer *et al.*, 2020b) (Equation (108)).

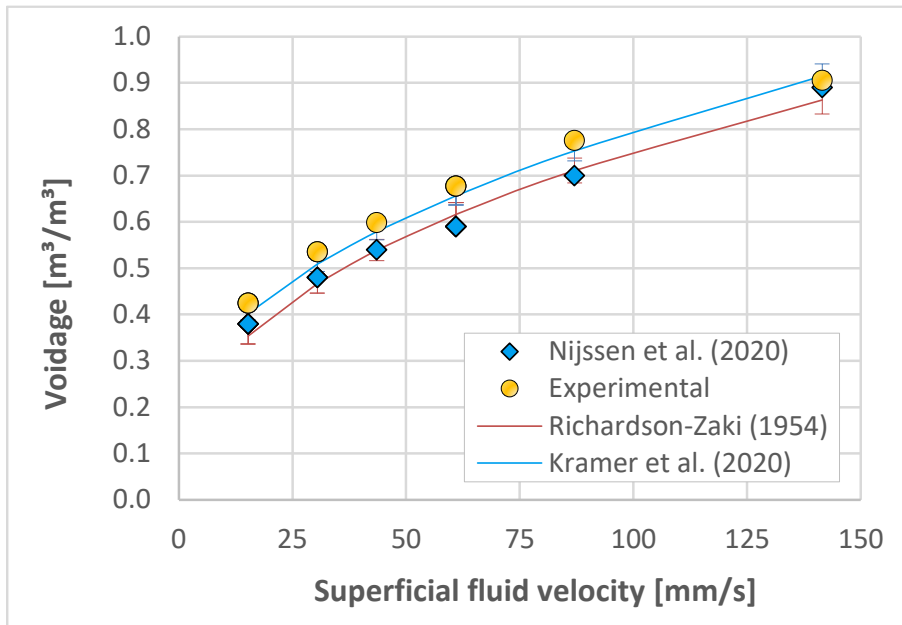


Figure 67 Experimentally measured mean voidage (circles), mean voidage predicted by CFD-DEM simulations (squares) (Nijssen *et al.*, 2020) (ARE = 10%), empirical data-driven model (blue line) (Kramer *et al.*, 2020b) (ARE = 2%), and a popular model (red line) (Richardson and Zaki, 1954) (ARE = 15%) for calcite pellets range $1.4 < d_p$ [mm] < 1.7.

The results presented in Figure 67 show that the CFD-DEM model under-predicts the voidage by a relative error of up to 10%, especially at intermediate flow rates. The voidage prediction for the Richardson–Zaki model has the largest discrepancy compared to the experimentally measured values, while the empirical model proposed by Kramer *et al.* shows the smallest deviation. The latter may not come as a surprise, since this data-driven model was calibrated for a variety of calcite pellet fractions.

Table 23 shows the basic bed characteristics obtained from the CFD-DEM simulations. The authors believe that the discrepancy with the experimental values in Table 23 is mainly caused by the non-spherical shape of the particles (Dharmarajah, 1982). Photographs of the calcite pellets are included in the Supplementary material (Section 1). Analysis of these images has indicated that the particle sphericity can be as low as 0.75. This aspect was not accounted for in the simulations. Nevertheless, the trend of the expansion is captured accurately, and analysis of the simulation results yields valuable insight into the bed behaviour.

Figure 68 shows an instantaneous CFD-DEM snapshot of the bed voidage in a cross-section through the centre of the bed, and Figure 69 shows the particle distribution (particles coloured by size) as viewed from the outside. The bed appears to be homogeneous when the particles are observed from outside the bed (Figure 69). However, Figure 68 shows the appearance of discrete water pockets at lower superficial liquid velocity, which transform into more complex structures at higher velocities. At the highest flow rate, the bed is composed of thin, interwoven particle-dense and dilute regions. Furthermore, it can be seen that only at high fluid velocity stratification of the bed is obtained. This indicates mobility of the particles but an absence of a large-scale mixing pattern. Separation of the smallest particles is observed at the lowest velocity, but stratification of the entire bed is not found.

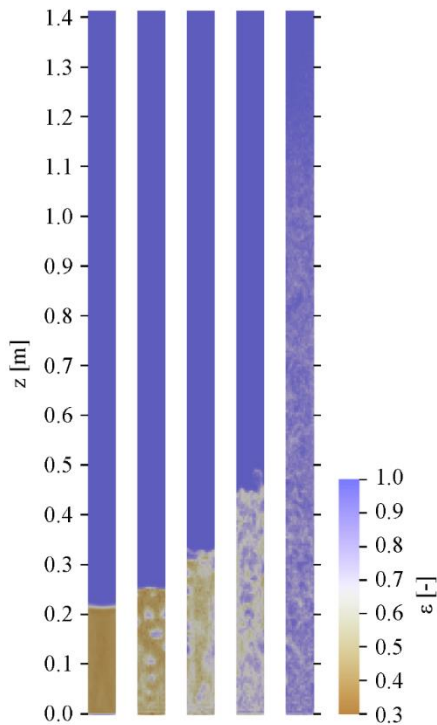


Figure 68 Instantaneous cross-sectional voidage snapshots for increasing superficial liquid velocity (15, 30, 61, 87 and 142 mm/s, respectively). Videos of the simulation can be assessed at: (Kramer and Nijssen, 2021a).

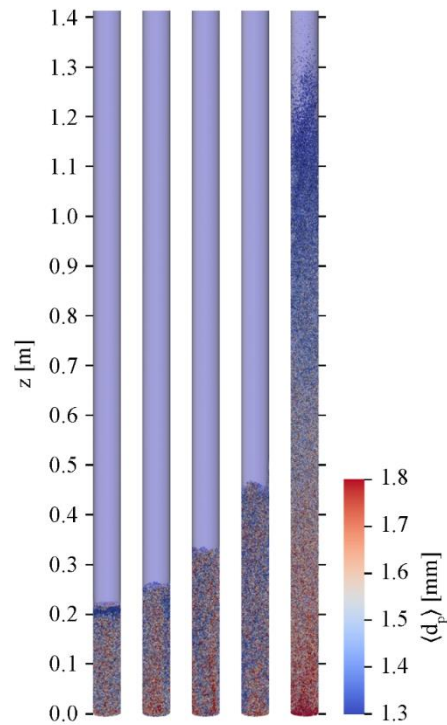


Figure 69 Instantaneous snapshots of particle distribution for increasing superficial liquid velocity (15, 30, 61, 87 and 142 mm/s, respectively). Colours indicate particle size.

The time-averaged solid mass flux was obtained from each simulation and is shown in Figure 70. This figure shows the vertical flux through a horizontal plane at height $z = L/2$. A weak overall solids circulation exists at intermediate velocity, which was also observed in the experiments. Depending on the superficial fluid velocity, upward particle movement can occur through the bed centre or along the walls. This indicates that the circulation pattern is rather unstable and might be highly susceptible to changes in the initial bed configuration or the liquid distribution. The unstable circulation is confirmed by standard deviations reported in Table 24, which were calculated at the centre of the bed. Above the lowest fluid velocity, the standard deviation is of the same order as the mean solid mass flux, indicating a widely varying solids movement.

The strongest circulation can be found at $v_s = 30$ mm/s, corresponding to water pockets moving up through the centre of the bed, as observed in Figure 68. At the highest liquid velocity, approaching the particle terminal velocity ($200 < v_t$ [mm/s] < 235), the time-averaged solids circulation vanishes. As can be seen from the standard deviation in Table 24, the fluctuating component persists. This lack of large-scale solids mixing combined with particle mobility allows for the stratification at high velocity as represented in Figure 69.

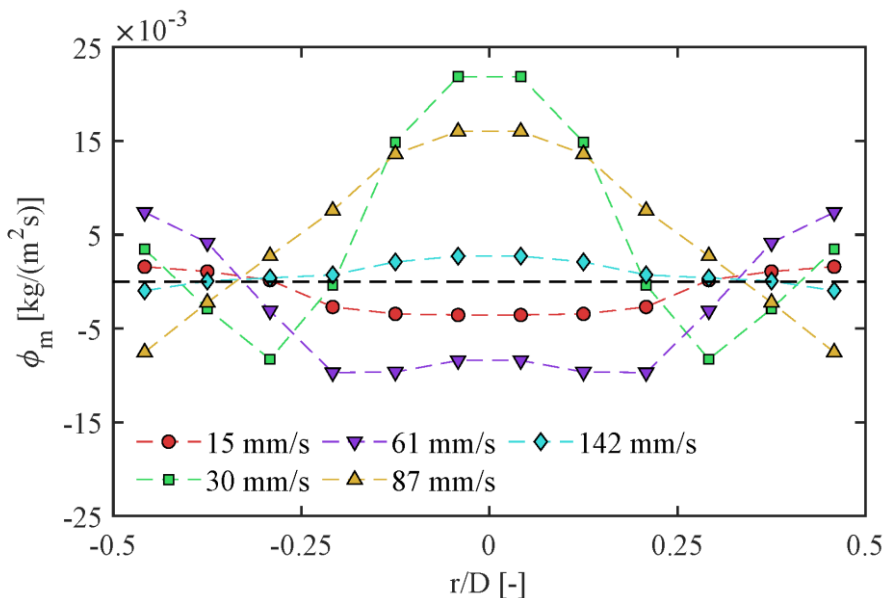
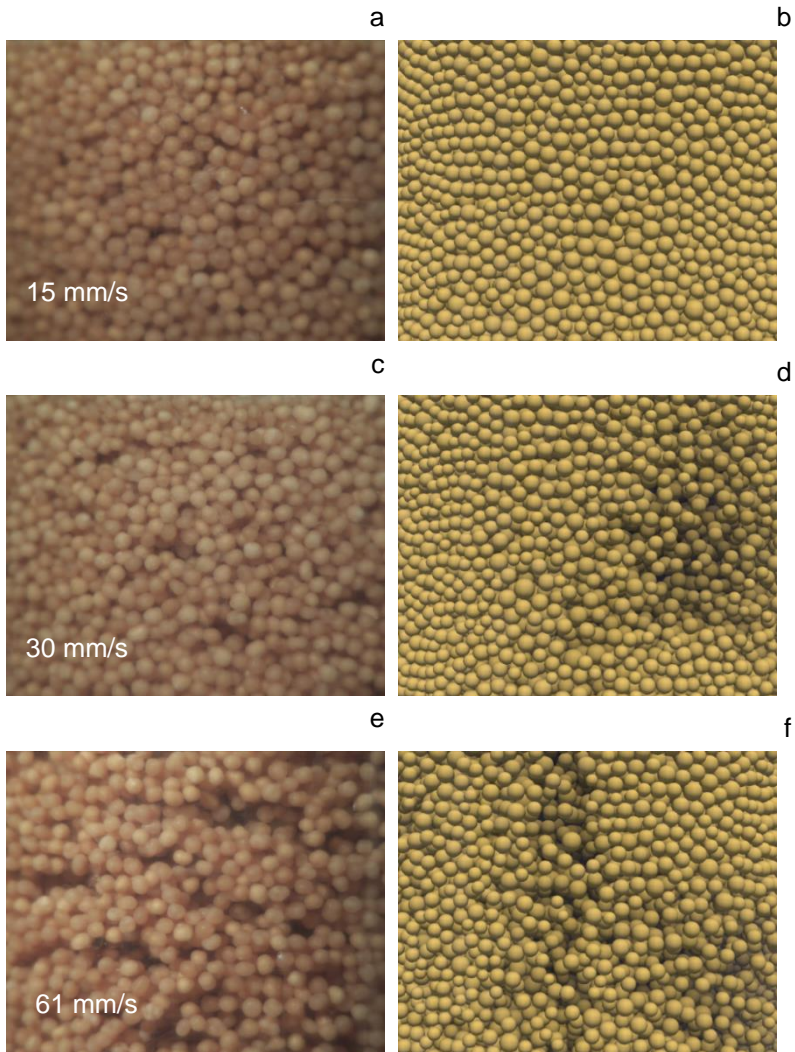


Figure 70 Time-averaged vertical solid mass flux at different superficial liquid velocity, measured at $z = L/2$.

Table 24 *Time-averaged vertical solid mass flux at the bed centre and corresponding standard deviation, measured at $z = L/2$*

Superficial fluid velocity	Mean solid mass flux	Solid mass flux standard deviation
[mm/s]	[kg/(m²h)]	[kg/(m²h)]
15	-12.8	0.84
30	78.7	45.2
61	-30.3	91.2
87	57.7	58.4
142	9.79	17.6

A visual comparison of void development in experiments and simulations with increasing fluid velocity is shown in Figure 71. At 30 mm/s (Figure 71c and d) the simulations predict large singular voids, while experiments show more numerous smaller pockets of water. At higher fluid velocity, the particle structure opens up further and voids merge into larger structures. This was captured both in experiments and in simulations. As the fluid motion is not resolved at the particle scale in the CFD-DEM method, prediction of the actual void shape is precarious. Still, a qualitative comparison of void size holds very well, especially at higher liquid velocities.



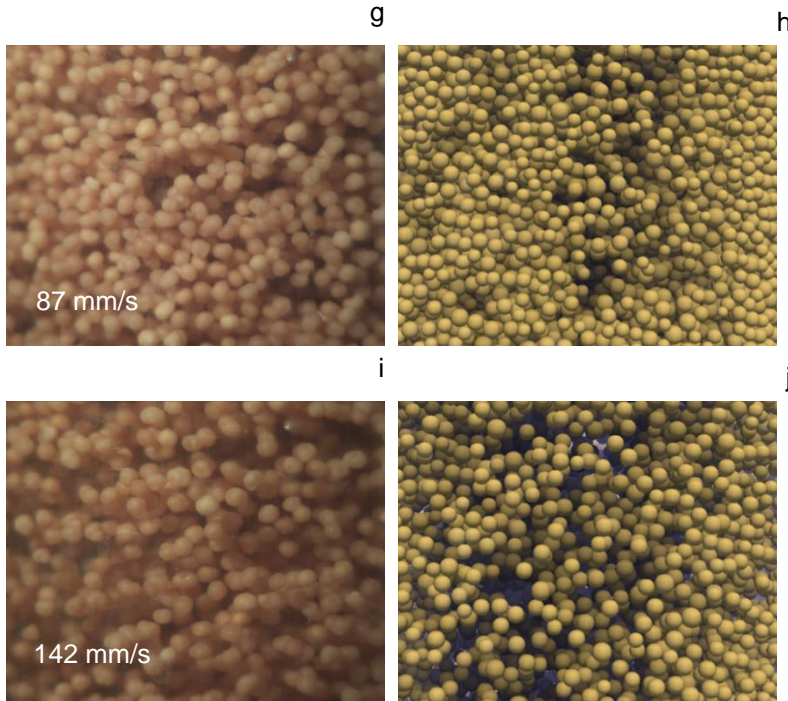


Figure 71 Visual comparison between experiments (left) and simulations (right), showing void development with increasing superficial liquid velocity (15, 30, 61, 87 and 142 mm/s, respectively).

To further quantify the influence of the observed voids on the operational efficiency of the LSF bed reactor, the probability density function (PDF, (Equation (87))) of the local voidage and its derived cumulative distribution function (CDF, Equation (88)) were evaluated. In the equations below, $V(\varepsilon)d\varepsilon$ denotes the total volume of cells having void fraction between ε and $\varepsilon + d\varepsilon$. Furthermore, a distinction has been made between the layer of cells bordering the reactor wall and those in the core of the reactor.

$$PDF(\varepsilon) d\varepsilon = \frac{V(\varepsilon)d\varepsilon}{\int_0^1 V(\varepsilon) d\varepsilon} \quad (87)$$

$$CDF(\varepsilon) = \int_0^\varepsilon PDF(\hat{\varepsilon}) d\hat{\varepsilon} \quad (88)$$

$$\langle \varepsilon \rangle = \int_0^1 PDF(\hat{\varepsilon}) \cdot \hat{\varepsilon} d\hat{\varepsilon} \quad (89)$$

$$\sigma_{\varepsilon}^2 = \int_0^1 PDF(\hat{\varepsilon}) \cdot (\hat{\varepsilon} - \langle \varepsilon \rangle)^2 d\hat{\varepsilon} \quad (90)$$

Where $\hat{\varepsilon}$ is a voidage integration variable. By way of illustration, Figure 72 shows the voidage PDF for the simulation with $v_s = 30$ mm/s. The results obtained at other fluid velocities are included in the Supplementary material (Section 4). The dashed lines indicate the mean voidage (Equation (89)) in the wall and core regions, while the dotted lines indicate the range of voidage encompassing 95% of the bed volume. Clearly, the void fraction distribution is not symmetrical, showing a peak at low voidage with a long tail reaching up to 90% liquid volume ($CDF(\varepsilon) = 2.5\%$ and 97.5%). This indicates the presence of high-voidage water bubbles in a denser emulsion phase. The broad distribution means that the mean bed voidage is not an adequate parameter to describe the LSF bed state, as a range of voidages should be considered instead.

Lastly, the voidage in the vicinity of the reactor walls was found to be up to 5% higher than in the bulk of the bed. This indicates an intrinsic limitation of optical voidage measurements in LSF bed experiments. The liquid volume fraction measured close to the wall is not representative of that in the core of the reactor. Simulations offer an advantage, as they provide full 3D void fraction information without the need for expensive measurement techniques, such as x-ray tomography, electrical capacitance tomography or optical probing.

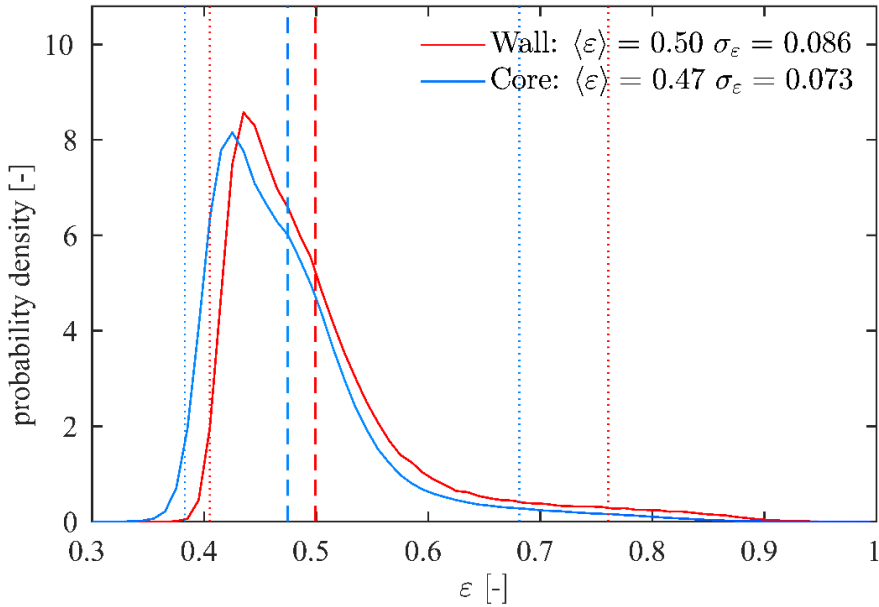


Figure 72 Voidage probability density function obtained at $v_s = 30$ mm/s. Dashed lines indicate mean voidage; dotted lines mark the range of voidages comprising 95% of the bed volume.

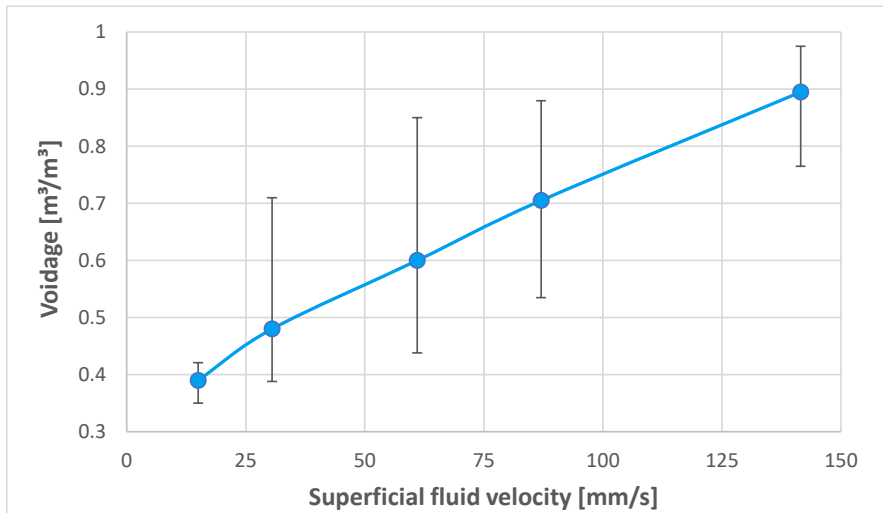


Figure 73 LSF bed expansion behaviour with increasing superficial liquid velocity. Symbols indicate mean voidage, error bars signify the range of voidages comprising 95% of the bed volume. Minimum fluidisation velocities: $v_{mf} = 13.6$ mm/s for $d_p = 1.4$ mm and $v_{mf} = 17.2$ mm/s for $d_p = 1.7$ mm calcite pellets.

The heterogeneity of the bed observed in the simulations is summarised in Figure 73. Symbols show the mean voidage plotted against superficial fluid velocity, while the error bars indicate the range of voidages comprising 95% of the bed volume. Interestingly, heterogeneity shows to be most pronounced slightly above the onset of fluidisation (Figure 73). At higher velocity, the range of observed voidages narrows as the discrete bubbles transform into more complex structures.

In order to show the influence of particle size on the bed heterogeneity, a simulation was repeated using smaller particles ($\langle d_p \rangle = 0.9$ mm, $\sigma_p = 0.08$ mm, $v_s = 30$ mm/s). The obtained voidage PDF is shown in Figure 74 and compared with previous results at $v_s = 61$ mm/s. These two simulations are compared in view of their similar expansion, *i.e.* mean voidage. However, the range of observed voidages is much narrower using smaller particles. This clearly indicates that larger particles favour a more heterogeneous bed configuration, as was previously shown by (Di Felice, 1995). In addition to being narrower, the distribution obtained from smaller particles is also more symmetric than the distribution found for the larger particles, indicating a less distinct separation between the emulsion and bubble phases.

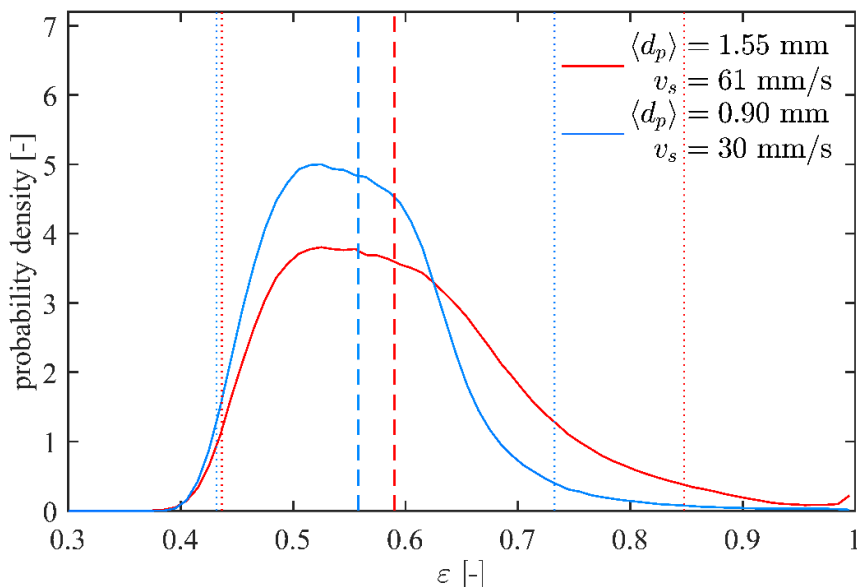


Figure 74 Comparison of voidage probability density functions for large particles ($\langle d_p \rangle = 1.55$ mm, $\sigma_p = 0.16$ mm, $v_s = 61$ mm/s) and small particles ($\langle d_p \rangle = 0.9$ mm, $\sigma_p = 0.08$ mm, $v_s = 30$ mm/s) at similar mean voidage. Dashed lines indicate mean voidage; dotted lines mark the range of voidages comprising 95% of the bed volume.

7.5 Conclusions

In this work, both experiments and simulations were employed to gain insight into the heterogeneous behaviour of drinking water softening reactors. In the literature, LSF systems are often considered to be homogeneous at modest velocities. Nevertheless, in the experiments with calcite grains, local voids were observed at relatively low fluid velocities and significant heterogeneous particle-fluid patterns at higher fluid velocities. A CFD-DEM simulation model was used, and its results compared with expansion measurements and high-speed videos and images. From this combination of experiments and simulations, it was concluded that homogeneous fluidisation virtually does not occur.

In the literature, fluidisation behaviour is usually investigated either through experimental work or numerical modelling. Considering their respective advantages and disadvantages, the combination of a numerical model and experiments proved to be a highly effective way to investigate this complex system. Experiments were needed to measure bed expansion, *i.e.* mean voidage, and to observe fluidisation features and patterns from the outside of the reactor (quasi 2D). The simulations made it possible to explore the fluidisation features and patterns even further, allowing measurements throughout the entire bed (3D). This has yielded important new insights into LSF behaviour.

The heterogeneity and onset of fluidisation behaviour obtained from the simulations and experimental observations were compared and found to agree reasonably well. The simulations showed distinct differences in void fraction in the cross-section of the columns. The voidage in the vicinity of the wall was not representative of that in the core of the reactor. Furthermore, the voidage distribution in the fluidised bed was found to be broadest at intermediate velocity. This information is of paramount importance for the chemical performance of the water softening reactor. Lastly, the solids circulation was investigated by measuring the solids flux. The circulation pattern was found to be unstable and prone to inversion. As expected, the solids flux vanished as the liquid velocity approached the particle terminal velocity.

7.6 Recommendations

It has been shown that CFD-DEM simulations are an effective and reliable tool for the analysis of LSF bed reactors. Using this method, much can be learned about liquid-solid fluidisation behaviour. The influence of particle shape and size distribution, liquid properties, as well as reactor scale are all subjects of major interest to which this method can be applied. The accuracy of the method can be improved further through the application of a sphericity correction to the interaction forces, as was discussed by (Mema and Padding, 2021). Unfortunately, such a correction is not yet available for the unsteady interaction forces. Additionally, a more elaborate model for the kinetic energy dissipation during immersed collisions and influence of lubrication forces will greatly benefit the accuracy of the method (Fries *et al.*, 2013; Peng *et al.*, 2014). In this research, unsteady behaviour was observed in LSF bed. It is recommended to conduct future research to better define and quantify the degree of heterogeneity, *i.e.* improve the fluidisation quality definitions and terms related to the fluid and particle properties. We have enabled future numerical and experimental studies to investigate the impact of these properties on reactor performance in full-scale treatment processes such as pellet-softening. Since it remains unclear whether heterogeneous behaviour could be beneficial or disadvantageous for chemical crystallisation efficiency in full-scale pellet-softening reactors, the CFD-DEM method could be used in future research with the aim to discover optimisation solutions. To this end, species transfer equations and chemical reactors can be added to the model to capture the influence of hydrodynamics and the chemical performance of the reactor.

7.6.1 Supplementary material

Supplemental data for this article can be accessed at:

<https://doi.org/10.1016/j.cesx.2021.100100>

<https://ars.els-cdn.com/content/image/1-s2.0-S2590140021000137-mmc1.docx>

Contents		page
1	Photographs of full-scale pellet-softening reactors and pellets	2
2	Fluidisation expansion experiments Standard operating procedure	3
	2.1 Expansion columns	3
	2.2 Operating procedure	5
3	Supporting videos of liquid-solid fluidisation experiments	7
4	Voidage distribution results	10
5	Fluidisation quality	13
6	References	14
7	Experimental data	15
	7.1 Calcite pellets (1.4-1.7 mm) repeated experiment at 20 [°C]	15
	7.2 Calcite pellets (0.8-0.9 mm) 2-35 [°C]	18
	7.3 Calcite pellets (1.4-1.7 mm) 2-35 [°C]	23-28

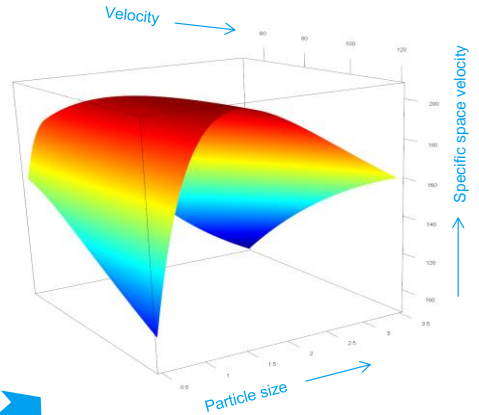
Full-scale drinking water pellet-softening reactors



Fluidisation experiments



Process improvements



Reactor performance indicators

Voidage prediction model

$$\varepsilon = (c_0 Re_p^{c_1} + c_2 Re_p^{c_3}) Fr_p^{c_4}$$



- ▶ A new explicit voidage prediction model for liquid-solid fluidised bed is proposed
- ▶ Voidage prediction accuracy is improved from 11% to 2% by combining Reynolds and Froude
- ▶ Specific surface area is of major importance in drinking water treatment processes
- ▶ Full-scale pellet-softening reactors can be optimised by using superficial space velocity

Keywords Drinking Water Treatment; Full-scale Water Softening; Fluidised Bed Reactors; Voidage Prediction; Data-Driven Modelling; Symbolic Computation

Chapter 8

Data-Driven Modelling

*"Everything should be made as simple as possible, but not simpler."
(Albert Einstein, 1879 – 1955)*

This article has been published as:

Accurate voidage prediction in fluidisation systems for full-scale drinking water pellet-softening reactors using data-driven models

O.J.I. Kramer, P.J. de Moel, J.T. Padding, E.T. Baars, Y.M.F. El Hasadi, E.S. Boek, J.P. van der Hoek

Journal of Water Process Engineering. **37**, 101481 (2020) pp. 1–15

The article can be found online at:

<https://doi.org/10.1016/j.jwpe.2020.101481>

8 Accurate voidage prediction in fluidisation systems for full-scale drinking water pellet-softening reactors using data-driven models

8.1 Abstract

In full-scale drinking water production plants in the Netherlands, central softening is widely used for reasons related to public health, client comfort and economic and environmental benefits. Almost 500 million cubic meters of water is softened annually through seeded crystallisation in fluidised bed reactors. The societal call for a circular economy has put pressure on this treatment process to become more sustainable. By optimising relevant process conditions, the consumption of chemicals can be reduced, and raw materials re-used. Optimal process conditions are feasible if the specific crystallisation surface area in the fluidised bed is large enough to support the performance of the seeded crystallisation process. To determine the specific surface area, crucial variables including voidage and particle size must be known. Numerous models can be found in the literature to estimate the voidage in LSF processes. Many of these models are based on semi-empirical porous-media-based drag relations like Ergun or semi-empirical terminal-settling based models such as Richardson–Zaki and fitted for monodisperse, almost perfectly round particles. In this study, we present new voidage prediction models based on accurate data obtained from elaborate pilot plant experiments and non-linear symbolic regression methods. The models were compared with the most popular voidage prediction models using different statistical methods. An explicit model for voidage estimation based on the dimensionless Reynolds and Froude numbers is presented here that can be used for a wide range of particle sizes, fluid velocities and temperatures and that can therefore be directly used in water treatment processes such as drinking water pellet-softening. The advantage of this model is that there is no need for applying numerical solutions; therefore, it can be explicitly implemented. The prediction errors for *classical* models from the literature lie between 2.7% and 11.4%. With our new model, the voidage prediction error is reduced to 1.9%.

8.2 Introduction

8.2.1 Drinking water softening

Water softening involves the removal of calcium, magnesium and other metal cations from water (Edzwald, 2011). Central softening of drinking water is currently frequently applied in several countries (e.g. the Netherlands, Belgium, Germany, France and the USA) while domestic softening is the most frequently applied way of softening in other countries (Cotruvo *et al.*, 2001; GWRC, 2007; Harms and Robinson, 1992). In full-scale drinking water production plants in the Netherlands, central softening is widely used for reasons related to public health, client comfort and economic and environmental benefits (van Amrners *et al.*, 1986; Groenendijk *et al.*, 2008; van der Bruggen *et al.*, 2009; Godskesen *et al.*, 2012). Specifically in areas with high water hardness, centralised drinking water softening can reduce the consumption of soap, detergents and other household chemicals and increase the service life and energy efficiency of household appliances such as coffee machines due to a reduction in calcium carbonate scaling (Beeftink *et al.*, 2021; Tang *et al.*, 2019b).

In the Netherlands, in 2020 almost 500 million cubic meters of water is softened annually through seeded crystallisation in fluidised bed reactors, a process known as pellet-softening (Hofman *et al.*, 2007), primarily removing calcium cations from the water. Pellet-softening was developed and introduced in the Netherlands in the 1970s (Graveland *et al.*, 1983). In other fields, crystallisation in fluidised bed reactors is also becoming increasingly popular. Examples include the removal of hardness from natural hard ground waters (Mahvi *et al.*, 2005), the recovery of CO₂ in direct air capture processes (Burhenne *et al.*, 2017), the improvement of pellet characteristics for re-use potentials (Tang *et al.*, 2019), reduced sludge production (Mercer *et al.*, 2005), groundwater softening in circulating pellet fluidised bed reactors usage in thermal power plants (Hu *et al.*, 2019) and organic micropollutant removal from groundwater (Maeng *et al.*, 2016). There is also a growing interest in fluidisation of biomass particles (Cui and Grace, 2007), fluidised bed reactors used in wastewater treatment (Akkoyunlu, 2003) and other liquid-solid fluidisation (LSF) techniques with many applications in engineering (Edzwald, 2011; Crittenden *et al.*, 2012; Epstein, 2003).

In pellet-softening reactors (van Dijk and Wilms, 1991), drinking water is treated in an up-flow fluidised cylindrical bed reactor (with flow velocity of 60-120 m/h). The Amsterdam reactor (van der Veen and Graveland, 1988) is currently a widely applied fluidised bed reactor (60-90 m/h). A strong chemical base, usually caustic soda or calcium hydroxide combined with a seeding material, is dosed to obtain supersaturated conditions in the water phase and is subsequently well mixed in the reactor. High pH leads to an alteration of the calcium carbonate equilibrium in which the solubility product is exceeded and CaCO_3 precipitates on the surface of the seeding material, thereby forming pellets. Seeds, typically quartz sand (Chen *et al.*, 2016), garnet sand (van Schagen *et al.*, 2006) or limestone calcite, are introduced in the reactor and fluidised under upward flow. The calcium carbonate crystallisation on the seeds mainly occurs in the lower region of the reactor (Graveland *et al.*, 1983; van der Veen and Graveland, 1988). Due to the crystallisation, the calcite pellets grow and migrate to the bottom of the reactor. When a defined grain size threshold is exceeded, a small part of the pellets is extracted from the bottom of the reactor (van Schagen *et al.*, 2008b).

The calcite pellets that are produced as a by-product in these plants can be re-used as seeding material, after grinding and sieving of the produced pellets (Palmen *et al.*, 2014). Pellets are the main by-product from the softening process and by identifying re-use applications, they potentially represent a resource rather than a waste product, thus promoting the establishment of a circular economy. The main advantages of this re-use are an expected significant decrease of the ecological footprint of both calcite as raw material and the drinking water treatment plants using pellet-softening and an increased valorisation of the pellets (Schetters *et al.*, 2015). Process optimisation (van Schagen *et al.*, 2008b) and control (van Schagen *et al.*, 2008a) has been focussed primarily on pellets grown on garnet sand as seeding material. The transition from garnet sand (Figure 75) as a seeding material to re-used crushed calcite (Figure 76) took place at Waternet from 2014 to 2016.

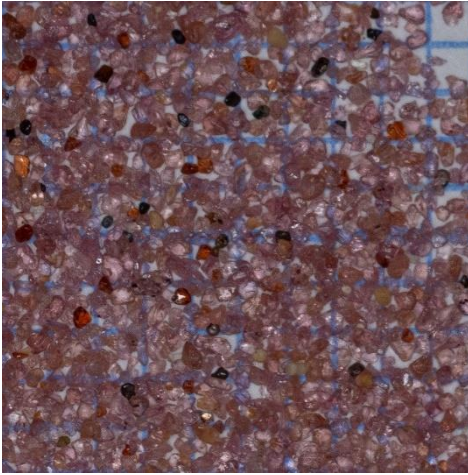


Figure 75 Garnet sand (mesh 80)
 $0.2 < d_p < 0.3 \text{ mm}$

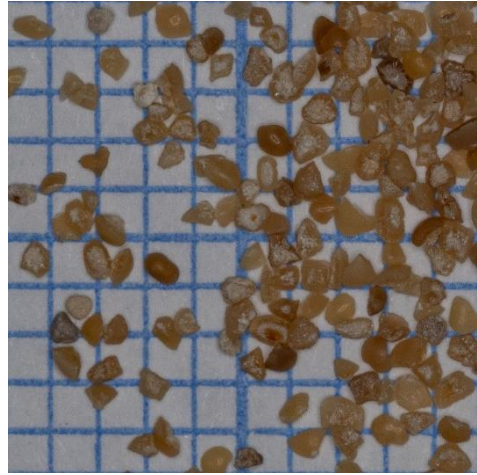


Figure 76 Crushed calcite
 $0.4 < d_p < 0.5 \text{ mm}$

8.2.2 Sustainability goals

There is a wide range of definitions of the concept of sustainability. The World Commission on Environment and Development (1987) defines sustainability as the ‘development that meets the needs of current generations without compromising the ability of future generations to meet their needs and aspirations’. The importance of continuing the development of a worldwide clean and sustainable water supply is increasing (Filho and Sümer, 2015). In general, drinking water suppliers have become more and more focussed on appropriate sustainable treatment technologies (Marques *et al.*, 2015). Optimal process conditions of water treatment processes contribute to the sustainability goals of public water organisations since fewer chemicals, less energy and fewer raw materials are needed (Ray and Jain, 2011; Gitis and Hankins, 2018).

The city of Amsterdam, the Netherlands, has the ambition to develop itself as a competitive and sustainable European metropolis (van der Hoek *et al.*, 2017). The flows of energy, water and resources within the urban environment offer a large potential to contribute to this ambition through a transition from the linear usage of resources and waste production towards the sustainable management of urban resources with circular flows of resources. Currently, the detrimental contributions of pellet-softening are in particular related to the consumption of chemicals like caustic

soda and raw materials such as garnet sand, mined in Australia and shipped to the Netherlands, both of which contribute to the carbon footprint and the environmental burden presented by the Dutch drinking water companies (Beeftink *et al.*, 2021). A life cycle assessment study has shown that pellet-softening can be improved in terms of eco-efficiency (Mohapatra *et al.*, 2002).

The role of more sustainable pellet-softening is twofold: it concerns the transition from garnet sand to re-used calcite pellets (Schetters *et al.*, 2015) as well as the reduced consumption of caustic soda (Beeftink *et al.*, 2021) in an optimal fluidised bed reactor. Both aspects imply the need for more accurate information of the fluidised bed conditions. To be able to acquire the process state of the fluidised bed, the most important process variable, *i.e.* the effective specific surface area (SSA) for the purpose of crystallisation, must be known. Therefore, the effective voidage must be determined. SSA is either based on the total reactor volume or on the water phase in the reactor, to be discussed in Section 8.3.2. An optimal operational configuration will lead to a sustainable operational approach for pellet-softening by using as little chemicals and raw materials as possible and ultimately leading to a more environmentally sustainable drinking water supply (Tang *et al.*, 2019a).

Waternet, the public water utility of Amsterdam and surroundings, is seeking a sustainable scenario for producing drinking water and offering services that fulfil the requirements of clients and regulations and, at the same time, maintaining a sound environmental performance while keeping costs as low as possible (Tapia *et al.*, 2008). To meet sustainability goals and to promote the development of a circular economy, Waternet has modified its pellet-softening processes (Schetters *et al.*, 2015), in which garnet grains have been replaced by calcite seeding particles that are based on crushed, dried, sieved and re-used calcium carbonate pellets. The garnet core inside the pellets hinders their potential application in market segments such as the glass, paper, food, cosmetics and feed industries. The pellet market value and the sustainability of the softening process can be increased through the substitution of the sand grain by a calcite grain of 0.5 mm (100% calcium carbonate). If the calcite pellets are crushed, dried and sieved, they can be re-used as a seeding material (Palmen *et al.*, 2014). To reduce the required amount of chemicals bases like caustic soda, a large crystallisation SSA for optimal crystallisation purposes is an essential condition. Smaller grains imply a larger SSA, but grains that are too small have a potential risk to be flushed out of the fluidised bed reactor.

8.2.3 Reactor technology conditions and research objective

The efficiency of the entire pellet-softening process can be expressed in terms of the amount of supersaturated calcium in the effluent, which can be determined by using the calcium carbonate crystallisation potential (CCCP). The CCCP determines the amount of chemicals used and the corresponding costs and CO₂-equivalent footprint of the pellet-softening process.

Chemical yield is defined as the amount of desired product produced relative to the amount that would have been formed if there were no by-products and the main reaction went to completion. For pellet-softening, a high yield implies the optimal capturing of calcium ions in calcite pellets with a minimum achievable CCCP. The overall chemical yield is strongly dependent on the specific crystallisation surface area in the reactor (Sobhan, 2019). For optimal process conditions, a large SSA in the fluidised bed is required. To be able to optimise pellet-softening processes, the SSA has to be determined, which is possible in case the voidage and the particle dimensions in the whole fluidised bed are known (Yang, 2003). Here, hydraulic process variables including superficial fluid velocity and viscosity, particle sizes and densities are crucial. To obtain optimal process states of fluidised bed processes, effective voidage prediction models can be used in process automation and intelligent control (van Schagen, 2009; Kramer *et al.*, 2019). Due to particle exchange in the pellet reactor, mainly caused by the extraction of calcite pellets and the dosage of seeding material, a certain particle size profile occurs over the reactor height. Due to the crushing process of calcite pellets (Schetters *et al.*, 2015), the seeding material consists of irregularly shaped particles. When they grow in size, they become increasingly round. If there is no difference in specific density, larger particles will migrate to the lower region of the reactor bed, and a stratified bed will evolve.

Since pellet-softening is a continuous process, boundary conditions must be monitored on a regular basis. As a consequence of the principle of seeded crystallisation, the most decisive boundary condition is to maintain the fluidised state permanently. Therefore, the risk of fixed bed state, caused by calcite pellets that are too large or water flows that are too low, must be avoided at all times. For water suppliers using surface water, the temperature also has consequences for process control strategies. In addition, flushing of the smallest grains out of the reactor, mostly the smallest fractions of seeding material, must be prevented due to its effect on subsequent treatment processes. In full-scale pellet-softening installations,

particle size mostly varies between 0.3-2.0 mm, and particle density between 2.5-4.0 kg/L. The current pellet size set-point in Amsterdam reactors is 1-1.2 mm. To retain fluidisation conditions, it is important that the largest pellets, usually those that are larger than the given set-point, are extracted from the reactor. They can then be used as a by-product in other processes or re-used as seeding material.

In full-scale reactors, the fluid-particle characteristics, *i.e.* homogeneous and heterogeneous flow regimes (Kramer *et al.*, 2020a), as well as many practical matters such as the fluid distribution through nozzles and the use of a by-pass flow in operational state (Rietveld, 2005) determine the process state and quality of the fluidised bed. In addition, pellet-softening can be seen as a combination of chemical and physical processes while the biological activity on the surface of the calcite pellets also affects the friction and the degree of bed expansion (Hammes *et al.*, 2011). The combination of a large SSA aim, the level of particle profile distribution over the reactor height, the degree of irregularity and size of the growing calcite pellets and finally environmental and process state conditions makes optimal control of a pellet-softening process a complex matter. Since the bed voidage is a critical process variable, the aim of this work is to develop a highly accurate voidage prediction model, as a function of fluid and particle properties which can be applied in full-scale pellet-softening fluidised bed unit operations.

A computational fluid dynamics (CFD) approach for obtaining an effective voidage prediction model is not preferable (Kramer *et al.*, 2020a), due to the above-mentioned non-ideal circumstances in combination with complex flow behaviour, numerous particle interactions (Cornelissen *et al.*, 2007) and the large amount of particles in full-scale industrial fluidised bed reactors, as is the case for water pellet-softening (up to 10,000,000,000 particles). This results in extremely high computational costs and a lower suitability for process optimisation and plant-wide control. To cope with constantly changing operational conditions in full-scale installations, more straightforward models are needed for optimal and robust process control. In particular, there is a need for an explicit and easily applicable voidage prediction model that effectively takes into account the local and global multiphase flow phenomena occurring in full-scale installations.

The aim of the current study was to develop a straightforward model based on the well-known dimensionless particle Reynolds and densimetric Froude numbers because they represent the inertial, viscous and gravitational forces in the multiphase system. The new model should be applicable for a wide range of particles, sizes, fluid velocities and temperatures and thus be of direct use in water

treatment processes like drinking water pellet-softening. For process control purposes, a direct relationship between particle size and voidage for a given water temperature and volumetric flow rate (default operational and design) is necessary.

8.3 Prediction models and performance indicators

8.3.1 Voidage prediction models

In a fluidised bed, the voidage, particle size and physical properties of the fluid and particles are inter-related. In the literature, numerous multiphase models are given to predict the voidage in fluidised bed reactors, mainly aimed at gas-solid systems (Holdich, 2002; Oka and Anthony, 2003; Crowe and Group, 2006; Rhodes, 2008; Seville and Yu, 2016; Yates and Lettieri, 2016) but also for liquid-solid systems (Di Felice, 1995; Peker *et al.*, 2008; Gibilaro, 2001; Dharmarajah, 1982; Yang, 2003). Specifically, for liquid-solid systems, the voidage can be predicted using classical models such as the Richardson–Zaki (1954) approach based on terminal settling velocity. The other frequently applied method is based on the idea of a flow through an assumed collection of channels in a bed of particles (Kozeny, 1927). In the Ergun approach (Ergun, 1952), the voidage is determined by the balance between the pressure gradient over the fluidised bed due to the mass of the pellets and the drag force of the water exerting on the pellets. The pressure gradient is accordingly given by the submerged weight of the pellets. The Carman–Kozeny model (Carman, 1937) is derived from a drag model where viscous and inertial forces are balanced using the modified particle Reynolds number. The impact of voidage is non-linear for both Kozeny–Carman and Ergun models (Sobieski and Zhang, 2014) and more pronounced at lower voidage. Since in water treatment the operational field lies in the vicinity of incipient fluidisation and, in addition, turbulent flow regimes are exceptional, a popular model adapted for the transitional flow regime is given by van Dijk *et al.* (1991). Foscolo *et al.* (1983) presented a similar tube flow approach, albeit with several model improvements. Foscolo considered a tortuosity factor, effective length of the fluid path and a forced interpolation to correct the limit of single-particle interaction to be obtained for dilute systems.

Another well-known relationship proposed by Wen and Yu (Wen and Yu, 1966; Hartman *et al.*, 1992) is based on the dependency of the drag coefficient on the

dimensionless Reynolds number (Kmiec, 1982) and on the assumption of a common voidage function for the entire flow regime. With this model, the voidage can explicitly be calculated for given particle Reynolds and Archimedes numbers. Di Felice (1995) investigated the voidage function and the dependency of the particle Reynolds number and proposed an improved Wen–Yu overall voidage relation. According to Akgiray and Soyer (2006), who provided an extended evaluation of expansion equations for fluidised solid–liquid systems, there is no general agreement regarding which equation is the most accurate. Akgiray proposed a voidage prediction model based on an improved drag relation. Kramer *et al.* (2020a) proposed an improved drag relation taking into consideration the fluidisation stability to cope with heterogeneity phenomena in LSF beds and increasing the overall voidage prediction accuracy. The traditional drag relation based on the particle Reynolds number was extended with the particle Froude number. One of the most popular and frequently used models for describing homogeneous LSF suspensions is the model developed by Richardson and Zaki (1953). The superficial fluid velocity and terminal settling velocity, together with an empirical index, enables determination of the fluid voidage in a straightforward way. Khan and Richardson (1989) proposed the same form of equation but only used the Archimedes number instead of the Reynolds terminal number. The reference point here for the Richardson–Zaki model is the terminal settling velocity. The model proposed by van Schagen (van Schagen, 2009; Rietveld *et al.*, 2006; van Schagen *et al.*, 2008b) was also based on the Richardson–Zaki principle and a fitted Schiller–Nauman Equation (Schiller and Naumann, 1933) to determine the terminal settling velocities for calcite pellets. To be able to predict voidage in the proximity of minimum fluidisation conditions, either the minimum fluidisation velocity must be known or the Richardson–Zaki index must be extremely accurate. Therefore, the Richardson–Zaki model was extended (Kramer *et al.*, 2019) with proven hydraulics-based models. The minimum fluidisation velocity is acquired with the Carman–Kozeny model (Carman, 1937) where the terminal settling velocity is acquired using the Brown–Lawler model (2003), an improved version of the well-known model developed by Schiller and Naumann (1933). In the literature, many velocity-voidage prediction models can be found, the most popular of which are given in Table 17.

Table 25 Voidage prediction models from the literature

Model	Equation ¹⁾	Parameters	Boundary conditions	Eq. nr.
Ergun, 1952	$(\rho_p - \rho_f)g(1 - \varepsilon) = c_1 \frac{v_s \eta (1 - \varepsilon)^2}{d_p^2 \varepsilon^3} + c_2 \frac{\rho_f v_s^2 (1 - \varepsilon)}{d_p \varepsilon^3}$	$c_1=150, c_2=1.75$		(91)
Carman, 1937 ²⁾	$(\rho_p - \rho_f)g(1 - \varepsilon) = c_1 \frac{v_s \eta (1 - \varepsilon)^2}{d_p^2 \varepsilon^3} + c_2 \frac{\rho_f^{1-c_1} v_s^{2-c_1} \eta^{c_1} (1 - \varepsilon)^{1+c_1}}{d_p^{1+c_1} \varepsilon^3}$	$c_1=180, c_2=2.9, c_3=0.1$	$Re_\varepsilon < 600$	(92)
van Dijk and Wilms, 1991	$(\rho_p - \rho_f)g(1 - \varepsilon) = c_1 \frac{\rho_f^{1-c_2} v_s^{1+c_2} \eta^{c_2} (1 - \varepsilon)^{1+c_2}}{d_p^{1+c_2} \varepsilon^3}$	$c_1=130, c_2=0.8$	$5 < Re_\varepsilon < 130$	(93)
Foscolo <i>et al.</i> , 1983	$(\rho_p - \rho_f)g(1 - \varepsilon) = \left(\frac{c_1}{Re_p} + c_2 \right) \frac{\rho_f v_s^2}{d_p} (1 - \varepsilon) \varepsilon^{c_3}$	$c_1=17.3, c_2=0.336, c_3=-4.8$		(94)
Akgiray and Soyer, 2006	$\frac{1}{6^3} Ar \frac{\varepsilon^3}{(1 - \varepsilon)^2} = c_1 Re_1 + c_2 Re_1^{c_3}$	$c_1=3.137, c_2=0.673, c_3=1.766$	$0.37 < \varepsilon < 0.90$ $-1.96 < \log Re_1 < 3.54$	(95)
Wen and Yu, 1966	$\varepsilon^{c_1} Ar = c_2 Re_p + c_3 Re_p^{c_4}$	$c_1=4.7, c_2=18, c_3=2.7, c_4=1.687$	$10^{-3} < Re_1 < 10^4$	(96)
Di Felice, 1995	$\varepsilon^\beta Ar = c_1 Re_p + c_2 Re_p^{c_3}, \beta = 4.7 - 0.65 e^{-c_6(c_7 - \log(Re_p))}$	$c_1=18, c_2=2.7, c_3=1.687,$ $c_4=4.7, c_5=0.65, c_6=0.5, c_7=1.5$		(97)
Richardson and Zaki, 1954	$\varepsilon^n = \frac{v_s}{v_t}$ $n = \begin{cases} Re_t < 0.2, & n = 4.65 \\ 0.2 \leq Re_t < 1, & n = 4.4 Re_t^{-0.03} \\ 1 \leq Re_t < 500, & n = 4.4 Re_t^{-0.1} \\ Re_t \geq 500, & n = 2.4 \end{cases}$		$\varepsilon_{mf} < \varepsilon < 1$	(98)
van Schagen <i>et al.</i> , 2008b	Equation (98), $C_D = \frac{24}{Re_t} (1 + 0.079 Re_t^{0.87})$, $C_D = \frac{4}{3} \frac{g d_p}{v_t^2} \left(\frac{\rho_p}{\rho_f} - 1 \right)$			(99)
RZ–Kramer ²⁾ Kramer <i>et al.</i> , 2019	Equation (98), $n = \frac{\log\left(\frac{Re_\varepsilon m_f (1 - \varepsilon_{mf})}{Re_t}\right)}{\log \varepsilon_{mf}}$			(100)
RIO 2 ²⁾ Kramer <i>et al.</i> , 2020a	$\frac{g d_p^2 (\rho_p - \rho_f)}{v_s \eta} \frac{\varepsilon^3}{1 - \varepsilon} = \left(\frac{c_1}{Re_\varepsilon + c_4 Fr_p^{\frac{1}{c_3}}} + \frac{c_2}{(Re_\varepsilon + c_4 Fr_p^{\frac{1}{c_3}})^{c_3}} \right) Re_\varepsilon$	$c_1=150, c_2=6.33, c_3=0.226,$ $c_4=3,883$	$\varepsilon_{mf} < \varepsilon < 0.95$	(101)

1) Dimensionless numbers are given in Table 1

2) Model abbreviation: RZ=Richardson–Zaki, RIO 2 model by Kramer

8.3.2 Reactor performance indicators

The particle size and voidage over the reactor height must be known to be able to estimate the SSA. The following reactor performance indicators are defined: specific surface area based on the reactor volume and the specific surface area based on the water phase as well as the specific space velocity (SSV). The most frequently presented definition of SSA in the literature (Edzwald, 2011; Crittenden *et al.*, 2012; Yang, 2003; Di Felice, 1995) of granular beds given as the total surface area of the particle material divided by the bed volume. $A_{s,r}$ represents the available area per m^3 reactor volume for crystallisation. For monodisperse spherical particles, the SSA, based on the reactor volume $A_{s,r}$, is given by:

$$A_{s,r} = 6 \frac{1 - \varepsilon}{d_p} \quad (102)$$

The SSA based on the water phase $A_{s,w}$ provides more adequate information for crystallisation of CaCO_3 on the available total particle surface. This performance indicator $A_{s,w}$ resembles the proper interaction area between water and reactive surface and is defined as:

$$A_{s,w} = \frac{A_{s,r}}{\varepsilon} \quad (103)$$

Mercer *et al.* (Mercer *et al.*, 2005) demonstrated that calcite seed crystals improved the removal of dissolved calcium during precipitative softening and that the optimal seed dose depended on the surface area available for crystal growth.

Van Schagen *et al.* (2008) showed that the pellet size, and consequently the SSA, had a significant influence on performance with respect to the water quality parameter. To keep the super-saturation in the pellet-softening reactor at acceptable levels, the SSA must be known to determine the crystallisation rate over the height of the reactor. Here, the voidage, particle size and temperature are important (Rietveld, 2005). Also, according to van der Veen and Graveland (1988), the SSA is strongly dependent on the water temperature.

Time also plays an important role in the mixing zone of the reactor, where the majority of the crystallisation reaction takes place. The caustic soda, the water and

seeding material must all be mixed in a minimum period of time in order to prevent undesirable carry-over of CaCO_3 precipitation. Consequently, the water that passes along the available specific surface area per unit of time must be at a maximum level. The following performance indicator, specific space velocity, is derived from 'space velocity' as used in the field of chemical reactor engineering (Levenspiel, 1999). Space velocity for homogeneous reactions, *i.e.* uniform fluids, is defined as the number of reactor volumes of feed at specific conditions which can be treated per unit of time. Regarding multiphase systems, the reactor volume is partly occupied by grains. In that case, the effective water volume must be used similar to the Empty Bed Contact Time (EBCT), defined as the volume of the empty bed divided by the flow rate (Edzwald, 2011; Crittenden *et al.*, 2012). Considering that crystallisation occurs in multiphase systems, space velocity can be translated into the rate in which the water passes the SSA or how often the water is renewed at the water layer above the particle surface. Due to the presence of grains and the effective residence time, the superficial fluid velocity must be corrected with respect to the voidage. The specific space velocity A_c is accordingly defined as the contact area per second per m^2 of transfer surface area:

$$A_c = A_{s,w} \frac{v_s}{\varepsilon} \quad (104)$$

Please note that A_c is an inverse time scale with units $[\text{s}^{-1}]$, while their counterparts $A_{s,r}$ and $A_{s,w}$ both are inverse length scales with units $[\text{m}^{-1}]$.

8.4 Materials and Methods

8.4.1 Empirical data-driven voidage prediction models

The fluidised bed voidage depends primarily on the fluid and particle properties. In general, one uses the mean particle size, assuming perfect spheres d_p , average particle density ρ_p , kinematic viscosity ν_r and superficial fluid velocity v_s . For the sake of simplicity, wall effect corrections, the influence of the fluid distributor, fluid circulations and the irregular distribution of the particles and other non-ideal

phenomena are ignored. More information about wall-effects is given Annex 2: Wall effects.

Voidage prediction models are only valid for a fluidised state. For this reason, it is important to determine the incipient fluidisation and maximum flushing point to check the prevailing state. Detailed elucidation and model derivations are presented in the Supplementary material (Sections 10, 11 and 12).

Voidage Prediction Polynomials (VPP)

A straightforward way to model the voidage for individual grain types is to use sets of polynomials as a function of velocity, viscosity and particle size, respectively, while considering the particle density to be constant, either indirectly or directly related to particle size. There are two ways to apply these polynomials. Both methods are based on an experimentally obtained dataset containing a wide range of data in fluid velocity covering the whole temperature regime and various particle diameters as well as a given particle density. A ‘floating polynomial model’ is given in the Supplementary material (Section 11). However, to keep the fitting procedure feasible for processing, a second approach using a one fit polynomial equation is proposed by means of Equation (105):

$$\varepsilon(v_s, v_T, d_p) = \sum_{i=0}^{i=l} \sum_{j=0}^{j=m} \sum_{k=0}^{k=n} c_{i,j,k} (v_s^i v_T^j d_p^k) \quad (105)$$

The advantage of this approach lies in the simplicity of having one single model for which fitting parameters can be obtained using non-linear regression software. The disadvantage, however, lies in the considerable computational time required for finding an acceptable prediction accuracy and the number of fitting parameters ($N = l \cdot m \cdot n$). The computational time increases substantially with the size of the experimental dataset. Using fit polynomials works well, although it demands strictly respecting the given boundary conditions to avoid overshoot and physically unrealistic voidage predictions.

Dimensionless Numbers Application (DNA)

The effective voidage can also be predicted using dimensionless Reynolds and Froude numbers based on an implicit drag relationship proposed by Kramer *et al.* (2020a). The Reynolds number deals with the relationship between viscous and inertial forces and determines the degree of laminar or turbulent flow regime (Bird *et al.*, 2007). The particle Reynolds number Re_p is defined as:

$$Re_p = \frac{\rho_f v_s d_p}{\eta} \quad (4)$$

The Froude number is defined as the ratio of inertial to gravity forces and is a proxy for the fluidisation quality from smooth homogeneous (particulate) fluidisation to heterogeneous or aggregative (bubbling) fluidisation (Kwauk and Li, 1996). The densimetric particle Froude number Fr_p is given by (Grace, 1986):

$$Fr_p = \frac{v_s}{\sqrt{\left(\frac{\rho_p}{\rho_f} - 1\right) g d_p}} \quad (14)$$

To find the voidage from these dimensionless parameters, a numerical method is needed.

Single Reynolds–Froude model (Rep1Frp)

To avoid numerical solutions, the following simple explicit Equation (106) is proposed in which the powers determine the dependence of the voidage on the ratio and magnitude of both dimensionless numbers with an added pre-factor:

$$\varepsilon = c_0 Re_p^{c_1} Fr_p^{c_2} \quad (106)$$

This equation can be rewritten as a straightforward function of velocity, viscosity, particle size and density. More information is presented in the Supplementary material (Sections 18 and 19).

Double Reynolds–Froude model (Rep2Frp)

Equation (106) is a rather straightforward approach which can be improved based on previous research in the field of chemical engineering (Albright, 2009). The general Reynolds number (Re) determines whether the flow is dominated by inertial or viscous forces, *i.e.* whether the flow is laminar or turbulent. Whitaker (Whitaker, 1972) proposed a heat transfer-based equation for the Nusselt number Nu as a function of the Reynolds number Re and Prandtl number Pr , for flow in pipes, around spheres and through packed beds as follows:

$$Nu = (0.5Re^{1/2} + 0.2Re^{2/3})Pr^{1/3} \quad (107)$$

Note that Nusselt numbers Nu between 1 and 10 are characteristic of laminar flow, while turbulent flow typically corresponds to Nu in the range 100 - 1,000 (White, 2015). Therefore, it can be understood qualitatively that Whitaker's expression for Nusselt increases with increasing Reynolds number and captures the influence of flow regimes on heat transfer (Whitaker, 1972). This understanding is supported by Bedingfield and Drew (Bedingfield and Drew, 1950; Yang, 2003), who showed a theoretical analogy between heat and mass transfer. Similarly, for LSF, we will formulate an expression for the voidage based on the sum of two terms that capture the influence of the flow regimes.

Here we use the Froude number instead of the Prandtl number. The reason for implementing the densimetric Froude number comes from the hypothesis (Kramer *et al.*, 2020a) that voidage is based on laminar-turbulent flow regimes as well as heterogeneity phenomena in LSF beds. The voidage can accordingly be predicted using Equation (108):

$$\varepsilon = (c_0Re_p^{c_1} + c_2Re_p^{c_3})Fr_p^{c_4} \quad (108)$$

Symbolic Regression Model (SRM)

Based on high quality datasets, highly accurate prediction models can be obtained using symbolic regression techniques as applied in genetic programming. Genetic programming is a random-based technique (Koza, 1992) for automatically learning computer programmes based on artificial evolution. It has been successfully used in many applications (Edwards, 2006; Barati *et al.*, 2014). The advantage of genetic programming is that there is no need to define the structure of a model *a priori*: the

technique randomly generates a population of several mathematical operators. Symbolic regression is the process of determining the symbolic function, which describes a dataset and effectively develops an empirical model (Awange and Paláncz, 2016). These types of models have two main features: complexity and accuracy. Generally, given a certain dataset, the process starts with the determination of very simple but inaccurate models. With time, more accurate but also more complex models are obtained. To prevent adverse modelling of measurement errors, data noise or deviation, a model should be taken as a compromise between complexity and accuracy. Voidage is a function of fluid velocity, viscosity and particle size and density given in a general form according to Equation (109):

$$\varepsilon = \varepsilon(v_s, v_T, d_p, \rho_p) \quad (109)$$

8.4.2 Experimental set-up

To calibrate and to validate the prediction models, liquid-solid expansion experiments were needed to obtain reliable datasets containing fluid viscosity and superficial velocity as well as particle size and density. Advanced laboratory and pilot plant apparatus were therefore especially designed for this purpose. In addition, drinking water-related grains were carefully prepared and selected. Standard operating procedure of fluidisation experiments is elucidated in Section 3.4.

8.4.3 Particle selection

For this research, calcite pellets and crushed calcite were fractionated using calibrated sieves given in Table 26.

Table 26 *Fractionated calcite pellets and crushed calcite*

Nr. ¹⁾	Mesh bottom sieve ²⁾ [μm]	Mesh top sieve [μm]
1	-	355
2	355	425
3	425	500
4	500	600
5	600	710
6	710	800
7	800	900
8	900	1000
9	1000	1120
10	1120	1250
11	1250	1400
12	1400	1700
13	1700	2000
14	2000	2360
15	2360	2800
16	2800	-

¹⁾ Nr. 3-15 were investigated with expansion experiments

²⁾ Available sieve sizes are usually regulated by standards such as ISO 3310-1, ISO 565, EN 933-2 and ASTM E11 (NEN-EN 933-2, n.d.)

Additional information can be found in the Supplementary material: particle selection (Section 3), particle characterisation (Section 8) and fluidisation expansion experiments (Section 9).

8.4.4 Particle and fluid characterisation and expansion experiments

The method to calculate the physical properties of water is given in the Materials and Methods Section 3.2. The methods to determine the physical properties of particles is given in Section 3.3. Accordingly, bed voidage and differential pressure equations are given in Section 3.4.

8.5 Results

8.5.1 Particle selection, properties, experimental set-up and fluidisation experiments

Liquid-solid expansion experiments were carried out at three locations: in Waternet's Weesperkarspel drinking water pilot plant located in Amsterdam, the Netherlands; at the University of Applied Sciences Utrecht, the Netherlands; and at Queen Mary University of London, United Kingdom.

In this study, we examined two kinds of particles, calcite pellets (100% CaCO₃) and crushed calcite seeding material grains (Schetters *et al.*, 2015), both applied in drinking water softening (Graveland *et al.*, 1983). Polydisperse calcite pellets were sieved and separated in order to acquire more uniformly dispersed samples. The morphological particle properties (Table 26) obtained with a Camsizer (Retsch-Technology, 2007) show that crushed calcite and the smallest fractionated calcite pellets have irregular shapes. The larger the grains become, the more spherically shaped they appear to be.

Detailed information about experimental expansion columns can be found in Section 3.1. The physical properties of water are given in Section 3.2. Photographs of granules are included in Annex 1: Photos and the Supplementary material (Sections 2 and 4). Standard operating procedure of fluidisation experiments is elucidated in Section 3.4.

8.5.2 Obtained physical properties of particles

Particle sizes and the number of individual fluidisation experiments regarding perfectly round spheres and natural gratins applied in water treatment processes are given in Table 27.

Table 27 Determined particle size and number of fluidisation experiments

Grain material	Mesh top sieve [μm]	ImageJ ⁶⁾ sphere size [mm]	Sphericity [-]	Number of experiments [#]	Geldart's type ⁷⁾
Calcite pellets	$d_p < 0.355$ mm	n.a.	0.84	0	B
	$0.355 < d_p < 0.425$ mm	n.a.	0.84	0	B
	$0.425 < d_p < 0.5$ mm	0.48	0.84	4	B
	$0.5 < d_p < 0.63$ mm	0.54	0.85 ⁵⁾	4	B
	$0.63 < d_p < 0.71$ mm	0.71 ¹⁾	0.90	4	B
	$0.71 < d_p < 0.8$ mm	0.83	0.91	4	B
	$0.8 < d_p < 0.9$ mm	0.94	0.94	7	B
	$0.9 < d_p < 1.0$ mm	1.03	0.95	4	D
	$1.0 < d_p < 1.12$ mm	1.17	0.96	5	D
	$1.12 < d_p < 1.25$ mm	1.25	0.96	4	D
	$1.25 < d_p < 1.4$ mm	1.41	0.97	5	D
	$1.4 < d_p < 1.7$ mm	1.62	0.98	5	D
	$1.7 < d_p < 2.0$ mm	1.96	0.98	4	D
	$2.0 < d_p < 2.36$ mm	2.25	0.98	6	D
$2.36 < d_p < 2.8$ mm	2.55	0.99	5	D	
$d_p > 2.8$ mm	n.a.	0.99	0	D	
Crushed calcite ³⁾	$0.425 < d_p < 0.5$ mm	0.49 ²⁾	0.84	7	B
	$0.5 < d_p < 0.63$ mm	0.57 ²⁾	0.84	16	B
	$0.63 < d_p < 0.71$ mm	n.a.	0.84	16	B
	$0.71 < d_p < 0.8$ mm	0.89 ²⁾	0.84	3	B

1) Estimated value

2) Determined with a Retsch Camsizer particle size analysis system

3) Purchased from the Calcite Factory Amsterdam

4) Mined calcite from Italy

5) Interpolated value

6) <https://imagej.nih.gov/ij/> (Ferreira and Rasband, 2012)

7) Geldart's particle classification (Geldart, 1973). Type B; sand-like particles and type D: spoutable particles

The acquired experimental dataset consisted of a matrix with varying temperatures, grain sizes and flow rates, as was required for a comparison of the theoretical fluidisation models. In total, 61 LSF experiments were carried out for a wide range of calcite pellets ($0.425 < d_p$ [mm] < 2.8), and a total of 42 experiments were carried out for crushed calcite ($0.4 < d_p$ [mm] < 1.12), summarised in Table 23. Additionally, in total, 89 additional independent LSF experiments were carried out for a wide range of calcite pellets ($0.71 < d_p$ [mm] < 2.36), ($2 < T$ [°C] < 36), ($v_{mf} < v_s$ [m/h] < 570). For validation purposes, additional LSF experiments for a wide range of different particles in fluid water systems were conducted at the three given locations. Data tabulation can be found in (Kramer *et al.*, 2019) and in the Supplementary material (Section 23).

8.5.3 Voidage prediction

Based on the expansion column experimental datasets from our experiments, several empirical data-driven models were derived using symbolic regression. Model parameters were found through non-linear curve fitting. For implicit models, the voidage prediction accuracy was found with a straightforward Bolzano's numerical intermediate value theorem. All equations, regression coefficients, fitting parameters and plots are given in the Supplementary material (Sections 10-12). The experiments cover a large range of variables, as given in Table 23, which is assumed to represent the boundary conditions for the presented models.

Table 28 *Model boundary conditions calcite pellets and crushed calcite*

Variable	Range calcite pellets	Range crushed calcite
Fluid temperature	$4 < T \text{ [}^\circ\text{C]} < 36$	$4 < T \text{ [}^\circ\text{C]} < 35$
Superficial fluid velocity	$v_{mf} < v_s \text{ [m/s]} < 0.13$	$v_{mf} < v_s \text{ [m/s]} < 0.073$
Particle diameter	$0.43 < d_p \text{ [mm]} < 2.8$	$0.40 < d_p \text{ [mm]} < 1.12$
Particle density	$2,575 < \rho_p \text{ [kg/m}^3\text{]} < 2,625$	$2,525 < \rho_p \text{ [kg/m}^3\text{]} < 2,675$

Voidage Prediction Polynomials (VPP)

Two different polynomials were tested. The first one is a triple quadratic polynomial (222), for which the voidage can be explicitly estimated based on velocity, viscosity and particle size with a constant assumed particle density. The second one is a 4th, 2nd and 3rd order polynomial (423) versus velocity, viscosity and particle size, also with a constant particle density. These polynomial expressions are relatively accurate for the voidage prediction in case the given boundary conditions are respected. However, when these boundary conditions are exceeded, these VPP models are unpredictable and rather inaccurate. Another disadvantage is the high computational effort required for the non-linear curve fitting process with the aim to find all the fitting parameters.

Dimensionless Numbers Application (DNA)

Single Reynolds–Froude model (Rep1Frp)

The fitting parameters for Equation (106), describing a combination of laminar versus turbulent flow regimes and homogeneous versus heterogeneous flow characteristics, are given in Table 29.

Table 29 Fitting parameters for Equations (106)¹⁾ and (4), (14)

Grain material	c_0	c_1	c_2	Correlation coefficient R^2
Calcite pellets	1.637	-0.1035	0.4339	0.974
Crushed calcite	1.814	-0.1354	0.3932	0.979

¹⁾ Boundary condition $\varepsilon_{mf} < \varepsilon < 0.95$

Double Reynolds–Froude model (Rep2Frp)

The fitting parameters for the improved Reynolds–Froude-based Equation (108) are given in Table 30.

Table 30 Fitting parameters in Equations (108)¹⁾ and (4), (14)

Grain material	c_0	c_1	c_2	c_3	c_4	Correlation coefficient R^2
Calcite pellets	1.688	-0.3504	0.5336	0.0565	0.4554	0.994
Crushed calcite	1.620	-0.1039	0.4925	-0.9166	0.3999	0.981

¹⁾ Boundary condition $\varepsilon_{mf} < \varepsilon < 0.95$

Model adjustments for process automation purposes without verifying boundary conditions are described in the Supplementary material (Section 19).

Symbolic Regression Model (SRM)

Based on the experimental expanded bed dataset, numerous solutions, *i.e.* multiple equations, were found when the software package Eureqa (Nuttonian, 2019) was used. We present two examples of equations: one for calcite pellets in Equation (110) and one for crushed calcite in Equation (111). Fitting parameters can be found in Table 31. The expressions are accurate within the given boundary conditions. However, as is the case with the polynomials, they are unpredictable and therefore inaccurate when the boundary conditions are violated.

Calcite pellets

$$\varepsilon = c_0 \frac{\rho_p}{\rho_f} + \ln(d_p) \left(c_1 \frac{\rho_p}{\rho_f} - c_3 - c_5 v_T - c_6 \ln v_s \right) - c_2 - c_4 v_s \ln(v_s) \quad (110)$$

Crushed calcite

$$\varepsilon = c_0 + c_1 v_T - c_4 d_p + c_2 d_p^2 - v_s (c_3 + c_5 \ln v_s) \quad (111)$$

Table 31 Fitting parameters in Equations (110) and (111)^{1) 2)}

Grain material	c_0	c_1	c_2	c_3	c_4	c_5	c_6	Correlation coefficient R^2
Calcite pellets	5.275	0.7977	14.82	2.326	1.681	12,099	0.0116	0.997
Crushed calcite	0.5998	109,096	279,245	8.663	742.3	6.42	-	0.984

1) Boundary conditions $\varepsilon_{mf} < \varepsilon < 0.95$

2) Note: be aware of velocity v_s and viscosity v_T used in equations (110) and (111).

Voidage-velocity graphs

In Figure 77 and Figure 78 we present our experimental voidage-velocity data in comparison with two models, respectively: the Richardson–Zaki Equation (98), as one of the most used and well-known models, and the new Reynolds–Froude Rep2Frp Equation (108) proposed in this study. Graphical results for all voidage prediction models are plotted and shown in the Supplementary material (Section 12).

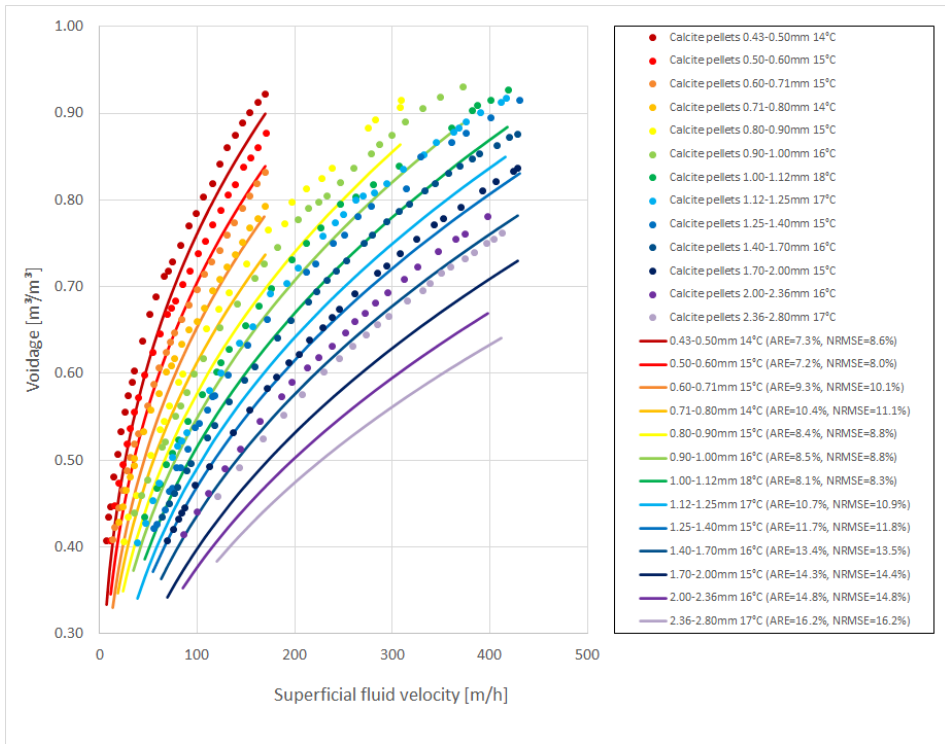


Figure 77 Experimental data in comparison with the Richardson–Zaki prediction model for calcite pellets at regular water treatment conditions. Voidage is plotted against superficial fluid velocity. Dots represent experimental data and curves represent the actual prediction model.

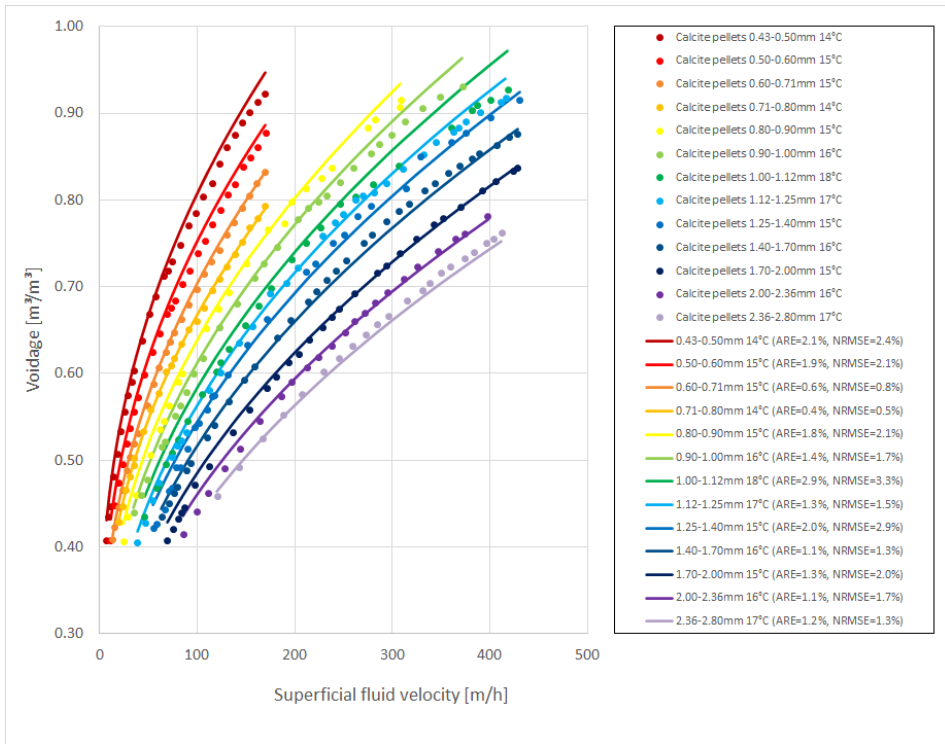


Figure 78 Experimental data in comparison with the Reynolds–Froude-based voidage prediction model for calcite pellets at global water treatment conditions. Voidage is plotted against velocity. Dots represent experimental data and curves represent the actual prediction model.

The voidage prediction models (Table 32) given in the literature ($N = 11$) as well as the models proposed in the current work ($N = 5$) were compared with the experimentally obtained data using five statistical methods: mean average error, average relative error, normalised root mean square error, logarithmic root mean squared error and Pearson’s correlation coefficient.

Table 32 Model overview voyage prediction accuracy calcite pellets arranged in descending order by accuracy: mean average error (MAE), average relative error (ARE), normalised root mean square error (NRMSE), logarithmic root mean squared error (LRMSE), Pearson's correlation coefficient (R^2). Model sources are given in Table 17

Model	MAE	Model	ARE	Model	NRMSE	Model	LRMSE	Model	R^2
Eureqa	0.0073	Eureqa	1.2%	Eureqa	1.5%	Eureqa	1.5%	Wen–Yu	0.999
Rep2Frp	0.0098	Rep2Frp	1.6%	Rep2Frp	1.9%	Rep2Frp	1.9%	RZ	0.999
RIO 2	0.0115	RIO 2	1.8%	RIO 2	2.1%	RIO 2	2.1%	Van Schagen	0.999
Akgiray	0.0124	Akgiray	2.1%	Akgiray	2.7%	Akgiray	2.8%	Rep1Frp	0.999
Poly423	0.0137	Poly423	2.3%	Poly423	3.0%	Poly423	2.9%	Foscolo	0.999
Poly222	0.0168	Poly222	3.0%	CK	3.8%	CK	3.7%	Eureqa	0.999
Rep1Frp	0.0179	Rep1Frp	3.1%	Rep1Frp	3.9%	Poly222	3.9%	Rep2Frp	0.998
CK	0.0232	CK	3.4%	Wen–Yu	4.0%	Rep1Frp	3.9%	Ergun	0.998
Wen–Yu	0.0250	Wen–Yu	3.6%	Poly222	4.1%	Wen–Yu	4.1%	RZ–Kramer	0.998
RZ–Kramer	0.0265	Ergun	3.9%	RZ–Kramer	4.3%	RZ–Kramer	4.4%	Akgiray	0.998
Ergun	0.0284	RZ–Kramer	3.9%	Ergun	4.9%	Ergun	4.7%	Di Felice	0.997
Van Schagen	0.0311	Van Schagen	5.1%	Van Schagen	5.6%	Van Schagen	5.8%	CK	0.996
Van Dijk	0.0495	Van Dijk	7.1%	Van Dijk	7.9%	Van Dijk	8.3%	RIO 2	0.988
Di Felice	0.0558	Di Felice	8.5%	Di Felice	8.6%	Di Felice	9.0%	Van Dijk	0.977
RZ	0.0694	Foscolo	10.1%	Foscolo	10.6%	Foscolo	11.3%	Poly423	0.974
Foscolo	0.0706	RZ	11.0%	RZ	11.4%	RZ	12.2%	Poly222	0.963

Note: Statistical methods are given in Annex 5: Statistical analysis.

8.5.4 Reactor performance indicators

The SSA is a relevant performance indicator concerning pellet-softening and can be estimated in case the voidage and particle size are known. The superficial fluid velocity determines for a great deal to what extent the bed expands. Based on Equation (102), describing the best-known SSA for the reactor volume, a 3D plot can be created. Figure 79 represents the SSA $A_{s,r}$ against the pellet size d_p and the linear flow rate v_s , for a given water temperature.

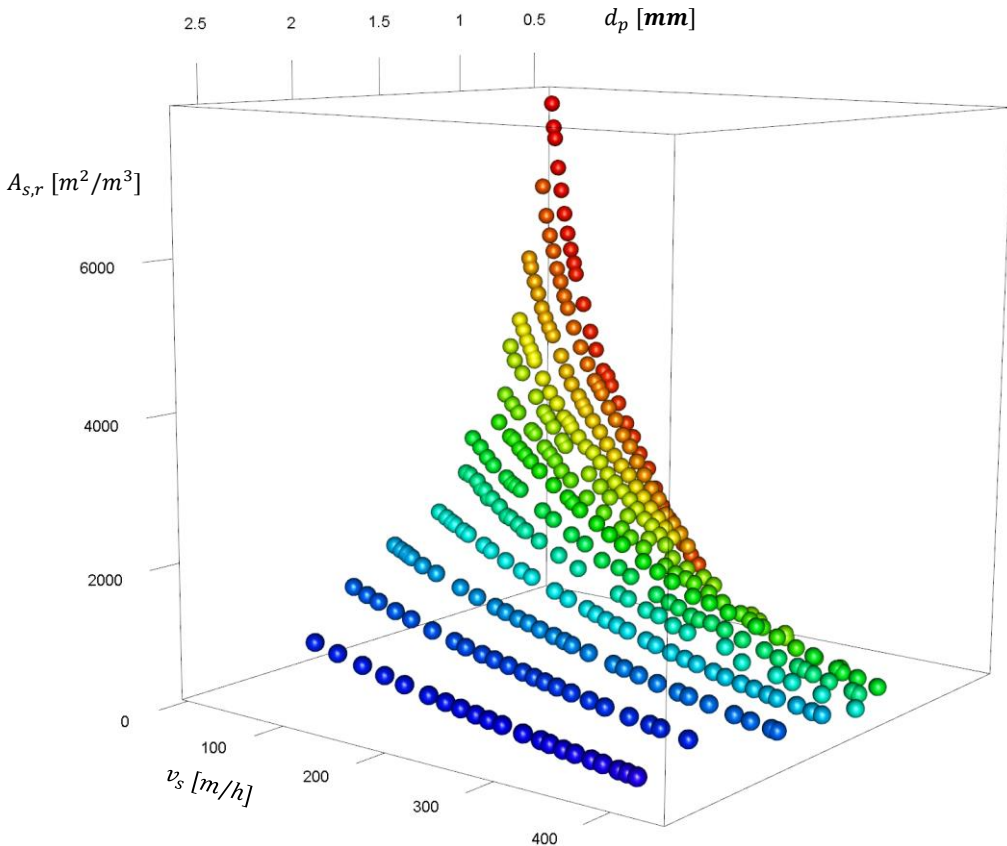


Figure 79 Specific surface area (reactor) versus superficial fluid velocity and particle size, for calcite pellets at regular water temperature and all experimental data $T \approx 15$ [°C]. For 5, 25 and 35 [°C] see Supplementary material (Section 13). Colour bar represents the measurement series.

However, the operation window for full-scale pellet-softening reactors is smaller ($60 < v_s \text{ [m/h]} < 120$): this is plotted in Figure 80. A surface plot, using Rep2Frp model (Equation (108)), is accordingly plotted in Figure 81.

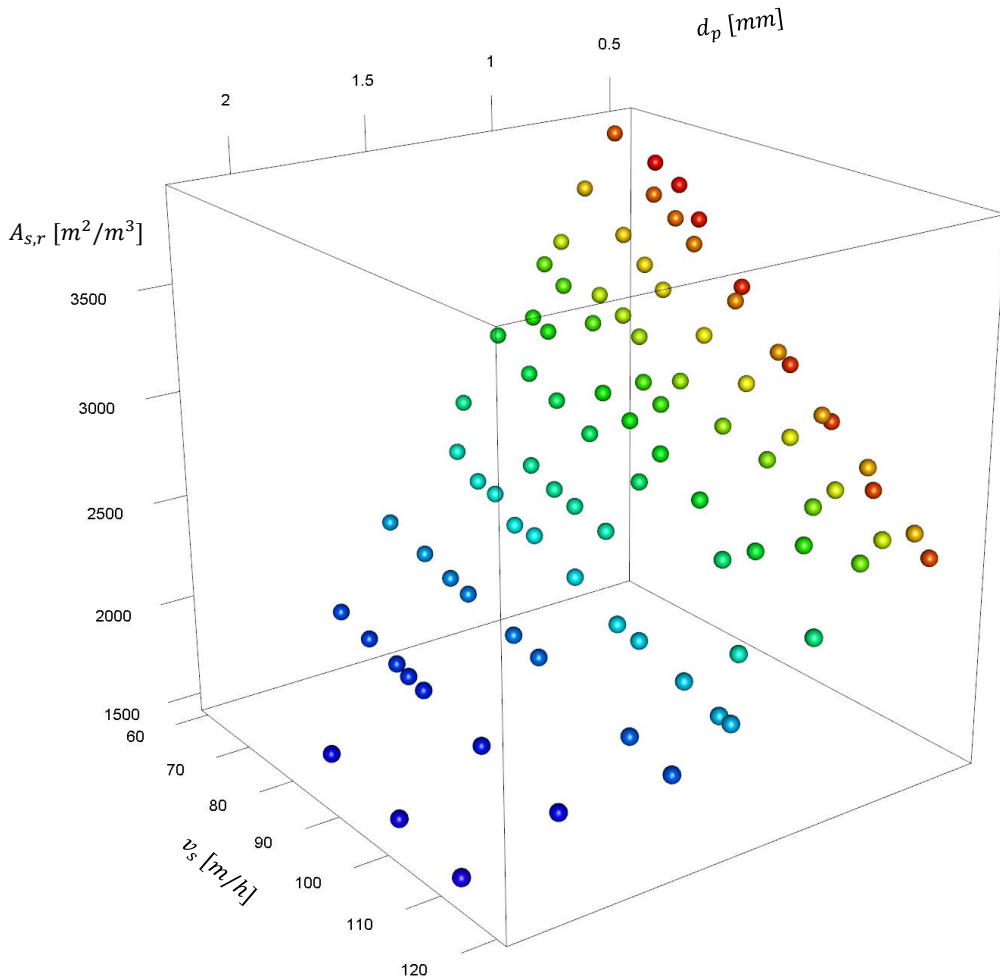


Figure 80 This is a segment of Figure 79. Specific surface area (reactor) versus superficial fluid velocity and particle size for calcite pellets at regular water temperature $T \approx 15 \text{ [}^\circ\text{C]}$ for the operation window for full-scale pellet-softening reactors ($60 < v_s \text{ [m/h]} < 120$). Smaller grains and lower linear flow rates provide a higher SSA.

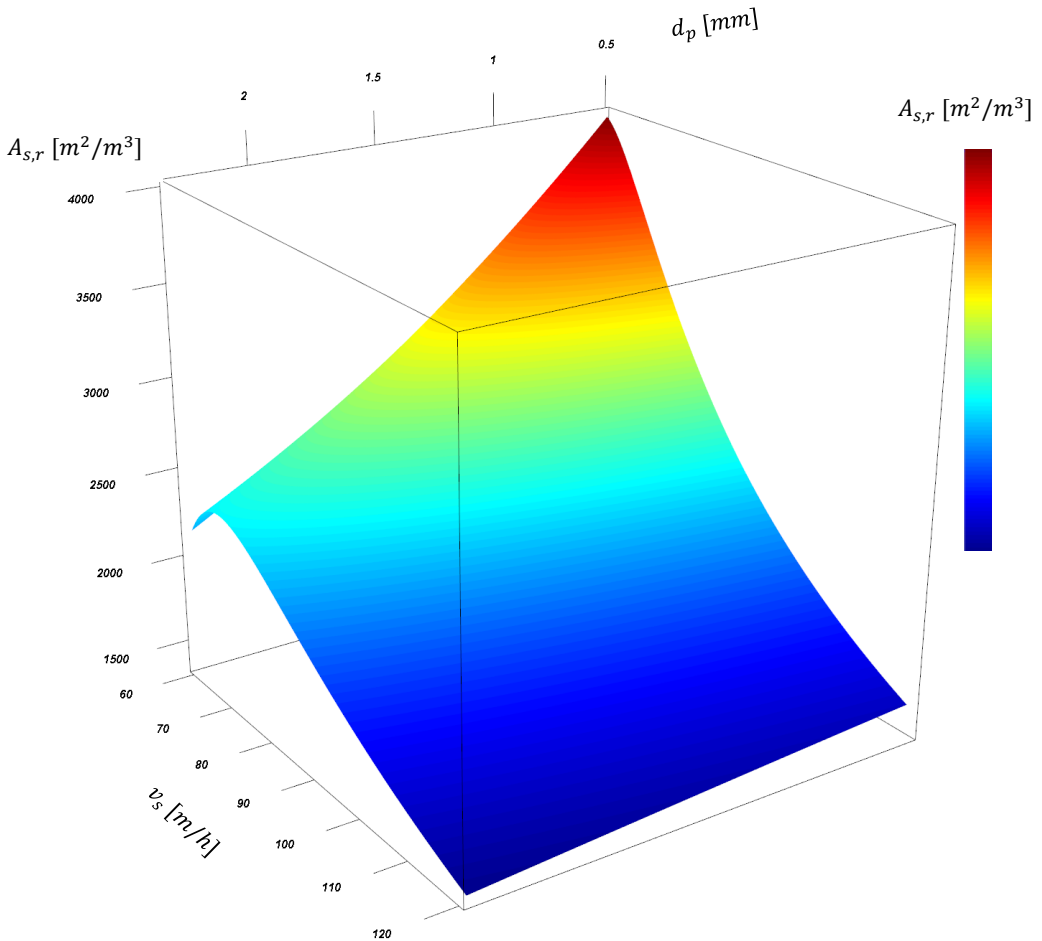


Figure 81 Surface plot: specific surface area (reactor) versus superficial fluid velocity and particle size using the Rep2Frp model (Equation (108) and (102)) at $T \approx 15$ [°C] for calcite pellets in a range ($60 < v_s$ [m/h] < 120). 1 [mm] calcite pellets, for instance, with a superficial fluid velocity $v_s = 80$ [m/h] result in an effective voidage $\varepsilon = 0.56$ and a specific surface area $A_{s,r} = 2,640$ [m^2/m^3].

In addition, the voidage ε is plotted against the pellet size d_p and the linear flow rate v_s in Figure 82. Another less familiar reactor performance indicator is the contact surface area per unit of time (Equation (104)) which is plotted Figure 83.

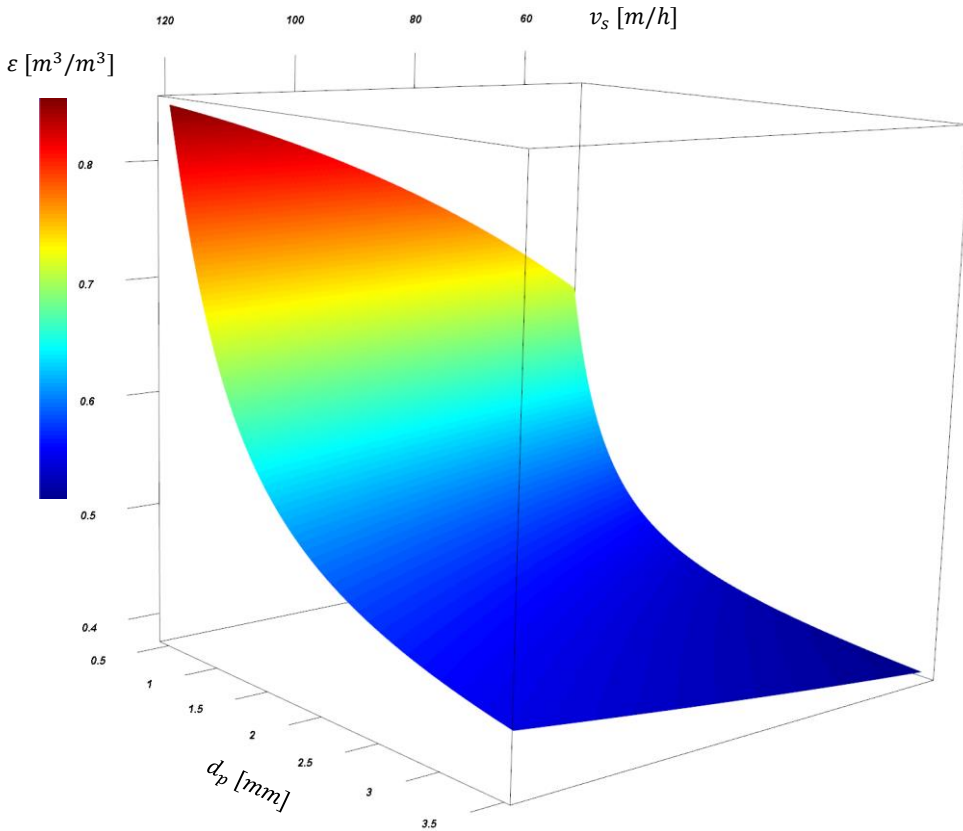


Figure 82 Surface plot: voidage versus superficial fluid velocity and particle size for calcite pellets at regular temperature $T \approx 15$ [°C] pellet-softening condition ($60 < v_s$ [m/h] < 120) using Rep2Frp model (Equation (108)). Larger grains and lower linear flow rates provide lower voidages and can therefore result in a fixed bed.

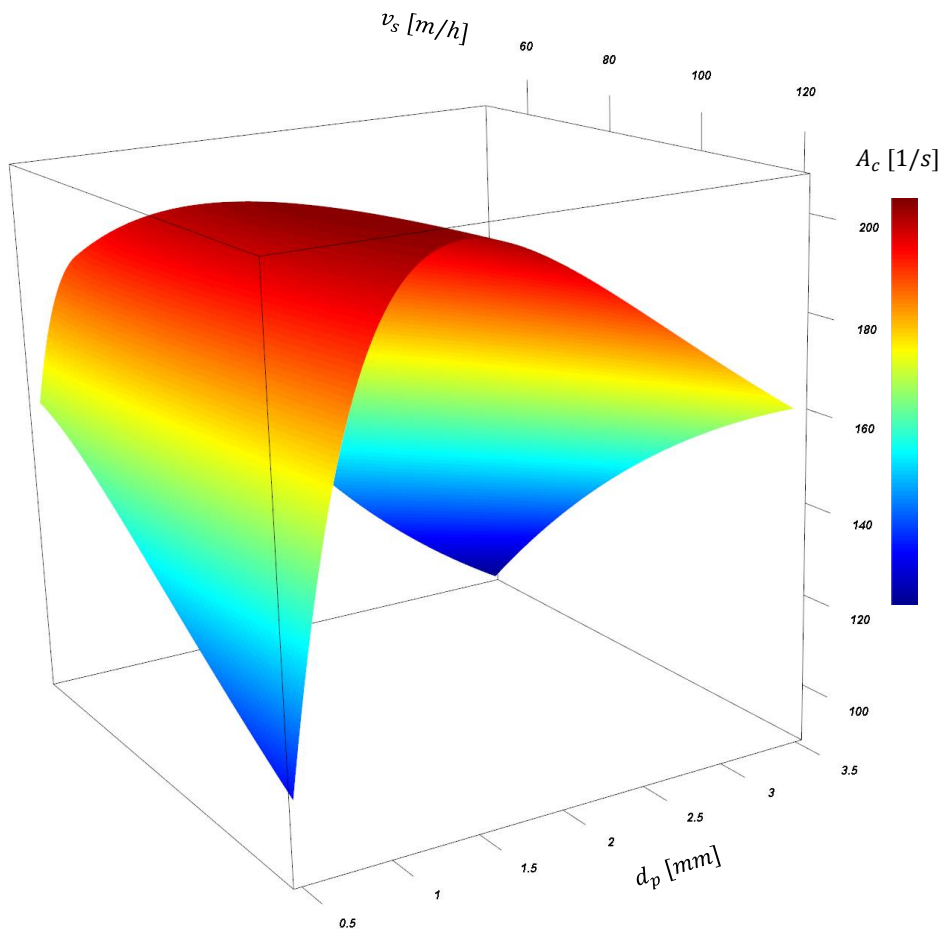


Figure 83 Surface plot: specific space velocity versus superficial fluid velocity and particle size for calcite pellets at regular temperature $T \approx 15$ [°C] pellet-softening condition ($60 < v_s$ [m/h] < 120). Higher linear flow rates lead to a higher SSV. However, changing the particle size of calcite pellets significantly determine the SSV. 1 [mm] calcite pellets with a superficial fluid velocity $v_s = 80$ [m/h] result in an effective voidage $\varepsilon = 0.56$ and a specific space velocity $A_c = 187$ [1/s]. In contrast to SSA, SSV has a maximum that can be calculated using Equations (108) and (104). The optimal pellet size for this example is between 0.8 and 1.2 [mm], which is in agreement with the practical operation experience. SSV plots for all experiments and surface plots during the seasons, are provided in the Supplementary material Sections 15 and 16.

8.6 Discussion

8.6.1 Voidage prediction models

Graphical exploration

The prediction models presented in this work, *i.e.* voidage prediction polynomials, dimensionless number applications and symbolic regression models, were compared with the most popular and familiar models known from the literature (Table 17). All voidage-velocity plots are included in the Supplementary material (Sections 11-12).

Before assessing the models in terms of statistical fit quality, we applied graphical exploration, as proposed by Anscombe (2010), to test the goodness of fit and to determine whether the model describes the experimental data adequately. Figure 78, for instance, shows both dots (experimental data) and lines (prediction model) that provide a visual image of the degree to which the dots and lines coincide, where the discrepancies appear, whether or not the dots are over-dispersed and whether the boundary conditions are violated and thus lead to unrealistic values.

Based on graphical explorations (Figure 77, Figure 78 and remaining figures in the Supplementary material), the Ergun model (Ergun, 1952) shows overprediction, in particular for higher velocities and larger grains. The Carman–Kozeny model (Carman, 1937) shows overprediction for smaller grains at low and intermediate velocities. Van Dijk’s model (van Dijk and Wilms, 1991) is originally fitted for a small operation window (Rietveld, 2005; van Schagen *et al.*, 2008b; van Schagen, 2009; Ashoor *et al.*, 2019) and therefore outliers can be found in and outside this specific region. The prediction quality of Foscolo’s model (Foscolo *et al.*, 1983) is relatively good at lower velocities but underpredicts in case the velocities are increased. Akgiray’s model (Akgiray and Soyer, 2006), on the other hand, works increasingly better for higher velocities. The Wen–Yu model (Wen and Yu, 1966) shows a good fit at low velocities and small grains but works less well for higher velocities and larger grains. The model modification proposed by Di Felice (1995) did not improve the fit quality. The RIO 2 model (Kramer *et al.*, 2020a) appears to work well in terms of fit quality, not including the smallest grains at maximum velocity. The Richardson–Zaki model (1954) in general underestimates the experimental data considerably (Figure 77) and, to a lesser extent, so does the van Schagen model (van Schagen *et al.*, 2008b). The other RZ-based model proposed by Kramer *et al.* (2019) starts to

show discrepancies for higher velocities and larger grains. Regarding the models presented in this study, the polynomial curves coincide with the dots except for the smallest grains and show unrealistic curvature caused by the fitting towards the maximum velocities. The empirical symbolic regression model shows appropriate slopes, albeit with a larger offset for increased velocities. The single Reynolds Froude-based model is not accurate for small grains at low velocities while the double Reynolds–Froude model shows good agreement with the experimental data.

Statistical exploration

Numerical voidage prediction accuracies are given in Table 32 for five statistical metrics (MAE, ARE, NRMSE, LRMSE and R^2). In general, the calculated errors of all examined models, based on experimental calcite pellets data, is a 12% or lower. The prediction errors of 11 of our 16 models are lower than 4%, and 5 out of 11 are lower than 2%. The following models have the lowest prediction error: Eureqa, Rep2Frp and the RIO 2 model, with the exception of R^2 . Based on an independent dataset, given in the Supplementary material (Sections 10), the prediction errors are slightly higher ($\approx 1\%$) and show the same top-three ranking. The differences in accuracy are mainly based on the use of older, and less accurate, versions of the experimental set-up and measurements devices.

Based on Pearson's correlation coefficient R^2 , it is impossible to make a well-argued choice for a preferable model or to determine which model is the most accurate. Almost all R^2 values are higher than 0.99, and in most cases, they are 0.999. The MAE measures the average magnitude of the errors in a set of predictions, regardless of their direction and where all individual differences have equal weight. The NRMSE gives a relatively high weight to large errors, and therefore the RMSE is more useful when large errors are particularly undesirable. In case of LRMSE, the outliers are drastically scaled down, thus nullifying their effect. Since we are looking for a highly accurate voidage prediction model, there is a slight preference for NRMSE as it penalises undesirably large errors.

Richardson–Zaki-based models

The Richardson–Zaki model, which is still highly popular in the literature, shows the highest prediction error. This can be explained by the fact that the terminal settling velocity is assumed to be determined by a maximum voidage $\varepsilon = 1$. However, the

observed voidage at maximum or entrainment state found in this research study was lower, namely approximately $\varepsilon \approx 0.95$. The Richardson–Zaki model uses terminal settling as a starting point and combined with an empirical index, which is also a function of terminal settling, the voidage can be predicted. When a voidage lies in the vicinity of incipient fluidisation, as is the case in pellet-softening processes, a relatively small inaccuracy in both the starting point and the index n in Equation (98) leads to a high prediction error. When *log-log* scales are used, these effects are clearly visible (Figure 77). Van Schagen solved this terminal settling issue through finding better fitting parameters for the Schiller–Naumann (1933) equation. He extrapolated expansion data for calcite pellets to terminal settling conditions. With this adjustment, the error was reduced by a factor of almost two. Kramer *et al.* (2019) introduced a second physical point. Besides the point of terminal settling, an extra point of minimum fluidisation was added from which the voidage can be interpolated. With these model improvements, despite some overprediction, the prediction error was reduced by a factor of nearly three.

Porous media-based drag relations

Based on statistical metrics only, it is not evident that the Ergun model is less accurate for the higher flow regime. The model has, however, shown a reasonable fit score at low flow, which was confirmed by Marshall and Li (2014). Based on statistics, the Carman–Kozeny model has a slightly higher fit score, but here too it remains unclear whether this model is actually more suitable in the transitional flow regime. The CK model overpredicts at low flow regimes. The models introduced by van Dijk, Foscolo, Wen–Yu and Di Felice have acceptable fit scores, but this is mainly at low flow regimes. For pellet-softening, voidage is overestimated by van Dijk, but underestimated by Foscolo and Di Felice. Akgiray, Wen–Yu and RIO 2 show conformity with the data.

Data-driven and numerical numbers-based models

The polynomial functions underpredict the voidage for the pellet-softening operational range, whereas the empirical symbolic regression model is less accurate at the borders, which is also the case for the single Reynolds–Froude-based model. The double Reynolds–Froude-based model has a high fit quality and is more reliable since this model is based on dimensionless numbers with a hydraulic physical

significance. This implies that, in case the boundary conditions were to be violated, the risk of run-away is smaller, compared to purely empirical data-driven models.

Modelling aspects

Several factors determine, to different levels and certain degrees, the fit prediction quality: these include non-ideal aspects such as particle polydispersity, morphological properties, density differences and particle interactions. Non-ideal circumstances such as fluid characteristics, heterogeneous flow phenomena and the influence of chemicals also play a role. Other determining factors include non-ideal matters related to the piece of apparatus used, such as flow distributor, column alignment, sensor inaccuracies and wall effects. The effort to incorporate all these aspects into a model is significant, but it also makes the model more complex. In full-scale, fully automated unit operations, a reliable, explicit and programmable model is preferred - despite the penalty it might bring in case the fit quality is slightly lower. The models can be fitted accurately when high-quality experimental data are used, based on calcite pellets extracted from the full-scale reactors.

Bed state control

To reach high performance levels in full-scale pellet-softening reactors, an optimal crystallisation process is important, but this is strongly dependent on the governing hydraulic state in fluidised beds. Pellet-softening in drinking water production processes is a continuous process. Discharging calcite pellets from reactors and subsequently dosing fresh seeding material are likewise continuous repetitive processes. These particle changes imply that the SSA also varies and will drift away from its ideal setpoint.

At the bottom of the reactor, the voidage is kept relatively low to obtain the highest crystallisation SSA; nevertheless, fixed bed situations must be avoided. The degree of voidage is dependent on the physical properties of the grains and the water viscosity. *De facto*, voidage, or fluid bed height, is kept constant through controlling the water flow in the reactor and, depending on water temperature, through particle bed management. In pellet-softening reactors, voidage is approximately $\varepsilon \approx 0.55$ at the bottom of the reactor and $\varepsilon \approx 0.8$ at the top.

Full-scale pellet-softening reactors are always installed in groups, and hard water containing a high concentration of calcium ions is often partly by-passed (Rietveld,

2005). Moreover, the total water production changes in volume periodically. In a full-scale operational pellet-softening reactor, the process state is subject to changes in water flow, temperature, depending on the season of the year, and ongoing variations in particle sizes, shaping the particle profile over the height of the reactor bed. To cope with these changes, constant process state monitoring is crucial. To control the required pellet sizes, as a standard conventional procedure, particle samples are regularly taken from the reactor bed manually and accordingly analysed in a laboratory. In that case, based on water flow, for a given temperature, together with the particle size, the voidage can be estimated. This is demonstrated in Figure 84. Engineers can check the quality of the SSA but also monitor the risk of a fixed bed state or flushing.

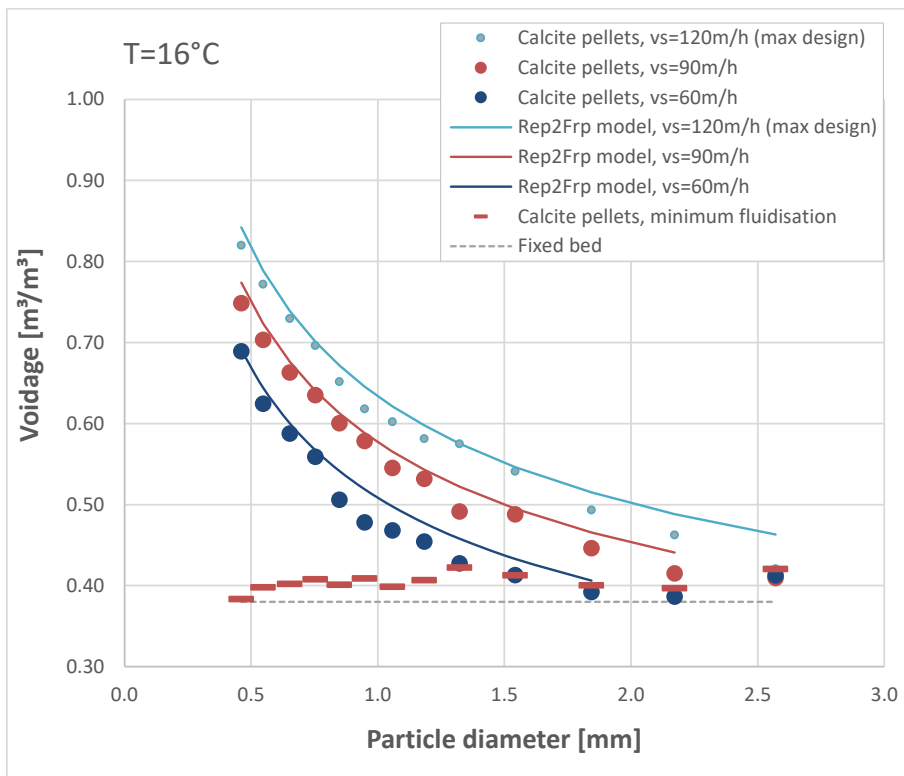


Figure 84 Voidage prediction and measurements for given particle diameters at global water treatment conditions. The green area covers crushed calcite and the blue area the calcite pellets in a full-scale pellet-softening reactor. For 5, 25 and 35 [°C] see Supplementary material (Section 17).

In industry, soft sensors are also implemented (van Schagen, 2009) with gauges at the bottom of the reactor in which the voidage and particle size is derived from flow, differential pressure and temperature. This is done by using models. The advantage of this method is the availability of on-line data results. However, a disadvantage is the vulnerability and consequently the sensitivity of the gauges due to the exposure to high lime scaling conditions in the lower zone of the reactor, resulting in less accurate predictions.

8.6.2 Reactor performance indicators

The SSA plotted in Figure 79 clearly shows that the $A_{s,r}$ decreases when the linear flow rate increases or particles become larger. This is similar for pellet-softening conditions (Figure 80 and Figure 81). This indicates why smaller particles, like seeding material, increase the SSA. Still, these crushed calcite grains migrate to the higher zones of the fluidised bed due to stratification and, in case the flow is too high, the risk of flushing out of the reactor emerges. At the same time, due to CaCO_3 crystallisation, particles grow and migrate to the lower zone of the reactor, where the chemical driving force is large and decisive. These larger grains cause the SSA to decrease fast and, in addition, they enlarge the risk of a fixed bed state. This can be seen in Figure 82, indicated by the dark blue zone. To maintain a maximum SSA, large calcite pellets should continuously be withdrawn and replaced by smaller crushed calcite seeds, which results in higher operational costs, mainly caused by transportation, and which also adversely affects the sustainability goals. Therefore, an optimum fluid velocity must be chosen very precisely. This substantiates the relevance of a voidage prediction model that is extremely accurate.

In Figure 83 a maximum specific space velocity A_c is reached for calcite pellets, with an average size slightly larger than 1 mm. With Equations (102) and (104), an optimal linear flow rate range ($75 < v_s \text{ [m/h]} < 85$) can be derived for an average water temperature, with a corresponding SSA: $A_{s,r} \approx 2,500 \text{ m}^2/\text{m}^3$. This is partly in agreement with the current operational window of the Amsterdam reactors at Waternet (Sobhan, 2019; Maeng *et al.*, 2016; Rietveld, 2005; Chiou, 2018; Chen *et al.*, 2000). Another complexity arises when the ratio of calcite pellet size to crushed calcite size is lower than would approximately be the case in a process state where the voidage is also in the vicinity of incipient fluidisation. In case the voidage is too

low, caused by either lower flow rate or higher water temperature, dosed crushed calcite remains trapped between the calcite pellets, leading to a non-stratified particle bed.

In full-scale installations with plant-wide control, complex models and the continuous challenge to find optimal numerical solutions are less desirable. Another disadvantage is that many models are semi-empirical and derived for monodispersed perfectly spherical particles. *De facto*, in all full-scale multiphase flow processes applied in water treatment processes, particles are irregularly shaped and often highly polydisperse. Due to the complex flow behaviour and large number of particles ($N \sim 10^{10}$), explicit particulate modelling of full-scale industrial fluidised bed system using Computation Fluid Dynamics is also challenging and as yet unachievable. Therefore, there is a pressing need for an explicit effective model to be able to accurately predict the overall voidage in fluidised beds that effectively takes into account the global multiphase flow phenomena and many other non-ideal matters occurring in full-scale installations. Based on these criteria and findings, an average optimal linear flow rate can be determined ($v_s \approx 85 \pm 5$ m/h). Due to the above-mentioned non-ideal circumstances, full-scale operational challenges and continuous changes in particle profile, further research is needed to find a more precise optimal process state that also takes into account hydraulic, chemical and biological phenomena. SSV plots for all experiments and surface plots during the seasons, are provided in the Supplementary material Sections 15 and 16.

8.7 Conclusions

The accurate calculation of voidage and specific surface area is of major importance in drinking water treatment processes like pellet-softening, because it determines the process conditions and treatment results. To maintain or provide optimal process conditions in pellet-softening reactors, it is important to accurately determine the fluidised bed voidage. Voidage is a crucial variable for determining the specific surface area, the minimum fluidisation and flushing conditions as well as the water and particle residence time. The voidage prediction accuracy of 11 models from the literature was compared with five types of data-driven and dimensionless numbers-based models. Accurate experimental datasets were used to validate the predictive power.

Porous media-based drag relations models RIO 2 and Akgiray's and the data-driven polynomial model 423 in general have a reasonable prediction quality (error < 3%). The model based on symbolic regression and the double Reynolds–Froude-based model has the best fit (error < 2%) for all examined statistical metrics. A majority of prediction models available from the literature (such as Foscolo, Akgiray, van Dijk, van Schagen Richardson–Zaki, RIO 2, Di Felice, Ergun and Carman–Kozeny) have the disadvantage that the voidage must be numerically solved. The polynomials, Wen–Yu and the Reynolds–Froude-based models provide explicit solutions for the voidage.

As mentioned above, in full-scale installations with plant-wide control, complex models and the continuous challenge to find optimal numerical solutions are less desirable. Therefore, there is a pressing need for an explicit effective model to be able to accurately predict the overall voidage in fluidised beds that effectively takes into account the global multiphase flow phenomena and many other non-ideal matters occurring in full-scale installations. As a consequence, and based on statistical metrics as well as graphical exploration, a preferable prediction model for a pellet-softening operational range ($60 < v_s \text{ [m/h]} < 120$) is the Rep2Frp model. The model is accurate, has a physical basis, is easy to use for process automation programmes and is therefore suitable for application in full-scale operational pellet-softening reactors.

8.8 Research data

Fit parameters for various additional granules regarding liquid-solid fluidisation models such as highly spherical particles and a variety of granules applied in drinking water treatment processes are shared at (Kramer *et al.*, 2020c): 4TU.Centre for Research Data: <https://doi.org/10.4121/13537121.v1>.

8.9 Supplementary material

Supplemental data for this article can be accessed at:

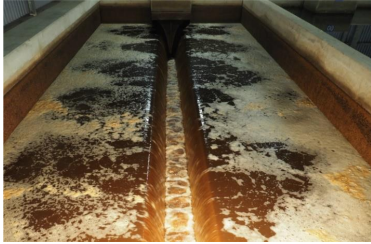
<https://doi.org/10.1016/j.jwpe.2020.101481>

<https://ars.els-cdn.com/content/image/1-s2.0-S2214714420303597-mmc1.docx>

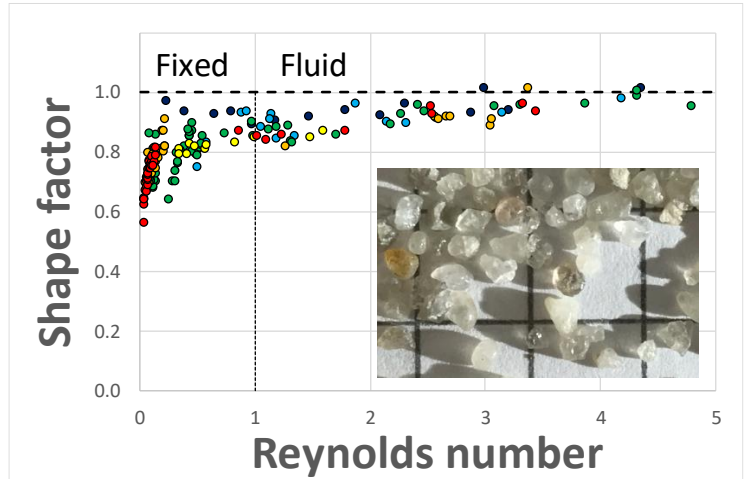
Contents		page
1	Proposed Rep2Frp model based on Reynolds and Froude numbers	1
2	Photographs of full-scale pellet-softening reactors	2
3	Particles selection	3
4	Photographs of examined calcite pellets	4
5	Expansion columns	5
6	Photographs and videos of fluidisation experiments	8
7	Wall effects	9
8	Particle and fluid characterisation	10
	8.1 Physical properties of water	10
	8.2 Physical properties of particles	10
	8.3 Average particle diameter	10
	8.4 Morphological properties	11
	8.5 Particle density	11
	8.6 Obtained particle properties	13
9	Fluidisation expansion experiments	14
	9.1 Standard operating procedure	14
	9.2 Flowmeter and differential pressure calibration	14
	9.3 Bed voidage and expansion	15
	9.4 Fluidisation expansion experiments	15
	9.5 Minimum and maximum fluidisation points	16
	9.5.1 Minimum fluidisation points	16
	9.5.2 Maximum fluidisation points	17
	9.5.3 Results regarding minimum and maximum fluidisation points	17
9.6	Statistical analysis	19
10	Fluidisation voidage prediction	20
	10.1 Calcite pellets	20
	10.2 Crushed calcite	20
11	Fitting parameters for models presented in this work	21
	11.1 Voidage Prediction Polynomials (VPP)	21
	11.1.1 Floating polynomial model	21
	11.1.2 Single polynomial model	21
	11.1.3 (222) polynomial	22
	11.1.4 (423) polynomial	24
	11.2 Dimensionless Numbers Application (DNA)	26
	11.3 Symbolic Regression Modelling (SRM)	29
12	Graphical voidage prediction results for examined models	31
	12.1 Water temperature $T \approx 5$ [°C]	31

12.2	Water temperature $T \approx 15$ [°C]	39
12.3	Water temperature $T \approx 25$ [°C]	47
12.4	Water temperature $T \approx 35$ [°C]	55
13	Specific surface area 3D plot versus velocity and particle size	63
14	Specific space velocity 3D data plot versus velocity and particle size	64
15	Specific space velocity 3D surface plot versus velocity and particle size	65
16	R script for 3D data and model surface plots	66
16.1	3D data plot using R	66
16.2	3D model surface plot using R	67
17	Full-scale reactor voidage prediction	68
18	Restructuring Rep1Frp model into Voidage Power Function	69
18.1	Rep1Frp voidage model	69
18.2	Rep1Frp velocity model	69
18.3	Rep1Frp particle diameter model	70
18.4	Voidage Power Function	70
19	Model adjustments for process automation without boundary conditions	71
19.1	Modified Rep2Frp model considering physical boundary conditions	71
19.2	Theoretical entrainment velocity	71
19.3	Practical entrainment velocity	72
19.4	Modified model results	72
19.5	Simplified entrainment velocity	73
20	Nomenclature	74
21	Bibliography	77
22	Acknowledgments	80
23	Experimental data	81
23.1	Calibration dataset for calcite pellets	81
23.2	Validation dataset for calcite pellets	102
23.3	Calibration dataset for crushed calcite	132-151

Filter backwash



Dynamic shape factors



- ▶ As particles are irregularly shaped, the Carman–Kozeny constant is not constant
- ▶ Fixed bed state is not fixed due to a rearrangement of particles in packing position
- ▶ Various shape factors for the same particles in fixed and fluid state are explained
- ▶ 1D spherical particle diameters in models must be replaced by 3D spheroids
- ▶ The successful Extended Terminal Sub-Fluidisation Wash can be explained hydraulically

Keywords Drinking Water Treatment; Multiphase Flows; Filter-Backwash; Hydraulics Drag Relations; Particle Orientation; Dynamic Particle Shape Factors

Chapter 9

Dynamic Shape Factors

“A correcting shape factor for fixed bed state which accordingly becomes redundant for the fluidised state, for the same particles when the flow rate increases, is peculiar. The actual cause of this is due to the re-orientation of particles in the bed and thus the changing drag.”

This article has been published as:

New hydraulic insights into rapid sand filter bed backwashing using the Carman–Kozeny model

O.J.I. Kramer, P.J. de Moel, J.T. Padding, E.T. Baars, S.B. Rutten, A.H.E. Elarbab, J.F.M. Hooft, E.S. Boek, J.P. van der Hoek
Water Research, **197**, 117085 (2021) pp. 1–11

The article can be found online at:

<https://doi.org/10.1016/j.watres.2021.117085>

9 New hydraulic insights into rapid sand filter bed backwashing using the Carman–Kozeny model

9.1 Abstract

Fluid flow through a bed of solid particles is an important process that occurs in full-scale water treatment operations. The Carman–Kozeny model remains highly popular for estimating the resistance across the bed. It is common practice to use particle shape factors in fixed bed state to match the predicted drag coefficient with experimentally obtained drag coefficients. In fluidised state, however, where the same particles are considered, this particle shape factor is usually simply omitted from the model without providing appropriate reasoning. In this research, it is shown that a shape factor is not a constant particle property but is dependent on the fluid properties as well. This dynamic shape factor for irregularly shaped grains increases from approximately 0.6 to 1.0 in fluidised state.

We found that unstable packed beds in moderate up-flow conditions are pseudo-fixed and in a setting state. This results in a decreasing bed voidage and simultaneously in a decreasing drag coefficient, which seems quite contradictory. This can be explained by the collapse of local channels in the bed, leading to a more uniform flow distribution through the bed and improving the available surface for flow-through. Our experimental measurements show that the drag coefficient decreases considerably in the laminar and transition regions. This is most likely caused by particle orientation, realignment and rearrangement in particles' packing position.

A thorough hydraulic analysis shows that up-flow filtration in rapid sand filters under backwash conditions causes the particle bed to collapse almost imperceptibly. In addition, an improved expression of the drag coefficient demonstrated that the Carman–Kozeny model constant, however often assumed to be constant, is in fact not constant for increasing flow rates. Furthermore, we propose a new pseudo-3D image analysis for particles with an irregular shape. In this way, we can explain the successful method using optimisation of the extended terminal sub-fluidisation wash (ETSW) filter backwashing procedure, in which turbidity and peaks in the number of particles are reduced with a positive effect on water quality.

9.2 Introduction

The downward flow of fluid through a bed of solid particles is an important process that occurs in full-scale water treatment operations (Crittenden *et al.*, 2012). In the field of drinking water treatment, rapid sand filtration (RSF) is the most common unit operation applied to capture fine particles from the water in the filter bed. Accumulated particles cause a gradual increase in head loss and reduce overall effectiveness of the filter bed (Howe *et al.*, 2012). When the head loss exceeds a certain threshold after a period of time, the filter is backwashed, usually assisted by some auxiliary scouring. During backwashing, an upward water flow expands the filter bed and flushes out the collected fine particles. After a filtration and backwashing sequence, the cycle starts again (Edzwald, 2011). To reduce the passage of particles through restarted filters immediately after a backwash procedure, Amburgey proposed the extended terminal sub-fluidisation wash method (ETSW) to remove significantly higher amounts of backwash remnant particles (Amburgey, 2005). ETSW is a proven method of terminating the backwash cycle with a sub-fluidisation wash for a time interval adequate to pass one theoretical filter volume of water upward through the filter (Amburgey and Amirtharajah, 2005).

ETSW is a relatively straightforward process comprising an appropriate additional sub fluidisation wash step at the end of a normal backwash procedure. The ETSW washing phase is started at the end of the backwash sequence with the purpose of rinsing out the remainder of the particles, sheared from the filter during the fluidisation stage of the backwash. The ESTW is set to a wash water flow rate below the minimum fluidisation velocity for a time sufficient to displace one entire filter volume of particle-laden water. The results presented by Amburgey (2005) show a significant improvement in water quality by reducing, or eliminating, the initial particle passage during the restart of a packed filter after backwashing. ETSW reduces the turbidity during filter maturation and particle number spikes in practice, but no hydraulic explanation for its effectiveness was provided.

In this paper, we report laboratory measurements in which up-flow filtration procedures were simulated. During the experiments, an unexpected reduction in both bed voidage and bed resistance was detected which could not be explained by traditional drag coefficient correlations as a function of the particle Reynolds number. We propose this *can* be explained by differences in preferred orientation of particles under different hydraulic conditions.

9.3 Hydraulic drag

9.3.1 Hydraulic models for fluid flow in particle beds

Well-known hydraulic models for flow through particle beds have been introduced for the laminar flow regime by (Blake, 1922) and (Kozeny, 1927) based on (Darcy, 1856), for the turbulent flow regime by (Burke and Plummer, 1928), and for the transitional flow regime by (Ergun, 1952) and (Carman, 1937) based on the Forchheimer flow conditions (Forchheimer, 1930). In the laminar regime, the fluid flows in smooth parallel layers without any disturbance between the layers, while in the turbulent flow regime, the fluid undergoes irregular fluctuations and changes in both magnitude and direction. Transitional flow is a mixture of laminar and turbulent flow, with turbulence in the centre of pore spaces and laminar flow near the particle surfaces. Each of these flows behaves in different ways in terms of their frictional energy loss.

De facto, the most commonly used and most accurate (Říha *et al.*, 2018) equation for expressing the relationship between permeability and voidage, particle size and tortuosity is the Carman–Kozeny equation. This equation is applied in various fields, such as groundwater flow, water treatment and many other water processes (Camp, 1946). The Carman–Kozeny equation is important not only for the determination of permeability in porous media (Yang, 2003), but also for the estimation of the voidage in a fluidised bed (Kramer *et al.*, 2020a). In groundwater flow, the flow regime is generally considered to be laminar (Crittenden *et al.*, 2012). In fluidised beds, however, not only laminar, but also transitional and, to a certain degree, turbulent flow regimes occur. The resistance of laminar flow through a granular bed can be calculated using the well-known equation proposed by (Blake, 1922), (Kozeny, 1927) and (Carman, 1937):

$$\frac{\Delta P}{\Delta L} = 180 \frac{v_s \eta (1 - \varepsilon)^2}{d_p^2 \varepsilon^3} \quad (Re_\varepsilon < 2) \quad (112)$$

Where: $\Delta P/\Delta L$ is the pressure drop head loss, v_s is the superficial velocity, η the dynamic fluid viscosity, d_p the average or equivalent particle diameter, ε the bed voidage and Re_ε the modified particle Reynolds number (Equation (6)). This equation shows that the resistance of laminar flow is linear with the viscosity and with the

superficial velocity, as is also known to be the case for laminar flow through pipes according to Hagen-Poiseuille (Munson *et al.*, 2020) and laminar flow through aquifers (Darcy, 1856). The experimentally obtained value of 180 is often indicated as the Kozeny drag coefficient (Kozeny, 1927). Further background information about the Carman equation is elucidated in the Supplementary material (Section 3). Since in water treatment the operational field lies in the vicinity of incipient fluidisation and since turbulent flow regimes are exceptional, there is a preference for using the Carman–Kozeny drag relation. Kozeny proposed a fixed pore shape factor $K = 180$ in Equation (74) to fit the model results to experimental data. In the literature, many other values are proposed (Ozgumus *et al.*, 2014); (Erdim *et al.*, 2015); (Hoyland, 2017); (Schulz *et al.*, 2019), of which $K = 150$ is also often used (Burke and Plummer, 1928); (Ergun, 1952); (Kramer *et al.*, 2020a). The factor 180 does not appear to be constant at higher velocities when the flow is no longer laminar ($Re_\varepsilon > 2$), as Carman (1937) showed. He introduced a drag coefficient, which can be written in the laminar form (f_L) (Equations 18 and 19) or in the turbulent form (f_T) (Equations 16 and 17) as a function of the Reynolds number Re_ε :

$$f_L = f_T Re_\varepsilon = 180 + 2.9 Re_\varepsilon^{0.9} \quad (Re_\varepsilon < 600) \quad (113)$$

Where f_L is the dimensionless drag coefficient (laminar representation) and f_T the dimensionless drag coefficient (turbulent representation) and where the modified particle Reynolds number Re_ε is defined as:

$$Re_\varepsilon = \frac{\rho_f d_p v_s}{\eta} \frac{1}{1 - \varepsilon} \quad (6)$$

Where ρ_f is the fluid density. The experimentally obtained relation for f_L or f_T will be indicated below as the Carman drag coefficient (Carman, 1937). For further background information on the many forms of this equation, reference is made to the literature (Erdim *et al.*, 2015) and model derivations given in the Supplementary material (Section 3).

9.3.2 Particle correction shape factors

Within hydraulic modelling, particles are often idealised to spheres for mathematical convenience. Water treatment-related particles generally have more complex geometric features, summarised under the term shape, including the geometric shape, the presence of surface disparities such as protuberances and re-entrant features as well as particle property irregularities. Shape is therefore difficult to define. Although the literature on particle shape is extensive (Gauvin and Katta, 1973); (Holdich, 2002); (Seville and Yu, 2016) and a number of shape factors and descriptors have been proposed (Clift *et al.*, 1978); (Allen, 1990), there is no universal agreement on how to define particle shape. Therefore, there is no agreement on how to correctly measure it, nor does the literature provide consistent methods to cope with naturally irregularly shaped particles that can be used in voidage prediction models for liquid-solid fluidisation systems. The size and shape of the particles has important implications for, for instance, filter design (Crittenden *et al.*, 2012), but there is no easy way to account for this.

In the literature (Wadell, 1933); (Cleasby *et al.*, 1981); (Michaelide *et al.*, 2017) particle shape is often characterised by sphericity, which is generally defined as the ratio of the surface area of an equal volume sphere to the surface area of the granule. That being said, sphericity has limited value in actual practice for several reasons. First, filter media are currently still routinely measured and specified using a laborious sieve analysis procedure, and less by means of advanced image analysis techniques. Second, in the literature there is no general consensus on how to apply sphericity for commercially available granular media. If the particle has a known geometric shape, sphericity can be calculated mathematically. However, for irregularly shaped particles, indirect methods are required. To determine shape factors, several empirical fitting models are available (Dharmarajah, 1982). Often, these models are based on head loss or voidage experiments. Carman (1937) proposed that the K -value was independent of media properties and introduced a correction factor to account for the non-spherical nature of filter grains, using sphericity and the shape factor (Fair *et al.*, 1933). According to (Yang, 2003), shape factors are open to criticism, because a range of granules with different shapes may have the same shape factor, which is inevitable if complex shapes are to be described by only a single parameter. (Wen and Yu, 1966) proposed shape factor corrections, used in the Ergun equation, based on experimental data for the minimum fluidisation voidage. According to the literature (Dharmarajah, 1982);

(Crittenden *et al.*, 2012), a commonly used particle shape factor in fixed bed state is necessary in order to match the Carman–Kozeny predicted drag coefficient with the experimentally obtained drag coefficient. The main drawback of this approach is that the model parameters often have no direct connection to the underlying porous medium structure (Schulz *et al.*, 2019), do not have a physical interpretation, or are difficult or even impossible to measure, especially by means of sieve analysis (di Felice, 1995).

In contrast, in the fluidised state, particle shape factors are usually omitted to match the Carman–Kozeny predicted drag coefficient with the experimentally obtained drag coefficient, without providing any explanation. Most likely this is done because these parameters are difficult to measure directly (de Jong and Nomden, 1974); (Hoyland, 2017); (Hunce *et al.*, 2018). This is remarkable at the very least since the same particles are involved, in fixed as well as fluidised states. In addition, particle shape factors as a function of fluid velocity and temperature in liquid-solid fluidised systems are rarely evaluated in the literature. In the practice of filtration (Crittenden *et al.*, 2012) and other forms of flow through granular beds, the measured resistance does not appear to correspond with the calculated resistance. To obtain a fit, an experimentally determined shape factor ϕ_s is used to modify the measured diameter (d) into an effective diameter (d_p):

$$d_p = \phi_s d \tag{114}$$

Where d is the measured diameter and ϕ_s the diameter shape correction factor. For further background information on the manifold empirical adjustments for flow resistance, reference is made to the literature (Říha *et al.*, 2018).

9.4 Research aims

Based on theoretical factors and the specific ETSW procedure as applied after filter backwashing, it is clear that in order to obtain a thorough understanding of the hydraulics of up-flow filtration systems applied in full-scale water treatment unit operation, several goals must be met. Initially, a more effective drag coefficient must be introduced to be able to visualise changes in drag for various velocities and temperatures. The magnitudes of particle correction shape factors must be shown in fixed and fluidised state. To demonstrate the degree of irregularity of considered granular material as well as to determine preferred particle orientation, an applicable image analysis method must be developed. In addition, a hydraulic explanation must be offered for the effective ETSW method for future optimisation purposes (water throughput and operational time) and to improve water quality.

9.5 Materials and methods

9.5.1 Particle selection and physical properties

For up-flow filtration and fluidisation experiments, rapid filtration sand grains were selected. The particle density was determined using measured differential pressures and a laboratory pycnometer. The hydraulic equivalent particle diameter (Dallavalle, 1948); (Crittenden *et al.*, 2012); (Davis, 2010) was calculated using the sieve diameters, expressed in Equation (28):

$$d_p = \sqrt{d_{s,1} d_{s,2}} \quad (28)$$

Where $d_{s,i}$ is the sieve mesh diameter. The dimensions of the particles were also determined by using ImageJ as a particle analyser (Ferreira and Rasband, 2012), for which a 4.188 g sample of filter sand was scanned on an A4 flatbed scanner, at a resolution of 2,400 dpi. Irregularly shaped particles, in particular elongated parts, tend to lie horizontally oriented. ImageJ determines for each individual particle which pixel in the 2D-image belongs to this particle. For each particle, the software determines some 34 size parameters, such as equivalent circle diameter, and

equivalent ellipse dimensions with related morphological particle properties (Table 33), such as aspect ratio, Ferret diameter, circularity and solidity. Statistical information such as mean, range and frequency distribution can be determined from all these measurements.

Table 33 *ImageJ morphological properties (Ferreira and Rasband, 2012)*

Property	Meaning
Aspect ratio	The width to height ratio of an elongated particle
Feret diameter	Distance between two parallel tangents on opposite sides of the image of a randomly oriented particle
Circularity	Perimeter of sphere of the same projected area divided by the actual projected perimeter of the particle
Solidity	The area of a particle divided by its convex hull area; the imaginary convex hull around it

The total mass and measured density were used to calculate the total volume of the particles. Assuming an ellipsoid based on length and width of the average of the 2D dimensions gives a pseudo-3D height as average value for all particles.

9.5.2 Hydraulic experimental set-up

Filtration and expansion experiments were carried out at three locations: in Waternet’s Weesperkarspel drinking water pilot plant located in Amsterdam, the Netherlands (Figure 9), at the University of Applied Sciences Utrecht, the Netherlands; and at Queen Mary University of London, United Kingdom (Figure 10) and at the University of Applied Sciences Utrecht, the Netherlands (Figure 11 and Figure 12). A schematic overview is presented in Figure 14.

Through filtration and expansion experiments, bed voidage and pressure drop were measured as a function of various linear fluid flow rates and temperatures. Hydraulic experiments were started in fixed bed state, obtained after an initial backwash with full fluidisation, which resembled the typical practical conditions of rapid sand and multimedia filters. By increasing the flow rate, the bed height was carefully observed and measured to determine any change in bed height and consequently average voidage. By measuring the differential pressure, the flow rate of the incipient fluidisation point was detected. By further increasing the flow rate, a sequence of bed voidages and differential pressures was measured to be able to compose an expansion curve. Based on acquired bed voidage, differential pressure, superficial

fluid velocity, particle size and kinematic fluid viscosity, the drag coefficients were determined as presented in Section 9.3.1.

Photographs of particles, technical information about experimental set-up devices and operational procedures can be found in the Supplementary material (Sections 1 and 2).

9.5.3 Dynamic shape factor determination

To investigate the variability of the particle shape factor, the ratio of the measured drag coefficient f_L and the drag coefficient for Carman–Kozeny $f_{L,CK}$, using Equation (54), was calculated. We hypothesised that this ratio would depend on the hydraulic state, *i.e.* on the ratio $Re_\varepsilon/Re_{\varepsilon,mf}$ of the actual modified particle Reynolds number (Equation 6) and that for incipient fluidisation. Inverting the Carman–Kozeny equation, for the measured voidage, velocity and viscosity, it was possible to estimate the average particle size. Accordingly, a *dynamic* shape factor could be determined for various flow rates using a numerical solving method based on Bolzano's numerical intermediate value theorem. This is a straightforward solving method described in: (Apostol, 1967). A simplified equation states:

$$\phi_s = \sqrt{\frac{f_{L,CK}}{f_L}} \quad (115)$$

Where $f_{L,CK}$ is the dimensionless drag coefficient (laminar representation for Carman–Kozeny).

9.6 Results and discussion

9.6.1 Particle properties

Samples of RSF granules were obtained from a full-scale RSF unit operation located at the Waternet facility in Loenderveen, the Netherlands. The applied filter sand range (see Figure 85) was obtained by using sieves of 0.80 and 1.25 mm. This was confirmed by sieving with 10 sieves between 0.6-2.8 mm (NEN-EN 933-2, n.d.), showing that 10 wt-% of the particles were smaller and 1 wt-% were larger than this range, which corresponds to a respective 20% and 1% in terms of the number of particles. We measured an average particle diameter of $d_{50} = 0.90$ mm based on particle counting.

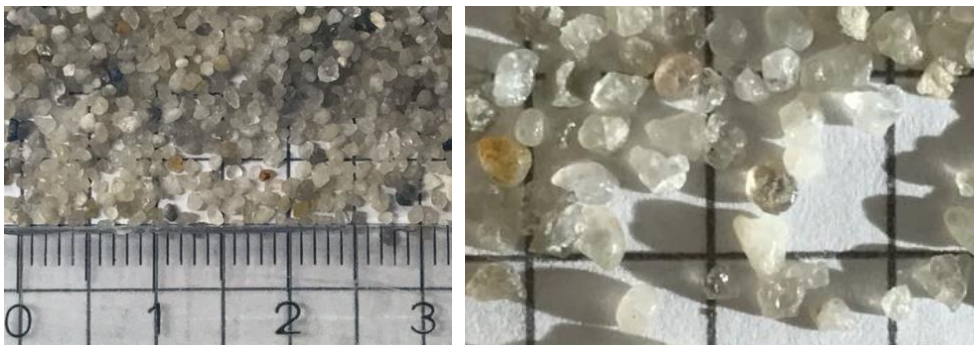


Figure 85 Rapid sand filter granules $0.8 < d_p < 1.25$ mm

The full-colour scan obtained from the A4 flatbed scanner was initially converted into a single-colour picture for maximum particle distinction from which a binary (black and white) picture was created with a pixel size of around 0.01 mm (2,400 dpi). The size of each (black) particle was measured through pixel counting. Observed particles with their particle numbers can be shown as outlines on top of the original scan (see Figure 86). The 4.188 g sample contained 2,040 particles, each analysed by its size, shape and other morphological properties in ImageJ.

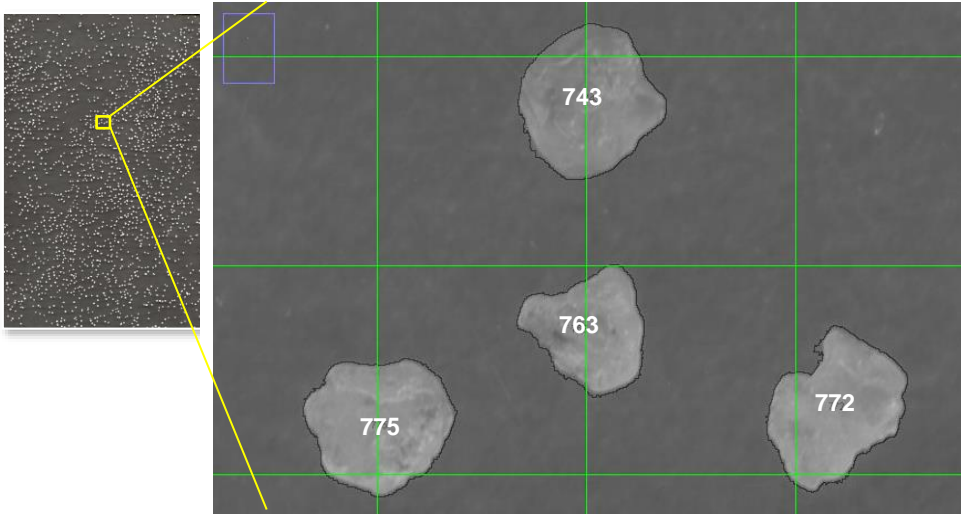


Figure 86 Scanned sample with particle analysis with ImageJ, with particle outlines and particle numbers, with 2 x 2 mm gridlines.

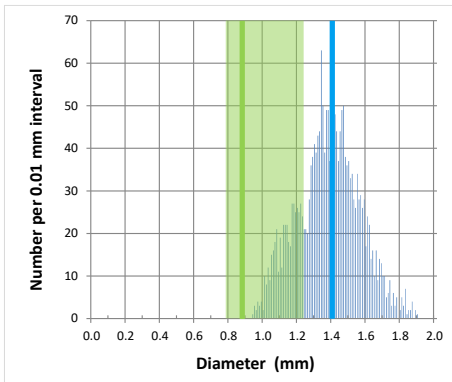


Figure 87 Equivalent diameter (assumed to be a circle): histogram of circle diameter from particle areas of ImageJ (in blue), compared to filter sand specifications (green area). The average diameters based on particle counting (d_{50}) are presented as vertical lines in green (sieve experiment) and blue (ImageJ), respectively.

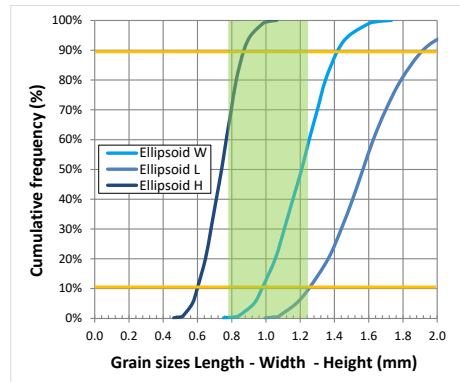


Figure 88 Cumulative frequency grain sizes

Figure 87 and Figure 88 show the measured distribution and cumulative frequency, respectively, of observed equivalent particle diameter. The green areas indicate the specification of the filter material based on information from the supplier of the two sieves (bottom sieve and top sieve). The projected area per particle, determined with ImageJ, was used to obtain the equivalent diameter of a circle resembling the basics of square sieve grids, as illustrated in Figure 87. Giving the exact contours per particle allows for the calculation of an equivalent ellipse with the same area for each particle, giving two independent diameters d_{50} of 1.57 and 1.21 mm on average, with an aspect ratio of 1.30. Assuming that an ellipsoid with these two axes has the same volume as the average particle gives the third diameter of 0.78 mm. This dimension explains the sieve passage as particles are passing sieves in an upright orientation, contrary to the scanned particles lying in a horizontal orientation.

Figure 88 illustrates how smaller particles are obtained which did not pass through the lowest sieve with the smallest mesh size, probably as a result of short sieving time. In contrast, hardly any larger particles were found since they did not pass through the top sieve with the largest mesh size. Figure 88 also shows that the particles are not perfect spheres, as a sieve curve would suggest, but that they are much better described as an ellipsoid with three distinct dimensions: width, height and length.

In sum, it can be concluded that the analysed RSF grains are moderately irregularly shaped, and far from spherical. In the next section, it will become clear why this information is important in relation to decreasing bed resistance for increasing flow rates. Particle analysis using flatbed scans with pseudo-3D image processing is superior to 1D sieve analyses. The determined particle properties of RSF grains are presented in Table 34.

Table 34 Particle properties rapid filtration sand grains

Variable	RSF grains	Unit
Particle sieve sizes	0.80 - 1.25	[mm]
Particle density	2,638 ± 11	[kg/m ³]
Equivalent circle diameter 2D (average) ²⁾	1.38	[mm]
Uniformity 2D (d_{60}/d_{10}) ²⁾	1.26	[-]
Circularity 2D (average) ²⁾	0.73	[mm]
Ellipsoid 3D- d_{50} ²⁾	1.57 - 1.21 - 0.78	[mm]
Ellipsoid aspect ratios 3D - l/b-b/h ²⁾	1.30 - 1.55	[-]
Geldart's type ³⁾	D	

¹⁾ Measured particle size distributions are given in the Supplementary material (Section 4)

²⁾ ImageJ (Ferreira and Rasband, 2012)

³⁾ Geldart's particle classification (Geldart, 1973) type D: spoutable particles

In industrial practice, samples of granules are still commonly sieved to obtain information about the particle size distribution for process monitoring. With this method, the morphological properties of the particles are lost. However, as irregularly shaped particles, and rod-like particles in particular, can realign and pass to lower sieves, this gives a distorted view of the actual particle sizes. The easily acquired particle information, *i.e.* average particle size, is entered accordingly into the drag coefficient or voidage prediction model. In practice, this classical method works well for spherical particles, but it is less accurate for irregularly shaped particles such as RSF grains (Figure 85). Irregularly shaped particles experience anisotropic drag in fixed and fluidised state, due to the surrounding fluid and interactions with adjacent particles and the wall (Mahajan *et al.*, 2018).

9.6.2 Hydraulic experiments and expansion curves

The hydraulic experiments we conducted provided crucial information about differential pressure and bed height in fixed, incipient and fluidised states, as a function of linear flow rates and water temperatures. In total, eight up-flow experiments were conducted for RSF grains at six different water temperatures (6-29 °C). Additional expansion experiments were performed at seven different water temperatures (5-36 °C) to determine the minimum or incipient fluidisation points, causing the first particles to expand as well as allowing the precise expansion behaviour of RSF grains to be determined. For up-flow filtration, the fluid flow was gradually increased until the incipient fluidisation point was reached, where the differential pressure levelled at a maximum value. For moderate fluidised state, the fluid flow was slightly further increased under constant maximum differential pressure. The expansion curve for RSF grains is presented in Figure 89. The measured voidage in fixed bed state varies between $\varepsilon_0 = 0.44 \pm 0.03$. The voidage at the minimum fluidisation velocity is $\varepsilon_{mf} = 0.45 \pm 0.01$. Figure 89 shows the expansion behaviour of RSF grains in the fluidised state. The measured bed voidages at various water temperatures agree reasonably well with the predicted values according to the Carman–Kozeny model. The influence of the water temperature in the fluidised state can be seen in Figure 90. The temperature effect in the fixed bed state was less clearly observable (Figure 89). A moderate linear relationship ($R^2 = 0.99$) between the degree of subsidence % of the packed bed and

water temperature (5-35 °C) was found: $\Delta\varepsilon/\varepsilon = -0.0001T + 0.008$. The temperature dependence of the bed setting is caused by the changes in viscosity of water, which affects the frictional forces acting on the filter bed.

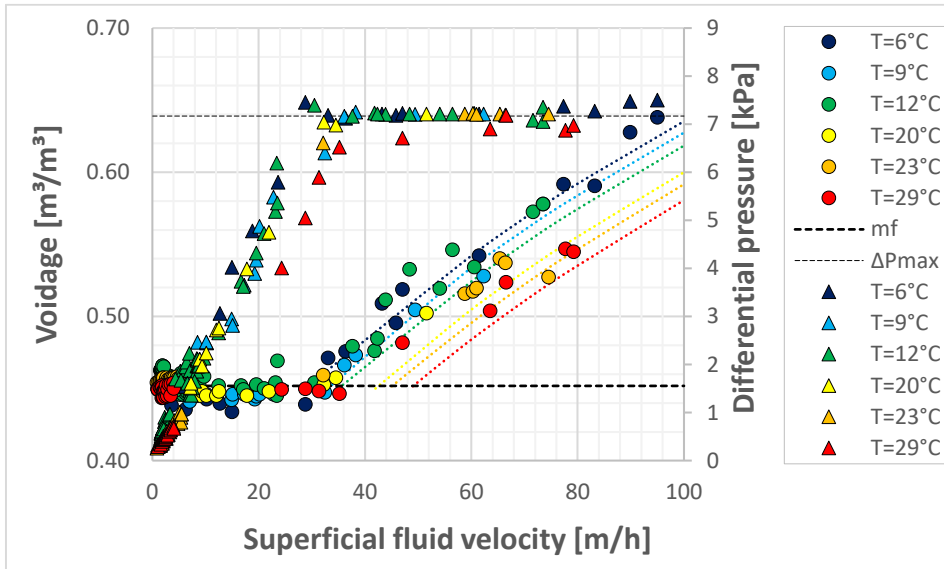


Figure 89 Up-flow filtration and expansion curve for rapid filter sand granules $0.8 < d_p < 1.25$ mm. Experimental voidage (circles), Carman–Kozeny predicted voidage (\cdots) and differential pressure (triangles) against superficial fluid velocity, (- - -) maximum pressure drop, (-.-) voidage at minimum fluidisation.

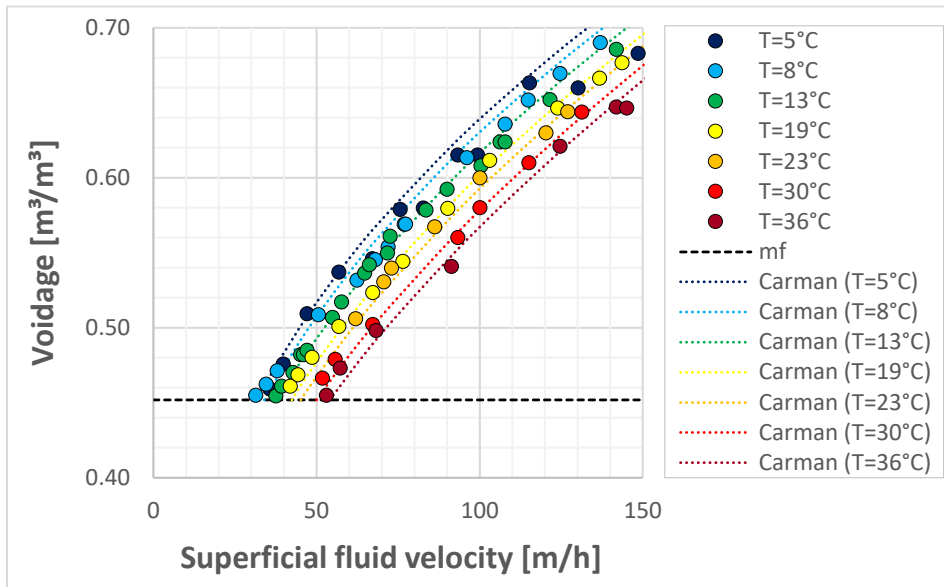


Figure 90 Fluidisation characteristics of rapid filter sand granules $0.8 < d_p < 1.25$ mm. Experimental voidage (circles) and Carman–Kozeny predicted voidage (---) against superficial fluid velocity for six different water temperatures.

Experimental data tabulation (Section 9), minimum fluidisation points (Section 5) and model predictions (Section 3) are given in the Supplementary material.

9.6.3 Measured and predicted drag coefficients

The drag coefficient against the modified Reynolds number Re_ε for RSF grains is presented in turbulent representation f_T in Figure 91 and in laminar representation f_L in Figure 92. In both figures, the Kozeny and Carman (Equation (54)) drag relations are plotted. Figure 91 shows a clear deviation between the measured and predicted values for low Reynolds numbers ($Re_\varepsilon < 10$). In most other literature references (Burke and Plummer, 1928); (Carman, 1937); (Ergun, 1952); (Gibilaro, 2001); (Bird *et al.*, 2007); (Hoyland, 2017), such deviations between measurements and drag models are artificially hidden by the use of logarithmic scales over several orders of magnitude.

For relatively high Reynolds numbers ($Re_\varepsilon > 10$), the predicted Carman values coincide relatively well with the measured values. For low Reynolds numbers

(especially $Re_\epsilon < 5$), the measured f_L values are significantly larger than the theoretically expected $f_L = 180$, corresponding to the Kozeny pore shape factor $K = 180$. The laminar representation of f_L makes changes in drag much more concise compared to the commonly used turbulent representation of f_T . Figure 92 clearly shows that the drag decreases considerably in case the fluid flow increases slightly, under laminar or transitional conditions. This is happening while the particles are still assumed to be packed in the fixed bed state.

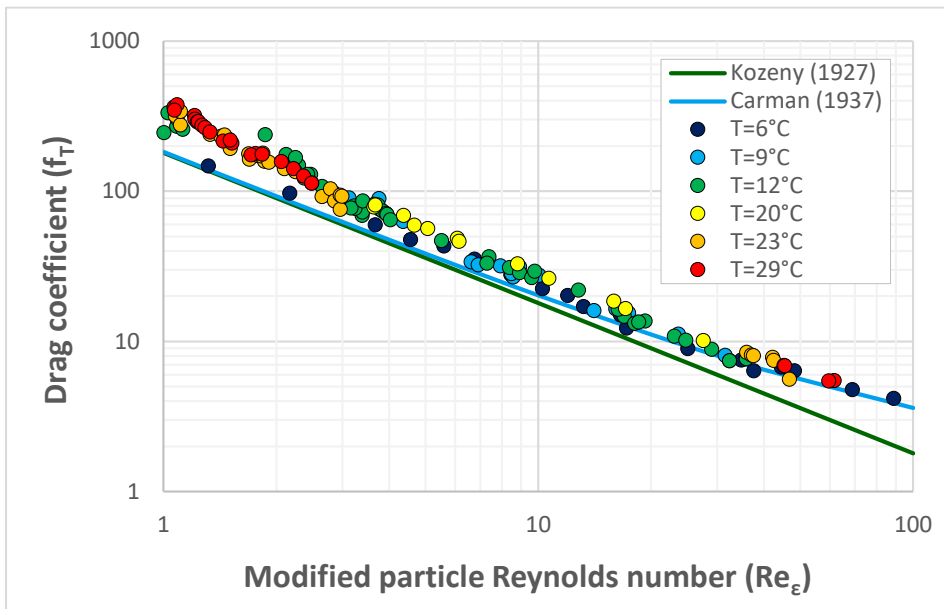


Figure 91 Drag (turbulent representation) f_T against modified Reynolds number for rapid filter sand granules $0.8 < d_p < 1.25$ mm.

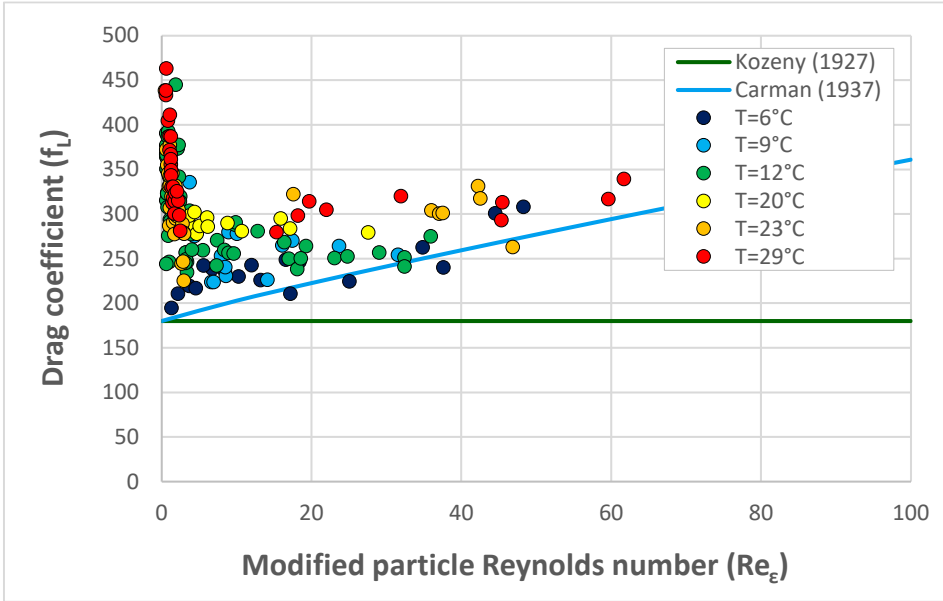


Figure 92 Drag (laminar representation) f_L against modified Reynolds number for rapid filter sand granules $0.8 < d_p < 1.25$ mm.

More information about the Carman model can be found in the Supplementary material (Sections 3).

To show explicitly that the drag decreases mainly in the (supposedly) fixed bed, the ratio of measured to predicted drag $f_L/f_{L,CK}$ is plotted against the Reynolds number ratio $Re_\epsilon/Re_{\epsilon,mf}$ in Figure 93. For increasing flow rates, where $Re_\epsilon/Re_{\epsilon,mf}$ is still well below 1, the ratio $f_L/f_{L,CK}$ decreases rapidly. For every percent that the bed voidage drops, the drag coefficient f_L decreases by a factor 4. The large ratio of measured to predicted drag occurs at $Re_\epsilon/Re_{\epsilon,mf} < 0.5$, which indicates that it cannot be explained by effects occurring around v_{mf} . This will be investigated further in the next subsection.

A practical approach is to use a particle shape factor to compensate for observed deviations in f_L . The use of a shape factor, however, becomes redundant in the fluidised state, since the prediction of the voidage is increasingly consistent with the models for ($Re_\epsilon > 10$) in Figure 92 and Figure 93. We reiterate that the common use of two different shape factors in the literature for fixed beds (Ergun, 1952); (Yang, 2003); (Li *et al.*, 2018) and fluidised beds (di Felice, 1995); (Gibilaro, 2001); (Rhodes, 2008) is remarkable, because it concerns the same particles. Using Equation 115, shape factors were calculated for RSF grains. Figure 94 shows that in the fixed bed

state, the particle shape factor varies between approximately $0.6 < \phi_s < 0.9$. In the fluidised state, however, the shape factor slowly approaches $\phi_s = 1$.

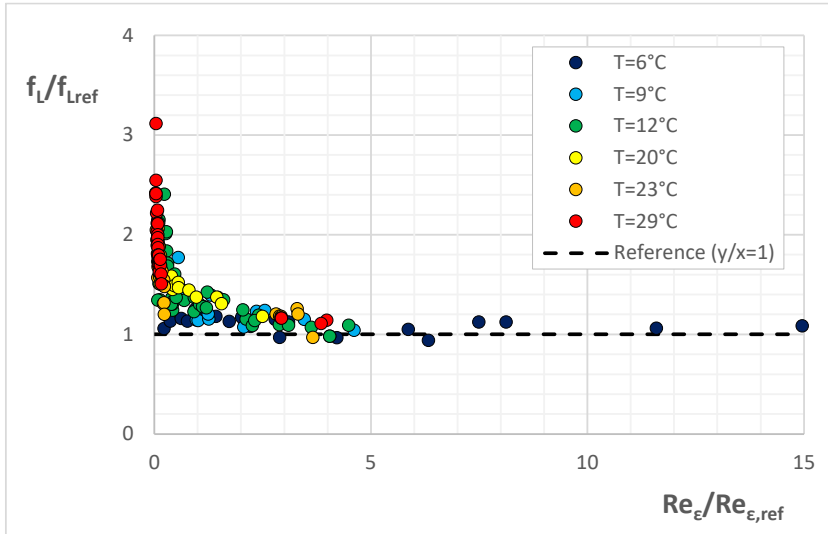


Figure 93 Drag (laminar representation) relative to the Carman–Kozeny drag against modified Reynolds numbers relative to modified Reynolds numbers at minimum fluidisation for rapid filter sand granules $0.8 < d_p < 1.25$ mm.

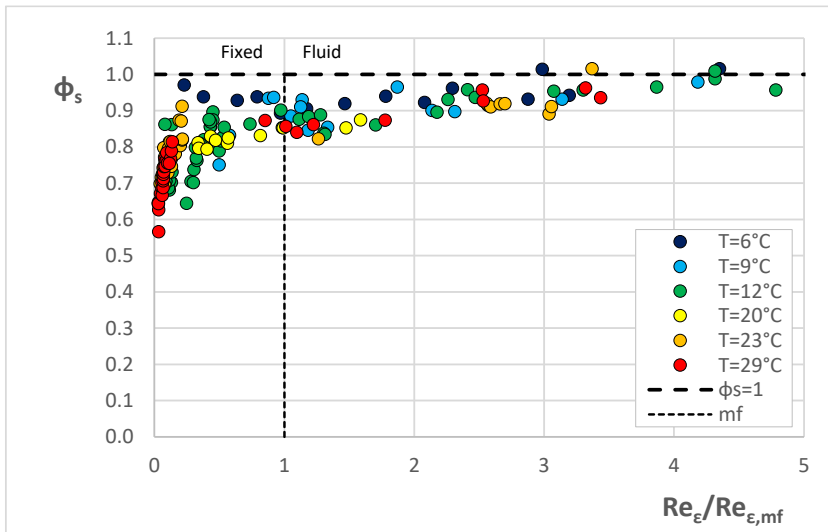


Figure 94 Shape factor against modified Reynolds numbers relative to modified Reynolds numbers at minimum fluidisation for rapid filter sand granules $0.8 < d_p < 1.25$ mm.

9.6.4 Hydraulic explanation for up-flow filtration and ETSW

When a fluid flows in upward direction through a particle bed in fixed state, the fluid exerts a certain drag on the particles. The transition from a fixed bed to a fluidised bed occurs when the pressure drop across a packed bed reaches a constant maximum value, after the fluid flow exceeds the minimum fluidisation velocity. The particles start to elevate, and irregularly shaped particles also show changing orientation, realignment and rearrangement in their packing position. During the pilot plant experiments, the observed bed height decreased slightly (approximately 1%), which can be seen in Figure 95. Videos of RSF grains (Kramer *et al.*, 2020g), as well as calcite pellets (Kramer *et al.*, 2020h), at flow rates well below the minimum fluidisation points, show clearly that particles already start to move locally while overall they remain in a fixed bed state. The collapse of the packed bed caused by ETSW is also demonstrated in four videos.



Figure 95a
Initial fixed bed



Figure 95b
*Fixed bed setting
after t=5 [min] ETSW*



Figure 95c
*Fixed bed setting
after t=30 [min] ETSW*

The collapse of the particles in the fixed beds below the incipient fluidisation point is most likely caused by particle orientation, realignment and rearrangement in their packing position. An unsteady packed bed in moderate up-flow conditions is pseudo-fixed and in a setting state. This results in a decreasing bed voidage and simultaneously in a decreasing drag coefficient, which seems quite contradictory. However, this can be explained by the collapse of local channels (Figure 97) in the

bed, leading to a more uniform flow distribution through the bed and improving the available surface for flow-through (Hassett, 1961). This is the reason why ETSW, as an additional method to a backwash filter recipe, works effectively (Figure 96), since it levels the voidage in the particle bed. In this way, the successful ETSW method proposed by Amburgey (2005) can be explained.



Figure 96 Full-scale RSF during collapse pulsing 40 m/h backwashing scour



Figure 97a Full-scale RSF during ETSW 5 m/h up-flow



Figure 97b Full-scale RSF during ETSW bed, spouting channels

During full-scale operational ETSW procedures, small (1-10 mm) spouting channels were observed: this is shown in Figure 97. The amount and intensity of spouts decreased during the procedure. A plausible explanation is that the up-flow filtration caused the channels to collapse in the bed, leading to a more uniform flow distribution through the bed and improving the available surface for flow-through. We hypothesise that this phenomenon has a positive effect on water quality, since the

magnitude of turbidity and particle count spikes decrease. Therefore, the successful optimisation ETSW filter backwashing procedure proposed by Amburgey (2005) can be explained hydraulically.

9.6.5 Preliminary considerations of hydraulics-based ETSW

According to Amburgey (2005), adjustments in fluid velocity should be limited to the minimal fluidisation velocity. Since this velocity depends on both the filter bed material and on water temperature, optimising the up-flow velocity could become complicated due to different packing materials and seasonal temperature fluctuations. Smaller RSF grains fluidise more easily compared to the larger RSF grains, resulting in a gradual transition. In other words, because of differences in particle size, the minimum fluidisation velocity cannot be determined exactly. In the event that during ETSW velocities occur that are too high, the benefits of bed setting, a more uniform flow distribution throughout the bed and better available surface for through-flow are nullified. Therefore, when optimising the ETSW time, it may be more important to focus on effective bed subsidence instead of focussing on incipient fluidisation. Amburgey (2005) assumed that at least one bed volume would be required to wash out remaining particles. As we provide a hydraulic explanation for improved water quality, this assumption does not need to apply. Therefore, considering this hydraulic explanation, the ETSW time could potentially be shortened to less than one bed volume. This would decrease down-time due to backwashing and increase up-time (filtration time) as breakthrough at restart will be significantly reduced, or even eliminated. With regard to water quality and costs, the elimination of breakthrough at restart will improve the overall bulk quality of the produced water, increase the total volume produced in between backwashes and subsequently save overall production costs. In practice, the first half hour of filtration, after backwashing, is discarded as this contains the highest concentrations of remaining particulates and contamination.

9.6.6 Full-scale consequences of utilising the ETSW procedure

Turbidity is a measure of the amount of particulate matter in water and is one of the most widely used parameters for measuring water quality prior to disinfection (Edzwald, 2011). High turbidity levels can reduce disinfection capacity. Adequate turbidity removal implies the partial removal of pathogens in water (Lechevallier *et al.*, 1991), since most pathogens tend to aggregate with particles. Before 2016, at the full-scale RSF in Loenderveen (the Netherlands), considerable turbidity spikes were detected in the first filtrate after backwash cycles. After a backwash cycle had been completed and the filter returned to operational mode, the turbidity of the first filtrate was measured in four filters (Figure 98). After approximately 30 minutes, the turbidity increased from 0.2 FTU up to 1-3 FTU. A similar elevated pattern could be seen for bacterial levels Enterococci ($N=4/10L$), E.coli ($N=14/10L$) and traces of sulphite-reducing Clostridia ($N=10^3/10L$). The WHO (World Health Organization, 2017) promotes a turbidity threshold of below 0.2 NTU.

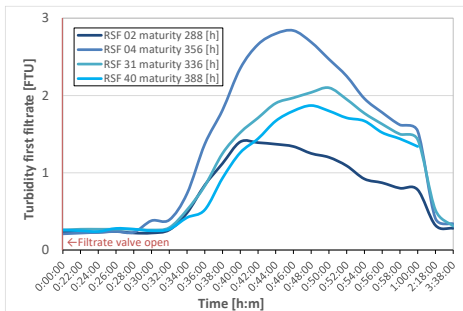


Figure 98 Turbidity measurements of four full-scale RSF first filtrates in Loenderveen before the ETSW procedure was established.

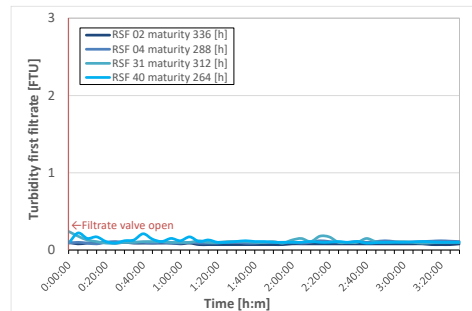


Figure 99 Turbidity measurements of four full-scale RSF first filtrates in Loenderveen after the ETSW procedure was established.

Accordingly, an optimisation process has been started at the full-scale facility in Loenderveen to improve water quality by reducing bacterial breakthroughs. The goal was to decrease the concentrations of bacteria to improve the oxidation and disinfection efficiency in the ozonation unit operation down-stream (van der Helm, 2007). The ETSW procedure was initialised on the full-scale facilities additional to the standard backwash procedure. Furthermore, we investigated whether it was desirable to remove the first filtrate for approximately three hours. After the ETSW

procedure was utilised, turbidity spikes in the first filtrates were excluded (Figure 99) in favour of water quality.

9.7 Conclusions

Our experiments showed that irregularly shaped particles such as RSF grains in fixed beds under moderate up-flow conditions show non-monotonous hydraulic behaviour related to changing orientation, realignment and rearrangement in particle packing position. This happens in such a manner that the bed offers the maximum flow passage, *i.e.* voidage to the fluid. Initially, the bed voidage, the flow-through interface available in the bed, as well the drag decrease and accordingly increase for larger fluid flows. These phenomena also affect the volume-based voidage prediction, something that to the best of our knowledge has not been elucidated in the literature.

In the field of engineering, a shape factor is applied to compensate for the above aspect in the fixed and incipient fluidisation but is omitted when the fluidised state is described. In this research, it was shown that such a shape factor is not a constant particle property but is dependent on the fluid properties as well. This dynamic shape factor for irregularly shaped RSF grains increases from approximately 0.6 until 1.0 in fairly fluidised state. The use of constant shape factors regarding natural, irregularly shaped granules is therefore not recommended. Our new straightforward image analysis method, based on a weighted particle sample to estimate the mean measures of spheroids, shows that sieve measures are not representative of natural, irregularly shaped granules. Based on experimental data obtained in this work, it is shown that, for increasing fluid flow rates, the fixed bed voidage decreases slightly (approximately 1%) while the drag coefficients decline to a considerable degree. The drag coefficient reached values up to 450 (in laminar representation), which is considerably larger than the well-known Kozeny value of 180.

The reduction in bed voidage as well as bed resistance is due to the realignment of the particles in the packed bed and the collapse of flow channels created during a normal backwash procedure. Particle orientation, realignment and rearrangement implies unstable fixed beds that become denser in laminar up-flow conditions. This results in a decreasing bed voidage and simultaneously in a decreasing drag coefficient. A complete fluidised state, *i.e.* exceeding the minimum fluidisation velocity, is not necessary. In addition, besides the particle size, also the particle

shape is a decisive factor in the phenomena occurring in the particle beds. The collapse of local channels in the bed leads to a more uniform flow distribution through the bed and improves the available surface for flow-through. In this way, the successful ETSW method proposed by Amburgey (2005) can be explained.

9.8 Recommendations

With the knowledge acquired during these experiments, the ETSW procedure can, in future research, be further optimised by adjustments to the up-flow velocity and time.

During our experiments, it was possible to capture the almost unnoticeable changes in the particle bed on video. In a full-scale installation, real-time monitoring of the particle collapse in the rapid sand filter bed is practically impossible. Thorough pilot plant research is required to fully understand the specific processes of a particular water treatment. Every water treatment plant has a different context *i.e.* water quality (load of particulate material), bed composition, different process strategies and different water temperatures.

Since the configuration of the particles in the packed filter bed is generated by frictional forces, it is recommended to investigate alternative methods that include frictional forces, so that subsidence can take place. Although filter resting could also be a solution to acquire bed setting and prevent the first filtrate turbidity spike after the backwash expansion, it reduces the operational up-time. In order to extend the hydraulic impact discussed here to an even more effective ETSW, a model to predict the permeability and bed setting of the filter bed needs to be further substantiated and developed to be able to optimise the ETSW procedure. The newly proposed pseudo-3D ImageJ analysis method can be used for future CFD modelling research, taking into account the influence of non-spherical particles, in which the obtained measures of the ellipsoids can be put to good use.

9.8.1 Supplementary material

Supplemental data for this article can be accessed at:

<https://doi.org/10.1016/j.watres.2021.117085>

<https://ars.els-cdn.com/content/image/1-s2.0-S0043135421002839-mmc1.docx>

Contents		page
1	Photographic material	1
1.1	Rapid sand filter granules	1
1.2	Filter bed setting in experimental set-up	1
1.3	Full-scale rapid sand filtration	2
1.4	Full-scale filtration states	2
2	Experimental set-up	3
2.1	Filtration and expansion columns	3
2.2	Concise drinking water treatment processes	3
2.3	Physical properties of water	4
2.4	Devices used for particle characterisation	4
2.5	Procedure expansion experiments	5
2.6	Procedure filtration experiments	5
2.7	Voidage and expansion calculation	5
3	The Carman–Kozeny model for laminar and turbulent flows	7
3.1	Laminar flow in granular beds	7
3.2	Emphasising different flow regimes	7
3.3	Transitional water flow in granular beds	9
3.4	Turbulent water flow in granular beds	10
3.5	Non-laminar water flow in granular beds	10
3.6	Drag coefficient reduction caused by voidage drop	11
4	Particle properties	12
5	Incipient fluidisation	13
6	Videos	14
7	Nomenclature	16
8	References	18
9	Experimental data	20
9.1	Rapid sand filter granules data (ETSW up-flow)	20
9.2	Rapid sand filter granules data (expansion data)	22-25

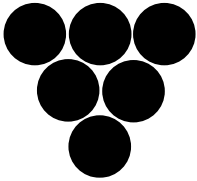
Granular activated carbon

fluidisation characteristics in water



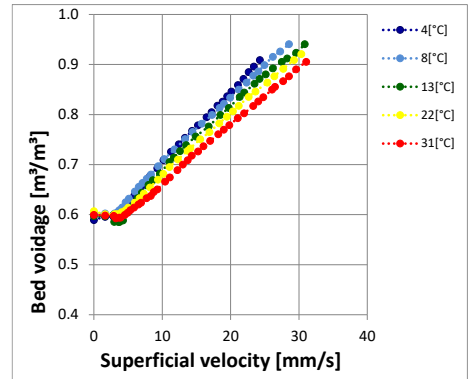
- Polydisperse
- Non-spherical
- Porous

$$\varepsilon \approx 0.6$$



- Monodisperse
- Spherical
- Solid

$$\varepsilon \approx 0.4$$



- ▶ Estimating the expansion of granular activated carbon (GAC) in water is complex
- ▶ The incipient porosity of GAC is much higher compared to solid particles
- ▶ Combining fluidisation and characterisation experiments enables fluidisation modelling
- ▶ GAC fluidisation modelling is complex but possible

Keywords Drinking Water Treatment; Liquid-Solid Fluidisation; Granular Activated Carbon; Green-based Materials; Expansion Characteristics; Porosity Prediction Modelling

Chapter 10

Carbon Expansion Conundrums

“The expansion behaviour of irregularly shaped, polydisperse and porous GAC grains is significantly more complex than the expansion behaviour of, monodisperse solid spherical particles. Nevertheless, they can resealable well be predicted with an empirical model, but GAC is subject of change due to attrition caused by an abrasive character of the bed during repetitive backwashing as well as particle growth due to biological activity.”

This article was accepted in *Advanced Powder Technology Journal* (17/6/2021).

Fluidisation characteristics of granular activated carbon in drinking water treatment applications

O.J.I. Kramer, C. van Schaik, P.D.R. Dacomba-Torres, P.J. de Moel, E.S. Boek, E.T. Baars, J.T. Padding, J.P. van der Hoek

The article can be found online at:

<https://doi.org/10.1016/j.appt.2021.06.017>

10 Fluidisation characteristics of granular activated carbon in drinking water treatment applications

10.1 Abstract

Granular activated carbon (GAC) filtration is an important unit operation in drinking water treatment. GAC filtration is widely used for its filtration and adsorption capabilities as a barrier for undesired organic macro- and micro-pollutants. GAC filtration consists of two successive phases: adsorption and filtration, capturing the impurities from the water in conjunction with a backwash procedure in which the suspended particles are flushed out of the system. Available literature predominantly focusses on adsorption. A less frequently discussed but nevertheless equally crucial aspect of this operation is the backwash procedure of GAC beds. To prevent accumulation of suspended particles and to avoid additional operation costs, optimal backwashing is required. Another factor is sustainability: water utilities are showing increasing interest in exploring new sustainable GAC media. As these have different bed expansion tendencies due to different GAC characteristics with varying geometries, operational developments are needed for prediction models to estimate the expansion degree during backwashing. The prediction of the bed expansion of GAC is complex as the particles are non-spherical, porous and polydisperse. Through a combination of advanced particle laboratory and fluidisation experiments, we demonstrate a new approach which leads to an improved expansion prediction model for the backwashing of GAC filters.

10.2 Introduction

Granular activated carbon (GAC) filtration is widely applied in advanced drinking water treatment plants for its filtration and adsorption capabilities as a barrier for undesired macro- and micro-pollutants (Bandosz, 2006); (Crittenden *et al.*, 2012); (Howe *et al.*, 2012). Increasing levels of organic micro-pollutants (OMP) in surface water used as source for drinking water production have led water supply companies in the Netherlands to integrate activated carbon technologies in their drinking water treatment plants (van der Hoek *et al.*, 1999). GAC is regenerated every 1-3 years to destroy the adsorbed components contained on its surface. The GAC filtration process consists of two successive phases. During the filtration and adsorption phase, suspended solids and dissolved organics are removed from the water through filtration and adsorption, respectively. Accumulation of suspended solids increases the head loss. When a head loss setpoint is exceeded, the accumulated particles are removed from the GAC filter during the backwash phase through an up-flow water stream and additional air scouring. For reliable and safe drinking water production, a precise specification of backwash rates for filter cleaning is needed. Therefore, robust and flexible treatment processes require thorough design specifications and process control of backwash rates for filter cleaning (Bosklopper *et al.*, 2004); (Rietveld, 2005). Regarding GAC filtration, the scientific literature focusses mainly on the adsorption capacity of GAC (Perrich, 1981); (Bansal and Goyal, 2005); (Marsh and Rodríguez-Reinoso, 2006); (Velten, 2008); (Çeçen and Aktaş, 2010); (Chowdhury *et al.*, 2012) and less on the backwashing insights and challenges posed by filters.

Although significant progress has been made in recent decades towards the accurate prediction of the expansion of uniform, non-porous and spherical media (Hunce *et al.*, 2018), limited work has been published on the fluidisation characteristics of polydisperse, non-spherical and porous GAC grains in water. Due to the growing importance of GAC filtration in the field of water treatment, a thorough understanding of the expansion behaviour of GAC facilitates the ability to improve the accuracy of bed expansion predictions. Operational constraints of the GAC filters, such as the degree of bed expansion and particle bed stratification, are determined by the water temperature, water flow, GAC particle size, density, shape and size distribution. Consequently, the accurate prediction of the expansion degree of GAC beds is complex. To cope with fluctuations and variations, full-scale GAC filters are commonly over-designed (Bosklopper *et al.*, 2004). To meet sustainability

goals (Ray and Jain, 2011); (Filho and Sümer, 2015); (Marques *et al.*, 2015), water companies are exploring the use of more sustainable raw materials for drinking water treatment. Traditionally, GAC is manufactured from coal, but the use of sustainable materials (Naushad and Lichtfouse, 2020) such as coconut shells and wood, is gaining popularity. Due to the differences in raw materials and manufacturing processes, different GAC granules also have different particle properties. Therefore, the transition to alternative GAC media also has implications for the process control of GAC filters, both in the filtration phase and in the backwashing phase. Changing GAC media can lead to two main operational problems: media washout and solids accumulation. If backwash velocities are too high, media washout is likely to happen. This results in high economic losses for water companies. If backwash velocities are too low, solids accumulation or the formation of mud balls can occur. This not only affects the filter performance, but it also leads to increased backwashing operations such as a higher frequency, again resulting in increased operational expenses. Another problem with fluidisation of GAC is that the particle size distribution (PSD) might adversely affect the water quality. GAC filters need to be stratified (Howe *et al.*, 2012); (Frank *et al.*, 2015) to prevent the movement of contaminant-saturated GAC particles to lower parts of the bed, which increases the risk of being desorbed and thus the risk of compromising the effluent of this treatment process. Understanding the fluidisation behaviour of porous media, and GAC in particular, can substantiate the decision of water companies to switch to more sustainable materials. Therefore, the need for knowledge about the GAC fluidisation behaviour is of major importance.

Scientific papers, with some dating back as far as to the 1920s (Kozeny, 1927); (Carman, 1937); (Ergun, 1952); (Richardson and Zaki, 1954), were originally derived specifically for spherical particles to describe the hydraulic behaviour of fluid flows through packed or fluidised beds. These models were often used to describe the hydraulic behaviour of non-spherical particles on the basis of particle shape correction factors intended to describe the particle's morphology through sphericity, surface area to volume ratios or other types of correlations using spheres. *De facto*, the granular media involved in water treatment processes, and especially GAC media, are non-spherical. Several experimental investigations concerning activated carbon fluidisation and particle size distributions have been performed. Experimental data presented by van Lier (1984) revealed that the different models applied to describe the fluidisation behaviour of different GAC types performed well only for specific carbon types and conditions. Similarly, findings reported by Akkoyunlu

(2003) show that the proposed models, based on the Richardson–Zaki model, seem to fit well but also had limitations in terms of accuracy and application. Dabrowski *et al.* (2008) proposed empirical models to predict the media expansion for specific GAC types assuming that the fluidisation velocity is inversely proportional to the water viscosity. The prediction accuracy increased when the model was corrected for temperature, depending on the type of commercial carbon that was analysed. Sholji (1987); Trussell and Chang (1999); Clements and Haarhoff (2004); Ujhidy *et al.* (2008) studied the expansion of filter media with Carman–Kozeny or Ergun-like equations using shape factors and model modifications to fit the experimentally obtained data or to improve the prediction accuracy. More recently, Nikam and Mandal (2020) used an Ergun-based approach to study the fluidisation of GAC particles, albeit in a gas-solid fluidised bed. Hoyland (2017) proposed a general model applicable to granular fixed and fluidised beds based on fundamental hydrodynamics for porous beads, based on the hydraulic conductivity approach of Carman–Kozeny. No detailed information was provided about the voidages of the examined particles, so it is unclear if this model is suitable for porous beads such as GAC. Hunce *et al.* (2016) and (2018) carried out accurate fluidisation experiments with porous media and laboratory experiments to obtain the particle and skeletal densities. For the expansion prediction, they used a specific drag relation based on similar Ergun and Carman–Kozeny principles. More recent research used computational fluid dynamics (CFD) modelling to study the behaviour of non-spherical particles: Cornelissen *et al.* (2007); Zhang *et al.* (2012); Samstag *et al.* (2016); Blais and Bertrand (2017); Mema and Padding (2021); Cahyadi *et al.* (2017) applied CFD for GAC media. Despite the academic insights reported in these works, neither effective voidage prediction models were proposed, nor thorough information was shared regarding scrutinised GAC particle properties. Still, this information is crucial to be able to describe the fluidisation behaviour of GAC in filter backwashing for water treatment processes.

In general, there is no agreement which model is the most adequate for describing the fluidisation characteristics, *i.e.* bed voidage, of irregularly shaped, polydisperse and porous media in liquid-solid fluidisation processes. It is common practice to use shape factors to correct for particle diameters to improve numerical results. In addition, regarding GAC grains, there is no consistent procedure detailing how to cope with the wide range of fixed bed porosities at minimum or incipient fluidisation. The *classical* models are based on fixed bed and incipient porosities for solid spherical particles with porosity values around 0.4. The porosities for GAC media at

minimum or incipient fluidisation are in general considerably higher, with values between 0.50-0.65 (Crittenden *et al.*, 2012). This is caused by the irregular shape combined with large particle size distribution of GAC media. During fluidisation, the bed stratifies: the large particles migrate to the bottom region of the bed and the smaller particles to the top of the bed (Clements, 2009). Since these large and small particles are then no longer mixed, the voidage will be determined by packing of highly irregular particle shapes and therefore relatively higher than for more spherical particles. The voidage, however, is relatively unstable, *i.e.* it is the loosest possible configuration and can decrease considerably under the influence of external factors (Kramer *et al.*, 2021c). This voidage can be determined by fluidising the GAC filter bed and then allowing the particles to settle gradually. The minimum fluidisation point thus gives crucial information (starting point) for determining the backwash operation (Anderson and Chescattie, 2003). The influence of the backwash on voidage is crucial and needs to be considered when measuring this variable, *i.e.* minimum fluidisation velocity and voidage (Clements, 2009); (Howe *et al.*, 2012).

Regarding fixed bed and incipient voidage of porous GAC, there is no agreement in the scientific literature either. Worch (2012) mentioned bed fixed porosities between 0.35-0.40. Sholji (1987); Knezev (2015) found similar values between 0.38-0.42. Velten (2008) and Clements (2009) found slightly higher values for several GAC types between 0.39-0.52 and van Lier (1984) measured fixed bed porosities for several GAC types between 0.58-0.62, which is in line with values reported in the standard work by Crittenden *et al.* (2012), and Chowdhury *et al.* (2012) gave more general values between 0.5-0.8. Regarding minimum fluidisation porosities, Nikam and Mandal (Nikam and Mandal, 2020) presented incipient porosities between 0.40 and 0.45. Pushnov (2006) mentioned the dependency of the fixed bed voidage on the ratios of the vessel to the grain diameter and the shape of the grains. This had already been found by Ergun (1952) for incipient porosities. In many publications considering filter backwashing, the degree of bed expansion as a function of the bed height: $E = L/L_{mf} - 1$ is used instead of the voidage: $L/L_{mf} = (1 - \epsilon_{mf})/(1 - \epsilon)$. This is most likely because operational GAC filters are typically expanded for 25% < E < 30% for 20-30 minutes with a main focus on bed heights and a smaller focus on porosities (Anderson and Chescattie, 2003). To our knowledge, no model exists that accurately describes the fluidisation behaviour of activated carbon grains that differ in particle size, PSD, shape and morphology and that have low particle-to-fluid density. The classical hydraulic models in the reviewed literature provide limited applicability for irregularly shaped media with high incipient porosities, which limits

their applicability. The present study seeks to close the knowledge gap regarding the fluidisation behaviour of activated carbon grains for drinking water production applications.

The aim of this research was to gain insight into the fluidisation behaviour and the relation with characteristics of granular activated carbon grains applied in water treatment processes. This was done by performing advanced laboratory measurements, conducting hydraulic multiphase flow experiments and exploring the possibility of modelling the voidage using classical models as well as empirical data-driven models based on symbolic regression. The following factors with regard to the expansion characteristics of GAC were investigated:

- Particle size and shape: high degree of non-sphericity, large polydispersity
- Particle density: due to the porous character of GAC media, multiple densities can be defined based on the packing and wettability on the rate of imbibition and adsorption of constituents from the water phase
- Particle behaviour: particle orientation and re-arranging and changing drag
- Particle change: attrition due to abrasive character of the bed during repetitive backwashing as well as particle growth due to biological activity

For an extensive exploration, nine different GAC types were examined with a wide variety of grain size, particle shape, degree of polydispersity and raw materials. This work focuses on the liquid-solid fluidisation. Air scouring is not taken into consideration.

10.3 Materials and Methods

10.3.1 Particle selection - a wide variety in properties and sources

For this research, nine different GAC samples were selected and analysed as presented in Table 35. The GAC types can be divided into three different categories: spherical (*balls*), non-spherical (*granular or rock-like*) and extruded (*rod-like*). An example of a granular GAC particle is shown in Figure 100.

Additional photographic material of examined GAC media is provided in the Supplementary material (Section 1).

Table 35 Examined GAC types ¹⁾

Grain material	Supplier	Source	Shape	d_{10} ³⁾	d_{50}	d_{90}
Aquasorb K-6300	Jacobi	Fossil-based	Granular	0.77	1.15	3.10
Aquasorb K-6300 ²⁾	Jacobi	Fossil-based	Granular	n.a.	n.a.	n.a.
Aquasorb KGA	Jacobi	Green materials-based	Granular	0.67	1.07	2.62
Filtrisorb 300C	Chemviron	Fossil-based	Granular	0.66	0.90	2.24
Filtrisorb TL830	Chemviron	Fossil-based	Granular	0.99	1.31	2.77
Norit GAC 830	Cabot	Green materials-based	Granular	0.64	1.01	2.73
Supra						
Norit RB 4C	Cabot	Green materials-based	Extruded	3.73	5.16	9.36
Norit ROW 0.8	Cabot	Green materials-based	Extruded	0.81	1.19	2.72
Supra						
Resorb HC	Jacobi	Fossil-based	Granular	0.60	0.90	2.64
Saratech Spherical	Blücher Technologies	Polymer-based	Spherical	0.41	0.42	0.53

¹⁾ Determined with a Camsizer (Retsch-Technology, 2007)

²⁾ Long-term GAC from a full-scale filter with a retention time of approximately 2-3 years

³⁾ $d_{10,min}$ is the particle size for which 10% of the particles are smaller. Min refers to the width of the particles

A Retsch (RT 6.5) sample splitter was used to obtain representative GAC samples for the reproducibility of the research analyses. Samples were washed to remove dust and fine particulate material, dried and stored for particle characterisation. GAC samples were then kept in water for six months before performing fluidisation experiments. Samples were periodically stirred to achieve the highest possible wetting degree of the internal pores. Locally produced drinking water was used in all experiments.

**Figure 100** Filtrasorb TL830 GAC

10.3.2 Porous media - dry and wet conditions

In the literature, the terms 'voidage' and 'porosity' are often used interchangeably. For this research, we use the term 'voidage' in the same way as for solid particles, defined as the fraction of the total volume, which is open space available for the fluid to flow around the particles; thus, the external porosity is similar to the voidage. The internal porosity is defined as the ratio of the internal pore volume to the whole nominal volume of a porous particle.

Unlike impermeable solid granular materials, porous GAC particles exhibit multiple densities and porosities based on different volumetric definitions (van Lier, 1984); (Sereno *et al.*, 2007); (Worch, 2012); (Hunce *et al.*, 2018). Inclusion of closed and/or open pores and absorption of water can significantly influence the density (Hunce *et al.*, 2016). For dry activated carbon, the mass and volume of pure coal without internal pores yields the absolute density ρ_a . The skeletal density ρ_s includes the closed pores as well. Including the (dry) open pores yields the particle (or envelope) density ρ_p . Taking the interparticle void space, or 'external porosity', into account yields the bulk density ρ_{bulk} which is usually the density provided by suppliers. A schematic overview is presented in Figure 102. Prolonged submersion of GAC causes the open pores to absorb water, increasing the mass of the particles. The volume of water absorbed per mass of dry GAC is defined as the open pore volume or OPV, usually expressed in litres per gram. Complete filling of the open pores can usually only be achieved under vacuum (Sereda and Feldman, 1970). As a vacuum is not applied in practice during the backwash of the investigated GAC particles, this is outside the scope of the current research. Therefore, in this research, open pores (Peel *et al.*, 1981) were defined as the internal voids penetrated by water upon prolonged immersion for at least six months. The particles used in the experiments were wetted before and submerged during the fluidisation experiments. A main emphasis is therefore placed on the 'wetted' state of activated carbon. Three states of wetting can be defined: oven dry (OD), saturated surface dry (SSD) and wet surface (WS) conditions, as respectively shown in Figure 101.

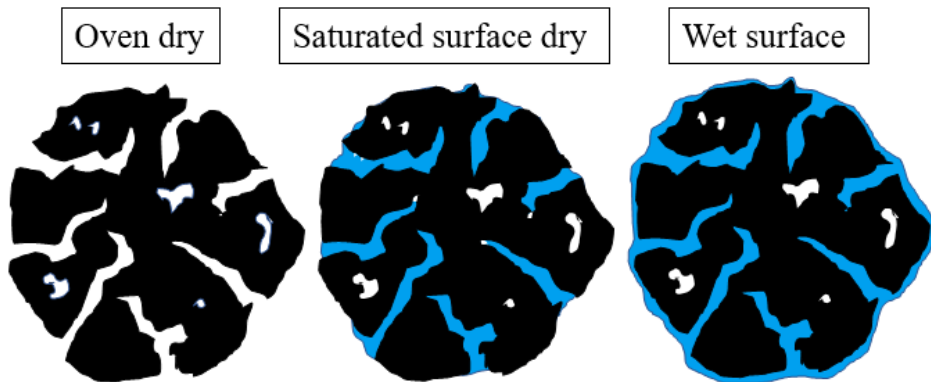


Figure 101 Illustrations of oven dry, saturated surface dry and wet surface granular activated carbon pore structure (Peel *et al.*, 1981).

The saturated surface dry mass (SSD mass) is defined as the oven dry mass (OD mass) added to the mass of water inside the open pores, excluding water on the surface of the particles, as visualised in Figure 101. In practice, a porous sample retrieved from immersion liquid is covered with a surface film that contributes non-negligibly to its mass (Wolf, 1995). This state is addressed as wet surface condition (WS condition), as seen in Figure 101. The difficulty in differentiating between mass contribution of water on surface and water in pores complicates determining the SSD condition, which was emphasised most recently by Hunce *et al.* (2018) and Cummins *et al.* (2017). To determine the SSD wet mass and wet density, information about the water permeable portion of the pores is required. Multiple experiments were used to acquire this information, ranging from immediate experiments to time-consuming experiments, the latter being eventually chosen to determine definitive values. According (Edzwald, 2011) and (Hunce *et al.*, 2016), a reproducible SSD condition is difficult to achieve and requires a certain level of experience and skill to perform. For this research, a schematic overview of a single GAC particle was used, presented in Figure 102, to distinguish external and internal parts of the particle. To differentiate the voids in the particle, open and closed pores are included as well as the solid part, which is called absolute carbon. Closed pores are defined as pores that are inaccessible to water. The open pores can be partially or entirely filled with water to indicate the wetting state of a particle. All necessary equations are based on the schematic representation of a single GAC particle (Figure 101) for OD, SSD and WS conditions, as discussed by Hunce *et al.* (2016). The model in Figure 102 was used accordingly to derive the equations regarding bulk, particle, skeletal, wet density and open pore volume.

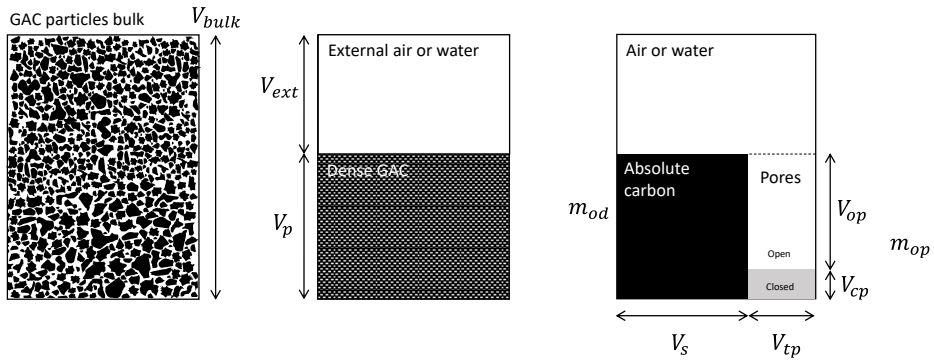


Figure 102 Schematic model representation of a GAC particle. V_{bulk} is the bulk volume or GAC particles including external voids, V_{ext} is the external volume of the external voids, V_p is particle volume including internal pores, m_{od} is the oven dry particle mass, V_{op} and m_{op} are the open pore volume and mass, V_{cp} the close por volume, m_{op} represents the open pore mass which can be dry or wet, V_s is the skeletal volume and V_{tp} is the total pore volume.

The relation between the bulk density ρ_{bulk} , (internally dry) particle density ρ_p and the external porosity ε_{ext} (voidage) is given by van Keulen (1973); Sereno *et al.* (2007); Worch, (2012); Huncce *et al.* (2016):

$$\varepsilon_{ext} = 1 - \frac{\rho_{bulk}}{\rho_p} \quad (116)$$

Next, the wet density ρ_{wet} (open pores filled with water) can be calculated as a function of the particle density, water density ρ_w and the open pore volume *OPV* (Worch, 2012) as:

$$\rho_{wet} = \rho_p(\rho_w OPV + 1). \quad (117)$$

The wet density ρ_{wet} as a function of the *OPV* and skeletal density ρ_s was derived accordingly as Equation (118).

$$\rho_{wet} = \rho_s \frac{1 + \rho_w OPV}{1 + \rho_s OPV} \quad (118)$$

Detailed information about GAC modelling, nomenclature and derivations can be found in the Supplementary material (Section 7).

10.3.3 Laboratory measurements - particle characterisation

Particle size and shape determination

A number of methods were used to define the size and morphology of particles. First, *classical* sieving, a frequently applied method, was used to physically separate particles using a mesh. Particles smaller than the mesh size can pass through to the next mesh and larger particles will be retained in the mesh. Second, static image analysis was used, where a referenced picture or scan of a GAC sample was analysed using specialised software such as ImageJ (Ferreira and Rasband, 2012) to analyse pixels and a microscope with internal software (Keyence, 2014). The software computes the size and different morph parameters of each particle in the picture. This method generates different dimensions of irregularly shaped particles and many other morphological parameters. Third, dynamic Camsizer image analysis was used (Retsch-Technology, 2007) to analyse a large number of falling particles with high-speed cameras coupled with specialised software. Detailed information about particle characterisation, applied methods and morphological properties of examined GAC media is provided in the Supplementary material (Section 2). Experimentally obtained data is also shared in (Kramer, 2021f).

Particle density and wetting degree determination

Oven dry mass and bulk density

The GAC samples were dried in an oven at 150 °C for two days, to guarantee optimal drying and at the same time prevent possible loss of material due to the heating. The weight m_{od} was measured on scale (type Kern FKB). The bulk density ρ_{bulk} was determined according to Equation (119) by measuring the bulk volume in a graduated cylinder (Clements, 2009).

$$\rho_{bulk} = \frac{m_{od}}{V_{bulk}} \quad (119)$$

Note that the bulk volume V_{bulk} and thus the external porosity is dependent on the arrangement of the particles. Variations can be observed once the bulk collapses when vibrations are applied and when particles are stratified, such as during the expansion experiments.

Skeletal density

Two methods were employed to determine the skeletal density.

Helium pycnometry

First, helium pycnometry (type using an AccuPyc 1330) (CEFIC, 1986); (Davidson and Perkin, 2013) was applied. Helium was added under pressure in the specialised apparatus, entering all accessible pores in a dry GAC sample. Based on the pressure increase and added helium, the helium impenetrable volume was determined which, combined with the dry mass of the sample, yields the skeletal density $\rho_s = m_{od}/V_s$. More detailed information is elucidated by Sereno (2007).

Hydrostatic weighing

Subsequently, hydrostatic weighing took place. This is an established technique for density determination (van Keulen, 1973); (Wolf, 1995) which applies the Archimedes principle (Nor et al., 2009) to determine the volume of a sample by measuring the weight loss upon submersion caused by the buoyant force. The skeletal or ‘in-accessible by water’ density was determined using:

$$\rho_s = \frac{\rho_w}{1 - \frac{m_{sub}}{m_{od}}} \quad (120)$$

Where m_{od} is the oven dry mass and m_{sub} the submerged SSD particle mass.

Detailed information about the helium pycnometry and hydrostatic weighing techniques can be found in the Supplementary material (Section 3) and in (Dacomba Torres, 2018) and (Kramer, 2021f).

Wet density and SSD mass

Three methods were employed to determine the water penetrable portion of the activated carbon samples.

Wet bulk

Wet bulk GAC samples were placed in a calibrated graduated cylinder. Water was removed until slightly above the sample and excess water was removed with a paper towel. Any air pockets were removed. The measured total particle volume in the graduated cylindrical column is indicated by V_{bulk} . The mixture was weighed m_{meas} , and the SSD mass of the GAC sample was defined as:

$$m_{ssd} = m_{meas} - \rho_w(V_w - V_{bulk}(1 - \varepsilon_{ext})) \quad (121)$$

To find m_{ssd} , the external porosity ε_{ext} obtained from the fluidisation experiments (Sections 10.3.4 and 10.4.3) was used.

Drained sieve

The wet samples were placed on a sieve and drained; excess water was wiped away with a paper towel until the samples appeared visually dry. This technique is commonly used (CEFIC, 1986); (Djerbi Tegger, 2012); (Hunce *et al.*, 2016) but the inability to determine exactly when SSD conditions are reached makes the results of this method rudimentary at best. The tendency to retain water on the surface differs between carbon types, and it was estimated that excess water was still present even after repeatedly wiping away the water, especially for the smaller grains such as Saratech Spherical and Norit ROW 0.8 Supra.

Drying log

To identify the SSD condition, or rather the more explicit (Equation (122)), a total of 42 drying logs were measured. Representative samples of 5-25 [g] of each GAC-type were administered in wet surface condition (Figure 101) in a thin layer on a non-absorbent surface. The weight of these samples was measured on a scale connected to a data logger for three to six days at room temperature in a closed fume hood with no ventilation. Initially, a linear, constant drying rate was expected, characterised by an excess of liquid in the surface pores of the porous particles (Yiotis *et al.*, 2007). The weight decrease during this period is assumed to be predominantly caused by the evaporation of the adhesion layer (water on the surface) (Wolf, 1995). The initial drying rate was expected to decrease significantly, or drop to zero, when surface dry conditions are met (Mujumdar, 2006). During this period, drying is controlled by mass transport mechanisms within the porous material (Yiotis *et al.*, 2006), which will not be discussed in this research. SSD mass, or m_{ssd} ,

was identified by extrapolating the last part of the drying log to $t=0$, as seen in Section 5.6, Figure 103. The water content at any point of the measurement could be determined after the oven dried mass m_{od} was acquired by placing the partially dried samples in an oven at 100 °C until the change in weight was negligible (≈ 8 hours). This resulted in Equation (122) for the OPV and Equation (118) for the wet density:

$$OPV = \frac{\frac{m_{ssd}}{m_{od}} - 1}{\rho_w} \quad (122)$$

More detailed information and visual displays concerning the drying log method can be found in the Supplementary material (Section 3).

Particle density

The particle density was determined indirectly by using the open pore volume and the skeletal density using the following:

Mass balance equation

Based on the GAC model (Figure 102), the particle density can be calculated when the OPV and skeleton density are known:

$$\rho_p = \frac{1}{\frac{1}{\rho_s} + OPV} \quad (123)$$

Image analysis

The particle envelope density could also be determined using the embedded image analysis software in a VHX microscope. This workflow consisted of obtaining a 3D model of the particles with the image processing software. This model helped determine the average height of several particles in the sample. After the average height of particles is determined, the area can also be easily calculated to obtain the volume of the particles in the sample. When this envelope volume is known, it suffices to know the mass of the analysed particles to determine the particle density. Detailed information about the particle density determination and GAC modelling can be found in the Supplementary material (Sections 3 and 7).

10.3.4 Fluidisation measurements - expansion characteristics

Expansion experiments for GAC grains were carried out at three locations: in Waternet's Weesperkarspel drinking water pilot plant located in Amsterdam, the Netherlands; at the University of Applied Sciences Utrecht, the Netherlands; and at Queen Mary University of London, United Kingdom.

For this research, a frequency modulated gear pump was used to enable a fluidisation velocity range suitable for the selected samples and prevent flow fluctuation. Differential pressure, superficial velocity, bed height and temperature were measured for 20-40 velocities, corresponding to a total of 53 fluidisation experiments for calibration and 30 for validation purposes. Water temperatures ranged from 4 to 40 °C. The velocity and temperature ranges were selected to cover the temperatures and velocities that are applied for the backwash procedure at Waternet throughout the year (5 to 20 °C).

Detailed information about experimental expansion columns can be found in Section 3.1, the physical properties of water in Section 3.2, the methods to determine the physical properties of particles in Section 3.3, bed voidage and differential pressure equations in Section 3.4, standard operating procedure of fluidisation experiments in Section 3.4.

Detailed information is included in the Supplementary material: photographic material and videos (Sections 1), particle characterisation (Section 2 and 3), technical details about used equipment (Sections 4), expansion experiments (Sections 5), fluidisation modelling (Sections 6), GAC modelling (Sections 7) and experimental data (Sections 8). In addition, information about wall-effects is given Annex 2: Wall effects.

10.3.5 Modelling aspects - voidage and incipient fluidisation

To predict the fluidisation behaviour, *i.e.* voidage (external porosity), of GAC, several important input parameters are required for the modelling exercise. The inputs consist of several particle characteristics (size, density, morphological properties), which were determined using various methods. For solid spherical monodisperse particles, the voidage can be predicted accurately as a function of fluid properties (velocity and viscosity) and particle properties (size and density) (Yang, 2003);

(Michaelide *et al.*, 2017); (Kramer *et al.*, 2020a,b). For non-spherical, polydisperse and porous GAC particles, the voidage prediction is considerably more complex. For the sake of convenience, the spherical particle size is commonly used in prediction models. Few models use morphological particle properties. Ergun (1952), however, included the particle shape factor. In the scientific literature, substantial knowledge is available regarding particle morphology: (Clift *et al.*, 1978); (Dharmarajah, 1982); (Allen, 1990); (Holdich, 2002); (Yang, 2003); (Soyer and Akgiray, 2005); (Masuda *et al.*, 2007); (Rhodes, 2008); (Marshall and Li, 2014); (Seville and Yu, 2016); (Barroso-Bogeat *et al.*, 2016). One of the most frequently used morphological properties is the sphericity proposed by Wadell (1933). However, in fixed beds, shape factors are more commonly used to match the predicted with experimentally obtained voidages (Kramer *et al.*, 2021c), or they are omitted. Voidage prediction models are only valid for a fluidised state. For this reason, it is important to determine the incipient fluidisation point to check the prevailing state. The onset of fluidisation from fixed to fluidised state occurs when the drag force is equal to the weight of the particles. Although numerous prediction models are proposed in the literature, such as (Wen and Yu, 1966); (Ergun, 1952); (Lippens and Mulder, 1993); (Yang, 2003); (Anantharaman *et al.*, 2018) there is no general agreement about the best approach. The degree of irregularity and polydispersity of particles as well as influences caused by the packing factor, surface forces and wall effects increase the complexity of accurate prediction.

The focus in this research lay on gaining insight into fluidisation characteristics and to a lesser extent on proposing accurate voidage prediction models. Nevertheless, the experimentally obtained expansion characteristics were compared to the most popular voidage prediction models proposed by Carman (1937); Ergun (1952) and Richardson and Zaki (1954). Accordingly, a data-driven model was used to predict the effective voidage proposed by Kramer *et al.* (2020a,b) based on dimensionless numbers (Rep1Frp model). In addition, a model based on symbolic regression was considered (Koza, 1992). Minimum fluidisation prediction, fluidisation modelling details and graphs are given in the Supplementary material (Section 6).

10.4 Results and discussion

10.4.1 Porous media - dry and wet conditions

Wetted GAC grains were analysed to obtain the open pore volume and wet density via the wet sieve method and drying log curve method. The results are presented in Figure 104. For most of the eight GAC types, the OPV values provided by manufacturers (orange bars) were slightly higher ($\approx 14\%$) than our experimentally determined drying log values (blue bars). The more commonly used sieve drying method (Hunce *et al.*, 2016) values (grey bars) are considerably higher ($\approx 77\%$), even with longer drying times.

Drying log

In the drying logs (example in Figure 103), we observe an initial linear decrease due to evaporation of external water. While it is possible that water from the largest pores might be transported to the surface through capillary forces during the initial constant rate period, the drying logs do in fact consistently show a sharp decrease of drying rate after a certain time depending on the GAC type used. The variations of the 42 measurements, caused a standard deviation of $\approx 7\%$ for the open pore volume, with a maximum of 20% for Aquasorb K-6300. The effect of the deviation or data spread in OPV on the error of the wet density was $\approx 1\%$ using Equation (118). An example of a drying log graph is shown in Figure 103. The drying methodology can be improved by using conditioned lab circumstances (taking the temperature and relative humidity into account) to increase the validity of this approach.

A large data set consisting of more than one million individual drying log measured data points is shared in (Kramer, 2021f), and additional methodology information about methylene blue adsorption can be found in the Supplementary material (Section 3).

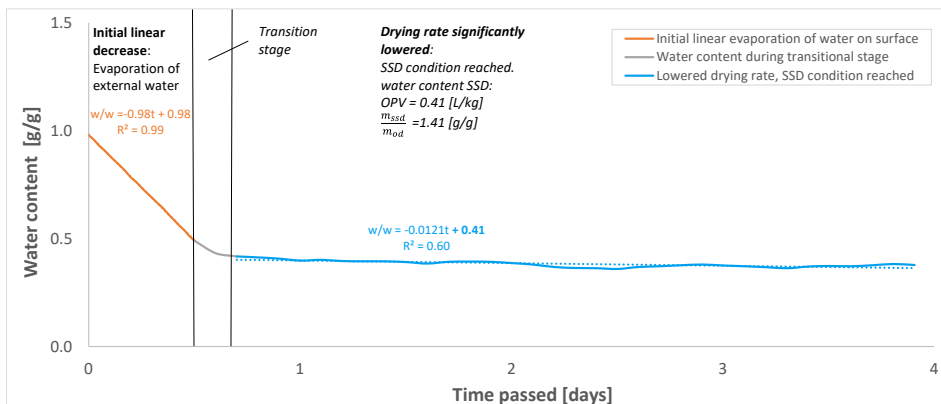


Figure 103 A typical drying log curve for Filtrasorb TL830. There are three stages: initial linear decrease with fast evaporation of external water, a transition stage and the saturated surface dry condition in equilibrium with the environment.

Wet sieve

Draining and wiping excess liquid seemed to remove the external bulk water only partially, as the wet mass found using this technique was substantially higher than the wet mass found using the other two techniques. Similar results were found by Hunce *et al.* (2016), who used a similar approach. Especially for the smaller particles such as Saratech Spherical and Norit ROW 0.8 Supra, in which water could not escape as easily, an increased mass was found.

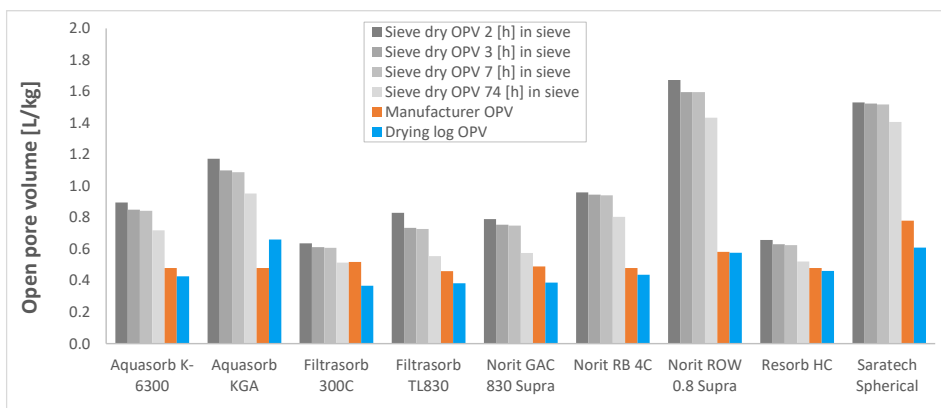


Figure 104 Open pore volumes, experimentally determined and provided by the suppliers.

10.4.2 Laboratory measurements - particle characterisation

Particle size and shape determination

Four methods were employed to determine the particle size of each sample, starting with the classical sieve analysis, microscope static image analysis, ImageJ static image analysis and accordingly a Camsizer dynamic image analysis, represented in Table 36. All other particle size and morphological GAC properties determined are provided in the Supplementary material (Section 2).

Table 36 Sieve analysis, microscope, ImageJ and Camsizer effective sizes ¹⁾

Shape	GAC type Note Variable Unit	Sieve		Microscope		ImageJ		Camsizer	
		$d_{10,sv}$	$d_{50,sv}$	min	max	min	max	min	max
		[mm]	[mm]	$d_{10,min,MIC}$	$d_{10,max,MIC}$	$d_{10,min,IJ}$	$d_{10,max,IJ}$	$d_{10,min,CS}$	$d_{10,max,CS}$
Granular	Aquasorb K-6300	1.27	1.67	1.33	1.96	1.41	2.02	0.77	1.15
Granular	Aquasorb KGA	0.89	1.38	0.95	1.41	1.08	1.42	0.67	1.07
Granular	Filtrisorb 300C	0.93	1.51	0.75	1.03	1.08	1.42	0.66	0.90
Granular	Filtrisorb TL830	1.27	1.56	0.86	1.26	1.35	1.92	0.99	1.31
Granular	Norit GAC 830 Supra	1.07	1.64	0.97	1.45	0.95	1.45	0.64	1.01
Granular	Norit RB 4C	3.15	4.55	3.79	6.05	4.05	5.29	3.73	5.16
Extruded	Norit ROW 0.8 Supra	0.81	0.86	0.82	1.64	0.85	1.57	0.81	1.19
Extruded	Resorb HC	0.94	1.48	0.84	1.22	1.26	1.82	0.60	0.90
Granular	Saratech Spherical	0.43	0.47	0.41	0.44	0.39	0.42	0.41	0.42

¹⁾ $d_{10,min}$ of minimum diameter (minor axis of ellipse) and $d_{10,max}$ of maximum diameter (major axis of ellipse)

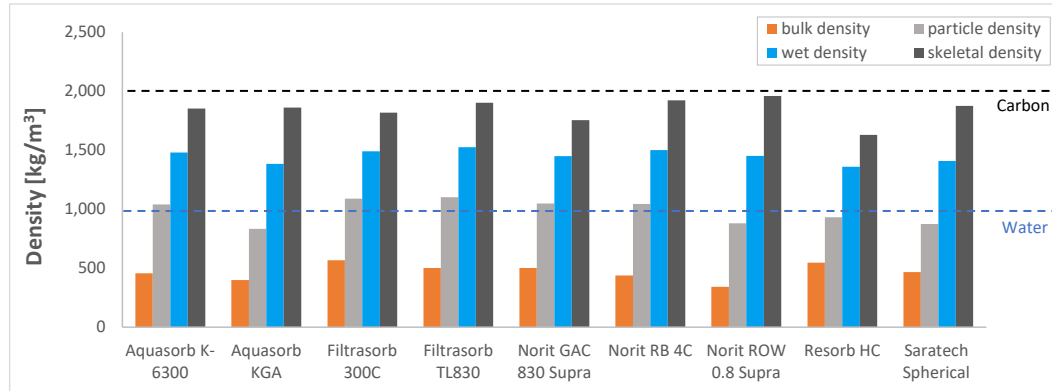


Figure 105 Experimentally determined densities. The absolute density of activated carbon (Mauguet et al., 2005) and water were added as a reference (Rumble, 2019).

Regarding spherical GAC particles, such as Saratech, the d_{10} for all four methods was, as expected, more or less the same 0.42 ± 0.02 mm. The granular GAC grains gave different results for the applied methods. Compared to the sieve analysis, the microscope d_{10} was approximately $\approx 15\%$ smaller but with a considerable standard deviation ($\approx 15\%$), possibly due to the fact that only a few grains were analysed compared to ImageJ where 10 or 100 times more grains were analysed per run. ImageJ measurements were approximately $\approx 10\%$ larger compared to the sieve analysis (with a slightly lower standard deviation $\approx 10\%$) due to the particle orientation. Elongated particles pass the sieve in a vertical orientation in contrast to the horizontally oriented grains on the scanner. The Camsizer measured considerably lower ($\approx 30\%$) d_{10} values compared with the sieve results. The $d_{10,max,CS}$ instead of the $d_{10,min,CS}$ agreed reasonably well with the $d_{10,sv}$.

GAC grains in general have a wide particle size distribution PSD. When these mixtures with a large PSD, *i.e.* with a wide range in particle sizes, are fluidised, the smallest particles have the tendency to expand the most. For that straightforward reason, the d_{10} (the particle size which corresponds to 10 percent finer on the cumulative PSD curve) or effective size is often used (Hunce *et al.*, 2018) to represent the input variable d_p in hydraulic models. The sieve analysis only provides 1D information. The microscope reveals more 3D information about GAC, but only a small number of grains can be investigated. The Camsizer analysis covers a larger number of grains, but the particle orientation is less clear compared with the ImageJ method. This latter method is more cost effective and a sufficient number of grains can be analysed, which is imperative when samples with a wide PSD are concerned. Detailed information about particle characterisation, applied methods and morphological properties of examined GAC media are provided in the Supplementary material (Section 2). Experimentally obtained data is shared at (Kramer, 2021f).

Density determination

The bulk, skeletal, particle and wet density (Equations (119), (120), (123) and (118)) were determined for the nine GAC types. The results are presented in Figure 105. The absolute density of activated carbon (Mauguet *et al.*, 2005) and water were added as a reference for comparison.

The error for the bulk density (orange bars) determined with the gradient cylinder compared with the manufacturer's value was $\approx 7\%$ and is in agreement with Chowdhury *et al.* (2012). The determined dry particle density (grey bars) fluctuated around the water density observed visually as some dry GAC particles floated and some slowly settled to the bottom of the jar. The skeletal density (dark grey bars) for all GACs was lower than the absolute density of activated carbon (Mauguet *et al.*, 2005); (Perrich, 1981); (Marsh and Rodríguez-Reinoso, 2006). The most relevant density for this research is the wet density (blue bars), which is used in the hydraulic models. For all nine GAC types, the average wet density was $1,450 \pm 50$ ($\approx 4\%$). Graphical results of densities, porosities and particle mass for each GAC type can be found in the Supplementary material (Section 3). The wet density was also determined with the differential pressure sensor of the expansion experimental set-up for validation purposes (Section 10.4.3).

Voidage determination

The voidage of non-stratified GAC (Figure 106) was determined with a graduated cylinder/pycnometer and with Equation (116) based on the particle density and bulk density or wet density (blue bars). The voidage of stratified GAC was also determined using the fixed bed in the expansion experiments (Section 10.4.3). The voidage at minimum fluidisation conditions is, as expected, slightly higher than the (stratified) fixed bed voidage but considerably higher than the non-stratified values. This is caused by the large PSD where smaller grains can fill the voids between the larger grains, thus decreasing the voidage. The common fixed bed voidage for solid spherical particles was added in Figure 106 as a reference. The voidage for granular GAC was found to be 0.57 ± 0.05 , considerably higher than some values obtained from the literature (Section 10.2), which is in line with the water standard works by Crittenden *et al.* (2012) (Crittenden *et al.*, 2012) and by van Lier (1984). Rod-like GAC had a slightly higher voidage 0.63 ± 0.02 , which is most likely caused by the elongated particle shape and degree of packing. Spherical GAC, in contrast, had a voidage of 0.47, which is lower than the other GAC types. The values determined by the expansion experiments (Section 10.4.3) were as follows: granular: 0.60 ± 0.05 , rod-like: 0.64 ± 0.02 and spherical 0.55, respectively.

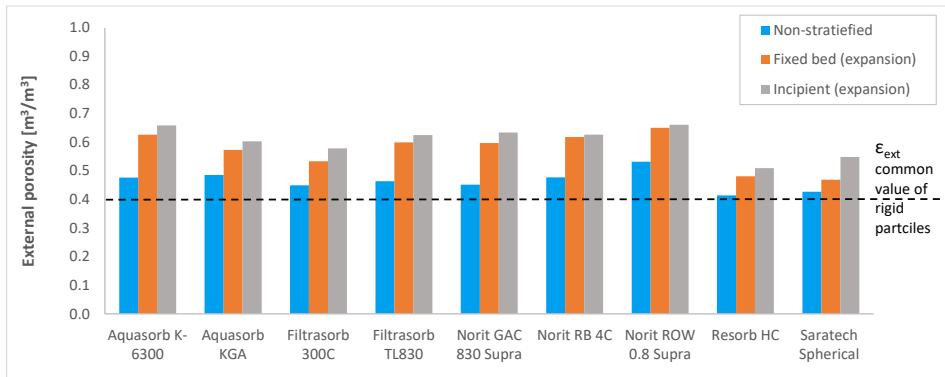


Figure 106 Experimentally determined voidage (external porosities). The commonly used fixed bed porosity for solid spherical particles was added as a reference (Yang, 2003).

10.4.3 Fluidisation measurements - expansion characteristics

A total of 48 liquid-solid fluidisation experiments were carried out to gain insight into the expansion characteristics of GAC grains. The obtained data was used to compare the experimentally obtained voidage with the prediction models. In addition, some models were calibrated with these expansion data. Thirty fluidisation experiments were used for model validation purposes. Five additional experiments were performed with long-term GAC obtained from a full-scale GAC filter. Figure 107 shows typical expansion curves for voidage (external porosity) and differential pressure as a function of superficial fluid velocity for temperatures between 4 °C and 31 °C.

The experimental dataset acquired consisted of a matrix with varying temperatures, grain sizes and flow rates.

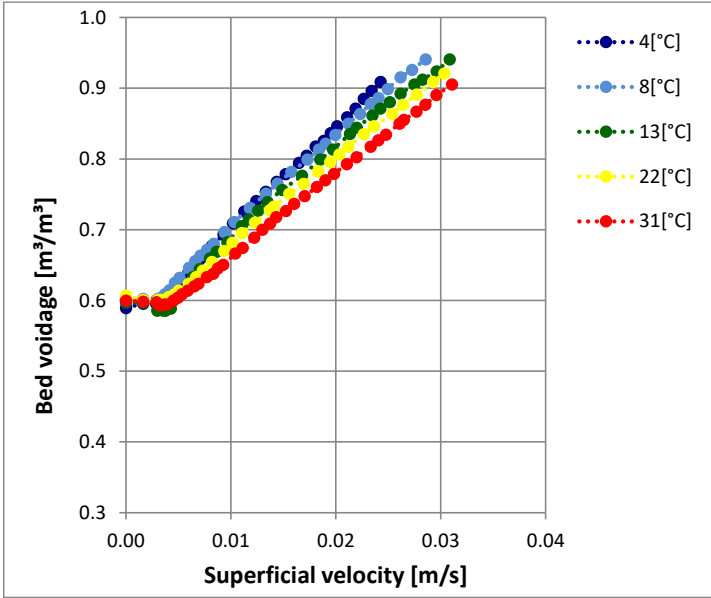


Figure 107a Experimental expansion characteristics of Norit GAC 830 Supra

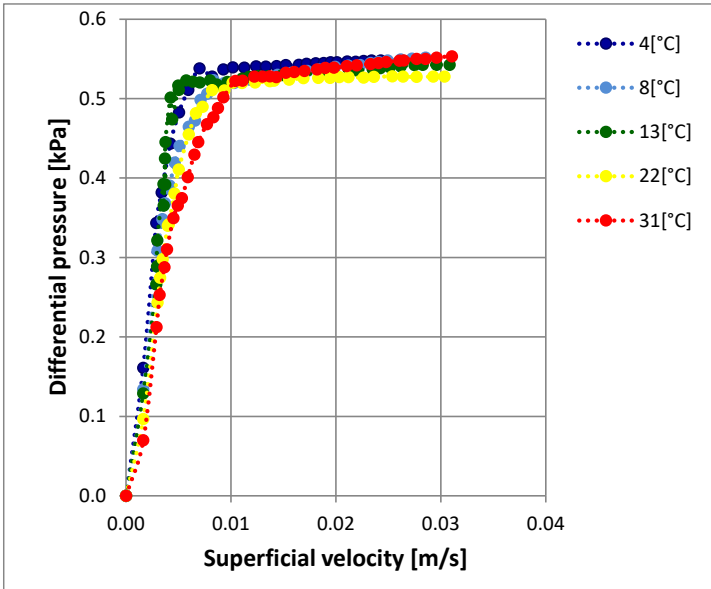


Figure 107b Differential pressures of Norit GAC 830 Supra

In the fixed bed state, the voidage is ≈ 0.6 (Table 37), which increases in the fluidised state for further elevated superficial fluid flows. The temperature (viscosity) effect is

clearly visible and follows the same characteristics compared to solid particles. The only difference is the incipient fluidisation point, which is significantly larger (≈ 0.6) compared to spherical particles (≈ 0.4) (Yang, 2003); (Gibilaro, 2001); (Michaelide *et al.*, 2017). The differential pressure shows a transition trajectory from fixed to fully fluidised state. Due to the large PSD, the smallest grains (≈ 0.64 mm) start to fluidise in an earlier state compared to the larger grains (≈ 2.73 mm). This confirms the complexity regarding the prediction of the incipient fluidisation of polydisperse GAC. Expansion curves for all GAC types are provided in the Supplementary material (Section 5).

10.4.4 Modelling aspects – voidage, morphology and incipient fluidisation

In the scientific literature, many models have been proposed to estimate the minimum fluidisation velocity as a function of the particle properties. The Wen–Yu model (Wen and Yu, 1966) is one of the most commonly used models. The average relative error between the predicted and measured minimum fluidisation velocity model was $\approx 38\%$ for granular grains, $\approx 14\%$ for rod-like grains and a considerable $\approx 78\%$ for spherical particles. In fact, the minimum fluidisation velocity is relevant for effective backwashing but can hardly be predicted accurately. Applying discretisation modelling, *i.e.* dividing the bed in separate layers with a distinct particle diameter related to this particular layer, could provide a solution for the particle size as input parameter in the prediction model. This approach does not, however, solve the other mentioned GAC-related challenges.

The well-known Carman–Kozeny model was used to estimate the incipient voidage under minimum fluidisation conditions. Table 37 presents the accurately measured fixed and incipient voidages as well as the estimated incipient voidage as determined with the Carman–Kozeny model. The average relative error between the predicted and measured incipient voidage was $\approx 19\%$ for granular grains, $\approx 38\%$ for rod-like grains and $\approx 27\%$ for spherical particles. Although the Carman–Kozeny model is a well-established and often used model for solid and relatively spherical particles, it is less suitable for GAC grains. More detailed information is given in the Supplementary material (Section 6).

Table 37 Experimentally determined and estimated fixed bed and incipient fluidisation voidages and average relative errors for individual GAC types

Grain material	Shape	ϵ_0	ϵ_{mf}	$\epsilon_{mf,CK}$ ²⁾	ARE
Aquasorb K-6300	Rocks	0.63	0.66	0.45	-31%
Aquasorb K-6300 ¹⁾	Rocks	0.62	0.65	0.54	-18%
Aquasorb KGA	Rocks	0.57	0.60	0.50	-18%
Filtrisorb 300C	Rocks	0.53	0.58	0.50	-13%
Filtrisorb TL830	Rocks	0.60	0.62	0.47	-24%
Norit GAC 830 Supra	Rods	0.60	0.63	0.54	-15%
Norit RB 4C	Rods	0.62	0.63	0.38	-40%
Norit ROW 0.8 Supra	Rocks	0.65	0.66	0.42	-36%
Resorb HC	Rocks	0.48	0.51	0.47	-7%
Saratech Spherical	Balls	0.47	0.55	0.69	27%

¹⁾ Long-term GAC from a full-scale filter with a retention time of approximately 2-3 years

²⁾ Carman-Kozeny (Carman, 1937) using Bolzano's numerical intermediate value theorem (Apostol, 1967)

The prediction of the voidage of GAC is complex as the particles are non-spherical, porous and polydisperse. Varying raw materials, manufacturing processes and pore structures further complicate the characterisation of the particles. Particularly the wet density, wet mass and the point of incipient fluidisation are difficult to determine. To be able to predict the voidage, these values must be known. In the literature, there is no general agreement regarding effective bed-voidage model prediction and employed spherical particles.

In this work, we combined advanced particle laboratory experiments and accurate liquid-solid fluidisation experiments. This led to the input parameters for the voidage prediction model. A schematic flowchart is given in Figure 108. The GAC scheme consists of ovals (dark red) representing laboratory experiments. Squares (black) indicate the particle properties that are needed in the whole system. Input data from suppliers and assumed values are coloured grey. Green stands for morphological particle properties. The squares in blue represent hydraulic fluidisation experiment data. Yellow arrows are the input values for the model that leads to a voidage prediction. Finally, the prediction error can be calculated based on the model output and measured voidage. The GAC scheme in Figure 108 shows the relationship between all the variables. Multiple routes are possible. We decided to choose the route with, at least to our knowledge, the highest reproducibility and transparency. This route is indicated by bold arrows.

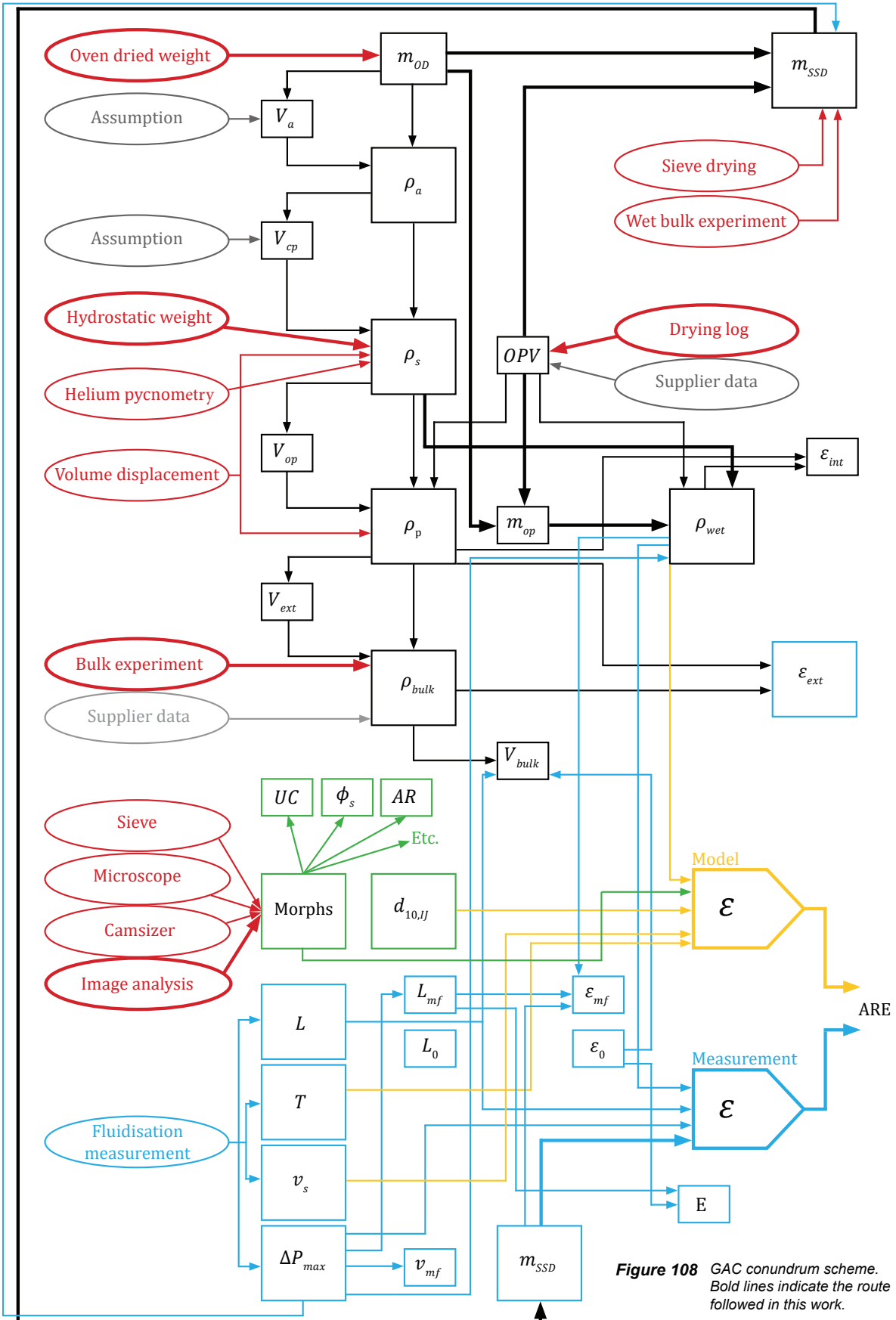


Figure 108 GAC conundrum scheme. Bold lines indicate the route followed in this work.

The starting point of the solution to the GAC conundrum, shown in Figure 109, is the SSD GAC particle (Figure 101). The oven dry particle mass m_{od} can be measured directly. The skeletal density ρ_s was determined using the hydrostatic weighing technique (Equation (120)) and accordingly the open pore volume using Equation (122). From the SSD conditions, the wet particle mass m_{ssd} and wet density ρ_{wet} can be calculated (Equation (118)). Regarding the particle size and shape, we chose the d_{10} . Various modelling results using symbolic regression can be found in the Supplementary material (Section 6). Voidage prediction including morphological properties and symbolic regression including morphological properties, however, were not the focus of this work. By using morphological properties such as ellipsoid sizes, the particle orientation could be taken into account for a more accurate understanding of fluidisation behaviour and characteristics. With the fluidisation experiments, the differential pressure ΔP_{max} could be used to validate the wet density ρ_{wet} or the SSD particle mass during fluidised bed state conditions (Equation (124)):

$$\rho_{wet} = \frac{\rho_f}{1 - \frac{\Delta P_{max} \pi D^2}{m_{ssd} g^4}} \quad (124)$$

Vice versa, the differential pressure or the external porosity could be checked with:

$$\frac{\Delta P_{max}}{L} = (\rho_{wet} - \rho_f)g(1 - \varepsilon_{ext}) \quad (\varepsilon > \varepsilon_{mf}) \quad (125)$$

The differential pressure gauge is a sensitive and rather accurate measurement device, but it only works well if the occurrence of trapped air is prevented. Especially for grains with a small particle-to-fluid density ratio ρ_{wet}/ρ_w such as GAC, an initial non-zero off-set adversely affects the accuracy of ΔP_{max} or ε_{ext} . Initial off-set ranging from 0.75-3.25 mbar was found, which was accounted for by subtracting the ΔP_{max} with the initial off-set. For this reason, the differential pressure was only used for validation purposes.

The fluidisation experiments could be used to determine the incipient voidage (Figure 106) reasonably well, using the differential pressure transition from an increasing to a constant value. Based on the bed height, SSD mass and the wet density ρ_{wet} , the voidage of the system could be calculated. The SSD mass and wet density are crucial model variables. Their validity is not ensured entirely but may be improved upon improving the reliability of the GAC conundrum scheme. Graphical

results of densities, porosities and particle mass can be found in the Supplementary material (Section 3).

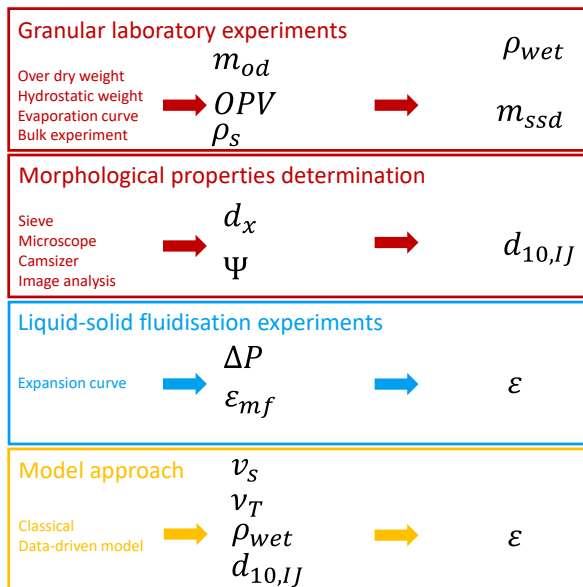


Figure 109 GAC conundrum solution scheme

The SSD particle mass m_{ssd} together with the wet density ρ_{wet} combined with the fluid properties (superficial fluid velocity and viscosity) and the ImageJ $d_{10,IJ}$ enabled average voidage prediction of the GAC beds. The most common hydraulic models were used to compare the estimated and experimental voidages. The voidages found experimentally were significantly higher compared to the classical predicted voidages estimated with the classical models. Finding fitting parameters for each of these models is fairly straightforward, but the usefulness of applying these fitted models is questionable (see Table 38).

Table 38 Voidage (external porosity) model prediction accuracy ¹⁾

Model	Reference	MAE	ARE	NRMSE	LRMSE	R ²
Carman–Kozeny	(Carman, 1937)	0.128	16.8%	17.3%	19.6%	0.99
Ergun	(Ergun, 1952)	0.143	16.5%	19.5%	22.4%	0.99
Richardson–Zaki	(Richardson and Zaki, 1954)	0.201	26.5%	26.7%	32.1%	0.99
Rep1Frp (fitted)	(Kramer <i>et al.</i> , 2020b)	0.034	4.5%	5.0%	5.0%	0.99

¹⁾ Mean average error (MAE), Average relative error (ARE), Normalised root mean square error (NRMSE), Logarithmic root mean squared error (LRMSE), correlation coefficient (R²). Equations are given in Annex 5: Statistical analysis.

The classical sieve analysis is still often used but provides only one-dimensional information about particles. It is also cumbersome. When the models must be improved, the sieve analysis is the least suitable method for further exploration. Other methods such as ImageJ analysis might be more suitable. The d_{10} can be used as an input parameter to deal with a large PSD. Discretisation modelling for GAC types with a large PSD could provide a more suitable solution.

Besides being non-spherical, GAC grains are polydisperse, porous and sensitive to attrition due to abrasive circumstances during backwashing and transport (Shpirt and Alben, 1986); (Deitz, 1997); (Mauguet *et al.*, 2005); (Frank *et al.*, 2015); (Barroso-Bogeat *et al.*, 2016); (Naushad and Lichtfouse, 2020). In addition, in full-scale filters, a biofilm layer may grow on GAC grains, affecting the drag and consequently the behaviour of the particles during fluidisation. Therefore, we compared one GAC type on its expansion characteristics. Aquasorb K-6300 virgin and Aquasorb K-6300 with a long-term retention of approximately three years in a full-scale drinking water filter were compared (Figure 110). The expansion degree of the virgin GAC was approximately 10% larger compared to the bio GAC. This is most likely caused by the reduction of fines which were flushed out of the system, a slightly increased density caused by intake of OMPs and the growing biofilm. The graphs can be found in the Supplementary material (Section 5).

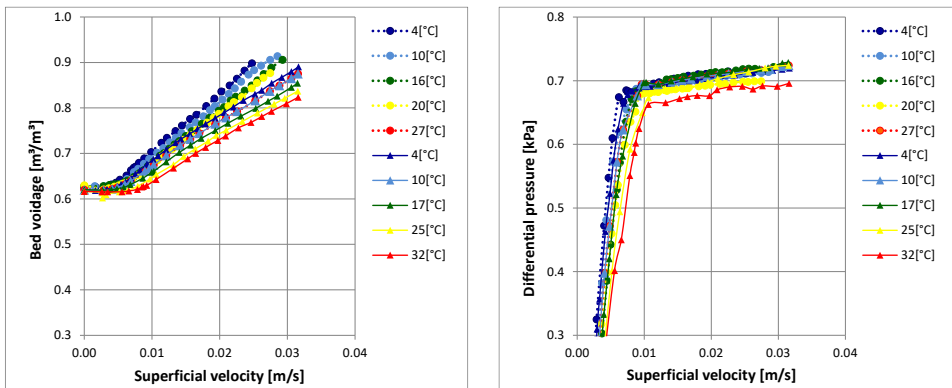


Figure 110 Experimental expansion behaviour of Aquasorb K-6300 virgin GAC (circles) and long-term Aquasorb K-6300 GAC (squares) from a full-scale filter with a retention time of approximately 2-3 years.

10.5 Conclusions

- Scientific conclusions

In this research we developed a new approach leading to new insight into the expansion characteristics of granular activated carbon grains used in water fluidisation processes. The scientific literature is not in agreement about how - and especially how accurately - the fluidisation characteristics of granular activated carbon (GAC) grains can be predicted. Some researchers propose empirical models and mention low prediction errors, but it is unclear how accurate these models will remain when GAC is used for a long period of time. We demonstrated that it is possible to combine GAC particle laboratory experiments with hydraulic experiments and mass balance-based equations. The incipient voidage, the saturated surface dry mass and wet density can be derived from both fluidisation and laboratory experiments. Consequently, it is possible to improve the validity of the variables which can be used to predict the voidage more accurately.

- Effect on design

In this work, we showed that fluidisation behaviour of GAC is very complex due to polydispersity, its porous character and non-spherical properties of the grains. Therefore, traditionally, full-scale GAC filters are commonly over-designed to cope with fluctuations and variations. For reliable and safe drinking water production however, a precise specification of backwash rates for filter cleaning is needed to prevent mudball, short circuiting and fixed bed formation, as well as flush out of fine particulate material with increased risk for pathogen and organic micropollutants breakthrough. In addition, optimal expanded bed discharges debris, suspended solids and dirt and allows the individual GAC grains to collide and scrub each other, resulting in an increased filter life and performance capacity. Therefore, robust and flexible treatment processes require thorough design specifications and process control of backwash rates for filter cleaning. Since the GAC grains do not remain constant, due to attrition, abrasive circumstances during backwashing and transport and due to biofilm layer growth on GAC grains, the fluidisation behaviour will change slowly but continuously. Engineers should be aware that prediction models have to be adjusted over time to cope with the process changes.

- *Effect on operations*

While it is possible to find a reasonably accurate voidage prediction model as a function of the fluid and particle properties, especially for individual GAC types, GAC is subject to change, and therefore it is most likely that the prediction accuracy will deteriorate rapidly. It is possible to fit a model for individual types of GAC, such as rock-like, rod-like and spherical particles with a considerably lower prediction error. Using advanced laboratory measurements, accurate morphological properties of GAC can be obtained. Including these morphs into hydraulic models increases the prediction accuracy, but it also increases the complexity of the models. Finally, it can be concluded that the incipient voidage of GAC is significantly higher (0.50-0.65) than the commonly used voidage for solid granular materials (0.40).

10.6 Recommendations

To improve the GAC modelling and prediction accuracy, the following topics should be addressed:

- In full-scale filters, GAC must be re-activated and partly replaced by virgin GAC. Mixing of different types of GAC must be investigated on their overall expansion (and filtration) characteristics.
- A model needs to be developed that considers biofilm growth for applied GAC filtration.
- Highly spherical nylon balls have a similar density to wetted GAC. The expansion degree is very well known. This can be used to improve current knowledge about the fluidisation behaviour of GAC.
- When the expansion behaviour must be known, for instance when new sustainable GAC types are introduced, it is recommended to perform pilot plant experiments. If this is not an option, a considered prediction model can be used, but it is important to take a high degree of spread into account.
- This research focused on voidage and showed that the determination of the incipient voidage is rather complex. In many articles, the voidage is avoided by applying the degree of expansion. An alternative and more effective approach should be developed that makes it possible to predict the overall bed expansion for establishing optimal backwashing protocols.

10.7 Supplementary material

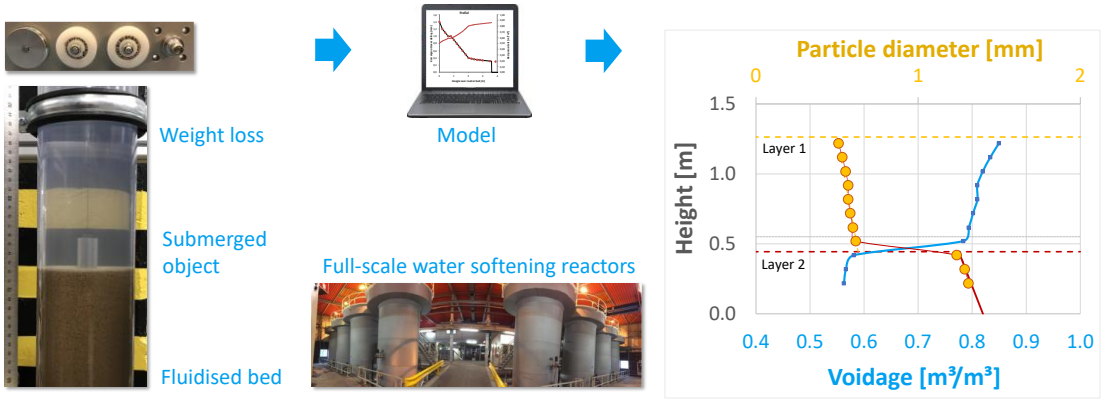
Supplemental data for this article can be accessed at:

<https://doi.org/10.1016/j.appt.2021.06.017>, (Kramer *et al.*, 2021f): [Data set].
4TU.ResearchData. <https://doi.org/10.4121/14229863.v1>

Contents		page
1	Supporting media of liquid-solid fluidisation experiments	4
1.1	Photographs of a full-scale granular activated carbon filtration unit	4
1.2	Photographs of fluidisation experiments with the expansion column	5
1.3	Photographs and main characteristics of examined GAC samples	6
1.4	Videos of liquid-solid fluidisation experiments	9
2	Particle characterisation	10
2.1	Classical sieve analysis	10
2.2	Microscope 3D models and sample profiles	10
2.3	ImageJ particle size results	16
2.4	Camsizer particle size results	18
3	Density laboratory experiments	24
3.1	Modified liquid pycnometry volume displacement technique	24
3.2	Drying log method	24
3.3	Skeletal density using helium pycnometry	26
3.4	Hydrostatic weighing	26
3.5	Particle envelope density	27
3.6	Methylene blue adsorption	27
3.7	Hygroscopic behaviour, water absorbed from air	27
3.8	Graphical results of densities, porosities and particle mass	28
4	Experimental set-up and fluidisation experiments	31
4.1	Expansion columns	31
4.2	Procedure expansion experiments	32
4.3	Voidage and expansion calculation	33
4.4	Fluid properties	34
4.4.1	Concise drinking water treatment processes	34
4.4.2	Physical properties of water	34
5	Experimental expansion curves	36
6	Fluidisation modelling	40
6.1	Voidage Power Function	40
6.2	Voidage predicting including morphological properties	46
6.2.1	UC of circular equivalent diameter and AR (ImageJ)	47
6.2.2	UC and equivalent diameter (sieve)	47
6.3	Voidage predicting, morphological properties, symbolic regression	48
6.3.1	Generated equation for rocks+rods+balls (ImageJ)	48
6.3.2	Generated equation for rocks+balls (ImageJ)	48
6.3.3	Generated equation for rods (ImageJ)	49
6.3.4	Generated equation for rocks+balls+rods (Camsizer)	49
6.3.5	Generated equation for rods:	50

6.4	Voidage predicting accuracies for different models	51
6.4.1	Voidage prediction Aquasorb K-6300	52
6.4.2	Voidage prediction Aquasorb KGA (full-scale long-term)	52
6.4.3	Voidage prediction Filtrasorb 300C	53
6.4.4	Voidage prediction Filtrasorb TL830	54
6.4.5	Voidage prediction Norit GAC 830 Supra	54
6.4.6	Voidage prediction Norit RB 4C	55
6.4.7	Voidage prediction Norit ROW 0.8 Supra	56
6.4.8	Voidage prediction Resorb HC	56
6.4.9	Voidage prediction Saratech Spherical	57
6.5	Statistical analysis	58
6.6	Minimum fluidisation points	59
6.7	Wall effects	61
7	GAC modelling	62
7.1	Schematic overview of a GAC particle	62
7.2	GAC nomenclature	62
7.3	Mass balance	63
7.4	Volume balance	63
7.5	Bulk, wet and particle density	63
7.6	External porosity	64
7.7	Open pore volume and wet particle mass	64
7.8	Open pore volume ratio	65
7.9	Relation between open pore volume and mass	65
7.10	Internal pore volume	66
7.11	Skeletal density	66
7.12	Skeletal density based on submerged mass	67
7.13	Relation between wet and skeletal density and open pore volume	67
7.14	Relation between particle density and skeletal density and OPV	68
7.15	Closed pores	68
7.16	Correction factor for closed pores	68
7.17	Ratio wet / dry mass	68
7.18	Hydraulic external porosity and differential pressure	69
8	Nomenclature	70
9	References	72
10	Experimental data	75
10.1	Calibration experiments	75
10.2	Full-scale long-term experiments with Aquasorb K-6300	92
10.3	Validation experiments	94-102

A novel sensor - measuring local voidage profile inside a fluidised bed reactor



- ▶ A method based on Archimedes to 'look' inside a fluidised bed reactor
- ▶ A sensor developed to hydrostatically weigh a submerged object in a fluidised bed
- ▶ The longitudinal voidage and particle diameter profile can be determined
- ▶ The hydraulic state can be estimated using an improved model

Keywords Fluidisation; Drinking Water Treatment; Pellet-Softening; Hydrostatic Soft Sensor; Hydraulic State

Chapter 11

Hydrometer

“Eureka! ... or Eureka?”
(Archimedes, 287 B.C. – 212 B.C.)

This article was accepted in: *Journal of Water Process Engineering*

A novel sensor measuring local voidage profile inside a fluidised bed reactor

O.J.I. Kramer, C. van Schaik, J.J. Hangelbroek, P.J. de Moel, M.G. Colin, M. Amsing, E.S. Boek, W.P. Breugem, J.T. Padding, J.P. van der Hoek
Journal of Water Process Engineering. 102091 (2021) pp. 1–15

The article can be found online at:

<https://doi.org/10.1016/j.jwpe.2021.102091>

11 A novel sensor measuring local voidage profile inside a fluidised bed reactor

11.1 Abstract

Liquid-solid fluidisation is frequently applied in drinking water treatment processes, often with the aim to obtain a large liquid-solid interfacial surface area. A large surface area is crucial for optimal seeded crystallisation in full-scale softening reactors. Due to crystallisation, particles grow and migrate to a lower zone in the reactor, which leads to a stratified bed. Larger particles adversely affect the surface area. To maintain optimal process conditions in fluidised beds, information is needed about the distribution of particle size, local voidage and available surface area, over the reactor height. In this work, a sensor is developed to obtain the hydraulic state gradient, based on *Archimedes'* principle. A cylindrical heavy object is submerged in the fluidised bed and lowered gradually while its weight is measured at various heights using a sensitive force measuring device. Based on accurate fluidisation experiments with calcite grains, the voidage is determined and a straightforward empirical model is developed to estimate the particle size as a function of superficial fluid velocity, kinematic viscosity, suspension density, voidage and particle density. The surface area and specific space velocity can be estimated accordingly; these represent key performance indicators regarding the hydraulic state of the fluidised bed reactor. The prediction error for voidage is $5 \pm 2\%$ and for particle size $9 \pm 4\%$. The newly developed soft sensor is a more time-effective method for determining the hydraulic state in full-scale liquid-solid fluidised bed reactors.

11.2 Introduction

11.2.1 Liquid-solid fluidisation applied in drinking water softening processes

Liquid-solid fluidisation is a commonly applied process in the treatment of drinking water, often to effectuate a large liquid-solid interfacial surface area (Crittenden *et al.*, 2012). In particular, pellet-softening, a process based on seeded crystallisation in fluidised bed reactors, requires a large surface area for crystallisation purposes (Graveland *et al.*, 1983). Another frequently applied treatment step in drinking water treatment is water softening (Edzwald, 2011). The removal of dissolved calcium from the water has benefits for public health, the environment, the economy and aesthetics. In addition, it counteracts limescale (Beefink *et al.*, 2021). In the Netherlands, more than 400 million m³ water is softened annually in drinking water treatment plants using fluidised bed pellet reactors (Hofman *et al.*, 2007). In these reactors, sand is traditionally dosed as seeding material. Calcite pellets are produced as a by-product (van Dijk and Wilms, 1991). To meet sustainability goals, calcite pellets are dried, grained, sieved and re-used as seeding material (Schetters *et al.*, 2015). By carefully dosing caustic soda, supersaturated conditions are created in the fluidised bed (Tang *et al.*, 2020), leading to calcium carbonate crystallisation on the surface of calcite grains. Crystallisation causes particles to grow and to migrate to a lower region in the reactor, which leads to a stratified bed and a certain particle size profile (0.2-2.0 mm) from the top to the bottom of the bed. Larger particles reduce the available surface area, which adversely affects the crystallisation efficiency. In addition, calcite pellets that are too large may cause detrimental clogging at the bottom of the reactor: this is due to the highly alkaline environment that is caused by caustic soda dosage if the superficial fluid velocity approaches the minimum fluidisation state. Therefore, when a certain particle size threshold is exceeded, calcite pellets are extracted from the bottom of the reactors. To maintain optimal process conditions, *i.e.* fast calcium carbonate crystallisation in the fluidised beds, information is needed about particle size, local voidage and specific surface area (SSA), over the reactor height (Kramer *et al.*, 2020b).



Figure 111 Full-scale pellet-softening reactors located at Waternet (Leiduin, The Netherlands) (van der Veen and Graveland, 1988).

In full-scale industrial pellet-softening reactors (Figure 111), the condition of the fluidised bed is not available to the operator in real time. To obtain direct particle information, on a frequent basis, laborious manual action is necessary such as particle sampling from the reactor bed or using hoses that might be hazardous in terms of water quality, *i.e.* violating hygiene requirements (World Health Organization, 2017). Moreover, particle samples must be dried, weighed, sieved and analysed accordingly, which is time consuming, expensive and only provides delayed information about a small section of the reactor.

Indirect fluidised bed information can also be acquired using online sensors (van Ammers *et al.*, 1986). The total pressure drop and bed height can be used to estimate the total average bed voidage. More advanced methods can also be applied in reactors equipped with a differential pressure measurement sensor between heights of 15 and 65 cm in the reactor (van Schagen, 2009). Using the fact that the hydraulic pressure drop must be equal to the submerged weight of the suspended bed material per unit cross-sectional area, it is possible to estimate the local voidage in the reactor zone with the highest supersaturation driving force. With hydraulic models such as Ergun (1952), Carman–Kozeny (Carman, 1937) or van Dijk (van Dijk and Wilms, 1991), the local average particle size can be estimated (van Schagen *et al.*, 2008). Knowing these values is operationally beneficial for determining effectivity and the point at which particles need to be removed. However, the information received is averaged and does not provide a complete description of the hydraulic state.

11.2.2 Hydraulic state determination of pellet-softening fluidised beds

Due to seasonal changes, surface water temperature in the Netherlands changes throughout the year and varies between 1 and 20 °C. This affects the degree of fluidised bed expansion in pellet-softening reactors. To maintain optimal process conditions for calcium carbonate crystallisation, sufficient particle surface area must be retained in the fluidised bed. Moreover, due to the transition from garnet sand as a seeding material to a more sustainable re-use of crushed calcite pellets (Schetters *et al.*, 2015); (Kramer *et al.*, 2020b), particle properties have changed. A consequence, however, is that altered particle size and shape of these granules affect the condition and performance of the distinct unit operation, causing an altering degree of expansion and a risk of particle flushing. In addition, when calcite pellet erosion occurs, with high turbidity as a result in the water phase, it often becomes impossible for the bed height sensor to detect the bed height. In practice, it is rather complex to comprehend the overall seeded crystallisation softening process that occurs in a stratified bed with a variety of large spherical and small highly non-spherical particles with different hydraulic behaviour. For this reason, operators have to build significant experience in operations: they often resort to "rules of thumb" (van der Helm, 2007) and professional experience to control and optimise the process (van der Veen and Graveland, 1988); (Hofman *et al.*, 2007); (Groenendijk *et al.*, 2008). Additional full-scale considerations to operations can be found in the Supplementary material (Section 6).

Up to this point, it has not been possible to fully determine the real-time dynamics of the fluidised bed from the outside of a reactor or based on overall process variables such as water temperature, flow, bed height and total differential pressure. The pellet-softening process has proven to be complex, and it is not completely understood if multiplicity, *i.e.* multiple process states, occur. For safe water production (Boccelli *et al.*, 2007) and optimal process conditions, a more flexible process control is needed (Bosklopper *et al.*, 2004). With regard to pellet-softening this means that an improvement is needed for the fast, online determination of the hydraulic state of the fluidised bed in pellet-softening reactors. The objective of this work is to experimentally measure the force acting on a submerged object in a liquid-solid fluidised bed and use this information to determine the suspension density and voidage along the bed height. The voidage measurement is based on *Archimedes'* principle, and is compared with the measured bed height and mass-based mean voidage. The overall aim of this research is to test the novel developed sensor to

obtain longitudinal information of the hydraulic state gradient in a drinking water pellet-softening reactor, where chemistry and hydraulics are inextricably interlinked. The approach in this work is a feasibility study to demonstrate that the Archimedes-based novel sensor, termed as ‘the Hydrometer’, works in a liquid-solid fluidised bed reactor. First, an overview is given of the existing scientific literature about submerged objects in fluidised beds and their applications. To explore the existence of a weight gradient, a preliminary trial was carried out in a full-scale reactor. An advanced experimental set-up was designed and constructed to investigate the possibility of measuring the weight changes of a submerged object for various heights in the fluidised bed. The novelty of this work lies in the combination of classical physics, *i.e.* Archimedes’ principle, and the translation into particle properties to serve as a semi-online sensor to determine the hydraulic state of a liquid-solid fluidised bed reactor.

11.3 Materials and methods

The experimental set-up is presented in Section 3.1.3. Experiments were executed in the experimental set-up with glass beads to scrutinise the dimensions of the submerged objects. A series of experiments were performed with a mixture of two sets of fractionised calcite grains from a pellet-softening reactor to investigate the possibility to distinguish the transition from one layer to another when the object is gradually lowered. Furthermore, two single fractions of calcite pellets were used to examine whether the spherically-assumed particle size can be predicted using a data-driven model based on the known particle and fluid properties. A sensibility analysis was conducted to determine the implications for the data conversion steps, *i.e.* the data transformation model (DTM). Key performance indicators (KPI) are also presented here to assess the hydraulic reactor performance. Finally, the practical utility in full-scale operation is discussed.

11.3.1 Particle selection

The focus of this research is the development of a novel sensor for pellet-softening fluidised bed reactors. For this reason, polydisperse calcite pellets (100% CaCO₃) were extracted from full-scale reactors. Relatively monodisperse fractions were obtained by sieving pellets batches with a AS 200 Retch Laboratory sieve shaker and calibrated US mesh sieves regulated by standards such as ISO 3310-1, ISO 565, EN 933-2 and ASTM E11 (NEN-EN 933-2, n.d.). In addition, crushed calcite grains (100% CaCO₃ from the Calcite Factory) were used to compose a two-fraction mixture. As a reference, spherical glass beads were used (Boom lab). Two representative samples from each fraction were scanned and analysed using ImageJ (Ferreira and Rasband, 2012) to validate the particle size and morphological properties. The sieved fractions were used to compose three different particle beds for the fluidisation experiments. Additional morphological particle properties, such as the sphericity, were determined with a Retsch Camsizer XT (Retsch-Technology, 2007). Additional photos of examined granules are given in Annex 1: Photos and in the Supplementary material (Section 2).

11.3.2 Fluidisation experiments

A straightforward pilot test was performed in a full-scale pellet-softening reactor to discover whether a submerged weight gradient was observed and measurable. Fluidisation measurements with glass beads were executed in a pilot set-up to analyse the influence of the dimensions of the submerged objects at maximum flow rate. Additionally, a series of fluidisation experiments was performed with different calcite particles for various flow rates to measure longitudinal gradients. During these fluidisation experiments, the weight loss of the submerged object was measured while the height of the object was altered. The fluid velocity and temperature as well as the bed height were logged.

11.3.3 Data transformation model

The buoyant weight gradient in the fluidised bed can be measured with the hydrometer sensor (Figure 112). The measured strain is converted through a calibration curve into weight loss. The pseudo-fluid or suspension density is calculated accordingly (explained in Section 11.4.1). The voidage can be derived based on a mass balance (Section 11.4.2). Since the initial particle mass and bed height were carefully measured, the particle mass, volume and total pressure drop are known (Section 11.4.4). With this information, the estimated variables can be validated (Section 11.4.6). Using a data-driven model, the particles size can be estimated (Section 11.4.7). By combining the voidage and particle size, the reactor key performance indicators can be approximated accordingly (Section 11.4.8). Corrections for the influence of the submerged object on the voidage are proposed in Section 11.4.5.

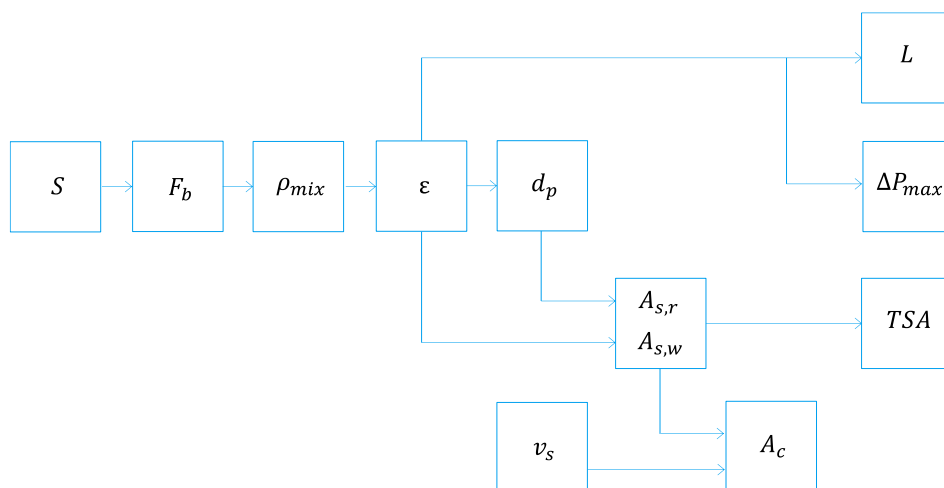


Figure 112 Schematic representation of the data transformation model. Direct strain measurement is converted into weight loss, suspension density and accordingly voidage and estimated particle size. Specific surface area based on the reactor and water phase and reactor key performance indicators (Section 11.4.8) can subsequently be calculated.

11.4 Theoretical hydraulic state determination

11.4.1 Suspension density

Fluidisation is the process of converting a granular material from a static solid-like state to a dynamic liquid-like state of a suspended particulate assembly by introducing upward flowing fluid (Gibilaro, 2001); (Yang, 2003). The apparent density of the particle-fluid mixture is larger than the fluid density itself. Assuming a homogeneous particle-fluid mixture in a fluidised bed (Di Felice, 1995), the average suspension density ρ_{mix} is directly related to the fluidised bed voidage ε (Di Felice *et al.*, 1989):

$$\varepsilon = \frac{(\rho_p - \rho_{mix})}{(\rho_p - \rho_f)} \quad (126)$$

Where ε is the voidage of the system, ρ_p the particle density and ρ_f the fluid density. Equation (126) is valid under homogeneous fluidisation conditions. The average pressure drop ΔP over a vertical length z of the bed according to an elementary force balance states:

$$\Delta P = \rho_{mix} g z \quad (127)$$

In Equation (127), fluid and solid wall friction from upward fluid flow is neglected when the column diameter is large. The pressure gradient (Equation (127)) is analogous to that in a Newtonian liquid, where the liquid density ρ_f is replaced by the suspension mixture ρ_{mix} . The suspension density gives rise to a buoyancy force F_b exerted on an object with volume V submerged in the suspension analogous to the Archimedean buoyancy for a static liquid (Nguyen and Grace, 1978):

$$F_b = \rho_{mix} g V \quad (128)$$

Equation (128) is valid if the submerged object size is considerably larger than the particle size.

11.4.2 Force balance

In the absence of a surrounding medium, a stationary object suspended on a wire experiences a net zero force ($F_g = F_s$), given by Equation (128), where F_g is the downward gravitational force and F_s a measurable upward strain force on the wire. In air, these forces are almost equal; in a fluidised bed, however, the considerable upward buoyancy force F_b causes a difference between the dry weight F_g and the apparent weight F_s . Another contribution to this weight loss, albeit less dominant, is the upward drag force F_d caused by the fluid flow. Together, this leads to Equation (129):

$$F_s = F_g - F_b - F_d - F_{col} \quad (129)$$

Where F_{col} is related to the surface integral of solid stress over the surface area of the object similar to F_d , the surface integral of fluid stress over surface area of the object. When there is a strong gradient in solid concentration over the object, a higher concentration at the object bottom will result in an upward net collision force, *i.e.* F_{col} will depend on the concentration. The stress depends on the Stokes number St . Concerning calcite pellets, $St = 0.2 \pm 0.05$ and therefore the collision forces (Goldschmidt *et al.*, 2001) are ignored or $F_{col} = 0$. An extensive analysis can be found in the Supplementary material (Section 4). Including other forces such as lift, added mass and Basset history forces leads to considerably more complex expressions (Cello *et al.*, 2010), but these are all negligible and therefore not the focus of this research.

11.4.3 Suspension density

Equation (129) can be transformed into Equation (130) accordingly:

$$m_{strain} = m_g - V_{object} \rho_{mix} - \frac{1}{2} \rho_{mix} v_i^2 \frac{A_{\perp}}{g} C_w \quad (130)$$

This approach is valid when the Stokes number is sufficiently small, such that the particles follow the flow. Combining Equations (130) and (126) leads to an explicit equation for the voidage, expressed as:

$$\varepsilon = \frac{\rho_p - \frac{m_g - m_{strain}}{V_{Displaced} + \frac{1}{2} \frac{A_{\perp}}{g} v_i^2 C_w}}{\rho_p - \rho_f} \quad (131)$$

Equation (131) may be used on the assumption of a small Stokes number, where the apparent liquid mass density in the drag force is ρ_{mix} . The drag coefficient C_w in Equation (131) is dependent on the particle-fluid suspension and flow velocity. To investigate the relevance of C_w and the hydrodynamic forces, the linear flow rate during the experiments was increased up to 230 m/h. Even at the highest flow velocity, the hydrodynamic drag term ($\frac{1}{2} \rho_{mix} v_i^2 A_{\perp} C_w$) is rather small compared to the buoyancy term ($\rho_{mix} g V_{object}$), and could therefore be neglected (max 0.16%), in particular regarding the operational window (60-90 m/h) of full-scale pellet-softening reactors. The influence of linear thermal expansion was also examined and could be neglected as well (max 0.06%). Derivations of given equations and tests in an empty column are provided in the Supplementary material (Section 4).

11.4.4 Total particle mass and differential pressure

The local voidage can be determined with Equation (131). The overall average voidage of the whole system can be calculated using Equation (33), based on the initial dry particle mass and total observed fluidised bed height:

$$\varepsilon = 1 - \frac{m}{\frac{\pi D^2 L \rho_p}{4}} \quad (36)$$

In this research, the differential hydraulic pressure over the bed height was not measured directly. However, based on the particle mass and density, calculating the maximum pressure drop indirectly for the fluidised state (Equation (33)) is straightforward. These values can be validated with data from previous research (Kramer *et al.*, 2020b):

$$\Delta P = \frac{mg}{\frac{\pi}{4}D^2} \left(1 - \frac{\rho_f}{\rho_p} \right) \quad (33)$$

11.4.5 Submerged object corrections

Constriction model to compensate velocity and voidage perturbations

Because the cylindrical object is suspended in the hydrometer tube, the superficial fluid velocity will be larger (approximately 3% - 12%) due to the decreased surface area (Figure 113 and Figure 114). This causes a locally increased voidage at the height of the object. Therefore, a correction is imperative to estimate the voidage for the lower velocity corresponding to the undistorted bed. Based on accurate expansion experiments (Kramer *et al.*, 2020b), an empirical relationship (Voidage Power Function) between the voidage and the superficial fluid velocity was derived and used to determine a correction for the voidage.

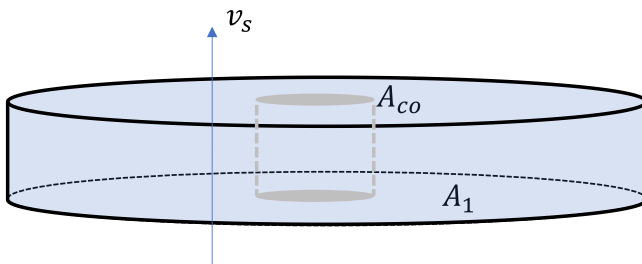


Figure 113 Constriction model: schematic overview of a cylindrical object submerged in a fluidised bed



Figure 114 Largest cylindrical object

From expansion experiments for a myriad of granules and expansion data found in the literature (Kramer *et al.*, 2020b), a general fit parameter was found. Subsequently, Equation (132) can be used to compensate the constriction effects caused by the cylindrical object submerged in the fluidised bed:

$$\varepsilon_1 = \varepsilon_2 \left(1 - \left(\frac{D_{co}}{D_{hm}} \right)^2 \right)^{\frac{1}{3}} \quad (\varepsilon_1 < \varepsilon_2); (\varepsilon_{mf} < \varepsilon < 0.95) \quad (132)$$

Where ε_1 is the (corrected) voidage at situation 1 with no distorted bed and ε_2 (uncorrected) at situation 2 where the flow is restricted due to submerged object in the fluidised bed. D_{co} is the diameter of the cylindrical object and D_{hm} the inner column diameter of the hydrometer. The derivation of Equation (132) is given in the Supplementary material (Section 4).

The influence of the object dimensions on the prediction accuracy

To investigate the influence of the object dimensions on the prediction accuracy, the fluidisation quality and the number of particles in the vicinity of the object were determined. The Froude number is defined as the ratio of inertial to gravity forces (Di Renzo *et al.*, 2017). The densimetric particle Froude number Fr_p (Grace, 1986); (Wirth, 1991); (Kramer *et al.*, 2020a) can be used as a proxy for the fluidisation quality from smooth homogeneous (particulate) fluidisation to heterogeneous or aggregative (bubbling) fluidisation, expressed in Equation (14):

$$Fr_p = \frac{v_s}{\sqrt{\left(\frac{\rho_p}{\rho_f} - 1 \right) g d_p}} \quad (14)$$

A transition occurs from particulate or smooth homogeneous fluidisation to heterogeneous or aggregative (bubbling) fluidisation at $Fr_p = 1$ (Bird *et al.*, 2007); (Yang, 2003); (Di Felice, 1995) mostly for gas-solid systems, but lower values are also proposed: $Fr_p < 0.13$ (Gupta and Sathiyamoorthy, 1999). In general, the transition from a homogeneous to a heterogeneous state is gradual.

The validity of the suspension mixture density ρ_{mix} depends on the number of solid particles around the submerged object. The estimate of the number of particles in a layer around the submerged object is based on the assumption that the particles are spherical and equidistant. The average distance between the centres of two spherical particles Δd_p in fluidised state can be calculated with Equation (133):

$$\Delta d_p = d_p^3 \sqrt{\frac{\pi}{(1 - \epsilon) 3\sqrt{2}}} \quad (133)$$

If the layer around the object is ξ particles thick, the number of particles N_p around the submerged object can be calculated with Equation (134):

$$N_p = \left(\frac{L_{co}}{\Delta d_p} + 2\xi - 1 \right) \left(\pi \left(\frac{D_{co}}{\Delta d_p} + 2\xi \right) - 1 \right) \quad (134)$$

Derivations can be found in the Supplementary material (Section 4).

11.4.6 Discretisation modelling

Bed height

The fluidised bed in the column can be subdivided into segments. By gradually lowering the submerged object, for every measurement, the position, weight loss and accordingly the voidage (Equation (131)) can be determined. This way, the gradient in the particle bed can be obtained. In principle, two constraints apply to the segment heights and local voidage values: first, the sum of N segment heights should be equal to the total bed height L (Equation (135)), and second, the total solid mass should be conserved (Equation (136)):

$$L = \sum_{i=1}^N \delta z_i \quad (135)$$

$$\sum_{i=1}^N (1 - \epsilon_i) \delta z_i = L_0 (1 - \epsilon_0) \quad (136)$$

In practice, a deviation between the sum of $(1 - \epsilon_i) \delta z_i$ and the total measured value $L_0 (1 - \epsilon_0)$ can be expected. Based on Equation (136), it is possible to calculate a correction factor f (universally applied to the estimated voidages at all heights) that can be used to compensate for the deviation:

$$f = \frac{L - L_0(1 - \varepsilon_0)}{\sum_{i=1}^N \delta z_i \varepsilon_i} \quad (137)$$

So, $\varepsilon_{i,corr} = f \varepsilon_i$ such that $\sum_{i=1}^N (1 - f \varepsilon_{i,corr}) \delta z_i = L_0(1 - \varepsilon_0) = L(1 - \varepsilon)$ hence:

$$L = f \sum_{i=1}^N \delta z_i \varepsilon_i = L_0(1 - \varepsilon_0) \quad (138)$$

Differential pressure

In a homogeneous steady fluidised state, the hydraulic pressure drop equals the weight of the particle bed, reduced by the buoyancy forces, per unit of bed volume according to Equation (22) (Bird *et al.*, 2007):

$$\frac{\Delta P_{max}}{\Delta L} = (\rho_p - \rho_f)g(1 - \varepsilon) \quad (139)$$

In the presence of a vertical gradient, the summed differential pressures per segment (Equation (140)) must be equal to the total pressure drop according to Equation (33):

$$\Delta P_{max} = g(\rho_p - \rho_f) \sum_{i=1}^N (1 - \varepsilon_i) \delta z_i \quad (140)$$

Where $\varepsilon_i = \varepsilon_{i,corr}$ from Equation (138).

Number of particles in the system

Assuming spherical particles, Equation (141) can be used to estimate the number of particles in one particular segment in the fluidised bed in a cylindrical column:

$$N_i = \frac{3}{2}(1 - \varepsilon_i) \frac{D^2}{d_p^3} \delta z_i \quad (141)$$

Accordingly, the total solid particle area in the bed volume is the sum of all the particle surfaces combined: $\sum N_i A_{1p}$ leading to the total surface area TSA in the entire fluidised bed:

$$TSA = \frac{3}{2}\pi D^2 \sum_{i=1}^N \frac{(1 - \varepsilon_i)}{d_{p,i}} \delta Z_i \quad (142)$$

11.4.7 Particle size estimation

Accurate expansion experiments (Kramer *et al.*, 2020b) combined with symbolic regression techniques (Koza, 1992) have provided an empirical data-driven model to predict the voidage as a function of the fluid and particle properties. This same approach was applied to predict the (spherical) particle size conversely as a function of the superficial fluid velocity, kinematic viscosity, particle density and measured voidage following Equation (143):

$$d_p = v_s^{c_0} v_T^{c_1} \left(\frac{\rho_p}{\rho_f} - 1 \right)^{c_2} (c_3 \varepsilon^{c_4} + c_5 \varepsilon^{c_6}) \quad (\varepsilon_{mf} < \varepsilon < 0.95) \quad (143)$$

Fitting parameters for calcite pellets, glass beads and highly spherical particles were obtained using non-linear regression software; these are given in Table 39. Model explanation, sources and further fitting parameters for other types of granules are given in the Supplementary material (Section 4). Fit parameters for other examined granules are provided in (Kramer *et al.*, 2020c).

Table 39 Fitting parameters in Equation (143)

Grain material	c_0	c_1	c_2	c_3	c_4	c_5	c_6	R^2
Glass beads	1.148	0.3060	-1.190	1.120	-3.050	5.875	1.475	0.990
Calcite pellets (calibrated data-set)	1.068	0.3101	-3.217	2.360	-3.069	11.73	1.059	0.968
Calcite pellets (validated data-set)	1.031	0.4264	-0.283	2.529	-3.161	6.938	0.808	0.915
Crushed calcite	0.613	0.4053	1.037	0.4764	-2.272	3,317	13.74	0.733

11.4.8 Model-based hydraulic state determination and reactor performance indicators

If the voidage and the (spherical) particle diameter are known, reactor Key Performance Indicators (KPIs) can be calculated (Kramer *et al.*, 2020b). The most commonly applied KPI is the specific surface area (SSA), which represents the available area per m³ reactor volume for crystallisation (Edzwald, 2011); (Crittenden *et al.*, 2012); (Yang, 2003). The reactor performance indicators used are the specific surface area based on the reactor volume $A_{s,r}$ and the specific surface area based on the water phase $A_{s,w}$:

$$A_{s,r} = 6 \frac{1 - \varepsilon}{d_p} \quad (102)$$

$$A_{s,w} = \frac{A_{s,r}}{\varepsilon} \quad (103)$$

In addition, the specific space velocity A_c is used (Kramer *et al.*, 2020b) defined as the contact area per second per m² of transfer surface area (Levenspiel, 1999). The specific space velocity (SSV) is defined as:

$$A_c = A_{s,w} \frac{v_s}{\varepsilon} \quad (104)$$

Please note that A_c is an inverse time scale with units [s⁻¹], while their counterparts $A_{s,r}$ and $A_{s,w}$ are both inverse length scales with units [m⁻¹].

In this research, the gradient in fluidised bed is studied. Consequently, the KPIs also have to be calculated. This is done with Equations (102), (103) and (104) on a longitudinal scale due to varying voidage and particle size. Since the measurements performed were discrete, the KPIs should also be calculated per segment over the bed height. The discretised KPIs can accordingly be found where the thickness of the layer is weighted: $\delta z_i = L/N$:

$$A_{s,r} = \frac{6}{N} \sum_{i=1}^N \frac{(1 - \varepsilon_i)}{d_{p,i}} \quad (144)$$

$$A_{s,w} = \frac{6}{N} \sum_{i=1}^N \frac{(1 - \varepsilon_i)}{\varepsilon_i d_{p,i}} \quad (145)$$

$$A_c = v_s \frac{6}{N} \sum_{i=1}^N \frac{(1 - \varepsilon_i)}{\varepsilon_i^2 d_{p,i}} \quad (146)$$

11.5 Results and discussion

11.5.1 Preliminary full-scale experiment

To explore the possibility of measuring a weight gradient in a liquid-solid fluidised bed, an object was submerged in a full-scale pellet-softening reactor (Figure 116) with a diameter of $D = 2.6$ m and a bed height of $L = 4.20$ m. The superficial fluid velocity was $v_s = 86$ m/h with a water temperature of $T = 12$ °C. A steel object was gradually submerged in the fluidised bed using a regular suspended scale. Additionally, 16 samples of calcite pellets were withdrawn at different heights. The grains were dried, sieved and analysed with image analysis software ImageJ (Ferreira and Rasband, 2012). The largest pellets were found at the bottom of the reactor ($d_p = 1.17$ mm) and the smallest at the top of the fluidised bed ($d_p = 0.47$ mm). The mass of the spherocylindrical object in air was 2.71 kg and submerged in water 2.45 kg. In Figure 115, the decreasing object mass is plotted in black circles against the position in the fluidised bed, *i.e.* height. The mass gradually decreased from 2.37 kg in the top region to 2.19 kg in the vicinity of the reactor's bottom region. The mass difference (decreased mixture mass density and hence the variation in particle volume concentration) in the fluidised bed was 0.18 kg, corresponding to 0.7 mm difference in particle size. Based on this indicative result, a new pilot plant set-up was designed in which 40 experiments were prepared and executed. These are discussed in the next Section.

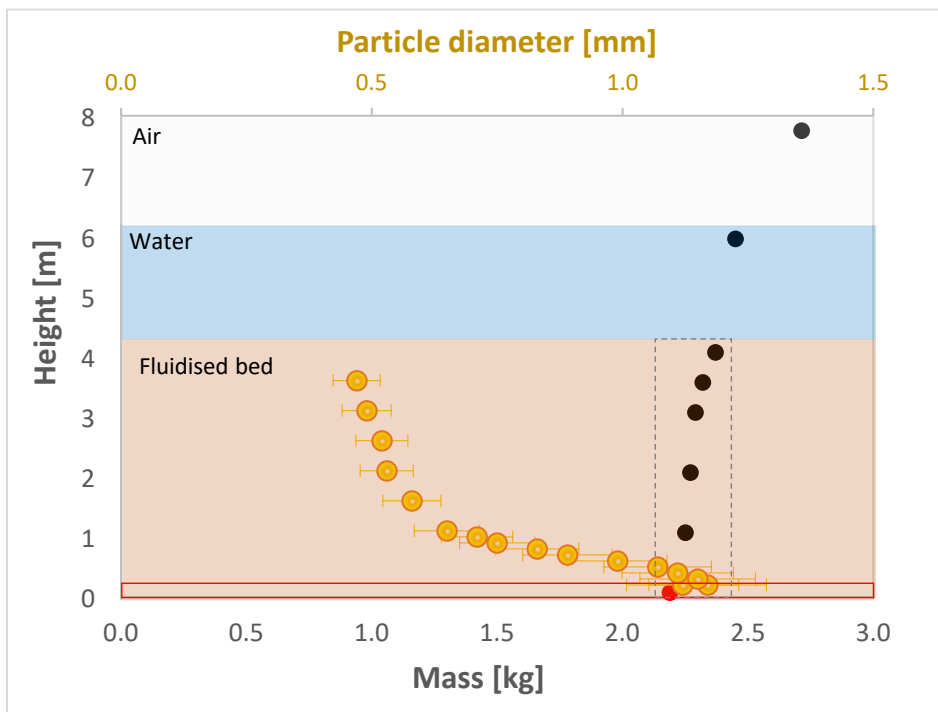


Figure 115 Object weight measured (middle object) in softening reactor (Figure 116) at various heights in air, water and fluidised bed. Superficial fluid velocity 86 m/h, water temperature 12 °C, bed height 4.20 m, maximum pressure drop 16.5 kPa. Steel spherocylindrical object 90 x 57 mm, volume 0.26 L, 2.71 kg in air, 2.45 kg submerged in water. The gradient difference in the fluidised bed $\Delta m/\Delta L \approx 0.045$ kg/m. Dotted grey frame indicates the measured gradient, ● the spherocylindrical submerged object, ● object near the reactor bottom, ● indicates the particle ImageJ/sieve diameter with error bars caused by the particle size distribution. Red frame indicates unstable zone caused by distributor ($z = 10$ cm).

11.5.2 Particle selection

For the fluidisation experiments, 5 kg of glass beads were purchased, and a total of 30 kg of calcite pellets was fractionated (Table 40) to obtain the best achievable monodisperse particles. The particle density was measured through a laboratory pycnometer with an error of 0.5%. The particles' sizes were measured using a classical sieve analysis, image analysis and additionally with a Camsizer for validation purposes. Compared to the sieve mesh size, the particle size of the

relatively spherical calcite pellets (sphericity $\phi_s \approx 0.95$) was approximately 5% larger when determined with the Camsizer and approximately 13% larger when determined with ImageJ. For the irregularly shaped, crushed calcite (sphericity $\phi_s \approx 0.90$), the differences were 14% and 36% for the Camsizer and ImageJ, respectively. These differences were presumably caused by the particle orientation. Particles pass through a sieve mesh vertically oriented, whereas scanned particles orient horizontally during the ImageJ analysis (Kramer *et al.*, 2021c). Photographs, particle properties and technical details of equipment used are provided in the Supplementary material (Sections 2 and 3).

11.5.3 Proof of concept of the hydrostatic weighing technique

Initially, nine fluidisation experiments were executed with glass beads (Figure 116) at high velocity to investigate the influence of the size of submerged objects on the accuracy of voidage determination. For this research, a total of 40 fluidisation experiments were conducted with calcite pellets and crushed calcite. To demonstrate the weight gradient over the bed height, nine fluidisation experiments were executed with a mixture of calcite and crushed calcite fractions (Table 40). Accordingly, to study the prediction accuracy of the voidage and (spherical) particle size, two relatively monodisperse particle samples of calcite pellets were used. Finally, four additional experiments were performed with an alternative submerged object material.

Table 40 Particle properties of examined granules used in the hydrometer measurements

Fraction [#]	Grain type	Geldart's particle type ¹⁾	Particle size min-max [mm] ²⁾	Dry weighted particle mass [kg]	Particle density [kg/m ³]	Sieve diameter [mm]	Camsizer diameter [mm]	ImageJ diameter [mm]	Sphericity [-]
Particle bed 0	Glass beads	D	3.03-3.14	4.95	2,515	-	-	-	0.99 ³⁾
Particle bed 1	Calcite pellets	B	0.80-0.90	10.00	2,614	0.95	0.99	1.06	0.94
Particle bed 2	Calcite pellets	D	0.90-1.00	10.00	2,625	0.56	0.64	0.76	0.95
Particle bed 3:	Calcite pellets +	B	0.50-0.63	4.00	2,560	1.32	1.37	1.50	0.90
(two fractions)	Crushed calcite	D	1.25-1.40	6.00	2,632	0.85	0.90	0.97	0.97

¹⁾ Geldart's particle classification (Geldart, 1973). Type B; sand-like particles and type D: spoutable particles

²⁾ The effective or average hydraulic equivalent particle diameter $d_p = \sqrt{d_{s,1} d_{s,2}}$, (Dallavalle, 1948); (Crittenden *et al.*, 2012)

³⁾ Sphericity of glass beads is obtained from literature (Dharmarajah, 1982); (Crowe and Group, 2006); (Kramer *et al.*, 2020a). Sphericity is the ratio of the surface area of an equal volume sphere to the surface area of the grain calculated from the perimeter P and project area



Figure 116
3 mm glass beads (Boom lab) at $v_s = 240$ m/h



Figure 117
Aluminium cylindrical objects, ($L_{co} = 100, 120, 160$ mm · $D_{co} = 20, 30, 40$ mm), $\rho_p = 2,701$ kg/m³



Figure 118
Titanium cylindrical object, ($L_{co} = 130$, · $D_{co} = 35$ mm), $\rho_p = 4,464$ kg/m³

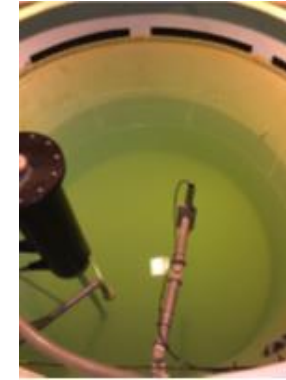


Figure 119
Full-scale pellet-softening reactor top view, reactor diameter ($D = 2.6$ m)

Submerged object dimensions

Experiments were executed in the experimental set-up with monodisperse glass beads (Figure 116) to scrutinise the dimensions of the submerged objects and to validate the constriction model (Equation (132)). A total of 9 aluminium cylinders (Figure 117) with varying dimensions were compared at a high superficial fluid velocity ($v_s = 240$ m/h). The reason for choosing aluminium objects was based on an expected voidage in the lowest region of the pellet-softening reactor. A usual voidage $\varepsilon \approx 0.55$ leads to a suspension density of $1,750$ kg/m³ (Equation (126)). To prevent floating, the density of the submerged object must be larger than the suspension density. It has, however, to be small enough to maintain an object mass within the measurement range, and to have a large enough object size to be within the correct limit of being much larger than the particle size. Based on the measured 'submerged object voidage' (Equation (131)) and the average voidage of the entire system (Equation (36)), the average relative prediction error (Equation 70) was calculated, indicated with blue circles in Figure 120, using Equation (131) and Equation (36):

$$ARE = \frac{1}{N} \sum_{i=1}^N \left(\frac{|\varepsilon_{calc,i} - \varepsilon_{exp,i}|}{\varepsilon_{exp,i}} \right) \quad (147)$$

The average relative error for the six aluminium objects ($L_{co} = 100$ and 120 mm) was 2%. For the three aluminium objects ($L_{co} = 160$ mm), the relative error was 6%. The objects were submerged approximately 10 cm in a fluidised bed of glass beads with an expanded bed height of 41 cm. The longest objects, only 14 cm in the vicinity of the fluid distributor, showed a larger error compared to the objects with a shorter length. This was probably caused by the heterogenous flow distribution in the bottom region of the column. The lowest error of 1% was found for the cylindrical objects with the largest width, presumably due to its higher mass, causing it to be more stable in the fluidised bed. In addition, elongated cylinders tend to rotate to maximise their cross-sectional area A_{\perp} of the object perpendicular to the flow. In addition, the error was calculated for all other fluidisation experiments and is presented in Figure 120. The overall average relative error was $5 \pm 2\%$. The results are not conclusive with respect to the choice of the most optimal object dimensions. There are certainly more effects governing the voidage prediction accuracy, such as object density, shape and (semi) homogeneous fluidisation. The effect of object dimensions, however, seems to have been compensated for by using the constriction model, as

shown in Equation (132). The effect of constriction was visible during the measurements. Upon lowering the object, a decreased weight was observed for a period of 5 to 10 seconds. Presumably, during this period, the fluidised bed voidage re-adjusted to the altered flow caused by the presence of the object. After this effect subsided, the average weight remained constant, however fluctuations were still present, especially in the lower regions of the column. This was most likely caused by an inhomogeneous particle bed in the vicinity of the water distributor at the bottom of the column resulting in object swaying. The maximum fluctuation was ± 2 g and is considered in the Data transformation model error analysis in Section 5 of the Supplementary material.

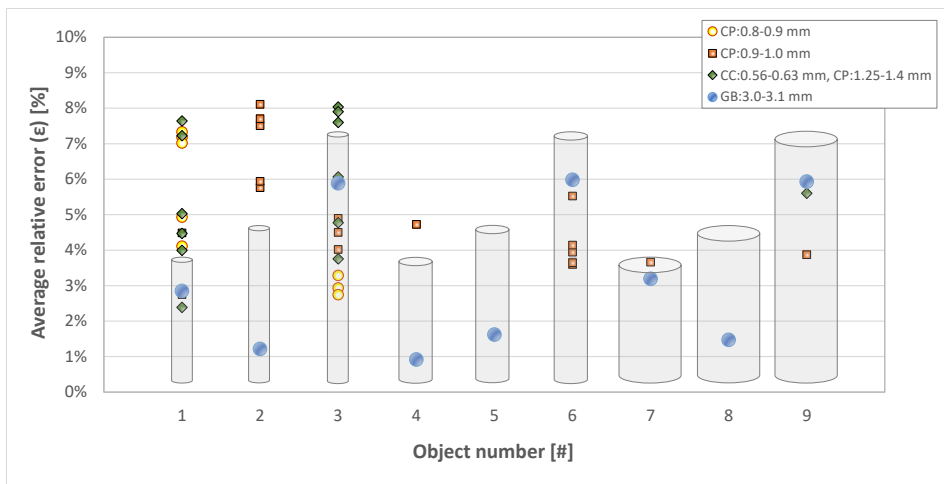


Figure 120 Average relative error (Table 31) estimated voidage against the cylindrical object number (Figure 117). Yellow circles: calcite pellets (0.80-0.90 mm), orange squares: calcite pellets (0.90-1.00 mm), green rhombus: mixture of crushed calcite (0.50-0.63 mm), calcite pellets (1.25-1.40 mm) and blue circles: glass beads (3 mm). The constriction model (Equation (132)) was used to compensate fluid velocity and voidage changes caused by the object in the cylindrical column.

To investigate the influence of the object density, four additional experiments were performed with a titanium cylindrical object ($L_{co} = 130$, $D_{co} = 35$ mm) as shown in Figure 118. The average prediction error for the voidage was $4 \pm 2\%$, but the observed instabilities in the lower region of the cylindrical column ($z < 10$ cm) did not decrease. Therefore, in this research we could not explicitly determine the optimal material density for the submerged object for the use in a pellet-softening reactor.

The densimetric particle Froude number Fr_p was calculated (Equation (14)) to obtain information about the prevailing fluidisation quality. Predictions errors against the Froude number does not indicate that heterogeneous unsteady behaviour (Di Renzo and Di Maio, 2007) is a determining factor. Figures can be found in the Supplementary material (Section 4). Equation (134) was used to estimate the number of particles in a layer around the submerged object to examine whether or not the suspension density assumption violated. When the layer around the object is ξ was set to 1, the minimum number of particles around the submerged object was approximately 1,000 (maximum 25,000), sufficient to apply the hydrostatic weighing technique to estimate the voidage. Although no adverse influence was found related to the number of surrounding particles, it is not clear below which number the accuracy will decrease. The glass beads measurements appear to be more accurate compared to pellets, but please note that the data spread for all grains examined is more or less the same at 5%. Figures with predictions errors can be found in the Supplementary material (Section 4).



Figure 121 *Single fraction experiment 0.9-1.0 mm calcite pellets*



Figure 122 *Two-fractions mixture: crushed calcite grains 0.50-0.63 mm at the top and calcite pellets 1.25-1.40 mm at the bottom*

Expansion experiments for the gradient determination with a two-fractions mixture

Fluidisation experiments were performed in four differently sized calcite fractions as shown in Table 40. The goal of the first experiment was to show that a sharp gradient in the longitudinal direction can be measured. To this end, a mixture of grains was composed of two fractions (Figure 122). The grains represent the extremes in particle size and position in a full-scale pellet-softening reactor: the largest calcite

pellets 1.25-1.40 mm can be found in the lowest region of the reactor while crushed calcite grains 0.50-0.63 mm can be found in the top of the fluidised bed. In a series of experiments ($N = 13$) with the double fraction calcite mixture, the object was gradually lowered in the fluidised bed as shown in Table 31. The weight gradient can be identified in Figure 123 ($0.3 < W_{sub} < 0.5$ N). During the experiments, instabilities were observed in the lower region of the cylindrical column ($z < 10$ cm). These values were omitted from the results (indicated in red). Supporting arguments for removing these data points are that in later optimising studies, instabilities can be prevented or resolved by better object design. All experimental data has been shared in (Kramer, 2021e) and in the Supplementary material (Section 9).

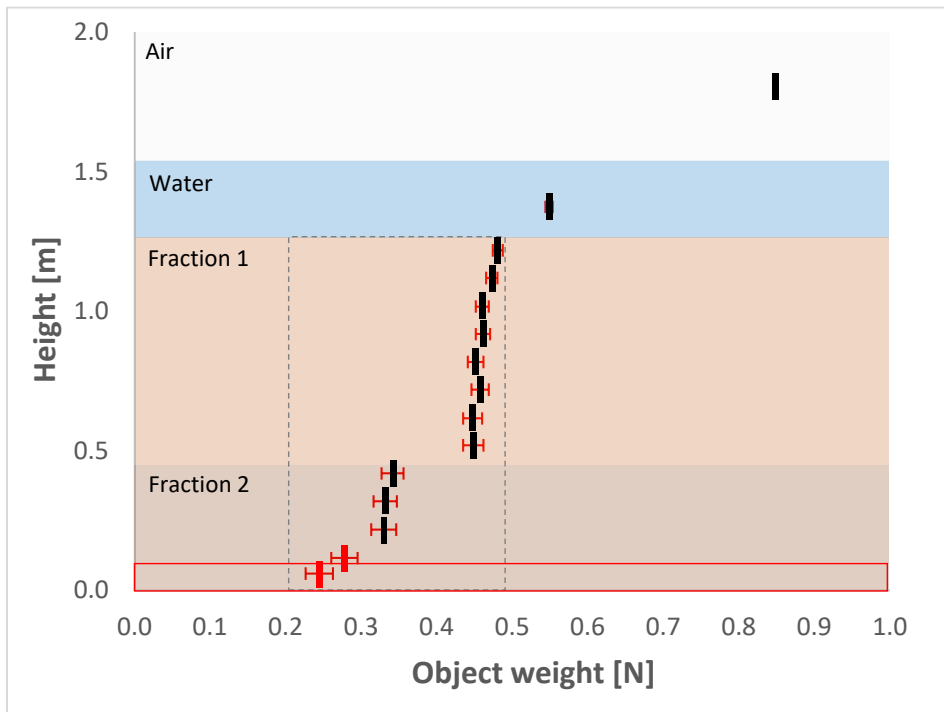


Figure 123 Experiment #31. Object weight was measured (middle object) at various heights in air, water, and fluidised bed fractions. Superficial fluid velocity 101 m/h. Water temperature of 11 °C. Aluminium cylindrical object 100.09 x 20.05 mm, volume 0.032 L, 0.85 N in air, 0.55 N submerged in water. Error bars indicate observed fluctuations during measurements. Dotted grey frame indicates the measured gradient. Red frame shows unstable zone caused by distributor instabilities ($\Delta z = 10$ cm). Measurements in this zone are excluded and marked red.

The density gradient (Equation (131)) is clearly visible in Figure 124. The green rhombuses represent the middle of the object where the gradient among the object length was averaged. The voidage, based on Archimedes' principle (Equation (131)) was compared with the bed height (Equation 136) and mass-based mean voidage (Equation (36)). In this way, the gradient could be validated. Figure 125 shows that there is an increasing deviation between the local voidage and the mean system voidage when lower regions are reached. This deviation was a generally consistent trend for the majority of the experiments. The observed slope in Figure 125 for the local voidage is caused by a prevalent stratification of grains in the range 0.50 to 0.63 mm where the 'largest' grains can be found in the lowest zone of this fraction and *vice versa*. The explanation for the absolute deviation can be explained by calibration inaccuracies, hysteresis and a non-optimal object density. Although the load cell was carefully calibrated to improve the strain measurement, errors were found between 0.5-1%. Every deviation in strain corresponds with a comparable degree of error in voidage prediction error. Information about hardware calibration is provided in the Supplementary material (Section 3).

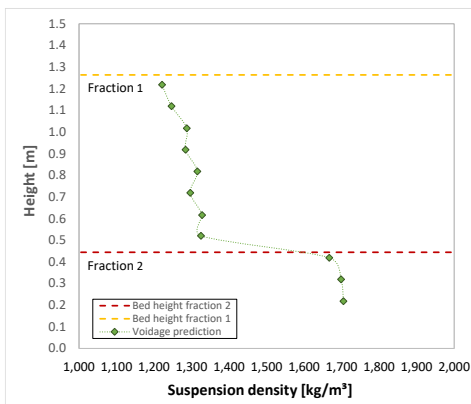


Figure 124 Suspension density ρ_{mix} derived from weight measurements at various heights. Individual fractions are presented by yellow and dark red dotted lines. The gradient difference in the fluidised bed $\Delta\rho_{mix} \approx 500$ (kg/m³)/m.

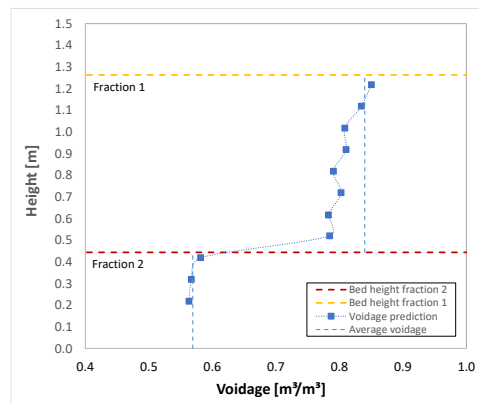


Figure 125 Voidage ε derived from weight measurements at various heights. Blue dotted lines show the average voidage in respective fractions calculated independently, based on initial particle mass, particle density and bed height. The gradient difference in the fluidised bed $\Delta\varepsilon \approx 0.3$ 1/m.

Figure 125 shows a zig-zag pattern, which was not only the result of the object ascending and descending within the fluidised bed but also due to hysteresis. The hardware shows a minor sensitivity of 3% of the total range (2 kg) for hysteresis. In addition, due to the shape of the cylindrical object, a few grains tend to settle on the top of the surface of the object. Approximately for every gram of *hitchhiking* grains, the voidage prediction error increases with 1%. In this research, aluminium cylindrical objects were used to match the expected fluid suspension density. In this research, the effect of adjusting the object density has not been investigated thoroughly. Despite the observed deviation, this experiment with two fractions clearly demonstrated the potential to measure a gradient and to estimate the voidage at any height except the lowest 10 cm.

Please note that in Figure 125 and Figure 126 the voidage was not corrected with Equation (138). Using a correction, the voidage prediction would be centred around the average voidage such that the average over the voidage prediction within a layer matches with the average voidage of that layer.

Table 41 Aluminium object measures and voidage prediction error ¹⁾

Object nr.	<i>D</i>	<i>L</i>	<i>A</i>	<i>m</i>	<i>m_{sub}</i>	<i>ARE</i> (ϵ) GB:3.0 mm	<i>ARE</i> (ϵ) CP:0.8-0.9 mm	<i>ARE</i> (ϵ) CP:0.9-1.0 mm	<i>ARE</i> (ϵ) CC:0.50-0.63 mm CP:1.25-1.40 mm
[#]	[mm]	[mm]	[mm ²]	[g]	[g]	[%]	[%]	[%]	[%]
1	20.05	100.09	316	88.03	56.22	2.8	6.1	3.6	5.1
2	20.08	120.06	317	104.86	66.76	1.2	-	7.0	-
3	20.17	160.00	320	141.29	89.90	5.9	3.0	4.5	6.4
4	29.92	100.38	703	202.16	131.50	0.9	-	4.7	-
5	29.92	120.13	703	230.70	146.42	1.6	-	-	-
6	29.92	160.00	703	320.72	208.34	6.0	-	4.1	-
7	40.06	100.52	1,260	342.76	216.68	3.2	-	3.7	-
8	40.00	120.09	1,257	408.52	258.18	1.5	-	-	-
9	40.01	160.00	1,257	545.26	344.32	5.9	-	3.9	5.6

¹⁾ GB: glass beads, CP: calcite pellets, CC: crushed calcite

Single fraction experiments

Next, two single fractions of calcite pellets were used to examine whether the spherical particle size could be predictive using a data-driven model (Equation (143)) based on the known particle fluid properties. Figure 126 demonstrates the existence of a gradient for both voidage and estimated (spherical) particle size (Equation (143)). The stratified bed and known sieve diameters enable the application of a linear interpolation of particle size over the length scale of the bed that better reflects the real situation.

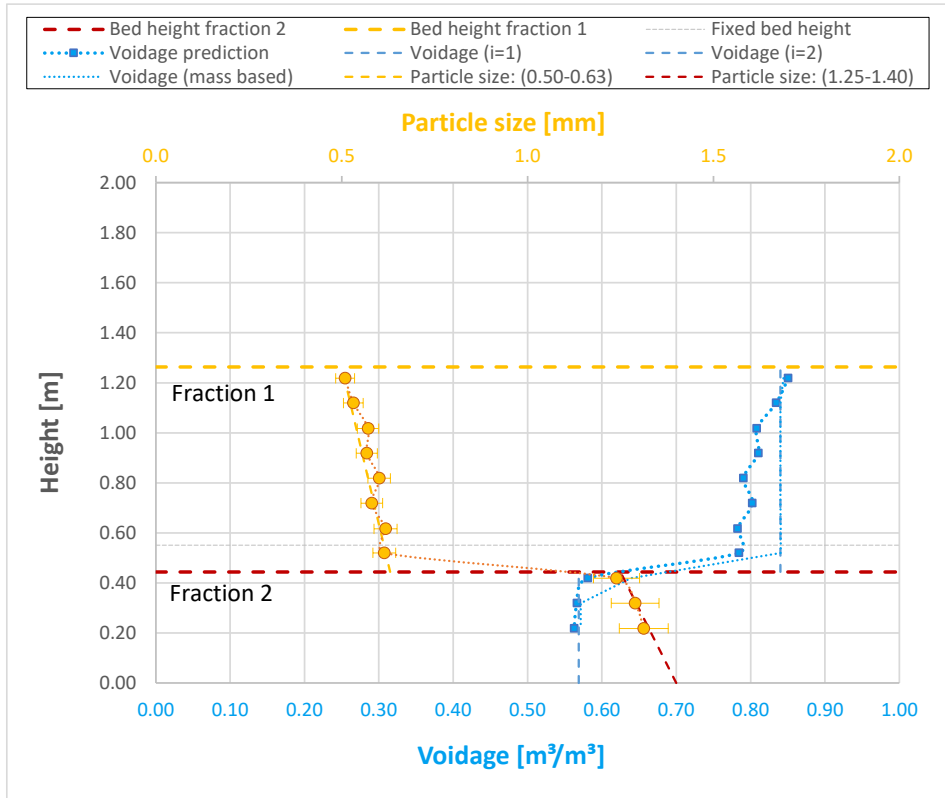


Figure 126 Experiment #31. Voidage and particle size prediction at various heights. Individual fractions are represented by yellow and dark red dotted lines. Blue dotted lines show the average voidage in respective fractions calculated based on initial particle mass, particle density and bed height. Yellow circles show the average particle size in respective fractions calculated based on the empirical prediction model according to Equation (143). The gradient difference in the fluidised bed $\Delta\varepsilon/\Delta L \approx 0.3 \text{ m}^{-1}$ and $\Delta d_p/\Delta L \approx 0.8 \text{ mm/m}$.

The voidage prediction results for all examined granules are presented in Table 31. The uncertainties regarding particle size comparison resulting from the different available image analysis methods are indicated with error bars (yellow). As the fixed and fluidised bed heights were measured during the experiments, the mass balance could be used to validate the total bed height (Equations (135) and (136)). In addition, the summed differential pressures per layer (Equation (140)) were used for a comparison with the total expected pressure drop (Equation (33)). The prediction error for ΔP_{max} was approximately 7% with a standard deviation of 5%, shown in

Table 42. The extent of the error for bed height and differential pressure is strongly dependent on the quality of the voidage prediction. When the correction factor expressed in Equation (137), was used, the overall voidage production accuracy was enhanced from 5% to 3%. This correction factor could be a solution in full-scale operations to cross validate measured and estimated process variables.

Table 42 Voidage, particle size and pressure drop prediction error. The last two columns are prediction errors after application of the voidage correction f (Equation (137)).

Object number	Average relative error						
	(ε)	(d_p) ¹⁾		$(\sum_{i=1}^N (1 - \varepsilon_i) \delta z_i)^2$	(ΔP_{max})	f	(ε)
[#]	[%]	[%]	[%]	[%]	[-]	[%]	[%]
GB:3 mm	4.7	8.8	9.5	9.5	1.06	2.9	11.8
CP:0.80-0.90 mm	5.0	11.2	7.1	7.1	1.04	3.9	15.6
CP:0.90-1.00 mm	5.7	7.9	10.8	7.9	1.05	3.2	9.1
CC:0.50-0.63 mm	3.2	5.3	3.1	3.1	1.03	0.8	3.6
CP:1.25-1.40 mm							
Total average	4.8	8.8	7.8	7.0	1.03	3.0	11.0
Standard deviation	1.9	3.8	5.1	4.7	0.03	1.3	5.7

¹⁾ Carman (1937) results for comparison, respectively: 11%, 9%, 10%, 5% and for Richardson–Zaki (1954) 21%, 17%, 18% and 13%

²⁾ Equations (136) and (138)

Table 42 shows the particle size prediction errors using the novel data-driven model (Equation (143)) and in addition, the prediction errors of the Carman–Kozeny and the Richardson–Zaki model. We prefer the data-driven model, fitted for non-spherical calcite pellets, besides for its slightly lower prediction error but also for the explicit expression for the particle diameter. The particle size prediction quality depends largely on the accuracy of the voidage ($d_p \cong \varepsilon^{-3}$). The dependency of the particle size on the voidage and figures with predictions errors can be found in the Supplementary material (Section 4). In addition, approximately 10% uncertainty can be expected due to calcite pellets being fractionated with sieves with the minimum difference between two successive sieve meshes ($d_{s,1}/d_{s,2} = 10^{1/20} = 1.12$). Consequently, particle size estimation is only functional when the voidage determination is reasonably accurate. In addition, calcite grains are not completely spherical (Table 40), which implies a discrepancy between estimated and real particle size (and shape). Bias is also expected from sieve analysis when particles are highly non-spherical, such as crushed calcite.

Data transformation model

A sensibility analysis was conducted to determine the implications for the data conversion steps, *i.e.* the data transformation model (DTM). The load cell measured the weight of the object expressed in voltage (error $\approx 0.6\%$). Through a calibrated relationship, the buoyant forces and weight loss were determined with the software (error $\approx 3\%$). Through a model (Equation (126)), the suspension density was calculated (error $\approx 3\%$). Accordingly, the voidage could be approximated with Equation (131) (error $\approx 5\%$). The particle volume, bed height and pressure drop based on the overall mass balance were used to optionally further validate these results (error: 7%). Based on the voidage, the spherical particle diameter could be estimated with Equation (143), albeit with a significant error $\approx 10\%$. Using the summarised propagated effect of errors (Ku, 1966) an error of 7% for ε , 12% for d_p and 14% for SSA was calculated. A detailed table of the data transformation model with the expected influence on the voidage prediction dependency can be found in the Supplementary material (Section 5). The hydraulic state determination error arises from a quantitative starting point to be considered. Nevertheless, in full-scale operation 10% uncertainty is acceptable for process monitoring and control, especially in view of the fact that currently there is no soft sensor available for such large scales.

11.6 Conclusions

A novel sensor has been developed, exploring the possibility of reasonably quick measurement of the hydraulic gradient in a liquid-solid fluidised bed applied in full-scale drinking water treatment plants. The preliminary test in a full-scale pellet-softening reactor at normal conditions was successfully performed to examine the existence of a gradient in the stratified bed. A mass loss of 10% was measured over the reactor bed, corresponding to 0.7 mm difference in particle size. This means that a lab-scale sensor was developed to measure the weight loss of a cylindrical submerged object while it was gradually lowered in the particle bed. During fluidisation experiments of a two-layer calcite grains system, a steep gradient between different layers could be measured, starting from 0.85 N in air, 0.55 N submerged in water, 0.48 N at the top and 0.24 N at the bottom of the column. A weight loss of 50% was measured over the fluidised bed, corresponding to 0.9 mm difference in particle size. Based on fluidisation experiments with two single layers

of calcite pellets, the particle size was estimated with a new data-driven model. Voidage could be estimated with an error of 5% and the spherical particle size with an error of approximately 10%. A developed constriction model was suitable to compensate for changes in fluid and voidage caused by objects suspended in the fluidised bed with different lengths and widths. The voidage prediction error could not be significantly decreased by choosing other submerged object dimensions, nor did the prediction accuracy improve when aluminium was replaced by titanium. As a consequence, measurements in the lowest region of the column were omitted as they were probably influenced by instabilities in the vicinity of the fluid distributor plate.

The new sensor was tested as a proof of concept. Despite a 5% prediction error for voidage, a 10% error for the spherical particle size and an overall propagated error of approximately 20% for the reactor key performance indicators, it was possible to measure a clear gradient in the liquid-solid fluidised bed during the experiments and in a full-scale reactor. This is promising for daily process control in full-scale reactors. The benefits of a longitudinal sensor for daily process control are quick access to the particle bed behaviour and, as a result, greater flexibility with changing water flow and process conditions. Impending problems such as fixed bed risk, flushing, hampering, or malfunctioning sensors such as differential pressure or bed height sensors can therefore be avoided. A potential downside compared to traditional differential pressure measurements is that the series of local measurements cost more time to process depending on the number of measurements performed. This could cause a delay for operational response to impending system changes. For the experimental set-up, 20 local measurements could be achieved in ± 30 minutes. If in future research the inaccuracies can be addressed and remedied, reactor key performance indicators can be calculated in real time to assess the hydraulic reactor's performance and to support optimal states.

11.7 Recommendations

To improve the accuracy and reliability of this novel sensor, several aspects must be improved.

- The decreasing accuracy in the lowest region of the reactor. This is relevant since the highest chemical driving force occurs in that particular zone. Solutions can be

found in the design of the submerged object, by optimising object dimensions, shape and density or using smart data filtering and processing.

- Combining the Archimedes-based hydrostatic weighing technique with an additional (submerged) differential pressure measurement device will make the discretised model validation more accurate.
- Adding a series of differential pressure meters over the height of the experimental fluidisation column will make validation of the results more accurate, along with making it possible to validate the gradient directly.
- The weight loss measurements with the new experimental set-up were executed and logged manually. Programming a routine (Q.monixx explained in Section 3.1.3 and in Supplementary material Section 1.1) can improve the data quality and decrease manual labour significantly.
- Substantiating a standard number of measurements sufficient for determining potential operational change, along with automation of the measurement could drastically decrease the time required for a profile measurement thereby minimizing the delay for operational response.
- During the measurements, the centre of the object was used as a reference point for the middle of a layer in which the voidage was averaged. By subdividing the column into more segments through introducing a gradual matrix data, more accurate voidage, particle size and surface area gradients can be determined.
- In full-scale pellet-softening reactors at the Waternet facility Weesperkarspel, a biomass growth process was detected on calcite pellets, caused by bacterial colonisation captured in calcite structures (Hammes *et al.*, 2011) forming porous calcium carbonate coatings. Grains with biomass growth have capricious shapes with different expansion behaviour, and accumulation in the fluidised bed causes a significantly higher degree of expansion. The sensor can be used to detect deviations in the preferred gradient.
- A sophisticated analysis of particle collisions with the Stokes number (Equation (13)) is useful for improving the voidage and particle diameter prediction accuracy.
- The scope of the novel sensor can be widened through fluidisation experiments with other types of granules, such as rapid filter sand, granular activated carbon and anthracite grains.
- Additional research is required to determine the effect of density on object swaying and weight fluctuation to substantiate choice of object material before implementation.

- Computational Fluid Dynamics simulations can help to improve particle-fluid-object interactions by including advanced detailed forces and hydraulic and hydrodynamic phenomena.
- The soft sensor could be used to derive more information from the fluidised bed by incorporating, for example, a turbidity meter, pH meter or thermometer.

Finally, in future research efforts, the hydraulic state should be combined with a chemical key performance indicator such as the calcium carbonate crystallisation potential (CCCP) (van Schagen, 2009); (Tang *et al.*, 2020). This will lead not only to further opportunities for reducing the chemical demand in pellet-softening reactors, but also to significant improvements in water treatment processes, such as more flexible operations, better water quality, reduced risks for approaching undesirable fluidisation states, reduced use of chemicals and greater sustainability. Recommendations, experimental raw data and additional details about the potential benefits of the novel sensor can be found in (Kramer, 2021e) and in the Supplementary material (Section 9).

11.8 Supplementary material

Supplemental data for this article can be accessed at:

<https://doi.org/10.1016/j.jwpe.2021.102091>

<https://ars.els-cdn.com/content/image/1-s2.0-S2214714421001781-mmc1.docx>

and (Kramer *et al.*, 2021e):

[Data set]. 4TU.ResearchData. <https://doi.org/10.4121/14204336.v1>

Contents		page
1	Photographs of full-scale pellet-softening reactors	3
2	Photographs of examined calcite pellets	4
	2.1 Calcite pellets	4
	2.2 Glass beads	5
3	Experimental set-up and standard operating procedure	6
	3.1 Hydrometer load cell and distance encoder schemes	6
	3.2 Data acquisition and GI.bench software	6
	3.2.1 Hardware and software	6
	3.2.2 Calibration measurements load cell and distance encoder	7
	3.3 Pre-design and photographs of the Hydrometer	9
	3.4 Particle size and shape measurements	10
	3.5 Particle size distribution of glass beads	10
	3.6 Morphological properties of calcite pellets	11
	3.7 Physical properties of particles	12
	3.8 Particle density and fixed and incipient voidage	12
	3.9 Differential pressure	13
	3.10 Physical properties of water	13
	3.11 Aluminium cylindrical objects	14
	3.12 Operating procedure	14
4	Derivations	15
	4.1 Suspension density	15
	4.2 Force balance	15
	4.3 Drag coefficient and equivalent liquid model	16
	4.4 Linear thermal expansion	17
	4.5 Constriction model	18
	4.5.1 Constriction effects - velocity	18
	4.5.2 First situation: no object in hydrometer tube	18
	4.5.3 Second situation: hydrometer hanging in tube	18
	4.5.4 Constriction effects - voidage	19
	4.5.5 Constriction effects - voidage cylinder	20
	4.6 Empty column test	20
	4.7 Empirical voidage and particle size prediction models	21
	4.8 Particle size prediction accuracy	22
	4.9 The influence of the object dimensions on the prediction accuracy	23
	4.10 Influences on the voidage prediction error	24

	4.11 The influence of collisions	26
5	Data transformation model	28
6	Full-scale consideration	29
	6.1 From robust to flexible water treatment process design	29
	6.2 Hydraulic state determination of pellet-softening fluidised beds	29
	6.3 An example of a scenario's for hydraulic state determination	29
	6.4 Operational window	31
	6.5 Relating hydraulic and chemical reactor performance indicators	32
	6.6 Future prospects and potential benefits of the soft sensor	33
7	Nomenclature	34
8	References	37
9	Experimental data	41
	9.1 Experiments with aluminium objects	41
	9.2 Experiments with a titanium object	65-66

Chapter 12

Synthesis

“To cope with future (un)expected circumstances, current full-scale water treatment plants should adapt and improve their design from robust to more flexible.”

12 Synthesis of research findings

Reliable drinking water can be produced and distributed to the consumer through a complex sequence of unit operations. Many of these unit operations involve multiphase flows using a variety of granules. This research focused on liquid-solid systems applied in drinking water treatment plants. With the lasting responsibility to produce reliable drinking water in the face of growing challenges, a flexible process control strategy is becoming increasingly crucial.

12.1 From a robust to a flexible process design

Traditionally, the granules used as raw material in pellet-softening of drinking water are mostly mined, and when these granules become waste material, they are often disposed of and de-valorised. For sustainability reasons, drinking water companies increasingly often investigate the possibility to initiate a transition from a linear to a more circular approach. For granules, new opportunities arise in this field if they can be processed and re-used in the treatment plant, which will subsequently lead to greater valorisation. A factor to be reckoned with in realising such opportunities, however, is the fact that particle properties of these granules (particle size and shape) change, affecting the condition and performance of the distinct unit operation: it will cause flushing and an altering degree of expansion. This means that the prediction of the particle bed expansion, *i.e.* voidage, is essential for ensuring reliable process control. It also has to be borne in mind that varying particle properties make the accurate prediction of voidage a complex affair. Different types of granules, such as rapid sand filter grains or crushed calcite pellets, are non-spherical and often also polydisperse, while activated carbon granules also have a porous structure. In addition, the particles can cause unsteady fluidisation behaviour, which makes the voidage prediction less precise. Hence, new fundamental knowledge was required to describe these multiphase flow systems. This study investigated three types of models to describe these systems: classical models, data-driven models and numerical models.

For optimisation and engineering, appropriate solutions are necessary to achieve pre-defined goals, such as effluent water quality requirements that comply with legal standards and operational norms. In addition, sustainability is becoming an

increasingly decisive factor when it comes to treatment process strategies, such as the use of other types of granules. Furthermore, it needs to be taken into account that drinking water companies are currently facing many more challenges, such as climate change (temperature), complex pollutions (reactor technology) and the increasingly intensive use of water catchment areas and sources required for the production and growing supply (throughput) of water (World Economic Forum, 2019). Still, the most important responsibility of drinking water companies remains public health, *i.e.* being responsible for providing sufficient, uninterrupted and safe drinking water to their customers. Traditionally, their treatment processes are robust (van Schagen, 2009) and designs are often over-dimensioned (Bosklopper *et al.*, 2004). For a water supplier to be future proof and to meet upcoming challenges, the concept of plant design should be revised and adjusted from robust to robust and flexible (Boccelli *et al.*, 2007). A similar example can be found in the way in which Japanese construction engineers improve the behaviour and response of buildings to earthquake hazards. Instead of building more and more solid and over-dimensioned structures, buildings are innovatively designed to be flexible in order to disperse the force of seismic motions.

In summary, drinking water is a vital resource for all of humanity, and water treatment plants can be resilient to impending changes that follow from different conditions by applying intelligent prediction models (Rietveld, 2005). Such models are an important part of adapting to changes when they have a fundamental basis and are suitable for adaptation in plant-wide process automation systems. Engineers should strive to find an optimal balance between straightforward models with acceptable prediction accuracy and model complexity.

12.2 Hydraulic modelling of liquid-solid fluidisation processes

Liquid-solid fluidisation processes are frequently applied in water treatment plants, often to achieve a large surface area. In this research, various models were examined and developed to predict the expansion or effective voidage of liquid-solid fluidised beds. To improve the prediction quality of the models and to be able to cope with changing circumstances, the process variables were considered for a wide range of areas, far beyond the usual operational working areas. The decisive input parameters of these models were particle and fluid properties *i.e.* density, size, viscosity and velocity. Several new experimental set-ups were designed, and a

myriad of experiments were conducted in order to obtain highly accurate data sets. These data sets were used to calibrate and validate the prediction models. The models and experiments have led to a better understanding of the principles of multiphase flow phenomena.

12.3 Particle size conundrum

Traditionally, and for convenience, spheres are used as a theoretical measure in voidage prediction models, even though natural or processed water-related grains are rarely perfectly round. When grains are more or less spherical, an average particle diameter, often based on sieves or scanning techniques, can be used as a model input parameter. Also, the use of a fixed particle shape factor such as sphericity can be used to compensate for the degree of irregularity. However, this pragmatic approach may provide reasonably acceptable expansion prediction in a limited working area only; it is of very little scientific value and offers few possibilities for fundamental improvements.

This research demonstrated that irregularly shaped particles show considerable re-orientation, realignment and positional rearrangement for increasing fluid velocity, thus changing the available surface for flow-through. The consequence of this phenomenon is that the concept of average and round particle diameter, and especially average sieve diameter, is less suitable for the accurate prediction of fixed and fluidised bed behaviour.

12.4 Model consideration

In this research, three types of models were considered: classical models, data-driven models and numerical models. Scientists are familiar with classical models since they are relatively easy to apply. A disadvantage of almost all of these models is that they are based on a theoretical concept of spherical particles, whereas in industrial processes, processed and natural grains are *de facto* non-spherical. Pragmatically, shape factors might provide an apparently simple solution. However, this is no longer feasible when new types of granules are introduced.

12.4.1 Classical models

The unwaveringly popular classical Richardson–Zaki model, based on a hindered settling correction to the terminal settling velocity of a single grain, is often applied for dilute gas-solid fluidised systems with high voidages. In water treatment processes, however, voidages are much lower due to the operational working area in the vicinity of the incipient fluidised state. The consequence of this large voidage difference is that the accuracy of Richardson–Zaki model's voidage prediction is relatively low. This is also caused by the estimation of the empirical index used in the model, despite the efforts by many researchers who have tried to find physical relevance (Siwiec, 2007a). It is therefore reasonable to conclude that the Richardson–Zaki model is less suitable in water treatment processes. The model prediction accuracy can be improved considerably by adding a hydraulic basis, but this does not solve the problem with irregularly shaped particles. Nevertheless, the model has several advantages. It is relatively straightforward and the predicted voidage cannot exceed the theoretical threshold, which might be useful for process automation. Other models lead to implicit expressions for the voidage and have to be solved through a numerical procedure, which is unwanted in full-scale automated industrial processes.

12.4.2 Data-driven models

The second type of approach involves the use of data-driven models. It is possible to generate a myriad of models using symbolic regression techniques (Koza, 1992), but the model including the particle Reynolds and densimetric Froude numbers provided exceptional prediction accuracy. Relatively simple and explicit equations were obtained, suitable for implementation in industrial environments. The model parameters always had to be fitted based on experimental data. The advantage of this type of model is that if it is used outside the range of training data, the predicted values will not run out of range, mainly owing to the use of hydraulic dimensionless numbers. When new types of grains are introduced with different particle properties, considering that the particles are more or less spherical, this degree of irregularity can be compensated by finding other fit parameters in the Reynolds-Froude-based models. The advantage is that no new experimental work is needed that would entail

considerable experimental investments. It has to be noted, however, that this method is less suitable if the grains are highly irregularly shaped and also polydisperse.

12.4.3 Numerical models

The third type of model is currently gaining significant ground: it is by far the most frequently discussed topic at multiphase flow conferences. Computational fluid dynamics modelling has a tremendous advantage because it is based on fundamental conservation laws and the potential of unprecedented visualisation. A simulation can be investigated from any state or preferred set-point. Many system parameters can be included which are not always accessible in experiments and, additionally, a deeper understanding of the phenomena occurring inside liquid-solid fluidised beds can be gained. Disadvantages of CFD simulations are long simulation times and high computational costs. This is especially the case when spherical particles are not suitable for representing the actual problem, *i.e.* when non-spherical particles have to be simulated or sometimes even fully resolved. The same problem arises when complex and large reactors, such as the pellet-softening reactor, have to be simulated.

12.4.4 Model selection

This research has shown that liquid-solid fluidised beds can be simulated using three types of models: classical, data-driven and numerical. Still, regarding irregularly shaped particles a large challenge remains with the question which particle size (and shape) should be used that properly represents the particle diameter.

When scientists face new liquid-solid fluidisation challenges, for example with new types of granules, and decide to initiate a modelling programme, they have the option to select one of the model approaches discussed above. Classical models are familiar and therefore often considered to be reliable, but they are *in principium* not developed and calibrated for non-spherical particles. Data-driven models are straightforward and effective. The degree of non-sphericity can sometimes even be partially compensated in the fit parameters. However, this requires prior experimental effort. In CFD models, spherical particles are mostly used as an input

parameter, but when predefined non-spherical measures such as ellipsoids and rods are used, for instance in applying the pseudo-3D scanning technique, the simulation of the real process is enhanced. This requires considerably more modelling skills and additional computational costs.

In (drinking) water treatment processes, granular material is often used. The most applied types are sand, calcite and carbon grains, but also anthracite and anionic exchange polymer resins are common. When these types of grains are used in treatment processes such as up-flow filtration, fluidisation or settling, shape is a decisive factor in addition to size. The influence of the shape of grains *i.e.* non-sphericity, on the hydraulic behaviour depends on the specific process itself. Regarding backwashing in rapid sand filtration according to a commonly used recipe, for instance when the water temperature is relatively constant, the shape is less important. But if the extended terminal sub-fluidisation wash procedure is used to optimise the water quality performance, the shape is extremely important, meaning that predictive models need to be adjusted. This research showed that the classical Carman–Kozeny model is reasonably accurate in the moderate fluidisation range; however, it was not suitable for predicting the considerably increased resistance for incipient up-flow conditions. In order to fully comprehend and further optimise the hydraulic insights into this system, CFD models must be deployed incorporating the non-spherical character of grains.

Typical of pellets-softening reactors is the use of a mixture of large almost spherical calcite pellets and smaller highly non-spherical pulverised calcite grains. The classical Richardson–Zaki model is less suitable for accurate voidage prediction and therefore unsuitable for determining the overall hydraulic state. For regular and stable process control (van Schagen, 2009), data-driven models can be used provided that the fit parameters are calibrated and amply cover the operational window. When the opportunity arises that the computational cost are no longer a limiting factor, CFD models hold great promise for coping with the hydraulics occurring in this system, in particular when the hydraulics are combined with chemistry.

Regarding granular activated carbon grains during backwashing conditions, predicting the expansion degree is a very complex matter. As long as the hydraulic behaviour of these polydisperse, non-spherical and porous particles is not understood, conducting experiments is more effective than solving the problem with many modelling conundrums. In future research, CFD appears to be an obvious and

highly suitable candidate for gaining new insights. Still, data-driven models may also be an interesting option when it comes to effective voidage prediction.

In general, classical models are useful for quick preliminary explorations, data-driven models can be used for effective usage in full-scale plants and CFD model are suitable for gaining academic insights. The choice between these approaches is up to the engineer who works to find optimal solutions for the short and the long term.

Chapter 13

Conclusions

“Round is not round (particle diameter).”

“Homogeneous is not homogeneous (fluidised bed).”

“Constant is not constant (180).”

13 Conclusions

13.1 Lessons learned through modelling and experiments

In this research, valuable lessons were learned from experiments and through modelling. Three types of models were examined to be able to estimate the effective voidage in liquid-solid fluidised systems and to gain hydrodynamic knowledge. Classical models such as the Richardson–Zaki model are still popular, but they have drawbacks when non-spherical particles are considered. Data-driven models are straightforward in their use but require experimental effort. Computational fluid dynamics (CFD) models are encouraging for finding fundamental answers, but these models require in-depth knowledge and computational costs. The best match regarding a suitable model approach depends on the situation and the challenge concerned.

13.2 Terminal settling and data spread

At first glance, the measurement of the terminal settling velocity of water-related granules, necessary for the Richardson–Zaki model, seemed relatively easy. It appeared that the almost 8,000 individual sedimentation data points, when averaged, agreed reasonably well with well-known drag coefficient prediction models. However, what is generally not emphasised in the literature is the occurrence of a large data spread around these average values. The extent and type of data spread is caused by the influence of natural variations in specific particle density, path trajectory instabilities, particle size, shape and orientation. This is important information for process engineering and the industrial design of water treatment systems when sedimentation of grains is involved.

13.3 Laminar-turbulent and homogeneous-heterogeneous flows

The literature provides limited accurate expansion data for liquid-solid fluidisation systems and virtually no data for perfectly round particles. For this reason, accurate expansion experiments were conducted using highly spherical monodisperse

particles as reference in the models. This reduced the uncertainty caused by irregularly shaped, polydisperse particles. Moreover, during these experiments, homogeneous state was not observed for a myriad of grains, temperatures and flow rates. In fact, heterogeneous fluidisation, showing bubbles and open spaces between agglomerates of particles, occurred at relatively low fluid velocities.

Many porous media-based models such as Ergun or Carman–Kozeny are based on the relationship between the drag coefficient and the modified particle Reynolds number, expressing the ratio of turbulent to laminar flow. To include the effect of heterogeneity in the fluidised beds, a new drag relation was proposed in which the overall voidage is not only dependent on the modified particle Reynolds number, but also on a densimetric Froude number, which acts as a proxy for the amount of heterogeneous versus homogeneous flow.

The proposed drag relation is suitable for fluidised bed applications, but what is perhaps more important is that it provides new insights related to the influence of the temporal-spatial heterogeneity on the effective hydrodynamic drag for large fluidised systems. The voidage prediction error decreased from approximately 5% (according to the best literature equations which use the Reynolds number only) to <2% (using both the Reynolds and the Froude number).

13.4 Computational fluid dynamics

A future-oriented step was explored for the use of numerical methods to study unsteady fluidised bed behaviour. To confirm that the heterogeneous flow is caused by physical forces inside the fluidised bed (as opposed to e.g. inhomogeneities in the fluid distributor plate or significant wall defects), an advanced CFD model was used to simulate calcite pellets and to obtain information about heterogeneous behaviour inside a fluidised bed. The simulations confirmed the existence of distinct differences in void fraction in the cross-section of the columns. An advantage of CFD simulations is that they can reveal additional phenomena such as voidage distribution and particle circulations which in experiments can only partially be observed from the outer container wall. To date, the detected unstable circulation pattern and heterogeneous behaviour has not been elaborated in the literature but may well be of paramount importance for the chemical performance of the water softening reactor.

13.5 Data-driven models

New data-driven models were synthesised based on non-linear symbolic regression methods and accurate expansion data obtained from elaborate pilot plant experiments, covering a large range of grain types, water flows and temperatures (viscosities). Dimensionless numbers were included to give the data-driven models a more physical basis. To calibrate and validate the developed models, more than 20,000 individual expansion data points were obtained through newly designed experimental set-ups. A model based on the Reynolds and Froude numbers resulted in very high voidage prediction accuracies (error < 2%) for a wide range of particle sizes, fluid velocities and temperatures. The advantage of this approach is that these straightforward data-driven models can directly be used in unit operations such as pellet-softening. However, although they can be very effective, considerable experimental effort is often required to find proper fit parameters.

13.6 From fixed to dynamic particle shape factors

Another relevant phenomenon was discovered during up-flow filtration experiments for non-spherical particles. It was found that a shape factor is not a constant particle property as is commonly assumed, but that this factor also depends on the fluid properties. The drag coefficient across the filter bed did not remain constant as initially expected. The considerable drag changes that were observed were caused by particle re-orientation in moderate up-flow filtration. The well-known pre-factor 180, a constant in the Carman–Kozeny model, turned out to vary considerably and become even larger than 400. This difference is often compensated for by using particle corrections or shape factors in the fixed bed state. The use of these shape factors in fluidised states, however, is generally not discussed and *de facto* omitted, which is remarkable given the fact that the same particles are considered here. Through a different presentation of the drag coefficient, it became possible to demonstrate that non-spherical particles re-orient in their position at increased flow rates. The fixed shape factor turned out to be dynamic, ranging from approximately 0.6 in the fixed bed state to 1.0 in the fluidised state. The degree of irregularity for considered particles such as rapid sand filter grains could be measured with a new image analysis method. The 2D dimensions of particles were determined using image analysis software and a flatbed scanner. When this was combined with the

measured mass and density of a particle sample, a pseudo-3D height of dimensioned shapes such as ellipsoids could be determined. This proposed and accessible method can be used for future CFD modelling that considers non-spherical particles.

13.7 Expansion of granular activated carbon grains

Besides pellet-softening and rapid sand filtration, granular activated carbon (GAC) filtration is of major importance in water treatment plants. A crucial part of the filtration cycle is the backwashing procedure of filters. Grains applied in this process are often highly polydisperse, irregularly shaped and porous. The literature does not provide general expansion prediction models for these kinds of grains. Accurate voidage prediction for GAC grains is very complex because the grains are highly non-spherical, monodisperse and have internal porous structures. By conducting a series of expansion experiments, it was possible to obtain expansion characteristics for a variety of grains and to provide insights into the complexities regarding the development of a reliable expansion prediction model. While in rapid sand filtration the considered particles are solid and relatively uniformly distributed in terms of size and shape, grains used in granular activated carbon filtration are a collection of smaller and larger grains. In addition, the grains often show disparities and protuberances and have a porous structure where the internal pores are filled with water. From a practical point of view, particles are often regarded as spheres in models, and with an easy to measure particle density it is possible to predict the bed expansion without too much effort. However, when considering granular activated carbon grains, the wetted and dry particle density, external and internal porosity and in particular the particle diameter of such highly irregularly shaped particles cannot directly be used in classical expansion prediction models. This makes predicting the degree of expansion for these types of grains in full-scale installations much more complex. By combining laboratory and expansion experiments, it was possible to solve some of these aspects of the “carbon grains conundrum”. In particular, it was possible to determine the wet density and external porosity using mass balances, hydraulic equations and experimental data.

13.8 A soft-sensor to determine the hydraulic state

An immersed object in a liquid-solid fluidised bed can be used as a soft-sensor to distinguish the gradient for local voidage and particle size. This hydrometer looks promising for functioning as a reactor key performance indicator to determine the hydraulic state. The pellet-softening reactor in full-scale, typically with respect to the Amsterdam reactor design, is characterised by a stratified fluidised particle bed. Small seeding grains are dosed at a high point of the reactor vessel, while the largest pellets migrate to the lowest zone of the reactor. The chemical driving force in that particular zone is the largest due to the caustic soda dosage. The higher part of the bed, however, is also important for the polishing effect of the softening process. Due to the complexity of determining a hydraulic state of the reactor, it was important to develop a new soft-sensor to determine the apparent hydraulic state and, derived from this, the performance in the reactor. The soft-sensor idea was based on the historical *Archimedes principle* where an immersed object experiences an upward force proportional to its volume and the effective suspension density of the submersion liquid. The gradually submerged weight of a cylindrical object was used to estimate the local effective density and bed voidage. The derived local voidage made it possible to estimate the particle size from which the available specific surface area for crystallisation purposes could be estimated. The sensor has its pros and cons. The disadvantage is the number of assumptions that were made, including homogeneous fluidisation which this research has proven to barely exist. Moreover, the model uses spherical particles, a theoretical concept that does not occur in water treatment plants. These assumptions were considered acceptable since the average unstable bubble size is small compared the size of the immersed object and since the pellets become fairly spherical as a result of calcium carbonate crystallisation. The opportunity of the Archimedes-based sensor is that a relationship can be established between the hydraulic and chemical reactor key performance indicators. More optimal states enable chemical savings, better water quality and reliable process control.

13.9 From robust to more flexible water treatment

For ensuring water treatment processes that are future proof and climate neutral, that are reliable in terms of water quality and continuous supply and that are economical and customer-friendly, there is a widely heard call for a transition from robust designs to more flexible designs. To achieve these goals, advanced (hydraulic) intelligent and plant-wide models can be used. Depending on the situation, scientists have to consider how to achieve an optimal balance between straightforward data-driven models with acceptable prediction accuracy and more advanced but more complex numerical models. In this study, both types of models have been considered and both can be used for making the next steps forward.

13.10 The expansion column benefits

Finally, this project enabled representatives from academia, industry and education to meet, converge, collaborate and strengthen each other. A vast majority of the data was obtained thanks to the experimental efforts of many university students who used the expansion columns developed for this research. The experimental data thus gathered formed the basis for model calibration and validation work that proved to be of major value for this research. At the same time, students were offered the chance to discover the professional environment in their field of expertise through problem-based learning, developed and applied throughout the research project. They were able to gather knowledge from experts, while industrial organisations were given the opportunity to work with talented graduate engineers (and occasionally offer them a career). Their collaborative research findings have opened new avenues for innovation, optimisation and the development of new processes. Large obtained and composed data sets were shared for new research goals such as the calibration of computational fluid dynamics models. The expansion column experiments have demonstrated that collaboration between research, education and professional practice forms part of the solution that makes it possible to realise the highly complex transition from a linear to a more circular-oriented economy.

Chapter 14

Recommendations

*“The only thing constant is change.”
(Heraclitus, 540 B.C. – 480 B.C.)*

14 Recommendations

This research examined hydraulic factors in liquid-solid fluidisation processes applied in drinking water treatment plants. Certain matters could not be resolved, such as the particle size conundrum in relation to models. Additionally, even though in water treatment plants other phenomena besides hydraulics are relevant, most notably chemistry, these phenomena were not taken into consideration. For more optimal process control, both multiphase flow hydraulics and aquatic chemistry have to be integrated. For a long-term vision with increasingly complex challenges ahead, such as the call for greater sustainability to promote the circular economy, fundamental knowledge is essential to be able to cope with necessary adjustments.

14.1 Objectives for optimisation

14.1.1 Relating hydraulic and chemical reactor performance indicators

This research focused on hydraulic aspects of liquid-solid fluidisation processes applied in drinking water treatment plants. For water softening, a frequently applied technique is seeded crystallisation in fluidised bed reactors. Here, hydraulics and chemistry are inextricably interlinked. Hence, a next step is to start a pilot plant study in which the performance of the softening process must be monitored on both terrains mentioned above: hydraulics and chemistry. The calcium carbonate crystallisation potential (CCCP) is a suitable key performance indicator which can be used to determine the amount of supersaturated calcium in the effluent of the reactor and to estimate the efficiency of the entire pellet-softening process. The CCCP can be calculated with PHREEQC (Parkhurst and Appelo, 2013; de Moel *et al.*, 2013) an abbreviation of 'pH, redox, equilibrium, calculation', a program to perform a wide variety of aqueous geochemical calculations. A practical value in full-scale operations ranges from 0.2-0.5 mmol/L. Experience-based CCCP with pellet-softening reactors ≈ 0.1 mmol/L are achievable under optimal fluidised bed and best reactor conditions. A large surface area must be available for efficient crystallisation (Tang *et al.*, 2020). Therefore, it is essential to implement a soft-sensor to determine the condition of the fluidised bed by determining the available total surface area (TSA) and specific space velocity (SSV). The TSA and SSV can be determined by

means of the hydrometer soft-sensor developed in this research. Optimal reactor performance, *i.e.* less chemical usage, can be derived from CCCP versus TSA and SSV scatter plots. This means that besides hydraulics, also chemistry needs further exploration, and in particular the integration of both worlds.

14.1.2 Optimal reactor performance and fluidisation quality

Based on field experience, the fluidisation quality of softening processes carried out at Waternet was observed during full-scale operational conditions and considered to be moderately heterogeneous. In addition, carry-over at the reactor effluent was detected, implying increasing CCCP values. Also, open spaces of water and unsteady behaviour was observed between the fluidised particles during experiments. Additional research is needed to investigate if heterogeneous behaviour affects chemical crystallisation efficiency, either negatively or positively. Larger open water spaces might increase the probability of spontaneous precipitation, while a heterogeneous flow regime could have a positive effect on the dispersion of chemical reactants in the water phase, due to vigorous agitation of the particles in contact with the fluid. A follow-up study could clarify how crystallisation proceeds in the presence of unsteady local voids during fluidisation. The research question is whether optimal fluidisation quality can be achieved for optimal chemical conversion, *i.e.* minimum reactor effluent CCCP.

14.2 Related ongoing research

In the Netherlands, more than 30 years of experience (Hofman et al., 2007) has been gained with pellet-softening reactors. The cylindrical (Amsterdam) reactor (van der Veen and Graveland, 1988) has been successfully applied alongside other types of reactors. The pellet reactor is an example of a clean technology (van Dijk and Wilms, 1991), and it is cost effective ($\approx 0.05 \text{ €/m}^3$). However, several aspects can be improved for better water quality, greater flexibility, less maintenance and a more limited need for chemicals, *i.e.* for ensuring greater sustainability. These factors should be considered in the new design of the pellet-softening reactor. For a further transition from a linear to a circular process, additional research is indispensable.

14.2.1 Alternatives to particles diameter in fluidisation models

In pellet-softening reactors, crushed calcite grains which start out as highly irregularly shaped seeds grow through crystallisation into increasingly spherical pellets. This research showed that for determining an average particle diameter, sieving (Rhodes, 2008) as a method is inferior to image analysis. Besides this, it is almost impossible to define a particle diameter for a non-spherical particle. The use of fixed shape factors proved unsuitable for diameter correction in hydraulic models. Dynamic shape factors might provide pragmatic solutions, but this requires much experimental effort. Therefore, new research is recommended to completely eliminate the average particle diameter from models. Pre-defined particle shapes such as rods or ellipsoids are more preferable candidates since particle orientation can be incorporated. A more fundamental approach could focus on alternatives for particle diameter such as specific surface area, hydraulic drag or dimensionless numbers representing particle-fluid interactions.

14.2.2 Distortion layers in the pellet-softening reactors

Pellet-softening is a process in which seeded crystallisation takes place in fluidised beds. In addition to this, in full-scale pellet-softening reactors at the Waternet facility Weesperkarspel, a biomass growth process was detected on calcite pellets, caused by bacterial colonisation captured in calcite structures (Hammes *et al.*, 2011) forming porous calcium carbonate coatings. Bacterial organisms proliferate in the presence of highly biodegradable nutrients in the water phase after the upstream ozonation. In fact, pellet-softening can be seen as a combination of chemical, hydraulic and biological processes. Grains with biomass growth have capricious shapes (Figure 127) with different expansion behaviour and accumulate in the fluidised bed; this is referred to as distortion layers.

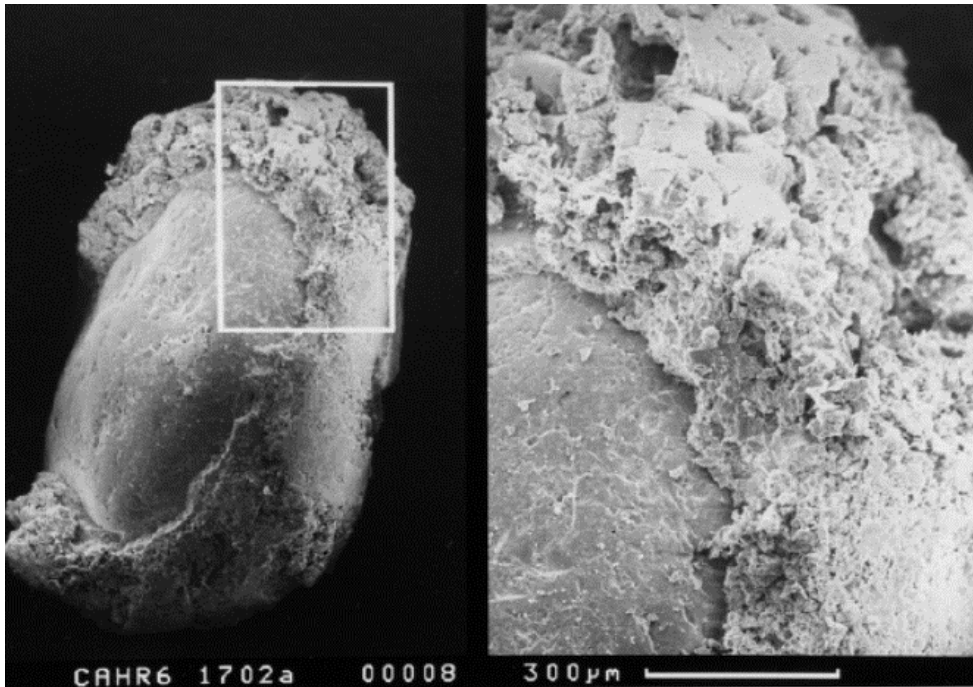


Figure 127 Porous calcium carbonate cauliflower-like growth in pellet-softening reactors (Dirken *et al.*, 1990)

These distortion layers have pros and cons. About half of the assimilable dissolved organic carbon (AOC) concentration in water is removed, which contributes to the biological stabilisation of the drinking water. Disadvantages are decreased efficiency of the downstream biologically activated carbon filters and the tendency of distortion layers to expand excessively, resulting in the need to take *ad hoc* manual curative measures. Another effect, which occurs for varying flow rates, is fluidised bed inversion (Figure 128). This phenomenon (Escudié *et al.*, 2006) reduces the available specific surface area for crystallisation since the bed voidage in distortion layers is lower compared to fluidised calcite pellets with the same size. This might adversely affect the reactor's performance (Bastiaan, 2020).

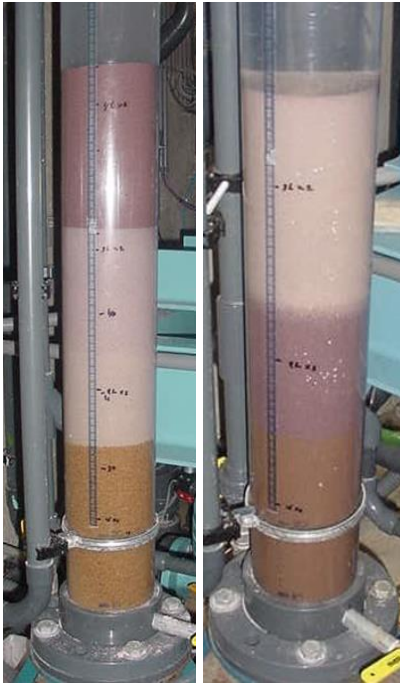


Figure 128 *Three-layer system: garnet sand (purple), distortion layer (beige), calcite pellets (dark yellow). Layer inversion with changing flow.*

New research should reveal whether it is useful to control the degree of biological activity in the fluidised bed. On the other hand, according to Wang *et al.* (2007), a fluidised pellet bed bioreactor is a promising technology for onsite wastewater treatment and re-use.

14.2.3 Computational fluid dynamics modelling

Computational fluid dynamics is a rapidly emerging field of expertise in water treatment processes and primarily used for the evaluation of hydraulic challenges. CFD is potentially more powerful for simulating integrated hydraulic, chemical and biological processes involved in processes on a spatial scale and for accelerating improvements in prediction models for design, control and optimised operations. Depending on the context, classical, data-driven or numerical models can be applied in many situations. This research discussed the pros and cons of the different model approaches. For future research, CFD looks set to become an extremely useful and

reliable method to cope with challenges, in particular when CFD modelling is combined with reliable experimental effort and with a clear practical goal in mind. Full-scale industrial pellet-softening reactors contain on the order of 10^{10} particles. Although CFD modelling is enormously promising (Samstag *et al.*, 2016), at least if its development follows Moore's law, which assumes that the number of transistors on a computer chip double about every 18-24 months, it is not yet feasible to simulate a complete reactor in full detail, and certainly not an entire sequence of softening reactors. By using smart strategies, for instance through choosing representative segments of a system or through coarse-graining, numerical solutions can correspond reasonably well to the real situation. This requires considerable computational cost and is therefore not suitable for real-time process control. Aspects such as reactor scale-up, vertical and circulating flow patterns, chemical and biological reactions, particle, fluid and chemicals mixing efficiency, unsteady behaviour of the bed, non-spherical particles, and finally the influence of the distributor enhance the quality of the numerical results, but make the simulation requirements even more complex. In the event that quantum computers become commercially available, CFD modelling may promise unlimited opportunities, but the technique is only reliable and meaningful when the user continues to respect the fundamental laws behind this tool.

In this research, a hydrometer soft-sensor was proposed to determine the hydraulic performance indicator gradient to be used in a full-scale pellet-softening reactor. CFD modelling should be executed to investigate the hydrometer's performance and to improve the proof of concept. Examples include the optimal immersed object dimensions, optimal material density related to the liquid-solid fluidised bed voidage and particle size and scale-up effects (Nauman, 2008; Albright, 2009; Duduković and Mills, 2015). Additionally, CFD is an excellent tool to investigate the influence of non-spherical particle orientation as a function of the altering fluid flow in fluidised bed systems.

14.2.4 General theory of liquid-solid and gas-solid fluidisation

While the basics of fluidisation are conceptually easy to comprehend, the hydrodynamic behaviour of fluidised beds is extremely complex (Beetstra, 2005). In this research, liquid-solid fluidisation was investigated. During experiments and in

full-scale processes, unsteady behaviour was observed of particles as well as fluid, *i.e.* bubbles (Kramer *et al.*, 2020a). The occurrence and behaviour of bubbles in gas-solid fluidisation is a popular topic that is frequently discussed in the scientific literature (Oka and Anthony, 2003). The appearance of bubbles in liquid systems raises the question whether there is a general overarching governing theory for both liquid-solid and gas-solid fluidisation. This is relevant since gas and liquid fluidisation as well as trickle flows are frequently encountered in water treatment processes. An interesting follow-up question to investigate is whether homogeneous fluidisation is a theoretical concept or that it actually exists in practical applications.

14.3 Avenues for future research

During this research project, new and simultaneous insights were gained into calcium carbonate crystallisation in the pellet-softening process. For future improvements of pellet-softening reactor performance, aspects such as supersaturation, seeded crystallisation reaction rate and inhibition need to be investigated further. To maximise overall softening reaction efficiency, additional research is necessary into factors such as supersaturation, seeded crystallisation reaction rate and inhibition, so as to be able to improve plant-wide water quality, reduce required chemical consumption and improve full-scale flexibility, for example by changing set-points and improving water quality.

In current pellet-softening reactors operations, mature calcite pellets are periodically withdrawn from the reactor and replaced with fresh seeding material. New research can provide answers to the question whether greater sustainability in this process can be introduced by applying a probe based on hydrodynamic or acoustic cavitation that converts *in situ* pellets into calcite seeds. Solutions may be found in the field of cavitation (Ozonek, 2012; Aldoukhi *et al.*, 2017).

The softening process (Amsterdam reactor) takes place via the dosage of caustic soda, which leads to an alteration of the calcium carbonate equilibrium whereby the solubility product is exceeded. Overall reactor efficiency is strongly dependent on the degree to which water, caustic soda and the seeding grains are mixed. To minimise CCCP levels, in addition to the current use of by-pass flows, not only recirculation flows should be investigated, but also the optimal number of nozzles.

Annexes

“Scientist should prevent getting lost in ‘noise’ e.g. by using shape factors to compensate naturally occurring variation in particle morphology.”

Annexes

	Page
Annex 1: Photos	370
- Photographs of examined calcite pellets	
- Photographs of examined granules	
Annex 2: Wall effects	375
Annex 3: Obtained particle properties	376
- Particle size	
- Particle density	
- Fixed and incipient voidage	
Annex 4: Morphological properties	378
Annex 5: Statistical analysis	379
Annex 6: Overview uncertainty analysis equations	380
Annex 7: Where research, education and professional practice meet	383

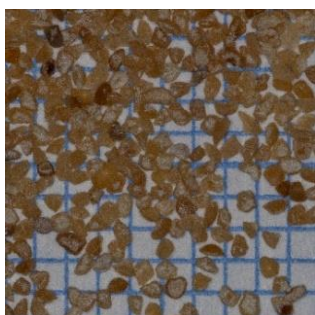
Annex 1: Photos

Source: (Kramer *et al.*, 2020b)
<https://doi.org/10.101z/j.jwpe.2020.101481>

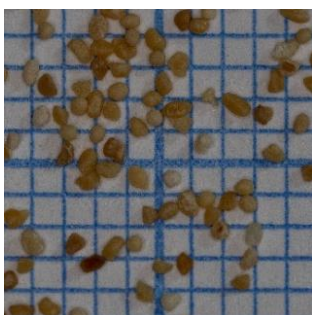
Source: (Kramer *et al.*, 2021b)
<https://doi.org/10.5194/dwes-14-53-2021>

Photographs of examined calcite pellets

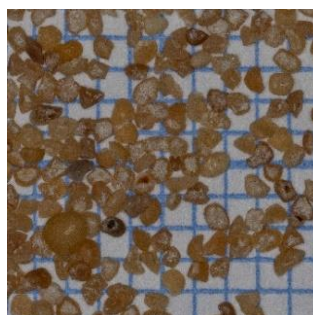
Calcite pellets were extracted from full-scale pellet-softening reactors located at the Waternet facility Weesperkarspel in Amsterdam. Accordingly, the pellets were fractionated using a Retsch sieve device and calibrated US mesh sieves regulated by standards such as ISO 3310-1, ISO 565, EN 933-2 and ASTM E11 (NEN-EN 933-2, n.d.). Photos of calcite grains were taken with a Nikon D500 camera using a Sigma 150 mm f/2.8 EX DG OS HSM lens.



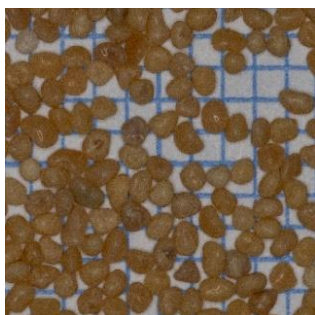
$0.36 < d_p < 0.43 \text{ mm}$



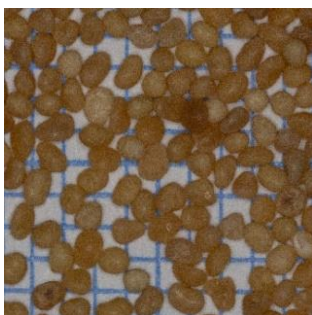
$0.43 < d_p < 0.50 \text{ mm}$



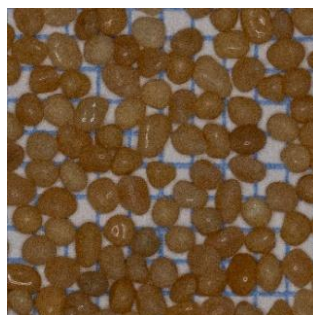
$0.50 < d_p < 0.63 \text{ mm}$



$0.63 < d_p < 0.71 \text{ mm}$



$0.71 < d_p < 0.80 \text{ mm}$



$0.80 < d_p < 0.90 \text{ mm}$

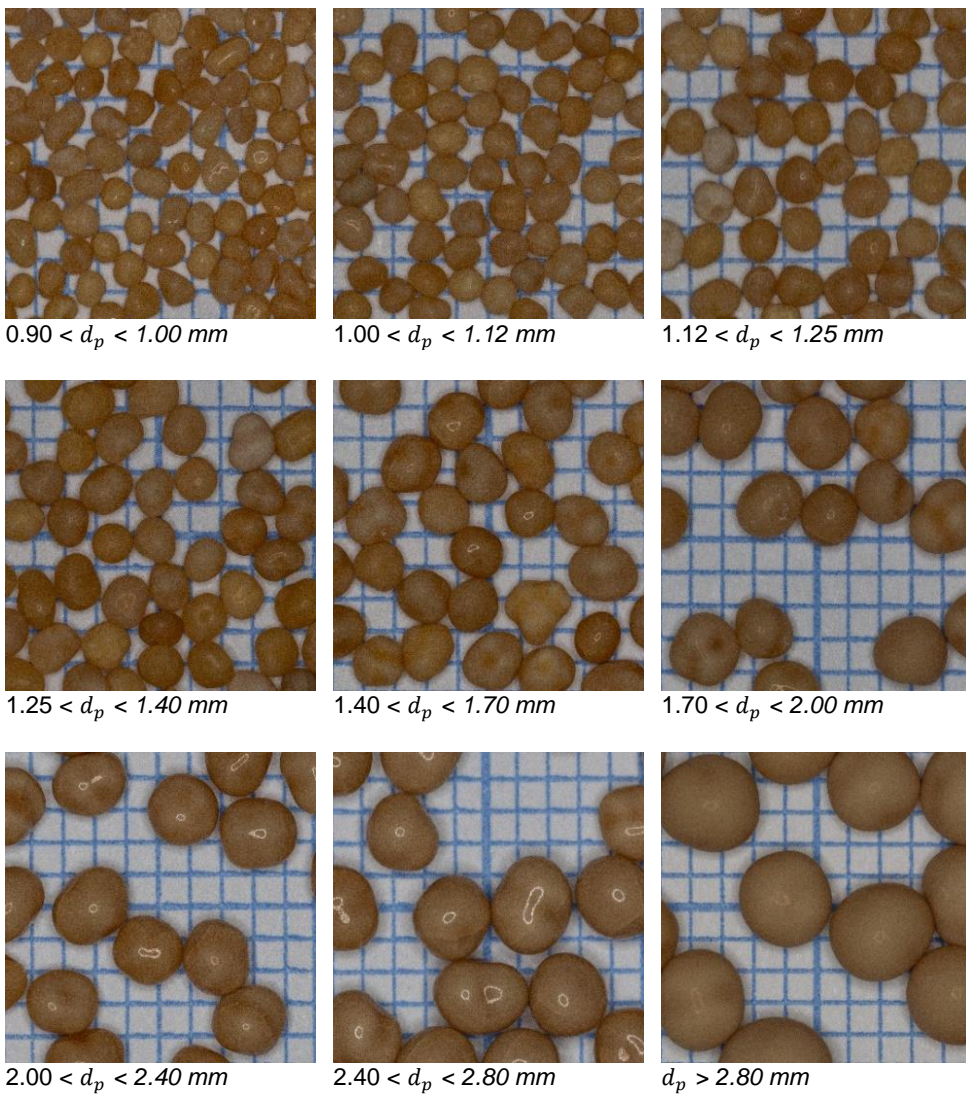
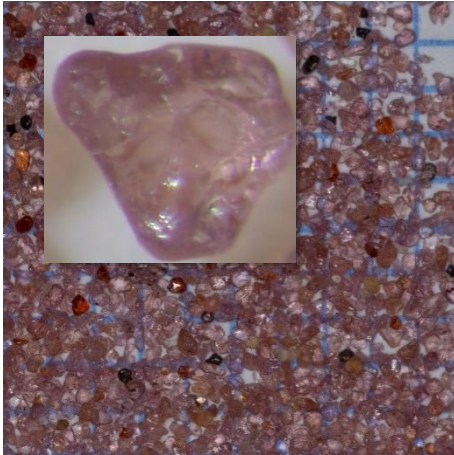


Figure 129 Photographs of examined calcite pellets

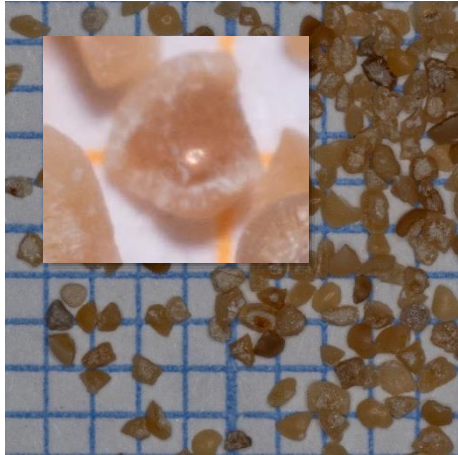
Scanning Electron Microscope photos of calcite pellets are presented by Dirken *et al.*, 1990).

Photographs of examined granules

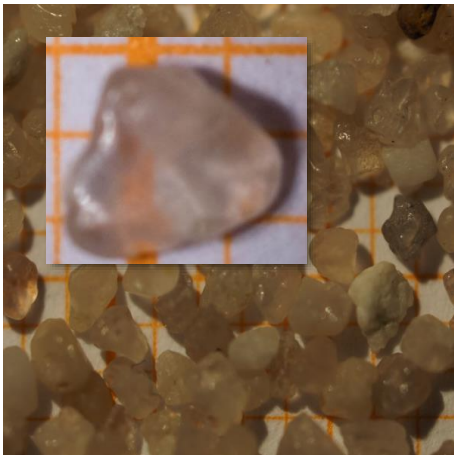
Besides calcite pellets, also many other granular material was investigated on the expansion and terminal settling behaviour in water represented in Figure 130.



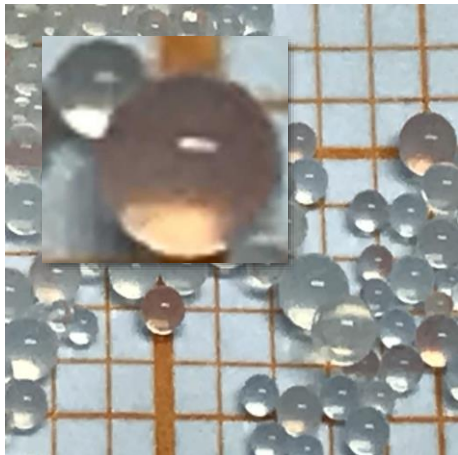
Garnet sand (mesh 80) $0.2 < d_p < 0.3$ mm



Crushed calcite $0.4 < d_p < 0.5$ mm



Rapid filter sand $0.8 < d_p < 1.25$ mm



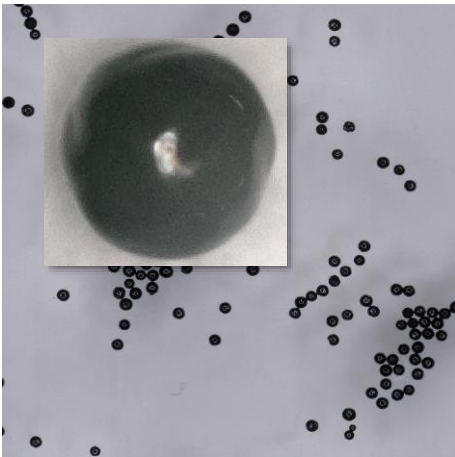
Anionic exchange resins $0.9 < d_p < 1.18$ mm



Olivin grains $0.5 < d_p < 0.9$ mm



Nylon balls (DitHolland) $d_p = 3.0$ mm



GAC grains (Saratech) $0.44 < d_p < 0.51$ mm

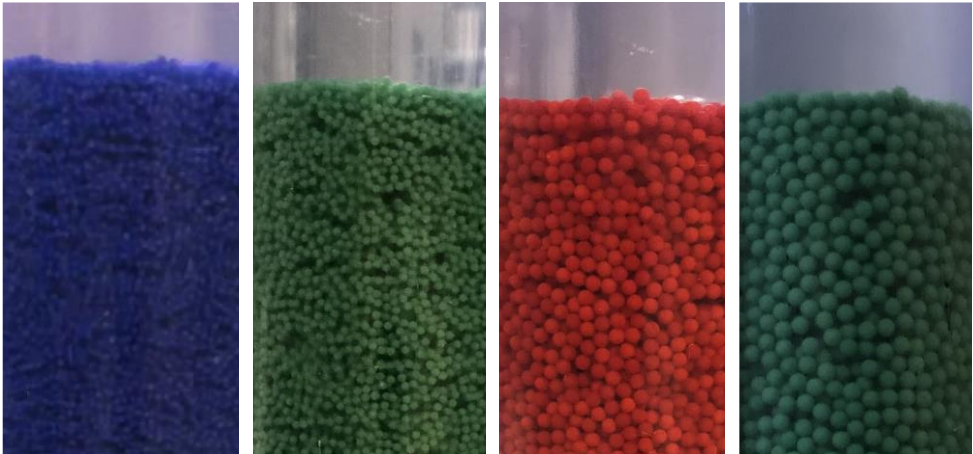


GAC (Norit ROW 0.8 Supra) $0.89 < d_p < 3.15$ mm

Figure 130 Photographs of examined granules



Figure 131 Glass bead $d_p=1.00$ mm



Glass beads
 $d_p=1.00$ mm

Glass beads
 $d_p=1.50$ mm

Glass beads
 $d_p=2.50$ mm

Glass beads
 $d_p=3.50$ mm

Figure 132 Photographs of spherical glass beads (SiLibeads)

Annex 2: Wall effects

Source: (Kramer *et al.*, 2020a)
<https://doi.org/10.1016/j.ijmultiphaseflow.2020.103261>

In the literature, many wall effect correction formulas can be found. These wall effects refer to the retardation of the motion of individual particles settling in a cylinder due to the displacement and opposing motion of the surrounding fluid (Clift *et al.*, 1978) and (Yang, 2003). Wall effects depend on the ratio of the particle diameter to the cylinder column diameter d_p/D and the sphere Reynolds number for terminal settling conditions (Di Felice, 1995), (Chhabra *et al.*, 2003) and (Di Felice and Gibilaro, 2004).

In the literature, correction formulas for liquid-solid fluidisation are also given in (Richardson and Zaki, 1954) and (Loeffler, 1953), often on an empirical basis. The effect of container walls can be neglected in most full-scale operations (Akgiray and Soyer, 2006). Regarding relatively small laboratory columns, wall effects might have to be considered because wall friction opposes the drag force acting on the particles during fluidisation. Numerous researchers including (Loeffler, 1953), (Dharmarajah, 1982), (Khan and Richardson, 1989), (Di Felice, 1995), (Rao *et al.*, 2010), (Whiten and Özer, 2015) and (do Nascimento *et al.*, 2016) proposed empirical equations, based on particle-to-column ratio, Reynolds number or velocity-ratio, to apply corrections. According to (Fidleris and Whitmore, 2002), the retarding effect of the wall decreases with increasing terminal Reynolds number, so that for ratios of ($d_p/D = 0.05 - 0.10$) the wall correction becomes less than 1% for Reynolds numbers exceeding 5 and 30, respectively. However, there is no general agreement in the literature. A straightforward critical value for particle-to-column ratio varies between 0.06 and 0.2. When we take $(d_p/D)_{crit} = 0.06$, then for all calcite pellet experiments, corrections are not needed. This is also the case for the majority of examined glass beads except 3.5 mm SiLibeads, where ($d_p/D = 0.061$). Data obtained from the literature violates this threshold occasionally. These data include 6.53 mm metal balls (Richardson and Zaki, 1954): ($d_p/D = 0.10$), for which the researchers applied their own wall effects correction: 5.2 mm glass beads (Wilhelm and Kwauk, 1948): ($d_p/D = 0.068$) and 3-5 mm glass beads (Loeffler, 1953): ($d_p/D = 0.061 - 0.19$). In our model analysis, we assumed no discernible difference in the bed expansion characteristics, and therefore wall effects corrections have not been implemented.

Annex 3: Obtained particle properties

Source: (Kramer *et al.*, 2020a)

<https://doi.org/10.1016/j.ijmultiphaseflow.2020.103261>

Particle size

The particle size of calcite pellets and crushed calcite determined with ImageJ is slightly higher (Table 27) compared to the average sieve diameter: ($R^2 = 0.994$). This can be explained by the fact that pellets and calcite are irregularly shaped due to the grinding process and therefore have a tendency to pass sieves more vertically oriented, while they are more horizontally oriented during static image analysis where particles are lying on a scanner. In case of calcite pellets, for modelling purposes, the average hydraulic equivalent particle diameter d_p is used (Equation (28)).

Particle density

The particle densities were determined through different methods and are given in Table 4 and Figure 133. For calcite pellets, the pycnometer density is the most accurate (average relative error = 0.8%) compared to the derived density based on the differential pressure sensor value, using Equation (33) (average relative error = 4.5%). For modelling purposes, the determined mean value was used.

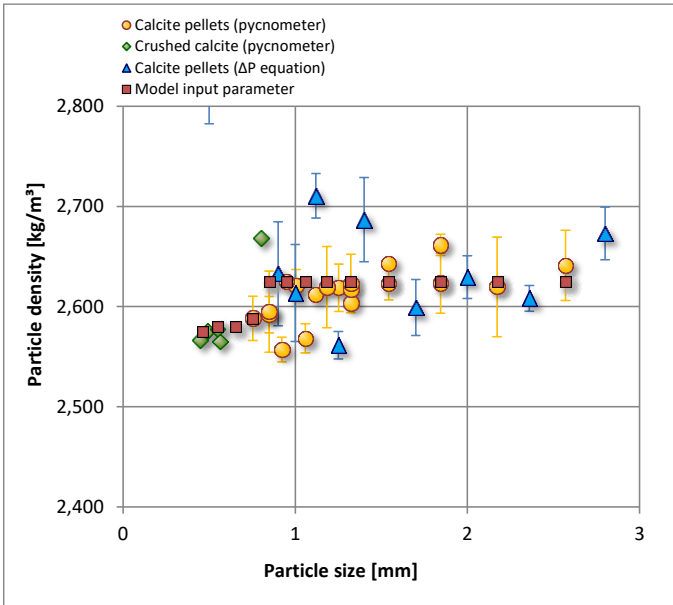


Figure 133 Particle densities of drinking water pellet-softening grains

Fixed and incipient voidage

The measured fixed and incipient bed voidage for calcite pellets (Table 4) agrees with the expected value of 0.4 for round spheres. Literature data which also contain more irregularly shaped particles show a slightly higher fixed bed and incipient porosity, which is also in agreement with findings reported in the literature (Wen and Yu, 1966a; Yang, 2003; Đuriš *et al.*, 2016).

Table 43 Overall determined particle properties

Grain material	Particle size [mm]	Particle density [kg/m ³]	Fixed bed porosity [m ³ /m ³]	Incipient porosity [m ³ /m ³]
Calcite pellets	0.43-2.80	2,613 ± 20	0.39 ± 0.02	0.40 ± 0.01
Crushed calcite	0.40-0.63	2,570 ± 32	0.49 ± 0.01	0.51 ± 0.02

Annex 4: Morphological properties

Source: (Kramer *et al.*, 2020b)

<https://doi.org/10.1016/j.jwpe.2020.101481>

The following morphological properties (Retsch Camsizer XT) are defined:

d_i	Effective sample size where $i\%$ of particles < than the particular size	[m]
UC	Non-uniformity coefficient d_{60}/d_{10}	[-]
Φ	Sphericity from the perimeter and area of the particle projection $\frac{4\pi A}{P^2}$	[-]
$Symm$	Symmetry, distances between centre of area to projection borders	[-]

Table 44 Determined particle properties of crushed calcite and calcite pellets using Retsch Camsizer XT

Diameter	$d_{s,min}$ [mm]	$d_{s,max}$ [mm]	d_p [mm]	d_{10} [mm]	d_{50} [mm]	d_{90} [mm]	UC [-]	Φ [-]	$Symm$ [-]
0.50 - 0.63	0.50	0.63	0.56	0.54	0.64	0.74	1.21	0.90	0.92
0.63 - 0.71	0.63	0.71	0.67	0.64	0.73	0.83	1.17	0.91	0.92
0.80 - 0.90	0.80	0.90	0.85	0.79	0.90	1.00	1.17	0.94	0.93
0.90 - 1.00	0.90	1.00	0.95	0.88	0.99	1.10	1.15	0.95	0.93
1.00 - 1.12	1.00	1.12	1.06	1.02	1.15	1.29	1.15	0.96	0.94
1.12 - 1.25	1.12	1.25	1.18	1.11	1.23	1.35	1.14	0.96	0.94
1.25 - 1.40	1.25	1.40	1.32	1.22	1.37	1.53	1.15	0.97	0.94
1.40 - 1.70	1.40	1.70	1.54	1.41	1.58	1.76	1.15	0.98	0.94
1.70 - 2.00	1.70	2.00	1.84	1.72	1.90	2.10	1.13	0.98	0.95
2.00 - 2.36	2.00	2.36	2.17	2.04	2.22	2.42	1.11	0.98	0.96
2.36 - 2.80	2.36	2.80	2.57	2.27	2.50	2.75	1.12	0.99	0.96
> 2.80	2.80	3.35	3.06	2.72	2.97	3.30	1.11	0.99	0.96
0.40 - 0.50	0.40	0.50	0.45	0.39	0.49	0.58	1.28	0.84	0.88
0.50 - 0.60	0.50	0.60	0.55	0.45	0.57	0.68	1.31	0.84	0.89

The sphericity for crushed calcite and calcite pellets can be interpolated using an empirical Morgan-Mercer-Flodin growth model with Equation (148).

$$\phi_s = \frac{c_0 c_1 + c_2 d_p^{c_3} [mm]}{c_1 + d_p^{c_3} [mm]} \quad (d_p [mm] > 0.4) \quad (148)$$

Table 45 Fitting parameters
MMF model $R^2 = 0.98$

Coefficient	Value
c_0	0.728
c_1	0.171
c_2	0.986
c_3	3.000

Annex 5: Statistical analysis

To compare the experimental data with the prediction models, several well-known statistical methods were used, given an experimentally determined value y_{exp} and a calculated predicted value y_{calc} .

The mean average error is given by:

$$MAE = \frac{1}{N} \sum_{i=1}^N (|y_{calc,i} - y_{exp,i}|) \quad (149)$$

The average relative error (Haider and Levenspiel, 1989) is given by:

$$ARE = \frac{1}{N} \sum_{i=1}^N \left(\frac{|y_{calc,i} - y_{exp,i}|}{y_{exp,i}} \right) \quad (150)$$

The normalised root mean squared error (Brown and Lawler, 2003) is given by:

$$NRMSE = \sqrt{\frac{1}{N} \sum_{i=1}^N \left(\frac{y_{calc,i} - y_{exp,i}}{y_{exp,i}} \right)^2} \quad (151)$$

The logarithmic root mean squared error is given by:

$$LRMSE = \sqrt{\frac{1}{N} \sum_{i=1}^N (\log(y_{calc,i}) - \log(y_{exp,i}))^2} \quad (152)$$

The Pearson correlation coefficient is given by:

$$R = \frac{\sum y_{exp,i} y_{calc,i} - \frac{(\sum y_{exp,i})(\sum y_{calc,i})}{N}}{\sqrt{\left(\sum (y_{exp,i})^2 - \frac{(\sum y_{exp,i})^2}{N} \right) \left(\sum (y_{calc,i})^2 - \frac{(\sum y_{calc,i})^2}{N} \right)}} \quad (153)$$

Annex 6: Overview uncertainty analysis equations

Table 46 Uncertainty analysis equations

Variable	Equation	Eq. nr.
Terminal Reynolds number	$\delta Re_t = \sqrt{\left(\frac{\partial Re_t}{\partial d_p} \delta d_p\right)^2 + \left(\frac{\partial Re_t}{\partial v_T} \delta v_T\right)^2 + \left(\frac{\partial Re_t}{\partial v_t} \delta v_t\right)^2}$	(154)
Drag coefficient	$\delta C_D = \sqrt{\left(\frac{\partial C_D}{\partial g} \delta g\right)^2 + \left(\frac{\partial C_D}{\partial d_p} \delta d_p\right)^2 + \left(\frac{\partial C_D}{\partial \rho_p} \delta \rho_p\right)^2 + \left(\frac{\partial C_D}{\partial \rho_f} \delta \rho_f\right)^2 + \left(\frac{\partial C_D}{\partial v_t} \delta v_t\right)^2}$	(155)
Particle density	$\delta \rho_p = \sqrt{\left(\frac{\partial \rho_p}{\partial m_p} \delta m_p\right)^2 + \left(\frac{\partial \rho_p}{\partial d_p} \delta d_p\right)^2}$	(156)
Terminal settling velocity	$\delta v_t = \sqrt{\left(\frac{\partial v_t}{\partial L} \delta L\right)^2 + \left(\frac{\partial v_t}{\partial t} \delta t\right)^2} \quad \delta t = c_0 + c_1 e^{-t}$	(157)

Table 47 Uncertainty analysis equations. Derivations are given in Kramer et al. (2021b) Supplementary material (Section 6)

Variable	Term	Equation	Equation number contribution to error
Terminal Reynolds number (Equation (3))	1 st	$\frac{\partial Re_t}{\partial d_p} = \frac{v_t}{v_T}$	(158)
	2 nd	$\frac{\partial Re_t}{\partial T} = \frac{d_p v_t}{c_6} \left(-\frac{c_7 \ln 10 (1 + \alpha \Delta T)}{(T + c_8)^2 10^{c_7/(T+c_8)}} - \frac{\alpha}{10^{c_7/(T+c_8)}} \right)$	(159)
	3 rd	$\frac{\partial Re_t}{\partial v_t} = \frac{1}{v_T} \left(d_p - \frac{c_2 d_p^2}{D} \right)$	(160)
Drag coefficient (Equation (41))	1 st	$\frac{\partial C_D}{\partial g} = \frac{4}{3} \frac{d_p}{v_t^2} \left(\frac{\rho_p}{\rho_f} - 1 \right)$	(161)
	2 nd	$\frac{\partial C_D}{\partial d_p} = \frac{\frac{4}{3} \frac{g}{v_t^2} \left(\frac{\rho_p}{\rho_f} - 1 \right)}{\left(d_p^{\frac{1}{2}} - c_2 \frac{d_p^{\frac{1}{2}}}{D} \right)^3} \left(d_p^{-\frac{3}{2}} + \frac{c_2}{D} d_p^{-\frac{1}{2}} \right)$	(162)
	3 rd	$\frac{\partial C_D}{\partial \rho_p} = \frac{4}{3} \frac{g d_p}{v_t^2 \rho_f}$	(163)
	4 th	$\frac{\partial C_D}{\partial T} = \frac{4}{3} \frac{g d_p}{v_t^2} \left(\rho_p \left(\frac{c_3 e^{c_3 T}}{c_4 - c_5 T^2} + \frac{2 c_5 T e^{c_3 T}}{(c_4 - c_5 T^2)^2} \right) - c_3 e^{c_3 T} \right)$	(164)
	5 th	$\frac{\partial C_D}{\partial v_t} = \frac{8}{3} \frac{g d_p}{v_t^3} \frac{\left(\frac{\rho_p}{\rho_f} - 1 \right)}{\left(1 - c_2 \frac{d_p}{D} \right)^2}$	(165)
Particle density (Equation (156))	1 st	$\frac{\partial \rho_p}{\partial m_p} = \frac{6}{\pi d_p^3}$	(166)
	2 nd	$\frac{\partial \rho_p}{\partial d_p} = -\frac{18 m_p}{\pi d_p^4}$	(167)
Terminal settling velocity (Equation (157))	1 st	$\frac{\partial v_t}{\partial L} = \frac{1}{t}$	(168)
	2 nd	$\frac{\partial v_t}{\partial r} = -\frac{L}{r^2}$	(169)

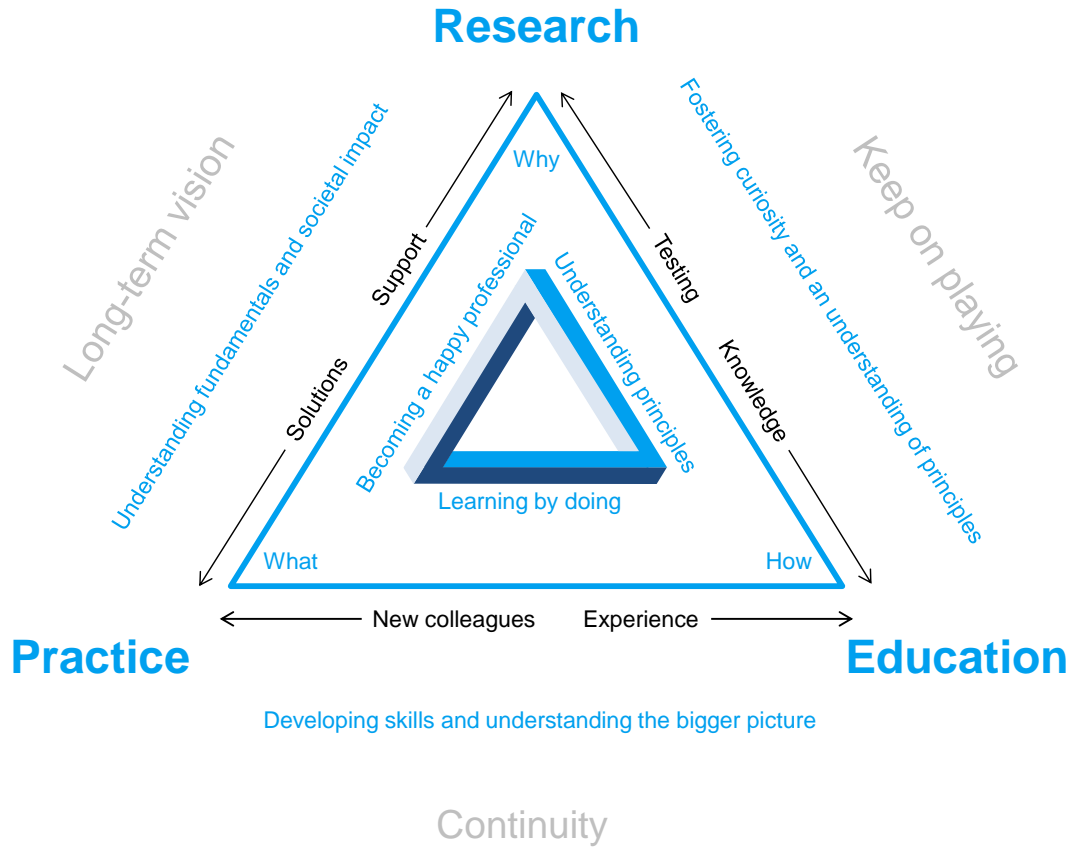


Figure 134 The symbiosis between research, education and professional practice

Annex 7: Where research, education and professional practice meet

The expansion column

A crucial part of this research was to obtain reliable experimental data for liquid-solid fluidisation systems. This high-quality data was not only suitable for calibrating and validating the prediction models, but it also provided a unique opportunity to explore alternative directions, such as including the Froude number next to the Reynolds number. University students were an indispensable and valuable link in the execution of countless experiments. They worked with the expansion column (EXC) (Figure 9) that was designed for this research project.

Ingredients for students to become engaged and committed

By conducting the experiments, the students learned about their useful contribution to the water sector. They learned that the transition from linear processes to more circular processes, such as moving from garnet sand to crushed calcite as seeding material, is accompanied by uncertain changes that had to be explored. More and more, today's students consider sustainability to be of paramount importance; they are inspired and intrinsically motivated by the increasing focus on sustainable drinking water with unlimited access for humanity. Through the experiments with the EXC, they make a modest contribution to this development by working out practical water treatment-related research questions. It allows them to discover how a multiphase flow system works when they change process variables and see what happens. In other words, they start playing and learning by doing. Simultaneously, and thanks to the feedback provided by committed and critical students, it was possible to improve the EXC step by step. In this way, students saw that the EXC experiments established a clear and valuable link between practice, education and research. To validate this observation, students were consulted and invited to complete a questionnaire (Figure 2).

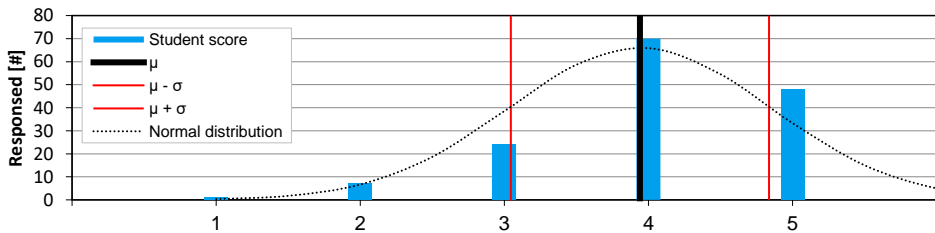


Figure 135 Questionnaire statement: “The expansion column experiment creates a valuable link between practice, education and research.” Answer options: 1 = strongly disagree, 2 = disagree, 3 = neutral agreement / undecided, 4 = agree and 5 = strongly agree. Student responses: $N = 150$, $\mu = 3.9$, $\sigma = 0.9$.

Developing curiosity and an investigating attitude

In addition to the experiments aimed at obtaining expansion, filtration and sedimentation data, the EXC was used to train students via group dynamics in a problem-based learning (PBL) experiment (Barrows and Tamblyn, 1980; Tan, 2003; Hunt et al., 2010) in which this piece of equipment was deployed. Groups of five students were asked to work on an industrial full-scale challenge which should be solved on the fly. Through a role-playing game, students had to supply the plant manager with an analysis of the problem. The technical issue concerned was caused by air inclusion in a pressure sensor. The air trapped inside caused malfunctioning of the reactor and should be solved as soon as possible. One student had to block the water flow so that air trapping could be prevented in the highest-pressure tap. A second student had to control the water flow and a third student had to release air from the pressure sensor using a spanner. A fourth student had to monitor the pressure sensor display. A fifth student was responsible for effective communication, coordination and handling. In this way, students were able to experience the challenges associated with working effectively in a group, the need to keep team spirits up and the need to achieve the best engineering results. The plant manager was watching the events closely.

A new generation of engineers in a circular economy

The EXC is an example of a straightforward low-budget experimental set-up with multiple purposes and applications. It ensures that students contribute to research and developments in sustainable water treatment and industrial multiphase flow processes during their study efforts. Furthermore, working with the EXC through PBL was clearly found to increase students' creativity and innovativeness. It showed how the role of universities in collaboration with the professional field can be enhanced (Kamp, 2016).

The connection between fundamental research and applications of scientific knowledge in professional practice can be improved through education (Figure 2). This type of cross-fertilisation benefits all actors involved. Following the quest for new fundamental knowledge, applied education can create and strengthen bonds between educational institutes and companies that find themselves faced with practical challenges. Solutions can be found by stimulating curiosity and through the development of investigating minds in an environment that is free and inviting. This is where responsibilities can be shared and where completely new (and sometimes even surprising) pathways and inventions can lead to a bright and sustainable future.

“Education can only be effective when teachers become tutors who truly ‘see’ their students and cater to their individual needs.”

References

*“It is easy to conceptualise 100 reason not to start something,
in the contrary there is often only 1 reason to actually start with it.”*

References

- Abraham, F.F., 1970. Functional dependence of drag coefficient of a sphere on Reynolds number. *Physics of Fluids* 13, 2194–2195.
<https://doi.org/10.1063/1.1693218>
- Akgiray, O., Soyer, E., 2006. An evaluation of expansion equations for fluidized solid-liquid systems. *Journal of Water Supply: Research and Technology – AQUA* 55, 517–525. <https://doi.org/10.2166/aqua.2006.040>
- Akkoyunlu, A., 2003. Expansion of granular water filters during backwash. *Environmental Engineering Science* 20, 655–665.
<https://doi.org/10.1089/109287503770736168>
- Al-Arkawazi, S., Marie, C., Benhabib, K., Coorevits, P., 2017. Modeling the hydrodynamic forces between fluid–granular medium by coupling DEM–CFD. *Chemical Engineering Research and Design* 117, 439–447.
<https://doi.org/10.1016/j.cherd.2016.11.002>
- Albright, J., 2009. *Albright's chemical engineering handbook*, 1st ed. CRC Press., New-York.
- Aldoukhi, A.H., Roberts, W.W., Hall, T.L., Ghani, K.R., 2017. Holmium laser lithotripsy in the new stone age: dust or bust? *Frontiers in Surgery*.
<https://doi.org/10.3389/fsurg.2017.00057>
- Allen, T., 1990. Particle size measurement – Powder Technology Series, 4th ed. Chapman and Hall, London. <https://doi.org/10.1007/978-94-009-0417-0>
- Almedeij, J., 2008. Drag coefficient of flow around a sphere: Matching asymptotically the wide trend. *Powder Technology* 186, 218–223.
<https://doi.org/10.1016/j.powtec.2007.12.006>
- Amburgey, J.E., 2005. Optimization of the extended terminal subfluidization wash (ETSW) filter backwashing procedure. *Water Research* 39, 314–330.
<https://doi.org/10.1016/j.watres.2004.09.020>
- Amburgey, J.E., Amiratharajah, A., 2005. Practical and theoretical guidelines for implementing the extended terminal subfluidization wash (ETSW) backwashing procedure. *Journal of Water Supply: Research and Technology-Aqua* 54, 329–337. <https://doi.org/10.2166/aqua.2005.0031>
- Anantharaman, A., Cocco, R.A., Chew, J.W., 2018. Evaluation of correlations for minimum fluidization velocity (U_{mf}) in gas-solid fluidization. *Powder Technology* 323, 454–485. <https://doi.org/10.1016/j.powtec.2017.10.016>
- Anderson, J.D., 1991. *Fundamentals of aerodynamics*, 2nd ed. McGraw-Hill, New York.
- Anderson, K., Chescattie, E., 2003. Incorporating filter bed expansion measurements into your backwashing routine, in: *AWWA Water Quality Technology Conference*.
- Anscombe, F.J., 2010. Graphs in statistical analysis. *The American Statistician* 27, 441–475. https://doi.org/10.1007/978-3-540-71915-1_35
- Anthony, J.W., Bideaux, R.A., Bladh, K.W., Nichols, M.C., 2003. *Calcite, handbook of mineralogy*, V, borates, carbonates, sulfates, mineral data publishing, 1st ed, Mineralogical Society of America. Mineralogical Society of America.

- Apostol, T.M., 1967. One-variable calculus, with an introduction to linear algebra, 2nd ed. John Wiley & Sons, Inc., New York.
- Ardekani, M.N., Costa, P., Breugem, W.P., Brandt, L., 2016. Numerical study of the sedimentation of spheroidal particles. *International Journal of Multiphase Flow* 87, 16–34. <https://doi.org/10.1016/j.ijmultiphaseflow.2016.08.005>
- Arsenijević, Z.L., Grbavčić, Ž.B., Garić-Grulović, R. v., Bošković-Vragolović, N.M., 2010. Wall effects on the velocities of a single sphere settling in a stagnant and counter-current fluid and rising in a co-current fluid. *Powder Technology* 203, 237–242. <https://doi.org/10.1016/j.powtec.2010.05.013>
- Ashoor, F.A.K., Zmat, A.D., AlDahhan, M.H., 2019. Pellet softening process for the removal of the groundwater hardness; modelling and experimentation. *Al-Qadisiyah Journal for Engineering Sciences* 12, 135–143. <https://doi.org/10.30772/qjes.v12i3.603>
- Asif, M., 1998. Generalized Richardson-Zaki correlation for liquid fluidization of binary solids. *Chemical Engineering and Technology* 21, 77–82.
- Auguste, F., Magnaudet, J., 2018. Path oscillations and enhanced drag of light rising spheres. *Journal of Fluid Mechanics* 841, 228–266. <https://doi.org/10.1017/jfm.2018.100>
- Awange, J.L., Paláncz, B., 2016. Geospatial algebraic computations, 1st ed, *Geospatial Algebraic Computations*. Springer, New York. <https://doi.org/10.1007/978-3-319-25465-4>
- Bagheri, G., Bonadonna, C., 2016. On the drag of freely falling non-spherical particles. *Powder Technology* 301, 526–544. <https://doi.org/10.1016/j.powtec.2016.06.015>
- Baldock, T.E., Tomkins, M.R., Nielsen, P., Hughes, M.G., 2004. Settling velocity of sediments at high concentrations. *Coastal Engineering* 51, 91–100. <https://doi.org/10.1016/j.coastaleng.2003.12.004>
- Bandosz, T.J., 2006. Activated carbon surfaces in environmental remediation, 1st ed. Academic Press, New York.
- Bansal, R.C., Goyal, M., 2005. Activated carbon adsorption, 1st ed. Taylor & Francis.
- Barati, R., Neyshabouri, S.A.A.S., 2018. Comment on “Summary of frictional drag coefficient relationships for spheres: Evolving solution strategies applied to an old problem” [*Chem. Eng. Sci.* 168 (2017) 339–343, doi: <https://doi.org/10.1016/j.ces.2017.04.037>]. *Chemical Engineering Science* 181, 90–91. <https://doi.org/10.1016/j.ces.2018.02.013>
- Barati, R., Neyshabouri, S.A.A.S., Ahmadi, G., 2014. Development of empirical models with high accuracy for estimation of drag coefficient of flow around a smooth sphere: an evolutionary approach. *Powder Technology* 257, 11–19. <https://doi.org/10.1016/j.powtec.2014.02.045>
- Bargieł, M., Tory, E.M., 2013. Extension of the Richardson-Zaki equation to suspensions of multisized irregular particles. *International Journal of Mineral Processing*. <https://doi.org/10.1016/j.minpro.2013.02.011>
- Barroso-Bogeat, A., Alexandre-Franco, M., Fernández-González, C., Gómez-Serrano, V., 2016. Particle size distribution and morphological changes in activated carbon-metal oxide hybrid catalysts prepared under different heating

- conditions. *Journal of Microscopy* 261, 227–242.
<https://doi.org/10.1111/jmi.12323>
- Batchelor, G.K., 1967. *An introduction to fluid dynamics*, 1st ed. Cambridge University Press, Cambridge.
- Batchelor, G.K., 1988. A new theory of the instability of a uniform fluidized bed. *Journal of Fluid Mechanics* 193, 75–110.
<https://doi.org/10.1017/S002211208800206X>
- Batchelor, G.K., 2012. *An introduction to fluid dynamics*. Cambridge University Press, Cambridge. <https://doi.org/10.1017/CBO9780511800955>
- Bedingfield, C.H., Drew, T.B., 1950. Analogy between heat transfer and mass transfer. *Industrial & Engineering Chemistry* 42, 1164–1173.
<https://doi.org/10.1021/ie50486a029>
- Beeftink, M., Hofs, B., Kramer, O.J.I., Odegard, I., Wal, van der, A., 2021. Carbon footprint of drinking water softening as determined by life cycle assessment. *Journal of Cleaner Production* 278, 1–10.
<https://doi.org/10.1016/j.jclepro.2020.123925>
- Beetstra, R., 2005. Drag force in random arrays of mono- and bidisperse spheres. Enschede.
- Beetstra, R., Hoef, M.A. van der, Kuipers, J.A.M., 2007. Drag force of intermediate Reynolds number flow past mono- and bidisperse arrays of spheres. *American Institute of Chemical Engineers Journal* 53, 489–501.
<https://doi.org/10.1002/aic.11065>
- Bird, R.B., Stewart, W.E., Lightfoot, E.N., 2007. *Transport phenomena*, revised, 2nd ed. John Wiley & Sons, Inc. International, New-York.
- Blais, B., Bertrand, F., 2017. CFD-DEM investigation of viscous solid–liquid mixing: Impact of particle properties and mixer characteristics. *Chemical Engineering Research and Design* 118, 270–285.
<https://doi.org/10.1016/j.cherd.2016.12.018>
- Blake, F.C., 1922. The resistance of packing to fluid flow. *Transactions of the American Institute of Chemical Engineers* 14, 415–421.
- Boccelli, D.L., Small, M.J., Diwekar, U.M., 2007. Drinking water treatment plant design Incorporating variability and uncertainty. *Journal of Environmental Engineering* 133, 303–312. [https://doi.org/10.1061/\(asce\)0733-9372\(2007\)133:3\(303\)](https://doi.org/10.1061/(asce)0733-9372(2007)133:3(303))
- Bolisetty, S., Peydayesh, M., Mezzenga, R., 2019. Sustainable technologies for water purification from heavy metals: review and analysis. *Chemical Society Reviews* 48, 463–487. <https://doi.org/10.1039/c8cs00493e>
- Bosklopper, Th.G. J., Rietveld, L.C., Babuska, R., Smaal, B., Timmer, J., 2004. Integrated operation of drinking water treatment plant at Amsterdam water supply. *Water Science and Technology: Water Supply* 4, 263–270.
<https://doi.org/10.2166/ws.2004.0116>
- Breakey, D.E.S., Vaezi, G., F., Masliyah, J.H., Sanders, R.S., 2018. Side-view-only determination of drag coefficient and settling velocity for non-spherical particles. *Powder Technology* 339, 182–191.
<https://doi.org/10.1016/j.powtec.2018.07.056>

- Brown, P.P., Lawler, D.F., 2003. Sphere drag and settling velocity revisited. *Journal of Environmental Engineering* 129, 222–231. [https://doi.org/10.1061/\(ASCE\)0733-9372\(2003\)129:3\(222\)](https://doi.org/10.1061/(ASCE)0733-9372(2003)129:3(222))
- Burhenne, L., Giacomini, C., Follett, T., Ritchie, J., McCahill, J.S.J., Mérida, W., 2017. Characterization of reactive CaCO₃ crystallization in a fluidized bed reactor as a central process of direct air capture. *Journal of Environmental Chemical Engineering* 5, 5968–5977. <https://doi.org/10.1016/j.jece.2017.10.047>
- Burke, S.P., Plummer, W.B., 1928. Suspension of macroscopic particles in a turbulent gas stream. *Industrial and Engineering Chemistry* 20, 1200–1204. <https://doi.org/10.1021/ie50227a026>
- Busciglio, A., 2011. Measurement techniques and modelling of multiphase systems. Palermo.
- Cahyadi, A., Yang, S., Chew, J.W., 2017. CFD study on the hydrodynamics of fluidized granular activated carbon in AnFMBR applications. *Separation and Purification Technology* 178, 75–89. <https://doi.org/10.1016/j.seppur.2017.01.023>
- Camp, T.R., 1946. Sedimentation and the design of settling tanks. *Transactions of the American Society of Civil Engineers* 111, 895–936.
- Capes, C.E., 1974. Particle agglomeration and the value of the exponent n in the Richardson-Zaki equation. *Powder Technology* 10, 303–306. [https://doi.org/10.1016/0032-5910\(74\)85005-9](https://doi.org/10.1016/0032-5910(74)85005-9)
- Carman, P.C., 1937. Fluid flow through granular beds. *Transactions, Institution of Chemical Engineers* 15, 32–48. [https://doi.org/10.1016/S0263-8762\(97\)80003-2](https://doi.org/10.1016/S0263-8762(97)80003-2)
- Cello, F., Di Renzo, A., Di Maio, F.P., 2010. A semi-empirical model for the drag force and fluid-particle interaction in polydisperse suspensions. *Chemical Engineering Science* 65, 2128–3139. <https://doi.org/10.1016/j.ces.2010.02.006>
- CEFIC, 1986. Test methods for activated carbon. Berlin.
- Çeçen, F., Aktaş, O., 2010. Activated carbon for water and wastewater Treatment - Integration of adsorption and biological treatment, 1st ed. Wiley-VCH, Istanbul. <https://doi.org/10.1002/9783527628926>
- Chen, Y.H., Fan, R., An, D., Cheng, Y., Tan, H., 2016. Water softening by induced crystallization in fluidized bed. *Journal of Environmental Sciences (China)* 50, 109–116. <https://doi.org/10.1016/j.jes.2016.08.014>
- Chen, Y.H., Yeh, H.H., Tsai, M.C., Lai, W.L., 2000. The application of fluidized bed crystallization in drinking water softening. *Journal of the Chinese institute of Environmental Engineering* 10, 177–184.
- Cheng, N.-S., 1997. Simplified settling velocity formula for sediment particle. *Journal of Hydraulic Engineering* 123, 149–152. [https://doi.org/10.1061/\(ASCE\)0733-9429\(1997\)123:2\(149\)](https://doi.org/10.1061/(ASCE)0733-9429(1997)123:2(149))
- Cheng, N.S., 2009. Comparison of formulas for drag coefficient and settling velocity of spherical particles. *Powder Technology* 189, 395–398. <https://doi.org/10.1016/j.powtec.2008.07.006>
- Cheremisinoff, N.P., 2002. Handbook of water and wastewater treatment technologies, 1st ed. Butterworth-Heinemann, Boston.
- Chhabra, R.P., Agarwal, S., Chaudhary, K., 2003. A note on wall effect on the terminal falling velocity of a sphere in quiescent Newtonian media in cylindrical

- tubes. *Powder Technology* 129, 53–58. [https://doi.org/10.1016/S0032-5910\(02\)00164-X](https://doi.org/10.1016/S0032-5910(02)00164-X)
- Chhabra, R.P., Basavaraj, M.G., 2002. *Coulson & Richardson's chemical engineering (volume 2)*, 6th ed. Butterworth-Heinemann, New York.
- Chien, S.F., 1994. Settling velocity of irregularly shaped particles. *SPE Drilling & Completion* 9, 281–289. [https://doi.org/10.1016/0148-9062\(95\)92494-3](https://doi.org/10.1016/0148-9062(95)92494-3)
- Chiou, E., 2018. An improved model of calcium carbonate crystallization: An improved kinetics-model for the calcium carbonate crystallization in the fluidized bed softening reactors at the Weesperkarspel drinking water treatment plant. Delft.
- Chong, Y.S., Ratkowsky, D.A., Epstein, N., 1979. Effect of particle shape on hindered settling in creeping flow. *Powder Technology* 23, 55–66. [https://doi.org/10.1016/0032-5910\(79\)85025-1](https://doi.org/10.1016/0032-5910(79)85025-1)
- Civan, F., 2007. Critical modification to the Vogel-Tammann-Fulcher equation for temperature effect on the density of water. *Industrial and Engineering Chemistry Research* 46, 5810–5814. <https://doi.org/10.1021/ie070714j>
- Clark, M.M., 2009. *Transport modeling for environmental engineers and scientists*, 2nd ed. John Wiley & Sons Ltd., New York.
- Cleasby, J.L., Arboleda, J., Burns, D.E., Prendiville, P.W., Savage, E.S., 1977. Backwashing of granular filters. *Journal American Water Works Association* 69, 115–126.
- Clements, M., Haarhoff, J., 2004. Practical experiences with granular activated carbon (GAC) at the Rietvlei water treatment plant. *Water SA* 30, 1–8.
- Clements, M., 2009. Granular activated carbon management at a water treatment plant.
- Clift, R., Gauvin, W.H., 1971. Motion of entrained particles in gas streams. *Canadian Journal of Chemical Engineering* 49, 439–448. <https://doi.org/https://doi.org/10.1002/cjce.5450490403>
- Clift, R., Grace, J.R., Weber, M.E., 1978. *Bubbles, drops, and particles*. Academic Press., San Diego, San Diego, C.A.
- Cloete, S., Cloete, J.H., Amini, S., 2018. Hydrodynamic validation study of filtered two fluid models. *Chemical Engineering Science* 182, 93–107. <https://doi.org/10.1016/j.ces.2018.02.032>
- Concha, F., Almendra, E.R., 1979. Settling velocities of particulate systems, 1. settling velocities of individual spherical particles. *International Journal of Mineral Processing* 5, 349–367. [https://doi.org/10.1016/0301-7516\(79\)90044-9](https://doi.org/10.1016/0301-7516(79)90044-9)
- Cornelissen, J.T., Taghipour, F., Escudie, R., Ellis, N., Grace, J.R., 2007. CFD modelling of a liquid-solid fluidized bed. *Chemical Engineering Science* 62, 6334–6348. <https://doi.org/10.1016/j.ces.2007.07.014>
- Cotruvo, J., Fawell, J.K., Giddings, M., Jackson, P., Magara, Y., Festo Ngowi, A. v., Ohanian, E., 2001. *Hardness in drinking-water: background document for development of WHO guidelines for drinking-water quality*, World health organisation. <https://doi.org/WHO/HSE/WSH/10.01/10/Rev/1>
- Coulson, J.M., Richardson, J.F., 1957. *Coulson Richardson chemical engineering (volume 2)*, 3rd ed. Pergamon Press, Oxford. <https://doi.org/10.1002/apj.5500010209>

- Cummins, B.M., Chinthapatla, R., Ligler, F.S., Walker, G.M., 2017. Time-dependent model for fluid flow in porous materials with multiple pore sizes. *Analytical Chemistry* 89, 4377–4381. <https://doi.org/10.1021/acs.analchem.6b04717>
- Crittenden, J.C., Trussell, R.R., Hand, D.W., Howe, K.J., Tchobanoglous, G., 2012. *MWH's water treatment: principles and design*, 3rd ed. John Wiley & Sons, New York.
- Crowe, C.T., Group, F., 2006. *Multiphase flow handbook*, 1st ed, Hemisphere. CRC Press, New York.
- Cui, H., Grace, J.R., 2007. Fluidization of biomass particles: A review of experimental multiphase flow aspects. *Chemical Engineering Science* 62, 45–55. <https://doi.org/10.1016/j.ces.2006.08.006>
- Dabrowski, W., Spaczyńska, M., Mackie, R.I., 2008. A model to predict granular activated carbon backwash curves. *Clean – Soil, Air, Water* 36, 103–110. <https://doi.org/10.1002/clen.200600033>
- Dacomba Torres, P.D.R., 2018. Fluidization behavior of granular activated carbon: For drinking water treatment applications. Delft.
- Dallavalle, J.M., 1948. *Micromeritics – the technology of fine particles*, 2nd ed. Pitman Publishing Ltd, London.
- Darby, R., Chhabra, R.P., 2001. *Chemical engineering fluid mechanics*, 2nd ed. Marcel Dekker Inc., New York.
- Darcy, H., 1856. *Les fontaines publiques de la ville de Dijon: Exposition et application des principes a suivre et des formules a employer dans les questions de distribution d'eau; ouvrage terminé par un appendice relatif aux fournitures d'eau de plusieurs villes au filtr.* Victor Dalmont, Libraire des Corps imperiaux des ponts et chaussées et des mines, Dijon.
- Davidson, S., Perkin, M., 2013. An investigation of density determination methods for porous materials, small samples and particulates. *Measurement: Journal of the International Measurement Confederation* 46, 1766–1770. <https://doi.org/10.1016/j.measurement.2012.11.030>
- Davidson, J.F., Clift, R., Harrison, D., 1985. *Fluidization*, 2nd ed. Academic Press, Inc., London.
- Davis, M., 2010. *Water and wastewater engineering – Design principles and practice*, 1st ed. McGraw-Hill, New-York.
- Dharmarajah, A.H., 1982. Effect of particle shape on prediction of velocity-voidage relationship in fluidized solid-liquid systems. Ames.
- Deitz, V.R., 1997. The heterogeneity of commercial granular activated carbons. *Carbon* 35, 579–584.
- De Moel, P.J., van der Helm, A.W.C., van Rijn, M., van Dijk, J.C., van der Meer, W.G.J., 2013. Assessment of calculation methods for calcium carbonate saturation in drinking water for DIN 38404-10 compliance. *Drinking Water Engineering and Science* 6, 1–10. <https://doi.org/10.5194/dwes-6-1-2013>
- De Moel, P.J., van Dijk, J.C., Verberk, J.Q.J.C., 2006. *Drinking water - principles and practices*. World Scientific Publishing Co Pte Ltd, New Jersey.
- Di Felice, R., 1995. Review article number 47: Of hydrodynamics of liquid fluidisation. *Chemical Engineering Science* 50, 1213–1245. [https://doi.org/10.1016/0009-2509\(95\)98838-6](https://doi.org/10.1016/0009-2509(95)98838-6)

- Di Felice, R., Foscolo, P.U., Gibilaro, L.G., 1989. The experimental determination of the force on spheres submerged in liquid interaction fluidized beds. *Chemical Engineering and Processing: Process Intensification* 25, 27–34. [https://doi.org/10.1016/0255-2701\(89\)85003-2](https://doi.org/10.1016/0255-2701(89)85003-2)
- Di Felice, R., Gibilaro, L.G., 2004. Wall effects for the pressure drop in fixed beds. *Chemical Engineering Science* 59, 3037–3040. <https://doi.org/10.1016/j.ces.2004.03.030>
- Di Felice, R., Rotondi, M., 2013. Solid suspension by an upflow mixture of fluid and larger particles. *Advances in Mechanical Engineering* 2013. <https://doi.org/10.1155/2013/859756>
- Di Renzo, A., Di Maio, F.P., 2007. Homogeneous and bubbling fluidization regimes in DEM-CFD simulations: Hydrodynamic stability of gas and liquid fluidized beds. *Chemical Engineering Science* 62, 116–130. <https://doi.org/10.1016/j.ces.2006.08.009>
- Di Renzo, A., Grassano, N., Di Maio, F.P., 2017. Force on a large sphere immersed in an expanded water-fluidized bed over a wide range of voidage values. *Powder Technology* 316, 296–302. <https://doi.org/10.1016/j.powtec.2016.12.045>
- Didwania, A.K., Homsy, G.M., 1981. Flow regimes and flow transitions in liquid fluidized beds. *International Journal of Multiphase Flow* 7, 563–580.
- Dioguardi, F., Mele, D., 2015. A new shape dependent drag correlation formula for non-spherical rough particles. Experiments and results. *Powder Technology* 277, 222–230. <https://doi.org/10.1016/j.powtec.2015.02.062>
- Dioguardi, F., Mele, D., Dellino, P., 2018. A new one-equation model of fluid drag for irregularly shaped particles valid over a wide range of Reynolds number. *Journal of Geophysical Research: Solid Earth* 123, 144–156. <https://doi.org/10.1002/2017JB014926>
- Djerbi Tegger, A., 2012. Determining the water absorption of recycled aggregates utilizing hydrostatic weighing approach. *Construction and Building Materials* 27, 112–116. <https://doi.org/10.1016/j.conbuildmat.2011.08.018>
- Do Nascimento, O.L., Reay, D.A., Zivkovic, V., 2016. Influence of surface forces and wall effects on the minimum fluidization velocity of liquid-solid micro-fluidized beds. *Powder Technology* 304, 55–62. <https://doi.org/10.1016/j.powtec.2016.05.013>
- Duduković, M.P., Mills, P.L., 2015. Scale-up and multiphase reaction engineering. *Current Opinion in Chemical Engineering* 9, 49–58. <https://doi.org/10.1016/j.coche.2015.08.002>
- Đuriš, M., Garić-Grulović, R., Arsenijević, Z., Jaćimovski, D., Grbavčić, Ž., 2013. Segregation in water fluidized beds of sand particles. *Powder Technology* 235, 173–179. <https://doi.org/10.1016/j.powtec.2012.10.004>
- Đuriš, M., Radočić, T.K., Arsenijević, Z., Garić-Grulović, R., Grbavčić, Ž., 2016. Prediction of bed expansion of polydisperse quartz sand mixtures fluidized with water. *Powder Technology* 289, 95–103. <https://doi.org/10.1016/j.powtec.2015.11.047>
- Ebrahimi Khabbazi, A., Ellis, J.S., Bazylak, A., 2013. Developing a new form of the Kozeny-Carman parameter for structured porous media through lattice-

- Boltzmann modeling. *Computers and Fluids* 75, 35–41.
<https://doi.org/10.1016/j.compfluid.2013.01.008>
- Edwards, R. v., 2006. *Processing random data: statistics for engineers and scientists*, 1st ed, Processing Random Data. World Scientific Pub Co Inc, New Jersey. <https://doi.org/10.1142/6133>
- Edzwald, J.K., 2011. *Water quality and treatment: a handbook on drinking water*, 6th ed. American Water Works Association, American Society of Civil Engineers, McGraw-Hill, New York.
- Einstein, A., 1906. Eine neue Bestimmung der Moleküldimensionen. *Annalen der Physik* 324, 289–306. <https://doi.org/10.1002/andp.19063240204>
- Eisfeld, B., Schnitzlein, K., 2001. The influence of confining walls on the pressure drop in packed beds. *Chemical Engineering Science* 56, 4321–4329.
[https://doi.org/10.1016/S0009-2509\(00\)00533-9](https://doi.org/10.1016/S0009-2509(00)00533-9)
- Van Engelenburg, J., van Slobbe, E., Teuling, A.J., Uijlenhoet, R., Hellegers, P., 2021. Sustainability characteristics of drinking water supply in the Netherlands. *Drinking Water Engineering and Science* 14, 1–41.
<https://doi.org/10.5194/dwes-14-1-2021>
- Epstein, N., 2003. Applications of liquid-solid fluidization. *International Journal of Chemical Reactor Engineering* 1, 1–16. <https://doi.org/10.2202/1542-6580.1010>
- Erdim, E., Akgiray, Ö., Demir, I., 2015. A revisit of pressure drop-flow rate correlations for packed beds of spheres. *Powder Technology* 283, 488–504.
<https://doi.org/10.1016/j.powtec.2015.06.017>
- Ergun, S., 1952. Fluid flow through packed columns. *Chemical Engineering Science* 48, 89–94.
- Escudié, R., Epstein, N., Grace, J.R., Bi, H.T., 2006. Layer inversion phenomenon in binary-solid liquid-fluidized beds: Prediction of the inversion velocity. *Chemical Engineering Science* 61, 6667–6690.
<https://doi.org/10.1016/j.ces.2006.06.008>
- Fair, G.M., Geyer, J.C., Okun, D.A., 1954. *Elements of water supply and waste water disposal*, 1st ed. John Wiley & Sons., New York.
- Fazle Hussain, A.K., 1986. Coherent structures and turbulence. *Journal of Fluid Mechanics* 173, 303–356. <https://doi.org/10.1017/S0022112086001192>
- Ferreira, T., Rasband, W., 2012. *ImageJ user guide*, ImageJ user guide IJ 1.46r.
<https://doi.org/10.1038/nmeth.2019>
- Fidleris, V., Whitmore, R.L., 2002. Experimental determination of the wall effect for spheres falling axially in cylindrical vessels. *British Journal of Applied Physics* 12, 490–494. <https://doi.org/10.1088/0508-3443/12/9/311>
- Filho, W.L., Sümer, V., 2015. *Sustainable water use and management examples of new approaches and perspectives*, 1st ed. Springer International Publishing, Cham, Switzerland. <https://doi.org/10.1007/978-3-319-12394-3>
- Flemmer, R.L.C., Banks, C.L., 1986. On the drag coefficient of a sphere. *Powder Technology* 48, 217–221. [https://doi.org/10.1016/0032-5910\(86\)80044-4](https://doi.org/10.1016/0032-5910(86)80044-4)
- Forchheimer, P., 1901. *Wasserbewegung durch boden*. *Zeitschrift des Vereines Deutscher Ingenieuer* 45, 1781–1788.
- Forchheimer, P., 1930. *Hydraulik*, 3rd ed. B.G. Teubner, Leipzig.
- Foscolo, P.U., Gibilaro, L.G., Waldram, S.P., 1983. A unified model for particulate expansion of fluidised beds and flow in fixed porous media. *Chemical*

- Engineering Science 38, 1251–1260. [https://doi.org/10.1016/0009-2509\(83\)80045-1](https://doi.org/10.1016/0009-2509(83)80045-1)
- Frank, J., Ruhl, A.S., Jekel, Martin., 2015. Impacts of backwashing on granular activated carbon filters for advanced wastewater treatment. *Water Research* 87, 166–174. <https://doi.org/10.1016/j.watres.2015.09.020>
- Fries, L., Antonyuk, S., Heinrich, S., Dopfer, D., Palzer, S., 2013. Collision dynamics in fluidised bed granulators: A DEM-CFD study. *Chemical Engineering Science* 86, 108–123. <https://doi.org/10.1016/j.ces.2012.06.026>
- Ganser, G.H., 1993. A rational approach to drag prediction of spherical and nonspherical particles. *Powder Technology* 77, 143–152. [https://doi.org/10.1016/0032-5910\(93\)80051-B](https://doi.org/10.1016/0032-5910(93)80051-B)
- Garside, J., Al-Dibouni, M.R., 1977. Velocity-voidage relationships for fluidization and sedimentation in solid-liquid systems. *Industrial and Engineering Chemistry Process Design and Development* 16, 206–214. <https://doi.org/10.1021/i260062a008>
- Geldart, D., 1973. Types of gas fluidization. *Powder Technology* 7, 285–292. [https://doi.org/10.1016/0032-5910\(73\)80037-3](https://doi.org/10.1016/0032-5910(73)80037-3)
- Geldart, D., 1990. Estimation of basic particle properties for use in fluid-particle process calculations. *Powder Technology* 60, 1–13. [https://doi.org/10.1016/0032-5910\(90\)80099-K](https://doi.org/10.1016/0032-5910(90)80099-K)
- Ghatage, S. v., Peng, Z., Sathe, M.J., Doroodchi, E., Padhiyar, N., Moghtaderi, B., Joshi, J.B., Evans, G.M., 2014. Stability analysis in solid-liquid fluidized beds: experimental and computational. *Chemical Engineering Journal* 256, 169–186. <https://doi.org/10.1016/j.cej.2014.06.026>
- Gibilaro, L.G., 2001. Fluidization-dynamics, the formulation and applications of a predictive theory for the fluidized state. Butterworth-Heinemann, Oxford.
- Gibilaro, L.G., Di Felice, R., Waldram, S.P., Foscolo, P.U., 1985. Generalized friction factor and drag coefficient correlations for fluid particle interactions. *Chemical Engineering Science* 40, 1817–1823.
- Gibilaro, L.G., Hossain, I., Foscolo, P.U., 1986. Aggregate behaviour of liquid fluidised beds. *Canadian Journal of Chemical Engineering* 64, 931–938. <https://doi.org/10.1002/cjce.5450640607>
- Girimonte, R., Vivacqua, V., 2011. The expansion process of particle beds fluidized in the voids of a packing of coarse spheres. *Powder Technology* 213, 63–69. <https://doi.org/10.1016/j.powtec.2011.07.006>
- Girimonte, R., Vivacqua, V., 2013. Design criteria for homogeneous fluidization of Geldart's class b solids upward through a packed bed. *Powder Technology* 249, 316–322. <https://doi.org/10.1016/j.powtec.2013.08.041>
- Gitis, V., Hankins, N., 2018. Water treatment chemicals: Trends and challenges. *Journal of Water Process Engineering* 25, 34–38. <https://doi.org/10.1016/j.jwpe.2018.06.003>
- Glasserman, P., Videla, D., Böhm, U., 1994. Liquid fluidization of particles in packed beds. *Powder Technology* 79, 237–245. [https://doi.org/10.1016/0032-5910\(94\)02822-2](https://doi.org/10.1016/0032-5910(94)02822-2)
- Godskesen, B., Hauschild, M., Rygaard, M., Zambrano, K., Albrechtsen, H.J., 2012. Life cycle assessment of central softening of very hard drinking water.

- Journal of Environmental Management 105, 83–89.
<https://doi.org/10.1016/j.jenvman.2012.03.030>
- Goldschmidt, M.J. v., Kuipers, J.A.M., van Swaaij, W.P.M., 2001. Hydrodynamic modelling of dense gas-fluidised beds using the kinetic theory of granular flow: effect of coefficient of restitution on bed dynamics. *Chemical Engineering Science* 56, 571–578.
- Goossens, W.R.A., 1998. Classification of fluidized particles by Archimedes number. *Powder Technology* 98, 48–53. [https://doi.org/10.1016/S0032-5910\(98\)00027-8](https://doi.org/10.1016/S0032-5910(98)00027-8)
- Goossens, W.R.A., 2019. Review of the empirical correlations for the drag coefficient of rigid spheres. *Powder Technology* 352, 350–359.
<https://doi.org/10.1016/j.powtec.2019.04.075>
- Grace, J.R., 1986. Contacting modes and behaviour classification of gas-solid and other two-phase suspensions. *Canadian Journal of Chemical Engineering* 64, 353–363. <https://doi.org/10.1002/cjce.5450640301>
- Grace, J.R., Bi, X., Ellis, N., 2020. *Essentials of fluidization technology*, 1st ed. Wiley-VCH, Vancouver.
- Graf, W.H., 1984. *Hydraulics of sediment transport*, 1st ed. Water Resources Publications, LLC, Colorado.
- Graveland, A.J., van Dijk, J.C., de Moel, P.J., Oomen, J.H.C.M., 1983. Developments in water softening by means of pellet reactors. *Journal AWWA – American Water Works Association* 75, 619–625.
- Green, H., Ampt, G.A., 1911. *Studies on Soil Physics*. *The Journal of Agricultural Science* 4, 1–24.
- Groenendijk, M., van de Wetering, T.S.C.M., van Nieuwenhuijze, R., 2008. Central water softening: Customer comfort is relevant in new WHO view. *Water Science and Technology: Water Supply* 8, 69–74. <https://doi.org/10.2166/ws.2008.036>
- Gupta, C.K., Sathiyamoorthy, D., 1999. *Fluid bed technology in materials processing*, 1st ed. CRC Press LLC., Boca Raton.
- GWRC, 2007. *Drinking water hardness: reasons and criteria for softening and conditioning of drinking water*, 1st ed. Global Water Research Coalition; Kiwa Water Research; AWWA Research Foundation, London.
- Haberman, W.L., Sayre, R.M., 1958. *Motion of rigid and fluid spheres in stationary and moving liquids inside cylindrical tubes*, Department of the Navy, David Taylor Model Basin, Hydromechanics Laboratory.
- Haider, A., Levenspiel, O., 1989. Drag coefficients and terminal velocity of spherical and nonspherical particles. *Powder Technology* 58, 63–70.
- Ham, J.M., Thomas, S., Guazzelli, E., Homsy, G.M., Anselmet, M.C., 1990. An experimental study of the stability of liquid-fluidized beds. *International Journal of Multiphase Flow* 16, 171–185. [https://doi.org/10.1016/0301-9322\(91\)90032-X](https://doi.org/10.1016/0301-9322(91)90032-X)
- Hammes, F., Boon, N., Vital, M., Ross, P., Magic-Knezev, A., Dignum, M., 2011. Bacterial colonization of pellet softening reactors used during drinking water treatment. *Applied and Environmental Microbiology* 77, 1041–1048.
<https://doi.org/10.1128/AEM.02068-10>
- Happel, J., Epstein, N., 1954. Cubical assemblages of uniform spheres. *Industrial & Engineering Chemistry* 46, 1187–1194. <https://doi.org/10.1021/ie50534a033>

- Harms, W.D., Robinson, R.B., 1992. Softening by fluidized bed crystallizers. *Journal of Environmental Engineering (United States)* 118, 513–529. [https://doi.org/10.1061/\(ASCE\)0733-9372\(1992\)118:4\(513\)](https://doi.org/10.1061/(ASCE)0733-9372(1992)118:4(513))
- Hartman, M., Trnka, D., Havlín, V., 1992. A relationship to estimate the porosity in liquid-solid fluidized beds. *Chemical Engineering Science* 47, 3162–3166. [https://doi.org/10.1016/0009-2509\(92\)87021-H](https://doi.org/10.1016/0009-2509(92)87021-H)
- Hartman, M., Trnka, O., Pohořelý, M., 2007. Minimum and terminal velocities in fluidization of particulate ceramsite at ambient and elevated temperature. *AIChE Journal – American Institute of Chemical Engineers* 46, 7260–7266. <https://doi.org/10.1021/ie0615685>
- Hassett, N.J., 1961. The mechanics of fluidization. *British Chemical Engineering* 19, 777–780.
- Hofman, J.A.M.H., Kramer, O.J.I., van der Hoek, J.P., Nederlof, M.M., Groenendijk, M., 2007. Twenty years of experience with central softening in the Netherlands, water quality, environmental benefits and costs, in: *Water 21, International Symposium on Health Aspects of Calcium and Magnesium in Drinking Water*, MD. International Life Sciences Institute, 24-26 April 2006. Washington, DC., USA, pp. 1–8.
- Holdich, R.G., 2002. *Fundamentals of particle technology, Fundamentals of particle technology*. Midland Information Technology and Publishing, Leicestershire. <https://doi.org/10.4236/ns.2010.210132>
- Hölzer, A., Sommerfeld, M., 2008. New simple correlation formula for the drag coefficient of non-spherical particles. *Powder Technology* 184, 361–365. <https://doi.org/10.1016/j.powtec.2007.08.021>
- Horowitz, M., Williamson, C.H.K., 2010. The effect of Reynolds number on the dynamics and wakes of freely rising and falling spheres. *Journal of Fluid Mechanics* 651, 251–294. <https://doi.org/10.1017/S0022112009993934>
- Howe, K.J., Hand, D.W., Crittenden, J.C., Rhodes Trussell, R., Tchobanoglous, G., 2012. *Principles of water treatment*, 1st ed. John Wiley & Sons, Inc., New Jersey.
- Hoyland, G., 2017. General combined model for the hydrodynamic behaviour of fixed and fluidised granular beds. *Water Research* 111, 163–176. <https://doi.org/10.1016/j.watres.2017.01.008>
- Hu, R., Huang, T., Wang, T., Wang, H., Long, X., 2019. Application of chemical crystallization circulating pellet fluidized beds for softening and saving circulating water in thermal power plants. *International Journal of Environmental Research and Public Health* 16, 1–12. <https://doi.org/10.3390/ijerph16224576>
- Hu, R.Z., Huang, T.L., Wen, G., Yang, S.Y., 2017. Modelling particle growth of calcium carbonate in a pilot-scale pellet fluidized bed reactor. *Water Science and Technology: Water Supply* 17, 643–651. <https://doi.org/10.2166/ws.2016.158>
- Hunce, S.Y., Soyer, E., Akgiray, Ö., 2018. On the backwash expansion of graded filter media. *Powder Technology* 333, 262–268. <https://doi.org/10.1016/j.powtec.2018.04.032>
- Hunce, S.Y., Soyer, E., Akgiray, Ö., 2016. Characterization of granular materials with internal pores for hydraulic calculations involving fixed and fluidized beds.

- Industrial and Engineering Chemistry Research 55, 8636–8651.
<https://doi.org/10.1021/acs.iecr.6b00953>
- Instruments GmbH, G., 2021a. Q.monixx – Smart edge device for monitoring applications.
- Instruments GmbH, G., 2021b. Gl.bench – Data acquisition software.
- Jamialahmadi, M., Müller-Steinhagen, H., 1992. Bed voidage in annular solid-liquid fluidized beds, *Chemical Engineering and Processing*.
- Jenny, M., Dušek, J., Bouchet, G., 2004. Instabilities and transition of a sphere falling or ascending freely in a Newtonian fluid. *Journal of Fluid Mechanics* 508, 201–239. <https://doi.org/10.1017/S0022112004009164>
- Johnson, M., Peakall, J., Fairweather, M., Biggs, S., Harbottle, D., Hunter, T.N., 2016. Characterization of multiple hindered settling regimes in aggregated mineral suspensions. *Industrial and Engineering Chemistry Research* 55, 9983–9993. <https://doi.org/10.1021/acs.iecr.6b02383>
- Johnson, R.W., 2016. *Handbook of fluid dynamics*, 2nd ed, *Journal of Fluid Mechanics*. CRC Press, Boca Raton.
<https://doi.org/10.1017/S0022112062211494>
- Joseph, G.G., Hunt, M.L., 2004. Oblique particle-wall collisions in a liquid. *Journal of Fluid Mechanics* 71–93. <https://doi.org/10.1017/S002211200400919X>
- Karamanev, D.G., 1996. Equations for calculation of the terminal velocity and drag coefficient of solid spheres and gas bubbles. *Chemical Engineering Communications* 147, 75–84. <https://doi.org/10.1080/00986449608936496>
- Keyence, 2014. *Digital microscope VHX-5000 user's manual*.
- Khan, A.R., Richardson, J.F., 1987. The resistance to motion of a solid sphere in a fluid. *Chemical Engineering Communications* 62, 135–150.
<https://doi.org/10.1080/00986448708912056>
- Khan, A.R., Richardson, J.F., 1989. Fluid-particle interactions and flow characteristics of fluidized beds and settling suspensions of spherical particles. *Chemical Engineering Communications* 78, 111–130.
<https://doi.org/10.1080/00986448908940189>
- Kmiec, A., 1982. Equilibrium of forces in fluidized bed – experimental verification. *The Chemical Engineering Journal* 23, 133–136. [https://doi.org/10.1016/0300-9467\(82\)80003-8](https://doi.org/10.1016/0300-9467(82)80003-8)
- Knezev, A., 2015. *Microbial activity in granular activated carbon filters in drinking water treatment*. Wageningen.
- Kolev, N.I., 2012. *Multiphase flow dynamics 2 mechanical interactions*, 4th ed, *Journal of Chemical Information and Modeling*. Springer-Verlag Berlin Heidelberg, Berlin. <https://doi.org/10.1007/978-3-642-20598-9>
- Koza, J.R., 1992. *Genetic programming: on the programming of computers by means of natural selection complex adaptive systems*.
- Kozeny, J., 1927. Über kapillare leitung des wassers im boden. *Akad. Wiss.Wien* 136, 271–306.
- Kramer, O.J.I., Jobse, M.A., Baars, E.T., van der Helm, A.W.C., Colin, M.G., Kors, L.J., van Vugt, W.H., 2015. Model-based prediction of fluid bed state in full-scale drinking water pellet-softening reactors, in: 2nd IWA New Developments in IT & Water Conference, 8-10 February. Rotterdam, The Netherlands, pp. 1–26.

- Kramer, O.J.I., de Moel, P.J., Baars, E.T., van Vugt, W.H., van der Hoek, J.P., 2017. Drinking water pellet-softening: prediction the terminal settling velocity of natural particles, in: 5th Young Water Professionals Benelux Conference, July 5-7. Ghent, Belgium, pp. 31–33.
- Kramer, O.J.I., de Moel, P.J., Baars, E.T., van Vugt, W.H., Padding, J.T., van der Hoek, J.P., 2019. Improvement of the Richardson–Zaki liquid-solid fluidisation model on the basis of hydraulics. *Powder Technology* 343, 465–478. <https://doi.org/10.1016/j.powtec.2018.11.018>
- Kramer, O.J.I., Padding, J.T., van Vugt, W.H., de Moel, P.J., Baars, E.T., Boek, E.S., van der Hoek, J.P., 2020a. Improvement of voidage prediction in liquid-solid fluidized beds by inclusion of the Froude number in effective drag relations. *International Journal of Multiphase Flow* 127. <https://doi.org/10.1016/j.ijmultiphaseflow.2020.103261>
- Kramer, O.J.I., de Moel, P.J., Padding, J.T., Baars, E.T., El Hasadi, Y.M.F., Boek, E.S., van der Hoek, J.P., 2020b. Accurate voidage prediction in fluidisation systems for full-scale drinking water pellet-softening reactors using data-driven models. *Journal of Water Process Engineering* 37, 1–15. <https://doi.org/10.1016/j.jwpe.2020.101481>
- Kramer, O.J.I., 2020c. Dataset underlying the research of: Fit parameters for liquid-solid fluidisation models applied in drinking water treatment processes [Data set] 4TU.Centre for Research Data. 4TU.ResearchData. <https://doi.org/10.4121/13537121.v1>
- Kramer, O.J.I., 2020d. Videos of liquid-solid fluidisation experiments of calcite pellets and glass beads in water [Data set] 4TU.Centre for Research Data. 4TU.Centre for Research Data, The Netherlands. <https://doi.org/10.4121/uuid:1b685d9e-4441-4a53-865c-86622ba49b25>
- Kramer, O.J.I., Castrejon-Pita, J.R., Boek, E.S., 2020e. Videos (high-speed camera) – liquid-solid fluidisation experiments (calcite-pellets 1.4-1.7 mm in water) [Data set] 4TU.Centre for Research Data. 4TU.Centre for Research Data, Amsterdam, The Netherlands. <https://doi.org/10.4121/uuid:41556e6c-b599-42cd-9f1d-bcf01dbe8576>
- Kramer, O.J.I., Raaghav, S.K.R., Breugem, W.P., 2020f. Videos of terminal settling experiments in water: path instabilities [Data set] 4TU.Centre for Research Data. 4TU.Centre for Research Data, The Netherlands. <https://doi.org/10.4121/UUID:3FFDFA51-38F0-4188-AEC5-8CD8FC8F1941>
- Kramer, O.J.I., van Schaik, C., 2020g. Videos of up-flow filtration velocities for rapid sand filter grains 0.8-1.25 mm in water [Data set] 4TU.Centre for Research Data. 4TU.Centre for Research Data, The Netherlands. <https://doi.org/10.4121/13337057.v1>
- Kramer, O.J.I., van Schaik, C., Nijssen, T.M.J., 2020h. Videos of fluidisation of calcite-pellets 0.8-0.9mm and 1.4-1.7 mm in water for various flow rates [Data set] 4TU.Centre for Research Data. 4TU.ResearchData, The Netherlands. <https://doi.org/10.4121/13277246.v1>
- Kramer, O.J.I., Nijssen, T.M.J., 2021a. Videos – CFD-DEM simulations: fluidisation of calcite-pellets in water [Data set] 4TU.Centre for Research Data. 4TU.Centre for Research Data, The Netherlands. <https://doi.org/10.4121/13663619>

- Kramer, O.J.I., de Moel, P.J., Raaghav, S.K.R., Baars, E.T., van Vugt, W.H., Padding, J.T., Peter van der Hoek, J., 2021b. Can terminal settling velocity and drag of natural particles in water ever be predicted accurately? *Drinking Water Engineering and Science* 14. <https://doi.org/10.5194/dwes-14-53-2021>
- Kramer, O.J.I., de Moel, P.J., Padding, J.T., Baars, E.T., Rutten, S.B., Elarbab, A.H.E., Hooft, J.F.M., Boek, E.S., van der Hoek, J.P., 2021c. New hydraulic insights into rapid sand filter bed backwashing using the Carman–Kozeny model. *Water Research* 197. <https://doi.org/10.1016/j.watres.2021.117085>
- Kramer, O.J.I., van Schaik, C., Hangelbroek, J.J., de Moel, P.J., Colin, M.G., Amsing, M., Boek, E.S., Breugem, W.P., Padding, J.T., van der Hoek, J.P., 2021d. A novel sensor for measuring local voidage and determining the hydraulic state inside a fluidised bed reactor. *Journal of Water Process Engineering* 102091, 1-15
- Kramer, O.J.I., 2021e. Dataset underlying the research of: A submerged cylindrical object in a liquid-solid fluidised bed – measuring local voidage and profile using a hydraulic weighing technique. 4TU.ResearchData. <https://doi.org/10.4121/14204336.v1>
- Kramer, O.J.I., 2021f. Dataset underlying the research of: New insights into the fluidisation characteristics of granular activated carbon for drinking water treatment applications. 4TU.ResearchData. <https://doi.org/10.4121/14229863.v1>
- Ku, H.H., 1966. Notes on the use of propagation of error formulas. *Journal of Research of the National Bureau of Standards, Section C: Engineering and Instrumentation* 70C, 263. <https://doi.org/10.6028/jres.070C.025>
- Kunii, D., Levenspiel, D., 1991. *Fluidization engineering*, 2nd ed. Butterworth-Heinemann, Boston.
- Kwauk, M., Li, J., 1996. Fluidization regimes. *Powder Technology* 87, 193–202. [https://doi.org/10.1016/0032-5910\(96\)03089-6](https://doi.org/10.1016/0032-5910(96)03089-6)
- Lapple, C.E., Shepherd, C.B., 1940. Calculation of particle trajectories. *Industrial and Engineering Chemistry* 32, 605–617. <https://doi.org/10.1021/ie50365a007>
- Leith, D., 1987. Drag on nonspherical objects. *Aerosol Science and Technology* 6, 153–161. <https://doi.org/10.1080/02786828708959128>
- Levenspiel, O., 1999. *Chemical reaction engineering*, 3rd ed, The Engineering Handbook, Second Edition. John Wiley & Sons, New York.
- Lewis, W.K., Gilliland, E.R., Bauer, W.C., 1949. Characteristics of fluidized particles. *Industrial & Engineering Chemistry* 41, 1104–1117. <https://doi.org/10.1021/ie50474a004>
- Lewis, W.K., Gilliland, E.R., Lang, P.M., 1962. Entrainment from fluidized beds. *Chemical engineering progress symposium series* 58, 65–78.
- Li, J., Kwauk, M., 1994. *Particle-fluid two-phase flow: the energy-minimization multi-scale method*. Metallurgical Industry Press, Beijing.
- Lichtfouse, E., Schwarzbauer, J., 2012. *Environmental chemistry for a sustainable world - Volume 2: remediation of air and water pollution*, 1st ed. Springer, Metz. <https://doi.org/10.1007/978-94-007-2439-6>
- Lindsey, W.F., 1938. *Drag of cylinders of simple shapes*. Cleveland, OH, United States.

- Lippens, B.C., Mulder, J., 1993. Prediction of the minimum fluidization velocity. *Powder Technology* 75, 67–78. [https://doi.org/10.1016/0032-5910\(93\)80026-7](https://doi.org/10.1016/0032-5910(93)80026-7)
- Liu, D., Kwauk, M., Li, H., 1996. Aggregative and particulate fluidization -The two extremes of a continuous spectrum. *Chemical Engineering Science* 51, 4045–4063. [https://doi.org/10.1016/0009-2509\(96\)00247-3](https://doi.org/10.1016/0009-2509(96)00247-3)
- Liu, G., Wang, P., Wang, S., Sun, L., Yang, Y., Xu, P., 2013. Numerical simulation of flow behavior of liquid and particles in liquid-solid risers with multi scale interfacial drag method. *Advanced Powder Technology* 24, 537–548. <https://doi.org/10.1016/j.apt.2012.10.007>
- Liu, G., Wang, P., Yu, F., Zhang, Y., Guo, W., Lu, H., 2015. Cluster structure-dependent drag model for liquid-solid circulating fluidized bed. *Advanced Powder Technology* 26, 14–23. <https://doi.org/10.1016/j.apt.2014.07.018>
- Loeffler, A.L., 1953. Mechanism of hindered settling and fluidization. Ames. <https://doi.org/10.31274/rtd-180813-14679>
- Loth, E., 2008. Drag of non-spherical solid particles of regular and irregular shape. *Powder Technology* 182, 342–353. <https://doi.org/10.1016/j.powtec.2007.06.001>
- Maeng, S.K., Rodriguez, C.N.A.S., Choi, J., Kim, S.H., Yu, Y., Kim, B.S., Hong, S.W., 2016. Organic micropollutant removal from groundwater: Comparison of pellet softening and nanofiltration. *Journal of Water Supply: Research and Technology – AQUA* 65, 453–464. <https://doi.org/10.2166/aqua.2016.114>
- Mahvi, A.H., Shafiee, F., Naddafi, K., 2005. Feasibility study of crystallization process for water softening in a pellet reactor. *International Journal of Environmental Science & Technology* 1, 301–304. <https://doi.org/10.1007/bf03325846>
- Marques, R.C., da Cruz, N.F., Pires, J., 2015. Measuring the sustainability of urban water services. *Environmental Science and Policy* 54, 142–151. <https://doi.org/10.1016/j.envsci.2015.07.003>
- Marsh, H., Rodríguez-Reinoso, F., 2006. Activated carbon. Elsevier Science & Technology Books.
- Marshall, J.S., Li, S., 2014. Adhesive particle flows, Adhesive Particle Flows. Cambridge University Press, New York. <https://doi.org/10.1017/cbo9781139424547>
- Masuda, H., Higashitani, K., Yoshida, H., 2007. Powder Technology: Fundamentals of particles, powder beds, and particle generation. CRC press - Taylor & Francis Group, LLC., New York.
- Maude, A.D., Whitmore, R.L., 1958. A generalized theory of sedimentation. *British Journal of Applied Physics* 9, 477–482. <https://doi.org/10.1103/RevModPhys.20.35>
- Mauguet, M.C., Montillet, A., Comiti, J., 2005. Macrostructural characterization of granular activated carbon beds. *Journal of Materials Science* 40, 747–755. <https://doi.org/10.1007/s10853-005-6316-7>
- Mema, I., Padding, J.T., 2021. Fluidization of elongated particles – Effect of multi-particle correlations for drag, lift, and torque in CFD-DEM. *AIChE Journal* 1–11. <https://doi.org/10.1002/aic.17157>
- Mercer, K.L., Lin, Y.P., Singer, P.C., 2005. Enhancing calcium carbonate precipitation by heterogeneous nucleation during chemical softening. *Journal*

- American Water Works Association 97, 116–125. <https://doi.org/10.1002/j.1551-8833.2005.tb07545.x>
- Michaelide, E., Crowe, C.T., Schwarzkopf, J.D., 2017. *Multiphase flow handbook*, 2nd ed. Taylor & Francis Inc, London.
- Mohapatra, P.K., Siebel, M.A., Gijzen, H.J., van der Hoek, J.P., Groot, C.A., 2002. Improving eco-efficiency of Amsterdam water supply: A LCA approach. *Journal of Water Supply: Research and Technology – AQUA* 51, 217–227. <https://doi.org/10.2166/aqua.2002.0019>
- Montillet, A., Akkari, E., Comiti, J., 2007. About a correlating equation for predicting pressure drops through packed beds of spheres in a large range of Reynolds numbers. *Chemical Engineering and Processing: Process Intensification* 46, 329–333. <https://doi.org/10.1016/j.cep.2006.07.002>
- Moody, L., 1944. Friction factors for pipe flow. *Transactions of American Society Mechanical Engineers* 66, 671–678.
- Morrison, F.A., 2013. *An introduction to fluid mechanics*. Cambridge University Press, New York. <https://doi.org/10.1017/cbo9781139047463>
- Mujumdar, A.S., 2006. *Handbook of industrial drying*, 4th ed. CRC Press.
- Munson, B.R., Rothmayer, A.P., Okiishi, T.H., Huebsch, W.W., 2020. *Fundamentals of fluid mechanics*, 7th ed. John Wiley & Sons, New York.
- Nauman, E.B., 2008. *Chemical Reactor Design, Optimization, and Scaleup*, 2nd ed. Wiley-AIChE. <https://doi.org/10.1036/007139558X>
- Naushad, M., Lichtfouse, E., 2020. *Environmental chemistry for a sustainable world - Green materials for wastewater treatment*. Springer. <https://doi.org/10.1007/978-3-030-17724-9>
- NEN-EN 933-2, 2020. Tests for geometrical properties of aggregates - Part 2: Determination of particle size distribution - Test sieves, nominal sizes of apertures, Dutch norm, ICS-code 91.100.15, 93.080.20.
- Newton, I., 1726. *Philosophiæ naturalis principia mathematica*, 3rd ed. University Press, Cambridge.
- Nguyen, T.H., Grace, J.R., 1978. Forces on objects immersed in fluidized beds. *Powder Technology* 19, 255–264. [https://doi.org/10.1016/0032-5910\(78\)80034-5](https://doi.org/10.1016/0032-5910(78)80034-5)
- Nijssen, T.M.J., Kramer, O.J.I., de Moel, P.J., Rahman, J., Kroon, J.P., Berhanu, P., Boek, E.S., Buist, K.A., van der Hoek, J.P., Padding, J.T., Kuipers, J.A.M., 2021. Experimental and numerical insights into heterogeneous liquid-solid behaviour in drinking water softening reactors. *Chemical Engineering Science: X* 100100, 1–11. <https://doi.org/10.1016/j.cesx.2021.100100>
- Nijssen, T.M.J., Kuipers, J.A.M., van der Stel, J., Adema, A.T., Buist, K.A., 2020. Complete liquid-solid momentum coupling for unresolved CFD-DEM simulations. *International Journal of Multiphase Flow* 132. <https://doi.org/10.1016/j.ijmultiphaseflow.2020.103425>
- Nor, F.H.M., Othman, H., Abidin, R.Z., 2009. Density measurement of tridecane by using hydrostatic weighing system at density laboratory, NML-SIRIM, in: *Frontiers in Physics, 3rd International Meeting, 2009 American Institute of Physics*. pp. 196–202.
- Nunes, C.A., Guerreiro, M.C., 2011. Estimation of surface area and pore volume of activated carbons by methylene blue and iodine numbers, in: *Quimica Nova*.

- Universidade Federal de Lavras, Departamento de Química, Brasil, São Paulo, pp. 472–476. <https://doi.org/10.1590/S0100-40422011000300020>
- Nutonian, 2019. Eureka, Genetic Programming and Evolvable Machines.
- Oka, S., Anthony, E.J., 2003. Fluidized bed combustion, Society. CRC Press, New-York. <https://doi.org/10.1201/9781420028454.ch2>
- Oke, O., Lettieri, P., Mazzei, L., 2015. An investigation on the mechanics of homogeneous expansion in gas-fluidized beds. *Chemical Engineering Science* 127, 95–105. <https://doi.org/10.1016/j.ces.2015.01.020>
- Olaofe, O.O., Buist, K.A., Deen, N.G., van der Hoef, M.A., Kuipers, J.A.M., 2013. Segregation dynamics in dense polydisperse gas-fluidized beds. *Powder Technology* 246, 695–706. <https://doi.org/10.1016/j.powtec.2013.05.047>
- Oseen, C.W., 1927. *Neuere methoden und ergebnisse in der hydrodynamik*, 1st ed. Leipzig: Akad. Verl.-Ges., Leipzig.
- Ouchene, R., Khalij, M., Arcen, B., Tanière, A., 2016. A new set of correlations of drag, lift and torque coefficients for non-spherical particles and large Reynolds numbers. *Powder Technology* 303, 33–43. <https://doi.org/10.1016/j.powtec.2016.07.067>
- Ozgunus, T., Mobedi, M., Ozkol, U., 2014. Determination of Kozeny constant based on porosity and pore to throat size ratio in porous medium with rectangular rods. *Engineering Applications of Computational Fluid Mechanics* 8, 308–318. <https://doi.org/10.1080/19942060.2014.11015516>
- Ozonek, J.O., 2012. *Application of hydrodynamic cavitation in environmental engineering*, 1st ed. CRC Press.
- Pal, D., Ghoshal, K., 2013. Hindered settling with an apparent particle diameter concept. *Advances in Water Resources* 60, 178–187. <https://doi.org/10.1016/j.advwatres.2013.08.003>
- Palmen, L.J., Schetters, M.J.A., van der Hoek, J.P., Kramer, O.J.I., Kors, L.J., Hofs, B., Koppers, H., 2014. Circular economy in drinking water treatment: re-use of grinded pellets as seeding material in the pellet-softening process, in: IWA World Water Congress and Exhibition, 21-26 September. Lisbon, Portugal, p. 1.
- Parkhurst, D.L., Appelo, C.A.J., 2013. Description of input and examples for PHREEQC version 3: A computer program for speciation, batch-reaction, one-dimensional transport, and inverse geochemical calculations, in: *Modeling Techniques, Groundwater, Techniques and Methods 6-A43*. U.S. Geological Survey, pp. 1–497. <https://doi.org/10.3133/tm6A43>
- Paudel, B., Feng, Z.G., 2013. Prediction of minimum fluidization velocity for binary mixtures of biomass and inert particles. *Powder Technology* 237, 134–140. <https://doi.org/10.1016/j.powtec.2013.01.031>
- Peel, R.G., Benedek, A., Crowe, C.M., 1981. A branched pore kinetic model for activated carbon adsorption. *AIChE Journal* 27, 26–32. <https://doi.org/10.1002/aic.690270106>
- Peker, S.M., Helvaci, Ş.Ş., Yener, B., Ikizler, B., Alparslan, A., 2008. *Solid-liquid two phase flow*, 1st ed, *Solid-liquid two phase flow*. Elsevier Science, Amsterdam. <https://doi.org/10.1016/B978-0-444-52237-5.X5001-2>
- Peng, Z., Ghatage, S. v., Doroodchi, E., Joshi, J.B., Evans, G.M., Moghtaderi, B., 2014. Forces acting on a single introduced particle in a solid-liquid fluidised bed.

- Chemical Engineering Science 116, 49–70.
<https://doi.org/10.1016/j.ces.2014.04.040>
- Perrich, J.R., 1981. Activated carbon adsorption for wastewater treatment, 1st ed. CRC Press, New York.
- Perry, R.H., Green, D.W., 2007. Perry's chemical engineers' handbook, 50th ed. McGraw-Hill Int., New York. <https://doi.org/10.1036/0071422943>
- Proudman, I., Pearson, J.R.A., 1957. Expansions at small Reynolds numbers for the flow past a sphere and a circular cylinder. *Journal of Fluid Mechanics* 2, 237–262. <https://doi.org/10.1017/S0022112057000105>
- Pushnov, A.S., 2006. Calculation of average bed porosity. *Chemical and Petroleum Engineering* 42, 14–17.
- Raaghav, S.K.R., 2019. Path instabilities of a rising or falling sphere in a fluid at rest – an experimental study. Delft.
- Rao, A., Curtis, J.S., Hancock, B.C., Wassgren, C., 2010. The effect of column diameter and bed height on minimum fluidization velocity. *AIChE Journal – American Institute of Chemical Engineers* 56, 2304–2311.
<https://doi.org/10.1002/aic.12161>
- Rapp, B.E., 2017. Microfluidics: modeling, mechanics and mathematics, 1st ed. Elsevier, Amsterdam.
- Ray, C., Jain, R., 2011. Drinking water treatment focusing on appropriate technology and sustainability introduction, 1st ed, *Drinking Water Treatment: Focusing on Appropriate Technology and Sustainability*. Springer Netherlands, Dordrecht. https://doi.org/10.1007/978-94-007-1104-4_1
- Retsch-Technology, 2007. Operating instructions / Manual particle size analysis system: Camsizer.
- Rhodes, M., 2008. Introduction to particle technology, 2nd ed, *Chemical Engineering and Processing*. John Wiley & Sons Ltd., Chichester.
<https://doi.org/10.1002/9780470727102>
- Riazi, A., Türker, U., 2019. The drag coefficient and settling velocity of natural sediment particles. *Computational Particle Mechanics* 6, 427–437.
<https://doi.org/10.1007/s40571-019-00223-6>
- Richardson, J.F., da S. Jerónimo, M.A., 1979. Velocity-voidage relations for sedimentation and fluidisation. *Chemical Engineering Science* 34, 1419–1422.
[https://doi.org/10.1016/0009-2509\(79\)85167-2](https://doi.org/10.1016/0009-2509(79)85167-2)
- Richardson, J.F., Zaki, W.N., 1954. Sedimentation and fluidisation: part I. *Transactions of the Institution of Chemical Engineers* 32, 35–53.
[https://doi.org/10.1016/S0263-8762\(97\)80006-8](https://doi.org/10.1016/S0263-8762(97)80006-8)
- Richardson, J.F., Zaki, W.N., 1979. Sedimentation and fluidisation. part I, This week's citation classic. *Transactions of the Institution of Chemical Engineers* 32, 35–53.
- Rietveld, L.C., 2005. Improving operation of drinking water treatment through modelling.
- Rietveld, L.C., van Schagen, K.M., Kramer, O.J.I., 2006. Optimal operation of the pellet-softening process, in: *AWWA, Workshop, American Water Works Association Inorganic Contaminants Proceedings*, 29-31 January. Austin, Texas, USA, pp. 1–14.

- Rowe, P.N., 1987. A convenient empirical equation for estimation of the Richardson-Zaki exponent. *Chemical Engineering Science* 43, 2795–2796. [https://doi.org/https://doi.org/10.1016/0009-2509\(87\)87035-5](https://doi.org/https://doi.org/10.1016/0009-2509(87)87035-5)
- Ruckenstein, E., 1964. Homogeneous fluidization. *Industrial and Engineering Chemistry Fundamentals* 3, 260–268. <https://doi.org/10.1021/i160011a015>
- Rumble, J., 2019. *Handbook of chemistry and physics*, 101th ed. CRC Press, New York.
- Samstag, R.W., Ducoste, J.J., Griborio, A., Nopens, I., Batstone, D.J., Wicks, J.D., Saunders, S., Wicklein, E.A., Kenny, G., Laurent, J., 2016. CFD for wastewater treatment: An overview. *Water Science and Technology* 74, 549–563. <https://doi.org/10.2166/wst.2016.249>
- Schetters, M.J.A., van der Hoek, J.P., Kramer, O.J.I., Kors, L.J., Palmen, L.J., Hofs, B., Koppers, H., 2015. Circular economy in drinking water treatment: re-use of ground pellets as seeding material in the pellet-softening process. *Water Science and Technology* 71, 479–486. <https://doi.org/10.2166/wst.2014.494>
- Schiaffino, S., Kytömaa, H.K., 1993. Steady fluidization of fine particles in a fixed bed of coarse particles. *Powder Technology* 77, 291–299. [https://doi.org/10.1016/0032-5910\(93\)85021-Z](https://doi.org/10.1016/0032-5910(93)85021-Z)
- Schiller, L., Naumann, A., 1933. Über die grundlegenden berechnungen bei der schwerkraftaufbereitung. *Zeitschrift des Vereines Deutscher Ingenieure* 29, 318–320.
- Sereda, P.J., Feldman, R.F., 1970. Wetting and drying of porous materials. *Canadian Building Digest* 10, 1–7. <https://doi.org/10.4224/40000703>
- Sereno, A.M., Silva, M.A., Mayor, L., 2007. Determination of particle density and porosity in foods and porous materials with high moisture content. *International Journal of Food Properties* 10, 455–469. <https://doi.org/10.1080/10942910600880736>
- Serway, R.A., Jewett, J.W., 2014. *Physics for scientists and engineers*, 9th ed. Physical Sciences: Mary Finch, Boston.
- Seville, J.P.K., Yu, C.Y., 2016. *Particle technology and engineering, an engineer's guide to particles and powders: fundamentals and computational approaches*, 1st ed. Butterworth-Heinemann.
- Sharqawy, M.H., Lienhard, V.J.H., Zubair, S.M., 2010. The thermophysical properties of seawater: a review of existing correlations and data accessed thermophysical properties of seawater: A review of existing correlations and data. *Desalination and Water Treatment* 16, 354–380. <https://doi.org/10.5004/dwt.2010.1079>
- Sholji, I., 1987. Expansion of granular filters during backwashing. *Journal of Environmental Engineering* 113, 516–531.
- Shpirt, E.A., Alben, K.T., 1986. Changes in particle size distributions on a fixed bed of granular activated carbon. *Water Science and Technology* 18, 31–42.
- Siwec, T., 2007. The experimental verification of Richardson-Zaki law on example of selected beds used in water treatment. *Electronic Journal of Polish Agricultural Universities. Series Civil Engineering* 10, 72–76.
- Slaa, S., van Maren, D.S., Winterwerp, J.C., 2012. On the hindered settling of silt-water mixtures, in: 4th International Conference on Estuaries and Coasts, 8-11 October 2012, Water Resources University, Vietnam. pp. 1–13.

- Smeets, P.W.M.H., Medema, G.J., van Dijk, J.C., 2009. The Dutch secret: How to provide safe drinking water without chlorine in the Netherlands. *Drinking Water Engineering and Science* 2, 1–14. <https://doi.org/10.5194/dwes-2-1-2009>
- Sobhan, R., 2019. An improved kinetic model and optimized configurations for pellet softening: Modeling and optimization of pellet-softening process in drinking water treatment. Delft.
- Sobieski, W., Zhang, Q., 2014. Sensitivity analysis of Kozeny-Carman and Ergun equations. *Technical Sciences / University of Warmia and Mazury in Olsztyn* 17, 235–248.
- Song, X., Xu, Z., Li, G., Pang, Z., Zhu, Z., 2017. A new model for predicting drag coefficient and settling velocity of spherical and non-spherical particle in Newtonian fluid. *Powder Technology* 321, 242–250. <https://doi.org/10.1016/j.powtec.2017.08.017>
- Soyer, E., Akgiray, Ö., 2005. Expansion of non-spherical media during fluidization, in: *Proceedings of IWA International Conference on Particle Separation*, Seoul, South Korea, June 1-5. pp. 579–586.
- Soyer, E., Akgiray, Ö., 2009. A new simple equation for the prediction of filter expansion during backwashing. *Journal of Water Supply: Research and Technology – AQUA* 58, 336–345. <https://doi.org/10.2166/aqua.2009.090>
- Stevens, B.L., Lewis, F.L., Johnson, E.N., 2016. *Aircraft control and simulation – dynamics, controls design, and autonomous systems*, 3rd ed. John Wiley & Sons, New York.
- Stokes, G.G., 1850. On the effect of the internal friction of fluids on the motion of pendulums. *Transactions of the Cambridge Philosophical Society* 4, 1–8. <https://doi.org/10.1017/CBO9780511702242.005>
- Tai, C.Y., Chang, M.C., Wu, C.K., Lin, Y.C., 2006. Interpretation of calcite growth data using the two-step crystal growth model. *Chemical Engineering Science* 61, 5346–5354. <https://doi.org/10.1016/j.ces.2006.03.047>
- Tang, C., Godsken, B., Aktor, H., van Rijn, M., Kristensen, J.B., Rosshaug, P.S., Albrechtsen, H.J., Rygaard, M., 2020. Procedure for calculating the calcium carbonate precipitation potential (CCPP) in drinking water supply: importance of temperature, ionic species and open/closed system. *Water* 13, 42. <https://doi.org/10.3390/w13010042>
- Tang, C., Jørgensen Hedegaard, M., Lopato, L., Albrechtsen, H.J., 2019. Softening of drinking water by the pellet reactor – Effects of influent water composition on calcium carbonate pellet characteristics. *Science of the Total Environment* 652, 538–548. <https://doi.org/10.1016/j.scitotenv.2018.10.157>
- Tang, C., Merks, C.W.M.A., Albrechtsen, H.J., 2019. Water softeners add comfort and consume water – Comparison of selected centralised and decentralised softening technologies. *Water Science and Technology: Water Supply* 19, 2088–2097. <https://doi.org/10.2166/ws.2019.088>
- Tapia, M., Siebel, M.A., van der Helm, A.W.C., Baars, E.T., Gijzen, H.J., 2008. Environmental, financial and quality assessment of drinking water processes at Waternet. *Journal of Cleaner Production* 16, 401–409. <https://doi.org/10.1016/j.jclepro.2006.07.053>
- Tavassoli, H., Peters, E.A.J.F., Kuipers, J.A.M., 2015. Direct numerical simulation of fluid-particle heat transfer in fixed random arrays of non-spherical particles.

- Chemical Engineering Science 129, 42–48.
<https://doi.org/10.1016/j.ces.2015.02.024>
- Teng, H., Zhao, T.S., 2000. An extension of Darcy's law to non-Stokes flow in porous media. *Chemical Engineering Science* 55, 2727–2735.
[https://doi.org/10.1016/S0009-2509\(99\)00546-1](https://doi.org/10.1016/S0009-2509(99)00546-1)
- Terfous, A., Hazzab, A., Ghenaim, A., 2013. Predicting the drag coefficient and settling velocity of spherical particles. *Powder Technology* 239, 12–20.
<https://doi.org/10.1016/j.powtec.2013.01.052>
- Tomkins, M.R., Baldock, T.E., Nielsen, P., 2005. Hindered settling of sand grains. *Sedimentology* 52, 1425–1432. <https://doi.org/10.1111/j.1365-3091.2005.00750.x>
- Trussell, R., Chang, M., 1999. Review of flow through porous media as applied to head loss in water filters. *Journal of Environmental Engineering* 125, 998–1006.
- Tsuchiya, K., Furumoto, A., Fan, L.S., Zhang, J., 1997. Suspension viscosity and bubble rise velocity in liquid-solid fluidized beds, *Chemical Engineering Science*.
- Turton, R., Levenspiel, O., 1986. A short note on the drag correlation for spheres. *Powder Technology* 47, 83–86. [https://doi.org/10.1016/0032-5910\(86\)80012-2](https://doi.org/10.1016/0032-5910(86)80012-2)
- Ujhidy, A., Bucsky, G., Németh, J., 2008. Hydrodynamic characteristics of activated carbon in air-and water-fluidized beds. *The Korean Journal of Chemical Engineering* 25, 1170–1177.
- US-IACWR, 1957. A study of methods used in measurement and analysis of sediment loads in streams. Some fundamentals of particle size analysis. Minneapolis, Minnesota.
- Valverde, J.M., Castellanos, A., 2008. A modified Richardson-Zaki equation for fluidization of Geldart B magnetic particles. *Powder Technology* 181, 347–350.
<https://doi.org/10.1016/j.powtec.2007.05.018>
- Van Ammers, M., van Dijk, J.C., Graveland, A.J., Nühn, P.A.N.M., 1986. State of the art of pellet softening, in: *Water Supply: Proceedings of the Specialized Conference on New Technologies in Water Treatment*, Organized by the International Water Supply Association, Amsterdam, 15 – 19 September 1986. pp. 223–235.
- Van der Bruggen, B., Goossens, H., Everard, P.A., Stengée, K., Rogge, W., 2009. Cost-benefit analysis of central softening for production of drinking water. *Journal of Environmental Management* 91, 541–549.
<https://doi.org/10.1016/j.jenvman.2009.09.024>
- Van der Helm, A.W.C., 2007. *Integrated modeling of ozonation for optimization of drinking water treatment*. Water Management Academic Press, Delft.
- Van der Hoek, J.P., Hofman, J.A.M.H., Graveland, A.J., 1999. The use of biological activated carbon filtration for the removal of natural organic matter and organic micropollutants from water. *Water Science and Technology* 40, 257–264.
[https://doi.org/10.1016/S0273-1223\(99\)00664-2](https://doi.org/10.1016/S0273-1223(99)00664-2)
- Van der Hoek, J.P., Strucker, A., de Danschutter, J.E.M., 2017. Amsterdam as a sustainable European metropolis: integration of water, energy and material flows. *Urban Water Journal* 14, 61–68.
<https://doi.org/10.1080/1573062X.2015.1076858>
- Van Keulen, J., 1973. Density of porous solids. *Materials and Structures* 6, 181–183.

- Van der Kooij, D., Drost, Y.C., Hijnen, W.A.M., Willemsen-Zwaagstra, J., Nobel, P.J., Schellart, J. A., 1995. Multiple barriers against micro-organisms in water treatment and distribution in the Netherlands. *Water Science and Technology: Water Supply* 13.
- Van der Veen, C., Graveland, A.J., 1988. Central softening by crystallization in a fluidized-bed process. *Journal American Water Works Association* 80, 51–58. <https://doi.org/10.1002/j.1551-8833.1988.tb03053.x>
- Van Dijk, J.C., Wilms, D.A., 1991. Water treatment without waste material-fundamentals and state of the art of pellet softening. *Journal Water Supply: Research and Technology: AQUA* 40, 263–280.
- Van Lier, W.C., 1984. The Influence of particle shape and particle size distribution on fluidisation behaviour of granular activated carbon in the aqueous phase. *Particle & Particle Systems Characterization* 1, 143–152. <https://doi.org/10.1002/ppsc.19840010125>
- Van Schagen, K.M., 2009. Model-based control of drinking-water treatment plants. Delft.
- Van Schagen, K.M., Babuška, R., Rietveld, L.C., Baars, E.T., 2006. Optimal flow distribution over multiple parallel pellet reactors: A model-based approach. *Water Science and Technology* 53, 493–501. <https://doi.org/10.2166/wst.2006.160>
- Van Schagen, K.M., Rietveld, L.C., Babuška, R., Baars, E.T., 2008. Control of the fluidised bed in the pellet softening process. *Chemical Engineering Science* 63, 1390–1400. <https://doi.org/10.1016/j.ces.2007.07.027>
- Van Schagen, K.M., Rietveld, L.C., Babuška, R., Kramer, O.J.I., 2008. Model-based operational constraints for fluidised bed crystallisation. *Water Research* 42, 327–337. <https://doi.org/10.1016/j.watres.2007.07.019>
- Veldhuis, C.H.J., Biesheuvel, A., 2007. An experimental study of the regimes of motion of spheres falling or ascending freely in a Newtonian fluid. *International Journal of Multiphase Flow* 33, 1074–1087. <https://doi.org/10.1016/j.ijmultiphaseflow.2007.05.002>
- Veldhuis, C.H.J., Biesheuvel, A., Lohse, D., 2009. Freely rising light solid spheres. *International Journal of Multiphase Flow* 35, 312–322. <https://doi.org/10.1016/j.ijmultiphaseflow.2009.01.005>
- Velten, S., 2008. Adsorption capacity and biological activity of biological activated carbon filters in drinking water treatment. Zürich. <https://doi.org/10.3929/ethz-a-005820821>
- Verloop, J., Heertjes, P.M., 1970. Shock waves as a criterion for the transition from homogeneous to heterogeneous fluidization. *Chemical Engineering Science* 25, 825–832. [https://doi.org/10.1016/0009-2509\(70\)85117-X](https://doi.org/10.1016/0009-2509(70)85117-X)
- Vogel, H., 1921. Das temperatur-abhängigkeitsgesetz der viskosität von flüssigkeiten. *Zeitschrift für Physik* 22, 645–646.
- Wadell, H., 1933. Sphericity and roundness of rock particles. *The Journal of Geology* 41, 310–31. <https://doi.org/10.1086/624040>
- Wallis, G.B., 1969. One dimensional two phase flow. McGraw-Hill Int., New York.
- Wang, Z.J., Tang, J., Lu, C.X., 2016. Fluidization characteristics of different sizes of quartz particles in the fluidized bed. *Petroleum Science* 13, 584–591. <https://doi.org/10.1007/s12182-016-0106-5>

- Wang, X.C., Yuan, H.L., Liu, Y.J., Jin, P.K., 2007. Fluidised pellet bed bioreactor: A promising technology for onsite wastewater treatment and reuse. *Water Science and Technology* 55, 59–67. <https://doi.org/10.2166/wst.2007.028>
- Wen, C.Y., Yu, Y.H., 1966a. A generalized method for predicting the minimum fluidization velocity. *American Institute of Chemical Engineers Journal* 12, 610–612. <https://doi.org/https://doi.org/10.1002/aic.690120343>
- Wen, C.Y., Yu, Y.H., 1966b. Mechanics of fluidization, in: *Chemical Engineering Progress, Symposium Series* 62. pp. 100–111.
- Whitaker, S., 1972. Forced convection heat transfer correlations for flow in pipes, past flat plates, single cylinders, single spheres, and for flow in packed beds and tube bundles. *AIChE Journal – American Institute of Chemical Engineers* 18, 361–371. <https://doi.org/10.1002/aic.690180219>
- White, F.M., 2016. *Fluid mechanics*, 8th ed. McGraw-Hill, New-York.
- Whiten, W.J., Özer, C.E., 2015. New relation for the computation of settling velocities and diameters of spheres. *Mineral Processing and Extractive Metallurgy Review* 36, 92–102. <https://doi.org/10.1080/08827508.2014.885904>
- Wilhelm, R.H., Kwauk, M., 1948. Fluidization of solid particles. *Chemical Engineering Progress* 44, 201–218.
- Wilkes, J.O., 2019. *Fluid mechanics for Engineers*, 3rd ed. Prentice Hall International Series in the Physical and Chemical Engineering Sciences, Boston. <https://doi.org/10.1007/978-3-642-11594-3>
- Wirth, K.E., 1991. Fluid mechanics of circulating fluidized beds. *Chemical Engineering & Technology* 14, 29–38. <https://doi.org/10.1002/ceat.270140105>
- Wolf, B., 1995. Application of hydrostatic weighing to density determination of tiny porous samples. *Review of Scientific Instruments* 66, 2578–2581. <https://doi.org/10.1063/1.1145591>
- World Commission on Environment and Development, 1987. *Our common future: report of the world commission on environment and development*, United Nations. New York.
- World Economic Forum, 2019. *Global Risks Report 2019*. Geneva Switzerland.
- World Health Organization, 2017. *Guidelines for drinking-water quality* 4th edition. World Health Organization.
- World Health Organization, UNICEF, 2017. *Progress on drinking water, sanitation and hygiene: 2017 update and SDG baselines*.
- Worch, E., 2012. *Adsorption technology in water treatment: Fundamentals, processes, and modeling*, 1st ed. Walter de Gruyter GmbH & Co., Dresden.
- Wu, W., Asce, M., Wang, S.S.Y., Asce, F., 2006. Formulas for sediment porosity and settling velocity. *Journal of Hydraulic Engineering* 132, 858–862. [https://doi.org/10.1061/\(ASCE\)0733-9429\(2006\)132:8\(858\)](https://doi.org/10.1061/(ASCE)0733-9429(2006)132:8(858))
- Wu, Y.C., Yang, B., 2019. An overview of numerical methods for incompressible viscous flow with moving particles. *Archives of Computational Methods in Engineering* 26, 1255–1282. <https://doi.org/10.1007/s11831-018-9277-0>
- Xu, P., Yu, B., 2008. Developing a new form of permeability and Kozeny-Carman constant for homogeneous porous media by means of fractal geometry. *Advances in Water Resources* 31, 74–81. <https://doi.org/10.1016/j.advwatres.2007.06.003>

- Yang, H., Fan, M., Liu, A., Dong, L., 2015. General formulas for drag coefficient and settling velocity of sphere based on theoretical law. *International Journal of Mining Science and Technology* 25, 219–223. <https://doi.org/10.1016/j.ijmst.2015.02.009>
- Yang, J., Renken, A., 2003. A generalized correlation for equilibrium of forces in liquid-solid fluidized beds. *Chemical Engineering Journal* 92, 7–14. [https://doi.org/10.1016/S1385-8947\(02\)00084-0](https://doi.org/10.1016/S1385-8947(02)00084-0)
- Yang, W.C., 2003. *Handbook of fluidization and fluid-particle systems*, 1st ed, Chemical Engineering. CRC Press, New-York. [https://doi.org/10.1016/S1672-2515\(07\)60126-2](https://doi.org/10.1016/S1672-2515(07)60126-2)
- Yates, J.G., 1983. *Fundamentals of fluidized-bed chemical processes*. Butterworth-Heinemann, London.
- Yates, J.G., Lettieri, P., 2016. *Fluidized-bed reactors: processes and operating conditions*. Springer International Publishing. <https://doi.org/10.1007/978-3-319-39593-7>
- Yiotis, A.G., Tsimpanogiannis, I.N., Stubos, A.K., Yortsos, Y.C., 2007. Coupling between external and internal mass transfer during drying of a porous medium. *Water Resources Research* 43, 1–12. <https://doi.org/10.1029/2006WR005558>
- Yiotis, A.G., Tsimpanogiannis, I.N., Stubos, A.K., Yortsos, Y.C., 2006. Pore-network study of the characteristic periods in the drying of porous materials. *Journal of Colloid and Interface Science* 297, 738–748. <https://doi.org/10.1016/j.jcis.2005.11.043>
- Zheng, Y., Zhu, J.X., Wen, J., Martin, S.A., Bassi, A., Margaritis, A., 1999. The axial hydrodynamic behavior in a liquid-solid circulating fluidized bed. *Canadian Journal of Chemical Engineering* 77, 284–290. <https://doi.org/10.1002/cjce.5450770213>
- Zhiyao, S., Tingting, W., Fumin, X., Ruijie, L., 2008. A simple formula for predicting settling velocity of sediment particles. *Water Science and Engineering* 1, 37–43. [https://doi.org/10.1016/s1674-2370\(15\)30017-x](https://doi.org/10.1016/s1674-2370(15)30017-x)
- Zhou, W., Dušek, J., 2015. Chaotic states and order in the chaos of the paths of freely falling and ascending spheres. *International Journal of Multiphase Flow* 75, 205–223. <https://doi.org/10.1016/j.ijmultiphaseflow.2015.05.010>

List of publications

List of publications

International refereed publications

Kramer, O.J.I., van Schaik, C., Dacomba-Torres, P.D.R., de Moel, P.J., Boek, E.S., Baars, E.T., Padding, J.T., van der Hoek, J.P., 2021, Fluidisation characteristics of granular activated carbon in drinking water treatment applications. This article accepted in *Advanced Powder Technology Journal* (17/6/2021) pp. 1-15. <https://doi.org/10.1016/j.appt.2021.06.017>.

Kramer, O.J.I., van Schaik, C., Hangelbroek, J.J., de Moel, P.J., Colin, M.G., Amsing, M., Boek, E.S., Breugem, W.P., Padding, J.T., van der Hoek, J.P., 2021. A new soft sensor for measuring local voidage and determining the hydraulic state inside a fluidised bed reactor. *Journal of Water Process Engineering* 100100, pp. 1-15. <https://doi.org/10.1016/j.jwpe.2021.102091>.

Nijssen, T.M.J., ^{*)} Kramer, O.J.I.^{*)}, de Moel, P.J., Rahman, J., Kroon, J.P., Berhanu, P., Boek, E.S., Buist, K.A., van der Hoek, J.P., Padding, J.T., Kuipers, J.A.M., 2021. Experimental and numerical insights into heterogeneous liquid-solid behaviour in drinking water softening reactors. *Chemical Engineering Science: X* 11, pp. 1-11. <https://doi.org/10.1016/j.watres.2021.117085>.

^{*)} shared authorship

Kramer, O.J.I., de Moel, P.J., Padding, J.T., Baars, E.T., Rutten, S.B., Elarbab, A.H.E., Hooft, J.F.M., Boek, E.S., van der Hoek, J.P., 2021. New hydraulic insights into rapid sand filter bed backwashing using the Carman–Kozeny model. *Water Research* 197, pp. 1-11. <https://doi.org/10.1016/j.watres.2021.117085>

Kramer, O.J.I., de Moel, P.J., Raaghav, S.K.R., Baars, E.T., van Vugt, W.H., Breugem, W.P., Padding, J.T., van der Hoek, J.P., 2021, Can terminal settling velocity and drag of natural particles in water ever be predicted accurately? *Drinking Water Engineering and Science* 14, pp. 53-71. <https://doi.org/10.5194/dwes-14-53-2021>

Kramer, O.J.I., de Moel, P.J., Padding, J.T., Baars, E.T., El Hasadi, Y.M.F., Boek, E.S., van der Hoek, J.P., 2020. Accurate voidage prediction in fluidisation systems for full-scale drinking water pellet-softening reactors using data-driven models. *Journal of Water Process Engineering* 37, pp. 1-15. <https://doi.org/10.1016/j.jwpe.2020.101481>

- Beeftink, M., Hofs, B., [Kramer, O.J.I.](#), Odegard, I., Wal, van der, A., 2021. Carbon footprint of drinking water softening as determined by life cycle assessment. *Journal of Cleaner Production* 278, 123925, pp. 1-10.
<https://doi.org/10.1016/j.jclepro.2020.123925>
- [Kramer, O.J.I.](#), de Moel, P.J., Baars, E.T., van Vugt, W.H., Padding, J.T., van der Hoek, J.P., 2019. Improvement of the Richardson–Zaki liquid-solid fluidisation model on the basis of hydraulics. *Powder Technology*, 343, pp. 465-478.
<https://doi.org/10.1016/j.powtec.2018.11.018>
- [Kramer, O.J.I.](#), Padding, J.T., Vugt, W.H. van, Moel, P.J. de, Baars, E.T., Boek, E.S., van der Hoek, J.P., 2020. Improvement of voidage prediction in liquid-solid fluidised beds by inclusion of the Froude number in effective drag relations. *International Journal of Multiphase Flow* 127, pp. 1-13.
<https://doi.org/10.1016/j.ijmultiphaseflow.2020.103261>
- Schetters, M.J.A., van der Hoek, J.P., [Kramer, O.J.I.](#), Kors, L.J., Palmen, L.J., Hofs, B., Koppers, H., 2015. Circular economy in drinking water treatment: reuse of ground pellets as seeding material in the pellet-softening process. *Water Science and Technology* 71, pp. 479-486.
<https://doi.org/10.2166/wst.2014.494>
- Van Schagen, K.M., Rietveld, L.C., Babuška, R., [Kramer, O.J.I.](#), 2008. Model-based operational constraints for fluidised bed crystallisation. *Water Research* 42, pp. 327-337. <https://doi.org/10.1016/j.watres.2007.07.019>

Conference proceedings and presentations

- [Kramer, O.J.I.](#), 2020. NPS17 (Netherlands Process Technology Symposium) Water Webinar organised by the Institute for Sustainable Process Technology (ISPT), 18 November - Panel member. <https://ispt.eu/events/nps17-water-webinar>
- [Kramer, O.J.I.](#), 2019. Smart drinking water production in Amsterdam, in: 2019 Korea International Water Industry Conference, 3 September. Seoul, Korea, www.waterindustry.kr
- [Kramer, O.J.I.](#), El Hasadi, Y.M.F., de Moel, P.J., Baars, E.T., Padding, J.T., van der Hoek, J.P., 2019. Accurate prediction of liquid-solid fluidised bed porosity in drinking water treatment processes using empirical data-driven genetic

- programming models, in: 10th International Conference on Multiphase Flow, 19-24 May. Rio de Janeiro, Brazil, pp. 1-2. www.icmf2019.com.br
- Kramer, O.J.I.**, 2019. Mysteries of drinking water – Seminar, 2 May. Queen Mary University of London, Division of Chemical Engineering, School of Engineering and Materials Science, United Kingdom
- Kramer, O.J.I.**, Boek, E.S., 2019. Fluidisation experiments – Queen Mary University of London, United Kingdom – Poster Erasmus+.
- Kramer, O.J.I.**, de Moel, P.J., Baars, E.T., van Vugt, W.H., Padding, J.T., van der Hoek, J.P., 2018. Improvement of the Richardson–Zaki liquid-solid fluidisation model on the basis of hydraulics, in: 16th Multiphase Flows Conference & Shore Course – Simulation, Experiment and Application, 13-16 November. Helmholtz-Zentrum Dresden Rossendorf, Dresden, Germany, p. 1, www.hzdr.de.
- Kramer, O.J.I.**, 2018. Call to adventure – Masterclass, 11 September. Utrecht, The Netherlands, HU University of Applied Sciences Utrecht, Institute Archimedes
- Kramer, O.J.I.**, 2018. Drinkwater in een circulaire economie (water-proces-circulair) – Masterclass, in: Lezingreeks: Grenzen aan de chemie – U-talent, 2-3, Utrecht University, November. Utrecht, The Netherlands, <https://u-talent.nl/>
- Kramer, O.J.I.**, 2018. Gezond drinkwater – Een doorkijk door de tijd van gezond drinkwater – Conference Masterclass, in: 28^e Woudschoten Chemie Conferentie, 2-3 November. Woudschoten, The Netherlands, pp. 1-2. www.fisme.science.uu.nl/woudschotenchemie/conferentie/
- Kramer, O.J.I.**, de Moel, P.J., Baars, E.T., van Vugt, W.H., van der Hoek, J.P., 2017. Drinking water pellet-softening: prediction the terminal settling velocity of natural particles, in: 5th Young Water Professionals Benelux Conference, July 5-7. Ghent, Belgium, pp. 31-33. www.ywpbenelux.org
- Hofs, B., Baars, E.T., Palmen, L.J., Elings, J., Kors, L.J., **Kramer, O.J.I.**, Koppers, H., van der Hoek, J.P., 2015. Increased sustainability of softening by producing pure calcite pellets for reuse, in: Conference Amsterdam, International, Water Week, AIWW Conference, Integrated Solutions for a Circular Economy and Resilient Cities, 2-6 November. Amsterdam, The Netherlands, pp. 1-2. <http://resolver.tudelft.nl/uuid:7fa65d83-6948-4467-943e-aff04c0deacf>
- Palmen, L.J., Schetters, M.J.A., van der Hoek, J.P., **Kramer, O.J.I.**, Kors, L.J., Hofs, B., Koppers, H., 2014. Circular economy in drinking water treatment: reuse of grinded pellets as seeding material in the pellet-softening process, in: IWA World Water Congress and Exhibition, 21-26 September. Lisbon, Portugal, pp. 1-2.

- Kramer, O.J.I.**, Jobse, M.A., Baars, E.T., van der Helm, A.W.C., Colin, M.G., Kors, L.J., van Vugt, W.H., 2015. Model-based prediction of fluid bed state in full-scale drinking water pellet-softening reactors, in: 2nd IWA New Developments in IT & Water Conference, 8-10 February. Rotterdam, The Netherlands, pp. 1-26. <http://resolver.tudelft.nl/uuid:a7bc1d77-5620-4b38-932c-c0a43e811fde>
- Van der Helm, A.W.C., **Kramer, O.J.I.**, Hooft, J.F.M., de Moel, P.J., 2015. Plant wide chemical water stability modelling with PHREEQC for drinking water treatment, in: 2nd IWA New Developments in IT & Water Conference, 8-10 February. Rotterdam, The Netherlands, pp. 1-5. <http://repository.tudelft.nl/view/ir/uuid:acd3c631-9d82-499b-95b5-afa6abdc5919/>
- Rietveld, L.C., van Schagen, K.M., **Kramer, O.J.I.**, 2006. Optimal operation of the pellet-softening process, in: AWWA, Workshop, American Water Works Association Inorganic Contaminants Proceedings, 29-31 January. Austin, Texas, USA, pp. 1-14.
- Hofman, J.A.M.H., **Kramer, O.J.I.**, van der Hoek, J.P., Nederlof, M.M., Groenendijk, M., 2007. Twenty years of experience with central softening in the Netherlands, water quality, environmental benefits and costs, in: Water 21, International Symposium on Health Aspects of Calcium and Magnesium in Drinking Water, MD. International Life Sciences Institute, 24-26 April 2006. Washington, DC., USA, pp. 1-8. <http://resolver.tudelft.nl/uuid:e43683de-0270-46c4-b736-c3ddfe9973e6>

National publications

- Kramer, O.J.I.**, van de Wetering, T.S.C.M., Huysman, K., Joris, K., 2020. Contactgroep Drinkwater Technologen; het succes van ruim 25 jaar kennis delen. H₂O tijdschrift voor watervoorziening en waterbeheer, pp. 1-8. www.h2owaternetwerk.nl/vakartikelen/contactgroep-drinkwater-technologen-het-succes-van-ruim-25-jaar-kennis-delen/
- Kramer, O.J.I.**, 2020. Q&A hardheid – drinkwater hardheid vragen en antwoorden. Amsterdam.
- Hofs, B., van der Wal, A., Beeftink, M., Odegard, I., **Kramer, O.J.I.**, 2020. Waterontharding door drinkwaterbedrijven voorkomt CO₂-uitstoot. H₂O tijdschrift voor watervoorziening en waterbeheer, pp. 1-7.

www.h2owaternetwerk.nl/vakartikelen/waterontharding-door-drinkwaterbedrijven-voorkomt-co2-uitstoot/

- [Kramer, O.J.I.](#), Maduro, A.F.E., Kors, L.J., Baars, E.T., van Vugt, W.H., 2018. Het Waterkwaliteitsverstoringsmodel. H₂O tijdschrift voor watervoorziening en waterbeheer, pp. 1-11. www.h2owaternetwerk.nl/vakartikelen/1771-het-waterkwaliteitsverstoringsmodel/
- Siegers, W., Hofman, J.A.M.H., [Kramer, O.J.I.](#), 2009. Kennisuitwisseling tussen Nederland en Duitsland over ontharding. H₂O tijdschrift voor watervoorziening en waterbeheer 2, pp. 9-10.
- Rietveld, L.C., [Kramer, O.J.I.](#), Bosklopper, K., van Dijk, J.C., 2004. Optimale besturing van ontharding. H₂O tijdschrift voor watervoorziening en waterbeheer 8, pp. 21-23.
- Van der Helm, A.W.C., [Kramer, O.J.I.](#), Bosklopper, K., Hofman, J.A.M.H., 2003. Hogere ambities vragen andere bedrijfsvoering. H₂O tijdschrift voor watervoorziening en waterbeheer 18, pp. 32-34.

Courses

- [Kramer, O.J.I.](#), Boek, E.S., van Schaik, C., 2020. Title: Virtual Lab: Fluidisation Experiments, online course for students chemical, civil or mechanical engineering. 4TU.ResearchData, The Netherlands.
<https://doi.org/10.4121/12881009>
- Stelt, M., [Kramer, O.J.I.](#), van Dijk, T., Philipse, F., Kors, L.J., 2020. Watertechnologie Process Development in The Chemical Industry, Cursusboek. Utrecht.
- Boek, E.S., [Kramer, O.J.I.](#), 2019. Drinking Water treatment Plant Design – Integrated Chemical Engineering Design Project, Queen Mary University of London.

Educational (first supervisor during my PhD project)

- Duijnmaijer, R., 2021. Implementatie van de hydrometer, Onderzoek naar de toepassing van de hydrometer in de bedrijfsvoering van de drinkwaterproductie van Waternet. Amsterdam.

- Malik, A., 2021. Drinking water pellet-softening modelling, Investigation to find alternates for the use of particle size in prediction models. Den Haag.
- Rahman, J., 2020. Homogenous fluidisation is not the main state for liquid-solid fluidisation. Amsterdam.
- Berhanu, P., 2020. Filtration with rapid filter sand. Amsterdam.
- Shao, V., 2020. Optimalisatie spoelprocedure Loenderveen. Amsterdam.
- Brakeboer, P., van Leusen, M., Sarkam, C., Duijnmaijer, R., Baars, J., 2020. Methode hydrometer – het principe van een dichtheidsmeter waarbij de dichtheid van een pseudovloeistof gemeten wordt. Utrecht.
- Ramjad, S., 2020. De invloed van onregelmatig gevormde korrels op het specifiek kristallisatie oppervlak in een gefluïdiseerd bed onthardingsproces in ten behoeve van drinkwaterbereiding. Utrecht.
- Sobhan, R., 2019. An improved kinetic model and optimized configurations for pellet-softening: Modeling and optimization of pellet-softening process in drinking water treatment. Delft.
- Van Schaik, C., 2019. Particle profile modelling. Amsterdam.
- Chiou, E., 2018. An improved model of calcium carbonate crystallization: An improved kinetics-model for the calcium carbonate crystallization in the fluidized bed softening reactors at the Weesperkarspel drinking water treatment plant. Delft.
- Van Bergen, T., Klok, H., Turk, S., Vrieswijk, M., 2018. Korrelgrootte analyse. Amsterdam, www.huontwikkelt.nl/institute-for-life-sciences-chemistry-werkt-mee-aan-zacht-drinkwater/
- Vantomme, J., 2018. Fluïdisatie-Procesmodel, Onderzoek naar het fysische gedrag van een vloeistof-vast gefluïdiseerd bed in pellet-onthardingsreactoren ten behoeve van de ontwikkeling en verbetering van een voorspellend rekenmodel. Amsterdam.
- Akcay, S., Kuijpers, R., 2018. Waternet expansiekolom. Amsterdam.
- Bokhorst, L.C., 2018. Fractioneren van calciëtpellets tijdens de ontharding van water een alternatieve methode voor het verkleinen van calciëtpellets tijdens het onthardingsproces. Utrecht.
- Dacomba Torres, P.D.R., 2018. Fluidization behavior of granular activated carbon: For drinking water treatment applications. Delft.
- Kuijpers, R., 2018. Lokaal verkleinen van calciëtpellets bij de ontharding, Scenariostudie met Multi-Criteria-Analyse (MCA) naar lokale calciëtpellet-

- verkleiningstechnieken bij de ontharding op basis van de criteria: kosten, kwaliteit, kwantiteit, bedrijfszekerheid, milieu en imago. Amsterdam.
- Elarbab, A.H.E., 2017. Hydraulische modellering van de korrelreactor ontwikkeling van een hydraulisch model voor de korrelreactor van het fluidisatiepunt tot aan het flushing point. Amsterdam.
- Van As, A., 2017. Modellering van de ontharding De hydraulica in de korrelreactor met Noord-Hollands calciëet als entmateriaal. Amsterdam.
- Rutten, S., 2017. ETSW-zetting, de hydraulische invloed van de Extended Terminal Subfluidisation Wash (ETSW) op de zetting van het gepakte filterbed en het uitblijven van de eerste filtraatpiek bij een filterspoeling. Amsterdam.
- Schoonhoven, S., 2016. Het waterkwaliteitsverstoringsmodel omzetten naar een gebruiksvriendelijke graphic-user-interface (GUI). Amsterdam.
- Steenbrink, J., 2016. Datastroom kaart voor het waterkwaliteitverstoringsmodel. Amsterdam.

Educational (co-supervisor during my PhD project)

- Abdulrahim, H. S., Mohamed, A., 2021. Life cycle analysis of carbon-neutral industrial processes: centralised water softening in the United Kingdom
- Kroon, J.P., 2020. Modelling of solid-liquid fluidization in the water softening process. Eindhoven.
- Bastiaan, T., 2020. The origin of carryover during softening and its influence on the softening process at Waternet. Amsterdam.
- Bögels, T., 2019. Calcite growth kinetics and mechanisms during water softening. Amsterdam.
- Carelse, P., Rademaker, J., Verduijn, B., 2019. Energiewinning uit waterstromen – Process Innovation Project. Amsterdam.
- Seepma, S.Y.M.H., 2018. Revision of CaCO₃ crystallisation kinetics in drinking water softening, an in-depth experimental research focusing on nucleation mechanisms and inhibition throughout CaCO₃ removal in pellet reactors during drinking water softening at Weesperkarspel. Amsterdam.
- Klok, H., 2018. Inventarisatie en optimalisatie procesregelingen LVN en WPK. Amsterdam.
- Haket, A., Jacobs, G., Reijnders, S., Gouka, T., Jhingoe, Y., 2019. Olivijn in praktijk – Watch your air get fresh again. Utrecht.

Graduation theses

- [Kramer, O.J.I.](#), 2001. Limit cycles, the elimination of limit cycles in a CISTR through the application of a feedback process controller, M.Sc. Thesis.
<https://doi.org/10.3929/ethz-a-004538529>
- [Kramer, O.J.I.](#), 1991. Fluid bed, theorie en praktijk, B.Sc. Thesis. Finalist NIRIA Dutch Royal Engineering Society annual graduation report contest

Website news

- [Kramer, O.J.I.](#), Boek, E.S., 2020. Fluidisation experiments – Queen Mary University of London – Erasmus+,
www.tudelft.nl/onderwijs/opleidingen/exchange/
- [Kramer, O.J.I.](#), 2019. Zwevend gedrag van kalkkorrels,
www.waternet.nl/innovatie/Verantwoorde-productie/zweefgedrag-van-kalkkorrels/
- [Kramer, O.J.I.](#), Baars, E.T., 2019. Kalk uit water halen met kalk,
www.waternet.nl/zoek/blog/gezond-water/kalk-uit-water-halen-met-kalk/
- Zijlstra, H., [Kramer, O.J.I.](#), 2019, Institute for life sciences and chemistry werkt mee aan zacht drinkwater, www.huontwikkelt.nl/institute-for-life-sciences-chemistry-werkt-mee-aan-zacht-drinkwater/
- [Kramer, O.J.I.](#), Baars, E.T., 2017. Waternet gaat kalkkorrels maken
www.waternet.nl/nieuws/2017/4/waternet-gaat-kalkkorrels-maken/

Videos

- [Kramer, O.J.I.](#), Nijssen, T.M.J., 2021. Videos – CFD-DEM simulations: fluidisation of calcite-pellets in water [Data set] 4TU.Centre for Research Data., Eindhoven, The Netherlands. <https://doi.org/10.4121/13663619>
- [Kramer, O.J.I.](#), van Schaik, C., 2020. Videos – up-flow filtration velocities for rapid sand filter grains 0.8-1.25 mm in water [Data set] 4TU.Centre for Research Data., Amsterdam, The Netherlands., <https://doi.org/10.4121/13337057.v1>
- [Kramer, O.J.I.](#), 2020. Videos – liquid-solid fluidisation experiments of calcite pellets and glass beads in water [Data set] 4TU.Centre for Research Data.,

Amsterdam, The Netherlands. <https://doi.org/10.4121/uuid:1b685d9e-4441-4a53-865c-86622ba49b25>

[Kramer, O.J.I.](#), Castrejon-Pita, J.R., Boek, E.S., 2020. Videos – (high-speed camera) – liquid-solid fluidisation experiments (calcite-pellets 1.4-1.7 mm in water) [Data set] 4TU.Centre for Research Data., London, United Kingdom., <https://doi.org/10.4121/uuid:41556e6c-b599-42cd-9f1d-bcf01d8e8576>

[Kramer, O.J.I.](#), Raaghav, S.K.R., Breugem, W.P., 2020. Videos – terminal settling experiments in water: path instabilities [Data set] 4TU.Centre for Research Data., Delft, The Netherlands. <https://doi.org/10.4121/UUID:3FFDFA51-38F0-4188-AEC5-8CD8FC8F1941>

[Kramer, O.J.I.](#), van Schaik, C., Nijssen, T.M.J., 2020. Videos – fluidisation of calcite-pellets 0.8-0.9mm and 1.4-1.7 mm in water for various flow rates [Data set] 4TU.Centre for Research Data. Amsterdam, The Netherlands. <https://doi.org/10.4121/13277246.v1>

[Kramer, O.J.I.](#), 2019, Studenten werken met Waternet aan beter drinkwater, www.hu.nl/voltijd-opleidingen/chemische-technologie/tijdens-de-opleiding JMBC, 2019 promotiefilm (TU Delft Process Technology Institute), www.tudelft.nl/dpti/

Hogeschool Utrecht, 2018, HU Waternet statische diameter analyse, www.youtube.com/watch?v=3wSsdSi4p3k

Research data

[Kramer, O.J.I.](#), 2021. Dataset underlying the research of: New insights into the fluidisation characteristics of granular activated carbon for drinking water treatment applications [Data set]. 4TU.ResearchData. <https://doi.org/10.4121/14229863.v1>

[Kramer, O.J.I.](#), 2021. Dataset underlying the research of: A submerged cylindrical object in a liquid-solid fluidised bed – measuring local voidage and profile using a hydraulic weighing technique [Data set]. 4TU.ResearchData. <https://doi.org/10.4121/14204336.v1>

[Kramer, O.J.I.](#), 2021. Dataset underlying the research of: Fit parameters for liquid-solid fluidisation models applied in drinking water treatment processes [Data set]. 4TU.Centre for Research Data. <https://doi.org/10.4121/13537121.v1>

Acknowledgements

“A civil servant should be able to make music all day, following the Cuban model.”

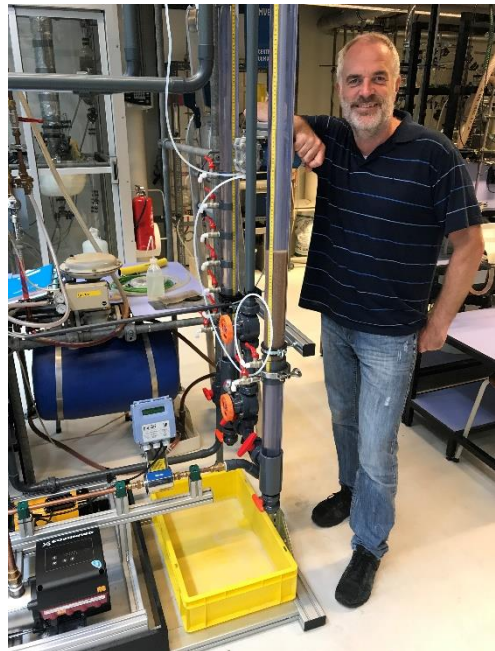
Acknowledgements

First and foremost, I would like to express my gratitude to my supervisors, professors Jan Peter van der Hoek and Johan Padding, my company manager Leon Kors, my project leader Michel Colin and my PhD advisers Eric Baars and Peter de Moel.

I would also like to express my gratitude to the dozens of inspiring graduates from different universities that I collaborated with during the course of my PhD trajectory. It was a true honour to be their supervisor. Another heartfelt word of thanks goes to my Waternet colleagues, who supported me in many different ways and who helped me complete this project.

I am grateful to have had the opportunity to meet and work with so many incredibly inspiring people from many different institutions and organisations. It is impossible to thank you all personally, but I am very much looking forward to the day that we will meet again. My final words of gratitude are for Karin: you are the very best that has ever happened to me!

Onno Kramer



A separate brochure with a more extensive and more personal word of thanks can be obtained from the author upon request.

Curriculum Vitae

*“There may be a hundred counter arguments,
but only one argument is needed to make the move.
Anyone who has never made a mistake has never tried anything new.”*

Curriculum Vitae

Onno Johannes Ignatius Kramer was born in Amsterdam, the Netherlands, on 5 May 1967. In 1991 he graduated from HTS-A in Amsterdam, where he studied Chemical Technology and was awarded for the Dutch Royal Engineering Society graduation annual graduation report contests. In 1993 he obtained his Bachelor's degree at the University of Twente's Department of Chemical Engineering.

From 1993 until 2001 Onno worked as a professional musician and, from 1998 until 2002, also as an ICT freelancer at Gelink Advies Groep in Enschede. In 2001 he finished his chemical engineering studies at the University of Twente. After spending time in Australia in 2002, he started working for the research project *Promicit* (Process Modelling and Intelligent Control of Integral water treatment), a consortium of WLB (Waterleidingbedrijf Amsterdam), ABB, TU Delft, DHV and Evers+Manders Consultancy. This work lasted from 2002 until 2004. In 2004, Onno applied for the position of process technologist at WLB. Since then, he has worked for the drinking water quality team of Waternet, the present public water utility of Amsterdam.

From 2005 onwards Onno has supervised dozens of Bachelor's and Master's students, and he has been a member of several committees: the 'Supervisory Committee', the 'Professional Fields Advisory Board' and the 'Audit Team' for HU Applied University of Utrecht, Institute for Life Sciences and Chemistry. In 2018 he initiated a preferred partnership between HU and Waternet. On behalf of Hobeon (Domain Applied Sciences), he assessed Avans University's Institute of Chemical and Environmental Engineering in 2017. Onno was a board member of the Dutch-Flemish Process Technologists Network from 2014 until 2020.

A number of Onno's students have been awarded prizes in annual graduation report contests: 1st and 2nd prize KNW in 2014, 2nd prize KNCV in 2015, 2nd prize KNW in 2016 and nominations for participation in the KNW contest in 2018 and 2019. In 2019 Onno received a grant within the framework of the Erasmus+ staff mobility programme for teaching and training at Queen Mary University of London, where he was appointed an honourable member and lifetime academic partner in the Division of Chemical Engineering. In 2016 Onno started his PhD research on *Hydraulic modelling of liquid-solid fluidisation in drinking water treatment processes*. This PhD research project was carried out at Delft University of Technology.

Stellingen

behorende bij het proefschrift

Hydraulic modelling of liquid-solid fluidisation in drinking water treatment processes

Onno Johannes Ignatius Kramer – Delft, 10 September 2021

1. Onregelmatig gevormde deeltjes vertonen een variabele deeltjesdiameter in gefluïdiseerde bedden bij wisselende vloeistofstroomsnelheden en porositeit. (dit proefschrift)
2. Het voorspellen van de weerstandscoefficiënt en porositeit in een vloeistof-vast gefluïdiseerd bed wordt verbeterd door het meenemen van het Froude kengetal in combinatie met het Reynolds kengetal. (dit proefschrift)
3. Het populaire model van Richardson en Zaki krijgt meer hydraulische betekenis en is betrouwbaarder wanneer het punt van minimale fluïdisatie met de terminale bezinkingssnelheid wordt verbonden. (dit proefschrift)
4. De prestaties van waterzuiveringsprocessen worden aanzienlijk verbeterd wanneer kennis en kunde op het gebied van zowel hydraulica als waterchemie worden gecombineerd. (dit proefschrift)
5. In wetenschap en techniek moet meer rekening worden gehouden met de ruime bandbreedte rondom berekende waarden die het gevolg is van natuurlijke variaties.
6. Het bepaalde specifieke contactoppervlak dat per seconde en per vierkante meter beschikbaar is in onthardingskorrelreactoren bewijst dat wateringenieurs de laatste dertig jaar uitstekend werk hebben verricht.
7. Om het hoofd te bieden aan toekomstige (on)verwachte omstandigheden, moeten de huidige grootschalige waterzuiveringsinstallaties hun ontwerp aanpassen en verbeteren van robuust naar meer flexibel.
8. Onderwijs kan alleen effectief zijn als docenten tutors worden die hun studenten echt 'zien' en voorzien in hun individuele behoeften.
9. De afgelegde weg van mensen is nooit kaarsrecht, net als de afgelegde weg van individuele deeltjes tijdens terminale bezinking. De kortste weg lijkt gemakkelijk en een omweg vaak moeilijk, maar een omweg levert op de lange termijn meer inzicht op.
10. Als je niet goed kijkt, dan zie je het niet.

Deze stellingen worden oponeerbaar en verdedigbaar geacht en zijn als zodanig goedgekeurd door de promotoren:

Prof. dr. ir. J.P. van der Hoek MBA en Prof. dr. ir. J.T. Padding.

Propositions

belonging to the thesis

Hydraulic modelling of liquid-solid fluidisation in drinking water treatment processes

Onno Johannes Ignatius Kramer – Delft, 10 September 2021

1. Irregularly shaped particles exhibit variable particle diameters in fluidised beds with varying fluid flow rates and voidage. (this thesis)
2. The prediction accuracy of the drag coefficient and voidage in liquid-solid fluidised beds is improved by including the Froude number in conjunction with the Reynolds number. (this thesis)
3. The popular model developed by Richardson and Zaki takes on more hydraulic significance and is more reliable when the minimum fluidisation point is connected to the terminal settling velocity. (this thesis)
4. The performance of water treatment processes is significantly improved when knowledge and skills in the fields of hydraulics as well as aquatic chemistry are combined. (this thesis)
5. In science and engineering, greater attention must be paid to the wide bandwidth around calculated values that results from natural variations.
6. The determined specific space velocity in pellet softening reactors proves that during the past thirty years water engineers have done an excellent job.
7. To cope with future (un)expected circumstances, current full-scale water treatment plants should adapt and improve their design from robust to more flexible.
8. Education can only be effective when teachers become tutors who truly 'see' their students and cater to their individual needs.
9. The trajectories followed by humans in the course of their lives and by irregularly shaped natural particles during terminal settling are extremely similar: they are never straight. While taking the shortest route may seem easier than taking a detour, the latter often yields better insights in the long term.
10. If you don't look closely, you will not see it.

These propositions are considered opposable and defensible and as such have been approved by the promotors:

Prof. dr. ir. J.P. van der Hoek MBA and Prof. dr. ir. J.T. Padding.

